EDITED and PUBLISHED quarterly at the offices of The American Society of Mechanical Engineers, United Engineering Center, 345 E. 47th St., New York, N. Y. 10017. ASME TWX No. 710-581-5267. Second-class postage paid at New York, N. Y., and at additional mailing offices.
CHANGES OF ADDRESS must be received at Society headquarters seven weeks before they are to be effective. Please send old label and new address.
PRICES: To members, $25.00, annually; to nonmembers, $50.00. Single copies, $15.00 each. Add $1.50 for postage to countries outside the United States and Canada.
STATEMENT from By-Laws. The Society shall not be responsible for statements or opinions advanced in papers or . . . printed in its publications (B 13, Par. 4).

INDEXED by the Engineering Index, Inc.

transactions of the ASME

Published Quarterly by
The American Society of
Mechanical Engineers
Volume 101 • Number 3
AUGUST 1979

journal of heat transfer

(*continued on page 426*)

TECHNICAL NOTES

ERRATA

ANNOUNCEMENTS

N. Seki
Professor.

S. Fukusako
Associate Professor.

K. Torikoshi[1]
Graduate Student.

Department of Mechanical Engineering
Hokkaido University
Sapporo 060, Japan

Characteristics of Fluidization of a Solid Particle Bed

A criterion to predict the characteristic of fluidization of particles bed was discussed by adopting a modified Froude number, $Fr_{\lambda c}$. The criterion derived from the hydrodynamic instability was compared with experimental data. In addition, the drag coefficient for particulate fluidized bed were found to be different from those measured for aggregative fluidized bed in a fully development fluidization.

1 Introduction

When the flow of fluid passes upwards through a particle bed and the drag force acting on the constituent particles is attained to balance the gravitational force exercised on the particles, the bed starts to be fluidized.

With a further increase in the flow rate, each particle is put in motion from its quiescent state to a continuously agitated state in the upward stream of fluid. Therefore such a fluidized bed—which is used for heat exchangers, chemical reactors and drying equipment, etc.—can well be expected to have an overall efficient contact of particles with fluid which results in an uniform temperature in the bed and a high rate of heat transfer between the exposed object and the bed.

In general, it is well known that the mixing state in the fluidized bed is classified into two categories, that is, a state of aggregative fluidized bed and that of particulate fluidized one. In the former case, bubbles form in the particle bed while, in the latter case, bubbles do not form.

Regarding the clarification of a characteristic difference between the two beds, some light has been thrown on the subject, experimentally or theoretically, by studies of pressure drop across the bed, drag force acting on the particles and interstitial flow between particles [1–6]. Nevertheless, presently it can be said that the essential characteristic distinction between the two fluidized beds and the criteria to predict these fluidizations, which are significantly related to the combination of particle, fluid and flow rate, have not been sufficiently clarified.

As for the aforementioned criterion, Wilhelm, et al. [1] proposed the use of the Froude number, $Fr_{mf} = u_{mf}^2/d_p g$, where u_{mf} and d_p are minimum fluidization velocity and particle diameter, respectively, based on a concept of interactive forces in the vicinity of bubbles generated. They predicted experimentally that the fluidized bed would become particulate if $Fr_{mf} < 0.13$ and aggregative if $Fr_{mf} > 1.0$. However, it might be considered that their proposed criterion has not given more clear-cut demarcation for predicting the future development of the particle bed to be fluidized. For instance, estimating their criterion of Froude number by using the Fetterman's experimental data [2], one finds that the evaluated critical Froude number results in less than 0.13, when the behavior of fluidization observed by him is found to still be aggregative.

This might be caused mainly by the fact that their resulting formulation was derived from only the interaction force balance at the minimum fluidization, as mentioned above. Romero, et al. [3] suggested a modified criterion of dimensionless groups including Froude number and Reynolds number, $Re_{mf} = u_{mf} d_p/\nu_f$, where ν_f is the kinematic viscosity of fluid, on the basis of the instability theory of the bed as developed by Wilhelm, et al. [4] whose bed stability theory is based on considering the fluidizing medium and dense bed as physically separate phases, especially when the interface of physical system pertinent to bed stability adopted in their study is perpendicular to the fluidizing fluid flow direction. They suggested that the criterion between particulate fluidized bed and aggregative fluidized bed is about 100 in a product of dimensionless groups, such as $(\rho_p - \rho_f)/\rho_f$, Fr_{mf}, Re_{mf}, and L_{mf}/D_c. Their prediction, however, is no more than agreeable to the experimental results in comparison with the Froude number criterion by Wilhelm, et al. [1]. Moreover, the use of a product of these groups as a criterion of fluidization is seen to be nebulous in the cases of air fluidization of glass balloon carried out in the present study. Jackson [5] and Pigford [6] carried out their investigations on a premise that the criterion should be based on a consideration of the stability or growth rate of disturbances. However, it might be said that they made their prediction without detailed discussions of whether the solution derived from the equation of motion would diverge or not. Concluding this, notwithstanding the recognition that one of the factors comprised in the criterion is Froude number, it should be noticed that these previous predictions for the criterion have not been met with satisfactory success. On the other hand, Harrison, et al. [7] predicted a stable bubble to be possibly generated in the particle bed after fluidization. The theory of Harrison, et al. [7] merely classifies fluidization into bubbling, transition and non-bubbling fluidization. However, it is clear that the theory does not predict in advance which types of fluidization in a given system would exhibit in future. Moreover, Verloop, et al. [8] confirmed analytically that the particles bed behaves homogeneously at a low voidage after minimum fluidization. These results may well suggest that both the generation of bubble nuclei and the homogeneous expansion of particles bed could be assumed in the vicinity of minimum fluidization. Furthermore, it is considered that these interpretations throw a meaningful light on the clarification of the criterion problem.

In the present study, based on these two affirmations by Harrison et al. [7] and Verloop, et al. [8], the criterion to predict the future development of particles bed after minimum fluidization is investigated theoretically by treating the particles-fluid motion as two-phase flow and compared with the experimental results.

2 Development of a Theoretical Model to Predict Fluidization Characteristics

Fundamental Consideration. In predicting how a given particles bed would behave at its fully developed stage, it is essential to discuss the characteristic particles-fluid motion at the beginning of and after fluidization.

It is experimentally well-known that the pressure drop across the bed after fluidization remains approximately in Carman-Kozeny equation. In the present study, the pressure drop across the bed before minimum fluidization is found to be given in linear logarithemic plots with increasing flow rate, and its general tendency is in agreement with previously reported results. When the fluid velocity has reached minimum fluidizing one, the pressure drop across the bed will be equal to the total weight of the constituent particles per unit area. At the moment of minimum fluidization or the onset of particles motion, the net gravitational force acting downwards on each particle is balanced by the upwards component of the drag force.

In order to ascertain the physical validity of Froude number as the criterion prediction, it is requisite to consider the particles motion released from their initial contact after onset of minimum fluidization. At the minimum fluidization, the well-known dimensional analysis of the particles motion under equilibrium is presented as follows,

[1] Concurrent position: Reseacher of Daikin Kogyo., Ltd., Sakai, Osaka

Contributed by the Heat Transfer Division for publication in the JOURNAL OF HEAT TRANSFER. Manuscript received by the Heat Transfer Division September 20, 1979.

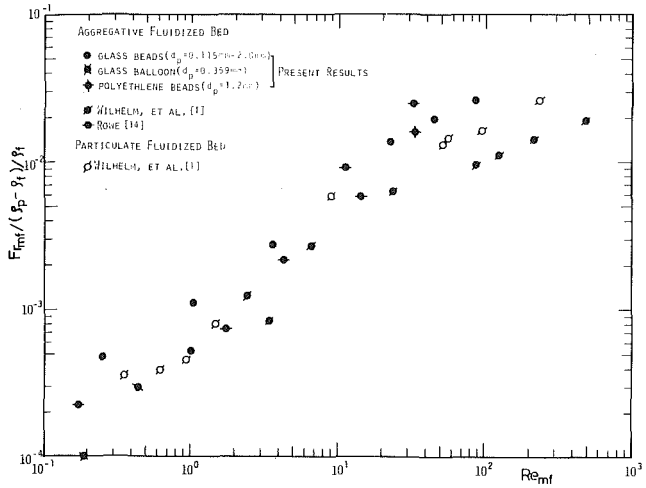

Fig. 1 Variation of Froude number with Reynolds number at minimum fluidization

$$u_{mf}{}^2/d_p g = 4/3(1/C_{dmf}')(\rho_p - \rho_f)/\rho_f,$$

$$C_{dmf}' = C_{dt} f(\epsilon) \tag{1}$$

where g is gravitational acceleration, ρ_p density of particle, ρ_f density of fluid, C_{dmf}' apparent drag coefficient of bed, C_{dt} drag coefficient of a single particle and $f(\epsilon)$ voidage function proposed by Wen, et al. [9]. Since the drag coefficient is usually a function of Reynolds number, $C_d = \phi(\mathrm{Re}_{mf})$. $u_{mf}{}^2/d_p g$ is the same Froude number as Wilhelm, et al. [1] proposed. Considering these facts, equation (1) could be rearranged as follows.

$$\mathrm{Fr}_{mf}/(\rho_p - \rho_f)/\rho_f = 4/3 f(\epsilon)\phi(\mathrm{Re}_{mf}) \tag{2}$$

Fig. 1 shows the experimental results of $\mathrm{Fr}_{mf}/(\rho_p - \rho_f)/\rho_f$ plotted against Re_{mf} together with the data by Wilhelm, et al. [1]. At a first glance of this figure, it is understood that $\mathrm{Fr}_{mf}/(\rho_p - \rho_f)/\rho_f$ increases with increasing Re_{mf} regardless of two categories. However, after carefully inspecting the relationship between $\mathrm{Fr}_{mf}/(\rho_p - \rho_f)/\rho_f$ and Re_{mf} in the range of the present study, it should be noticed that the demarcation between the results obtained from two fluidized beds is not clearly distinguished due to their scattered data. This fact may suggest that the previously proposed estimation of Froude number for the criterion should be reconsidered from the standpoint of more sharp prediction for the characteristic discrimination of particles bed.

In order to clarify the characteristic difference between two types of fluidized bed, it may primarily be necessary that the pressure drop, ΔP, across the bed and the amount of bed expansion, which are closely related to the drag force F_d acting on the particles bed are examined. Because the pressure drop across the bed is expected to be dissipated as the energy suspending the particles bed,

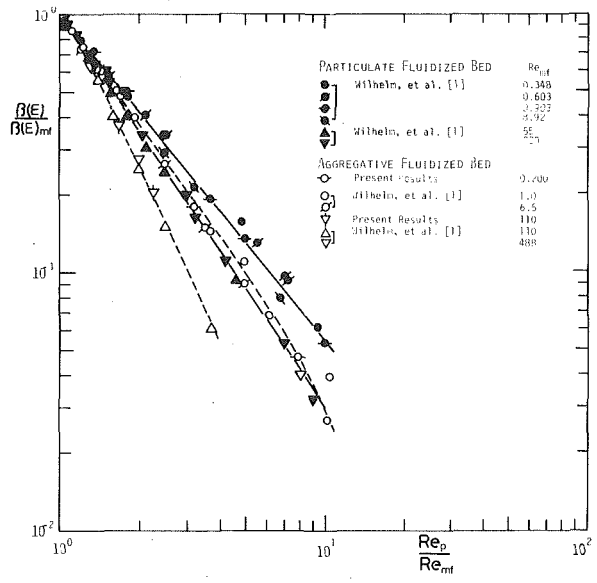

Fig. 2 Variation of drag coefficient in particulate fluidized bed and aggregative fluidized one in a fully developed region

$$\Delta P/L = F_d f(\epsilon) N = \beta(\epsilon) u_f \tag{3}$$

where L is bed height, $f(\epsilon)$ voidage function, N the number of particles per unit volume and $\beta(\epsilon)$ drag coefficient. The relation presented in equation (3) is based on an assumption that the drag force on the particles bed would be expected to depend on the relative velocity $(u_f - v_p)$ between the fluid and the constituent particles as reported by Jackson [5]. However, in the steady state, v_p is negligibly small and also the available domain for equation (3) is approximately $\mathrm{Re}_p < 500$. Accordingly it is expected that the bed expansion could be evaluated by equation (3) when $\beta(\epsilon)$ is obtained.

In Fig. 2, the relation between $\beta(\epsilon)/\beta(\epsilon)_{mf}$ and $\mathrm{Re}_p/\mathrm{Re}_{mf}$ whose data are those obtained by the present study using solid-gas system and also Wilhelm, et al. [1] using solid-gas system, is demonstrated. In the present study, in order to estimate the $\beta(\epsilon)$, the amount of bed expansion is directly measured under the condition of atmospheric pressure and the pressure drop across the bed is evaluated from manometer readings under constant inlet temperature of the bed. The difference between $\beta(\epsilon)/\beta(\epsilon)_{mf}$ for aggregative fluidized bed and that for particulate fluidized one is examined by using the experimental results by Wilhelm, et al. [1] for the latter and the present experi-

Nomenclature

A, B = constants
C_{dmf}' = apparent drag coefficient
C_{dt} = drag coefficient for a single isolated particle
c = wave propagation velocity
D_c = column diameter
d_p = particle diameter
F_d = drag force acting on the particles bed
$\mathrm{Fr}_{mf} = u_{mf}{}^2/d_p g$, Froude number at minimum fluidization
$\mathrm{Fr}_t = u_t{}^2/d_p g$, Froude number under terminal free-falling conditions
$\mathrm{Fr}_{\lambda c} = u_{mf}{}^2/\lambda c g$, a modified Froude number defined by equations (9) and (10)
$f(\epsilon)$ = voidage function defined by equation (1)
g = gravitational acceleration
k = wave number
L = bed height
N = number of particles per unit volume
ΔP = pressure drop across the bed
$\mathrm{Re}_{mf} = u_{mf} d_p/\nu_f$, Reynolds number at minimum fluidization
$\mathrm{Re}_p = u_f d_p/\nu_f$, Reynolds number
$\mathrm{Re}_t = u_t d_p/\nu_f$, Reynolds number under terminal free-falling conditions
$\mathrm{Re}_{\lambda c} = u_{mf}\lambda c/\nu_f$, Reynolds number based on wavelength, λc
t = time
u_f = overall superficial fluid velocity
u_f' = fluid phase local mean velocity
u_{mf} = superficial minimum fluidization velocity
u_t = terminal free-falling fluid velocity
v_p = particle velocity
v_p' = particle phase local mean velocity
x, y = co-ordinates in direction parallel and normal to particles and fluid phase flows, respectively
Y_0 = maximum amplitude
$\beta(\epsilon)$ = drag coefficient defined by equation (3)
$\beta(\epsilon)_{mf}$ = drag coefficient at minimum fluidization
η = distance perpendicular to the interface at given time and position
λc = wavelength
σ = surface tension
ρ_p, ρ_f = densities of particle and fluid, respectively
ν_f = kinematic viscosity of fluid
ϕ_p, ϕ_f = velocity potentials for practice velocity field and for fluid velocity field, respectively

Subscripts

p refers to particle
f = fluid

mental results for the former. In Fig. 2, it is indicated that $\beta(\epsilon)/\beta(\epsilon)_{mf}$ could be well correlated with Re_p/Re_{mf} in both cases of fluidized bed. Special note should be taken of the fact that all the data for aggregative fluidized bed lie below those for particulate fluidized bed at each Reynolds number of comparable magnitude adopted in the present study. Moreover, the difference between both data arranged in this figure decrease with decreasing Re_p/Re_{mf}. From this discussion, it might be thought that the particles-fluid motion in aggregative fluidized bed and that in particulate fluidized bed have a similar characteristic behavior approaching the transitional state adjacent to the minimum fluidization.

On the other hand, in the case of the particulate fluidized bed, the particle spacing increases with increasing Re_p/Re_{mf} and, hence, the drag coefficient for the constituent particles approaches the drag coefficient for a single particle monotonically, as estimated from this figure. In the case of aggregative fluidized bed, the apparant drag coefficient also approaches that for a single particle after steeply decreasing with increasing Re_p/Re_{mf} since the particle spacing is not increased corresponding to the increasing fluid velocity, as compared with that for particulate fluidized bed.

Based on the aforementioned consideration of the behavior of the particle bed, the following prediction of the criterion for the demarcation between the particulate fluidized bed and the aggregative fluidized bed might be introduced.

The Criterion for Two Types of Fluidized Bed. In the foregoing paragraph, the fact that the employment of previously defined Froude number as a dimensionless number expressing the criterion of characteristic discrimination for two different types of fluidized bed may not provide a useful formulation of the criterion is discussed. This might be caused by the fact that the previous studies to determine the criterion have been achieved in a situation where the criterion is to be derived from only the interactive force balance between fluid and particles in the state of minimum fluidization.

On the other hand, when the flow rate increases after minimum fluidization, it is well recognized that the fluidized bed would develop in either the particulate fluidized bed where the constituent particles expand, keeping an interactive force balance acting on the particles, or in the aggregative fluidized bed where the constituent particles are mixed by plume-like bubbles generated in the bed. Moreover, it can be said that these two categories of a fully developed fluidization probably depend on the original physical characteristic of the bed, which is significantly related to a combination of fluid-particles adopted. Therefore, in establishing the aforementioned criterion, it is felt that attention should be turned to the instability problem in a transitional state soon after minimum fluidization, where the interactive balance between drag and bouyant forces acting on the particles, and also the bubble nuclei comprising an escape dome to be generated in the bed, as Nicklin [10] described, could be assumed to hold. From this standpoint, the present approach to establishing the criterion is developed by treating the fluid-particles motion in the aforementioned transitional state as an instability problem of two-phase flow motion which it may be possible to treat as the Taylor-Helmhortz instability problem, as indicated schematically in Fig. 3. The figure on the left in Fig. 3 indicates a model for the present theoretical treatment confined to a situation at minimum fluidization,

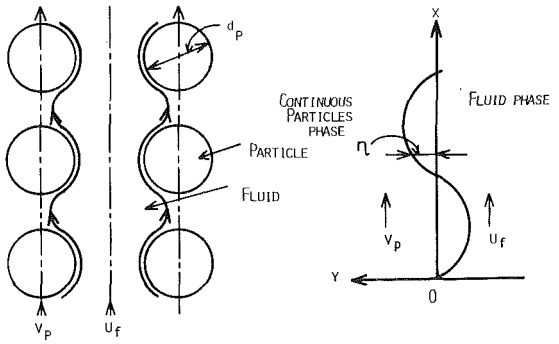

Fig. 3 Schematic description and system of co-ordinates of two-phase flow model for fluidized bed behavior

in which the fluid flows through the particle bed, while the figure on the right represents the co-ordinate system of the particles-fluid phase interface and the gravitational direction acting downwards in the negative x-direction. As shown in Fig. 3, it is noted that the present physical model in which the particles-fluid interact is vertically arranged, is clearly different from the one adopted by Wilhelm, et al. [4].

If the two-phase flow is assumed to be continuous and incompressible, and the fluid phase is nonviscous while the particles phase is continuous, the velocity potentials of particles and fluid phases, ϕ_p and ϕ_f, are generally taken in the following forms:

$$\phi_p = -v_p'x + \mathbf{A}e^{ky}\cos k(x - ct),$$
$$\phi_f = -u_f'x + \mathbf{B}e^{-ky}\cos k(x - ct) \tag{4}$$

where v_p' and u_f' are mean velocity of particles phase and that of fluid phase respectively, c wave propagation velocity, t time, **A, B** arbitrary constants, k wave number, and x and y co-ordinates, respectively. The co-ordinate of y corresponds to the upwards flow direction.

At the interface between two phases without mixing, the following boundary conditions are given:

$$(\partial\eta/\partial t) + v_p'(\partial\eta/\partial x) = -(\partial\phi_p/\partial y)_{y=\eta},$$
$$(\partial\eta/\partial t) + u_f'(\partial\eta/\partial x) = -(\partial\phi_f/\partial y)_{y=\eta} \tag{5}$$

where η is distance perpendicular to the interface. The wavy interface is described by the displacement of the surface from a plan surface ($y = 0$) where no perturbation exists. The solutions satisfying these boundary conditions are given by using the form of the interface as $\eta = Y_0 \sin k(x - ct)$, where Y_0 is maximum amplitude shown in Fig. 4.

$$\phi_p = -v_p'x + (c - v_p')Y_0\mathbf{e}^{ky}\cos k(x - ct)$$
$$\phi_f = -u_f'x - (c - u_f')Y_0\mathbf{e}^{-ky}\cos k(x - ct) \tag{6}$$

If these velocity potentials are adopted, one obtains the pressures exerting on the interface as follows.

$$p_p = \rho_p[k(c - v_p')^2 - g]Y_0 \sin k(x - ct)$$
$$p_f = -\rho_f[k(c - u_f')^2 + g]Y_0 \sin k(x - ct) \tag{7}$$

On the other hand, it is known that the pressure difference across the interface is usually given by $p_p - p_f = -\sigma(\partial^2\eta/\partial x^2)$.

Substituting the above-mentioned pressures into the expression of $(p_p - p_f)$, the general solution of the two-phase flow yields the following relation,

$$\rho_p(c - v_p')^2 + \rho_f(c - u_f')^2 = (\rho_p - \rho_f)g/k + \sigma k \tag{8}$$

If the surface tension of fluid is negligible small, the wavelength at the neutral state corresponding to the state of minimum fluidization is given by the following correlation after expanding of equation (8) with respect to c.

$$\lambda\mathbf{c} = 2\pi(\rho_p\rho_f/(\rho_p{}^2 - \rho_f{}^2))u_{mf}{}^2/g \tag{9}$$

As will be seen in equation (9), the wavelength, $\lambda\mathbf{c}$, is a function of physical properties of fluid and particle. Moreover, taking into account of the present derivation, the value of $\lambda\mathbf{c}$ should correspond to the magnitude of the assumed bubble nuclei of escape dome to be generated in the bed at minimum fluidization.

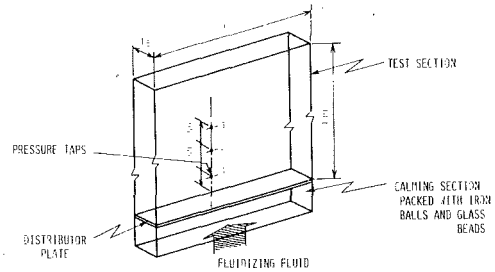

Fig. 4 Schematic drawing of test section

3 Experimental Determination of Fluidization Characteristics

Experimental Apparatus and Procedure. One of the purposes of the present study is to discuss the effective parameters dominating the behavior of particles fluidized by fluid. Accordingly, an attempt to establish a theoretical model which might be more pertinent to the behavior of fluidized bed is made for a two-dimensional fluidized bed. For this purpose a two-dimensional test bed in which solid particles are fluidized by air under atmospheric pressure is constructed.

Main test section of the present experimental apparatus is depicted in Fig. 4. Inside dimension of the section is 100 mm × 15 mm × 300 mm, while another dimension of 200 mm × 15 mm × 300 mm is used for checking the size effect of bed. The test section as a particles bed container is made of acrylic plate in order to visually observe the two-dimensional particles motion in the bed. The calming section, through which the compressed air used to fluidize the particles bed is initially calmed, is packed with iron balls 10 mm in diameter and glass beads 6 mm in diameter which are supported by an acrylic plate distributor 5 mm in thickness. The distributor has many holes of 0.6 mm in diameter, which are arranged in order every 5 mm in pitch. A silk screen is placed on the surface of the distributor in order to prevent the solid particles to be fluidized from dropping into the calming section. The three pressure taps, 8 mm OD and 0.8 mm ID, are installed on one of the vertical walls of the test section to measure the static pressure gradient in the bed and also to check the uniformity of the flow. They are made of brass and are connected to each manometer from which the pressure drop across the bed is evaluated.

In the present experiments, the flow rate of supplied compressed air is measured by an orifice meter or a gas flow meter which is carefully calibrated by a standard pressure gauge. Furthermore, the minimum fluidizing velocity is evaluated by the pressure drop-superficial fluid velocity curve to be obtained.

The solid particles adopted in the present experiments are glass beads, polyethlene beads and glass balloons having several diameters of each. The physical properties of these particles are given in Table 1. The arithmetic average diameter listed in this table is evaluated by the mesh screen analysis and by measuring each diameter of the particles with a micrometer. Prior to each run the particles bed is prefluidized to insure uniformity of packing. The pressure drop across the bed is measured before and after fluidization.

In a fluidizing state, the expansion of the bed is also measured. All the experimental data are obtained under a steady state and represented by their time mean values. A relation between pressure drop and flow rate of air is examined for several height of bed ranging from 10 mm to 100 mm.

Determination of λc. In order to clarify the characteristic of λc, the relation between the λc and the rising velocity, u_{mf} which could be evaluated from Ergun's prediction [11], is examined.

Fig. 5 shows the relation between u_{mf} and $\lambda c g$. As mentioned above, u_{mf} is the minimum fluidization velocity and also is adopted by using the graph of pressure drop against superficial velocity as is usual. In order to examine the effect of wall interaction on the two-dimensionality in the present study, an attempt to compare the prediction of minimum fluidization velocity u_{mf} by Ergun [11] with the experimental results is made. Except for very large particles, the experimental results of u_{mf} in the present study are ascertained to agree with the predicted criterion of the demarcation between two types of fluidized bed within a deviation of 8 percent, in general. Therefore, it is considered that the data obtained may give comparatively reliable results, though the wall interaction may have a significant effect on the formation of the bubble. As can be seen in Fig. 5, it is clear that the presentations where u_{mf} is proportional to $(\lambda c g)^{0.5}$ appear approximately in this figure for both fluidized beds and that there is a difference between both relations. Furthermore, it should be noted that such a λc corresponds well to the diameter of bubble nuclei in the experimental correlation proposed by Davies, et al. [12]. From these discussions it might be concluded that u_{mf} and λc have important roles in the demarcation between the two fluidized bed behaviors. λc is an especially meaningful key for the determining whether the initial bubble nuclei will grow or not with increasing flow rate since the initial voidage minimum fluidization is closely connected with the magnitude of bubble nuclei. Furthermore, it may be noted that the proportional constant is taken from Fig. 5 and the constant for aggregative fluidized bed is larger than that for a particulate fluidized bed. As a consequence, it might be said that an inherent constant pertinent to the discrimination of whether fluidization become aggregative or particulate presumably exists.

Fig. 6 shows a relation between $Re_{\lambda c}$ (= $u_{mf}\lambda c/\nu_f$) and Re_{mf}(= $u_{mf}d_p/\nu_f$). In Fig. 6, it may be clearly understood that the relation between λc and d_p for aggregative fluidized bed is a little different from that for particulate fluidized bed.

Table 1 Experimental conditions

Solid Material [−]	Mean Particle Diameter [mm]	Particle Density [Kg/m³]	Fluidizing Fluid [−]
Glass beads	0.115		
	0.230		
	0.387		
	0.850		
	1.100	2500	Air
	1.531		
	2.000		
Polyethylene beads	1.200	1087	Air
Glass balloon	0.359	190	Air

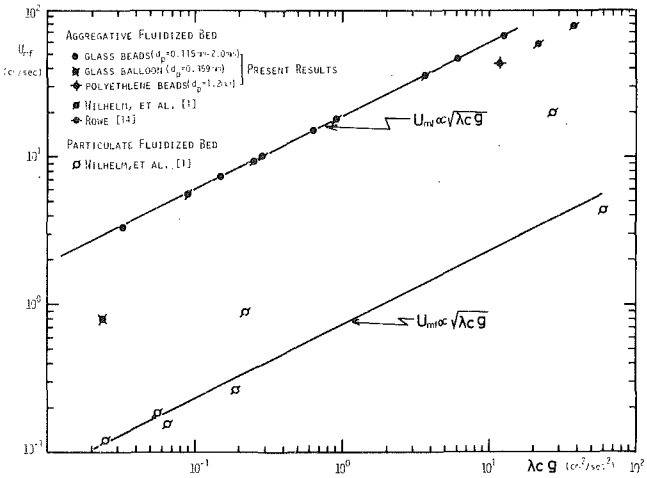

Fig. 5 Relations between u_{mf} and λc g

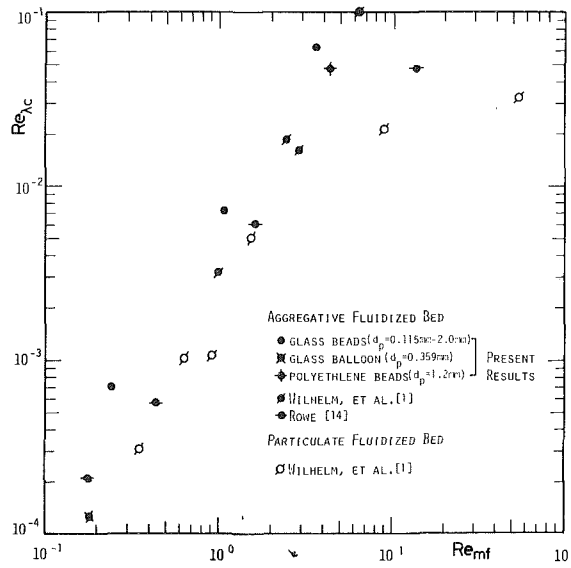

Fig. 6 Wavelength as a function of Reynolds number at minimum fluidization for particulate fluidized bed and aggregative fluidized one

4 Comparison of Theory and Experiment

In order to distinguish the characteristic difference between two types of fluidized bed more clearly, the voidage function, $f(\epsilon)$, which is obtained from the drag force ratio between the particles and for a single isolated particle, is discussed in connection with λc.

In the transitional state the following relation is described since the drag force for a single particle-fluid motion and that for the present particles-fluid motion can be equated:

$$\tfrac{1}{2}C_{dt}(\pi/4)d_p{}^2u_t{}^2 = \tfrac{1}{2}C_{dmf}'(\pi/4)d_p{}^2u_{mf}{}^2,$$

$$C_{dmf}'/C_{dt} = u_t{}^2/u_{mf}{}^2 = f(\epsilon) \tag{10}$$

where u_t is the terminal velocity. Thus a function of voidage, $f(\epsilon)$ in (10) which is defined in equation (1) might be estimated by using both u_{mf} and u_t, while a function of voidage $f(\epsilon)$ is dependent on Reynolds number based on the terminal velocity and varies from 200 to 10^4.

Rowe [13] showed experimentally the constant $(u_t/u_{mf})^2$ of 68.5 whose root square corresponds approximately to 8.72 predicted by Pinchbeck, et al. [14], who predicted u_t/u_{mf} being a function of $C_{dt}\mathrm{Re}_t$ and approaching the aforementioned value from 90 with increasing Reynolds number. Therefore, the present range of variation of $f(\epsilon)$ may be reasonable. In the range of interest, that is, $0.4 < \mathrm{Re}_t (= u_t d_p/\nu_f) < 500$, the drag force coefficient, C_{dt} for the estimation of u_t is chosen as $C_{dt} = 10/\mathrm{Re}_t{}^{0.5}$ [15]. In order to clarify the relation between λc and $f(\epsilon)$, dimensionless wavelength $d_p/\lambda c$ is plotted against C_{dmf}'/C_{dt} in Fig. 7. Inspecting this figure carefully it should be noticed that a difference between the tendency for particulate fluidized bed and that for aggregative fluidized bed exists within the range of the present study and all the data of the dimensionless term $d_p/\lambda c$ for the latter lie below the data for the former. In this figure, it could be understood that the criterion for the discrimination between two types of future development of fluidized bed corresponds well to a demarcation line whose slope is approximately constant at 1.67 in the range of $0.4 < \mathrm{Re}_t < 500$. Namely, the criterion for the aforementioned discrimination is presented as follows:

For particulate fluidized bed,

$$d_p/\lambda c > 1.54 \times 10^{-3}(u_t{}^2/u_{mf}{}^2)^{1.67},$$

or

$$\mathrm{Fr}_{mf}/\mathrm{Fr}_{\lambda c} > 1.54 \times 10^{-3}(\mathrm{Re}_P/\mathrm{Re}_{mf})^{1.34}$$

For aggregative fluidized one,

$$d_p/\lambda c < 1.54 \times 10^{-3}(u_t{}^2/u_{mf}{}^2)^{1.67},$$

or

$$\mathrm{Fr}_{mf}/\mathrm{Fr}_{\lambda c} > 1.54 \times 10^{-3}(\mathrm{Re}_P/\mathrm{Re}_{mf})^{1.34}$$

The above-mentioned criterion based on the λc, which is derived from two-phase flow motion instability and is a function of density ratio $(\rho_p - \rho_f)/\rho_f$, viscosity ν_f, and minimum fluidization velocity u_{mf}, may possibly apply for solid-liquid system as well as solid-gas system, as Simpson, et al. [16] mentioned that there is no fundamental difference between these two types of fluidization. Moreover, in obtaining the present study for the particulate fluidized bed data by Wilhelm, et al. [1], who carried out experiments in a solid-liquid system, are also used.

5 Conclusions

The useful characteristic criterion to predict the future development of aggregative and particulate fluidized beds are obtained by adopting a modified Froude number, $\mathrm{Fr}_{\lambda c}$, as defined in this study. The usefulness of the present proposed criterion is ascertained by using experimental data including previously reported data under the condition of atmospheric pressure.

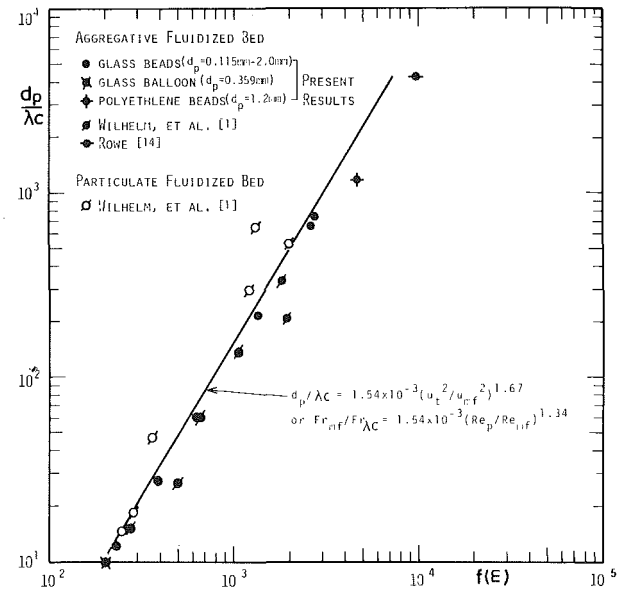

Fig. 7 Empirical correlation of criterion prediction for two fluidized beds. Solid line is discrimination line

References

1 Wilhelm, R. H., and Kwaulk, M., "Fluidization of Solid Particles," *Chem. Engng. Progr.*, Vol. 44, 1978, pp. 201–217.

2 Fetterman, C. P., M. S. Thesis, University of Washington, 1958.

3 Romero, J. B., and Johanson, L. N., "Factors Affecting Fluidized Bed Quality," *Chem. Engng. Progr. Symp. Ser.*, Vol. 58, 1962, pp. 28–37.

4 Wilhelm, R. H., and Rice, W. J., "Surface Dynamics of Fluidized Beds and Quality of Fluidization," *AIChE Journal*, Vol. 4, 1958, pp. 423–429.

5 Jackson, R., "The Mechanics of Fluidised Beds Part 1," *Trans. Inst. Chem. Engrs.*, Vol. 41, 1963, pp. 13–21.

6 Pigford, R. L., and Baron, T., "Hydrodynamic Stability of a Fluidized Beds," *Ind. Eng. Chem. Fund.*, Vol. 4, 1965, pp. 81–87.

7 Harrison, D., Davidson, J. F., and Kock, J. W., "On the Nature of Aggregative and Particulate Fluidisation," *Trans. Inst. Chem. Engrs.*, Vol. 39, 1961, pp. 202–211.

8 Verloop, J., and Heertjes, P. M., "Shock Wave as a Criterion for the Tension from Homogeneous to Hetregeneous Fluidisation," *Chem. Engng. Sci.*, Vol. 25, 1971, pp. 825–831.

9 Wen, C. Y., and Yu, Y. H., "Mechanics of fluidization," *Chem. Eng. Prog. Symp. Ser.*, Vol. 62, 1966, pp. 100–108.

10 Nicklin, J., "Two-phase Flow in Vertical Tubes," Ph.D. Thesis, University of Cambridge, 1961.

11 Ergun, S., "Fluid Flow through Packed Column," *Chem. Engng. Progr.*, Vol. 48, 1952, pp. 89–96.

12 Davies, R. M., and Taylor, G. I., "The Mechanics of Large Bubble Rising through Extended Liquids and through Liquids in Tubes," *Proc. Roy. Soc. Lond. Ser. A*, Vol. 200, 1950, pp. 375–390.

13 Rowe, P. N., "Drag Forces in a Hydraulic Model of a Fluidized Bed, Part 2," *Trans. Inst. Chem. Engrs., Lond.*, Vol. 39, 1961, pp. 175–180.

14 Pinchbeck, P. H., and Popper, F., "Critical and Terminal Velocities in Fluidization," *Chem. Engng. Sci.*, Vol. 6, 1956, pp. 57–65.

15 Kunii, D., and Levenspiel, O., *Fluidization Engineering*, Willey and Toppan, 1969, pp. 76.

16 Simpson, H. C., and Rodger, B. W., "The Fluidization of Light Solids by Gases under Pressure and Heavy Solids by Water," *Chem. Engng. Sci.*, Vol. 16, 1962, pp. 179–186.

F. W. Staub

General Electric Company,
Corporate Research and Development,
Schenectady, New York 12301
Fellow ASME

Solids Circulation in Turbulent Fluidized Beds and Heat Transfer to Immersed Tube Banks

In gas fluidized beds of large particles, a change in flow regime from bubbling flow to turbulent flow has been observed as the superficial gas velocity is increased. Solids flow and heat transfer models based on the bubbling flow regime are not generally adequate in the turbulent flow regime. A turbulent flow model is given here that is supported by limited solids flow measurements. A simplified model of the heat transfer to tube banks immersed in fluidized beds, that employs the solids flow model, is also given and is shown to be supported by data over a wide gas pressure and temperature range with particles in the 350μm to 2600μm size range.

Introduction

In recent years increased consideration of the use of large gas fluidized beds in the power generation application area has influenced a trend toward higher gas velocity, larger particle systems. While the maximum energy density fluidized bed operation conditions, attractive to power generation application, have not yet been defined, an information gap does exist between the relatively low gas velocity, small particle systems common to the chemical process industries and the high velocity systems now being investigated in the power generation field. Our early modeling studies [1] in particular indicated solids flow regime transition from the more intensively studied bubbling or slugging regimes to the bubble-free turbulent regime in the particle sizes and superficial gas velocity range of interest to the power generation application. A review of prior work did not uncover an existing turbulent fluidized bed flow model applicable to larger particle fluidization. In view of the above, a turbulent flow model is given here that contains the most essential elements of the observed flow process and that provides the phase flow rates required by a heat transfer model for immersed tube bank performance. While basic measurements, coupled with macroscopic models of the particle-surface interaction process, are still required to generate sufficient fundamental understanding of the heat transfer at surfaces immersed in fluidized beds, the simplified heat transfer model presented here is needed to improve correlations to be used by designers and to guide measurements planned for the future.

Flow Regimes

Above the minimum fluidization point it is generally recognized [2] that isolated bubbly flow exists, followed by rapidly growing, coalescing bubbly flow as the gas flow is increased. The behavior of the bubbling flow has been modeled with considerable success by Davidson and Harrison [3], Kunii and Levenspiel [2] and others. The transition from bubbly to turbulent flow has been studied by Davidson and Kehoe [4] and Yerushalmi, Cankurt, Geldart and Liss [5] who also observed and discussed the turbulent flow regime and who ascribe its first identification to Lanneau [6]. While Yerushalmi, et al. [5] and Lanneau [6] dealt with very small particles, where the turbulent regime is accompanied by significant bed loss, hence recycle, our observed large particle transition to turbulent flow is at a gas superficial velocity well below the particle terminal velocity [1]. The transition to turbulent flow as described in [1] occurred at a reduced velocity of 0.55–0.65 for 650μm particles and 0.30–0.35 for 2600μm particles. The reduced velocity is defined here as the ratio of the superficial gas velocity-to-single particle terminal velocity. In the absence of tube banks in the fluidized bed, the turbulent flow regime consisted of superimposed solids eddy motion on cocurrent and counter-current solid-gas flow. In the presence of tube banks [1] the turbulent flow regime becomes more ordered with obvious cocurrent and counter-current particle streaming motion.

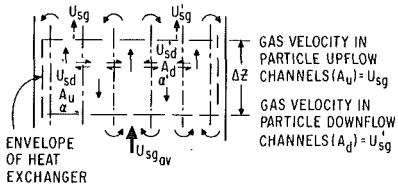

Fig. 1 Turbulent flow model

Turbulent Flow Model

The initial purpose of the flow model given here is to provide a basis for predicting the average heat transfer to a tube bank. A secondary purpose is to permit the prediction of the solids velocities which are of importance to the understanding of solids-internals interaction, i.e., erosion, and to allow the prediction of the solids axial dispersion coefficient which is required to predict solids mixing rates.

While the observed solids flow behavior in the turbulent regime directly suggests the use of a cocurrent and counter-current gas-solids flow model with superimposed lateral mixing, such a modeling approach has also been employed by VanDeemter [7] in bubbling flow where the upward flowing (cocurrent) streams are taken to include all gas bubbles. Although VanDeemter's effective diffusion coefficient is expressed in terms of the volume fraction occupied by the upflow and downflow solids respectively, these variables imply the knowledge of the bubble void fraction.

The turbulent gas-solids flow model assumed here is shown schematically in Fig. 1. The primary assumptions inherent in this flow model are:

- The bed is divided into multiple particle upflow channels (ΣA_u) and particle downflow channels (ΣA_d) that consider lateral particle exchange between flow channels. Inlet effects due to the distributor and exit effects due to disengagement at the top of the dense bed region are neglected; i.e., the local void fraction and phase velocities are constant in the axial direction in each flow channel.
- In the upward channels, the particulates and gas are in cocurrent steady flow at superficial velocities of U_{sd} and U_{sg}, respectively. In the downward flow channels, the particulates are in counter-current steady flow with respect to the net upward gas flow at superficial velocities of U'_{sd} and U'_{sg}, respectively. Simple corrections can be made to the channel gas flow velocities to include gas backmixing but these have not been made here.
- A uniform or single mean (such as surface mean) particle size is

Contributed by the Heat Transfer Division for publication in the JOURNAL OF HEAT TRANSFER. Manuscript received by the Heat Transfer Division July 28, 1978.

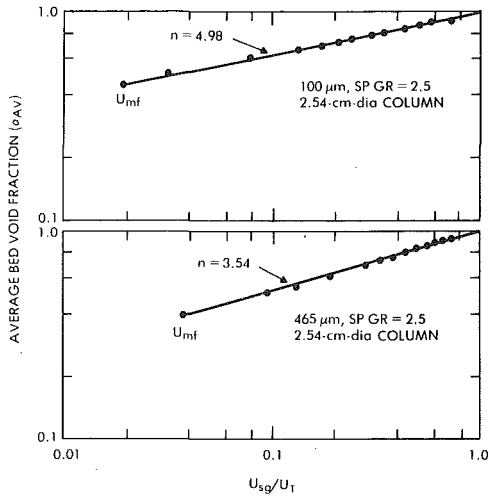

Fig. 2 Correlation of liquid fluidized void fraction data for 100μm particles [9] and 465μm particles [10]

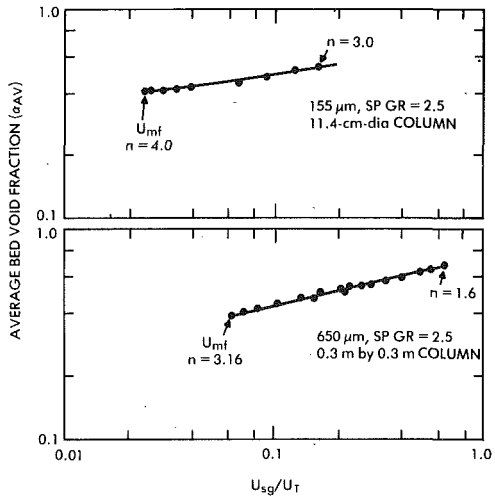

Fig. 3 Correlation of gas fluidized void fraction data for 155μm particles [11] and for 650μm particles [1]

assumed to exist in the bed with no "dead" or zero flow regions within the bed.

- A mixing length concept is employed that is defined by the bed height needed for the mean lateral flow exchange of particles to be equal to their axial through flow rate. Any flow resistance to particle flow due to bed internals is lumped in the mixing length definition. Lateral gas mixing between flow channels is neglected.
- The heat exchanger offers a uniform flow resistance over its cross-section. While the relations given here are based on bed cross-sectional areas, they can easily be employed based on the mean particle plus gas flow area actually available within the exchanger.

The average void fraction in a fluidized bed can be well represented by equation (1) as shown by Richardson and Zaki [8] where U_T is the terminal velocity of a single particle in the gas stream.

$$\frac{U_{sg_{av}}}{U_T} = \alpha_{av}{}^n \tag{1}$$

For liquid fluidized beds, n is normally constant in equation (1) (see Fig. 2), while for gas fluidized beds, n decreases with increasing superficial velocity (see Fig. 3). While an improved correlation method for the average bed void fraction has been developed [1], the form given by equation (1) is employed here for simplicity. Note that the presence of the tube bank has a negligible effect on α_{av} in view of its small volume in relation to the bed [1].

When both phases are in steady flow it can be shown that [12], in the upward and downward (counter-current) flow channels, equations (2) and (3) give the relations between the superficial phase velocities using equation (1) for the void fraction correlation form.

$$U_{sg} = U_T\alpha^m + \frac{\alpha}{1-\alpha}U_{sd} \tag{2}$$

$$U'_{sg} = U_T\alpha'^p - \frac{\alpha'}{1-\alpha'}U'_{sd} \tag{3}$$

Note that, in view of the variation of the exponent n with superficial velocity in gas fluidized beds, the exponents m and p are employed in equations (2) and (3). The prime designation refers to the downward (particle) flowing channel conditions.

Conservation of mass and continuity yield equations (4, 5) and (6) with no particle loss from the bed:

$$\Sigma A_d U'_{sd} = \Sigma A_u U_{sd} \tag{4}$$

$$\frac{\Sigma A_d(1-\alpha') + \Sigma A_u(1-\alpha)}{\Sigma A_d + \Sigma A_u} = 1 - \alpha_{av} \tag{5}$$

$$\frac{\Sigma A_d U'_{sg} + \Sigma A_u U_{sg}}{\Sigma A_d + \Sigma A_u} = U_{sg_{av}} \tag{6}$$

Equation (7) represents the time and space averaged ratio of up-

Nomenclature

A_u, A_d = cross-sectional area of a representative upflow channel and downflow channel, respectively
A_i = interfacial area between representative upflow channel and downflow channels
C = ratio of particle upflow-to-particle downflow cross-sectional areas in bed (see equation (7))
d_p = particle diameter
g = acceleration due to gravity
h = average heat transfer coefficient
M = length ratio defined by equation (10)
Nu, Nu_g = Nusselt number at the same superficial velocity for heat transfer to bed internals in a fluid bed and without particles present, respectively
Nu_u, Nu_d = Nusselt number for bed internals located in upflow and downflow channels, respectively
P = perimeter of representative upflow channel
ΔP = static pressure difference
U = velocity
$U_{sg_{av}}$, $U_{sd_{av}}$ = superficial gas velocity and superficial solids velocity, respectively, based on total bed cross-section
U_{sg}, U'_{sg} = superficial gas velocity in particle upflowing and particle downflowing channels, respectively
U_{sd}, U'_{sd} = superficial particle velocity in particle upflowing and particle downflowing channels, respectively
U_T = particle terminal velocity
w = lateral particle mass velocity per channel in bed in one direction
W = axial particle mass velocity per channel (in upflow)
ΔZ = axial length of bed region under consideration
ΔZ_m = mixing length (see equation (11))
α_{av} = overall average void fraction based on mean bed height
α, α' = void fraction in particle upflowing and particle downflowing channels, respectively
ρ_s = particle density
ρ_g = gas density
τ_i = interfacial shear between particle upflow and particle downflow channels

Subscripts

av = average over bed cross-section
su = in channel with upward flow
sd = in channel with downward flow

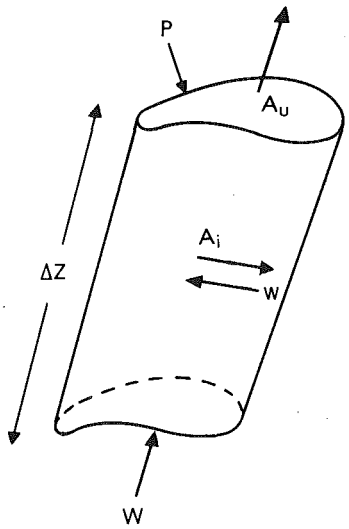

Fig. 4 Schematic of typical upflow channel

flowing and downflowing channel cross-sectional areas:

$$\frac{\Sigma A_u}{\Sigma A_d} = C \tag{7}$$

Considering an axial length ΔZ in the bed removed from the distributor and the top bed region, we can write the force balance for a representative upflowing channel as given by equation (8), where A_i is the interfacial area between the representative upward and downward flowing channels and A_u is the cross-sectional area of a representative upflowing channel (see Fig. 4). As will be shown below, as long as the mixing length is constant over the bed cross-section, the individual channel cross-sectional areas need not be all equal in this model.

$$\Delta P_u = \rho_s g(1-\alpha)\Delta Z + \tau_i \frac{A_i}{A_u} \tag{8}$$

The interfacial shear stress is expressed by equation (9) in terms of the transverse particle mass velocity exchange w at the interface, where for simplicity, the mean particle velocity difference is taken as the gradient at the interface. The frictional flow resistance offered by bed internals is introduced subsequently in terms of the mixing length employed when tube banks are present. The gas phase shear stress is neglected.

$$\tau_i = w\left(\frac{|U_{sd}|}{1-\alpha} + \frac{|U'_{sd}|}{1-\alpha'}\right) \tag{9}$$

If we define the mixing length (ΔZ_m) by equations (10) and (11)

$$\Delta Z_m = M\Delta Z \tag{10}$$

then equation (11) gives the relation between the lateral, w, and axial, W, upward flowing particle mass velocities in a representative channel.

$$w = \left(\frac{A_u}{P\Delta Z_m}\right)(W) = \left(\frac{A_u}{P\Delta Z_m}\right)(\rho_s U_{sd}) \tag{11}$$

From equations (5, 7, 9, 10) and (11), we obtain equation (12)

$$\tau_i \frac{A_i}{A_u} = \rho_s {U_{sd}}^2 \left(\frac{1}{1-\alpha} + \frac{C}{1-\alpha'}\right) \tag{12}$$

It can now be seen that, by including the flow resistance due to internals in the mixing length ratio, M—i.e., decreasing mixing length caused by increased shear stress—one can include such flow resistance by measuring or assuming the mixing length. Equation (12) also shows that in this model the shear term in the force balance (equation (8)) is independent of the representative channel cross sectional area.

Similarly, the force balance on the downward flowing channels yields equation (13).

$$\Delta P_d = \rho_s g(1-\alpha')\Delta Z - \tau_i \frac{A_i}{A_d} \tag{13}$$

If no lateral static pressure gradients exist, equation (14) relates the channel force balances where ΔZ is taken to be ΔZ_m.

$$\Delta P_{av} = \rho_s g(1-\alpha_{av})\Delta Z_m = \Delta P_u = \Delta P_d \tag{14}$$

From equations (8, 12) and (14) we now obtain equation (15)

$$U_{sd} = \left\{\frac{g\Delta Z(\alpha - \alpha_{av})}{\dfrac{1}{M(1-\alpha)} + \dfrac{C}{M(1-\alpha')}}\right\}^{1/2} \tag{15}$$

With the exponents n, m, and p given by the average void correlation, equations (3, 4, 5, 6) and (7) relate U_{sd}, C, and α in terms of equation (16) with U_{sd} given by equation (15).

$$U_{sg_{av}}(1+C) - C\left[U_T\alpha^m + \frac{\alpha}{1-\alpha}U_{sd}\right] = U_T\left[1 - \{(1-\alpha_{av}) + C(\alpha-\alpha_{av})\}\right]^p - \frac{CU_{sd}[1-\{(1-\alpha_{av}) + C(\alpha-\alpha_{av})\}]}{(1-\alpha_{av}) + C(\alpha-\alpha_{av})} \tag{16}$$

As $C \to 0$, $m = p = n$ so that the model yields a uniform superficial velocity equal to $U_{sg_{av}}$. The mixing length ΔZ_m, as well as the fraction of total cross-sectional area in upflow are still inputs for which data are lacking. For this reason, a parametric set of calculations has been carried out to examine the effect of varying C and ΔZ_m over the range of superficial velocities, particle sizes and measured bed void fraction (n, m, and p values) of interest. These calculations have yielded the following results:

1 For a constant value of the exponent n, as in liquid fluidized beds, there is no solution when equation (1) is employed; i.e., the counter-current flow model does not exist. This is in agreement with observations if one neglects wall effects.

2 There are always solutions provided the exponent n in equation (1) decreases with increasing superficial velocity. This is also in agreement with gas fluidized data.

3 The circulating particle mass velocity is proportional to the 0.4 power of the mixing length.

4 The circulating particle mass velocity per unit bed cross-sectional area increases and then decreases as C increases from zero at a constant mixing length. There is a maximum upflow cross-sectional area fraction above which there is no solution.

5 As the superficial gas velocity approaches U_T, the solids circulation rate approaches zero.

At given mixing lengths, the maximum calculated upflow and downflow superficial solids velocities, given the average superficial gas velocity, using equations (15) and (16) yielded reasonably good linear correlation with respect to the average solids fraction $(1-\alpha_{av})$. Using a value of $\Delta Z_m = 0.305$m, the values of U_{sd} and U'_{sd} calculated over a relatively wide range of gas properties in the 650μm–2600μm particle size range (2.5 specific gravity) are shown in Fig. 5. The maximum solid circulation rates shown in Fig. 5 resulted at values of $C = 0.4$ to 0.5. Eighty percent of the calculated values fall within ±20 percent of those given by equations (17) and (18) at a constant mixing length of 0.305m.

$$U_{sd} = 0.404\,(1-\alpha_{av})\ \text{(m/s)} \tag{17}$$

$$U'_{sd} = 0.193\,(1-\alpha_{av})\ \text{(m/s)} \tag{18}$$

While no direct measurements of the mixing length in fluidized beds are available some indirect support exists for the use of the bed diameter as the mixing length in deep beds without internals and for the use of the spacing of bed internals as the mixing length when such internals exist in beds. In bubbling flow an increasing value of the mixing length with superficial gas velocity is expected [7, 13], until the bubble diameters have reached values determined by the equipment. In turbulent deep fluidized beds without internals the limiting mixing length is thus assumed equal to bed diameter until more data become available. In the presence of tube banks, the observation and calculation of Hoke, et al. [14], that the tube row spacing appears to dictate mixing length, is supported by the size of the solids circulation

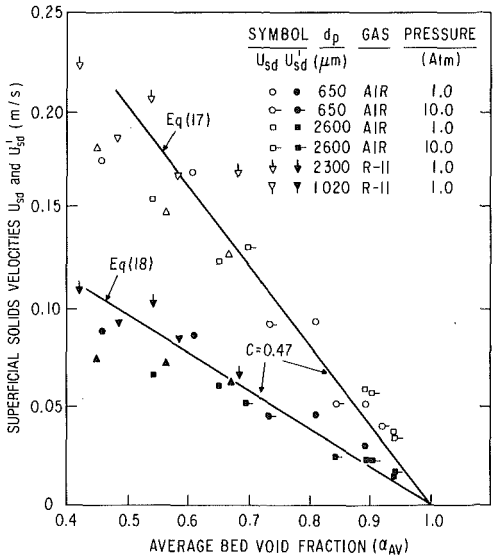

Fig. 5 Superficial solids velocities in upflow and downflow channels as calculated for ΔZ_m = 0.305m using equations (15) and (16) (symbols) and as approximated using equations (17) and (18)

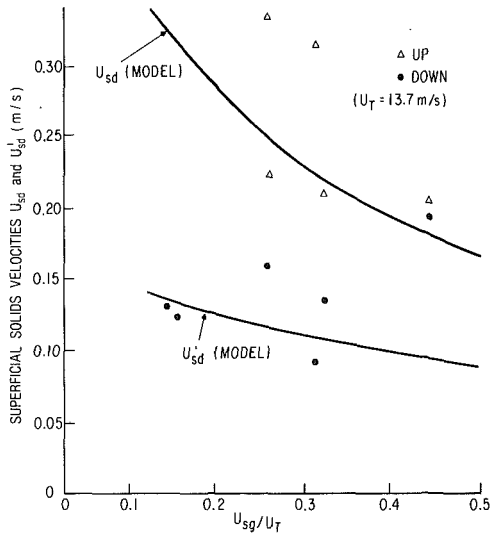

Fig. 6 Comparison of measured and calculated superficial solids velocities for 2600μm dia glass solids in a 0.305m bed fluidized with air at 1Atm

cells observed in this investigation [1]. Again, until further data are available, the average spacing between tubes in a tube bank is taken here to be equal to the mixing length ΔZ_m when a tube bank is immersed in the bed.

Some initial measurements of particle mass velocity have been carried out to compare with the model prediction. Using a calibrated traversing particle impact probe, which employed a 0.25cm dia piezoelectric pressure transducer and suitable data handling equipment to measure the individual particle impact rate, the mean upflowing and downflowing solids superficial velocities were experimentally determined in a 0.305m × 0.305m atmospheric pressure fluidized bed. A narrow size distribution of 2600μm glass particles was employed with a perforated plate distributor using a 40cm static bed height over a range of superficial air velocities. These data are compared with the model calculation in Fig. 6 where ΔZ_m = 0.305m and C = 0.45 at the maximum calculated solids circulation. Note that reasonable agreement with the model exists in the magnitude of both U_{sd} and U'_{sd}. The mean calculated absolute particle velocities of 0.35 to 0.5 m/s in upflow and 0.15 to 0.2 m/s in downflow were within 25 percent of the mean impact velocities measured by the data in Fig. 6. Note also that, while bubbling flow tended to predominate for values of U_{sg}/U_T less than about 0.3 in Fig. 6, the solids circulation data scatter about the model prediction about equally in both flow regimes. No bubble frequencies or sizes could be measured with any accuracy under the flow conditions in Fig. 6 so that a solids circulation model based on bubbling flow, such as that of Kunii, Yoshida and Levenspiel [13], could not be employed to compare to the data. While more particle flow data need to be obtained using other particle sizes and densities, as well as other bed geometries, the initial flow model comparison in Fig. 6 is promising.

Until more particle circulation data become available, it will be assumed that the most likely solution, at a given mixing length, is the value of C for which the total particle circulation rate is a maximum. This assumption has been employed to date in the heat transfer model presented below.

Heat Transfer Model

To formulate a heat transfer model in the flow regime that can be approximated by the quasi-steady counterflow particle model outlined above, it seems reasonable to relate previous correlations for the heat transfer in tubes carrying gas fluidized particles in transport to our case where the particles flow up or down over immersed surfaces.

The heat transfer to cocurrent gas-particulate flow in tubes has been studied by several workers. Schluderberg, et al. [15] and Hawes and Holland [16] used particle sizes <20μm at particle loading ratios ($\rho_s U_{sd}/\rho_g U_{sg}$) up to 100 while Danziger [17] and Wilkinson and Norman [18] used mean particle sizes up to 70μm at particle loading ratios up to 450. Danziger's mean particle size of 50μm included a 10μm–210μm particle size range. These workers correlated their heat transfer data using equation (19) with negligible effect of particle size.

$$\frac{\mathrm{Nu}}{\mathrm{Nu}_g} = \left(1 + \frac{\rho_s U_{sd}}{\rho_g U_{sg}}\right)^{0.45} \tag{19}$$

Jepson, Poll, and Smith [19] showed agreement with equation (19) using 250μm particles at a large particle loading ratio and decreasing heat transfer coefficients with increasing particle size at all loading ratios. The effect of larger particles on the heat transfer in fluidized beds was investigated by Baskakov [20] who determined the particle size proportionality shown in equation (20). While Baskakov [20] correlated the maximum coefficient value using equation (20) this proportionality is employed here over the range of gas superficial velocities of interest as a first approximation and in view of the fact that the ratio of the coefficients to the maximum coefficient with varying gas velocity was nearly the same for all particle sizes investigated. To include

$$\begin{aligned} h &\sim (d_p)^{-1/3} \quad 20\mu\mathrm{m} < d_p < 1000\mu\mathrm{m} \\ h &\approx \text{constant} \quad 1000\mu\mathrm{m} < d_p < 3000\mu\mathrm{m} \end{aligned} \tag{20}$$

this particle size effect in the heat transfer correlation equation (21) employs a reference particle diameter of 150μm as a compromise between the data of Danziger [17], Wilkinson and Norman [18], Jepson, et al. [19], and Baskakov [20].

$$\frac{\mathrm{Nu}}{\mathrm{Nu}_g} = \left[1 + \left(\frac{150}{d_p(\mu\mathrm{m})}\right)^{0.73}\left(\frac{\rho_s U_{sd}}{\rho_g U_{sg}}\right)\right]^{0.45} \tag{21}$$

for $20\mu\mathrm{m} < d_p < 1000\mu\mathrm{m}$

for $1000\mu\mathrm{m} < d_p < 3000\mu\mathrm{m}$, d_p = 1000 in equation (21)

It is suggested that, for both the upflowing and downflowing channels in the flow model given here, the heat transfer to an immersed surface can also be correlated by an equation that has the form of equation (21). If the boundary layer disturbance by the particles and the transient conduction to particles impacting the surface are applicable phenomena, then the local void fraction and local gas velocity should be more important than whether or not the particles are in cocurrent or counter-current flow. Vreedenberg's data [22] lend a little support to this point.

To employ equation (21), Nu_g is evaluated for the tube bank ge-

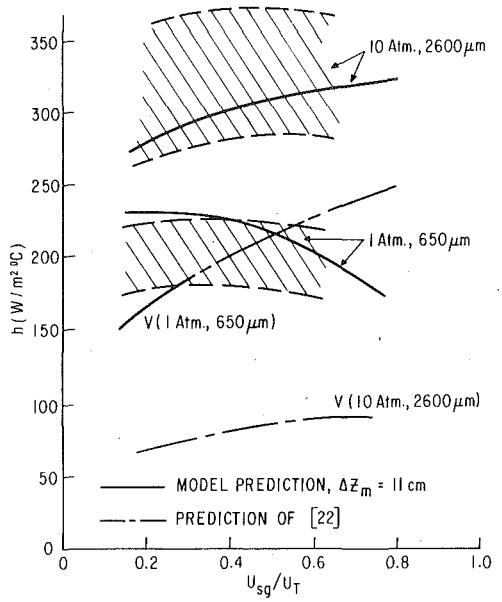

Fig. 7 Comparison of measured and calculated heat transfer coefficients to a horizontal staggered tube bank immersed in an air fluidized bed at 20°C. The hashed region represents the range of coefficients for different tube locations in the bank.

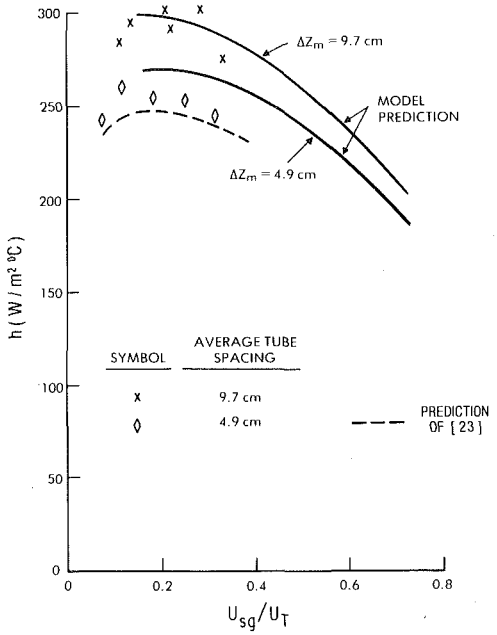

Fig. 8 Comparison of measured and calculated heat transfer coefficients to a horizontal staggered tube bank immersed in an air fluidized bed at 1atm and 20°C using 350μm particles [23]

ometry in question using existing heat transfer correlations. The value of Nu is then calculated using the gas and solid superficial velocities pertinent to the upflow and downflow regions calculated using the flow model. That is, the values of U_{sg} and U_{sd} in upflow as well as U'_{sg} and U'_{sd} in downflow as calculated from equations (5, 7, 15) and (16) are substituted in equation (21) to obtain the Nusselt number in the upflow region, Nu_u, and downflow region, Nu_d, respectively. The average Nusselt number, Nu, is then obtained from equation (22).

$$\mathrm{Nu} = \frac{C\mathrm{Nu}_u + \mathrm{Nu}_d}{(1+C)} \tag{22}$$

When this implicit method was applied, over the range of particle sizes and gas conditions shown in Fig. 5, to horizontal tube bundles immersed in the fluidized bed, it was found that, using the average gas superficial velocity with the area mean superficial solids velocity ($U_{sd_{av}}$) as given in equations (23) and (24), the calculated heat transfer coefficients were within 10 percent of those calculated using the more exact implicit method.

$$U_{sd_{av}} = \frac{2C}{(1+C)} U_{sd} = (0.639)(0.65)(1-\alpha_{av})\Delta Z_m{}^{0.4} \tag{23}$$

$$U_{sd_{av}} = 0.42(1-\alpha_{av})\Delta Z_m{}^{0.4}\ (\mathrm{m/s}) \tag{24}$$

with ΔZ_m in meters

Equation (23) comes from equation (17) and Fig. 5 where ΔZ_m = 0.305m and where C = 0.47. Equation (24) is then employed with equation (25), where the tube bank convection Nusselt number ($\mathrm{Nu}_{g_{av}}$) is based on $U_{sg_{av}}$ in the absence of particles.

$$\frac{\mathrm{Nu}}{\mathrm{Nu}_{g_{av}}} = \left[1 + \left(\frac{150}{d_p(\mu\mathrm{m})}\right)^{0.73}\left(\frac{\rho_s U_{sd_{av}}}{\rho_g U_{sg_{av}}}\right)\right]^{0.45}$$

$$\text{for } 20\mu\mathrm{m} < d_p < 1000\mu\mathrm{m} \tag{25}$$

for $1000\mu\mathrm{m} < d_p < 3000\mu\mathrm{m}$, $d_p = 1000\mu\mathrm{m}$ in equation (25)

Considering the assumptions in this heat transfer model and the implicit nature of equations (15) and (17) the simplified expressions given by equations (24) and (25) were employed in the comparisons with tube bank heat transfer data shown in Figs. 7–9.

The hashed regions in Fig. 7 include the range of measured heat transfer coefficient for a ten row horizontal staggered 3.18cm OD tube bank having 10.2cm horizontal tube-to-tube spacing and a 5.7cm vertical row-to-row spacing. A 40–70cm static bed height of closely sized 2600μm glass ballotini (2.5 s.g.) were employed in a 0.305m ×

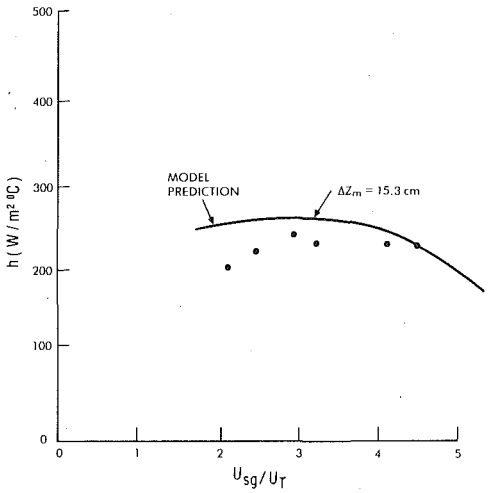

Fig. 9 Comparison of measured and calculated heat transfer coefficients to a horizontal staggered tube bank immersed in a coal combustion fluidized bed at 1atm, 815°C using a 700μm mean particle size [24]

0.305m bed. The solid line is that calculated from equations (24) and (25), with the $\mathrm{Nu}_{g_{av}}$ determined using the tube bank heat transfer correlation of McAdams [21]. The dotted line represents the prediction using the often employed correlation of Vreedenberg [22] established at one atmosphere for smaller particles in fluidized beds under bubbling flow conditions. It is clear that, as one proceeds into the turbulent regime at 1 atm, i.e., above $U_{sg}/U_T = 0.35$ in Fig. 7, the heat transfer correlation of Vreedenberg [22], established in the bubbling regime, is increasingly in error. The extrapolation of the bubbling bed correlation of Vreedenberg [22] to 10 atm and to larger particles is also obviously not proper as shown in Fig. 7 while the application of the turbulent bed model gives reasonable prediction without changing any of the model assumptions involved. The latter implies again that, for large particles at high velocities, existing heat transfer models and correlations based on bubbling flow and small particle sizes are not satisfactory. The horizontal tube bank data of Gel'perin and Ainshtein [23] are compared in Fig. 8 to that calculated by the same method for two horizontal tube spacings to show that,

when ΔZ_m is selected on the basis of the average tube spacing, reasonable correlation is achieved. Note the smaller particle size in the data of Gel'perin and Ainshtein [23]. The dotted line in Fig. 8 represents the bubbling bed model prediction from Gel'perin and Ainshtein [23] and it shows that even where bubbling flow is present, the turbulent bed model given here predicts the heat transfer data about as well as a bubbling bed model.

The heat transfer data of Mesko [24] in an 815°C fluidized bed combustor, to a horizontal staggered 5.1 cm OD tube bank with a 15.3 cm horizontal tube-to-tube spacing and a 7.6 cm vertical row-to-row spacing are shown in Fig. 9 when compared to the calculation using the model given here. The radiation heat transfer component determined by Baskakov [20] with cool immersed surfaces was employed to reduce the heat transfer coefficient measured by Mesko [24] by seven percent in order to obtain the convective fluidized bed coefficient. This combustion bed contained a broad particle size distribution whose weighted mean size was given as 700μm.

Conclusion

In the turbulent fluidized bed flow regime solids flow and heat transfer correlations based on bubbling bed flow are not expected to, and do not, predict measured performance.

The turbulent fluidized bed solids flow and heat transfer model given here shows satisfactory agreement with immersed tube bank heat transfer data and with limited solids velocity measurements. It also appears to predict reasonably well the tube bank heat transfer when some bubbling flow was seen to persist.

Acknowledgment

The author is indebted to G. S. Canada and S. Brzozowski for their development of the solids flow measurement technique as well as the General Electric Company and the Electric Power Research Institute who supported this research effort.

Special recognition is given to Novak Zuber, now with the NRC, Washington, DC, whose modeling approach to two-phase flow has been applied throughout this work.

References

1 Staub, F. W., and Canada, G. S., "Effect of Tube Bank and Gas Density on Flow Behavior and Heat Transfer in Fluidized Beds," *Fluidization,* Cambridge University Press, 1978, pp. 339–344.

2 Kunii, D., and Levenspiel, O., "Fluidization Engineering," Robert E. Krieger, 1977.

3 Davidson, J. F., and Harrison, D., *Fluidized Particles,* Cambridge University Press, 1963.

4 Davidson, J. F., and Kehoe, P. W. K., Inst. Chem. Eng. Symp. Series 33, 97, London, 1971.

5 Yerushalmi, J., Cankurt, N. T., Geldart, D., and Liss, B., Paper No. 119a, 69th Annual Meeting AIChE, Chicago, Ill., Nov. 29, 1976.

6 Lanneau, K. P., *Trans. Inst. Chem. Eng. 38,* 125, 1960.

7 VanDeemter, J. J. in Drinkenburg, A. A. H. (Ed.), *Proceedings of the International Symposium on Fluidization,* 1967, Amsterdam, Netherlands University Press, p. 334.

8 Richardson, J. F., and Zaki, W. N., "Sedimentation and Fluidization," *Transactions of the Institution of Chemical Engineers,* Vol. 32, 1954, p. 35.

9 Price, B. G., Lapidus, L., and Elgin, J. C., "Mechanics of Vertical Moving Fluidized Systems," *Am. Inst. Chem. Eng. J.,* Vol. 5, No. 1. 93, 1959.

10 Struve, D. C., "The Mechanics of Moving Vertical Fluidized Systems," *Canadian J. of Chemical Engineers,* Aug. 1958, p. 141.

11 Lewis, W. K., Gilliland, E. R., and Bauer, W. C., "Characteristics of Fluidized Particles," *Ind. Eng. Chem.,* Vol. 41, No. 6, 1949, p. 1104.

12 Wallis, G. B., *One-Dimensional Two-Phase Flow,* McGraw-Hill, New York, 1959.

13 Kunii, D., Yoshida, K., and Levenspiel, O., "Axial Movement of Solids in Bubbling Fluidized Beds," *I. Chem. E. Symposium Series,* No. 30, Instn. Chem. Engrs., London, 1968, pp. 79–84.

14 Hoke, R. C., Hodges, J. L., and Bertrand, R., "Prediction of Temperature Profiles in Fluid Bed Boilers," ASME Paper 76-HT-66, ASME/AIChE Heat Transfer Conference, St. Louis, Mo., Aug. 1976.

15 Schluderberg, D. C., Whitelaw, R. L., and Carlson, R. W., "Gaseous Suspensions—A New Reactor Coolant," *Nucleonics,* Vol. 19, No. 8, Aug. 1961, pp. 67–76.

16 Hawes, R. J. and Holland, E., "An Experimental Investigation into Heat Transfer and Pressure Drop of Gaseous Suspensions of Solids," AEEW-R244, 1964, U.K. Atomic Energy Authority.

17 Danziger, W. J., "Heat Transfer to Fluidized Gas-Solids Mixtures in Vertical Transport," *Industr. Eng. Chem. Progress Design & Devel.,* Vol. 2, No. 4, Oct. 1963, pp. 269–276.

18 Wilkinson, G. T. and Norman, J. R., "Heat Transfer to a Suspension of Solids in a Gas," *Trans. Instn. Chem. Engrs.,* Vol. 45, 1967, T314–T318.

19 Jepson, G., Poll, A., and Smith, W., "Heat Transfer from Gas to Wall in a Gas/Solid Transport Line," *Trans. Instn. Chem. Engrs.,* Vol. 41, 1963, pp. 207–211.

20 Baskakov, A. P., "Heat Transfer to Objects Immersed in Fluidized Beds," *Powder Technology,* Vol. 8, 1973, pp. 273–282.

21 MaAdams, W. H., *Heat Transmission,* Third Edition, McGraw-Hill, New York, 1954.

22 Vreedenberg, H. A., "Heat Transfer Between a Fluidized Bed and a Horizontal Tube," *Chemical Engineering Science,* Vol. 9, 1958, p. 52.

23 Gel'perin, N. I. and Ainshtein, V. G., "Heat Transfer Between a Fluidized Bed and Staggered Bundles of Horizontal Tubes," *International Chemical Engineering,* Vol. 9, No. 1, Jan. 1969, pp. 137–142.

24 Mesko, J. E., *Multicell Fluid Bed Boiler Design, Construction and Test Program,* ERDA Contract E(49-18) 1237, Pope, Evans and Robbins Corporation, Status Report No. 37, Oct. 1975.

N. S. Grewal
S. C. Saxena

Department of Energy Engineering,
University of Illinois at Chicago Circle,
Box 4348
Chicago, IL. 60680

Effect of Surface Roughness on Heat Transfer from Horizontal Immersed Tubes in a Fluidized Bed

Experimental results of the total heat transfer coefficient between 12.7 mm dia copper tubes with four different rough surfaces and glass beads of three different sizes as taken in a 0.305 m × 0.305 m square fluidized bed as a function of fluidizing velocity are reported. The comparison of results for the rough and technically smooth tubes suggests that the heat transfer coefficient strongly depends on the ratio of pitch (P_f) to the average particle diameter ($\overline{d}_p$), where P_f is the distance between the two corresponding points on consecutive threads or knurls. By the proper choice of ($P_f/\overline{d}_p$) ratio, the maximum total heat transfer coefficient for V-thread tubes (h_{wfb}) can be increased by as much as 40 percent over the value for a smooth tube with the same outside diameter. However, for values of ($P_f/\overline{d}_p$) less than 0.95, the maximum heat transfer coefficient for the V-thread rough tubes is smaller than the smooth tube having the same outside diameter. The qualitative variation of the heat transfer coefficient for rough tubes with ($P_f/\overline{d}_p$) is explained on the basis of the combined effect of contact geometry between the solid particles and the heat transfer surface, and the solids renewal rate at the surface. The present findings are critically compared with somewhat similar investigations from the literature on the heat transfer from horizontal or vertical rough tubes and tubes with small fins.

Introduction

Fluidized-bed combustion systems are being rapidly developed for the generation of electric power from sulfur rich coal. In such systems, immersed boiler tubes are employed to remove the heat of coal combustion and the steam thus generated is used to drive turbines. The efficiency of heat removal from the fluidized bed will therefore depend upon the coefficient of heat transfer between the immersed tubes and the bed. Any feature that can augment the value of this coefficient will be very useful for design purposes. The existing literature for heat transfer from rough surfaces in a fluidized bed is somewhat limited and was reviewed recently by Saxena, et al. [1]. Relatively much more work has been done on heat transfer from smooth tubes immersed in a fluidized bed [1]. These investigations on smooth tubes suggest that the mechanism of heat transfer between boiler tubes and the fluidized bed is very complicated because of the involvement of many fluidized-bed variables such as particle size and size distribution, particle shape, particle density, particle and gas thermal properties, reactor geometry and type of gas distributor; and the variations in heat transfer tube design such as size, shape, spacing (gap), pitch and material. For rough tubes, in addition to the above variables one will have to include in the analysis of heat transfer process such variables as the type of surface roughness, size of surface roughness and pitch to particle diameter ratio.

Neukirchen and Blenke [2], and Gelperin, et al. [3] have reported measurements of heat transfer rate between a rough horizontal tube and a fluidized bed. Their results are reviewed by Saxena, et al. [1]. Both groups have employed three types of rough tubes viz., longitudinal, transverse, and a network of crosswise grooves. In Neukirchen and Blenke [2], experiments, the groove depth was varied from 0.6 to 1.9 mm and bed material was glass beads of 700 μm average diameter. Gelperin, et al. [3] on the otherhand varied the groove depth from 0.5 to 0.7 mm and used quartz sand of 350 μm average diameter. The two works lead to similar results when the groove depth was close to the particle diameter viz., the heat transfer rate for rough tubes compared to smooth tubes of the same outside diameter either did not change at all or decreased. The decrease was particularly marked (30–40 percent) for tubes with crosswise grooves.

D'Albon, et al. [4], and Vijayaraghavan and Sastri [5] have investigated the heat transfer from rough vertical tubes immersed in a fluidized bed and these works are also reviewed in [1]. D'Albon, et al. [4] examined the effect of metric threads on heat transfer between a vertical cylindrical tube and a fluidized bed of sand particles of average diameter 50 and 100 μm. For the latter case, they [4] found that the maximum heat transfer coefficient for a tube with threads (h_{wfb}) of height 3.9 mm was about 25 percent greater than a smooth tube having the same outside diameter. However, a vertical tube with threads of height 1.7 mm the maximum heat transfer coefficient was smaller by about the same amount as compared to a smooth tube. Vijayaraghavan and Sastri [5] studied the effect of surface roughness on heat transfer between an electrically heated vertical tube, 35 mm in diameter and 200 mm in length, and a fluidized bed of glass spheres (−250 to +160 μm and −630 to +500 μm). The tubes were roughened with transverse and longitudinal 60 deg V-grooves, and fine and coarse cross knurling. The pitch for V-grooves and coarse knurling was 0.8 mm and only 0.1 mm for fine knurling. The longitudinal V-grooves produced the largest increase in heat transfer rate for the smaller particles in comparison to the smooth tube. For coarse knurling, the increase in heat transfer rate was relatively smaller. Heat transfer rate was smaller for transverse grooved tube as compared to smooth tube and it was smallest for tubes with fine cross knurling. Similar qualitative results were obtained for larger particles.

Korolev and Syromyatnikov [6] investigated the effect of surface roughness on heat transfer from an electrically heated vertical plate and fluidized beds of corundum ($\overline{d}_p$ = 120 μm), chamotte ($\overline{d}_p$ = 320 μm), and polystyrene ($\overline{d}_p$ = 720 μm). The transverse and longitudinal V-grooves with 0.4 mm height and 0.5 mm pitch were machined on the surface. They also examined two other plates on which the surface roughness was obtained by the treatment of surfaces with a jet of corundum particles. The average height of the roughness on the two plates was 2 and 10 μm and the average pitch between projections was 0.06 and 0.10 mm, respectively. For fine particles (120 and 230 μm) when ($P_f/\overline{d}_p$) < 1, an increase in surface roughness height resulted in the reduction of heat transfer rate as compared to that for a smooth vertical plate. When the height and pitch of V-grooves were greater than the particle size, the heat transfer coefficients for rough plates were larger as compared to the smooth plate. In the fluidized bed of larger particles ($\overline{d}_p$= 720 μm), the surface roughness of these plates did not effect the heat transfer coefficient. Further, the heat transfer coefficient for the longitudinal V-groove plate was larger than that for the transverse V-groove plate.

A number of investigations have been reported in the literature on the performance of transverse [7–12, 14–16] and longitudinal [13]

Contributed by the Heat Transfer Division for publication in the JOURNAL OF HEAT TRANSFER. Manuscript received by the Heat Transfer Division June 29, 1978.

finned horizontal tubes, and transverse fins on vertical tubes [9, 17, 18]. Most of these investigations involve fins of widely different shape, height and pitch. These influence the solids movement and gas flow around the surface quite differently than the rough tubes examined in the present work. To shed some light on the effect of surface roughness on heat transfer coefficient, we have conducted a series of experiments on smooth and rough horizontal tubes in a fluidized bed of glass beads. Further, we have compared the results of the present investigation with only those existing studies where the operating conditions and the $P_f/\overline{d}_p$ values are close to our values. In the next section, we briefly describe our experimental facility and the procedure for making a run.

Experimental Apparatus and Procedure

The experimental arrangement consists of a fluidization column, air supply system, electrical system for heat transfer tubes, and an off-gas system. The fluidized bed system is instrumented for the measurement of temperature, pressure, air flow rate, and power supplied to the heat transfer tubes. The fluidization column is constructed from 3 mm sheet steel, 2.1 m in height and 30.5 by 30.5 cm in cross-section and is shown in Fig. 1. The fluidizing air which is introduced at the bottom of the column flows through the air-jet breaker plate in the calming section and then through the fluidized bed distributor plate which is located at the top of the calming section. The heat transfer tubes, 12.7 mm outside diameter and made of copper, are mounted horizontally and 213 mm above the perforated plate distributor. The details of V-thread and knurled tubes are shown in Fig. 2. The rough tubes consist of 60 deg V-threads with pitches of 0.79 mm ($^1/_{32}$ in.), 0.40 mm ($^1/_{64}$ in.) and 0.24 mm ($^1/_{108}$ in.), and a knurled tube of diametral pitch equal to 32. The diametral pitch is the ratio of total number of teeth on the circumference of a transverse plane perpendicular to the axis of rotation of the tube, to the basic blank tube diameter. The knurled surface has diagonal teeth with 30 deg helix angle. The shape of the teeth is pyramid with rhomboidal base. The distributor consists of two perforated steel plates with a coarse cloth sandwiched between them. One cm diameter holes are drilled in both the plates at a triangular pitch of 14 mm. The open area being 37.5 percent.

The fluidizing air is supplied by a compressor and its rate is measured on calibrated rotameters with an accuracy of ±1 percent. The pressures in the fluidized bed at various locations are measured by liquid manometers. The heat transfer tubes are electrically heated

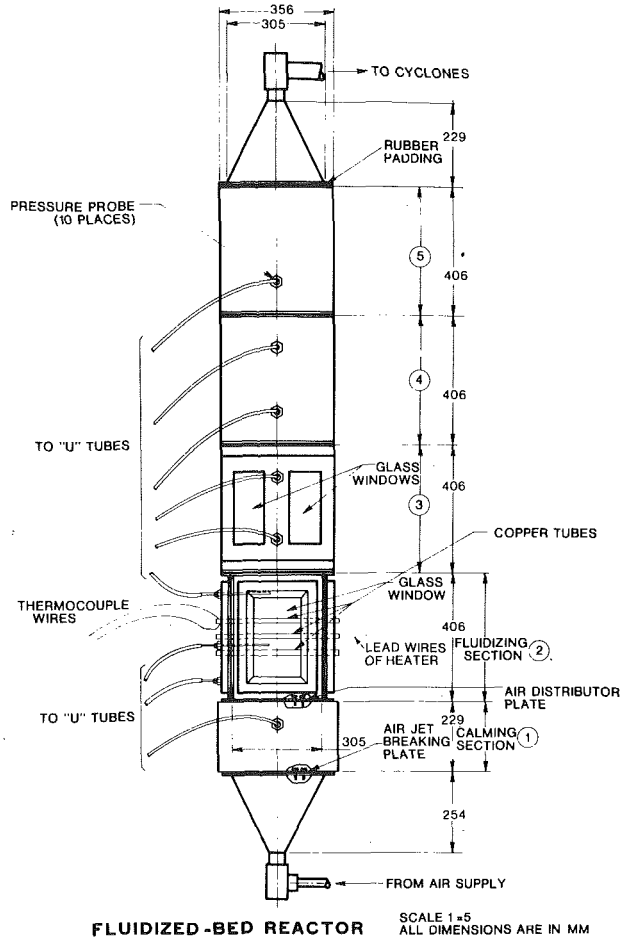

Fig. 1 Experimental 30.5 × 30.5 cm square fluidized bed

by a calrod heater 9.4 mm in diameter and 30.5 cm long as shown in Fig. 3. Two iron-constantan thermocouples are silver soldered at the center of the tube, 90 deg apart. The temperatures indicated by the two thermocouples on the top and the side of the heat transfer tubes differed mostly by about 1K both for smooth and rough tubes. This

Nomenclature

A_w = surface area of a smooth tube, m^2

A_{wb} = surface area of a smooth tube with outside diameter equal to the fin tip diameter of a given finned tube, m^2

A_{wft} = total surface area of a finned tube, m^2

C_{pg} = specific heat of air at constant pressure, kJ/kg K

$\overline{d}_p$ = average particle diameter defined by equation (1), m

d_{pi} = arithmetic average diameter of the successive screens, m

D_b = bed diameter, m

D_T = outside diameter of smooth tube or fin tip diameter of a finned tube, m

g = acceleration due to gravity, m/s^2

G = mass fluidizing velocity, kg/m^2s

G_{mf} = velocity at minimum fluidizing conditions, kg/m^2s

h = heat transfer coefficient, W/m^2K

h_w = total heat transfer coefficient for smooth tube, W/m^2K

h_{wfb} = total heat transfer coefficient for finned tube based on the surface area of a smooth tube with outside diameter equal to finned tube tip diameter, W/m^2K

h_{wft} = total heat transfer coefficient for finned tube based on actual surface area of the finned tube, W/m^2K

$h_{w\ max}$ = maximum heat transfer coefficient for smooth tube, W/m^2K

$h_{wfb\ max}$ = maximum heat transfer coefficient for finned tube based on the surface area of a smooth tube with outside diameter equal to finned tube tip diameter, W/m^2K

$h_{wft\ max}$ = maximum heat transfer coefficient for finned tube based on actual surface area of the finned tube, W/m^2K.

H = distance between pressure probes, m

H_s = static height of bed, m

k_f = thermal conductivity of the fluidizing air, W/m K

ℓ = fin height, m

Nu_{wT} = Nusselt number for smooth tube based on heat transfer tube diameter, $(h_w D_T)/k_f$, dimensionless

Nu_{wftT} = Nusselt number for rough or finned tube based on tube diameter, $(h_{wft} D_T)/k_f$, dimensionless

P_f = pitch, for V-threaded tubes it is the distance between two identical points of the consecutive threads; for knurled tubes this distance is measured along the tube axis only, m

Pr = Prandtl number, $(\mu C_{pg})/k_f$, dimensionless

Q = electrical power supplied to heater, W

T_b = average fluidized bed temperature, K

T_w = average surface temperature of the heat transfer tube, K

w_i = weight fraction of particles in a specified size range, dimensionless

β = ratio of the maximum heat transfer coefficient for a rough tube to its value for a smooth tube having the same outside diameter, dimensionless

ΔP = pressure drop across the probes, Pa

ϵ = bulk bed porosity, dimensionless

$1 - \epsilon$ = volume fraction occupied by particles, dimensionless

ρ_f = fluid density, kg/m^3

ρ_s = density of solid particles, kg/m^3

μ = viscosity of the fluidizing gas, Ns/m^2

ϕ = fin effectiveness factor, h_{wft}/h_w, dimensionless

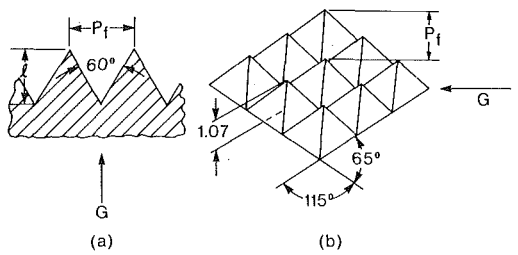

Fig. 2 Details of the rough tubes: (*a*) V-thread tube and (*b*) knurled tube

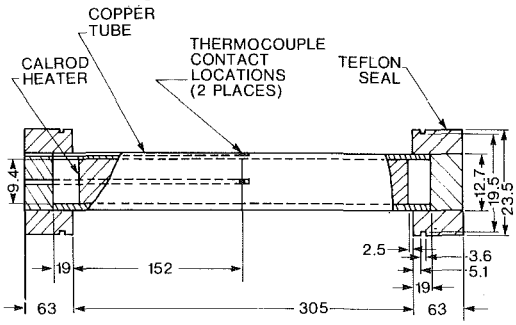

Fig. 3 Details of copper tube and heater assembly. All dimensions are in mm

uniformity of temperature distribution is due to the high thermal conductivity of copper of which these tubes are made. The ends of the tubes are provided with teflon support to reduce axial heat loss. The end heat loss is estimated to be less than one percent. In all runs, one of the thermocouples is kept at the top side of the tube. A d-c power supply with voltage regulation of ±0.01 percent is used to energize the heater. Precision voltmeters and ammeters are employed to determine the power fed to the heater. Two thermocouples to measure the temperature of the fluidizing bed are located 13.3 cm above and below the center of the heated tube, and an average value has been used in the calculation of heat transfer coefficient. In our experiments for $G/G_{mf} > 1.3$, the difference between the temperatures indicated by the two thermocouples never exceeded 0.16K (0.3°F). The top thermocouple readings were always higher than the bottom thermocouple. For $G/G_{mf} > 1.3$, the average heater surface and bed temperatures are in ranges of 315 to 340 K and 298 to 310 K, respectively. The average temperature difference between the tube surface and the fluidized bed varies between 16 to 44 K depending on particle size, fluidizing velocity and the tube surface roughness. The thermocouples are connected to a Leeds and Northrup Numatron temperature recorder with 0.1 K resolution and 21 column digital printer.

In these experiments, spherical glass beads of three different sizes have been used as bed material and the size distribution is given in Table 1. The particles have a size distribution in each case but about 95 percent of them are confined in a relatively close range. The average diameter, $\bar{d}_p$, of the particles is obtained from the sieve analysis of glass beads on a sonic sifter and the following relation:

$$\bar{d}_p = \frac{1}{\sum_i (w/d_p)_i} \tag{1}$$

Here w_i is the weight fraction of the particles of diameter d_{p_i} in the sample. The $\bar{d}_p$ values are given in Table 1. The particle density of glass beads, ρ_s, is determined by the displacement of methanol in a graduated cylinder and these are reported in Table 2. The minimum fluidizing velocity for a given bed of glass beads is determined in the conventional fashion [19] by measuring the bed pressure drop as a function of fluidizing velocity. The minimum fluidizing velocity is established by the intersection of the two linear plots describing the constant and decreasing pressure drop with decreasing fluidizing velocity [20]. Minimum mass fluidizing velocity, G_{mf}, values for all the three glass beads are also listed in Table 2.

The settled bed height in all the experiments is kept the same at 35 cm. The electrical current, voltage, and pressure drops in the vicinity of the heat transfer tube are recorded. The steady state is assumed to be established when the bed temperature variation is less than 0.4 K per hour. The temperatures at each of the other locations are recorded over a period of time and an arithmetic average value is used. The total heat transfer coefficient, h_w, is determined from the following relation:

$$h_w = \frac{Q}{A_w(T_w - T_b)} \tag{2}$$

The total heat transfer coefficient for rough or finned tubes, h_{wft}, is also calculated from equation (2), where A_w is replaced by the total surface area of the rough or finned tube. Another way of defining the total heat transfer coefficient for rough or finned tube is to base it on the surface area of a smooth tube whose outside diameter is equal to the tip diameter of the rough tube and is represented by h_{wfb}.

The pressure loss in a fluidized bed, ΔP, is equal to the weight of the bed per unit cross-sectional area i.e.,

$$\Delta P = H(1 - \epsilon)(\rho_s - \rho_f) \tag{3}$$

ΔP, H, ρ_s and ρ_f are known and therefore the above relation is used to compute the bulk porosity, ϵ, of a portion of the bed which contains the heat transfer tube. The specific measurements and their discussion is given below.

Table 1 Cumulative particle size distribution for glass beads

Sieve dia (μm)	Percent less than the stated size		
	$\bar{d}_p$ = 265 μm	$\bar{d}_p$ = 357 μm	$\bar{d}_p$ = 427 μm
1000	—	—	100.0
850	—	—	99.5
600	—	100.0	99.5
500	—	99.9	96.9
425	100.0	99.0	47.1
355	99.3	46.6	1.4
300	95.6	1.9	0.2
250	20.6	0.3	0.0
212	2.1	0.2	—
180	0.2	0.0	—
150	0.1	—	—
125	0.0	—	—
105	—	—	—

Table 2 Size, density and minimum fluidizing velocity of glass beads

Material	$\bar{d}_p$, μm	ρ_s, kg/m^3	G_{mf}, kg/m^{2}s
Glass beads	265	2490	0.071
Glass beads	357	2490	0.127
Glass beads	427	2490	0.196

Results and Discussion

Figs. 4–6 show the results of the variation of the total heat transfer coefficient for the various rough tubes, h_{wfb}, and the smooth tube, h_w, for the glass beads of three different sizes as a function of the reduced excess mass fluidizing velocity. It is clear from these figures that heat transfer rates depend upon the fluidizing velocity, surface roughness and particle diameter. The qualitative variation of the dependence of h_w on fluidizing velocity as shown in these figures is in complete accord with the reported trends observed by earlier investigators [19–21]. The heat transfer coefficient for smooth tubes increases with increase in the value of reduced excess mass fluidizing velocity, $(G - G_{mf})/G_{mf}$. The increase is larger in the beginning but decreases as the gas velocity is increased; h_w, however, decreases for large gas velocity and attains its maximum value at some intermediate value. These qualitative features can be explained on the basis of "particle mode" of heat transfer [22, 23]. The heat transfer is proportional to the number of particles close to the surface, and to the period for which they stay there, i.e., residence time. The initial increase of h_w is due to decrease in particle residence time resulting from particle mixing caused by rising bubbles. However, the number of particles close to the heat transfer surface decreases with increase in the fluidizing velocity which cause a reduction in the heat transfer rate. At a particular fluidizing velocity, the magnitude of h_w depends upon the net contribution of these two opposing factors. Further, for a smooth tube it is found here that h_w always decreases with increase

in solid particle diameter and this result is in complete conformity with the reported findings in the literature [1, 20–22]. The decrease in h_w with increase in the particle diameter is explained as predominantly due to the increase in the gas conduction paths for such particles. Further, the particle surface area per unit volume of the bed is large for small particles and therefore small particles are more efficient in exchanging heat with the surface than the large particles.

The experimental heat transfer data for smooth tubes are compared in terms of the Nusselt number with the existing seven correlations [7, 9, 24–28], listed in Table 3, in Fig. 7 for $G/G_{mf} > 1.3$. The root-mean-square deviations for the smooth tube data are given in column 4 of this table.

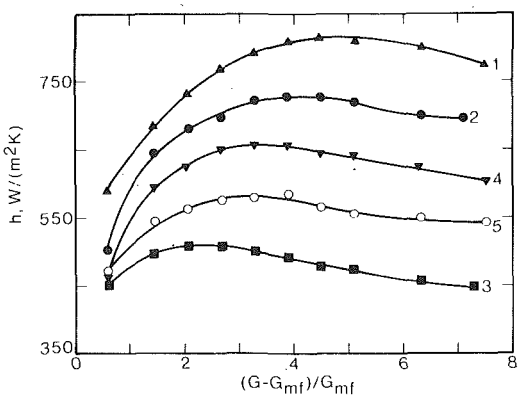

Fig. 4 Variation of h with $(G - G_{mf})/G_{mf}$ for glass beads ($\bar{d}_p$ = 265 μm) and an electrically heated 12.7 mm copper tube with different surface roughness. Curves 1 through 3 refer to surface with V-threads of pitch 0.79 mm, 0.40 mm and 0.24 mm, respectively; curve 4 is for a knurled surface of diameteral pitch 32; and curve 5 is for a technically smooth surface

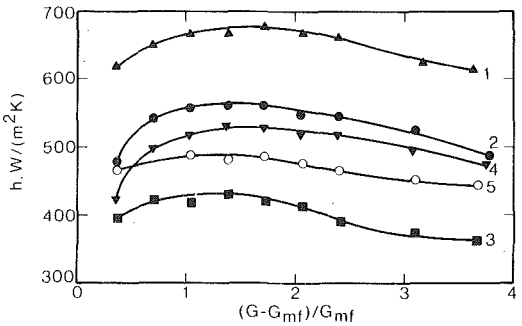

Fig. 5 Variation of h with $(G - G_{mf})/G_{mf}$ for glass beads (d_p = 357 μm) and an electrically heated 12.7 mm copper tube with different surface roughness. Curves 1 through 3 refer to surface with V-threads of pitch 0.79 mm, 0.40 and 0.24 mm, respectively; curve 4 is for a knurled surface of diameteral pitch 32; and curve 5 is for a technically smooth surface

The best agreement is obtained for the correlation of Ternovskaya and Korenberg [28], the RMS deviation being 12.8 percent. Further, as seen from Fig. 7, most of the calculated values lie within ± 20 percent of the data points. The data also scatter with almost equal frequency on either side of the 0 percent deviation line. Based on such considerations we have inferred that the correlations of [24, 27] and [9] though quite good are not as accurate as that of [28] for glass beads and the operating conditions of our experiments.

The dependence of h_{wfb} for rough tubes on $(G - G_{mf})/G_m$ is qualitatively similar to that for smooth tubes. However, the maximum value of h_{wfb} is reached at a higher value of reduced excess mass fluidizing velocity as compared to the smooth tube. Figs. 4–6 also show that h_{wfb} values for a rough tube can be larger or smaller in comparison to a smooth tube depending upon the size of pitch in relation to the particle diameter. Since in practice, it will be advantageous to operate the system under conditions where the heat transfer rates are maximum, therefore, only the maximum heat transfer coefficient values have been discussed in greater detail in the following with $P_f/\bar{d}_p$ as an independent parameter. Further, we examine the ratio of the maximum value of h_{wfb} to the maximum value of h_w, which is denoted here by β. Thus, β is directly a measure of the relative efficiency of heat transfer for a fin tube over a smooth tube occupying the same bed volume.

The dependence of β on $(P_f/\bar{d}_p)$ is displayed in Fig. 8. The values of β as obtained from the present work for V-thread rough tubes first

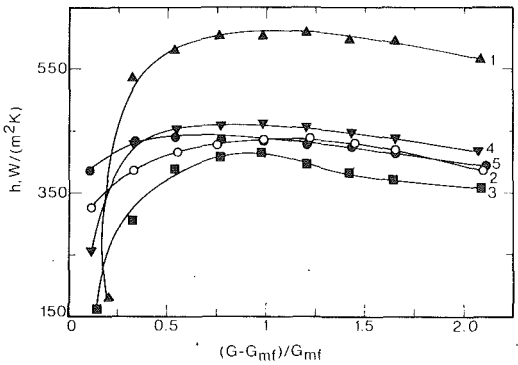

Fig. 6 Variation of h with reduced fluidizing velocity for glass beads ($\bar{d}_p$ = 427 μm) and an electrically heated 12.7 mm copper tube with different surface roughness. Curves 1 through 3 refer to surface with V-threads of pitch 0.79 mm, 0.40 mm and 0.24 mm, respectively; curve 4 is for a knurled surface of diameteral pitch 32; and curve 5 is for a technically smooth surface

Table 3 Comparison of experimental and predicted heat transfer rates from various correlations for smooth and rough tubes

Reference	Correlation: Smooth Tube	Correlation: Rough Tube	Percent RMS Dev.: Smooth Tube	Percent RMS Dev.: Rough Tube
Vreedenberg [25]	$\mathrm{Nu}_{wT} = 420\left[\left(\frac{GD_T\rho_s}{\rho_f\mu}\right)\left(\frac{\mu^2}{\bar{d}_p{}^3\rho_s{}^2 g}\right)\right]^{0.3}\mathrm{Pr}^{0.3}$	$\mathrm{Nu}_{wftT} = \phi\,\mathrm{Nu}_{wT}$	21.5	21.5
Ternovskaya and Korenberg [28]	$\mathrm{Nu}_{wT} = 2.9\left[\left(\frac{1-\epsilon}{\epsilon}\right)\left(\frac{G\bar{d}_p}{\mu}\right)\right]^{0.4}\mathrm{Pr}^{0.33}(D_T/\bar{d}_p)$	$\mathrm{Nu}_{wftT} = \phi\,\mathrm{Nu}_{wT}$	12.8	11.8
Petrie, et al. [7]	$\mathrm{Nu}_{wT} = 14\,(G/G_{mf})^{1/3}\,\mathrm{Pr}^{1/3}\,(D_T/\bar{d}_p)^{2/3}$	$\mathrm{Nu}_{wftT} = \phi\,\mathrm{Nu}_{wT}$	18.8	18.5
Ainshtein [26]	$\mathrm{Nu}_{wT} = 5.76\,(1-\epsilon)\left(\frac{G\bar{d}_p}{\mu\epsilon}\right)^{0.34}\mathrm{Pr}^{0.33}\,(H/D_b)^{0.16}(D_T/\bar{d}_p)$	$\mathrm{Nu}_{wftT} = \phi\,\mathrm{Nu}_{wT}$	16.9	16.9
Andeen and Glicksman [24]	$\mathrm{Nu}_{wT} = 900\,(1-\epsilon)\left[\left(\frac{GD_T}{\rho_f\mu}\rho_s\right)\left(\frac{\mu^2}{\bar{d}_p{}^3\rho_s{}^2 g}\right)\right]^{0.326}\mathrm{Pr}^{0.3}$	$\mathrm{Nu}_{wftT} = \phi\,\mathrm{Nu}_{wT}$	15.0	15.0
Gelperin, et al. [27]	$\mathrm{Nu}_{wT} = 4.38\left[\frac{1}{6(1-\epsilon)}\left(\frac{G\bar{d}_p}{\mu}\right)\right]^{0.32}\left(\frac{1-\epsilon}{\epsilon}\right)(D_T/\bar{d}_p)$	$\mathrm{Nu}_{wftT} = \phi\,\mathrm{Nu}_{wT}$	14.0	14.0
Genetti, et al. [9]	$\mathrm{Nu}_{wT} = \left[\frac{11\,(1-\epsilon)^{0.5}}{1 + 0.2512/\left(\frac{G\bar{d}_p}{\mu}\right)^{0.24}(\bar{d}_p/0.000203)^2}\right]^2(D_T/\bar{d}_p)$	$\mathrm{Nu}_{wftT} = \phi\,\mathrm{Nu}_{wT}$	15.6	15.5

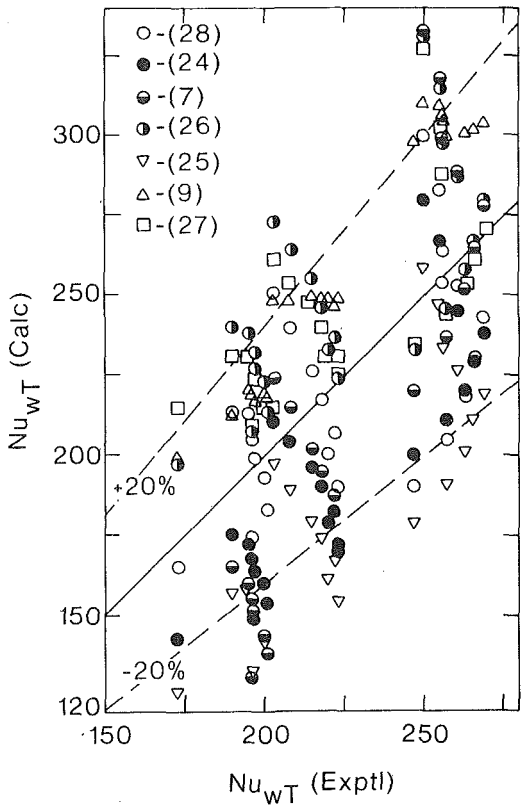

Fig. 7 Comparison of experimental and calculated heat transfer coefficient for a smooth tube

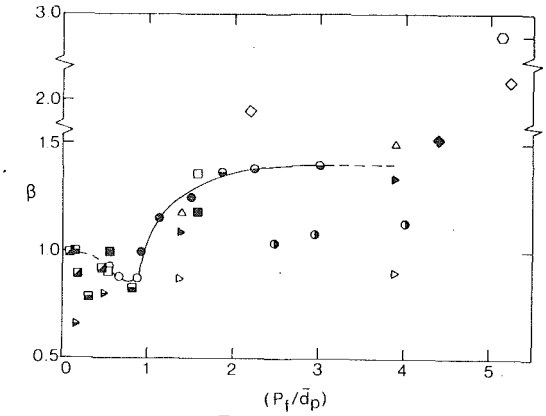

Fig. 8 Variation of β with $P_f/\bar{d}_p$. For symbols and other related details see Table 4. The continuous curve is drawn on the basis of present data for V-thread tubes and dashed curves are extrapolations

decreases with increase in value of $(P_f/\bar{d}_p)$ up to about 0.8, attains a minimum value, and then steadily increases with $(P_f/\bar{d}_p)$. However, the rate of increase decreases with increase in $(P_f/\bar{d}_p)$ and tends to a constant value for larger values of $(P_f/\bar{d}_p)$.

It is well known [1, 22] that the principal mode of heat removal is by unsteady state conduction to the moving solid particles at temperatures where radiation can be neglected (<900K) and for non-pressurized systems involving particles of sufficiently small size so that gas convection is negligible (<1mm). Thermal energy is propagated by conduction through the interstitial gas phase enclosed between the heater wall and the absorbing particles and between the absorbing particles. The amount of heat removed from the heater surface depends on the average bed porosity in the vicinity of the heater or gas conduction paths between solid particles and the heat transfer surface, and particle residence time. Although the surface area of a V-thread tube of 0.24 mm pitch is about 1.98 times the surface area of a smooth tube of the same outside diameter, the heat transfer rates for the former are smaller for all the three sizes of glass beads. This can be explained by referring to Figs. 9(*a*) and 9(*b*) and

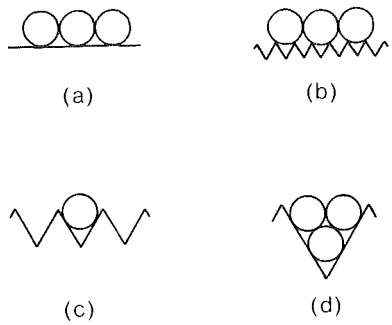

Fig. 9 Particle and heat transfer surface contact for (*a*) smooth tube, (*b*) tube with fine roughness, P_f/d_p = 0.5, (*c*) tube with matching roughness, P_f/d_p = 1.2, and (d) tube with coarse roughness, P_f/d_p = 2.5

following a somewhat similar argument as given by Korolev and Syromyatnikov [6] and by Vijayaraghavan and Sastri [5], while explaining their heat transfer data for a rough surface. As the value of $(P_f/\bar{d}_p)$ is increased from zero, the value of average porosity or conduction path between heat transfer surface and first row of solid particles, increases as is evident from a comparison of Figs. 9(*a*) and 9(*b*). The resistance to heat flow is greater for the case shown in Fig. 9(*b*) than for the case corresponding to Fig. 9(*a*) because of longer heat conduction path or larger value of porosity in the vicinity of the heat transfer surface. Further, due to the irregularities of the surface the particle residence time close to the heat transfer surface will increase. Thus, as $(P_f/\bar{d}_p)$ increases from 0 to about 0.8, the heat conduction path increases while the particle residence time increases. As a result $h_{wfb\ max}$ for rough tubes or β decreases.

Fig. 9(*c*) represents a typical case when $(P_f/\bar{d}_p)$ is greater than 1 but less than 2. In this case, most of the solid particles have multiple contact with the heat transfer surface and therefore more surface area of the glass spheres is available for heat transfer from the heated tube surface in comparison to the case of a smooth tube, Fig. 9(*a*). This will enhance the heat transfer rate. The increase in $h_{wfb\ max}$ for a V-thread tube $(P_f/\bar{d}_p = 1.8)$ is about 34 percent over a smooth tube. The actual increase in the value of $h_{wfb\ max}$ will depend upon whether or not any of the V-threads have been clogged by bed particles. Particle clogging was observed in our experiments with 0.40 mm pitch V-threads while the threads remained unclogged for 0.79 mm pitch V-threads. When the particle size is much smaller than the pitch, i.e., $P_f/\bar{d}_p > 2$, there will be only limited number of particles having multiple contact with the heat transfer surface and their number will further decrease with increase in $(P_f/\bar{d}_p)$. Thus the rate of increase of β would decrease with the increase in $(P_f/\bar{d}_p)$. The maximum heat transfer coefficient for rough tubes with $(P_f/\bar{d}_p) = 3$ is found to be about 40 percent greater than for smooth tubes in present experiments (Fig. 8). The heat transfer coefficient for the V-thread tube having a pitch 0.79 mm (Curve 1) is found to be always larger than the heat transfer coefficient for the knurled tube (Curve 4) for all the three particle sizes. This is probably because V-threads are less effective in hampering the solids motion in the bed close to the tube surface than the knurled tube surface.

Fig. 8 also illustrates the effect of $(P_f/\bar{d}_p)$ on maximum heat transfer for knurled tube. In this case the increase in $h_{wfb\ max}$ is smaller than for V-thread tubes. For example, when $P_f/\bar{d}_p = 4$, the maximum heat transfer coefficient is only about 13 percent larger than for a smooth tube.

Values of bulk bed porosity, ϵ, for particles of $\bar{d}_p = 265\ \mu$m as obtained from equation (3) and measurement of ΔP by probes located 13.3 cm above and below the tube vary between 0.43 and 0.48 over the entire mass fluidizing velocity range of 0.11 to 0.60 kg/m^{2}s. The value is insensitive to the surface roughness of the tube as expected, but shows a slight decrease with increase in particle diameter. Bulk bed porosity also influences the rate of heat transfer from an immersed surface in a fluidized bed and therefore this parameter has been used frequently to correlate the heat transfer data [1]. In our experiments, the value of the bulk bed porosity has not changed significantly and consequently the variations in the heat transfer coefficient from one

Table 4 Key to Figs. 8 and 10

Symbol	Reference	Tube Orientation	Nature of surface roughness	Orientation of surface roughness	ℓ, mm	P_f, mm	Solid particles Material	$\bar{d}_p$, μm
○	Present	Horizontal	60°-v Threads	Transverse	0.204	0.235	Glass beads	265,357,427
●	Present	Horizontal	60°-v Threads	Transverse	0.344	0.397	Glass beads	265,357,427
◒	Present	Horizontal	60°-v Threads	Transverse	0.687	0.794	Glass beads	265,357,427
◑	Present	Horizontal	Knurling	Diagonal	1.07	1.06	Glass beads	265,357,427
△	[5]	Vertical	60°-v Threads	Longitudinal	0.687	0.794	Glass beads	205,565
▷	[5]	Vertical	60°-v Threads	Transverse	0.687	0.794	Glass beads	205,565
▶	[5]	Vertical	Knurling	—	—	0.80	Glass beads	205,565
▶	[5]	Vertical	Knurling	—	—	0.10	Glass beads	205,565
□	[6]	Vertical plate	V-grooves	Longitudinal	0.400	0.500	Chamotte Polystyrene	320 720
■	[6]	Vertical plate	V-grooves	Transverse	0.400	0.500	Chamotte Polystyrene	320 720
◪	[6]	Vertical plate	Treated with corundum particles	—	0.002	0.06	Corundum Chamotte Polystyrene	120 320 720
▬	[6]	Vertical plate	Treated with corundum particles	—	0.010	0.10	Corundum Chamotte Polystyrene	120 320 720
♦	[17, 18]	Vertical	helical fins	Transverse	1.47	2.674	Glass beads	610
◇	[17, 18]	Vertical	helical fins	Transverse	1.50	1.33	Glass beads	610,254
○	[12]	Horizontal	helical fins	Transverse	5.94	2.82	Glass beads	551

surface to the other for a given particle size and mass fluidizing velocity cannot be attributed to bulk bed porosity.

Comparison with Earlier Studies

The values of β obtained from the present work are compared with the similar values of previous investigations [5, 6, 12, 17] in Fig. 8. For transverse groove horizontal and longitudinal groove vertical, and knurled surfaces, the values of β are in qualitative agreement with each other. The β values for rough surfaces are smaller than unity when $(P_f/\bar{d}_p) < 1$, and are greater than unity when $(P_f/\bar{d}_p) > 1$ [2, 3, 5, 6]. Vijayaraghavan and Sastri [5] have not reported the average particle diameter, but have mentioned that the size range was narrow. We have, therefore, approximated the average particle sizes as 205 μm and 565 μm. The values of β obtained in the present study for transverse V-thread horizontal tube and by Vijayaraghavan and Sastri [5] for longitudinal V-groove vertical tube and by Korolev and Syromyatnikov [6] for longitudinal V-groove vertical plate are in good agreement with one another. This is easily understandable when one recalls that in all these three cases [5, 6] not only the fin shape is similar but also their orientation with respect to flow is identical. The values β for small fins [12, 17] are greater than the values found in the present study. This is mainly due to the larger area of the heat transfer surface provided by finned tubes for the same $(P_f/\bar{d}_p)$ ratio as shown below.

Another way of comparing the performance of rough and finned tubes is to consider the quantity, ϕ, which is defined as the ratio of the effective heat transfer coefficient for rough or finned tubes based on the total surface area of the tube, h_{wft}, to the heat transfer coefficient for a smooth tube, h_w, both referring to identical fluidized bed conditions. The quantity ϕ is plotted in Fig. 10 as a function of $(P_f/\bar{d}_p)$ for those values of $(G - G_{mf})/G_{mf}$ where maximum values of h_{wft} and h_w are found. Once again there is a good agreement between the present and the previous investigations [5, 6, 12] for longitudinal V-thread vertical tube and surface [5, 6], transverse finned horizontal tube [12], and present results for transverse V-thread finned horizontal tube. However, values of ϕ for transverse V-groove vertical tube [5] and vertical plate [6] are smaller as compared to the values of ϕ for longitudinal V-groove vertical tube [5] and vertical plate [6] for similar values of $(P_f/\bar{d}_p)$ ratio, height of projections and fluidizing conditions. The reason for this is that the projections perpendicular to flow cause greater obstruction to particle flow than the projections parallel to the flow. This will result in an increase in particle residence time for tubes having projections perpendicular to flow which decrease ϕ. The values of Chen and Withers [17] referring to a vertical tube with transverse fins appear to be greater than the rest of the data.

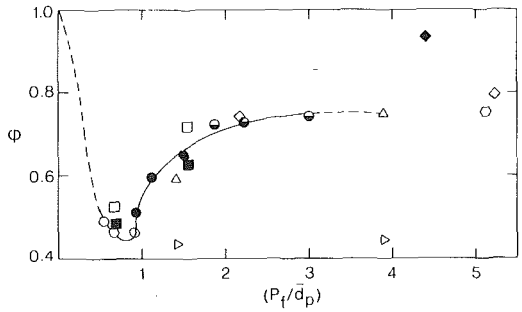

Fig. 10 Variation of ϕ with $P_f/\bar{d}_p$. Rest of the legend is same as in Fig. 8

Proposed Correlation

For $(P_f/\bar{d}_p) > 0.95$, the values of ϕ for the present data for V-thread tubes and for $G/G_{mf} > 1.3$, are correlated by the following equation:

$$\phi = 0.549 + 0.227\,[1 - (P_f/\bar{d}_p)^{-1.91}] \quad (4)$$

Further, it follows from the definition of ϕ that

$$\mathrm{Nu}_{wftT} = \mathrm{Nu}_{wT}.\ \phi \quad (5)$$

where Nu_{wT} can be calculated from the correlations for smooth tubes given in Table 3.

The present data for V-thread tubes are compared with the predicted values of Nu_{wftT} and the results are given in Table 3. It is to be noted that the modified correlation of Ternovskaya and Korenberg [28] gives the best predictions. As seen in Fig. 11, almost all the predicted values are within ±20 percent of the experimental values of Nu_{wftT}.

Concluding Comments

Hager and Thomson [29] studied bubble motion around the horizontal tubes with longitudinal and transverse fins. They observed that bubbles do not penetrate into the space between fins and thus solids have a poor renewal rate. This situation is more serious with close spaced fins, and much of the advantage in using large number of fins is neutralized. Genetti, et al. [9] observed a reduction in heat transfer in some cases for finned tubes and attributed this to particle hold up. This reduction is due to the inability of bubbles to penetrate the fin space and subsequently solids are defluidized in fin spacing. Due to the small height of the surface roughness in our experiments, the bubbles are able to renew the solids in the grooves. A practical economic advantage of the V-thread rough tubes over the finned tubes is the ease and the cost of fabrication. However, it may be noted that

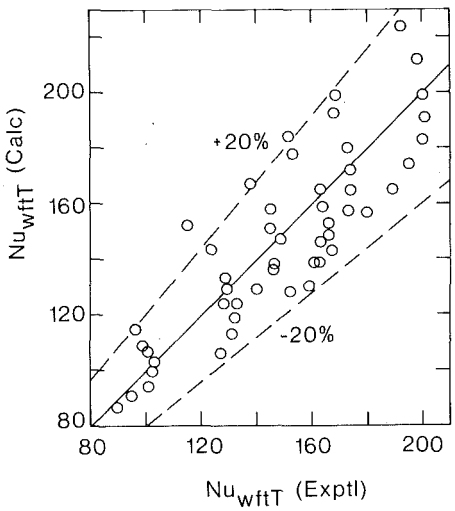

Fig. 11 Comparison of predicted and experimental Nusselt numbers for V-thread tubes

for rough surfaces when $P_f/\overline{d}_p < 1$, the heat transfer process is more efficient for smooth tubes than for rough tubes both having the same outside diameter. Therefore, the design of boiler tubes must consider values for $P_f/\overline{d}_p > 1$.

From the above discussion it is clear that the mechanism of heat transfer from surfaces is sensitively dependent on the $P_f/\overline{d}_p$ ratio. For $P_f/\overline{d}_p < 1$, the heat transfer coefficient for a rough surface is always less than the smooth surface of the same size and it is due to the increase in the heat conduction path. Such surfaces where this mechanism is solely responsible for reducing the heat transfer rate may be called a rough surface. For $P_f/\overline{d}_p > 1$, the heat transfer coefficient value is controlled by many factors, viz., (1) the effective area of the heat transfer surface, (2) the effective area of the particle which exchanges heat with the surface, and (3) the residence time of the particles. The relative roles of these factors may be understood in relation to fin geometry. For example, for V-thread tubes the contribution of (2) predominates when $1 < P_f/\overline{d} < 2$ and the net heat transfer increases. For $P_f/\overline{d}_p > 2$, the bulk of the increase in heat transfer is attributed to (1). In general, whenever the heat transfer coefficient is augmented by (1), it seems appropriate to call it a finned surface. These remarks may help in classifying the rough and finned surfaces based on the mechanism of heat transfer.

Acknowledgments

This research is partly supported by the Department of Energy under contract No. EX-77-C-01-1787 and partly by National Science Foundation under Grant No. ENG77-08780A01.

References

1 Saxena, S. C., Grewal, N. S., Gabor, J. D., Zabrodsky, S. S., and Galershtein, D. M., "Heat Transfer Between a Gas Fluidized Bed and Immersed Tubes," *Advances in Heat Transfer*, Vol. 14, 1978, pp. 149–247.

2 Neukirchen, B. and Blenke, H., "Design of Horizontal Tube Bundles in Gas-Fluidized Bed Reactors From a Thermal Engineering Viewpoint," *Chem. Ing. Tech.*, Vol. 45, 1973, pp. 307–312.

3 Gelperin, N. I., Einshtein, V. G., Toskubaev, I. N., and Vasiliev, S. K., "Characteristics of Heat Transfer From Low-finned Tubes," *Trudy MITKhT*, Moscow, Vyp. 11, 1974, pp. 116–118.

4 D'Albon, G., Peretz, D., Cernescu, V., Bendescu, I., Clotan, V., and Lozonschi, Gh., "Trecerea Caldurii in Cazul Corpuriler cu Microaripioare Imersate Inter-un Strat Fluidizat," *Bul. Inst. Politechnic din Jasi*, Vol. XVII, Sec. IV, N 3–4, 1971, pp. 101–106.

5 Vijayaraghavan, M. R., and Sastri, V. M. K., "Effect of Surface Roughness on Heat Transfer in Fluidized Beds," Conference on Future Energy Production, Int. Center Heat and Mass Transfer, Dubrovnic, 1975, pp. 571–578.

6 Korolev, V. N. and Syromyatnikov, N. I., "Heat Transfer from a Surface with Artificial Roughness to a Fluidized Bed," *Journal of Engineering Physics*, Vol. 28, No. 6, 1975, pp. 698–700.

7 Petrie, J. C., Freeby, W. A., Buckham, J. A., "In-Bed Heat Exchangers," *Chem. Engr. Progr.*, Vol. 64, No. 7, 1968, pp. 45–51.

8 Bartel, W. J., Genetti, W. E. and Grimmett, E. S., "Heat Transfer from a Horizontal Discontinuous Finned Tube in a Fluidized Bed," *Chem. Eng. Progr. Sym. Ser.*, Vol. 116, No. 67, 1971, pp. 85–89.

9 Genetti, W. E., Schmall, R. A. and Grimmett, E. S., "The Effect of Tube Orientation on Heat Transfer With Bare and Finned Tubes in a Fluidized Bed," *Chem. Engr. Progr. Sym. Ser.*, Vol. 116, No. 67, 1971, pp. 90–96.

10 Bartel, W. J. and Genetti, W. E., "Heat Transfer from a Horizontal Bundle of Bare and Finned Tubes in an Air Fluidized Bed," *Chem. Eng. Progr. Sym. Ser.*, Vol. 69, No. 128, 1973, pp. 85–93.

11 Priebe, S. J. and Genetti, W. E., "Heat Transfer from a Horizontal Bundle of Extended Surface Tubes to an Air Fluidized Bed," *AIChE Sym. Ser.*, Vol. 73, No. 161, 1977, pp. 38–43.

12 Genetti, W. E. and Kratovil, M. T., "Heat Transfer from Helical Finned Tubes in a Fluidized Bed," Paper No. 4b, 83rd National AIChE meeting held in Houston, Texas, March 20–24, 1977.

13 Natusch, H. J., and Blenke, H., "Zur Wärmeübertragung an Horizontalen Längsrippenrohren in Gas-Fliesbetten," *Verfahrenstechnik*, Vol. 8, No. 10, 1974, pp. 286–293.

14 Natusch, H. J., and Blenke, H., "Wärmeübertragung an Rippenrohren in Gas-Fliesbetten," *Verfahrenstechnik*, Vol. 7, No. 10, 1973, pp. 293–296.

15 Gelperin, N. I., Einshtein, V. G., and Toskubaev, I. N., "Heat Transfer Between Finned Tubes and Fluidized Bed of Granular Material," *Khim. Tekhnolog. Topliv i Masel*, Vol. 2, 1972, pp. 42–43.

16 Gelperin, N. I. Einshtein, V. G.; Toskubaev, I. N., Vasiliev, S. K. and Ryspaev, N. S., Fluidized Bed-to-Finned Tubes Heat Transfer," *Trudy TITChT*, Vyp. 1, 1974, pp. 165–168.

17 Chen, J. C. and Withers, J. G., "An Experimental Study of Heat Transfer from Plain and Finned Tubes in Fluidized Beds," AIChE Paper No. 34, The 15th National Heat Transfer Conference, San Francisco, Aug. 12, 1975.

18 Chen, J. C., "Heat Transfer to Tubes in Fluidized Beds," ASME paper No. 76-HT-75, 16th National Heat Transfer Conference, St. Louis, Aug. 9–11, 1976.

19 Kunii, D., and Levenspiel, O., *Fluidization Engineering*, John Wiley, New York, 1969.

20 Grewal, N. S., and Saxena, S. C., "Investigations of Heat Transfer From Immersed Tubes in a Fluidized Bed," 4th Natl. Heat Mass Transfer Conf., India, 1977, pp. 53–58.

21 Zabrodsky, S. S., *Hydrodynamics and Heat Transfer in Fluidized Beds*, The M.I.T. Press, Cambridge, Massachusetts, 1966.

22 J. S. M. Botterill, *Fluid-Bed Heat Transfer*, Academic Press, New York, 1975.

23 Ziegler, E. N., Koppel, L. B., and Brazelton, W. T., *Ind. Eng. Chem. Fund.*, Vol. 3, No. 4, 1964, pp. 324–328.

24 Andeen, B. R. and Glicksman, L. R., "Heat Transfer to Horizontal Tubes in Shallow Fluidized Beds," ASME—AIChE Heat Transfer Conference, St. Louis, Mo. Aug. 9–11, 1976 Paper No. 76-HT-67.

25 Vreedenberg, H. A., "Heat Transfer Between a Fluidized Bed and A Horizontal Tube," *Chem. Engr. Sci.*, Vol. 9, 1958, pp. 52–60.

26 Ainshtein, V. A., "An Investigation of Heat Transfer Process Between Fluidized Beds and Single Tubes Submerged in the Bed," in Zabordsky, S. S., "Hydrodynamics and Heat Transfer in Fluidized Beds," M.I.T. Press, Cambridge, Massachusetts, 1966, pp. 270–272.

27 Gelperin, N. I., Kruglikov, V. Ya., and Ainshtein, V. G., in Ainshtein, V. G., and Gelperin, N. I., "Heat Transfer between a Fluidized Bed and a Surface," *Inter. Chem. Engrg.*, Vol. 6, No. 1, 1966, pp. 67–73.

28 Ternovskaya, A. N. and Korenberg, Yu.G., "Fluidized Bed Furnaces and Heat Exchangers," *Naukova Dumka*, Kiev, 1973.

29 Hager, W. R., and Thomson, W. J., "Bubble Behavior Around Immersed Tubes in a Fluidized Bed," *AIChE Sym. Ser.* No. 128, Vol. 69, 1973, pp. 68–77.

E. M. Sparrow
Fellow ASME

J. E. Niethammer
Department of Mechanical Engineering,
University of Minnesota,
Minneapolis, Minn. 55455

Natural Convection in a Ternary Gas Mixture—Application to the Naphthalene Sublimation Technique

An analysis is made of natural convection mass transfer in a ternary gas mixture adjacent to a vertical plate. The main feature of the analysis is the proper mathematical description of the buoyancy force and of the boundary conditions. With regard to the latter, account is taken of the selective impermeability of the plate to certain components of the mixture. The governing boundary layer equations are shown to admit a similarity solution, and a numerical scheme for solving the similarity equations and boundary conditions is outlined. The general formulation is specialized to the case of sublimation from a solid, vertically oriented naphthalene plate situated in a humid air environment. Solutions were obtained for temperature levels corresponding to those encountered in practice and for relative humidities of water vapor between zero and one. It was found that the mass transfer results were unaffected by the presence of humidity, and this finding gives license to the utilization of the naphthalene technique without special concern about the humidity level. In addition, the transverse velocity at the plate surface associated with the mass transfer was too small to affect the magnitude of the mass transfer.

Introduction

In this paper, natural convection flow and mass transfer in a ternary gas mixture adjacent to a vertical plate is analyzed in general and then specialized to the sublimation of naphthalene in humid air. The initial motivation for the analysis was the need to appraise the influence of humidity on the results provided by the naphthalene sublimation technique. This mass transfer technique has been used extensively in conjunction with the analogy between heat and mass transfer to determine results for complex heat transfer systems.

In the application of this technique, the surface(s) for which the transfer coefficients are desired is fabricated from solid naphthalene (e.g., by casting). During a data run, air is passed over the surface for a metered period of time, and vapor sublimes from the surface into the air stream. The overall transfer coefficient is obtained by measuring (via a sensitive balance) the change of mass of the naphthalene wall, while local coefficients are determined by measurement of the local recession of the surface. The transfer coefficients are based on the difference in the concentrations of naphthalene vapor at the surface and in the bulk flow. A typical value of the vapor concentration at the surface is 4×10^{-7} gm/cm^3.

In the execution of the experiments, it is customary to take air from the laboratory room and, without dehumidification, pass it through the apparatus, thereby accepting the existent humidity. The humidity level may vary appreciably with climatic conditions and with the season. Even at moderate values of relative humidity, the concentration of water vapor in the air is appreciably larger than the aforementioned naphthalene vapor concentration.

The transport of naphthalene vapor takes place by convection and diffusion, with the diffusion process being dominant near the surface. The naphthalene concentration gradients, which are the driving potential for the diffusion, are exceedingly small. While the gradients are primarily established by the surface concentration of the naphthalene vapor, they are also affected by the concentrations of the other gaseous species that are present. Therefore, the self-consistency of naphthalene mass transfer results corresponding to the random and uncontrolled presence of water vapor in the air may be questioned.

The naphthalene sublimation technique can also be employed to study natural convection as well as forced convection. Since naphthalene vapor is heavier than air, a density difference is created which induces a natural convection downflow adjacent to the naphthalene surface (analogous to that for a cooled heat transfer surface). The driving force for the natural convection is the difference in the densities of the gaseous mixtures at the surface and in the free stream. This difference is extremely small and might well be affected by the presence of different amounts of water vapor corresponding to randomly different levels of humidity. The possible influence of the water vapor on the concentration gradients which drive the naphthalene vapor diffusion, as discussed in the preceding paragraph, is also applicable to natural convection.

In view of the foregoing considerations, it may be concluded that if the presence of water vapor does influence the naphthalene mass transfer results, the effects will be greater for natural convection than for forced convection. A natural convection problem was, therefore, selected to study the possible effects of the water vapor.

Contributed by the Heat Transfer Division for publication in the JOURNAL OF HEAT TRANSFER. Manuscript received by the Heat Transfer Division, September 22, 1978.

In addition to the naphthalene sublimation technique, there are, presumably, other applications where natural convection mass transfer in multi-component gas mixtures is encountered. Therefore, the analysis will first be performed for a general ternary mixture and then specialized to the naphthalene vapor/water vapor/air system. For the latter, numerical solutions are carried out in order to obtain quantitative information about the possible influences of the presence of water vapor. It should also be noted that once the analytical approach for ternary mixtures has been established, then the generalization to a large number of species components follows without difficulty.

A schematic diagram of the situation being studied is presented in Fig. 1. As pictured there, a vertical plate is situated in an otherwise quiescent environment in which there is a gaseous ternary mixture characterized by mass fractions $W_{1\infty}$, $W_{2\infty}$, $W_{3\infty}$, respectively for species 1, 2, and 3. Depending on the boundary conditions at the plate, the density of the fluid adjacent to the surface will be either greater or less than that of the ambient fluid, giving rise to either a downflow or an upflow. For concreteness, a downflow will be analyzed here. The analysis for an upflow is identical to that for a downflow except for a change of sign in the buoyancy term.

Although the boundary layer thickness is shown schematically in Fig. 1 as a single dashed line, there are, in actuality, four boundary layers whose respective thicknesses may differ from each other. The four boundary layers are that for the velocity and those for the concentrations of each of the three species.

The entire system is isothermal so that there are no heat transfers, and density differences result solely from differences in the concentrations of the individual components. It is also assumed that the flow is laminar.

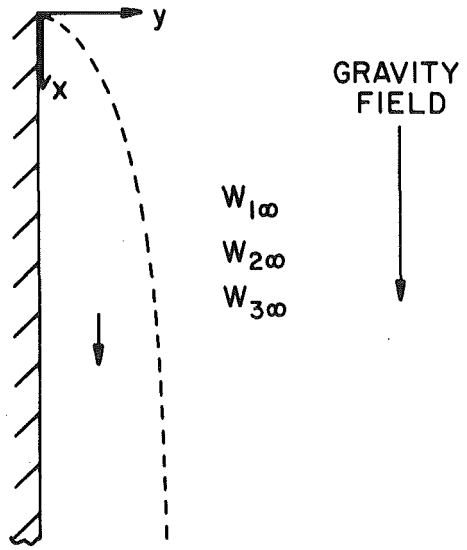

Fig. 1 Schematic diagram of the vertical plate problem

Analysis

Governing Equations. The first objective of the analysis is to derive the buoyancy force which drives the natural convection. At any position x, y in the boundary layer, the local buoyancy force per unit mass f_B is

$$\rho f_B = -\partial p/\partial x + \rho g \tag{1}$$

or

$$f_B = g(1 - \rho_\infty/\rho) \tag{2}$$

where, in accordance with boundary layer theory, $\partial p/\partial x$ has been evaluated in the ambient fluid as $\rho_\infty g$. In equation (2), both ρ and ρ_∞ represent mixture densities, respectively at x, y and in the ambient. To recast equation (2) in a form that is useful for the further analysis of the problem, it is necessary to express the density ratio ρ_∞/ρ in terms of the mass fractions $W_i (i = 1, 2, 3)$ of the components.

To this end, the mixture is treated as a perfect gas so that

$$\rho = p/(\overline{R}/M)T, \quad \rho_\infty = p_\infty/(\overline{R}/M_\infty)T_\infty \tag{3}$$

For a boundary layer, the total pressure is constant at a given elevation x, so that $p = p_\infty$ and, furthermore, $T = T_\infty$ since the fluid is isothermal. From this, it follows that

$$\rho_\infty/\rho = M_\infty/M \tag{4}$$

where both M_∞ and M denote mixture molecular weights.

For a ternary mixture of perfect gases, it is well known that

$$M = x_1M_1 + x_2M_2 + x_3M_3 \tag{5}$$

where the x_i are mole fractions. In addition, the relationship between the mole fraction x_i and mass fraction W_i, which are respectively defined as

$$x_i = p_i/p, \quad W_i = \rho_i/\rho \tag{6}$$

is

$$x_i = W_i(M/M_i) \tag{7}$$

and since $p = p_1 + p_2 + p_3$ and $\rho = \rho_1 + \rho_2 + \rho_3$, then

$$x_1 + x_2 + x_3 = 1, \quad W_1 + W_2 + W_3 = 1 \tag{8}$$

With the aid of equations (7) and (8), the molecular weight expression (5) can be written as

$$M = M_1M_2M_3/(M_1M_2 + W_1M_2M_3 + W_2M_1M_3 - W_1M_1M_2 - W_2M_1M_2) \tag{9}$$

where, for reasons which will be discussed shortly, W_3 has been eliminated. An equation similar to (9) can be written for M_∞ by replacing W_1 and W_2 with $W_{1\infty}$ and $W_{2\infty}$.

Nomenclature

c = constant in similarity variable, equation (23a)
D_i = diffusion coefficient of component i in mixture
F = reduced stream function, equation (24)
f_B = buoyancy force per unit mass
g = acceleration of gravity
j_i = diffusive mass flux of component i
K = mass transfer coefficient, equation (41)
L = plate length
M = molecular weight of mixture
M_i = molecular weight of component i
$\dot{M}$ = surface-integrated mass transfer rate
$\dot{m}$ = local mass flux
$\dot{m}_i$ = local mass flux of component i
p = system pressure
p_i = partial pressure of component i
$\overline{R}$ = universal gas constant
Sc_i = Schmidt number of component i
Sh = Sherwood number, equation (41)
T = temperature
U = dimensionless streamwise velocity, equation (56)
u = streamwise velocity
V = dimensionless transverse velocity, equation (55)
v = transverse velocity
W_i = mass fraction of component i, ρ_i/ρ
x = streamwise coordinate
x_i = mole fraction of component i, p_i/p
y = transverse coordinate
η = similarity variable, equation (23)
θ_i = scaled mass fraction, equation (24)
μ = mixture viscosity
ν = mixture kinematic viscosity
ρ = mixture density
ρ_i = density of component i
ϕ = relative humidity
ψ = stream function

Subscripts

0 = corresponds to $\phi = 0$
00 = corresponds to $\phi = 0$ and $v_w = 0$
p = principal
s = supplementary
w = at the wall
ϕ = corresponds to relative humidity ϕ
∞ = in the ambient
1, 2, 3 = mixture components

Then, the expression $1 - (M_\infty/M) = 1 - (\rho_\infty/\rho)$ can be evaluated and the buoyancy force f_B (equation (2)) follows as

$$f_B/g = \frac{(W_1 - W_{1\infty})(M_1 - M_3)/M_1 + (W_2 - W_{2\infty})(M_2 - M_3)/M_2}{1 - W_{1\infty}(M_1 - M_3)/M_1 - W_{2\infty}(M_2 - M_3)/M_2} \quad (10)$$

This equation shows that the buoyancy force can be expressed as a linear combination of the mass fraction differences $(W_1 - W_{1\infty})$ and $(W_2 - W_{2\infty})$. The factors which multiply these quantities reflect the transformation of densities into mass fractions and the elimination of W_3 via the relation $W_3 = 1 - W_1 - W_2$.

The natural convection mass transfer problem is governed by the momentum equation for the mixture and mass conservation equations for the individual species. For laminar boundary layer flow, the momentum conservation equation is

$$u(\partial u/\partial x) + v(\partial u/\partial y) = f_B + (1/\rho)\partial/\partial y(\mu \partial u/\partial y) \quad (11)$$

in which ρ and μ respectively denote local mixture properties. Mass conservation can be expressed in either of two equivalent formats. In one, a conservation equation is written for each component. In the second, conservation equations are written for two of the three components along with a mass conservation equation for the mixture (the latter is identical to the continuity equation for a single component flow). The second approach is simpler to employ and will be adopted here.

For components 1 and 2, the species conservation equations are

$$u(\partial W_1/\partial x) + v(\partial W_1/\partial y) = (1/\rho)\partial/\partial y(\rho D_1 \partial W_1/\partial y) \quad (12)$$

$$u(\partial W_2/\partial x) + v(\partial W_2/\partial y) = (1/\rho)\partial/\partial y(\rho D_2 \partial W_2/\partial y) \quad (13)$$

In these equations, D_1 and D_2 denote the ternary diffusion coefficients of components 1 and 2, respectively. For the mixture, mass conservation takes the form

$$\partial(\rho u)/\partial x + \partial(\rho v)/\partial y = 0 \quad (14)$$

Equations (11–14), supplemented by the buoyancy force representation (10), describe the local physical processes in the flow. The four equations contain four unknowns, the velocity components u and v and the mass fractions W_1 and W_2. The thermophysical properties ρ, μ, and D which appear in these equations may depend on the mass fractions as well as on the given values of the pressure p and temperature T. It may be noted that the governing equations do not explicitly involve the mass fraction W_3. The elimination of W_3 as an active unknown was accomplished by algebraic manipulation during the derivation of equation (10) and by choosing to use the mixture mass conservation equation in lieu of a species conservation equation for component 3. This elimination is advantageous because it reduces the number of active unknowns from five to four. Once W_1 and W_2 have been determined, then W_3 follows as $1 - W_1 - W_2$.

To complete the formulation of the problem, the boundary conditions have to be dealt with.

Boundary Conditions. It is necessary to provide boundary conditions both at the plate surface and in the ambient fluid beyond the boundary layer. The latter are of simpler form and are dealt with first.

As was implied in the problem description stated in the Introduction, the mass fractions of the components in the ambient fluid are regarded as known. Furthermore, the streamwise (i.e., vertical) velocity is zero beyond the boundary layer. These boundary conditions can be formally stated as

$$W_1 = W_{1\infty}, \quad W_2 = W_{2\infty}, \quad u = 0 \text{ as } y \to \infty \quad (15)$$

At the plate surface, two physically relevant mass transfer boundary conditions will be considered: (1) prescribed vapor pressure or concentration, and (2) surface impermeability. Each component of the mixture may be assigned either one or the other of these boundary conditions (except that the assignment of the impermeability condition to all three components suppresses the natural convection altogether).

The two types of surface boundary conditions can be illustrated by considering the natural convection problem for sublimation of naphthalene from a vertical plate to a humid air environment. The naphthalene plate is isothermal and equal in temperature to that of the surroundings. By employing the vapor pressure—temperature relationship, the naphthalene vapor pressure at the wall can be calculated and then used to compute the vapor density (i.e., the concentration) via the perfect gas law. On the other hand, the naphthalene plate is impermeable to both the air and the water vapor.

The mathematical representation of the mass transfer boundary conditions at the plate surface will now be considered. To this end, attention will be focused on the representative case where the vapor pressure p_{1w} at the surface is known for component 1 and the surface is impermeable to both components 2 and 3.

From the given values of the vapor pressure p_{1w} and the total pressure p, the mole fraction x_{1w} can be evaluated and thereby regarded as known. Then, by employing equations (5), (7), and (8),

$$W_{1w} = \frac{x_{1w}M_1(1 - W_{2w} + W_{2w}M_3/M_2)}{x_{1w}(M_1 - M_3) + M_3} \quad (16)$$

This equation interrelates the wall values of W_1 and W_2.

Another relationship can be obtained from the impermeability conditions for components 2 and 3. At any surface location x, it is required that the local mass fluxes $\dot{m}_2(x)$ and $\dot{m}_3(x)$ are zero. There are two contributions to $\dot{m}_i$, namely, a convective contribution $\rho_{iw}v_w$ (where $v_w(x)$ is the transverse velocity at the wall) and a diffusive contribution j_{iw}. Therefore, for components 2 and 3

$$\rho_{2w}v_w + j_{2w} = 0, \quad \rho_{3w}v_w + j_{3w} = 0 \quad (17)$$

from which it follows that $j_{2w}/\rho_{2w} = j_{3w}/\rho_{3w}$. Furthermore, by the definition of the diffusive fluxes [1], $j_1 + j_2 + j_3 = 0$, so that

$$j_{2w} = -j_{1w}\rho_{2w}/(\rho_w - \rho_{1w}) \quad (18)$$

in which ρ_{3w} has been eliminated via the relation $\rho = \rho_1 + \rho_2 + \rho_3$. The diffusive flux j_i is connected to the gradient $\partial W_i/\partial y$ by Fick's law

$$j_i = -\rho D_i(\partial W_i/\partial y) \quad (19)$$

which can be incorporated into equation (18), giving

$$(\partial W_2/\partial y)_w = -(\partial W_1/\partial y)_w(D_1/D_2)W_{2w}/(1 - W_{1w}) \quad (20)$$

Equations (16) and (20) provide the needed relationships between the wall values of W_1, W_2, $\partial W_1/\partial y$, and $\partial W_2/\partial y$.

The impermeability conditions (17) also yield a boundary condition for the wall velocity v_w. By adding these equations and then eliminating j_{3w} and ρ_{3w} as in the derivation of equation (18), there results

$$v_w = j_{1w}/(\rho_w - \rho_{1w}) = -D_1(\partial W_1/\partial y)_w/(1 - W_{1w}) \quad (21)$$

The final boundary condition at the wall stems from the no-slip condition, which gives

$$u = 0 \quad \text{at} \quad y = 0 \quad (22)$$

All told, taking account of both the plate surface and the ambient fluid, there are seven boundary conditions, respectively expressed by equations (15, 16, 20, 21), and (22).

Similarity Transformation. It will now be demonstrated that the governing equations and boundary conditions admit a similarity solution. First, a similarity variable is introduced as

$$\eta = cx^{-1/4}\int_0^y (\rho/\rho_\infty)dy \quad (23)$$

where

$$c^4 = \frac{g(M_1 - M_3)(W_{1w} - W_{1\infty})/4\nu_\infty^2}{M_1 - W_{1\infty}(M_1 - M_3) - W_{2\infty}(M_1/M_2)(M_2 - M_3)} \quad (23a)$$

In addition, new dependent variables are defined by

$$F(\eta) = \psi/4\nu_\infty cx^{3/4}, \quad \theta_1(\eta) = (W_1 - W_{1\infty})/(W_{1w} - W_{1\infty}), \quad \theta_2(\eta) = (W_2 - W_{2\infty})/(W_{2w} - W_{2\infty}) \quad (24)$$

It may be noted that the makeup of the constant c was selected to give the transformed momentum equation a filial resemblance to the momentum equation of the conventional (thermal) natural convection problem. The mixture properties ρ_∞ and ν_∞ in the ambient fluid were selected as reference values because the mass fractions needed for their evaluation are assumed known.

The continuity equation (14) is satisfied by taking

$$(\rho/\rho_\infty)u = \partial\psi/\partial y, \quad (\rho/\rho_\infty)v = -\partial\psi/\partial x \tag{25}$$

and momentum conservation (11) becomes, after transformation,

$$\frac{d}{d\eta}\left[\frac{\rho\mu}{(\rho\mu)_\infty}F''\right] + 3FF'' - 2(F')^2 + \theta_1 + \theta_2\left[\frac{W_{2w}-W_{2\infty}}{W_{1w}-W_{1\infty}}\right]\left[\frac{M_1(M_2-M_3)}{M_2(M_1-M_3)}\right] = 0 \tag{26}$$

where the primes denote differentiation with respect to η. The species conservation equations (12) and (13) for components 1 and 2 are then transformed and become

$$\frac{d}{d\eta}\left[\frac{\rho^2 D_1}{(\rho^2 D_1)_\infty}\theta_1'\right] + 3(\mathrm{Sc}_1)_\infty F\theta_1' = 0 \tag{27}$$

$$\frac{d}{d\eta}\left[\frac{\rho^2 D_2}{(\rho^2 D_2)_\infty}\theta_2'\right] + 3(\mathrm{Sc}_2)_\infty F\theta_2' = 0 \tag{28}$$

in which Sc_1 and Sc_2 denote Schmidt numbers

$$\mathrm{Sc}_1 = \nu/D_1, \quad \mathrm{Sc}_2 = \nu/D_2 \tag{29}$$

For a given pressure p and temperature T, the properties ρ, μ, and D depend, at most, on the local mass fractions. With this in mind, examination of equations (26–28) indicates that the similarity transformation has been successful, that is, x and y have been banished and only functions of η appear.

Attention will now be turned to the transformation of the boundary conditions. From the definition of θ_1 and θ_2, there follows

$$\theta_1(0) = \theta_2(0) = 1, \quad \theta_1(\infty) = \theta_2(\infty) = 0 \tag{30}$$

and, in addition, since $u = 0$ at the surface and in the ambient fluid

$$F'(0) = F'(\infty) = 0 \tag{31}$$

Although equations (30) are attractive from a cosmetic viewpoint, they do not address the realities of the problem since they provide no information about W_{1w}, $W_{1\infty}$, W_{2w}, and $W_{2\infty}$ which appear explicitly in equation (26). In general, $W_{1\infty}$ and $W_{2\infty}$ can be regarded as known. The values of W_{1w} and W_{2w} have to be extracted from the boundary conditions at the plate surface for the specific problem in question. In addition, the given boundary condition for the transverse velocity v_w at the surface has to be translated into a condition for $F(0)$. To illustrate how this is done, consideration may be given to the plate-surface boundary conditions expressed by equations (16, 20), and (21).

Equation (16) is left as is since it provides a direct interrelationship between W_{1w} and W_{2w} for a given value of x_{1w}, but equations (20) and (21) are transformed, with the result

$$\theta_2'(0) = -\theta_1'(0)(D_1/D_2)W_{2w}(W_{1w} - W_{1\infty})/(1 - W_{1w})(W_{2w} - W_{2\infty}) \tag{32}$$

$$F(0) = \theta_1'(0)(W_{1w} - W_{1\infty})(\rho_w/\rho_\infty)^2/3(\nu_\infty/D_1)(1 - W_{1w}) \tag{33}$$

The procedure for using these equations will be discussed as part of the description of the numerical solution method that follows.

Numerical Solutions. The governing equations (26–28) for the similarity solution, when taken together, comprise a coupled nonlinear ordinary differential system of order seven. Correspondingly, there are seven boundary conditions, four at the plate surface ($\eta = 0$) and three in the ambient fluid ($\eta = \infty$). The solution can be carried out by employing a numerical forward-integration method (for instance, the well-known Runge-Kutta method), starting at $\eta = 0$ and integrating out to $\eta = \eta_\infty$, which is a numerical approximation of $\eta = \infty$.

In the forthcoming description of the solution scheme, it will be assumed that algebraic equations are available for computing the mixture properties ρ, μ, and D. For concreteness, the scheme will be described for the illustrative set of boundary conditions that have been carried through the preceding sections of the paper, namely, prescribed values of $W_{1\infty}$, $W_{2\infty}$, p_{1w}, p, and T, with the surface being impermeable to components 2 and 3, and with $u = 0$ at the surface and in the ambient.

A forward integration procedure requires that all of the boundary conditions be specified at the starting point of the integration. For the problem under consideration, the integration is initiated at $\eta = 0$ and the required input quantities are

$$F(0), \quad F'(0), \quad F''(0), \quad \theta_1(0), \quad \theta_1'(0), \quad \theta_2(0), \quad \theta_2'(0) \tag{34}$$

As will be demonstrated shortly, information equivalent to four of these is given, so that guesses have to be made for the equivalent of the other three. Once these guesses have been made, numerical values of all seven starting quantities are available and the integration from $\eta = 0$ to $\eta = \eta_\infty$ can be performed. The resulting values of θ_1, θ_2, and F' at $\eta = \eta_\infty$ are examined and compared with the given boundary conditions $\theta_1(\infty) = \theta_2(\infty) = F'(\infty) = 0$. If agreement between the computed values and the given boundary conditions does not fall within a given tolerance, a new set of guesses is made and the procedure repeated until satisfactory agreement is attained. In the refinement of the guesses, it was found to be advantageous to use a shooting method.

Attention will now be focused on the starting values for the numerical integration. Among the seven quantities listed in equation (34), the numerical values of $F'(0)$, $\theta_1(0)$, and $\theta_2(0)$ are directly available from equations (30) and (31). In addition, x_{1w} is known via the given values of p_{1w} and p, and equations (16, 32), and (33) provide interrelations between W_{1w}, W_{2w}, $\theta_1'(0)$, $\theta_2'(0)$, and $F(0)$. By assigning values to (i.e., guessing) two of these quantities, the other three can be determined. There is some degree of arbitrariness in the choice of the two quantities for which guesses are to be made. With an eye to the subsequent computations for the naphthalene/air/water vapor system, W_{1w} and $\theta_1'(0)$ have been selected here.

For a guessed value of W_{1w} and with x_{1w} known, equation (16) yields W_{2w}. With these and with the values of $W_{1\infty}$ and $W_{2\infty}$, and with a guess for $\theta_1'(0)$, a value of $\theta_2'(0)$ can be obtained from equation (32). These inputs also enable $F(0)$ to be calculated from equation (33). Finally, a guess is made for $F''(0)$.

Thus, the guesses of W_{1w}, $\theta_1'(0)$, and $F''(0)$ complete the specification of the boundary conditions at $\eta = 0$ and, at the same time, provide the values of W_{1w} and W_{2w} needed as input to the transformed momentum equation (26). The numerical solution can then be carried out and the guesses refined in the manner that was discussed in a preceding paragraph.

Surface Mass Transfer. The main objective of the analysis is to determine the local and average mass transfer rates at the surface. If $\dot{m}$ denotes the local mass transfer per unit time and unit area, then

$$\dot{m} = \dot{m}_1 + \dot{m}_2 + \dot{m}_3 \tag{35}$$

where the component mass fluxes are given by

$$\dot{m}_i = \rho_{iw}v_w + j_{iw} \tag{36}$$

When (36), with $i = 1$, 2, and 3, is substituted into (35) and note is taken of the fact that $\rho_1 + \rho_2 + \rho_3 = \rho$ and that $j_1 + j_2 + j_3 = 0$, the mass transfer expression reduces to

$$\dot{m} = \rho_w v_w \tag{37}$$

Furthermore, when v_w is evaluated in terms of the similarity variables via equations (25, 24) and (23) we obtain

$$\dot{m} = -3\mu_\infty c F(0)/x^{1/4} \tag{38}$$

where c is the constant that scales the similarity variable η and is given by equation (23a). The value of $F(0)$ is one of the results that is obtained from the numerical solutions of the similarity equations. Once it is available, $\dot{m}$ follows directly from equation (38).

The overall rate of mass transfer $\dot{M}$ for a streamwise (i.e., vertical) length L and for unit width is found by integrating $\dot{m}$ from $x = 0$ to $x = L$, with the result

$$\dot{M} = -4\mu_\infty c F(0) L^{3/4} \tag{39}$$

Equations (38) and (39) are general expressions for the local and average mass transfer rates and are, therefore, applicable for any set of boundary conditions that are consistent with a similarity solution. Alternative expressions for the mass transfer can be derived for specific boundary conditions. For instance, for the case that has been dealt with in the prior sections of the paper (i.e., p_{1w} specified, $\dot{m}_2 = \dot{m}_3 = 0$), $F(0)$ may be eliminated from equation (38) in favor of $\theta_1'(0)$ by employing equation (33). After making this substitution, there is obtained, after rearrangement

$$\frac{\dot{m}}{(\rho_{1w} - \rho_{1\infty})} \frac{x}{D_1} = -\theta_1'(0) c x^{3/4} \frac{(W_{1w} - W_{1\infty})(\rho_w/\rho_\infty)^2}{((\rho_{1w} - \rho_{1\infty})/\rho_\infty)(1 - W_{1w})} \tag{40}$$

Since $\dot{m} = \dot{m}_1$ for the case under consideration, it is natural to select $(\rho_{1w} - \rho_{1\infty})$ as the driving potential for mass transfer and to define a mass transfer coefficient K and Sherwood number Sh as

$$K = \dot{m}/(\rho_{1w} - \rho_{1\infty}), \quad \mathrm{Sh} = Kx/D_1 \tag{41}$$

Furthermore, the group $cx^{3/4}$ is, in essence, a Grashof number.

Equation (40) can be simplified by adopting a constant property model of the type normally employed in thermal natural convection. For such a model, no distinction is made between ρ_w and ρ_∞, and equation (40) reduces to

$$\mathrm{Sh} = -\theta_1'(0) c x^{3/4}/(1 - W_{1w}) \tag{42}$$

It may also be noted that if the contribution of the transverse velocity v_w at the wall is ignored, that is, if $\dot{m} = \dot{m}_1 = j_{1w}$, then for the constant property model

$$\mathrm{Sh} = -\theta_1'(0) c x^{3/4} \tag{43}$$

By comparing equations (42) and (43), it is seen that the factor $1/(1 - W_{1w})$ represents the contribution of the transverse velocity to the surface mass transfer.

Naphthalene Sublimation in Humid Air

Problem Definition and Solution. Attention will now be focused on sublimation from a solid naphthalene plate to ambient air in which the relative humidity ϕ may be arbitrarily prescribed.[1] In keeping with experimental practice, the concentration of naphthalene vapor in the ambient is zero. The temperature and pressure are given and from the former, the naphthalene vapor pressure at the plate surface can be evaluated from the vapor pressure—temperature relation (e.g., [2]). The plate is impermeable to both air and water vapor.

To specialize the foregoing analysis, let

$$1 \sim \text{naphthalene vapor}, \quad 2 \sim \text{water vapor}, \quad 3 \sim \text{air} \tag{44}$$

Then, the given information for the present problem can be expressed as

(a) at $\eta = \infty$

$$p_{1\infty} = 0, \quad p_{2\infty} = \phi p_{2,\mathrm{sat}}, \quad p_{3\infty} = p - p_{2\infty} \tag{45}$$

$$W_{1\infty} = 0, \quad W_{2\infty} = \frac{p_{2\infty}/p}{p_{2\infty}/p + (p_{3\infty}/p)(M_3/M_2)} \tag{46}$$

(b) at $\eta = 0$

$$p_{1w} = \text{known}, \quad x_{1w} = p_{1w}/p, \quad \dot{m}_2 = \dot{m}_3 = 0 \tag{47}$$

where both $p_{2,\mathrm{sat}}$ (saturation pressure of steam) and p_{1w} are functions of temperature.

To adapt the governing equations (26–28) to the naphthalene problem, the thermophysical properties have to be dealt with. For all cases of practical interest in the application of the naphthalene sublimation technique, the naphthalene vapor is no more than a minute trace. For example, in the most extreme case considered in the forthcoming numerical studies, W_1 varies from 0.0008 to zero as η ranges from zero to infinity. Therefore, with regard to property ratios such as $\rho\mu/(\rho\mu)_\infty$ and ρ/ρ_∞, ρ and μ can be evaluated for an isothermal, uniform-composition air/water vapor mixture, which means that $\rho\mu/(\rho\mu)_\infty = 1$ and $\rho/\rho_\infty = 1$.

The naphthalene diffusion coefficient D_1 for the ternary mixture was evaluated from Blanc's law [3], which requires the *binary* diffusion coefficients for naphthalene/air and naphthalene/water vapor as input. The former is available [2] while the latter was evaluated from the correlation of Fuller, Schettler, and Giddings [3]. It was found that the extreme deviation of D_1 from the naphthalene/air binary diffusion coefficient D_{na} is about one percent. Since the value of D_{na} is uncertain by more than one percent, deviations between D_1 and D_{na} were not further considered. From a similar calculation, the water vapor diffusion coefficient D_2 for the ternary mixture was found to deviate by a maximum of 0.06 percent from the binary water vapor/air diffusion coefficient, and so the binary coefficient was used for D_2. Furthermore, the binary diffusion coefficients are independent of composition [3].

With this, equations (26–28) reduce as follows:

1 The first term of equation (26) becomes F'''.

2 The first term of equation (27) becomes θ_1'' and $(\mathrm{Sc}_1)_\infty$ becomes Sc_1.

3 The first term of equation (28) becomes θ_2'' and $(\mathrm{Sc}_2)_\infty$ becomes Sc_2. Furthermore, $\mathrm{Sc}_1 = 2.5$ [2], while Sc_2 was calculated to be 0.6 by employing Table 10.1 of [4] and Table 7 of [5].

Turning next to the boundary conditions, the values of $W_{1\infty}$ and $W_{2\infty}$ are already expressed by equation (46), and $\theta_1(\infty) = \theta_2(\infty) = F'(\infty) = 0$. At the wall ($\eta = 0$), the value of x_1 from equation (47) is used as input to equation (16), and the impermeability conditions (32) and (33) are employed to find the starting values for the numerical solution as was described earlier. In equation (32), D_1/D_2 may be replaced by $(\mathrm{Sc}_2/\mathrm{Sc}_1)$ and, in equation (33), $(\rho_w/\rho_\infty)^2 = 1$ and $(\nu_\infty/D_1) = \mathrm{Sc}_1$.

The numerical solutions are performed according to the scheme outlined in a previous section of the paper. The cases selected for study were chosen to correspond to realistic experimental conditions. For the system temperature T, values of 10, 20, and 30°C (50, 68, and 86°F) were assigned, and this seemingly small temperature range corresponds to a change of more than a factor of seven in the naphthalene vapor pressure at the wall. The system pressure was taken to be one atmosphere, and the relative humidity ϕ was given values of 0, 0.5, and 1.0.

The $\phi = 0$ case corresponds to a binary boundary layer (naphthalene/air) which is governed by equations (26) and (27) (suitably simplified as just discussed) and with $W_{2w} = W_{2\infty} = 0$. Equation (16) with $W_{2w} = 0$ yields W_{1w}, and only one impermeability condition, that for air, is appropriate. That condition is suitably expressed by equation (33), modified as already discussed.

In addition to the foregoing solutions for $\phi = 0$, another set was performed in which the transverse velocity v_w was suppressed altogether. This problem is governed by

$$F''' + 3FF'' - 2(F')^2 + \theta_1 = 0 \tag{48}$$

$$\theta_1'' + 3\mathrm{Sc}_1 F \theta_1' = 0 \tag{49}$$

$$\theta_1(0) = 1, \quad \theta_1(\infty) = F(0) = F'(0) = F'(\infty) = 0 \tag{50}$$

These equations and boundary conditions are identical to those for the classical thermal natural convection problem for the vertical plate. Thus, by employing a model where water vapor is ignored and the transverse velocity v_w is neglected, the mass transfer problem loses its special identity and merges with a well-known heat transfer problem.

Results and Discussion. The quantities of most immediate interest are the local and overall surface mass transfer rates, $\dot{m}$ and $\dot{M}$, respectively. Since the results will be presented in ratio form and since there is proportionality between $\dot{m}$ and $\dot{M}$ for a similarity solution, ratios involving $\dot{m}$ are identical to corresponding ratios involving $\dot{M}$. For concreteness, the results will be presented in terms of $\dot{m}$.

[1] In the temperature range of practical interest, water vapor can be treated as a perfect gas since its compressibility factor Z is in the range from 0.997 to 1 ([4], Fig. 1.4).

Two ratios will be examined, $\dot{m}_\phi/\dot{m}_0$ and $\dot{m}_0/\dot{m}_{00}$. Among these quantities, $\dot{m}_\phi$ is the local naphthalene mass transfer rate to air with relative humidity ϕ, $\dot{m}_0$ is the value of $\dot{m}_\phi$ when $\phi = 0$ (no water vapor), and $\dot{m}_{00}$ is for $\phi = 0$ and $v_w = 0$. The latter corresponds to an interchange of Sh for Nu and of Sc for Pr in the classical vertical plate heat transfer solution. Thus, the departure of $\dot{m}_\phi/\dot{m}_0$ from unity is a direct measure of the effect of changes in humidity, while $\dot{m}_0/\dot{m}_{00}$ shows the effect of accounting for the transverse velocity at the plate surface.

From equation (42), for fixed values of the system pressure and temperature, it follows that

$$\frac{\dot{m}_\phi}{\dot{m}_0} = \frac{[\theta_1'(0)c/(1 - W_{1w})]_\phi}{[\theta_1'(0)c/(1 - W_{1w})]_0} \tag{51}$$

where c is given by equation (23a). It should be noted that since c contains W_{1w}, ν_∞, and $W_{2\infty}$, the values of which depend on ϕ, it follows that $c_\phi/c_0 \neq 1$. Numerical information needed for the evaluation of $\dot{m}_\phi/\dot{m}_0$ is listed in Table 1 for temperatures equal to 10, 20, and 30°C and $\phi = 0$, 0.5, and 1.

If $\dot{m}_\phi/\dot{m}_0$ is evaluated for each of the fixed temperature levels that appears in the table, it is found that the deviations of $\dot{m}_\phi/\dot{m}_0$ from unity are well within one percent. To provide some insights into this finding, consider the case $T = 30$°C and $\phi = 1$. The evaluation of equation (51), up to the point of introducing the properties, yields

$$\dot{m}_\phi/\dot{m}_0 = 1.0056\sqrt{\nu_0/\nu_\phi} \tag{52}$$

Thus, even if the differences in the properties were to be ignored, only a half percent error would be incurred. The densities that appear in the ν_0/ν_ϕ ratio are readily evaluated from the information given in Table 1. However, the viscosity μ_ϕ of humid air is not known to high precision. For the case in question, we have estimated a value of $\mu_\phi/\mu_0 = 0.995$ from the information given in [5]. When the properties are introduced into (52), $\dot{m}_\phi/\dot{m}_0 = 1$ to within a few hundredths of a percent.

The foregoing finding indicates that the naphthalene mass transfer rates are insensitive to the absence or presence of water vapor. It now remains to assess the influence of the transverse velocity v_w at the wall, and this is done via the ratio $\dot{m}_0/\dot{m}_{00}$. It is easily shown that

$$\dot{m}_0/\dot{m}_{00} = [\theta_1'(0)]_0/[\theta_1'(0)]_{00}(1 - W_{1w}) \tag{53}$$

The value of $[\theta_1'(0)]_{00}$ is -0.76986 for Sc = 2.5. With this, and with the values of $[\theta'_1(0)]_0$ in Table 1, it is found that $\dot{m}_0/\dot{m}_{00} = 1.00006$, 1.00015, and 1.00040, respectively for $T = 20$, 30, and 40°C. These results clearly indicate that the mass transfer is unaffected by the wall velocity v_w.

The results of the preceding paragraphs have shown that the naphthalene mass transfer is neither affected by humidity nor by the wall velocity v_w. Therefore, naphthalene sublimation experiments can be performed at any humidity level that might be present in the laboratory without concern about errors. Furthermore, the insignificant role of v_w means that the naphthalene mass transfer coefficients can be interpreted, via the analogy, as heat transfer coefficients corresponding to an impermeable wall. For the analogy, Sh → Nu, Sc → Pr, and the corresponding Grashof numbers are

$$\mathrm{Gr} = g[(M_1 - M_3)/M_1]W_{1w}x^3/\nu^2, \quad \mathrm{Gr} = g\beta\Delta Tx^3/\nu^2 \tag{54}$$

Further perspectives on the mass transfer results will now be presented. From an examination of the transformed momentum equation (26), it is seen that there are two components of the buoyancy force, namely, the principal buoyancy term θ_1 and the supplemental buoyancy which constitutes the last term of the equation. A main contributor to the supplemental buoyancy term is the quantity $(W_{2w} - W_{2\infty})$ which expresses the difference in the mass fractions of the water vapor at the wall and in the ambient. From an examination of Table 1, it is seen that this difference is very small in all of the cases investigated, which suggests that the supplemental buoyancy will, itself, be small.

A comparison of the principal and supplemental buoyancies presented in Fig. 2 confirms the smallness of the latter, thereby rationalizing the insensitivity of the mass transfer to the presence of the water vapor. The comparison shown in the figure is for the case where $T = 30$°C and $\phi = 1$ which, among the various cases studied, gives rise to the largest supplemental buoyancy. The figure also compares the principal buoyancy distributions for $\phi = 0$ and $\phi = 1$ and indicates only a very slight difference. For all of the cases, the last column of Table 1 lists wall values of the ratio of supplementary buoyancy $f_{B,s}$ to principal buoyancy $f_{B,p}$. The listing confirms that the supplemental buoyancy for the other cases is even smaller than that for the case depicted in Fig. 2.

Table 1 Results of the numerical solutions ($p = 1$ atm)

T(°C)	ϕ	$-\theta_1'(0)$	10^3W_{1w}	10^2W_{2w}	$10^2W_{2\infty}$	$10^2(f_{B,s}/f_{B,p})_w$
10	0	0.76982	0.10789			
	0.5	0.77044	0.10814	0.37744	0.37746	0.14893
	1.0	0.77107	0.10838	0.75662	0.75666	0.29862
20	0	0.76974	0.30354			
	0.5	0.77093	0.30486	0.72030	0.72041	0.28448
	1.0	0.77211	0.30621	1.4468	1.4470	0.57057
30	0	0.76955	0.79745			
	0.5	0.77169	0.80381	1.3120	1.3125	0.51769
	1.0	0.77383	0.81027	2.6450	2.6461	1.0416

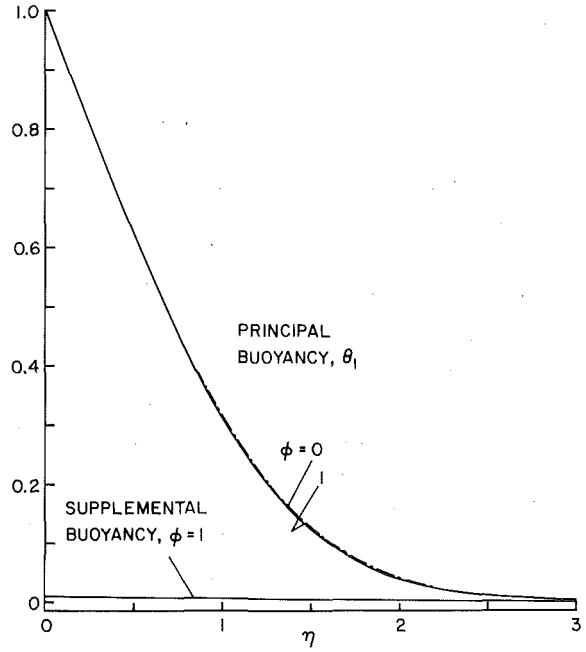

Fig. 2 Distributions of the principal and supplemental buoyancy components: $T = 30$°C, $p = 1$ atm

To provide perspective about the role of the wall velocity v_w, distributions of the transverse velocity in the near-wall region are presented in Fig. 3. The ordinate variable V is an abbreviation for $vx^{1/4}/\nu c$ which, from the similarity solution, is given by

$$V = vx^{1/4}/\nu c = \eta F' - 3F \tag{55}$$

The curves for $\phi = 0$ and $\phi = 1$ that are shown in the figure correspond to $T = 30$°C and, in addition, the curve representing the results for $v_w = 0$ and $\phi = 0$ is also plotted. There are two features of this figure that are worthy of note, namely, the sign of V and its magnitude.

In the conventional thermal natural convection problem as well as in the mass transfer problem with $v_w = 0$ and $\phi = 0$, V is negative throughout the entire boundary layer because the natural convection process draws fluid from the ambient toward the surface. On the other hand, for sublimation mass transfer, V must be positive at the surface as shown in the figure. It may be seen, however, that the region of positive V does not penetrate very deeply into the boundary layer so that, for the most part, V is negative as in the conventional case.

To obtain a measure of the size of the positive V values, they may be compared to V_∞, the magnitude of which is about 1.1. Against this

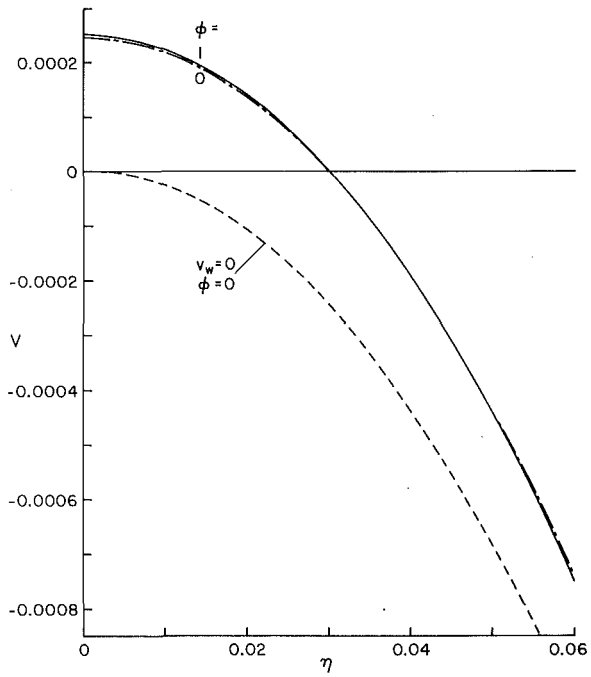

Fig. 3 Distributions of the transverse velocity in the near-wall region: T = 30°C, p = 1 atm

standard, the wall value of V (the largest positive V), which is about 0.00025, is clearly very small. Also, the distribution of V is insensitive to whether $\phi = 0$ or $\phi = 1$.

The foregoing discussion underscores the fact that the transverse velocities generated by the surface mass transfer are too weak to affect the magnitude of the mass transfer. Information about V_w and V_∞ for all the cases that were investigated can be obtained from the $F(0)$ and $F(\infty)$ listings of Table 2, with $V_w = -3F(0)$ and $V_\infty = -3F(\infty)$.

To complete the presentation of results, velocity distributions are presented in Fig. 4 in terms of the variable U defined by

$$U = u/4\nu c^2 x^{1/2} = F' \tag{56}$$

The curves are for the T = 30°C case, which yields the highest supplemental buoyancy and wall velocity among the temperatures investigated. It is seen from the figure that there is only a slight spread between the $\phi = 0$ and $\phi = 1$ curves and, furthermore, that the $\phi = 0$ ($v_w \neq 0$) curve overlaps that for $v_w = 0$ and $\phi = 0$. Therefore, the velocity profiles are essentially unaffected by the presence of the water vapor.

As a final matter, it is of interest to briefly examine the validity of the isothermal flow assumption that was employed in the analysis. It can be reasoned that since the latent heat of sublimation has to be supplied to the subliming solid, the surface temperature of the solid must be depressed in order to set up and maintain the requisite heat flow. If it is assumed that all of the heat required for the sublimation process is transferred by natural convection from the ambient air to the surface, then it can be shown that the depression of the surface temperature relative to the ambient is less than 0.1°C. The smallness of this temperature difference validates the isothermal flow model.

Concluding Remarks

In response to the need to assess the effect of humidity on experiments involving the naphthalene sublimation technique, an analysis of natural convection in a ternary gas mixture was performed. The main issues in the mathematical formulation of the problem were the derivations of the appropriate buoyancy force and the boundary conditions. In the latter, consideration had to be given to the fact that the bounding wall is selectively impermeable to certain of the components of the mixture. The analysis took full account of possible variations of the fluid properties. It was demonstrated that the problem yielded a similarity solution, and a numerical scheme for solving the similarity equations and boundary conditions was described.

The general formulation was specialized to natural convection sublimation from a solid, vertically oriented naphthalene plate situated in humid air. Numerical solutions were performed for three temperature levels that bracket the practical range. At each temperature level, the relative humidity of water vapor in the air was varied from zero to one. It was found that the mass transfer results were unaffected by the presence of humidity. Careful diagnosis revealed that both the supplemental buoyancy associated with the presence of humidity and the transverse velocity at the wall associated with the mass transfer are very small.

This finding gives license to the utilization of the naphthalene sublimation technique without special concern about the humidity in the air. Upon application of the heat/mass transfer analogy, the resulting heat transfer coefficients correspond to an impermeable bounding wall.

Table 2 Velocity-related results of the solutions (p = 1 atm)

T(°C)	ϕ	$F''(0)$	$-10^4F(0)$	$F(\infty)$
10	0	0.54890	0.11075	0.37549
	0.5	0.54977	0.11110	0.37722
	1.0	0.55065	0.11144	0.37871
20	0	0.54891	0.31162	0.37549
	0.5	0.55058	0.31347	0.37844
	1.0	0.55225	0.31533	0.38145
30	0	0.54893	0.81888	0.37550
	0.5	0.55196	0.82772	0.38092
	1.0	0.55501	0.83669	0.38610

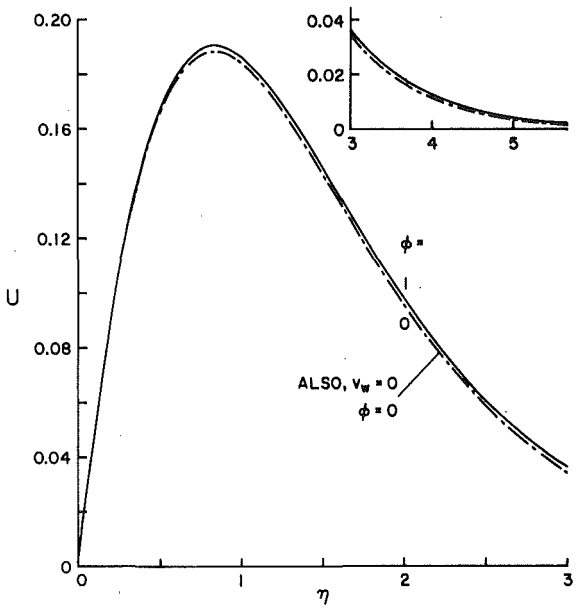

Fig. 4 Velocity distributions: T = 30°C, p = 1 atm

Acknowledgment

This research was performed, in part, under the auspices of NSF Grant ENG77-06762.

References

1 Eckert, E. R. G., and Drake, Jr., R. M., *Analysis of Heat and Mass Transfer*, McGraw-Hill, New York, 1972, Chapters 19–21.

2 Sogin, H. H., "Sublimation from Disks to Air Streams Flowing Normal to Their Surfaces," *Trans. ASME*, Vol. 80, 1958, pp. 61–69.

3 Reid, R. C., Prausnitz, J. M., and Sherwood, T. K., *The Properties of Gases and Liquids*, 3rd ed., McGraw-Hill, New York, 1977.

4 Threlkeld, J. L., *Thermal Environmental Engineering*, Prentice-Hall, Englewood Cliffs, N. J., 1970.

5 Mason, E. A., and Monchick, L., "Survey of the Equation of State and Properties of Moist Air," in *Humidity and Moisture*, A. Wexler, ed., Vol. 3, Reinhold, New York, 1965.

R. Rana
Department of Mechanical Engineering
University of Hawaii,
Honolulu, Hawaii 96822

R. N. Horne
Department of Petroleum Engineering,
Stanford University,
Stanford, CA 94305

P. Cheng
Department of Mechanical Engineering,
University of Hawaii
Honolulu, Hawaii 96822

Natural Convection in a Multi-Layered Geothermal Reservoir

The effect of layered structure of rock formation on free convection in a geothermal reservoir is investigated in this work. The model examined is that of a rectangular reservoir comprised of three horizontal permeable layers with different permeabilities. The reservoir is considered to be bounded by impermeable surfaces on the sides and at the bottom. The upper boundary of the aquifer is permeable, which permits the recharge and discharge of water to and from the aquifer. A transient two-dimensional convective flow is developed when the impermeable boundaries are raised suddenly to high temperatures. The governing nonlinear partial differential equations with appropriate boundary and initial conditions are solved numerically by finite difference methods. Application of the direct method for solving Poisson's equation for stream function made it possible to carry out the solution for a much longer time than possible with iterative techniques. Numerical results are obtained for various parameters and configurations of the geothermal reservoir. The influence of a less permeable middle layer on the flow and heat transfer characteristics in the aquifer is discussed. The computed vertical temperature profiles are similar in shape to the complex temperature profiles observed at the HGP-A well.

Introduction

It is well known that many geothermal reservoirs are comprised of layers of rock formations with different permeabilities and porosities. One example of such a reservoir is the newly developed geothermal field near Pahoa, Hawaii where the core samples collected at different depths in the drilled hole (i.e., the HGP-A well) confirm the existence of horizontal layers with widely different permeabilities. Analyses of the fluid samples collected from the well indicate that the water has a generally low chloride concentration which leads to the speculation that there are impermeable barriers (such as dike-like formations) between the reservoir and the sea, and that the reservoir is probably recharged from a freshwater source along the top permeable boundary. The present paper is a study of free convection in such a geothermal reservoir.

The geothermal reservoir is modelled as a saturated porous medium with a rectangular cross-section which is bounded by impermeable surfaces on the sides and bottom. The top boundary is permeable so that recharge and discharge of water to and from the aquifer through the upper boundary is possible. Furthermore, it is assumed that the aquifer is comprised of three layers with different permeabilities and thicknesses: the middle one being the least permeable and the upper and lower layers having high and moderate permeabilities. When the aquifer is heated suddenly from the sides by a dike complex as well as from the bottom by shallow intrusives, it is assumed that a two-dimensional convective flow is initiated. It should be noted that the convective flow in a porous medium can be two-dimensional even in a three-dimensional region [12], so the physical existence of an infinitely long trench need not be bothersome.

To investigate the transient behavior of the geothermal reservoir, it is necessary to use the transient form of the equations and examine the development of the flow and isothermal pattern over a long period of time. The transient behavior of natural convection in porous medium has been studied previously by various authors. Elder [8] studied the development of flow and isotherms in an enclosed two-dimensional porous medium when the base is suddenly heated. The problem of transient three-dimensional natural convection in a confined porous medium was studied numerically by Holst and Aziz [9]. The experimental studies of Caltagirone, et al. [3] and Combarnous and Le Fur [7] indicated possible unsteady flows for the uniformly heated case, and later numerical experiments by Horne and O'Sullivan [11] showed different possible convective patterns when a two-dimensional enclosed porous medium is heated uniformly and non-uniformly along the base. Horne and O'Sullivan observed both steady and fluctuating flows for the uniformly heated case, and only oscillatory flows when the base is partially heated. This was also noticed by Caltagirone [4] who obtained a numerical solution for transient natural convection in a horizontal porous layer placed between two isothermal surfaces. Caltagirone noticed the dependence of oscillatory flows on the aspect ratio of convective cells. Cheng and Teckchandani [6] numerically studied the transient response of an aquifer with recharge from the sides when suddenly heated non-uniformly from below. In all of the above mentioned studies, investigators have considered a homogeneous porous medium for analysis. The purpose of the present work is to study the effect of layered structure of the rock formation on the free convection in a geothermal reservoir, which has not been investigated previously.

The governing partial differential equations describing the transient flow and heat transfer chracteristics in the geothermal reservoir are solved by finite difference techniques similar to those employed by Horne and O'Sullivan in a previous study. Computations were carried out for different values of the governing parameters and for various boundary conditions. The numerical results show that the convection pattern and the vertical temperature profiles are greatly influenced by the presence of a less permeable middle layer. Because of the flow restriction imposed by the less permeable middle layer, the temperature variations in the middle and upper layers become smaller and the lower overall heat transfer rate is less. Moreover, it is found that steady-state convection is reached for aspect (length to height) ratios of one and two, but changes to oscillatory convection when the aspect ratio is increased to four. This shows the dependence of oscillatory flow on the aspect ratio. However, since we are more concerned with steady heat flows in this paper, the additional aspects of the fluctuating flows are reported elsewhere [14].

Mathematical Formulation

The reservoir is modeled as a two-dimensional rectangular porous region consisting of three horizontal porous layers with different thicknesses and permeabilities as shown in Fig. 1. It is bounded by impermeable dikes on the sides and by impermeable hot bedrock at the bottom. The upper boundary of the top layer is permeable, which permits the recharge and discharge of water to and from the aquifer. The form of the equations describing the flow depends on the simplifying assumptions made. Basically, the behavior of fluid in a porous medium is governed by conservation of mass, momentum, energy, and the equation of state. For the present analysis, the working fluid is

Contributed by the Heat Transfer Division for publication in the JOURNAL OF HEAT TRANSFER. Manuscript received by the Heat Transfer Division May 30, 1978.

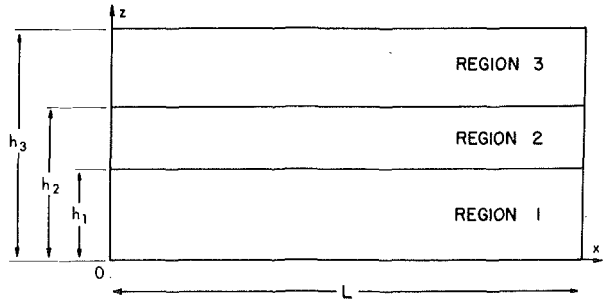

Fig. 1 Physical model of a multi-layered geothermal reservoir

taken to be pure water. To simplify the mathematical formulation without losing sight of main characteristics, the following assumptions are made: (1) The saturating fluid is assumed to be incompressible; (2) the porous medium and fluid are in local thermal equilibrium at each point; (3) thermal conductivity, permeability, diffusivity and viscosity are assumed invariant with temperature; (4) the Boussinesq approximation is employed, implying that density effects are significant only in the buoyancy terms; and (5) Darcy's law is assumed to be applicable—this requires that Reynolds number (based on pore space) must be less than unity, which in turn implies that velocities in the porous medium are very low.

When the pressure is eliminated from Darcy's law, the resulting equation in terms of stream function and temperature is [8, 11]

$$\nabla^2\psi_i = -\frac{K_i}{\mu}\rho_0 g\beta\frac{\partial T_i}{\partial x} \tag{1}$$

where

$$u_i = \frac{\partial\psi_i}{\partial z} \quad \text{and} \quad v_i = -\frac{\partial\psi_i}{\partial x} \tag{2a, b}$$

with the subscripts $i = 1, 2, 3$ denoting the bottom, middle, and top layer (see Fig. 1). The energy equation in terms of stream function and temperature is

$$\lambda_i\frac{\partial T_i}{\partial t} + \left(\frac{\partial\psi_i}{\partial z}\frac{\partial T_i}{\partial x} - \frac{\partial\psi_i}{\partial x}\frac{\partial T_i}{\partial z}\right) = \alpha_i\nabla^2 T_i \tag{3}$$

Initially, the reservoir is at uniform temperature T_0 and motionless elsewhere, i.e., $u(x, y, 0) = v(x, y, 0) = 0$ and $T(x, y, 0) = T_0$. If temperature on the bottom impermeable surface is suddenly raised to a higher temperature, T_m, the thermal boundary condition on the bottom is

$$T_1(x, 0, t) = T_m, \quad t > 0 \tag{4}$$

where T_m is the prescribed bedrock temperature which is assumed to be uniform. For the vertical impermeable boundaries, both a heated case and an insulated case will be considered. For the heated case, a linear temperature distribution is assumed, i.e.,

$$T_i(0, z, t) = T_i(L, z, t) = T_0 + (1 - z)(T_m - T_0), \quad t > 0 \tag{5a, b}$$

whereas for the insulated boundaries, the conditions are

$$\frac{\partial T_i}{\partial x}(0, z, t) = \frac{\partial T_i}{\partial x}(L, z, t) = 0, \quad t > 0 \tag{5c, d}$$

where L is the horizontal length of the reservoir. The corresponding hydrodynamic boundary conditions on the vertical and bottom impermeable surfaces for both cases are

$$u_i(0, z, t) = u_i(L, z, t) = v_1(x, 0, t) = 0, \quad t > 0 \tag{6}$$

The upper permeable boundary allows the recharge and discharge of water to and from the reservoir. A simple calculation shows the effect of energy discharged through the top permeable boundary with geothermal fluid is small. If we assume that the occurrances of fumeroles are much more localized than the overall scale of the system, then we can use the approximation of air temperature, T_0, at the ground surface. Thus, the boundary conditions along the top permeable surface are

$$u_3(x, h_3, t) = 0 \quad \text{and} \quad T_3(x, h_3, t) = T_0, \quad t > 0 \tag{7a, b}$$

where h_3 is the height of the aquifer.

The continuity of pressure and normal flow across the interface boundaries gives the following conditions to be satisfied along these boundaries:

$$p_1(x, h_1, t) = p_2(x, h_1, t), \qquad v_1(x, h_1, t) = v_2(x, h_1, t), \quad t > 0 \tag{8a, b}$$

$$p_2(x, h_2, t) = p_3(x, h_2, t), \qquad v_2(x, h_2, t) = v_3(x, h_2, t), \quad t > 0 \tag{9a, b}$$

where h_1 and h_2 are the locations of the horizontal interfaces measured from the bottom impermeable surface (see Fig. 1). The continuity in temperature and heat flow across the interface requires the following conditions to be satisfied:

$$T_1(x, h_1, t) = T_2(x, h_1, t), \qquad k_1\frac{\partial T_1}{\partial z}(x, h_1, t) = k_2\frac{\partial T_2}{\partial z}(x, h_1, t), \quad t > 0 \tag{10a, b}$$

$$T_2(x, h_2, t) = T_3(x, h_2, t), \qquad k_2\frac{\partial T_2}{\partial z}(x, h_2, t) = k_3\frac{\partial T_3}{\partial z}(x, h_2, t), \quad t > 0 \tag{11a, b}$$

where k_i ($i = 1, 2, 3$) is the thermal conductivity of the respective porous layers.

With the aid of equations (2), velocity boundary conditions in equations (6–9) can be expressed in terms of stream function to give:

$$\psi_i(0, z, t) = \psi_i(L, z, t) = \psi_1(x, 0, t) = 0, \quad t > 0 \tag{12a, b, c}$$

Nomenclature

A = reservoir aspect ratio
g = gravitational acceleration
H = dimensionless distance of the upper boundary of the porous layer from the bottom impermeable surface
h = dimensional distance of the upper boundary of the porous layer from the bottom impermeable surface
k = thermal conductivity of the porous layer
K = permeability of the porous medium
L = width of the reservoir
p = pressure
Ra = Rayleigh number
t = time
T = temperature
T_m, T_0 = maximum and minimum values of T
u = Darcy's velocity component in the x-direction
v = Darcy's velocity component in the z-direction
U = dimensionless Darcy's velocity component in the X-direction
V = dimensionless Darcy's velocity component in the Z-direction
x, z = dimensional horizontal and vertical coordinates
X, Z = dimensionless coordinates
λ = ratio of the volumetric heat capacity of the saturated medium to that of the fluid
θ = dimensionless temperature defined by equation (16)
ρ = density of fluid
ρ_0 = density of fluid at T_0
μ = viscosity of fluid
α = thermal diffusivity
β = thermal expansion coefficient
τ = dimensionless time defined by equation (16)
ψ = dimensional stream function
Ψ = dimensionless stream function

Subscript

i = variable for the ith layer

$$\frac{\partial \psi_1}{\partial z}(x, h_1, t) = \frac{\partial \psi_2}{\partial z}(z, h_1, t),$$

$$\psi_1(x, h_1, t) = \psi_2(x, h_1, t), \quad t > 0 \quad (13a, b)$$

$$\frac{\partial \psi_2}{\partial z}(x, h_2, t) = \frac{\partial \psi_3}{\partial z}(x, h_2, t),$$

$$\psi_2(x, h_2, t) = \psi_3(x, h_2, t), \quad t > 0 \quad (14a, b)$$

$$\frac{\partial \psi_3}{\partial z}(x, h_3, t) = 0, \quad t > 0 \quad (15)$$

To express the governing equations and boundary conditions in dimensionless form, the following dimensionless variables are introduced:

$$\theta_i = \frac{T_i - T_0}{T_m - T_0}; \quad \Psi_i = \frac{\psi_i}{\alpha_i}; \quad \tau = \frac{1}{\lambda_3}\left(\frac{\alpha_3}{h_3^2}\right)t;$$

$$Z = \frac{z}{h_3}; \quad A = \frac{L}{h_3}; \quad H_i = \frac{h_i}{h_3}, \quad (16)$$

where A is the aspect ratio of the aquifer. Equations (1) and (2) in terms of dimensionless variables become:

$$\nabla^2 \Psi_i = -\mathrm{Ra}_i \frac{\partial \theta_i}{\partial X} \quad (17)$$

$$\frac{\lambda_i}{\lambda_3}\frac{\alpha_3}{\alpha_i}\frac{\partial \theta_i}{\partial \tau} + \left(\frac{\partial \Psi_i}{\partial Z}\frac{\partial \theta_i}{\partial X} - \frac{\partial \Psi_i}{\partial X}\frac{\partial \theta_i}{\partial Z}\right) = \nabla^2 \theta_i \quad (18)$$

where Ra_i is the Rayleigh number for each layer and is defined as $\mathrm{Ra}_i = K_i \rho_0 g \beta (T_m - T_0) h_3 / \mu \alpha_i$ with different values of K_i and α_i for each layer. For the special case of a reservoir with homogeneous thermal properties, we have $\alpha_i = \alpha$ and $\lambda_i = \lambda$ in equations (17) and (18); the resulting equations with subscripts omitted, are the same equations used in most of the literature on geothermal convection problems. Note that the present formulation differs from that of Chan, et al. [5] in that the present formulation is based on Darcy's law while that of Chan, et al.'s is based on a modification of Darcy's law with an added viscous term. The neglection of this additional term is both normal [4, 8, 10] and justifiable in large scale geothermal convection problems.

Hydrodynamic boundary conditions in terms of dimensionless variables along the impermeable surfaces are:

$$\Psi_i(0, Z, \tau) = \Psi_i(A, Z, \tau) = \Psi_1(X, 0, \tau) = 0, \quad \tau > 0 \quad (19a, b, c)$$

For the bedrock the thermal boundary condition is

$$\theta_1(X, 0, \tau) = \theta_L, \quad \tau > 0 \quad (20)$$

Along the vertical impermeable boundaries, the boundary conditions for the heated case are

$$\theta_i(0, Z, \tau) = \theta_i(A, Z, \tau) = 1 - Z, \quad \tau > 0 \quad (21a, b)$$

whereas those for the insulated case are

$$\frac{\partial \theta_i}{\partial X}(0, Z, \tau) = \frac{\partial \theta_i}{\partial X}(A, Z, \tau) = 0, \quad \tau > 0 \quad (21c, d)$$

Along the two horizontal interfaces, the dimensionless boundary conditions are

$$\Psi_1(X, H_1, \tau) = \frac{\alpha_2}{\alpha_1}\Psi_2(X, H_1, \tau),$$

$$\theta_1(X, H_1, \tau) = \theta_2(X, H_1, \tau), \quad \tau > 0 \quad (22a, b)$$

$$\Psi_2(X, H_2, \tau) = \frac{\alpha_3}{\alpha_2}\Psi_3(X, H_2, \tau),$$

$$\theta_2(X, H_2, \tau) = \theta_3(X, H_2, \tau), \quad \tau > 0 \quad (23a, b)$$

and

$$\frac{\partial \Psi_1}{\partial Z}(X, H_1, \tau) = \left(\frac{\alpha_2}{\alpha_1}\right)\left(\frac{K_1}{K_2}\right)\left(\frac{\partial \Psi_2}{\partial Z}\right)(X, H_1, \tau), \quad \tau > 0 \quad (24)$$

$$\frac{\partial \Psi_2}{\partial Z}(X, H_2, \tau) = \left(\frac{\alpha_3}{\alpha_2}\right)\left(\frac{K_2}{K_3}\right)\left(\frac{\partial \Psi_3}{\partial Z}\right)(X, H_2, \tau), \quad \tau > 0 \quad (25)$$

$$\frac{\partial \theta_1}{\partial Z}(X, H_1, \tau) = \left(\frac{\alpha_2}{\alpha_1}\right)\left(\frac{\partial \theta_2}{\partial Z}\right)(X, H_1, \tau), \quad \tau > 0 \quad (26)$$

$$\frac{\partial \theta_2}{\partial Z}(X, H_2, \tau) = \left(\frac{\alpha_3}{\alpha_2}\right)\left(\frac{\partial \theta_3}{\partial Z}\right)(X, H_2, \tau), \quad \tau > 0 \quad (27)$$

The dimensionless boundary conditions along the top permeable surfaces are

$$\frac{\partial \Psi_3}{\partial Z}(X, 1, \tau) = \theta_3(X, 1, \tau) = 0, \quad \tau > 0 \quad (28)$$

Equations (17) and (18) with boundary conditions (19–28) are to be solved by numerical methods.

Finite Difference Solutions

The numerical solutions of equation (17) for stream function and equation (18) for temperature are obtained by finite difference methods. The solution of the elliptic equation for the stream function is obtained by an extension of Buneman's odd-even reduction algorithm [2], which is by no means straight-forward because of the complicated derivative boundary conditions along the interfaces (see [14] for details). This direct method is much faster than the usual iterative methods for regions with simple shapes and is therefore superior in both accuracy and economy. For the energy equation, Arakawa's scheme for the finite difference representation of advection terms is used. The scheme, involving a nine-node representation of the advection terms, can avoid the nonlinear instability that arises from aliasing errors. Due to the complex nature of the method, the use of an implicit time difference scheme is not practical. For this reason an explicit scheme with forward time differencing is used to approximate the time derivative in the energy equation.

To express the derivative boundary conditions in finite difference form for stream function along the interfaces, definition of imaginary nodes outside the physical domain of the adjacent layers is required. The stream function at the imaginary nodes is then eliminated from the boundary conditions based on the central difference approximation and the finite difference equations for the interior nodes. If similar procedures are used for the derivative boundary conditions of temperature, it would result in a set of very involved and lengthy mathematical equations. To avoid this problem, imaginary nodes for temperature are not used. Instead, the derivative boundary conditions for temperature are approximated by a three-point formula relating the nodal points at the interface and the interior nodes in the two adjacent layers.

Numerical Results and Discussion

Numerical computations were carried out for the following three cases with different Rayleigh numbers and thermal boundary conditions:

Case I. $\mathrm{Ra}_1 = 300$, $\mathrm{Ra}_2 = 120$, $\mathrm{Ra}_3 = 750$ with heated vertical boundaries where thermal boundary conditions are given by equations (20) and (21a, b).

Case II. $\mathrm{Ra}_1 = 300$, $\mathrm{Ra}_2 = 50$, $\mathrm{Ra}_3 = 750$ with heated vertical boundaries, i.e., the thermal boundary conditions as Case I.

Case III. $\mathrm{Ra}_1 = 300$, $\mathrm{Ra}_2 = 120$, $\mathrm{Ra}_3 = 750$ with insulated vertical boundaries where thermal boundary conditions are given by equations (20) and (21c, d).

For each case considered, it is assumed that (1) the values of α_i and λ_i are the same for all layers, (2) $H_1 = 7/16$, $H_2 = 11/16$, and (3) $A = 2$. The values chosen for H_1 and H_2 are roughly corresponding to field data at the Pahoa geothermal field. Other cases with different values of aspect ratio are presented in [14].

Case I. The different Rayleigh numbers chosen for the three layers imply that the permeability ratios for the layers are $K_1/K_2 = 2.5$ and $K_3/K_2 = 6.25$ which are the approximate permeability ratios for the rock formations at Pahoa, Hawaii. These ratios represent a highly permeable top layer, low permeability middle layer, and a moderately permeable bottom layer. Fig. 2 is a plot of the horizontal velocity

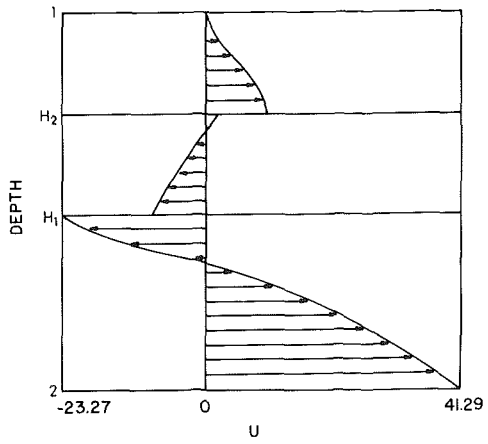

Fig. 2 Dimensionless horizontal velocity profiles at $X = 0.72$ for Case I

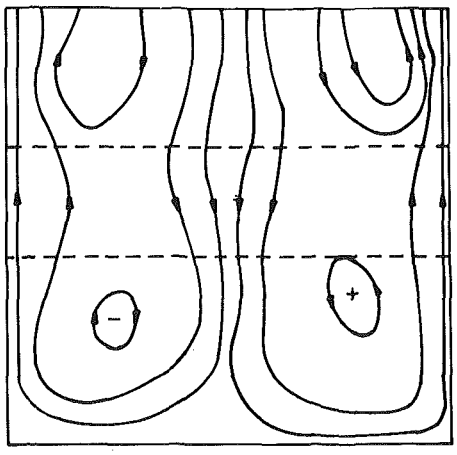

Fig. 3 (*a*)

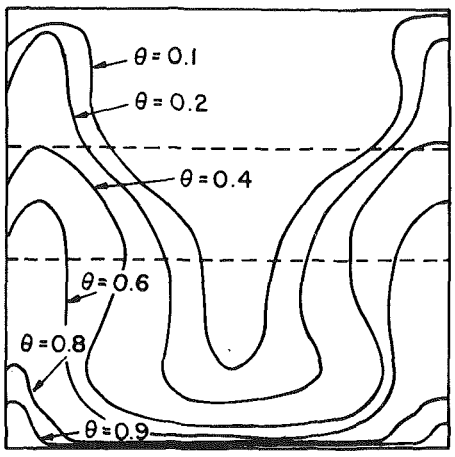

Fig. 3 (*b*)

Fig. 3 Convection patterns and isotherms for Case I

profiles on the vertical cross section at $X = 0.72$, which shows that discontinuity of horizontal velocity exists at the interfaces of two adjacent layers with different permeabilities. Mathematically, it can easily be shown from Darcy's law that if pressure is continuous across the interface of two layers with different permeabilities, the Darcy's velocity component at the interface and in the direction parallel to the interface must be discontinuous. The existence of the Darcy's velocity slip is physically necessary if we note that Darcy's velocity is defined as an average velocity flux, rather than the velocity at a point as in the classical viscous flow theory.

Fig. 3(*a*) shows the steady-state convection pattern for the left half of the domain of Fig. 1. The reservoir approaches steady state at a time level of 0.0754 corresponding to 1.5×10^4 year. The extreme values

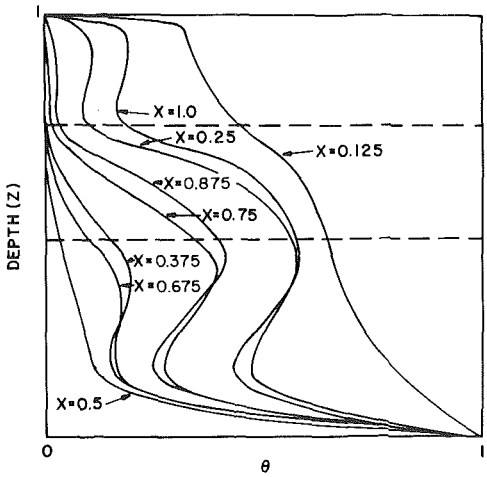

Fig. 4 Dimensionless vertical temperature profiles for Case I

of stream function for the double cellular convection pattern (with cell width of 0.5) are 13.1 and −12.7, respectively. It is interesting to note that recirculating convective cells exist only in the top and bottom layers where the permeabilities are high, but are absent in the middle less permeable layer. This demonstrates that some of the water recharge from the top does not penetrate into the lower layers and that some of the hot water in the bottom layer never rises to the upper layers because of the presence of the less permeable middle layer. From the isotherms shown in Fig. 3(*b*), it can be concluded that regions of high temperature are at a distance slightly away from the heated sides and in the middle of the reservoir as the hot rising plumes are located near these regions. Consequently, when the flow is at steady state, the heated sides act as heat sinks instead of heat sources. The Nusselt number (defined as the heat transfer over the top permeable boundary compared to that transferred by conduction alone) is found to be 3.9.

Fig. 4 shows the vertical temperature profiles at different locations for Case I. The large temperature inversions in the top and bottom layers indicates the strong convection currents there. On the other hand, the almost linear temperature profile in the middle layer shows that recirculation is not important in the less permeable layer.

Case II. This case with still lower permeability for the middle layer is run in order to highlight the effects of the low permeability layer. The Rayleigh numbers for the three layers imply the permeability ratios of $K_1/K_2 = 6$ and $K_3/K_2 = 15$. The solution reaches a steady state at a time level of 0.0686 corresponding to 1.4×10^4 years. The convection pattern is shown in Fig. 5(*a*) for the left half of the domain of Fig. 1. The extreme values for the stream function in the two convective cells are 5.08 and −13.67 indicating that the convection current is much larger for the convective cell at the left. The less permeable middle layer prohibits the development of double-cellular convection pattern as in Case I. The suppression of a second plume rising in the central portion of the aquifer leads to lower temperature in the top and the middle layers (Fig. 5(*b*)). The almost linear vertical temperature profiles in the middle layer (see Fig. 6) shows the effects of the diminished convection current there. The Nusselt number along the top boundary is 2.2, which has decreased because of the inability of heat to convect through the middle layer.

Case III. To study the effects of insulated sides, a case is run with Rayleigh numbers identical to Case I. The steady state solutions for streamlines and isotherms are plotted in Figs. 7(*a*) and 7(*b*), respectively. It is shown that as a result of less heat being supplied to the reservoir, the number of hot plume is reduced from two in Case I to one in the present case. The computed Nusselt number along the top boundary for this case is also less than that of Case I. The vertical temperature plot of Fig. 8 shows that the temperature of the fluid in the top and the middle layers are lower than the corresponding locations in Case I and that temperature inversions in the bottom layer are less pronounced in the present case, both owing to the weaker convection circulation in these regions in this case. On the other hand, Fig. 8 shows that temperature inversions also take place in the middle

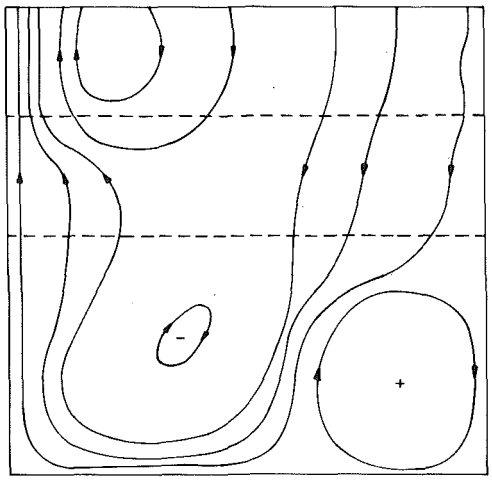

Fig. 5 (*a*)

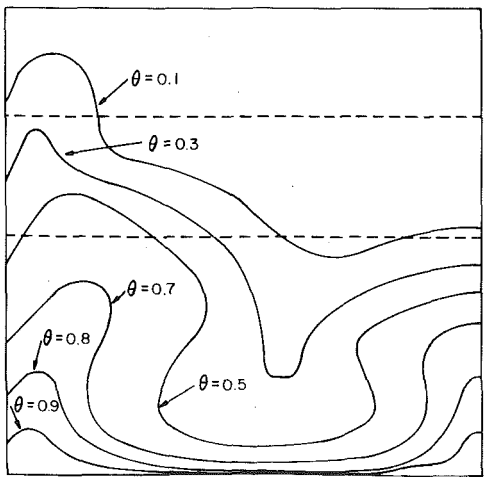

Fig. 5 (*b*)

Fig. 5 Convection patterns and isotherms for Case II

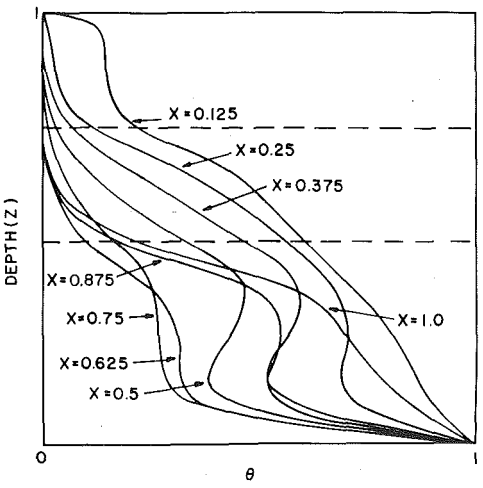

Fig. 6 Dimensionless vertical temperature profiles for Case II

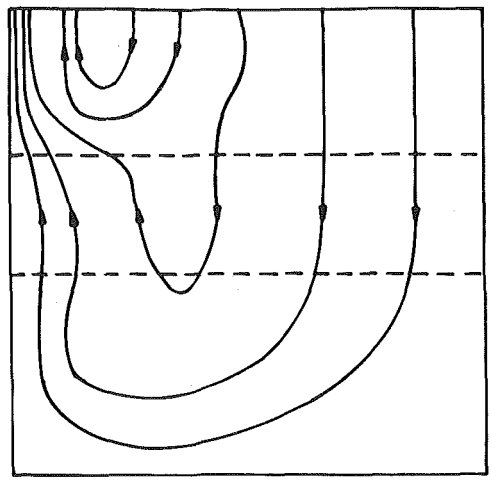

Fig. 7 (*a*)

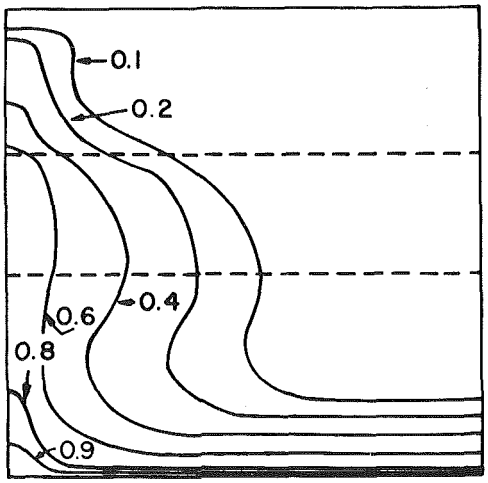

Fig. 7 (*b*)

Fig. 7 Convection patterns and isotherms for Case III

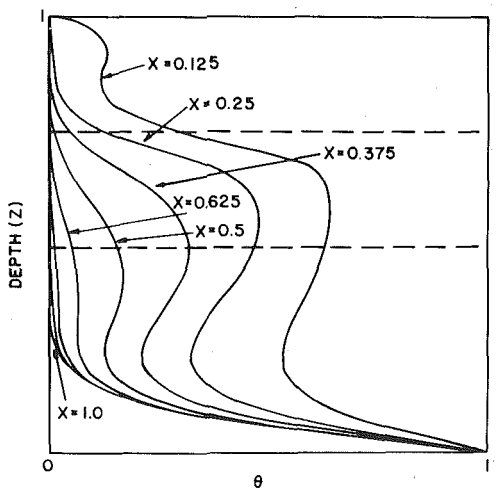

Fig. 8 Dimensionless vertical temperature profiles for Case III

less permeable layer indicating that convective recirculation exists in the middle layer (see also Fig. 7(*a*)).

Comparison with the Case of Uniform Permeability and Field Data. For comparison purposes numerical results are also obtained for the case of uniform permeability with a Rayleigh number (Ra = $K\rho_0 g\beta(T_m - T_0)h_3/\mu\alpha$) of 350. The vertical temperature profiles for this case are plotted in Fig. 9, where it is shown that temperature inversions in the upper portion of the layered reservoir (see Fig. 4) do not exist in the present case. Comparison of computed vertical temperature profiles in Figs. 4, 6, and 8 to the field data taken on different dates at the HGP-A well [13], as plotted in Fig. 10, shows that they are similar in shape. Since the main purpose of the present work is to study qualitatively the effect of layered formation on free convection in a geothermal reservoir, no attempt has been made to match the exact field data to that of the computed profiles. In fact, it would be difficult, if not impossible, to match the field data to that of the computed data exactly since the physical boundaries of the Pahoa geothermal field are at unknown positions and it is likely that the

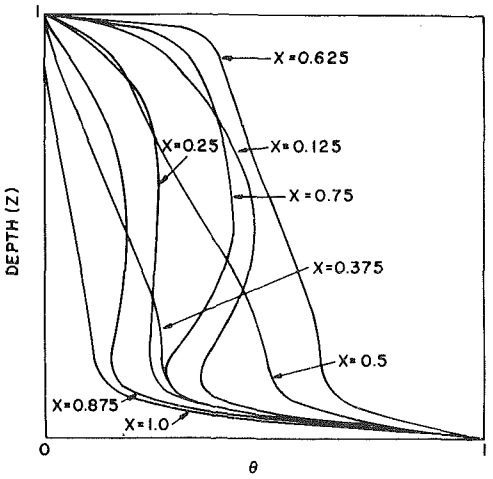

Fig. 9 Dimensionless vertical temperature profile for a reservoir with uniform permeability

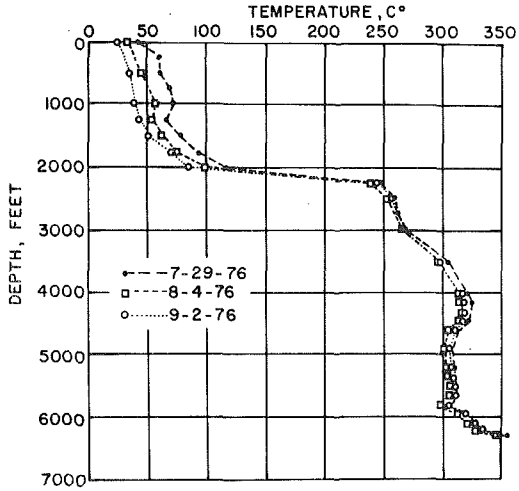

Fig. 10 Vertical temperature profiles from the HGP-A well

temperature profiles measured at the HGP-A well reflect a transient situation rather than a steady state.

Summary and Conclusions

A numerical study has been conducted to investigate the transient free convection in a multi-layered geothermal reservoir. The model is comprised of three horizontal permeable layers with different permeabilities and thicknesses. The study shows that the presence of a lower permeability middle layer can impose a restriction on flow through the layer resulting in a multi-cellular convection pattern. As a result of this restriction, the overall heat transfer rate is reduced. The convection pattern depends not only on the values of the permeability ratios but also on the thermal boundary conditions. The computed vertical temperature profiles near the thermal plumes have temperature inversions in the top and bottom (more permeable) layers while the temperature profiles in the middle (less permeable) layer are relatively straight. The computed temperature profiles for a multi-layered geothermal reservoir are qualitatively similar in shape to those of the field data taken from the HGP-A well.

Acknowledgment

This work was supported in part by the Hawaii Geothermal Project (funded by ERDA through Grant No. E 04-3-1093), by the Stanford Geothermal Program (funded by NSF under Grant No. AER-72-03490), and the National Science Foundation (through Grant No. ENG 77-27527). All the authors were guests of the Stanford Geothermal Program during the course of this research. The authors wish to thank the reviewers for their discussion which has led to the considerable improvement in the manuscript.

References

1 Arakawa, A., "Computational Design for Long-Term Numerical Integration of the Equation of Fluid Motion: Two-Dimensional Incompressible Flow," Part I. *Journal of Computational Physics*, Vol. 1, 1966, pp. 119–143.

2 Busbee, B. L., Golub, G. H., and Nielsen, C. W., "On Direct Methods for Solving Poisson's Equations," *SIAM Journal of Numerical Analysis*, Vol. 7, 1970, pp. 627–655.

3 Caltagirone, J. P., Cloupeau, M., and Combarnous, M., "Convection Naturelle Fluctante dans une Couche Poreuse Horizontale," *Comptes Rendus*, Vol. B273, 1971, pp. 833–836.

4 Caltagirone, J. P., "Thermoconvective Instabilities in a Horizontal Porous Layer," *Journal of Fluid Mechanics*, Vol. 72, 1975, pp. 269–287.

5 Chan, B. K. C., Ivey, C. M., and Barry, J. M., "Natural Convection in Enclosed Porous Media with Rectangular Boundaries," ASME JOURNAL OF HEAT TRANSFER, Vol. 92, 1970, pp. 21–27.

6 Cheng, P., and Teckchandani, L. D., "Numerical Solutions for Transient Responses of a Liquid Dominated Geothermal Reservoir," AGU Monograph No. 20, *The Earth's Crust—Its Nature and Physical Properties*, ed. J. G. Heacock, et al., AGU, Washington, D.C., 1977, pp. 705–721.

7 Combarnous, M. and Le Fur, B., "Transport de Chaleur par Convection Naturelle dans une Couche Poreuse Horizontale," *Comptes Rendus*, Vol. B269, 1969, pp. 1009–1012.

8 Elder, J. W., "Transient Convection in a Porous Medium," *Journal of Fluid Mechanics*, Vol. 27, 1967, pp. 609–623.

9 Holst, P. H. and Aziz, K., "Transient Three-Dimensional Natural Convection in Confined Porous Media," *Int. Journal Heat Mass Transfer*, Vol. 15, 1972, pp. 73–90.

10 Horne, R. N., "Transient Effects in Geothermal Convective Systems," Ph.D Thesis, University of Aukland, School of Engineering, 1975.

11 Horne, R. N. and O'Sullivan, M. J., "Oscillatory Convection in a Porous Medium Heated from Below," *Journal of Fluid Mechanics*, Vol. 66, 1974, pp. 339–352.

12 Horne, R. N., "Three-Dimensional Natural Convection in a Confined Porous Medium Heated from Below," to appear in *Journal Fluid Mech.*, 1979.

13 Progress Report for the First Quarter of Federal FY77, The Hawaii Geothermal Project, Phase II—Well Testing and Analysis, Jan. 1, 1977.

14 Rana, R., "Numerical Simulation of Free Convection in a Multi-Layer Geothermal Reservoir," M.S. Thesis, Dept. of Mechanical Engineering, University of Hawaii, Aug. 1977.

A. Bejan
Assistant Professor,
Department of Mechanical Engineering,
University of Colorado,
Boulder, Col. 80309
Assoc. Mem. ASME

J. Imberger
Professor,
Department of Civil Engineering,
University of Western Australia,
Nedlands, Western Australia, 6009

Heat Transfer by Forced and Free Convection in a Horizontal Channel with Differentially Heated Ends

The effect of net longitudinal flow on natural convection in a horizontal cavity with different end temperatures is discussed. The flow is studied using an asymptotic expansion in the aspect ratio $A \ll 1$, the Grashof, Prandtl and Peclet numbers being arbitrary but fixed. It is shown that unlike the natural counterflow with zero longitudinal net flow [1] a net discharge leads to a nonparallel flow structure characterized also by a variable longitudinal temperature gradient. The influence of parameters A, Gr, Pr and Pe on the flow structure is discussed. An asymptotic expression for the Nusselt number for longitudinal heat transport through the cavity is derived in the limit $A \to 0$ and Gr, Pr, Pe fixed.

Introduction

The heat transfer in a long horizontal slender cavity with a longitudinal temperature was discussed in a series of papers by Cormack, et al. [1, 2] and Imberger [3]. The cavity had adiabatic top and bottom walls and the circulation in the center of the cavity was driven by the longitudinal temperature gradient. The flow was found to be horizontal, proceeding towards the cold end in the upper half of the channel and returning in the lower half after being cooled by the cold vertical end wall. It was shown that steady state was reached when a vertical temperature gradient was established sufficient to diffuse an amount of heat from the top layer to the bottom layer necessary to balance the convective transports. The natural counterflow represents an effective mechanism for convective heat transfer between the ends of the cavity.

The solution was shown to depend on the Prandtl number Pr, the Grashof number Gr and the aspect ratio A. The limit considered was $A \to 0$ and Pr and Gr fixed. In this limit there was excellent agreement between the analytical results, the numerical solutions and the experimental measurements.

Cormack, et al. [4] replaced the adiabatic boundary condition along the top wall and found solutions for a top boundary with heat transfer and one which moved longitudinally. Their analysis was similar to the earlier techniques. However, since the natural convection velocity was selected as velocity scale, the results of Cormack, et al. are most meaningful in cases where the surface effect (velocity, heat flux) is small when compared with the natural convection effect in the horizontal fluid layer. This condition requires a top velocity no greater than the natural convective velocity, and a top surface heat transfer rate no greater than the net heat transfer rate in the horizontal direction through the cavity.

Many applications of the cavity flow process involve net discharge through the cavity from one end to the other. Such a flow leads to a form of forced convection since the longitudinal temperature gradient is convected by the flow. Distinct from the natural counterflows previously investigated, a net discharge leads to a net transportation of heat down the cavity. With adiabatic walls this cannot be balanced by vertical diffusion. In this paper we show how the temperature field compensates for the net flow by developing a sufficient x variation in temperature for longitudinal diffusion to balance the forced convection.

Mathematical Formulation

Fig. 1 shows a parallel-plate channel with the height H considerably smaller than its length L. The channel is filled with a Newtonian incompressible fluid. The long horizontal boundaries $y' = 0, H$ are adiabatic and impermeable. As shown on the figure, the two ends are kept at different temperatures $T_a < T_b$. The fluid is forced to move through the channel at a known volumetric flowrate per unit width Q [m^2/s]. The positive sense of this net flow is chosen to coincide with the positive x direction.

We are interested in the flow and temperature field in the core of the cavity in the limit $A = H/L \to 0$. For this to be a meaningful limit the flow must retain the relative balance between natural and forced convection as $A \to 0$. If $\Delta T = T_b - T_a$ is the temperature difference across the cavity, then the baroclinic pressure difference will be of the order of $(\beta \Delta T \rho_0 g H)$. On the other hand, if Q is the net flow through the cavity then there must exist a barotropic pressure across the cavity of the order of $(\rho_0 \nu Q L/H^3)$. We require in the limit $A \to 0$ that $(\beta \Delta T \rho_0 g H) = (\text{constant})(\rho_0 \nu Q L/H^3)$. It is easy to see that the constant in this proportionality is equal to

$$\frac{\beta \Delta T \rho_0 g H}{\rho_0 \nu Q L/H^3} = \mathrm{Ra}\,\frac{A\alpha}{Q}$$

where Ra is the Rayleigh number based on the channel vertical dimension H,

$$\mathrm{Ra} = \frac{g\beta \Delta T H^3}{\alpha \nu}.$$

From the preceeding argument we conclude that in the limit $A \to 0$ Q must also approach zero so that Q/A remains constant. In other words, for scaling purposes it is inappropriate to use the flow rate Q, for one cannot regard Q as constant and still talk about a balance between free and forced convection in the slender channel limit. Therefore, we define $Q_1 = Q/A$ and use Q_1 as the independent flow scaling parameter which has the property that it remains fixed in the limit $A \to 0$. From Poiseuille fow between two parallel plates it is known that Q_1 is of order $H^2 \Delta P/\mu$, where ΔP is the end-to-end pressure difference applied across the channel. In conclusion, using Q_1 (fixed) as independent flow scaling parameter is equivalent to using the end-to-end ΔP, assumed arbitrary but fixed. The dimensionless group which characterizes the forced convection effect in the channel is the Peclet number based on Q_1 (or ΔP) defined as $\mathrm{Pe} = Q_1/\alpha$.

The most consistent nondimensionalization for this limit is thus

$$x = \frac{x'}{L};\ y = \frac{y'}{H};\ \theta = \frac{T - T_a}{T_b - T_a};\ \psi = \frac{\psi'}{\mathrm{Gr\,Pr}\,A\alpha},$$

where the dashed variables are physical quantities and

$$\mathrm{Pr} = \frac{\nu}{\alpha};\ \mathrm{Gr} = \frac{g\beta H^3 (T_b - T_a)}{\nu^2};\ \mathrm{Ra} = \mathrm{Gr\,Pr}.$$

In terms of these variables the equations describing conservation of mass, momentum and energy in steady-state, subject to the usual Boussinesq approximation, are

$$\mathrm{Gr}\,A^2 \frac{\partial(\omega, \psi)}{\partial(x, y)} = A^2 \frac{\partial^2 \omega}{\partial x^2} + \frac{\partial^2 \omega}{\partial y^2} + \frac{\partial \theta}{\partial x}, \tag{1}$$

$$A^2 \frac{\partial^2 \psi}{\partial x^2} + \frac{\partial^2 \psi}{\partial y^2} = -\omega, \tag{2}$$

Contributed by the Heat Transfer Division for publication in the JOURNAL OF HEAT TRANSFER. Manuscript received by The Heat Transfer Division November 29, 1978.

$$\mathrm{GrPr}\, A^2 \frac{\partial(\theta, \psi)}{\partial(x, y)} = A^2 \frac{\partial^2 \theta}{\partial x^2} + \frac{\partial^2 \theta}{\partial y^2}, \tag{3}$$

where ω is the dimensionless vorticity.

The following boundary conditions apply at the solid horizontal walls

$$\psi = \mathrm{Pe/Ra}; \frac{\partial \psi}{\partial y} = \frac{\partial \theta}{\partial y} = 0 \text{ at } y = 1, \tag{4}$$

$$\psi = \frac{\partial \psi}{\partial y} = \frac{\partial \theta}{\partial y} = 0 \text{ at } y = 0. \tag{5}$$

The scaling of the governing equation reveals that the flow and temperature field in the channel depend on four dimensionless parameters: the Grashof number Gr, the Prandtl number Pr, the aspect ratio A and the forced flow Peclet number $\mathrm{Pe} = Q_1/\alpha$.

Asymptotic Solution $A \to 0$. (Gr, Pr, Pe Fixed)

The solution follows from the procedure outlined by Cormack, et al. [1], by which the unknown functions, θ, ψ and ω are expanded in series form,

$$\theta = \theta_0 + A^2\theta_2 + A^4\theta_4 + \tag{6}$$

$$\psi = \psi_0 + A^2\psi_2 + A^4\psi_4 \tag{7}$$

$$\omega = \omega_0 + A^2\omega_2 + A^4\omega_4 \tag{8}$$

and then substituted back into equations (1–3).

The zeroth order equations are:

$$\frac{\partial^2 \omega_0}{\partial y^2} + \frac{\partial \theta_0}{\partial x} = 0; \frac{\partial^2 \psi_0}{\partial y^2} = -\omega_0; \frac{\partial^2 \theta_0}{\partial y^2} = 0 \tag{9}$$

with the boundary conditions

$$\psi_0 = \mathrm{Pe/(PrGr)}; \frac{\partial \psi_0}{\partial y} = \frac{\partial \theta_0}{\partial y} = 0 \text{ at } y = 1 \tag{10}$$

and

$$\psi_0 = \frac{\partial \psi_0}{\partial y} = \frac{\partial \theta_0}{\partial y} = 0 \text{ at } y = 0. \tag{11}$$

A solution to this problem is

$$\theta_0 = F_0(x) \tag{12a}$$

$$\psi_0 = \frac{dF_0}{dx}\left(\frac{y^4}{24} - \frac{y^3}{12} + \frac{y^2}{24}\right) - \frac{\mathrm{Pe}}{\mathrm{PrGr}}(2y^3 - 3y^2). \tag{12b}$$

The first part of the streamfunction describes the natural convection flow induced by the longitudinal temperature gradient dF_0/dx. The second component is the plane Poiseuille flow necessary to carry the net mass flow Q_1.

The unknown function $F_0(x)$ may be obtained by considering the second order temperature equation

$$\mathrm{GrPr}\frac{\partial \psi_0}{\partial y}\frac{\partial \theta_0}{\partial x} = \frac{\partial^2 \theta_0}{\partial x^2} + \frac{\partial^2 \theta_2}{\partial y^2}. \tag{13}$$

Integrating this with respect to y between 0 and 1 and invoking the appropriate boundary conditions, i.e., $\partial\theta_2/\partial y = 0$ at $y = 0, 1$, yields

$$\frac{d^2 F_0}{dx^2} - \mathrm{Pe}\frac{dF_0}{dx} = 0, \tag{14}$$

which has the solution

$$F_0 = \frac{C_0}{\mathrm{Pe}}(e^{\mathrm{Pe}x} - 1) + C_0^* \tag{15}$$

The two constants of integration C_0 and C_0^* must be determined from the end boundary conditions.

Proceeding in an identical manner, the solution may be determined up to an arbitrary order. The aggregate expression for the temperature and the streamfunction correct to second order is given by:

$$\theta = \frac{K}{\mathrm{Pe}}(e^{\mathrm{Pe}x} - 1) + K^* + A^2\left[K^2\,\mathrm{PrGr}\, e^{2\mathrm{Pe}x}\left(\frac{y^5}{120} - \frac{y^4}{48} + \frac{y^3}{72}\right) - K\mathrm{Pe}\, e^{\mathrm{Pe}x}\left(\frac{y^4}{2} - y^3 + \frac{y^2}{2}\right) - \frac{K\mathrm{Pe}}{210}e^{\mathrm{Pe}x}(\mathrm{Pe}x - 1) - \frac{K^2\mathrm{GrPr}}{1440}(e^{2\mathrm{Pe}x} - 1) + \frac{K^3\,\mathrm{Pr}^2\,\mathrm{Gr}^2}{241920}\left(\frac{e^{\mathrm{Pe}x} - 1}{\mathrm{Pe}} - \frac{e^{3\mathrm{Pe}x} - 1}{3\mathrm{Pe}}\right)\right] + 0(A^4) \tag{16}$$

and

$$\psi = Ke^{\mathrm{Pe}x}\left(\frac{y^4}{24} - \frac{y^3}{12} + \frac{y^2}{24}\right) - \frac{\mathrm{Pe}}{\mathrm{PrGr}}(2y^3 - 3y^2) + A^2\left[\left\{-\frac{K\mathrm{Pe}^3}{210}xe^{\mathrm{Pe}x} - \frac{K^2\mathrm{PePrGr}}{720}e^{2\mathrm{Pe}x} + \frac{K^3\mathrm{Pr}^2\mathrm{Gr}^2}{241920}(e^{\mathrm{Pe}x} - e^{3\mathrm{Pe}x})\right\}\left\{\frac{y^4}{24} - \frac{y^3}{12} + \frac{y^2}{24}\right\} + \frac{K^2\mathrm{PePrGr}}{362880}e^{2\mathrm{Pe}x}(2y^9 - 9y^8 + 12y^7 - 20y^3 + 15y^2) - \frac{K\,\mathrm{Pe}^2}{10080}e^{\mathrm{Pe}x}(3y^8 - 12y^7 + 42y^6 - 84y^5 + 70y^4 - 14y^3 - 5y^2) + \frac{K^2\,\mathrm{PeGr}}{725760}e^{2\mathrm{Pe}x}(10y^9 - 45y^8 + 84y^7 - 84y^6 + 42y^5 - 10y^3 + 3y^2) - \frac{K\,\mathrm{Pe}^2}{3360\mathrm{Pr}}e^{\mathrm{Pe}x}(5y^8 - 20y^7 + 28y^6 - 14y^5 + y^2)\right] + 0(A^4). \tag{17}$$

The parameters K and K^* are shorthand for the sum of integration constants such that,

$$K = C_0 + A^2C_2 + \ldots, \tag{18}$$

$$K^* = C_0^* + A^2C_2^* + \ldots. \tag{19}$$

There are various ways in which parameters K and K^* could be determined from conditions at the two ends of the channel. One definite possibility would be to first specify the systems with which the channel communicates at $x' = 0, L$ (Fig. 1), and then specify the temperature and flow conditions along the rigid boundaries of these new subsystems. This route would be required in cases in which the discharge flow into the neighboring reservoirs is of primary interest. An alternative procedure is to specify the temperature at one point in each of the two mouths of the channel. This procedure is well-established, having been used effectively in connection with free convection

Nomenclature

A = aspect ratio, H/L
C_0, C_0^* = constants of zeroth order solution
F_0 = zeroth temperature distribution, equation (15)
g = gravitational acceleration
Gr = Grashof number
H = channel vertical dimension
k = fluid thermal conductivity
K, K^* = parameters of asymptotic core solution, equations (18, 19)
L = channel length
Nu = Nusselt number
Pe = Peclet number
Pr = Prandtl number
ΔP = end-to-end pressure difference
q = heat transfer rate in the horizontal direction, W/m
Q = volumetric flow rate per unit width, m^2/s
Q_1 = flow scaling parameter, Q/A
Ra = Rayleigh number, GrPr
T = fluid temperature
T_a, T_b = end temperatures
ΔT = temperature difference, $T_b - T_a$
x = horizontal position
x_f = horizontal position of wedge front, Fig. 3
y = vertical position
α = thermal diffusivity
β = coefficient of thermal expansion
θ = dimensionless temperature
ν = kinematic viscosity
ρ_0 = fluid density
ψ = streamfunction
ω = vorticity function
$(\,)'$ = dimensional variables

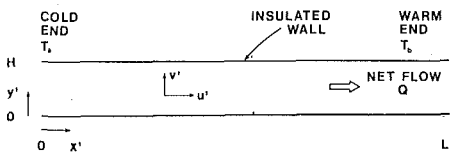

Fig. 1 Schematic of horizontal channel with net flow and different end temperatures

phenomena in slender channels communicating with arbitrary, much larger, fluid reservoirs [5–7]. In the next section we use this technique for evaluating parameters K and K^*; we shall refer to this procedure as "pinning" the channel flow to reservoir-imposed end-temperatures.

At this point it is appropriate to comment on the choice of having expanded θ, ψ and ω in series of even powers of A, equations (6–8). A series expansion in all powers of A (odd and even) was also considered by the authors. Proceeding along this path it was found that the $0(A)$ components $\theta_1, \psi_1, \omega_1$ have exactly the same analytical form as the $0(A^0)$ solution $\theta_0, \psi_0, \omega_0$. The only difference between the two solutions is the two-constant package, (C_1, C_1^*) versus (C_0, C_0^*). Likewise, the $0(A^3)$ solution is analytically identical to the $0(A^2)$ solution. Summing up these solutions, the terms can be grouped two at a time, $0(A^0) + 0(A^1)$, $0(A^2) + 0(A^3)$, etc. The result of this "condensation" is a series expansion in powers of A^2, as proposed from the outset in equations (6–8). Therefore, in expressions such as (18, 19), C_0 and C_0^* are actually shorthand notation for $(C_0 + AC_1)$ and $(C_0^* + AC_1^*)$, respectively. Earlier analyses of natural convection in very shallow channels [1, 4] also revealed the fact that the $A \to 0$ asymptotic solution can be condensed in series from containing only even powers of A.

Discussion of Flow and Temperature Fields

The basic features of the flow in the cavity are best illustrated by describing the zeroth and second order solution separately.

The Zeroth Order Solution. We shall assume that the end region flow is such that at $x = 0$ the flow is described by equations (16) and (17) and that $\theta_0 = 0$. Equally, it will be assumed that at $x = 1$ the flow is again given by the solutions (16) and (17) with $\theta_0 = 1$. With this pinning of the core flow,

$$K = \frac{\mathrm{Pe}}{(e^{\mathrm{Pe}} - 1)}; K^* = 0. \qquad (20a, b)$$

The temperature and flow fields are plotted in Figs. 2 and 3 for different values of the Peclet number and the Rayleigh number Ra = PrGr.

The longitudinal temperature gradient K, at $x = 0$, decreases as the flow rate parameter Pe increases. At the same time, the temperature gradient near $x = 1$ increases sharply. We see that for Peclet numbers of the order of 10 and higher most of the channel length is nearly isothermal. Consequently, for Pe > 10 the free convection effects will be felt in the close proximity of the discharge. If Pe is negative (i.e., the net flow proceeds from right to left on Fig. 1), the resulting temperature distributions are obtained by antisymmetric reflection about the Pe = 0 distribution.

The streamfunction is shown in Fig. 3 as lines of constant $\mathrm{PrGr}\psi_0/\mathrm{Pe}$. The figure was constructed with the intention of showing the competition between the forced convection effect (Pe) and free convection effect (Ra). Increasing the Rayleigh number while keeping the Peclet constant (Pe = 2), the flow pattern progresses from a nearly plane Poiseuille flow at $K\mathrm{Ra} = 20$ to a parallel counterflow approaching the core flow discussed by Cormack, et al. [1]. As Ra increases, more and more warm fluid which enters from the right penetrates the channel. If the Rayleigh number is high enough, a portion of the fluid originating from the warm end will reach the cold end.

The critical parameters deciding the relative importance of forced convection versus free convection are Pe and $K\mathrm{Ra}$. Parameter $K\mathrm{Ra}$ is essentially a Rayleigh number based on the longitudinal temperature gradient at $x = 0$. One way of assessing the relative importance of Pe and $K\mathrm{Ra}$ is by examining the position of the wedge front, i.e.,

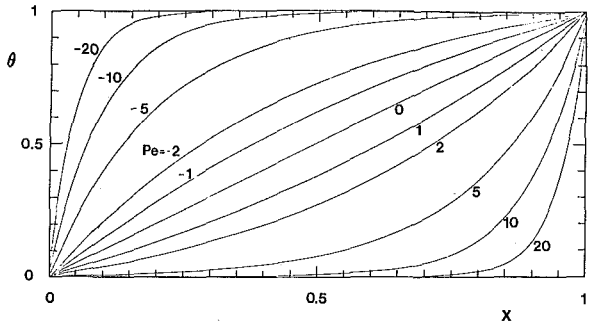

Fig. 2 Zeroth order longitudinal temperature distribution in the channel

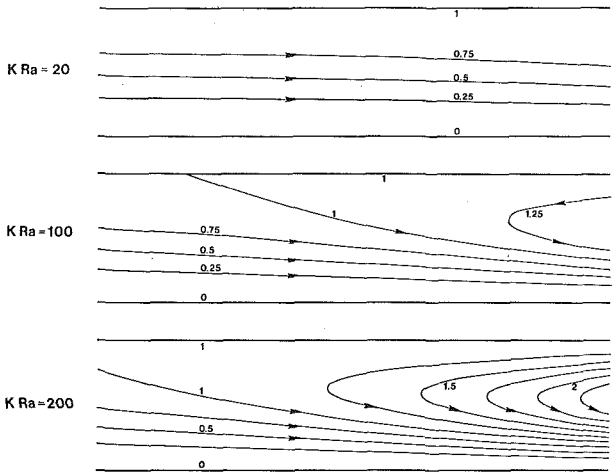

Fig. 3 Zeroth order streamfunction for Pe = 2 and increasing KRa. The numbers on the figure indicate the value of $\psi_0\mathrm{PrGr}/\mathrm{Pe}$.

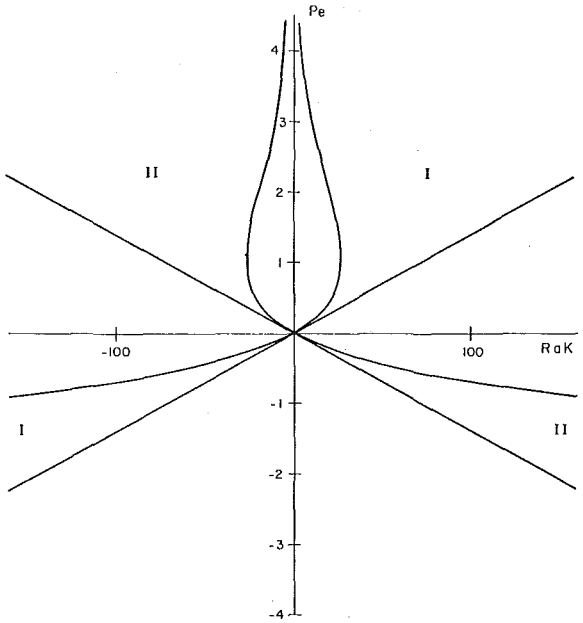

Fig. 4 Two-dimensional field Pe-KRa showing domains I and II based on the zeroth order solution

the furthest point reached by fluid entering from the warm end. As shown in Fig. 3, if Pe and Ra are both positive, the wedge front (a point of zero shear) occurs along the top wall

$$\partial^2\psi/\partial y^2 = 0 \text{ at } y = 1. \qquad (21)$$

The position of the front follows from condition (21),

$$x_{f,y=1} = \frac{1}{\mathrm{Pe}} \ln\left(72 \frac{\mathrm{Pe}}{K\mathrm{Ra}}\right). \qquad (22)$$

Now, for the front to reside in the channel we must have $0 \leq x_{f,y=1} \leq 1$. This condition is met by combinations (Pe, KRa) situated in the domain labeled I on Fig. 4. As an example, the second set of streamlines shown on Fig. 3 (Pe = 2, KRa = 100) belongs to a case situated in domain I. We see also that domain I extends into the third quadrant of Fig. 4, for cases in which Pe and Ra are both negative. When Pe and Ra are of opposite sign the tip of the wedge lies on the bottom, its position being given by

$$x_{f,y=0} = \frac{1}{\text{Pe}} \ln\left(-72\frac{\text{Pe}}{K\text{Ra}}\right). \tag{23}$$

The condition $0 \leq x_{f,x=0} \leq 1$ is met throughout domain II shown on Fig. 4. The remaining four areas not covered by domains I and II are characterized by a flow pattern which approximates either a plane Poiseuille flow, as in the top drawing of Fig. 3, or a Cormack, et al. [1] counterflow in which the Pe effect is much smaller than the Rayleigh number effect.

The zeroth order solution with K, K^* given by (20a, b) is complete, regardless of the type of subsystems bordering the slender horizontal channel. We showed that in the limit $A \to 0$ the temperature field depends only on x, equation (15). This feature is to be expected in the limit $A \to 0$ when, say, L is fixed and H tends to zero. The flow is isothermal across the mouths of the channel because the channel is physically of zero height. In this limit, the mouth temperature from $y = 0$ to $y = 1$ equals the neighboring isothermal reservoir temperature, regardless of the shape and size of the reservoir. In this context, it is important to distinguish between the limit $A \to 0$ with (Ra, Pe, Pr) fixed, considered in the present paper, and the more common "weak free convection" limit Ra $\to 0$ with (A, Pe, Pr) fixed. In the latter, if Pe = 0, the zero order temperature field is determined by conduction, and the resulting temperature distribution across each mouth is non-isothermal.

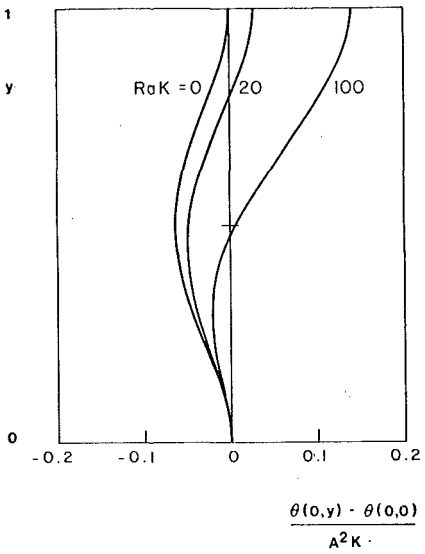

Fig. 5 (a) Cold end

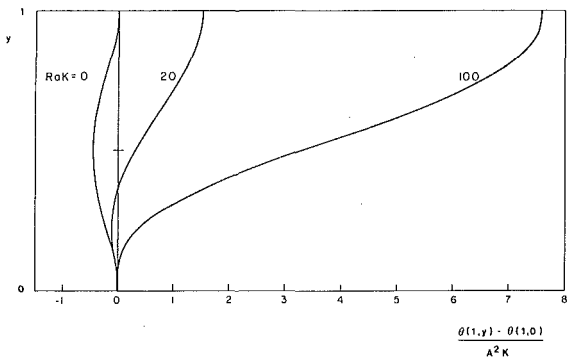

Fig. 5 (b) Warm end

Fig. 5 Second order effects on the temperature distribution

The Second Order Solution. We now turn our attention to the effect of a small but finite aspect ratio A on the $A \to 0$ solution discussed above. The temperature effect is, as expected, a variation with vertical position which becomes more pronounced as the Rayleigh number based on axial temperature gradient KRa increases. Figs. 5(a, b) illustrate this effect for Pe = 2 and increasing KRa, at $x = 0$ and $x = 1$, respectively. The stratification is considerably more pronounced near the discharge end where, as illustrated in Figs. 2 and 3, the free convection effect is felt more strongly as the modified Rayleigh number KRa increases. Figs. 5(a, b) were constructed based on the $0(A^2)$ correction to the temperature field. Hence, the temperature variation shown in the figures scales up as A^2.

The effect of finite A on the streamfunction is somewhat more complex. Examining the aggregate formula (17) we find that the Prandtl number (Pr) appears now as an individual parameter in the solution. We used the Prandtl number to systematically display the second order effect on streamfunction. For example, Fig. 6(a) shows the variation in the limiting case Pr $\to \infty$. To construct Fig. 6(a), we kept the net flow constant, Pe = 2, and increased KRa. The ensuing secondary pattern changes considerably as KRa increases, from a counterclockwise motion at KRa = 0 to a predominantly clockwise movement as KRa goes well over 100. As KRa increases, the top counterclockwise pattern is gradually pushed out of the picture, to the left if both Pe and Ra are positive.

The opposite limit, Pr $\to$ 0, was considered in the sequence of streamline patterns displayed in Fig. 6(b). With Pe = 2, the pattern changes drastically as the Rayleigh number increases. The bottom drawing of Fig. 6(b) illustrates a secondary flow prevalent at high KRa where fluid enters the core region at midheight exiting almost symmetrically along the top and bottom walls. This flow, like the others shown in Fig. 6(a, b), takes place near the discharge end of the channel.

Heat Transport

An interesting aspect of the flow discussed here is the heat transfer between the two ends of the channel. As shown by Cormack, et al. [1], in the absence of net flow the heat transfer rate is due to both con-

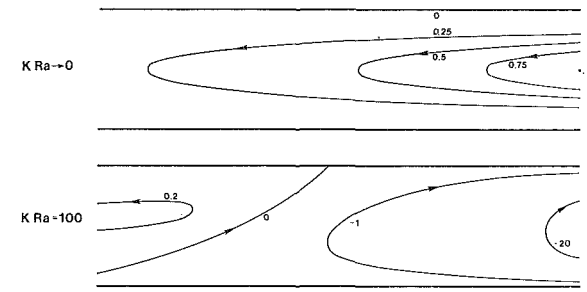

Fig. 6 (a)

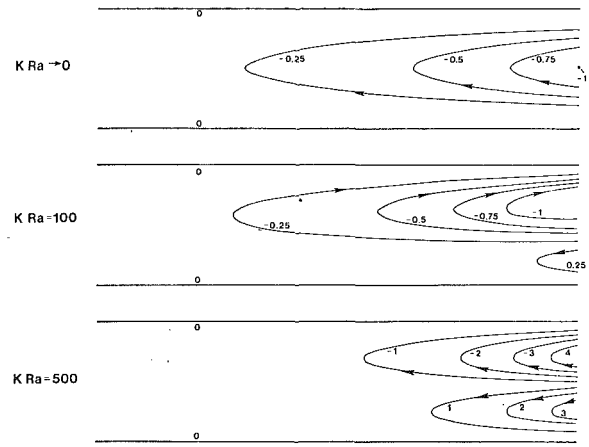

Fig. 6 (b)

Fig. 6 Second order streamfunction for Pe = 2 and increasing KRa: (a) Pr $\to \infty$, b) Pr $\to$ 0. The numbers on the figure indicate the value of: (a) 2.56 $\times$ $10^3\psi_2$, (b) 3.21 $\times$ $10^3\psi_2$Pr.

duction and free convection, the free convection mode becoming the dominant mechanism as the group RaA exceeds roughly 500. In our case, the net flow Q_1 is directed against the naturally occurring flow of heat. For a given end-to-end ΔT and increasing Q_1 we expect the net heat transfer rate to decrease.

We can estimate the net heat transfer rate per unit width q[W/m], positive from right to left on Fig. 1, by performing an energy flux analysis along any x = constant cross-section in the core region of the channel. Dividing q by the estimate based on pure conduction we define the Nusselt number for horizontal heat transfer

$$\mathrm{Nu} = \frac{qL}{Hk(T_b - T_a)} = \int_0^1 \left(\frac{\partial\theta}{\partial x} - \mathrm{Ra}\,\theta\,\frac{\partial\psi}{\partial y}\right) dy. \qquad (24)$$

Using the aggregate expressions (16, 17), the integral (24) yields

$$\mathrm{Nu} = K - \mathrm{Pe}K^* + \frac{K^3\mathrm{Ra}^2A^2}{362880}\left(1 - 252\,\frac{\mathrm{Pe}}{K\mathrm{Ra}}\right) + 0(A^4) \qquad (25)$$

As a useful check on the extensive algebra associated with evaluating integral (24), all x-dependent terms inherited from both θ and ψ drop out; the longitudinal heat transfer rate (25) is independent of position as required by conservation of energy. If Pe = 0, the Nusselt number formula becomes identical to the result developed by Bejan and Tien [8] for heat transfer by free convection in horizontal enclosures. Compared with the Cormack, et al. [1] expression for Nu, expression (25) with Pe = 0 differs only slightly, the factor 1/362880 appearing in (25) being only 3.6 percent smaller than the 2.86×10^{-6} arrived at numerically by Cormack, et al.

Examining the Nusselt number expression (25), we find that Nu decreases appreciably when Pe increases while Ra is kept constant. This effect manifests itself two ways, first via a decreasing K (see equation (20)) and, second, in the last term of expression (25). Fig. 7 illustrates the dependence of Nu on the net flow Pe, for $A = 10^{-2}$ and increasing Ra.

Finally, the Nusselt number result (25) may be used to determine the parametric domain in which the present asymptotic solution is applicable. From the condition that, in (25), the $0(A^2)$ term must never exceed the 0(1) term we find an upper bound for the aspect ratio A,

$$A < 602.4\,(K\mathrm{Ra})^{-1}\left(1 - 252\,\frac{\mathrm{Pe}}{K\mathrm{Ra}}\right)^{-1/2}. \qquad (26)$$

In writing this result we used the zeroth order estimate for K^*, equation (20b). The K formula (20a) can now be coupled with expression (26) to calculate the maximum A for which the present analysis is a realistic approximation.

Concluding Remarks

We analyzed the effect of a net discharge on the natural counterflow set-up in a horizontal parallel-plate channel with the two ends maintained at different temperatures. The analysis was based on an asymptotic expansion in the aspect ratio $A = H/L \to 0$. The flow field and heat transfer in the two dimensional channel was shown to depend on the aspect ratio A, the Rayleigh number Ra, the Peclet number characteristic of the net discharge Pe, and the Prandtl number Pr. The analytical expressions reported for streamfunction, temperature distribution and net horizontal heat transfer rate are valid strictly in the limit $A \to 0$, with Ra, Pe and Pr considered finite and fixed. An estimate of the domain of applicability of these results is contained in expression (26) with the axial temperature gradient parameter given by (20a).

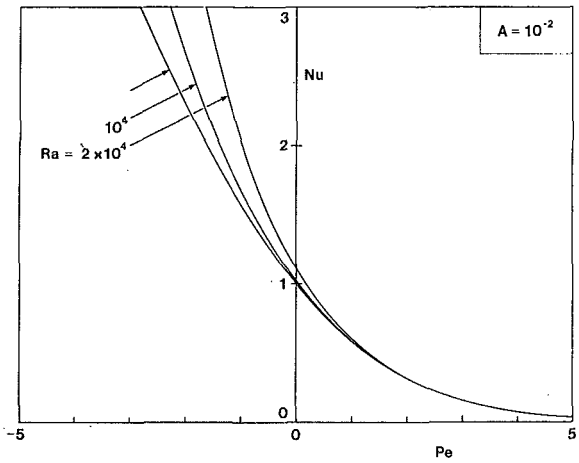

Fig. 7 The Nusselt number versus the Peclet number for $A = 10^{-2}$ and varying Ra

Acknowledgment

The authors thank Professors C. L. Tien, F. S. Sherman and G. M. Corcos, Department of Mechanical Engineering, University of California, Berkeley, for many fruitful discussions. This work was supported in part by a postdoctoral fellowship awarded to A. Bejan by the Miller Institute for Basic Research in Science, University of California, Berkeley. This research was conducted while J. Imberger was an Associate Professor of Civil Engineering at the University of California, Berkeley.

References

1 Cormack, D. E., Leal, L. G. and Imberger, J., "Natural Convection in a Shallow Cavity with Differentially Heated End-Walls. Part 1. Asymptotic Theory," *Journal of Fluid Mechanics*, Vol. 65, 1974, p. 209.

2 Cormack, D. E., Leal, L. G. and Seinfeld, J. H., "Natural Convection in a Shallow Cavity with Differentially Heated End-Walls. Part 2. Numerical Solutions," *Journal of Fluid Mechanics*, Vol. 65, 1974, p. 231.

3 Imberger, J., "Natural Convection in a Shallow Cavity with Differentially Heated End-Walls. Part 3. Experimental Results," *Journal of Fluid Mechanics*, Vol. 65, 1974, p. 247.

4 Cormack, D. E., Stone, G. P. and Leal, L. G., "The Effect of Upper Surface Conditions on Convection in a Shallow Cavity with Differentially Heated End-Walls," *International Journal of Heat and Mass Transfer*, Vol. 18, 1975, p. 635.

5 Lighthill, M. J., "Theoretical Considerations on Free Convection in Tubes," *Quarterly Journal of Mechanics and Applied Mathematics*, Vol. 6, 1953, p. 398.

6 Ostrach, S., and Thornton, P. R., "On the Stagnation of Natural Convection Flows in Closed-End Tubes," *Trans ASME*, Vol. 80, 1958, p. 363.

7 Bejan, A. and Tien, C. L., "Laminar Free Convection Heat Transfer through Horizontal Duct Connecting Two Fluid Reservoirs at Different Temperatures," ASME JOURNAL OF HEAT TRANSFER, Vol. 100, 1978, p. 725.

8 Bejan, A. and Tien, C. L., "Laminar Natural Convection Heat Transfer in a Horizontal Cavity with Different End Temperatures," ASME JOURNAL OF HEAT TRANSFER, Vol. 100, 1978, p. 641.

A. Mucoglu
Department of Mechanical Engineering,
Villanova University,
Villanova, PA

T. S. Chen
Department of Mechanical and Aerospace Engineering,
University of Missouri-Rolla,
Rolla, MO
Mem. ASME

Mixed Convection on Inclined Surfaces

An analysis is performed to study the effects of buoyancy force on the heat transfer characteristics of laminar forced convection flow over an inclined flat surface which is either maintained at a uniform temperature or subjected to a uniform heat flux. Numerical results are presented for Prandtl numbers of 0.7 and 7 over a wide range of values of the buoyancy force parameters, with the angle of inclination ranging from 0 to 90 deg from the vertical. In general, it is found that for both surface heating conditions, the local friction factor and the local Nusselt number increase with increasing buoyancy force for assisting flow and decrease with increasing buoyancy force for opposing flow. In addition, the effects of the buoyancy force on these two quantities are found to diminish as the angle of inclination increases. A comparison is also made of the results between the case of uniform wall temperature and the case of uniform surface heat flux.

Introduction

Mixed forced and free convection in laminar boundary layer flow has been analyzed extensively for vertical and horizontal flat plates (see, for example, [1, 2] and the references cited therein). In general, it has been found that for both flow configurations, the rate of surface heat transfer increases when the buoyancy force assists the forced flow and decreases when it opposes the forced flow. The present study deals with mixed convection along an inclined flat plate, with the angle of inclination ranging from 0 to 90 deg from the vertical. The plate is maintained at a uniform temperature or subjected to a uniforce surface heat flux. Both buoyancy assisting and opposing flows are treated, with the forced flow being either above or below the inclined plate.

Analysis

Consider a laminar forced flow aligned parallel to a flat plate that is inclined with an acute angle γ from the vertical. The forced flow is above the plate when γ is measured in the clockwise direction and below the plate when it is measured in the opposite direction. On the basis of boundary layer assumptions, along with the use of Boussinesq approximation, the governing equations for the problem under consideration can be written as

$$\frac{\partial u}{\partial x}+\frac{\partial v}{\partial y}=0 \tag{1}$$

$$u\frac{\partial u}{\partial x}+v\frac{\partial u}{\partial y}=-\frac{1}{\rho}\frac{\partial p}{\partial x}\pm g\beta(T-T_\infty)\cos\gamma+\nu\frac{\partial^2 u}{\partial y^2} \tag{2}$$

$$0=-\frac{1}{\rho}\frac{\partial p}{\partial y}\pm g\beta(T-T_\infty)\sin\gamma \tag{3}$$

$$u\frac{\partial T}{\partial x}+v\frac{\partial T}{\partial y}=\alpha\frac{\partial^2 T}{\partial y^2} \tag{4}$$

The streamwise pressure gradient induced by the buoyancy force can be related to the temperature difference through equation (3) as

$$-\frac{1}{\rho}\frac{\partial p}{\partial x}=\pm g\beta\sin\gamma\frac{\partial}{\partial x}\int_y^\infty (T-T_\infty)\,dy \tag{5}$$

where the plus and minus signs on the right-hand side of the equation pertains, respectively, to flows above and below the plate. The second term on the right-hand side of equation (2) represents the buoyancy force, and its plus and minus signs refer to upward and downward forced flows, respectively. The boundary conditions for equations (1–4) are

$$u=v=0,\quad T=T_w \text{ or } q_w=-k\,\partial T/\partial y \text{ at } y=0$$
$$u\to u_\infty,\ T\to T_\infty \text{ as } y\to\infty \tag{6}$$

Equation (2), along with equation (5), reduces to that for a vertical plate without the buoyancy induced streamwise pressure gradient term when $\gamma = 0$ deg and to that for a horizontal plate without the buoyancy force term when $\gamma = 90$ deg. For the case of an inclined plate, both the streamwise pressure gradient term and the buoyancy force term exist, but they have different magnitudes depending on the angle of inclination of the plate. An order of magnitude analysis on equation (3) yields $p/\rho\delta \sim g\beta(T-T_\infty)\sin\gamma$ from which the streamwise pressure gradient term $(\partial p/\partial x)/\rho$ becomes of the order of $p/\rho x \sim (\delta/x)g\beta(T-T_\infty)\sin\gamma$. The buoyancy induced streamwise pressure gradient term can then be neglected in comparison with the buoyancy force term in equation (2) when the condition $(\partial p/\partial x)/\rho \ll g\beta(T-T_\infty)\cos\gamma$ or equivalently the condition $(\delta/x)g\beta(T-T_\infty)\sin\gamma \ll g\beta(T-T_\infty)\cos\gamma$ prevails. That is

$$\frac{\delta}{x}\tan\gamma \ll 1 \tag{7}$$

Since $\eta_\delta = \delta(u_\infty/\nu x)^{1/2}$ and $\delta/x = \eta_\delta/\mathrm{Re}_x^{1/2}$ the above condition leads to

$$\tan\gamma \ll \mathrm{Re}_x^{1/2}/\eta_\delta \tag{8}$$

For the mixed convection boundary layer flow considered here, the Reynolds number Re_x may range from 10^3 to 10^5 and the dimensionless boundary layer thickness η_δ is about 10. The values of $\mathrm{Re}_x^{1/2}/\eta_\delta$ will then lie between 3 and 30. Thus, equation (8) will be valid for $\tan\gamma \sim 1$ or $\gamma \le 45$ deg when $\mathrm{Re}_x \sim 10^3$. As Re_x increases, the approximation becomes even more valid for larger angles. At $\mathrm{Re}_x = 10^5$, for example, the γ values may run as high as 80 deg.

Within the framework of the condition given by equation (8), the x-momentum equation (2) can be simplified to

$$u\frac{\partial u}{\partial x}+v\frac{\partial u}{\partial y}=\pm g\beta(T-T_\infty)\cos\gamma+\nu\frac{\partial^2 u}{\partial y^2} \tag{9}$$

Thus, the governing equations for the problem under study are described by equations (1–6) or can be approximated by equations (1, 9, 4), and (6). The next step in the analysis is to transform these equations into a dimensionless form. This is most conveniently carried out separately for the cases of uniform wall temperature and uniform surface heat flux.

Uniform Wall Temperature Case. Let the dimensionless coordinates be

$$\xi=\xi(x),\quad \eta=y(u_\infty/\nu x)^{1/2} \tag{10}$$

and introduce the dimensionless stream function $f(\xi,\eta)$ and the dimensionless temperature $\theta(\xi,\eta)$, respectively, as

$$f(\xi,\eta)=\psi(x,y)/(\nu\,u_\infty\,x)^{1/2},\quad \theta(\xi,\eta)=(T-T_\infty)/(T_w-T_\infty) \tag{11}$$

where the dimensional stream function $\psi(x, y)$ satisfies the continuity equation (1) with

$$u=\partial\psi/\partial y,\quad v=-\partial\psi/\partial x \tag{12}$$

Contributed by the Heat Transfer Division and presented at the Winter Annual Meeting, San Francisco, California, December 10–15, 1978. Manuscript received by the Heat Transfer August 31, 1978. Paper No. 78-WA/HT-46.

Introducing equations (10–12) into equations (9, 4), and (6), one arrives at the following system of equations

$$f''' + \frac{1}{2}ff'' \pm \xi\,\theta = \xi\left(f'\frac{\partial f'}{\partial \xi} - f''\frac{\partial f}{\partial \xi}\right) \tag{13}$$

$$\frac{1}{\mathrm{Pr}}\theta'' + \frac{1}{2}f\,\theta' = \xi\left(f'\frac{\partial \theta}{\partial \xi} - \theta'\frac{\partial f}{\partial \xi}\right) \tag{14}$$

$$f'(\xi, 0) = f(\xi, 0) = 0,\ \theta(\xi, 0) = 1;\ f'(\xi, \infty) = 1,\ \theta(\xi, \infty) = 0 \tag{15}$$

where the primes stand for partial differentiation with respect to η and the buoyancy force parameter $\xi(x)$ has the expression

$$\xi = |\mathrm{Gr}_x|\cos\gamma/\mathrm{Re}_x{}^2 \tag{16}$$

with

$$\mathrm{Gr}_x = g\beta(T_w - T_\infty)x^3/\nu^2, \quad \mathrm{Re}_x = u_\infty x/\nu \tag{17}$$

denoting the local Grashof number and the local Reynolds number, respectively. On the other hand, when the transformation is performed on equations (2–6), one arrives at

$$f''' + \frac{1}{2}ff'' \pm \frac{1}{2}\Omega\sin\gamma\left(\eta\theta + \int_\eta^\infty \theta d\eta + \Omega\int_\eta^\infty \frac{\partial\theta}{\partial\Omega}d\eta\right) \pm \xi\,\theta = \frac{1}{2}\Omega\left(f'\frac{\partial f'}{\partial\Omega} - f''\frac{\partial f}{\partial\Omega}\right) \tag{18}$$

$$\frac{1}{\mathrm{Pr}}\theta'' + \frac{1}{2}f\theta' = \frac{1}{2}\Omega\left(f'\frac{\partial\theta}{\partial\Omega} - \theta'\frac{\partial f}{\partial\Omega}\right) \tag{19}$$

$$f'(\Omega, 0) = f(\Omega, 0) = \theta(\Omega, \infty) = 0, \quad f'(\Omega, \infty) = \theta(\Omega, 0) = 1 \tag{20}$$

where

$$\Omega = |\mathrm{Gr}_x|/\mathrm{Re}_x{}^{5/2} = \xi/(\cos\gamma\ \mathrm{Re}_x{}^{1/2}) \tag{21}$$

Equation (18) reduces to that for a horizontal boundary layer flow [2] when $\gamma = 90$ deg (i.e., $\sin\gamma = 1$ and $\xi = 0$). When the buoyancy induced pressure gradient terms involving $\sin\gamma$ are neglected, it reduces to equation (13) since $\Omega\partial/\partial\Omega = 2\,\xi\partial/\partial\xi$.

It is noted that the parameter $\xi(x)$ or $\Omega(x)$ measures the *magnitude* of the buoyancy force effect, and the plus and minus signs that appear on the left-hand side of equation (13) and (18) pertain to assisting and opposing flows respectively.[1] As $\cos\gamma$ appears in the Grashof number, the solution of equations (13–15) can be carried out, for a prescribed value of ξ, independently of γ.

The physical quantities of interest include the velocity distribution $u/u_\infty = f'(\xi, \eta)$, the temperature distribution $(T - T_\infty)/(T_w - T_\infty) = \theta(\xi, \eta)$, the local Nusselt number Nu_x, and the local friction factor C_f. The last two quantities are defined by

$$\mathrm{Nu}_x = \frac{q_w}{T_w - T_\infty}\frac{x}{k}, \quad C_f = \frac{\tau_w}{\rho u_\infty{}^2/2} \tag{22}$$

From the definition of the wall shear stress $\tau_w = \mu(\partial u/\partial y)_{y=0}$ and Fourier's law $q_w = -k(\partial T/\partial y)_{y=0}$, along with the use of equations (10) and (11), it can be shown that

$$\mathrm{Nu}_x\mathrm{Re}_x{}^{-1/2} = -\theta'(\xi, 0), \quad C_f\mathrm{Re}_x{}^{1/2} = 2\,f''(\xi, 0) \tag{23}$$

Uniform Surface Heat Flux Case. For this case, let

$$\chi = \chi(x), \quad \eta = y(u_\infty/\nu x)^{1/2} \tag{24}$$

$$F(\chi, \eta) = \psi(x, y)/(\nu u_\infty x)^{1/2}, \quad \Phi = (T - T_\infty)\mathrm{Re}_x{}^{1/2}/(q_w x/k) \tag{25}$$

Substitution of equations (24, 25), and (12) into equations (9, 4), and (6) yields the system of equations

$$F''' + \frac{1}{2}FF'' \pm \chi\,\Phi = \frac{3}{2}\chi\left(F'\frac{\partial F'}{\partial\chi} - F''\frac{\partial F}{\partial\chi}\right) \tag{26}$$

$$\frac{1}{\mathrm{Pr}}\Phi'' + \frac{1}{2}F\,\Phi' - \frac{1}{2}F'\,\Phi = \frac{3}{2}\chi\left(F'\frac{\partial\Phi}{\partial\chi} - \Phi'\frac{\partial F}{\partial\chi}\right) \tag{27}$$

$$F(\chi, 0) = F'(\chi, 0) = \Phi(\chi, \infty) = 0, \quad F'(\chi, \infty) = 1, \quad \Phi'(\chi, 0) = -1 \tag{28}$$

where the buoyancy force parameter χ is given by

$$\chi = |\mathrm{Gr}_x{}^*|\cos\gamma/\mathrm{Re}_x{}^{5/2} \tag{29}$$

with the modified Grashof number $\mathrm{Gr}_x{}^*$ defined as

$$\mathrm{Gr}_x{}^* = g\beta q_w x^4/k\nu^2 \tag{30}$$

The velocity distribution is given by $F'(\chi, \eta) = u/u_\infty$ and the temperature distribution by $\Phi(\chi, \eta)/\Phi(\chi, 0) = (T - T_\infty)/(T_w - T_\infty)$. The local Nusselt number and the local friction factor now have the expressions

$$\mathrm{Nu}_x\mathrm{Re}_x{}^{-1/2} = 1/\Phi(\chi, 0), \quad C_f\mathrm{Re}_x{}^{1/2} = 2\,F''(\chi, 0) \tag{31}$$

Results and Discussion

Equations (13–15) were solved by the local nonsimilarity method (see, for example, [2–3]) and also by an efficient and accurate finite-difference method similar to that described in [4], whereas equations (26–28) were solved by the finite-difference method only. Local similarity solutions were also carried out for equations (13–15) and equations (18–20). Each of the systems of equations for the local nonsimilarity model and local similarity model was solved by the Runge-Kutta integration scheme in conjunction with Newton-Raphson method to satisfy the conditions at the edge of the boundary layers. Numerical results were obtained for Prandtl numbers of 0.7 and 7, which are typical for air and water. In the computations, the buoyancy force parameters $\mathrm{Gr}_x\cos\gamma/\mathrm{Re}_x{}^2$ and $\mathrm{Gr}_x{}^*\cos\gamma/\mathrm{Re}_x{}^{5/2}$ for the uniform wall temperature (UWT) and uniform surface heat flux (UHF) ranged from -0.25 to 5.0 for both, with the positive values in the parameters refering to buoyancy force assisting flow and the negative values to buoyancy force opposing flow.

To illustrate the validity of the numerical results that have been obtained under the condition $\tan\gamma \ll \mathrm{Re}_x{}^{1/2}/\eta_\delta$, the Nusselt number results for the UWT case from solutions of the local similarity model

[1] It is noted here that the plus and minus signs associated with the term $\frac{1}{2}\Omega\sin\gamma\,(\eta\theta + \ldots)$ in equation (18) pertain, respectively, to $T_w > T_\infty$ and $T_w < T_\infty$ for flow above the plate and to $T_w < T_\infty$ and $T_w > T_\infty$ for flow below the plate. Likewise, the plus sign in front of the $\xi\theta$ term in both equations (13) and (18) refers to upward forced flow with $T_w > T_\infty$ and downward forced flow with $T_w < T_\infty$, whereas the minus sign refers to downward forced flow with $T_w > T_\infty$ and upward forced flow with $T_w < T_\infty$, for both flows above and below the plate. However, for flow below the plate, the temperature difference in the Grashof number Gr_x that is contained in the Ω and ξ expressions needs to be replaced with $(T_\infty - T_w)$.

Nomenclature

C_f = local friction factor
f, F = reduced stream functions
g = gravitational acceleration
$\mathrm{Gr}_x, \mathrm{Gr}_x{}^*$ = Grashof numbers, $g\beta(T_w - T_\infty)x^3/\nu^2, g\beta q_w x^4/k\nu^2$
k = thermal conductivity
Nu_x = local Nusselt number, $q_w x/(T_w - T_\infty)k$
p = static pressure difference
Pr = Prandtl number
q_w = local surface heat transfer rate per unit area
Re_x = Reynolds number, $u_\infty x/\nu$
T = fluid temperature
T_w, T_∞ = wall and free stream temperatures
u, v = velocity components in x and y directions
u_∞ = free stream velocity
x, y = axial and normal coordinates
α = thermal diffusivity
β = volumetric coefficient of thermal expansion
γ = angle of inclination from vertical
δ = boundary layer thickness
η = pseudo-similarity variable
η_δ = dimensionless boundary layer thickness
θ, Φ = dimensionless temperatures
μ, ν = dynamic and kinematic viscosity
ξ, χ = buoyancy force parameters, $|\mathrm{Gr}_x|\cos\gamma/\mathrm{Re}_x{}^2, |\mathrm{Gr}_x{}^*|\cos\gamma/\mathrm{Re}_x{}^{5/2}$
ψ = stream function
Ω = buoyancy force parameter, $|\mathrm{Gr}_x|/\mathrm{Re}_x{}^{5/2}$

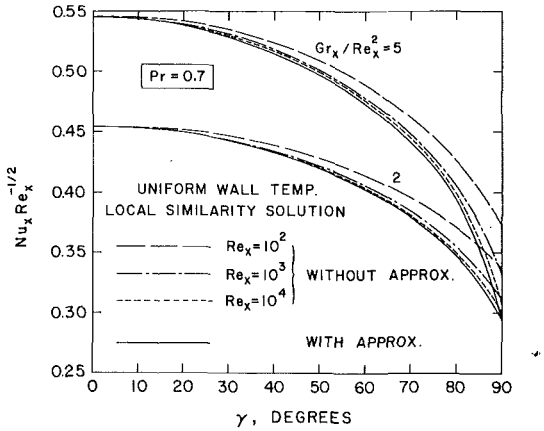

Fig. 1 A comparison of the local Nusselt numbers for uniform wall temperature with and without the approximation $\tan\gamma \ll Re_x^{1/2}/\eta_\delta$, Pr = 0.7

of equations (13–15) are compared with those from solution of the local similarity model of equations (18–20). This is shown for Pr = 0.7 in Fig. 1 for two values of $Gr_x/Re_x^2 = 2$ and 5, each with $Re_x = 10^2$, 10^3, and 10^4, respectively. As can be seen from the figure, the two sets of curves for each Gr_x/Re_x^2 value are in good agreement for the entire range of angles γ from 0 to 90 deg, particularly for $\gamma < 75$ deg and $Re_x \geq 10^3$. Thus, the condition $\tan\gamma \ll Re_x^{1/2}/\eta_\delta$ is valid for 0 deg $\leq \gamma <$ 90 deg for all practical purposes when Re_x is not small. With $Re_x = 10^4$ and $\eta_\delta = 10$, one has $Re_x^{1/2}/\eta_\delta = 10$ and the condition corresponds to the requirement that $\tan\gamma \ll 10$. For larger values of Re_x, $Re_x^{1/2}/\eta_\delta > 10$ and the approximation will be even better for larger angles γ. With the validity of the condition $\tan\gamma \ll Re_x^{1/2}/\eta_\delta$ thus established, the results of engineering interest will be presented next.

Fig. 2 shows the local Nusselt numbers as a function of the buoyancy force parameter $Gr_x \cos\gamma/Re_x^2$ for the UWT case. The results from the local nonsimilarity solution are seen to be in close agreement with those from the finite difference solution. Indeed, the difference between the two sets of results for Pr = 0.7 is less than 0.6 percent so that they cannot be distinguished by curves in the figure. The local similarity model, on the other hand, is seen to provide results that are of relatively low accuracy. A similar trend is observed in the accuracy of the local friction factor results among the three models (Fig. 3) with the results for Pr = 7 between the local nonsimilarity and finite-difference solutions being within 0.3 percent and undistinguishable in the figure. The local Nusselt numbers and the local friction factors as a function of the buoyancy force parameter $Gr_x^* \cos\gamma/Re_x^{5/2}$ for the case of UHF are shown in Figs. 4 and 5, respectively. The results are from the finite-difference solution.

An inspection of Figs. 2–5 reveals that both the local Nusselt number and the local friction factor for both UWT and UHF cases increase with increasing buoyancy force for assisting flow and decrease with increasing buoyancy force for the opposing flow. It is also seen that for a given value of $Gr_x \cos\gamma/Re_x^2$ for UWT or $Gr_x^* \cos\gamma/Re_x^{5/2}$ for UHF, the local Nusselt numbers for Pr = 7 is larger than that for Pr = 0.7. This is because as the Prandtl number increases, the thermal boundary layer thickness decreases and the surface temperature gradient increases (see Fig. 9) which results in a higher rate of heat transfer from the surface. On the other hand, the buoyancy force is seen to have a larger influence on the friction factor for Pr = 0.7 than for Pr = 7. This outcome is due to the lower density of air which exhibits a greater sensitivity to the buoyancy force effect, thereby causing a larger change in the velocity gradients at the wall (see Fig. 8) and, hence, the wall shear results.

From the definitions of the buoyancy force parameters ξ for UWT and χ for UHF, it can be seen that $\xi_{\text{inclined plate}}/\xi_{\text{vertical plate}} = \chi_{\text{inclined plate}}/\chi_{\text{vertical plate}} = \cos\gamma$. That is, as the plate is inclined from the vertical, the buoyancy force effect decreases as $\cos\gamma$. Accordingly, to induce the same effects on the heat transfer and wall shear results at an angle $\gamma > 0$ deg as at $\gamma = 0$ deg (i.e., a vertical plate), the buoyancy force intensity Gr_x/Re_x^2 for UWT or $Gr_x^*/Re_x^{5/2}$ for UHF must be increased by a factor of $1/\cos\gamma$. This trend is true for both

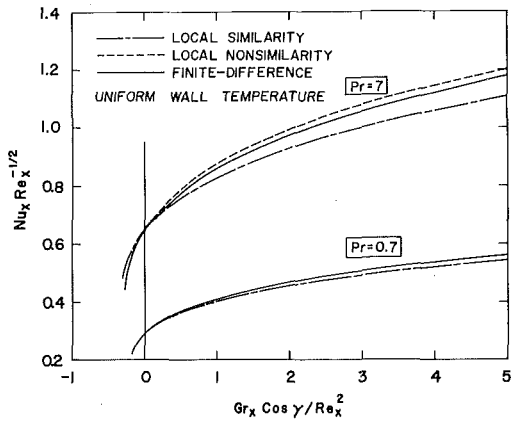

Fig. 2 Local Nusselt number results for uniform wall temperature, Pr = 0.7 and 7

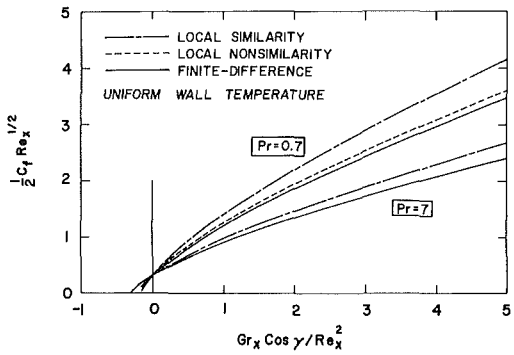

Fig. 3 Local friction factor results for uniform wall temperature, Pr = 0.7 and 7

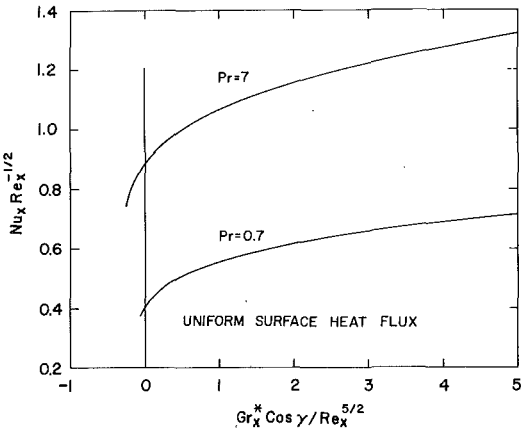

Fig. 4 Local Nusselt number results for uniform surface heat flux, Pr = 0.7 and 7

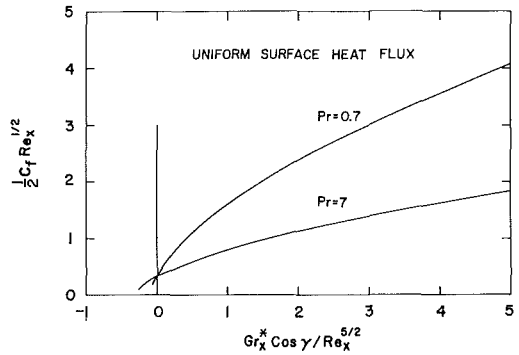

Fig. 5 Local friction factor results for uniform surface heat flux, Pr = 0.7 and 7

assisting and opposing flows. The effects of the buoyancy force intensity on the local Nusselt number at several angles of inclination are illustrated in Figs. 6 and 7 for the UWT and UHF cases, respectively. As can be seen from these figures, the buoyancy force effect diminishes as γ increases.

Representative velocity and temperature profiles for several values of Gr_x/Re_x^2 at two typical angular positions $\gamma = 0$ and 60 deg are shown in Figs. 8 and 9 for the UWT case. It is seen from Fig. 8 that for assisting flow ($Gr_x/Re_x^2 > 0$), the velocity gradient at the wall increases as the buoyancy force increases. This is accompanied by an increase in the velocity near the wall and for $Pr = 0.7$ an overshooting of the velocity beyond its free stream value. For the opposing flow ($Gr_x/Re_x^2 < 0$), the buoyancy force reduces the velocities and the velocity gradients at the wall as compared to those for pure forced convection ($Gr_x/Re_x^2 = 0$), and S-shaped profiles typical of retarded

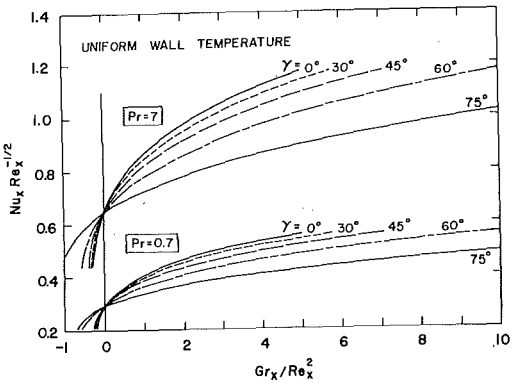

Fig. 6 The effect of angle of inclination on the local Nusselt number for uniform wall temperature, Pr = 0.7 and 7

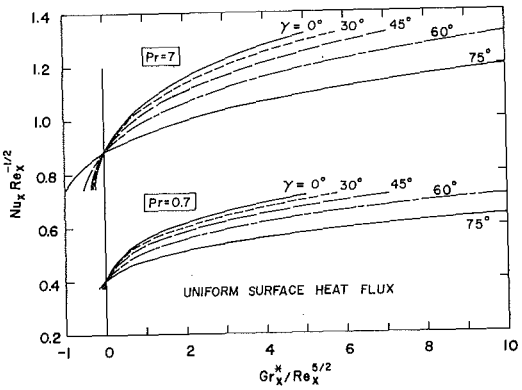

Fig. 7 The effect of angle of inclination on the local Nusselt number for uniform surface heat flux, Pr = 0.7 and 7

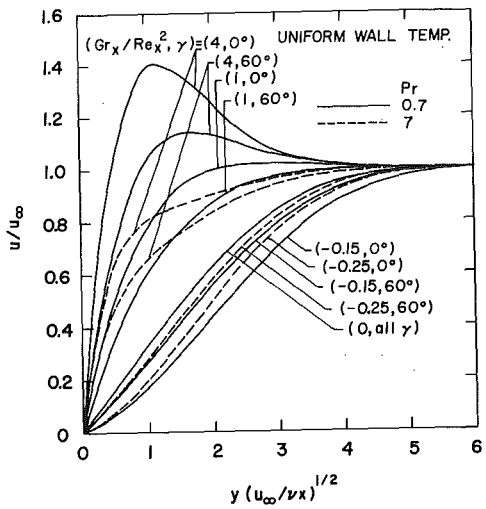

Fig. 8 Representative velocity profiles at various angles of inclination for uniform wall temperature, Pr = 0.7 and 7

boundary layer are in evidence. The effect of buoyancy force on the velocity field, however, diminishes for both assisting and opposing flows as γ increases. With regard to the temperature profiles (Fig. 9), the temperature gradient at the wall is seen to increase as the buoyancy force increases, with an accompanying decrease in the thermal boundary layer thickness, for the case of assisting flow. This trend is seen to reverse for the case of opposing flow. It is noted that the temperature gradient at the wall for $Pr = 7$ is steeper than that for $Pr = 0.7$, as is expected. In addition, just as in the velocity field, the effect of buoyancy force on the temperature field decreases as γ increases. The velocity and temperature profiles for the UHF case are similar to those of the UWT case and, to conserve space, they are therefore omitted.

A direct comparison of the local Nusselt number results between the UHF and UWT cases is of practical interest. To facilitate such a comparison, it is necessary to define an equivalent buoyancy force parameter for the UHF case in terms of the local wall temperature $T_w(x)$ such that

$$\xi_e = [g\beta|T_w(x) - T_\infty|x^3/\nu^2] \cos\gamma/Re_x^2 \tag{32}$$

where

$$|T_w(x) - T_\infty| = |q_w|\,(x/k)Re_x^{-1/2}\Phi(\chi, 0) \tag{33}$$

from the Φ expression in equation (25). Substituting equation (33) into equation (32) and making use of equation (29), one obtains

$$\xi_e = \chi\,\Phi(\chi, 0) \tag{34}$$

For $\xi = \chi\,\Phi(\chi, 0)$, one can write from the Nu_x expressions in equations (23) and (31) that

$$(Nu_x)_{UHF}/(Nu_x)_{UWT} = -1/[\Phi(\chi, 0)\,\theta'(\xi, 0)] \tag{35}$$

The $(Nu_x)_{UHF}/(Nu_x)_{UWT}$ ratio versus $\xi_e = \chi\,\Phi(\chi, 0)$ is plotted in Fig. 10. It can be seen from the figure that, for an equivalent buoyancy

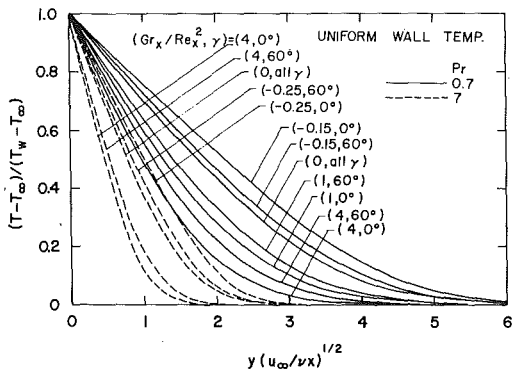

Fig. 9 Representative temperature profiles at various angles of inclination for uniform wall temperature, Pr = 0.7 and 7

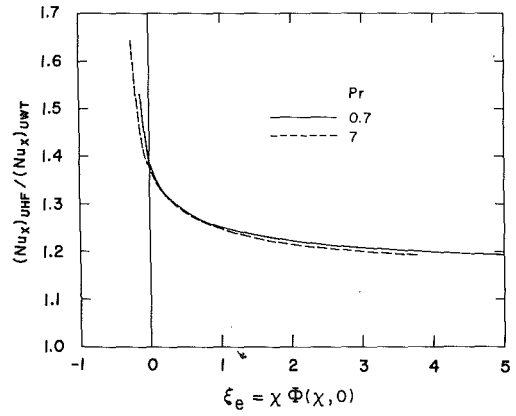

Fig. 10 A comparison of the local Nusselt numbers between uniform surface heat flux and uniform wall temperature, Pr = 0.7 and 7

force parameter as defined by equation (34), heating by uniform surface heat flux provides local Nusselt numbers that are larger than heating by uniform wall temperature. In addition, the Nusselt number ratio decreases as ξ_e increases and becomes essentially constant for large values of ξ_e.

Acknowledgment

This study was supported in part by a grant from the National Science Foundation (NSF ENG 75-15033 A01).

References

1 Oosthuizen, P. H. and Hart, R., "A Numerical Study of Laminar Combined Convective Flow Over Flat Plates," ASME JOURNAL OF HEAT TRANSFER, Vol. 95, 1973, pp. 60–63.

2 Chen, T. S., Sparrow, E. M., and Mucoglu, A., "Mixed Convection in Boundary Layer Flow on a Horizontal Plate," ASME JOURNAL OF HEAT TRANSFER, Vol, 99, 1977, pp. 66–71.

3 Sparrow, E. M. and Yu, H. S., "Local Non-similarity Thermal Boundary-Layer Solutions," ASME JOURNAL OF HEAT TRANSFER, Vol. 93, 1971, pp. 328–334.

4 Cebeci, T. and Bradshaw, P., *Momentum Transfer in Boundary Layers*, Chapter 7, Hemisphere Publishing Corp., Washington, D.C., 1977.

R. W. Douglass
Associate Professor,
Department of Mechanical Engineering,
University of Nebraska,
Lincoln, Neb. 68588
Assoc. Mem. ASME

E. J. Shaughnessy
Assistant Professor,
Department of Mechanical Engineering
and Materials Science,
Duke University,
Durham, N. C. 27706
Mem. ASME

B. R. Munson
Associate Professor,
Department of Engineering Science and Mechanics
and the Engineering Research Institute,
Iowa State University,
Ames, Iowa 50011
Assoc. Mem. ASME

Small Reynolds Number Convection in Rotating Spherical Annuli

A fourth order regular perturbation expansion in powers of the Reynolds number is used to investigate the steady convection of a stratified Boussinesq fluid in rotating spherical annuli. The results include the primary and secondary flow patterns, temperature distributions, total heat flux, and torque characteristics emphasizing their dependence on a wide range of radius and angular velocity ratios. Maximum usable Reynolds numbers were found and usually were larger than 10. The optimum configuration for convective heat transfer is a radius ratio of 0.35 and an angular velocity ratio of +1/3. This same configuration gives the largest torque as well.

1 Introduction

Combined convection in spherical geometries has been the subject of increased study in recent years because of its geophysical and astrophysical applications. Previous work can be divided into two broad classifications: those concerned with the convection in concentric spherical annuli, and those investigating the limiting case of a single rotating sphere immersed in an infinite expanse of fluid. Within each classification research has included both analytical and experimental studies.

As might be expected, early research emphasized convection due to a single sphere rotating in a very large volume of fluid. In 1960, Singh [1] reported results for the forced convection boundary layer problem in such a geometry. His solution was based on a truncated sine series. Later, Bentwich [2] used a perturbation solution technique to study the entire flow field surrounding a rotating sphere subjected to a uniform heat flux. Experimental results for this single sphere case are summarized in Nordlie and Kreith [3] and Kreith, et al. [4]. These works include cases ranging from natural to forced convection. In [4] analytical results are also given using a technique quite similar to that used in [1].

Research into the heat transfer aspects of the more general concentric sphere geometry appears to have been initiated by Erdogan [5, 6]. In these papers results are presented for a variety of boundary conditions with the effect of viscous dissipation included. However, secondary flows were excluded since Stokes flow was assumed. The time dependent convection problem was investigated by Smith and Charles [7] for a flow similar to that of Erdogan. They also assumed that secondary flows were not present, and viscous dissipation was neglected. The annular fluid was allowed to generate heat in an arbitrary fashion while the outer sphere's temperature was taken as an unspecified function of time. The angular velocities of the spheres were specified. Their results include closed form solutions for the velocities and temperature of the fluid in terms of double infinite series of Legendre and Bessel functions.

Avudainayagam [8] studied the heat flux due to a slowly rotating inner sphere and a fixed outer sphere. He allowed the temperature of the outer sphere to depend on both longitude and latitude with the inner sphere held at a fixed temperature. Using the Stokes flow hypothesis, the problem was solved using a technique developed by Saffman [9].

Riley [10] and Riley and Mack [11] were the first to include secondary flow convection effects in the energy equation. They further assumed the fluid to be slightly compressible (Boussinesq) so that natural and combined convection could be considered. The body force field was taken parallel to the rotation axis. Solutions were obtained using a perturbation expansion in powers of the Reynolds number through second order. Their principal finding was that the secondary flow is significant and that its nature is strongly dependent on the degree of natural convection.

The linearized problem of convection in a narrow annulus in almost rigid rotation was investigated by Pedlosky [12]. The bounding surfaces were subject to given uniform heat fluxes. The fluid was stratified with a uniform radial gravity field. Detailed results include velocity and temperature distributions in the Ekman layers, the geostrophic interior of the northern latitudes, and in the equatorial boundary layer. Experimental results for the concentric annulus configuration have been reported by Askin [13] and Maples, et al. [14]. They present data for the Nusselt number dependence on the Reynolds number. Buoyancy effects were included in the experiments, leading to results for several types of combined convection.

In this paper, we consider the analytical solution of subcritical, small Reynolds number combined convection in rotating spherical annuli. The fluid is heated from the inner sphere and is in a uniform radial gravity field. Results include the primary and secondary flow patterns, temperature distributions, total heat flux, and torque characteristics for a wide range of radius and angular velocity ratios. The perturbation solutions are found to be complicated functions of buoyancy and rotational effects as well as of the geometry.

2. The Governing Equations and Method of Solution.

The geometry for the spherical annulus flow is shown in Fig. 1. A viscous Boussinesq fluid [15] fills the gap between the inner and outer spheres which are of radii R_1 and R_2, have uniform temperatures T_1 and T_2, and rotate about a common axis with constant angular ve-

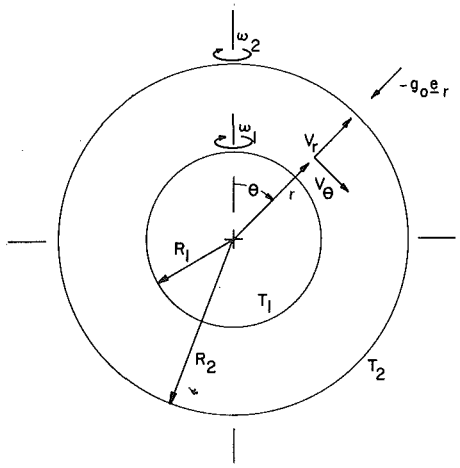

Fig. 1 The flow geometry and notation

Contributed by the Heat Transfer Division for publication in the JOURNAL OF HEAT TRANSFER. Manuscript received by the Heat Transfer Division November 29, 1979.

locities ω_1 and ω_2, respectively. Viscous dissipation is neglected and all fluid properties are assumed constant. Secondary flows in the meridian plane drive the convection. These secondary flows are due in part to the differential rotation of the spheres and to the fluid's variable density interacting with the uniform gravity field, $\underline{g} = -g_0\underline{e}_r$, shown in Fig. 1. This results in the completely coupled system of governing equations shown below. Since the flow is assumed to be independent of the longitude, ϕ, the dimensionless Navier-Stokes equations and energy equation are written in terms of a stream function in the meridian plane, ψ, an angular momentum function, Ω, and a temperature function, ζ. In spherical coordinates (r, θ, ϕ) fixed in space, these equations are as follows (Douglass [16]):

$$\frac{1}{\mathrm{Re}}\tilde{D}^2\Omega = \frac{1}{r^2\sin\theta}\frac{\partial(\Omega,\psi)}{\partial(r,\theta)}, \tag{1}$$

$$\frac{1}{\mathrm{Re}}\tilde{D}^4\psi = -\frac{\mathrm{Gr}}{\mathrm{Re}^2}\sin\theta\frac{\partial\zeta}{\partial\theta} + \frac{1}{r^2\sin\theta}\left\{\frac{2}{r\sin\theta}\right.$$
$$\left.\times\left[\Omega\frac{\partial(-r\sin\theta,\Omega)}{\partial(r,\theta)} + \tilde{D}^2\psi\frac{\partial(-r\sin\theta,\psi)}{\partial(r,\theta)}\right] + \frac{\partial(\tilde{D}^2\psi,\psi)}{\partial(r,\theta)}\right\}, \tag{2}$$

and

$$\frac{1}{\mathrm{Re}}\nabla^2\zeta = \frac{\mathrm{Pr}}{r^2\sin\theta}\frac{\partial(\zeta,\psi)}{\partial(r,\theta)}, \tag{3}$$

where

$$\tilde{D}^2 = \partial^2/\partial r^2 + r^{-2}(\partial^2/\partial\theta^2 - \cot\theta\,\partial/\partial\theta),$$
$$\tilde{D}^4 = \tilde{D}^2(\tilde{D}^2),$$

and ∇^2 is the Laplacian operator in spherical coordinates. Jacobian notation for the derivatives has been used. Thus, for example,

$$\frac{\partial(A,B)}{\partial(r,\theta)} = \frac{\partial A}{\partial r}\frac{\partial B}{\partial\theta} - \frac{\partial A}{\partial\theta}\frac{\partial B}{\partial r}.$$

The flow is assumed to be symmetric with respect to the equator so that the range of independent variables is $R_1 \le \hat{r} \le R_2$ and $0 \le \theta \le \pi/2$. Representative results are then presented for the upper right quadrant of the annulus of Fig. 1.

The actual physical variables are obtained from

$$\hat{v}_r = R_2\omega_0\frac{\partial\psi/\partial\theta}{r^2\sin\theta}$$
$$\hat{v}_\theta = -R_2\omega_0\frac{\partial\psi/\partial r}{r\sin\theta} \tag{4}$$
$$\hat{v}_\phi = R_2\omega_0\frac{\Omega}{r\sin\theta}$$
$$\hat{T} = (T_2 - T_1)\zeta + T_1.$$

The angular velocity of the primary flow about the axis of rotation is given by $\hat{\omega} = \omega_0[\Omega/(r^2\sin^2\theta)]$, or in dimensionless form by $\omega = \Omega/(r^2\sin^2\theta)$.

Various dimensionless groups arise from the nondimensionalization of the governing equations. The nondimensionalization employs R_2, ω_0^{-1}, and $(T_2 - T_1)$ as the characteristic length, time and temperature scales. Among the dimensionless groups are the radius ratio $\eta = R_1/R_2$, the angular velocity ratio $\tilde{\mu} = \omega_2/\omega_1$, the Reynolds number, the Prandtl number, and the Grashof number. The Reynolds number is defined as $\mathrm{Re} = \omega_0 R_2^2/\nu$. The Prandtl number appearing in the energy equation (3) is $\mathrm{Pr} = \mu c/\kappa$.

The remaining dimensionless parameter is the Grashof number $\mathrm{Gr} = g_0\beta(T_2 - T_1)R_2^3/\nu^2$ which appears in equation (2) in the combination $\mathrm{Gr}/\mathrm{Re}^2$. If the inner sphere is warmer than the outer sphere, $T_1 > T_2$ and Gr is negative. This situation may be thermally unstable, and in the absence of rotation is analogous to the Bénard problem. When the spheres are rotating at different rates, heating either sphere modifies the basic shear driven secondary flow. The extent of this modification is a complex function of all the parameters of the problem.

It proves convenient in combined convection calculations to consider values of the ratio $\mathrm{Gr}/\mathrm{Re}^2$. The forced convection problem is given by $\mathrm{Gr}/\mathrm{Re}^2 = 0$, thereby uncoupling equations (2) and (3). Here we consider the values $\mathrm{Gr}/\mathrm{Re}^2 < 0$, corresponding to the unstably stratified combined convection problem. In some cases, the Grashof number may become quite large and perhaps lead to supercritical values of the Rayleigh number ($\mathrm{Ra} = \mathrm{GrPr}$). However, stability is not the concern of this work. The authors are not acquainted with any existing research into the thermal stability of a fluid in a differentially rotating spherical annulus. The stability of the results presented here is, then, still open for further research.

The boundary conditions which complete the formulation of the problem are as follows:

$$\psi = \frac{\partial\psi}{\partial r} = 0 \text{ on } r = \eta, 1,$$

$$\zeta = 0 \text{ on } r = \eta,\ \zeta = 1 \text{ on } r = 1,$$

and either

$$\Omega = \eta^2\sin^2\theta \text{ on } r = \eta \text{ and } \Omega = \tilde{\mu}\sin^2\theta \text{ on } r = 1 \tag{5}$$

if ω_1 is the characteristic angular velocity ($\omega_0 = \omega_1$), or

$$\Omega = \frac{\eta^2}{\tilde{\mu}}\sin^2\theta \text{ on } r = \eta \text{ and } \Omega = \sin^2\theta \text{ on } r = 1$$

if ω_2 is the characteristic angular velocity. In general, ω_0 is taken to be ω_2 unless $\omega_2 = 0$. Then ω_0 is ω_1.

There are three dependent variables in the system of coupled governing equations (1, 2,) and (3); $\psi(r,\theta)$, $\Omega(r,\theta)$, and $\zeta(r,\theta)$. The solution of the system for small Reynolds numbers is found by "perturbing" these variables about their creeping flow (very small Re, negligible inertia) solutions. This is accomplished by assuming solutions of the form

Nomenclature

c = specific heat
e_r = radial unit vector
f_{mn} = component function for Ω_n
g_0 = gravitational acceleration constant
g_{mn} = component function for ψ_n
Gr = Grashof number $= g_0\beta(T_2 - T_1)R_2^3/\nu^2$
h_{mn} = component function for ζ_n
M = torque required to rotate the spheres
$P_m(\theta)$ = Legendre polynomial of the first kind of degree m
Pr = Prandtl number $= \mu c/\kappa$
Q = total heat transfer rate
r = radial coordinate
R_1, R_2 = inner and outer radius of the spheres
Ra = Rayleigh number = GrPr
Re = Reynolds number $= \omega_0 R_2^2/\nu$
$\mathrm{Re}_{\max}$ = largest permissible value of Re
$T(r,\theta)$ = fluid temperature
T_1, T_2 = inner and outer surface temperatures
v = velocity component
β = coefficient of volume expansion of the fluid
ϵ = relative size of each pair of consecutive terms in the expansions
$\zeta(r,\theta)$ = dimensionless temperature function
η = radius ratio $= R_1/R_2$
θ = latitudinal coordinate
κ = thermal conductivity
μ = viscosity of the fluid
$\tilde{\mu}$ = angular velocity ratio $= \omega_2/\omega_1$
ν = kinematic viscosity
$\pi = 3.1415\ldots$
ϕ = longitudinal coordinate
$\psi(r,\theta)$ = stream function
$\omega(r,\theta)$ = angular velocity of the fluid
ω_0 = reference angular velocity
ω_1, ω_2 = angular velocity of the inner and outer spheres
$\Omega(r,\theta)$ = angular momentum function

Subscripts

c = conduction
r, θ, ϕ = vector components

Superscript

$\hat{(\ )}$ = physical variable

$$\psi(r, \theta) = \sum_{n=0}^{N} \mathrm{Re}^n \psi_n(r, \theta),$$

$$\Omega(r, \theta) = \sum_{n=0}^{N} \mathrm{Re}^n \Omega_n(r, \theta), \tag{6}$$

and

$$\zeta(r, \theta) = \sum_{n=0}^{N} \mathrm{Re}^n \zeta_n(r, \theta),$$

implying that each additional term is a small correction to the previous ones. In addition, it is necessary to restrict both Pr and $\mathrm{Gr/Re}^2$ to unit order in this solution.

This technique has been used by several other investigators including Riley [10] for a problem related to the one presented here, and Munson [17, 18] for isothermal spherical annulus flows. Ovseenko [19] has proven that for sufficiently small Re, the isothermal flow problem can be presented by the expansion for ψ and Ω as given in equation (6). He was also able to show that such an expansion provides a unique solution. Since the equations for angular momentum and temperature are analogous, ζ is also expanded in a power series in Re. At the present time no proof of uniqueness or convergence of this expansion is available.

Substituting equation (6) into (1–3) and equating like powers of the Reynolds number results in

$$\tilde{D}^2 \Omega_n = \frac{-1}{r^2 \sin\theta} \sum_{m=0,2,\ldots}^{n-1} \frac{\partial(\psi_{n-m-1}, \Omega_m)}{\partial(r, \theta)},$$

$$\nabla^2 \zeta_n = \frac{-\mathrm{Pr}}{r^2 \sin\theta} \sum_{m=0,2,\ldots}^{n-1} \frac{\partial(\psi_{n-m-1}, \zeta_m)}{\partial(r, \theta)},$$

and (7)

$$\tilde{D}^4 \psi_n = -\left(\frac{\mathrm{Gr}}{\mathrm{Re}^2}\right) \sin\theta (\zeta_{n-1})_\theta - \frac{1}{r^2 \sin\theta} \sum_{m=1,3,\ldots}^{n-2} \left\{ \frac{\partial(\psi_{n-m-1}, \tilde{D}^2 \psi_m)}{\partial(r, \theta)} + \frac{2}{r \sin\theta} \left[\tilde{D}^2 \psi_m (\cos\theta r (\psi_{n-m-1})_r - \sin\theta (\psi_{n-m-1})_\theta) + \sum_{l=0,2,\ldots}^{m+1} \Omega_l (\cos\theta r (\Omega_{n-l-1})_r - \sin\theta (\Omega_{n-l-1})_\theta) \right] \right\}$$

with r and θ subscripts referring to partial differentiation.

In equation (7) the summation index, n, is even for Ω_n and ζ_n, and odd for ψ_n. This is due to the symmetries of the flow field as demonstrated in [16, 17]. The boundary conditions for each order become

$$\psi_n(\eta, \theta) = \psi_n(1, \theta) = \frac{\partial \psi_n}{\partial r}(\eta, \theta) = \frac{\partial \psi_n}{\partial r}(1, \theta) = 0,$$

$$\Omega_n(\eta, \theta) = \sin^2\theta \eta^2 \delta_{n0}, \ \Omega_n(1, \theta) = \sin^2\theta \tilde{\mu} \delta_{n0} \quad \text{if } \omega_0 = \omega_1$$

or (8)

$$\Omega_n(\eta, \theta) = \sin^2\theta (\eta^2/\tilde{\mu}) \delta_{n0}, \ \Omega_n(1, \theta) = \sin^2\theta \delta_{n0} \quad \text{if } \omega_0 = \omega_2,$$

and

$$\zeta_n(\eta, \theta) = 0, \ \zeta_n(1, \theta) = \delta_{n0},$$

where $\delta_{ij} = \begin{cases} 0, & i \neq j \\ 1, & i = j \end{cases}$ is the Kronecker delta function.

It is necessary to solve system (7), subject to boundary conditions (8), order by order beginning with the $n = 0$ case. The closed spherical geometry and the form of the operators $\tilde{D}^2$ and ∇^2 suggest the use of separation of variables as a solution method. The dependent variables are appropriately written as

$$\psi_n(r, \theta) = \sum_{m=1,3,\ldots}^{n} g_{mn}(r) \sin^2\theta P_m(\theta),$$

$$\Omega_n(r, \theta) = \sum_{m=0,2,\ldots}^{n} f_{mn}(r) \sin^2\theta P_m(\theta),$$

and (9)

$$\zeta_n(r, \theta) = \sum_{m=0,2,\ldots}^{n} h_{mn}(r) P_m(\theta),$$

where $P_m(\theta)$ is the Legendre polynomial of the first kind of order m. Note that this form is identical to that suggested by Bentwich [2]. The θ dependence of ψ, Ω, and ζ separates from the r dependence for this perturbation solution and allows the governing equations to be written as a system of linear, inhomogeneous ordinary differential equations for the component functions $f_{mn}(r)$, $g_{mn}(r)$, and $h_{mn}(r)$. Only N terms in the expansions are included, introducing the approximation to the exact solutions. N is equal to 4 for the results presented here, giving solutions through Re^4.

The equations for the various component functions can be solved successively with the solutions written in the following general form:

$$\Phi_{mn}(r) = \sum_{i,j} \alpha_{mn}{}^{ij} r^i (\ln r)^j. \tag{10}$$

Here, α represents an array of constant coefficients for the appropriate f, g, or h function. These coefficients are given in terms of the various parameters involved: η, $\tilde{\mu}$, Pr, and $\mathrm{Gr/Re}^2$.

Due to the uncoupling of the momentum and energy equations in forced convection flows, the f_{mn} and g_{mn} functions are the same for this forced convection problem as they are for the isothermal flow [17]. A detailed account of the solution method and a listing of the numerous α coefficients (through terms of order Re^4) can be found in Douglass [16]. It is noted that a solution consisting of f_{00}, g_{11}, and h_{00} represents a very small Reynolds number primary flow with its relatively small secondary flow and a conduction temperature profile, respectively.

3 Discussion of Results

There are five dimensionless parameters governing the flow and heat transfer in the rotating annulus. Two of these (η, $\tilde{\mu}$) are determined by the geometry and boundary conditions, two (Re, $\mathrm{Gr/Re}^2$) are measures of dynamical effects, and the last (Pr) depends on the fluid properties. The results presented here have a Prandtl number of unity and $\mathrm{Gr/Re}^2 = -1$. These parameter values model the combined convection of a fluid such as air or saturated Freon filling a rotating spherical annulus.

The authors have reported results elsewhere which emphasize strong buoyancy and Reynolds number effects [16, 20], and stable stratification [21]. Other results for Reynolds numbers as large as 200 may be found in [22, 23]. The present study complements these earlier numerical simulations in that it includes an extensive examination of the analytical dependence of the flow and heat transfer on the geometry and boundary conditions.

The Validity Criterion. In order to find the largest Reynolds number for which a particular perturbation solution is valid, we employed a criterion similar to that used by Custer and Shaughnessy [24]. Since the solutions to the governing equations are found in terms of an expansion in powers of the Reynolds number, the relative size of each term is used as a gauge to determine the maximum Reynolds number for which the expansion remains valid. The expansion is presumed valid for values of Re such that the absolute value of each term in the expansion is less than 10 percent of the preceding term. This is a more stringent criteria than that used by Riley [10] in his two-term solution for gravity parallel to the rotation axis. The limiting Reynolds number was defined to be that which causes the second term in the series to be $\frac{1}{3}$ (in some cases $\frac{1}{4}$) as great as the first.

The permissible values of Re were obtained by searching the solution at each order for its maximum absolute value and then forming ratios of the maxima. For example, we have

$$\psi(r, \theta) \simeq \mathrm{Re}\, \psi_1 + \mathrm{Re}^3 \psi_3.$$

The gauge of relative size, ϵ, is then defined as

$$\epsilon = \frac{|\mathrm{Re}^3 \psi_3|_{\max}}{|\mathrm{Re} \psi_1|_{\max}} = C(\eta, \tilde{\mu}; \mathrm{Pr}, \mathrm{Gr}) \mathrm{Re}^2 \tag{11}$$

Values of C are calculated for several radius and angular velocity ratios, with Pr and $\mathrm{Gr/Re}^2$ fixed, for each of ζ, ψ, and Ω. Once these are known, the largest of the C values are used to find the upper limit on Reynolds number such that

$$\mathrm{Re}_{max}(\eta, \tilde{\mu}) = (0.1/C_{max})^{1/2}. \quad (12)$$

These values are shown in Figs. 2 and 3. As expected, these Reynolds numbers depend strongly on η and $\tilde{\mu}$. Generally, the largest values of Re are greater than 10, provided η is less than 0.6 and $\tilde{\mu}$ is not near $-1/3$ or $+1$. When $\tilde{\mu} = +1$, the spherical annulus is rotating as a rigid body with no secondary flows and the heat transfer is by conduction. The flow field is then exactly determined. Fig. 3 illustrates that for $\tilde{\mu}$ becoming very large, Re_{max} approaches a limit. This value is the same for $\tilde{\mu} = \pm\infty$. It further appears that for particular values of η and $\tilde{\mu}$, Re_{max} can become quite large, nearing 100. These values of Re_{max} are comparable to those calculated by Riley [10]; however, his values are generally larger.

The Flow Field. The characteristics of the flow between rotating concentric spheres are principaplly dependent on the secondary flow as represented by the stream function, $\psi(r, \theta)$. The convective effects on both energy and momentum are directly coupled to ψ, as seen in the governing equations. The magnitude of ψ generally correlates with Re, increasing as Re increases. It also, of course, depends on Pr, $\mathrm{Gr}/\mathrm{Re}^2$, $\tilde{\mu}$, and η. Prandtl number effects have not yet been fully explored in the literature; however, the Grashof number dependence has been investigated, as mentioned earlier.

The phenomenon of secondary flow in the annulus is due in part to the presence of body forces and in part to the differential rotation of the spherical boundaries. Considering only the rotating boundary source, it is the inequality of the centrifugal accelerations generated at each boundary and their relative magnitudes that determine the nature of the secondary circulation. That is, the centrifugal acceleration, a_i, generated at a given boundary depends on both the radius and angular velocity as:

$$a_i = \sin^2\theta R_i \omega_i^2$$

or

$$\frac{a_2}{a_1} = \frac{R_2\omega_2^2}{R_1\omega_1^2} = \frac{\tilde{\mu}^2}{\eta}.$$

Note that ω_i is squared deleting the direction of rotation from the acceleration. This rotation effect is perhaps most easily seen in the angular velocity ratio ($\tilde{\mu}$) since it determines the relative rotation rates of the boundaries. The angular velocity ratio dependence has been discussed by Munson [17] and by Riley and Mack [11] for forced convection (no body force) situations. Generally, their results show that the direction of secondary flow is a strong function of $\tilde{\mu}$, since again it appears in the boundary conditions. As observed in the northeastern quadrant of the annulus, they show that the clockwise circulation for $\tilde{\mu} = \infty$ changes to counterclockwise for $\tilde{\mu} = 0$ with both of these eddies appearing for certain values of $\tilde{\mu}$ (say, $-1/3$).

A similar sort of behavior is observed for specific values of $\tilde{\mu}$ with η allowed to vary. Consider the large radius ratio ($\eta = .7$) results of Fig. 4(a) first. In each of the following $\tilde{\mu} = -1/3$ which means that the inner sphere is rotating three times as fast as the outer, but in the opposite direction. Here, $R_1 \simeq R_2$ and from the above acceleration ratio it is seen that

$$\frac{a_2}{a_1} \simeq \tilde{\mu}^2 = \frac{1}{9}.$$

Thus, the acceleration generated by the inner sphere is nearly an order of magnitude larger than that of the outer boundary and the circulation is counterclockwise. In the small η case ($\tilde{\mu}$ fixed), the centrifugal acceleration of the inner sphere is comparatively small due to its relatively small radius. Even though it is rotating relatively fast, its small size does not allow its acceleration to compete favorably with the dominating acceleration generated by the outer sphere. Thus, the secondary flow for small η is clockwise as shown in Fig. 4(c). For intermediate values of η, each sphere, to varying degrees, dominates part of the flow field causing two eddies to exist together as shown in Fig. 4(b). The clockwise eddy is near the outer boundary while the counterclockwise eddy is near the inner sphere.

Figs. 5 and 6 demonstrate the effect of annulus size on the fluid's angular velocity, $\omega(r, \theta) = \Omega(r, \theta)/(r^2 \sin^2\theta)$, and temperature, $\zeta(r, \theta)$.

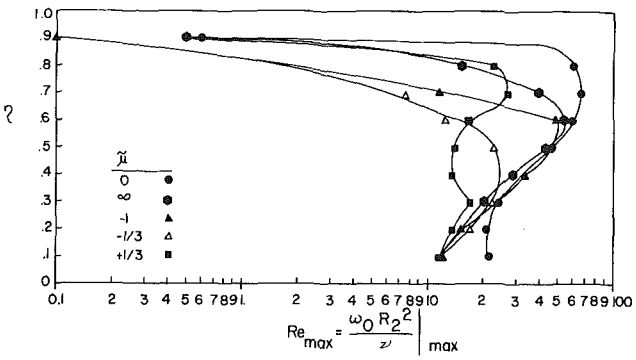

Fig. 2 Limiting Reynolds numbers such that the ratio of any one term in the solutions to its predecessor is less than 0.1: radius ratio dependence

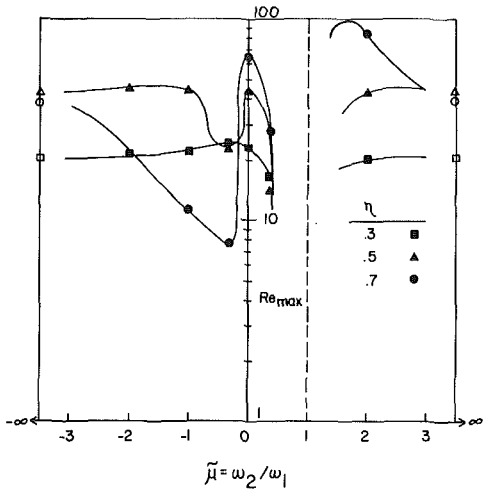

Fig. 3 Limiting Reynolds numbers such that the ratio of any one term in the solutions to its predecessor is less than 0.1: angular velocity ratio dependence. Asymptotes for $\tilde{\mu} = \pm\infty$ are shown with open symbols

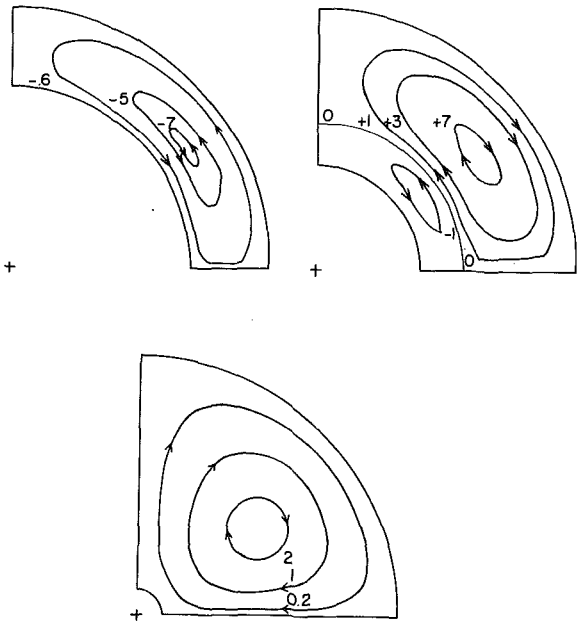

Fig. 4 Secondary flow dependence on the radius ratio. Values shown are multiplied by 10^5. a) $\eta = 0.7$, b) $\eta = 0.4$, and c) $\eta = .1$ for $\mathrm{Re} = \omega_2 R_2^2/\nu = 1$, $\mathrm{Pr} = 1$, $\mathrm{Gr}/\mathrm{Re}^2 = -1$, and $\tilde{\mu} = -1/3$

For the relatively small value of the Reynolds number (Re = 1) in these figures the contours are essentially concentric spherical shells. Hence, the secondary flow has altered neither the primary flow nor the isotherms to any noticeable degree. As Re becomes large, however, these contours as well as those for $\psi(r, \theta)$ become distorted (cf. [23], indicating the importance of the secondary flow's convective effect on momentum and energy). The perturbation solution through order

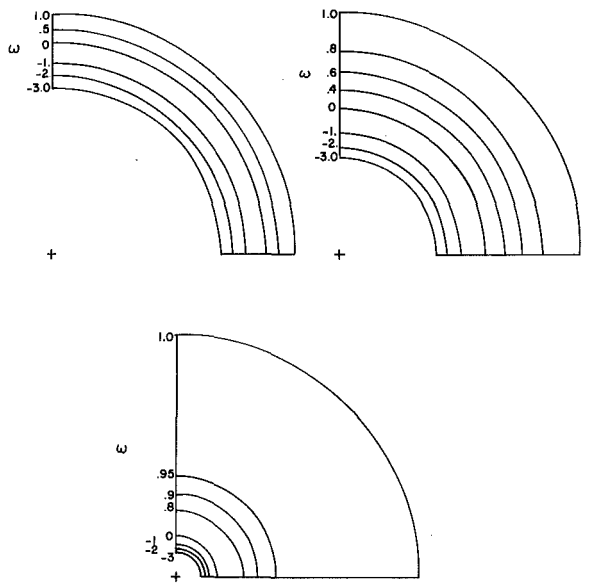

Fig. 5 Angular velocity dependence on the radius ratio. a) $\eta = 0.7$, b) $\eta = 0.4$, and c) $\eta = 0.1$ for $\mathrm{Re} = \omega_2 R_2^2/\nu = 1$, $\mathrm{Pr} = 1$, $\mathrm{Gr/Re}^2 = -1$, and $\tilde{\mu} = -1/3$

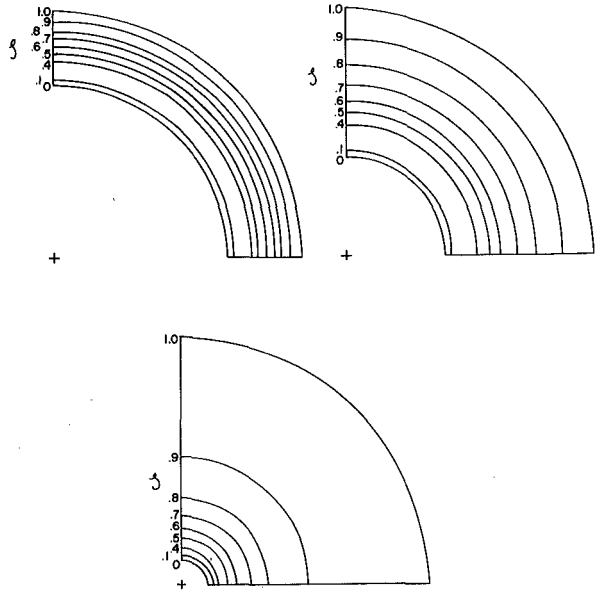

Fig. 6 Isotherm dependence on the radius ratio. a) $\eta = 0.7$, b) $\eta = 0.4$, and c) $\eta = 0.1$ for $\mathrm{Re} = \omega_2 R_2^2/\nu = 1$, $\mathrm{Pr} = 1$, $\mathrm{Gr/Re}^2 = -1$, and $\tilde{\mu} = -1/3$

Re^4 does not allow an accurate observation of these distortions.

Each of the angular velocity contours of Fig. 5 has a locus of zero azimuthal velocity (i.e., $\omega = 0$). This follows since the spheres rotate in opposite directions. It is interesting to note that in illustration (*c*) for $\eta = .1$, a rather large volume of fluid moves at an angular velocity close to that of the outer sphere. This region covers nearly 60 percent of the annulus.

Heat Flux and Torque Calculations. In addition to the dependence of the flow field on the various dimensionless groups, such overall characteristics as the total heat flux due to convection and the torque required to rotate the spheres are of interest. Since the perturbation solution provides exact solutions for the dependent variables, explicit statements of these quantities may be obtained.

The total heat flux, $\hat{Q}$, is found to be

$$\hat{Q} = 4\pi\kappa R_2(T_2 - T_1) \sum_{m=0,2,\ldots}^{N} \mathrm{Re}^m[r^2 h_{0m}'(r)]|_{\eta,1}. \tag{13}$$

The total heat flux due to conduction alone is given by the $m = 0$ term,

$$\hat{Q}_c = 4\pi\kappa R_2(T_2 - T_1)\eta/(1 - \eta). \tag{14}$$

This conduction flux is used to normalize the total flux of (13) giving, for $N = 4$,

$$\frac{\hat{Q}}{\hat{Q}_c} = 1 + A(\eta, \tilde{\mu}; \mathrm{Gr/Re}^2)(\mathrm{PrRe}^2)^2. \tag{15}$$

The parameter A is a measure of the increase in heat transfer due to convection. $A(\mathrm{PrRe}^2)^1$ term is not present in (15) since h_{02} in (13) is identically zero. Thus, the convective heat transfer is at least a fourth order effect. This is in contrast to the case of gravity parallel to the rotation axis in which the heat transfer is at least a third order effect [10, 25].

Values of A are shown in Figs. 7 and 8 for several values of η and $\tilde{\mu}$. From Fig. 7, the optimum value of η for convection is roughly 0.35. The data for $\tilde{\mu} = +1/3$ are nearly an order of magnitude larger than those for other $\tilde{\mu}$ shown. It is also shown that convective effects decrease very sharply as η departs from 0.35.

The general shape of the data is parabolic except for $\tilde{\mu} = -1/3$. In this case, the heat flux data reflect the changes in the secondary flow field as indicated in Fig. 4. Once the two-eddy pattern is well established in the annulus, the total heat flux drops by nearly an order of magnitude.

In Fig. 8, the dependence of A on $\tilde{\mu}$ is shown. Again, the asymptotes of A for $\tilde{\mu} = \pm\infty$ are given. For the wider annuli ($\eta \lesssim .6$) the convective effect generally increases as $\tilde{\mu}$ approaches zero from $-\infty$. For $\tilde{\mu} = 0$, however, the values of A decrease significantly due to the generally weaker secondary flows generated when only the inner sphere rotates. As the outer sphere begins to rotate in the same direction as the inner sphere ($\tilde{\mu} > 0$), the convective effect reaches a maximum, provided $\tilde{\mu} < +1$. At $\tilde{\mu} = +1$, A must be zero since the fluid is moving as a rigid body and secondary flows are nonexistent. In this case, then, the only mode of heat transfer is conduction, and from equation (15) the value of A is obvious. This result is true even for $\mathrm{Gr/Re}^2 \neq 0$ since the body force field is radial (e.g., the spherical Bénard problem), and stratification has been assumed subcritical. For larger $\tilde{\mu}$, A increases asymptotically to its value for $\tilde{\mu} = \infty$.

The torque required to rotate a sphere, $\hat{M}$, is found by integrating the shear stress over the sphere's surface to obtain

$$\hat{M} = \frac{8}{3}\pi\mu\omega_0 R_2^3 \left\{ r^2 \left[f_{00}' - \frac{2}{r} f_{00} + \mathrm{Re}^2 \left(f_{02}' - \frac{1}{5} f_{22}' \right) \right] \right\}\Bigg|_{\eta,1} \tag{16}$$

The fourth order terms do not contribute to the torque since their integrals are zero. The creeping flow torque, $\hat{M}_0$, is the zeroth order term,

$$\hat{M}_0 = \frac{8\pi\mu R_2^3 \omega_2 \eta^3 (1 - \tilde{\mu})}{\tilde{\mu}(1 - \eta^3)} \tag{17}$$

and is used to normalize $\hat{M}$ as

$$\frac{\hat{M}}{\hat{M}_0} = 1 + B(\eta, \tilde{\mu}; \mathrm{Gr/Re}^2, \mathrm{Pr})\mathrm{Re}^2. \tag{18}$$

The quantity B is, again, a function indicating the effect of convection of momentum on the torque required to rotate the spheres. This effect is seen to be second order in the Reynolds number.

The values of B are shown in Figs. 9 and 10. These data are of the same general form as those for the heat flux, since the generation mechanisms involved are the same. The maximum torque occurs for $\eta \simeq .35$ and $\tilde{\mu} = +1/3$, and B is zero for $\tilde{\mu} = +1$ due to rigid rotation.

4 Conclusions

The fourth order regular perturbation solution discussed herein has presented results valid for relatively small values of the Reynolds number and $\mathrm{Pr} = \mathrm{Gr/Re}^2 = 1$. For such Re, the character of the flow field is shown to depend strongly on the angular velocities of the boundaries as well as the size of the annular gap. In contrast to the flow situation with the body force parallel to the rotation axis, radial stratification has a relatively slight effect on the flow field. Further, the values of η and $\tilde{\mu}$ for maximum heat flux are also those for maximum torque.

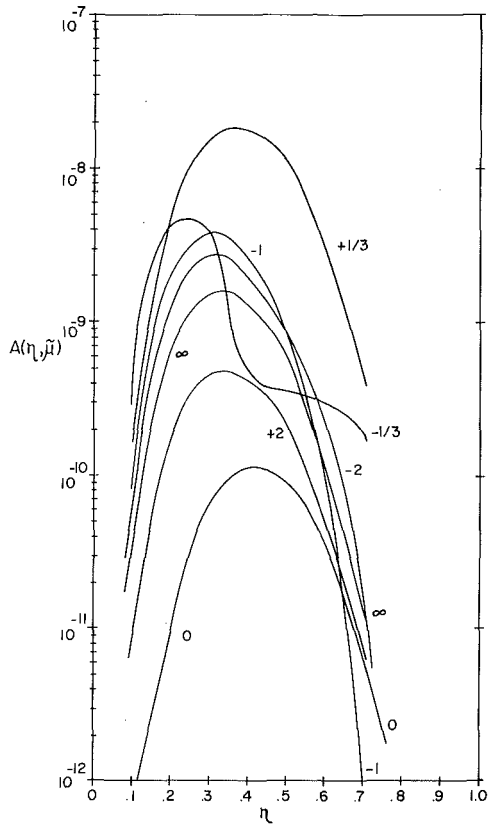

Fig. 7 Convective enhancement of the total heat flux: radius ratio dependence

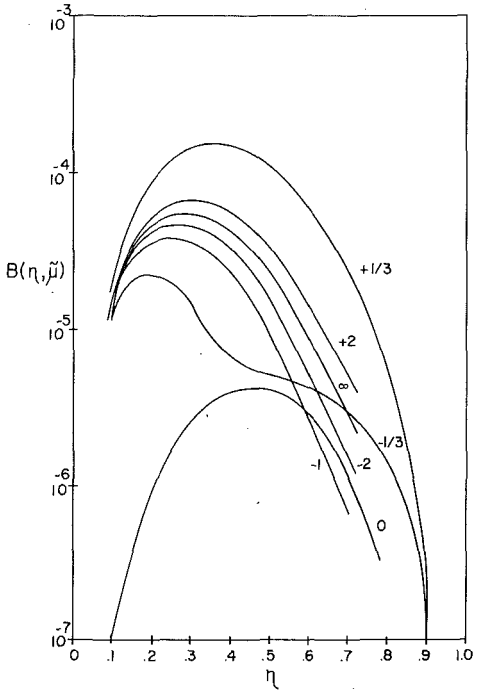

Fig. 9 Convective enhancement of torque: radius ratio dependence

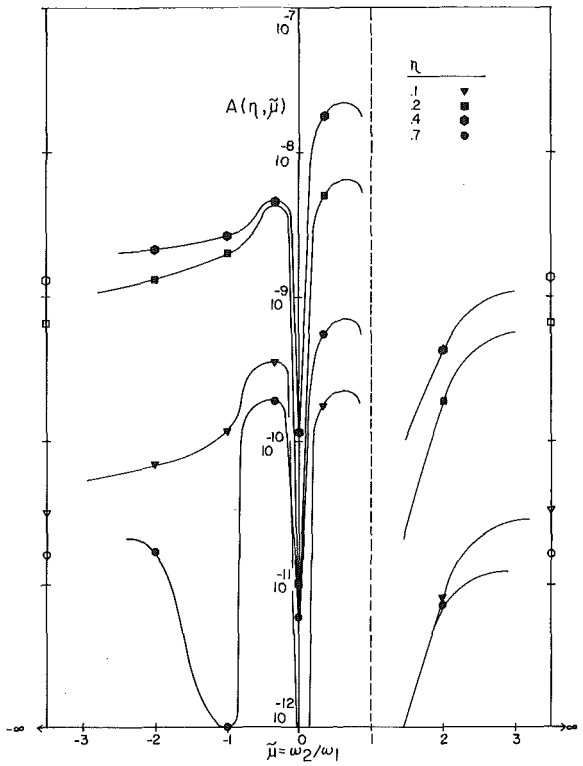

Fig. 8 Convective enhancement of the total heat flux: angular velocity ratio dependence. Asymptotes for $\tilde{\mu} = \pm\infty$ are shown with open symbols

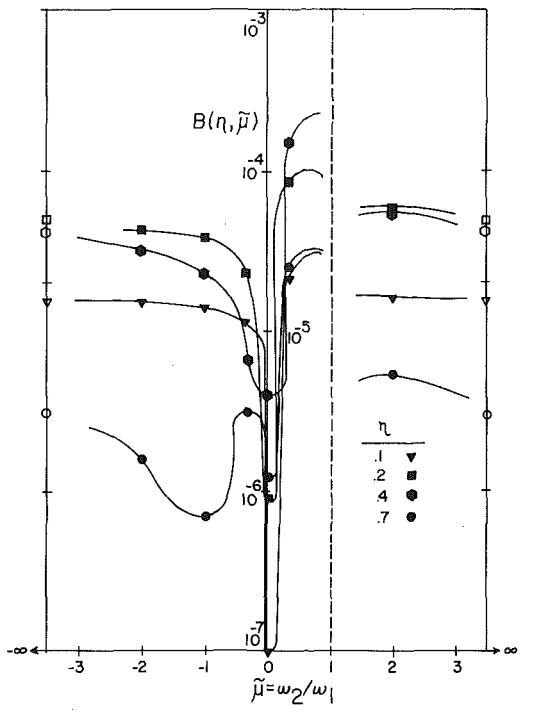

Fig. 10 Convective enhancement of torque: angular velocity radio dependence. Asymptotes for $\tilde{\mu} = \pm\infty$ are shown with open symbols

References

1 Singh, S., "Heat Transfer by Laminar Flow from a Rotating Sphere," *Applied Scientific Research*, Vol. 9, 1960, pp. 197 ff.

2 Bentwich, M., "The Temperature Distribution Inside a Rotating Sphere and in the Entire Flow Field Around It," *Israel Journal of Technology*, Vol. 9, 1971, pp. 1–6.

3 Nordlie, R. and Kreith, F., "Convection Heat Transfer from a Rotating Sphere," in *International Developments in Heat Transfer, Proc. 1961–62 Heat Transfer Conf.*, pp. 461–467.

4 Kreith, F., Roberts, L. Sullivan, J., and Sinha, S., "Convection Heat Transfer and Flow Phenomena of Rotating Spheres," *International Journal of Heat and Mass Transfer*, Vol. 6, 1963, pp. 881–895.

5 Erdogan, M., "Transmission de la Chaleur à un Fluide Visquex se Mouvant Entre Deux Sphères Concentriques Tournantes," *Z.A.M.P.*, Vol. 15, 1964, pp. 66–67.

6 Erdogan, M., "Heat Transfer in an Incompressible Viscous Fluid Between Two Concentric Rotating Spheres," *Bulletin of the Istanbul Technical University*, Vol. 17, 1964, pp. 77–86.

7 Smith, P. and Charles, M., "Unsteady Spherical Couette Flow," in *Developments in Theoretical and Applied Mechanics*, Vol. 5, 1970.

8 Avudainayagam, A., "Heat Transfer from a Slowly Rotating Sphere," *Applied Scientific Research*, Vol. 26, 1972, pp. 18–22.

9 Saffman, P., "The Lift on a Small Sphere in a Slow Shear Flow," *Journal of Fluid Mechanics*, Vol. 22, 1965, pp. 385–400.

10 Riley, T., "Thermal Influence on the Slow Viscous Flow Between Rotating Concentric Spheres," Ph.D. Thesis, Department of Aerospace Engineering and Engineering Mechanics, The University of Texas at Austin, 1971.

11 Riley, T. and Mack, L., "Thermal Effect on Slow Viscous Flow Between Concentric Spheres," *International Journal of Non-linear Mechanics*, Vol. 7, 1972, pp. 275–288.

12 Pedlosky, J., "Axially Symmetric Motion of a Stratified, Rotating Fluid in a Spherical Annulus of Narrow Gap," *Journal of Fluid Mechanics*, Vol. 36, 1969, pp. 401–415.

13 Askin, K., "Convective Heat Transfer from a Rotating Inner Sphere to a Stationary Outer Sphere," M.S. Thesis, Auburn University, Auburn, Ala., 1971.

14 Maples, G., Dyer, D., Askin, K., and Maples, D., "Convective Heat Transfer from a Rotating Inner Sphere to a Stationary Outer Sphere," ASME JOURNAL OF HEAT TRANSFER, Vol. 95, 1973, pp. 546–547.

15 Gray, D. and Giorgini, A., "The Validity of the Boussinesq Approximation for Liquids and Gases," *International Journal of Heat and Mass Transfer*, Vol. 19, 1975, pp. 545–551.

16 Douglass, R., "Combined Natural and Forced Thermal Convection in a Rotating Spherical Annulus," Ph.D. Thesis, Department of Mechanical Engineering and Materials Science, Duke University, Durham, N. C., 1975

17 Munson, B., "Hydrodynamic Stability of Flow Between Rotating Spheres and Rotating Sliding Cylinders," Ph.D. Thesis, University of Minnesota, Minneapolis, Minn., 1970.

18 Munson, B. and Joseph, D., "Viscous Incompressible Flow Between Concentric Rotating Spheres. Part 1: Basic Flow," *Journal of Fluid Mechanics*, Vol. 49, 1971, pp. 289–303.

19 Ovseenko, Yu, "On the Movement of Viscous Liquids Between Two Rotating Spheres," Izv.oVyssh. Uchebo Zaved., Matematica, No. 4, 1963, pp. 129ff.

20 Shaughnessy, E., Custer, J., and Douglass, R., "Partical Spectral Expansions for Problems in Thermal Sciences," ASME JOURNAL OF HEAT TRANSFER, Vol. 100, 1978, pp. 435–441.

21 Shaughnessy, E. and Douglass, R., "The Effect of Stable Stratification on the Motion in a Rotating Spherical Annulus," *International Journal of Heat and Mass Transfer*, Vol. 21, 1978, pp. 1251–1259.

22 Douglass, R., Munson, B., and Shaughnessy, E., "Thermal Convection in Rotating Spherical Annuli, Part I: Forced Convection," *International Journal of Heat and Mass Transfer*, Vol. 21, 1978, pp. 1543–1553.

23 Douglass, R., Munson, B., and Shaughnessy, E., "Thermal Convection in Rotating Spherical Annuli, Part II: Stratified Flows," *International Journal of Heat and Mass Transfer*, Vol. 21, 1978, pp. 1555–1564.

24 Custer, J. R., and Shaughnessy, E. J., "Thermoconvective Motion of Low Prandtl Number Fluids within a Horizontal Cylindrical Annulus," ASME JOURNAL OF HEAT TRANSFER, Vol. 99, 1977, pp. 596–602.

25 Dallman, R. J., "Combined convection in a rotating spherical annulus," M.S. Thesis, University of Nebraska, Lincoln, Nebraska, 1978.

S. V. Patankar
E. M. Sparrow
Fellow, ASME

Department of Mechanical Engineering,
University of Minnesota,
Minneapolis, Minn. 55455

Condensation on an Extended Surface

An analysis is made of film condensation on a vertical fin which is attached to a cooled vertical plate or cylinder. This is a three-dimensional problem in which the condensation process on the fin surface is tightly coupled to conduction within the fin. A physically meaningful similarity solution of the problem was formulated and numerically evaluated. Beyond the range where the similarity solution is valid, a finite-difference marching solution of the governing partial differential equations was carried out. The heat transfer results from the similarity solution, which are represented by simple algebraic formulas, appear to be applicable for the operating range encountered in practice. It was found that the calculated fin heat transfer is markedly less than that which would be predicted by an isothermal fin model, so that the use of such a model substantially overestimates the performance of the fin.

Introduction

Condensation is one of the basic modes of convective heat transfer and, as such, has been studied extensively since the pioneering work of Nusselt in 1916. In the main, the published analyses of film condensation on external surfaces have dealt with primary heat transfer surfaces rather than with extended surfaces (i.e., fins). Furthermore, it appears that the external condensation problems analyzed thus far have involved condensate films whose thickness varies in only one coordinate direction, while the surface temperature is either constant or varies along the direction of film growth. In practice, on the other hand, the use of finned condensers is quite common. Therefore, information about the condensation heat transfer rates on fins has direct relevance to design.

In the present investigation, an analysis is made of film condensation on a vertical fin which is attached to a cooled vertical plate or vertical cylinder. A schematic diagram of the situation under study is presented in Fig. 1. As seen there, a pure saturated vapor (temperature T_{sat}) occupies the space adjacent to a finned plate or cylinder. The vapor is quiescent except for motions induced by the condensation process. The temperature of the plate or cylinder—hereafter called the base surface—is uniform and equal to T_w, with $T_w < T_{sat}$ so that condensation occurs.

It will be assumed that the condensate forms a smooth continuous film on the surface of the fin. Furthermore, it is assumed that if there is an array of fins, the spacing between the fins is sufficiently large so that the respective condensate films do not interact. The thickness of the fin is $2t$ and its transverse length is L. In accordance with the thin-fin model, temperature variations across the thickness of the fin will be neglected.

The condensation process on the fin will now be discussed in order to show that the film thickness δ depends not only on the vertical coordinate z, as in Nusselt-type problems, but also on the transverse coordinate x, i.e., $\delta = \delta(x, z)$. In addition, the fin temperature also depends on both x and z, so that $T = T(x, z)$.

As is true for fins in general, the fin temperature in the present condensation problem varies in the direction transverse to the base surface. In particular, at any z, the fin temperature increases with x, starting with a value $T = T_w$ at $x = 0$. Correspondingly, the condensation rates will be highest in the neighborhood of $x = 0$, i.e., near the base, and will decrease with increasing x. The film thickness mirrors

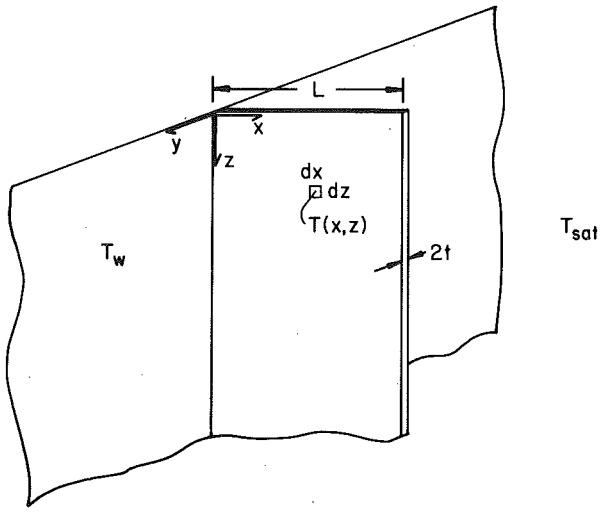

Fig. 1 Schematic diagram of the fin condensation problem

Contributed by the Heat Transfer Division for publication in the JOURNAL OF HEAT TRANSFER. Manuscript received by The Heat Transfer Division September 29, 1978.

the variation of the condensation rate, so that at any z it decreases monotonically from the base to the tip.

Under the action of gravity, the film flows downward along the fin. In the course of its flow, more condensate is added to the film and its thickness grows with z. The effect of this growth is to increase the thermal resistance of the film, thereby decreasing both the condensation rate and the heat flow. The decreased heat flow tends to diminish the transverse temperature gradients in the fin, so that the extent of the temperature variation from base to tip is less at large z than at small z.

The foregoing discussion affirms the dependence of both the condensate film thickness and the fin temperature on both x and z. It can also be demonstrated that the velocity and temperature distributions in the film are three-dimensional. Furthermore, it is necessary to simultaneously solve the conduction problem in the fin and the fluid flow--heat transfer problem in the condensate.

In the forthcoming presentation, an analytical model will be formulated which will make this complex problem tractable. It will be shown that this model admits a similarity-type solution for a wide range of practical operating conditions. Although similarity solutions are well-known in boundary layer work and are also obtainable in a limited class of conduction problems, a similarity solution for a conjugate solid—fluid heat transfer and fluid flow problem is a novelty.

The similarity solution enables the heat transfer results to be presented in a form that is comparable in simplicity to that of the basic Nusselt problem. Beyond the range where the similarity solution is applicable, a finite-difference marching solution of the governing equations for the conjugate problem was performed. It is noteworthy that the dimensionless heat transfer results from both the similarity and nonsimilarity solutions are free of parameters. In addition to local and average heat transfer results, fin temperature distributions and profiles of the condensate layer thickness are also presented.

From a search of the published literature, it appears that the analysis of condensation on fins has been confined to relatively simple situations. In [1], the conventional one-dimensional fin analysis was modified by assuming that the fin was covered with a uniform film of condensate. [2], which is contemporaneous with the present investigation, dealt with a vertical fin whose lower end is maintained at a fixed temperature. Variations of the condensate film thickness and fin temperature were confined to the z, i.e., vertical, direction, so that the problem is of the Nusselt type.

Analysis

Formulation of the Model. The conjugate heat transfer problem encompassing the fin in Fig. 1 and its condensate film will now be formulated in mathematical terms. For the fin, an energy balance for a typical volume element $2tdxdz$ at x, z (Fig. 1) involves conduction heat flows within the fin in the x and z directions and an inflow of heat from the condensate which washes the exposed surfaces of the element. As was noted earlier, it will be assumed that the fin is sufficiently thin so that temperature variations across its thickness can be neglected. If the vertical height of the fin is substantially greater than the transverse length L, then the z conduction—i.e., the streamwise conduction—in the fin is negligible compared with the x conduction. With this, the fin energy balance can be written as

$$-k_f(2tdz)(\partial^2 T/\partial x^2)dx = q(x, z)(2dxdz) \tag{1}$$

in which k_f is the thermal conductivity of the fin and $q(x, z)$ is the local heat flux from the condensate to the fin at x, z. The factor of two on the right-hand side of equation (1) accounts for the presence of a condensate film on both faces of the fin, and the partial derivative appearing on the left is necessary since $T = T(x, z)$.

Attention will now be turned to the evaluation of the condensation heat flux $q(x, z)$. It has been demonstrated in [3] and [4] that conduction is the dominant mode of energy transport in the condensate film, with convection playing a second order role. This is because the film is so thin (~0.1 mm) that the energy released by the subcooling of the condensate is very small compared with that liberated as latent heat during the condensation process. The effect of convection on the heat transfer coefficient is governed by the magnitude of the Jakob number, $c_p\Delta T/\lambda$, where ΔT is the temperature difference across the condensate film. Even for a high value of the Jakob number such as 0.1, the accounting of convection has only a 1.5 percent effect on the transfer coefficient. Since the present research is concerned with the identification of much larger effects, it is reasonable to neglect the contribution of convection.

With convection neglected, the energy equation for a fluid element in the condensate film reduces to $\nabla^2 T_{\text{cond}} = 0$. Among the three derivatives appearing in the Laplacian, $\partial^2 T_{\text{cond}}/\partial y^2$ is overwhelmingly large compared with the x and z derivatives. This is because the scale of the y coordinate ($0 \le y \le \delta$) is much, much smaller than the scales of the x and z coordinates. Therefore, the energy equation for the condensate becomes

$$\partial^2 T_{\text{cond}}/\partial y^2 = 0 \tag{2}$$

the solution to which is a linear temperature distribution

$$T_{\text{cond}}(x, y, z) = T(x, z) + (T_{\text{sat}} - T(x, z))(y/\delta) \tag{3}$$

which reduces at $y = 0$ to the local fin temperature $T(x, z)$ and at $y = \delta$ to the temperature of the saturated vapor T_{sat}. The local heat flux from the condensate to the fin then follows as

$$q(x, z) = \frac{k(T_{\text{sat}} - T(x, z))}{\delta(x, z)} \tag{4}$$

where $\delta(x, z)$ is the local thickness of the film.

The substitution of equation (4) into the right-hand side of (1) serves to eliminate q, so that

$$\frac{\partial^2 T}{\partial x^2} = \frac{k(T - T_{\text{sat}})}{k_f t\delta} \tag{5}$$

This differential equation, when solved, provides a means for obtaining the fin temperature distribution $T(x, z)$, but the fact that $\delta(x, z)$ is unknown precludes such a solution at this stage. In order to obtain an equation which governs the variation of δ with x and z, consideration has to be given to the mass flow in the film and to the condensation process which produces the flow.

Nomenclature

g = acceleration of gravity
F = condensate thickness variable, Δ^4/Z
k = thermal conductivity of condensate
k_f = thermal conductivity of fin
L = transverse length of fin
$\dot{m}$ = condensate flow rate
p = pressure
Q_f = overall rate of fin heat transfer
q = local heat flux at fin surface
q_f = local fin heat flux per unit area of fin-base contact area
T = fin temperature
T_{cond} = condensate temperature
T_{sat} = saturation temperature
T_w = fin base temperature
t = fin half thickness
w = vertical velocity component
X = dimensionless coordinate, x/L
x = transverse coordinate
y = coordinate normal to fin surface
Z = dimensionless coordinate, equation (13)
$\hat{Z}$ = changeover point from similarity to non-similarity solution
z = vertical coordinate
Δ = dimensionless film thickness, equation (12)
Δ_0 = value of Δ at $X = 0$
δ = condensate film thickness
η = similarity variable, equation (23)
η_∞ = numerical approximation for $\eta = \infty$
θ = dimensionless temperature, equation (12)
λ = latent heat of condensation
μ = viscosity of condensate
ρ = density of condensate

Superscript

* = for the ideal (isothermal) fin

To derive the governing equation for δ, consideration is first given to the z-, i.e., streamwise, momentum equation. In [4], it was demonstrated that for all condensed liquids other than liquid metals, the inertia terms have an entirely negligible effect on the heat transfer coefficient. This result stems from the extreme thinness of the condensate film. Since the film thicknesses in the present problem should be even smaller than those encountered in [4], the inertia terms can be neglected without error. Consequently, the z-momentum equation reduces to a balance between the viscous, pressure, and gravity terms. The viscous terms encompass three contributions, $\mu(\partial^2 w/\partial x^2)$, $\mu(\partial^2 w/\partial y^2)$, $\mu(\partial^2 w/\partial z^2)$. In a manner similar to that used in analyzing the energy equation for the condensate, it can be argued that $\mu(\partial^2 w/\partial y^2)$ is much, much larger than the other terms, thereby enabling them to be deleted. Then, the z-momentum equation for the condensate becomes

$$\mu(\partial^2 w/\partial y^2) = \partial p/\partial z - \rho g = \rho_v g - \rho g \simeq -\rho g \tag{6}$$

where the vapor density ρ_v has been neglected relative to the liquid density ρ.

As soon as the boundary conditions are specified, equation (6) can be integrated to give the velocity distribution across the condensate film at any position x, z. The velocity at the fin surface $y = 0$ is zero. At the liquid-vapor interface ($y = \delta$), the vapor exerts a very slight drag on the liquid. In [5], the interfacial drag was shown to have an insignificant effect on the heat transfer coefficient (~one percent for $c_p \Delta T/\lambda \sim 0.1$) for all condensed liquids other than liquid metals. Therefore, the zero shear boundary condition, $\partial w/\partial y = 0$, at the liquid-vapor interface is appropriate. Then, the integration of equation (6) along with the application of the aforementioned boundary conditions yields

$$w(x, y, z) = (g\rho/\mu)(y\delta - \tfrac{1}{2}y^2) \tag{7}$$

The rate $\dot{m}$ at which condensate passes through an area element δ by dx which spans the thickness of the film at position x, z and has a transverse width dx is obtained by integrating equation (7)

$$\dot{m}(x, z) = \int_{y=0}^{\delta} \rho w dx dy = (g\rho^2\delta^3/3\mu)dx \tag{8}$$

The change of $\dot{m}$ in the streamwise direction between x, z and $x, (z + dz)$ then follows by differentiation

$$d\dot{m} = (\partial\dot{m}/\partial z)dz = (g\rho^2\delta^2/\mu)(\partial\delta/\partial z)dxdz \tag{9}$$

This change in $\dot{m}$ is caused by the addition of condensate at the liquid-vapor interface. Another potential contribution to the change may result from transverse velocities which might exist in the film. If such velocities exist, they are very small since there is no direct forcing function (e.g., pressure gradient, body force, free stream velocity) which brings them into being. We believe that the effects of the transverse velocities are fully negligible, so that $d\dot{m}$ can be equated to the rate of condensate addition at the liquid-vapor interface. Consequently, the rate at which latent heat is liberated per unit surface area at x, z follows as

$$\frac{\lambda d\dot{m}}{dxdz} = \frac{\lambda g\rho^2\delta^2}{\mu}\frac{\partial\delta}{\partial z} \tag{10}$$

It may also be noted that since the condensate temperature profile, equation (3), is linear, the energy liberated at the interface is deposited without augmentation or diminution at the surface of the fin. Therefore, equations (4) and (10) may be equated, yielding

$$\frac{\partial(\delta^4)}{\partial z} = \frac{4k\mu}{\lambda g\rho^2}(T_{\text{sat}} - T) \tag{11}$$

Upon examining the foregoing development, it is seen that the key equations are (5) and (11). These constitute a coupled pair of partial differential equations for determining the distributions of T and δ as functions of the coordinates x and z. To reduce the problem to its essence, dimensionless variables are introduced as follows

$$\theta = \frac{T - T_{\text{sat}}}{T_w - T_{\text{sat}}}, \qquad \Delta = \left[\frac{k_f t}{kL^2}\right]\delta \tag{12}$$

$$X = \frac{x}{L}, \qquad Z = \frac{4k\mu(T_{\text{sat}} - T_w)}{\lambda g\rho^2}\left[\frac{k_f t}{kL^2}\right]^4 z \tag{13}$$

With these, equations (5) and (11) become

$$\frac{\partial^2\theta}{\partial X^2} - \frac{\theta}{\Delta} = 0 \tag{14}$$

$$\frac{\partial(\Delta^4)}{\partial Z} - \theta = 0 \tag{15}$$

It is noteworthy that the change of variables has eliminated all parameters from the governing equations.

To complete the formulation of the problem, it remains to specify the boundary conditions. At the junction of the fin and the base surface ($x = 0$), temperature continuity requires that $T = T_w$, where T_w is a specified constant. The situation at the fin tip ($x = L$) is quite complex and cannot be analyzed with a high degree of certainty. Since the tip is not expected to contribute significantly to the overall fin heat transfer, it appears sufficient to employ the insulated-tip boundary condition $\partial T/\partial x = 0$. Only a single boundary condition is needed for the film thickness δ, namely $\delta = 0$ at $z = 0$. The mathematical statement of the boundary conditions in terms of the transformed variables is

$$\theta = 1 \text{ at } X = 0, \qquad \partial\theta/\partial X = 0 \text{ at } X = 1, \qquad \Delta = 0 \text{ at } Z = 0 \tag{16}$$

The foregoing formulation has focused the task of solving the conjugate problem on equations (14–16). Although not lengthy, these equations are quite complex because they involve strongly coupled, nonlinear partial differential equations. An analytical solution appears out of the question. However, as will be demonstrated shortly, there is a range of conditions where it is possible to transform the partial differential equations into ordinary differential equations and then to obtain similarity solutions. Outside of that range, the actual partial differential equations (14) and (15) will be solved.

The key result that is to be extracted from the solution is the fin heat transfer rate. At any station, z, the local heat flux from the fin to the base surface (per unit fin-base contact area), can be obtained from Fourier's law

$$q_f(z) = k_f(\partial T/\partial x)_0 \tag{17}$$

or, in terms of the variables of equations (12) and (13),

$$q_f(Z) = [k_f(T_{\text{sat}} - T_w)/L](-\partial\theta/\partial X)_0 \tag{18}$$

The overall rate of heat transfer from fin to base over a vertical height from $z = 0$ to $z = z$ then follows by integration

$$Q_f(z) = \int_0^z q_f(z')2tdz' \tag{19}$$

where z' is a dummy variable. If dimensionless variables are introduced, the expression for Q_f becomes

$$Q_f(Z) = \frac{\lambda g\rho^2 L}{2\mu}\left[\frac{kL^2}{k_f t}\right]^3 \int_0^Z \left[-\frac{\partial\theta}{\partial X}\right]_0 dZ' \tag{20}$$

The foregoing heat transfer equations will be evaluated later when numerical values of $(\partial\theta/\partial X)_0$ are available from the solutions.

Solution of the Governing Equations. The motivation to seek a similarity solution stems from certain physical characteristics of the problem that will now be discussed. At small values of z, the condensate layer is thin and the fin heat transfer rates are high. As a consequence, at a fixed z, the fin temperature distribution, starting from $T = T_w$ at $x = 0$, increases sharply with x and attains a value $T \cong T_{\text{sat}}$ well before $x = L$. Thus, at such z stations, the fin heat transfer would be the same regardless of whether the transverse length of the fin were L, $5L$, or infinity, so that the $X = 1$ boundary condition of equation (16) can be replaced by

$$T = T_{\text{sat}} \text{ or } \theta = 0 \text{ at } X = \infty \tag{21}$$

It may also be noted that as z becomes progressively smaller, the increase of T with x (at a fixed z) becomes sharper and sharper, with the result that the range of x where $T < T_{\text{sat}}$ diminishes. In the

limit,

$$T = T_{sat} \text{ or } \theta = 0 \text{ at } Z = 0 \text{ and } X > 0 \tag{22}$$

with a singularity at $X = 0$ and $Z = 0$.

The characteristics of θ that are indicated in equations (21) and (22) are reminiscent of those encountered in boundary layer work. It can also be argued that Δ possesses the same characteristics at $X = \infty$ and at $Z = 0$ as does θ.

With the foregoing as background, a similarity solution will be sought for equations (14) and (15). The boundary conditions to be satisfied are stated by equation (16), with the $X = 1$ condition replaced by equation (21). The leading edge condition, equation (22), need not be imposed as a separate constraint; rather, it will be automatically satisfied by the similarity solution.

A similarity variable η is now introduced as

$$\eta = X/Z^{1/8} \tag{23}$$

with dependent variables

$$\theta = \theta(\eta), \qquad F(\eta) = \Delta^4/Z \tag{24}$$

With these, the governing equations become

$$\theta'' - \theta/F^{1/4} = 0, \qquad F - \eta F'/8 - \theta = 0 \tag{25}$$

subject to the boundary conditions

$$\theta(0) = 1, \qquad \theta(\infty) = 0, \qquad F(\infty) = 0 \tag{26}$$

where the primes denote differentiation with respect to η. It can be seen from equations (25) and (26) that the similarity transformation has been successful, that is, X and Z have been banished and only functions of η appear.

An analytical solution of equations (25) and (26) is out of reach, and a numerical technique was, therefore, employed. The θ'' and F' equations (25) were recast in finite difference form, and the resulting difference equations were solved iteratively. The solution was carried out in a domain $0 \le \eta \le \eta_\infty$. Several candidate values of η_∞ were employed to obtain final results that are independent of η_∞. In this connection, it may be noted that the calculated fin heat transfer changed by about 0.08 percent when η_∞ was varied from 3.0 to 3.8; the change was about 0.01 percent between $\eta_\infty = 3.8$ and 6.

For the heat transfer computation, the key result that is needed from the similarity solution is $\theta'(0)$, the value of which was found to be

$$\theta'(0) = -1.080 \tag{27}$$

It can also be shown by analyzing equations (25) (as well as from the numerical solutions) that $F(0) = 1$, so that $\Delta = Z^{1/4}$ at $X = 0$ (adjacent to the fin base). The physical implications of this result will be discussed later.

The similarity solution is valid for z stations at which $T \cong T_{sat}$ (i.e., $\theta \cong 0$) at $x = L$. At those stations where θ is noticeably different from zero at $x = L$, the similarity form of the governing equations cannot be used and, instead, the original partial differential equations (14) and (15) must be solved. The changeover from the similarity equations to the nonsimilarity equations was made by associating η_∞ (which corresponds to $\theta = 0$) with the tip of the fin (i.e., $x/L = 1$), which gives the Z value at changeover as

$$\hat{Z} = (1/\eta_\infty)^8 \tag{28}$$

where $\eta_\infty = 3.8$ was employed in the calculations. The suitability of this choice was supported by the fact that for a substantial range of $Z > \hat{Z}$, the nonsimilarity solution yielded heat transfer results which, when properly scaled, were virtually identical to those from the similarity solution.

For $Z > \hat{Z}$, finite difference solutions of equations (14) and (15) were carried out. Prior to deriving the difference equations, Δ was replaced by $Z^{1/4}F^{1/4}$ in (14) and Δ^4 by ZF in (15). To initiate the solution, the similarity results were used to provide values of θ and F as functions of X at $\hat{Z}$. The finite difference procedure was structured to operate successively on equations (14) and (15). First, equation (14) was solved to obtain the θ versus X distribution at a fixed Z, using the boundary conditions $\theta = 1$ at $X = 0$ and $\partial\theta/\partial X = 0$ at $X = 1$. The F distribution needed as input to (14) was taken from the station just upstream of Z. Then, equation (15) was stepped forward in Z (at fixed values of X) to yield the F distribution. The forward marching was continued to Z values (up to $Z = 10$) that are larger than those for which a laminar film is expected to exist. This extended range was employed to enable the trends with Z to be clearly established.

For the heat transfer computations, the value of $(\partial\theta/\partial X)$ at $X = 0$ was extracted from the solution at each Z station in the finite difference grid.

Results and Discussion

Heat Transfer. In presenting the heat transfer results, it will be advantageous, both to achieve generality and to point out certain physical characteristics, to employ dimensionless ratios. As a reference quantity, i.e., for the denominator of the ratio, it is appropriate to use the heat transfer corresponding to an ideal fin whose temperature is everywhere uniform and equal to T_w. Such an isothermal fin is identical to the isothermal vertical plate analyzed by Nusselt, for which the condensation heat transfer results appear in numerous texts. The ideal fin results will be denoted by an asterisk.

For the ideal fin, the film thickness δ^* depends only on z and is given by (e.g., [6], Ch. 11)

$$\delta^*(z) = [4k\mu(T_{sat} - T_w)z/\lambda g\rho^2]^{1/4} \tag{29}$$

or

$$\Delta^* = Z^{1/4} \tag{30}$$

Furthermore, the local heat flux from the condensate to the fin surface is given by

$$q^*(x, z) = q^*(z) = k(T_{sat} - T_w)/\delta^* \tag{31}$$

For a horizontal strip of fin situated at station z and having surface area L by dz, the rate of heat transfer from the condensate to the fin is $q^*(z)Ldz$; this quantity is doubled to account for condensation on both faces of the fin. It then follows that the rate at which heat is delivered from the fin to the base at z, per unit fin-base contact area, is

$$q_f^*(z) = \frac{2q^*(z)Ldz}{2tdz} = \frac{k(T_{sat} - T_w)L}{\delta^* t} \tag{32}$$

which becomes, with the aid of equations (12) and (30),

$$q_f^*(Z) = [k_f(T_{sat} - T_w)/L]/Z^{1/4} \tag{33}$$

The local heat flux ratio comparing the actual fin with the ideal fin is evaluated using equations (18) and (33), with the result

$$q_f/q_f^* = (-\partial\theta/\partial X)_0 Z^{1/4} \tag{34}$$

For the similarity regime, $(\partial\theta/\partial X)_0 = \theta'(0)/Z^{1/8}$ and, upon taking note of equation (27), there follows

$$q_f/q_f^* = 1.080Z^{1/8} \tag{35}$$

Equation (34) has been evaluated using the $(\partial\theta/\partial X)_0$ values from the nonsimilarity solution and is plotted in Fig. 2 along with equation (35) which represents the similarity solution. The figure is subdivided into upper and lower portions. The latter spans the range of Z values between 0.0001 and 0.1, while the former spans the Z range between 0.01 and 10 (the overlap in the ranges is to provide continuity). The two parts of the figure have separate ordinate scales.

Inspection of the figure shows that q_f/q_f^* is substantially less than unity at small values of Z and increases as Z increases. Therefore, the local heat transfer for a real fin may be substantially less than that for an ideal (isothermal) fin. To provide perspective for this finding, an example was worked out for steam at 20°C (68°F) condensing on a copper fin with half thickness $t = 0.127$ cm (0.05 in.), transverse length $L = 2.54$ cm (1 in.), and vertical height $z_{max} = 152.4$ cm (5 ft). The temperature difference $T_{sat} - T_w$ was taken to be 5.6°C (10°F). Upon evaluating equation (13) for these conditions, it is found that

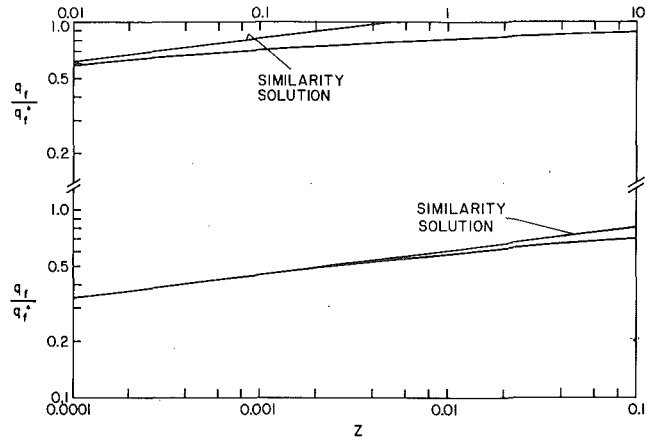

Fig. 2 Local fin heat transfer results

$0 \le Z \le 0.0014$. Correspondingly, Fig. 2 shows that $0 \le q_f/q_f^* \le 0.47$. Thus, the use of an isothermal fin model, which is equivalent to using the simple Nusselt theory, gives rise to significant errors in the local fin heat transfer.

It may be noted that the foregoing value of $Z_{max} = 0.0014$ is quite small even though a rather large vertical height was chosen for the example. For smaller heights, Z_{max} would be proportionately smaller, giving even larger departures from the results of the Nusselt theory.

Further inspection of Fig. 2 shows that the results from the similarity solution are essentially identical to those of the nonsimilarity solution up to a Z value of 0.001. Thereafter, there is a growing deviation, but the difference is only five percent at $Z = 0.01$ and 15 percent at $Z = 0.1$. Therefore, for most practical purposes, the q_f from the similarity solution, which is expressed by

$$q_f = 1.080[k_f(T_{sat} - T_w)/L]Z^{1/8} \tag{36}$$

is sufficient. Use of equation (36) enables the local fin heat transfer to be calculated with the same degree of ease as for the calculation of the ideal fin heat transfer (which uses the Nusselt formula for an isothermal vertical plate).

Another interesting perspective on the local heat transfer results can be obtained by examining the behavior of the quantity

$$q_f/1.080[k_f(T_{sat} - T_w)/L]Z^{1/8} \tag{37}$$

which is plotted in Fig. 3 as a function of Z. Again, as in Fig. 2, the figure is subdivided into two parts in order to cover a wide range of Z values. For the similarity solution, the plotted quantity is equal to unity for all Z, and this is portrayed by horizontal lines in both the lower and upper graphs. On the other hand, for the ideal fin, the plotted quantity equals $1/1.080Z^{1/8}$, and this is represented by a down-sloping line at the right of the upper graph.

If attention is focused on the upper graph, it is seen that the similarity solution and the ideal fin solution, taken together, form an envelope curve which bounds the actual fin heat transfer results. The maximum deviation of the results from the envelope is about 20 percent. This relationship between the envelope curve and the actual solution curve is reminiscent of similar relationships that are encountered in a variety of heat transfer problems. For instance, in [7], a similar relationship was demonstrated for the problem of combined forced and natural convection on a vertical plate. There, too, the maximum deviation between the envelope and the solution curve was about 20 percent.

Attention will now be turned to the overall rate of heat transfer Q_f from fin to base over a vertical height from $z = 0$ to $z = z$. The results will be presented in terms of the ratio Q_f/Q_f^*, in which Q_f^* corresponds to the ideal fin and is given by

$$Q_f^*(z) = (8/3\sqrt{2})[\lambda g \rho^2 k^3 (T_{sat} - T_w)^3 L^4 z^3/\mu]^{1/4} \tag{38}$$

or

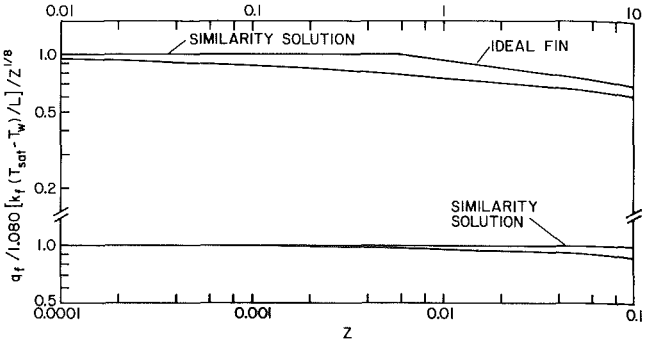

Fig. 3 Envelope curves and their relationship to the local heat transfer results

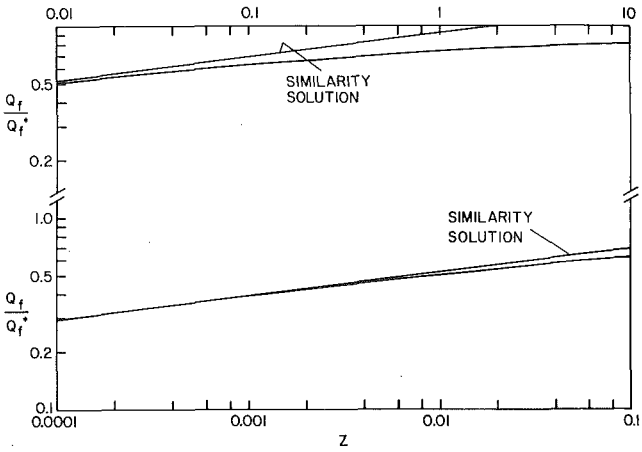

Fig. 4 Overall fin heat transfer results

$$Q_f^* = \frac{2\lambda g \rho^2 L}{3\mu}\left[\frac{kL^2}{k_f t}\right]^3 Z^{3/4} \tag{39}$$

Then, referring to equation (20), the ratio Q_f/Q_f^* follows as

$$\frac{Q_f}{Q_f^*} = \frac{3}{4Z^{3/4}}\int_0^Z \left[-\frac{\partial\theta}{\partial Z}\right]_0 dZ' \tag{40}$$

In particular, for the similarity regime

$$\frac{Q_f}{Q_f^*} = 0.9257Z^{1/8} \tag{41}$$

The Q_f/Q_f^* ratios from equations (40) and (41) have been plotted as a function of Z in Fig. 4. It is seen that in the range of small Z, Q_f is substantially less than Q_f^*. For instance, for the example that was discussed earlier (for which Z at the lower edge of the fin was 0.0014), the actual overall heat transfer from the fin is about 40 percent of that for an ideal fin. Therefore, the use of the ideal fin model (i.e., the Nusselt model) can lead to a significant overestimation of the heat transfer capabilities of the fin. The deviations between Q_f and Q_f^* diminish as Z increases, but in the range of practical Z values the deviations are significant.

It may be noted by comparing Figs. 2 and 4 that $Q_f/Q_f^* < q_f/q_f^*$ at any given value of Z. This relationship is plausible because Q_f is based on integration which encompasses stations where q_f/q_f^* is less than the q_f/q_f^* value at the given Z.

Further examination of Fig. 4 indicates that the deviations between the results from the similarity and non-similarity solutions are less than five percent for $Z \le 0.01$. Therefore, for almost all practical purposes, Q_f can be computed with high accuracy from the similarity solution, which is expressed by

$$Q_f = \frac{0.6171\lambda g \rho^2 L}{\mu}\left[\frac{kL^2}{k_f t}\right]^3 Z^{7/8} \tag{42}$$

This equation enables the overall fin heat transfer to be easily computed.

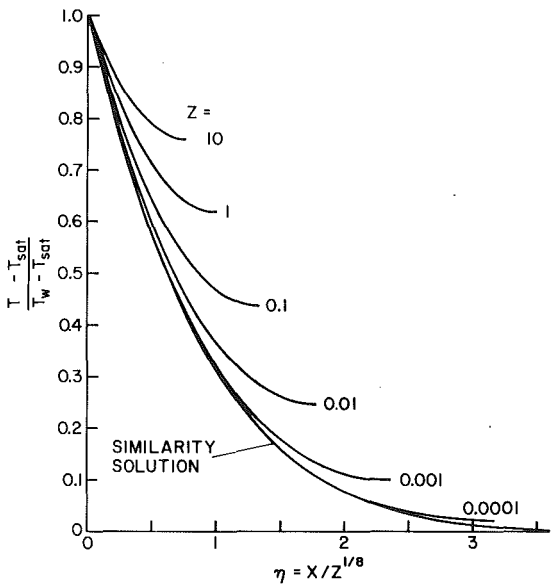

Fig. 5 Fin temperature distributions

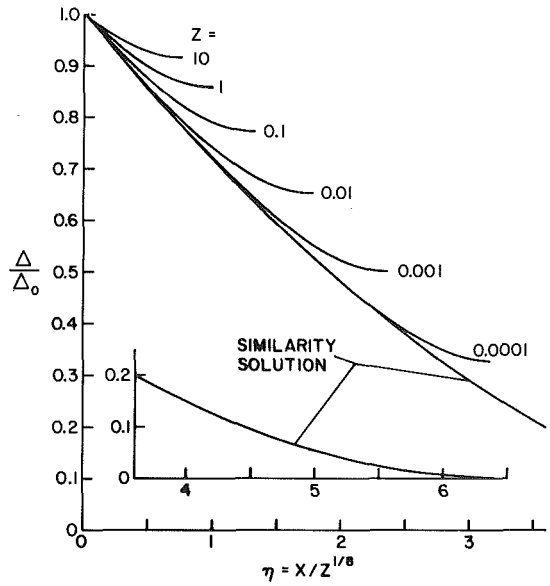

Fig. 6 Distributions of the condensate film thickness

Fin Temperature and Condensate Film Thickness. Representative results for the transverse variation of the fin temperature at various fixed Z stations have been taken from the similarity and nonsimilarity solutions and are presented in Fig. 5. The ordinate is the dimensionless temperature $\theta = (T - T_{sat})/(T_w - T_{sat})$, while the similarity variable η was chosen as the abscissa variable so that all Z stations in the similarity regime would be represented by a single curve. The temperature distributions for the nonsimilarity regime are respectively parameterized by the Z station to which they correspond. Since these distribution curves terminate at $X = 1$, the range of the variable $X/Z^{1/8}$ decreases as Z increases. This is the reason why the curves for higher Z values span an increasingly smaller portion of the abscissa.

It is seen from the figure that the transverse variations of the fin temperature diminish in the streamwise direction, i.e., with increasing Z. Furthermore, since larger ordinate values mean lower temperatures (note that $T_w < T_{sat}$), the general level of the fin temperature decreases with increasing Z. Thus, the fin approaches more closely to the ideal isothermal fin ($T = T_w$) as Z increases, and this is consistent with the heat transfer results of Figs. 2 to 4. Unfortunately, this approach occurs for large Z values where the relatively thick condensate films impose a high thermal resistance.

For small Z, the temperature distributions from the non-similarity solutions are essentially coincident with that for the similarity solution except in the neighborhood of $X = 1$. This explains why the heat transfer results from the similarity solution continue to be valid in the nonsimilarity regime.

Attention will now be turned to the condensate film thickness. It was noted earlier that the similarity solution yielded $\Delta = Z^{1/4}$ at $X = 0$ (adjacent to the fin base) and an identical result can be obtained from the non-similarity differential equations. Furthermore, from equation (30), Δ^* for the ideal fin also equals $Z^{1/4}$, so that

$$\Delta(0, Z) \equiv \Delta_0 = \Delta^* = Z^{1/4} \tag{43}$$

Consequently, the F variable can be rephrased as

$$F = (\Delta/\Delta_0)^4 \text{ or } \Delta/\Delta_0 = F^{1/4} \tag{44}$$

Distributions of Δ/Δ_0 are plotted in Fig. 6 both for the similarity solution and for the non-similarity solution, the latter being parameterized by Z values between 0.0001 and 10. These distribution curves show the transverse variation of the film thickness at fixed Z stations. It can be seen that the film thickness generally decreases in the direction from the fin base to the fin tip. The thickness of the film is highly nonuniform at small Z but becomes more and more uniform as Z increases. This trend toward uniformity is accompanied by a general growth in the film thickness, since $\Delta_0 = Z^{1/4}$. It is this growth which diminishes the local fin heat transfer at larger Z.

The significant variations of film thickness in evidence in Fig. 6, especially those at small Z, indicate that the uniform film thickness assumption which formed the basis of the analysis of [1] is not correct.

Concluding Remarks

The conjugate multi-dimensional heat transfer problem encompassing condensation on a fin attached to a cooled vertical plate or cylinder has been made tractable by a mathematical model which includes the essential physical processes. It was demonstrated that the model yields a physically meaningful similarity solution. Whereas similarity solutions are commonly encountered in boundary layer theory and are also possible in selected transient conduction problems, such solutions for conjugate problems are novel. Beyond the range where the similarity solution is valid, a finite-difference marching solution of the governing partial differential equations was carried out.

It appears that the similarity solution can be employed over essentially the entire range of operating conditions that are of practical interest. The heat transfer results from the similarity solution, equations (36) and (42), are algebraic forms whose simplicity is comparable to that for the classical Nusselt condensation problem.

The main finding of the study is that the fin heat transfer is much lower than that which would be predicted by an isothermal fin model, i.e., Nusselt model. For an illustrative example, it was found that the overall fin heat transfer was 40 percent of that for an isothermal fin. Thus, the use of predictions based on an isothermal fin significantly overestimates the heat transfer performance.

The present analytical model employs the same assumptions about film stability and absence of ripples and surface waves that are used in analyzing condensation on an isothermal wall. It is expected, therefore, that the applicability of the present results to fin practice will be comparable to the applicability of the isothermal wall predictions to condensation on actual isothermal surfaces. Although, as noted in the Introduction, finned condensing surfaces are very commonly encountered in practice, it does not appear that carefully controlled experiments on fin condensation have been reported.

Acknowledgment

This research was performed under the auspices of NSF Grant ENG 75-18141 A01.

References

1 Threlkeld, J. L., *Thermal Environmental Engineering,* second ed.,

Prentice-Hall, Englewood Cliffs, N. J., 1970, pp. 257–259.

2 Nader, W. K., "Extended Surface Heat Transfer with Condensation," Paper CS-5, Sixth International Heat Transfer Conference, Toronto, Canada, Aug. 1978.

3 Rohsenow, W. M., "Heat Transfer and Temperature Distribution in Laminar Film Condensation," Trans. ASME, Vol. 78, 1956, pp. 1645–1648.

4 Sparrow, E. M. and Gregg, J. L., "A Boundary Layer Treatment of Laminar Film Condensation," ASME JOURNAL OF HEAT TRANSFER, Vol. 81, 1959, pp. 13–18.

5 Koh, J. C. Y., Sparrow, E. M., and Hartnett, J. P., "The Two Phase Boundary Layer in Laminar Film Condensation," *International Journal of Heat and Mass Transfer*, Vol. 2, 1961, pp. 69–82.

6 Karlekar, B. V. and Desmond, R. M., *Engineering Heat Transfer*, West Publishing Company, St. Paul, Minn., 1977.

7 Lloyd, J. R. and Sparrow, E. M., "Combined Forced and Free Convection on Vertical Surfaces," *International Journal of Heat and Mass Transfer*, Vol. 13, 1970, pp. 434–438.

C. Bonacina
S. Del Giudice

Instituto di Fisica Tecnica,
Facoltà di Ingegneria,
Università di Padova,
Padova, Italy[1]

G. Comini

Instituto di Fisica Tecnica,
Facoltà di Ingegneria,
Università di Trieste,
Trieste, Italy[1]

Dropwise Evaporation

Evaporation of atomized liquids on hot surfaces is identified as an interesting technical process, characterized by very high values of specific heat fluxes. An experimental apparatus, expressely built for the evaluation of heat transfer mechanisms in mist cooling with low excess temperatures, is described. A mathematical model, based on the assumption of dropwise evaporation, is used to correlate the experimental results.

Introduction

Atomized liquids are widely used to enhance heat transfer with hot surfaces. Extensive reviews of spray and/or mist cooling techniques utilized in heat exchanger operations and in metallurgical, nuclear and electronic industries can be found in the literature [1, 2].

Most applications concern heat transfer processes where surface temperature are, in general, much lower or much higher than the saturation temperature of the atomized liquid. As a consequence, in most mathematical models either negligible rates of evaporation or film boiling conditions are assumed [3, 4].

So far as we know, only Kopchikov, et al. [5] and Toda [6, 7] dealt with moderate as well as high surface temperatures. Their main achievement, however, appears to be the investigation of thermal behaviour of continuous liquid films on heated plates.[2]

Instead we operated with relatively low flow rates of atomized liquid and visual observations indicated that our heat transfer surfaces were only wetted in spots.

Our aim, in fact, was to realize a process, characterized by relatively low values of excess temperatures, where only a fraction of the total heat transfer surface is covered by droplets.

In the context of dropwise condensation studies it has long been established that heat transfer rates are increased substantially whenever formation of liquid films on the heat transfer surface is prevented. We ascertained that the same principle holds good for dropwise evaporation. Besides, we found out that, unlike dropwise condensation, dropwise evaporation of atomized liquids on hot surfaces can be induced, controlled and maintained without difficulty for any amount of time.

A mathematical model, based on the assumption of dropwise evaporation is presented here to explain and correlate the very high values of heat transfer coefficients obtained in our experiments. Heat conduction through the liquid patches on the plate is assumed to be the leading heat transfer mechanism. In fact film boiling effects have been ruled out because of the relatively low values of wall superheat investigated while nucleate boiling effects have been disregarded as statistically insignificant.

Heat transfer measurements, performed during the initial stage of this research, already seemed to support this theory [8]. Optical observations, carried out later and described in the text, allowed us to confirm the assumptions made and to estimate accurately the values of the empirical constants used in the model. This way quite satisfactory predictions were made possible both for heat transfer coefficients and for fractions of heat transfer areas covered by droplets.

[1] Also with Laboratorio per la Tecnica del Freddo del C.N.R., Cas. Post. 1075, 35100 Padova, Italy.

[2] As a matter of fact, the heating surface is described in [5] as completely covered by a continuous liquid film while the same point is not clearly made in [6, 7]. On the other hand, all results reported in [6, 7] concern experiments where heat flux density values, q, are always larger, and often much larger, than the corresponding products of mass flux densities of liquids (w_s) by equivalent heat effects, λ'. As a consequence, Toda's test sections could not possibly evaporate all the incoming atomized liquid and thus, we infer, were constantly overflowed.

Contributed by the Heat Transfer Division for publication in the JOURNAL OF HEAT TRANSFER. Manuscript received by the Heat Transfer Division August 25, 1977.

Physical Aspects

When a liquid is sprayed over a surface whose temperature is higher than the saturation temperature of the liquid itself, the average heat transfer coefficient can be advantageously defined as [5, 6, 7, 9]:

$$h = Q/[A(T_w - T_{vs})] \tag{1}$$

where $(T_w - T_{vs})$ is the excess temperature. Experimental measurements on mist cooling, in fact, are well correlated by characteristics curves $q(=Q/A)$ versus $(T_w - T_{vs})$ which are practically independent on the degree of subcooling $(T_{vs} - T_\ell)$ of the impinging liquid droplets [5, 6, 7, 8].

As is shown in Fig. 1, characteristic curves for mist cooling exhibit different regions in correspondence with low, intermediate and high values of excess temperatures, respectively [6, 7]. For low excess temperatures the liquid is in contact with the heated surface and evaporation occurs from the upper liquid-vapour interface. For high excess temperatures the liquid rests on a layer of its own vapour which is maintained there by the intensive evaporation from the lower liquid-vapor interface. For intermediate excess temperatures a transition between the evaporation and the film boiling regime is observed [6, 7].

There is not much agreement in the literature on the role of nucleate boiling in the patches of liquid on heated plates at low and moderate excess temperatures. In [5] nucleate boiling is assumed to be the only significant heat transfer mechanism while in [6, 7] the effects of nucleate boiling on the heat transfer characteristics are considered negligible.

The aim of this research was the investigation of heat transfer mechanisms during mist cooling at relatively low excess temperatures. For the range of excess temperatures we investigated, our optical observations showed a statistically negligible number of nucleation sites. Nucleate boiling with the formation of liquid domes seemed to take place only in a few exceptionally large droplets. Thus we decided to disregard nucleate boiling effects in our model.

We decided also that the behavior of a single droplet on a heated surface had to be completely clarified before considering the behaviour of a spray of droplets. Studies of this kind are described in [7, 10] but they concern droplets of several millimeters in diameter impinging at high velocity on copper, glass and stainless steel surfaces. Instead, in our experiments, an aluminum surface was used, droplet

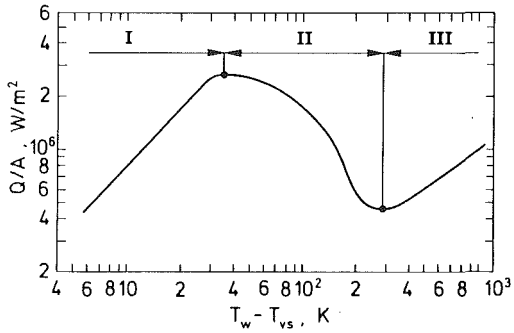

Fig. 1 Characteristic curve: heat flux density Q/A versus excess temperature ($T_w - T_{vs}$) for mist cooling. (I) low excess temperature zone, (II) intermediate excess temperature zone, (III) high excess temperature zone (from Toda [7]).

mean diameters in the spray were of the order of 50 to 100 μm only [11] and impingment velocities were relatively low. Thus we made some optical observations under our own experimental conditions.

Actually we discovered droplet behavior similar to that described by Toda [7]. As a consequence, single droplet analyses by Toda [7] and ourselves could not differ much.

We observed the behaviour of liquid droplets on the heated surface with the aid of a high-speed camera. Photographs from a typical sequence are shown in Fig. 2 and a typical behavior is schematized in Fig. 3.

As can be seen, immediately after their arrival on the plate, the droplets spread out to assume a disk shaped form whose diameter, in our experiments, was approximately four to five times larger than the original diameter of the droplet in the spray. Afterwards, the diameter of the liquid patch remains constant for the entire lifetime on the plate. At the end, when the continuous evaporation from the upper liquid-vapour interface has made the patch thickness negligibly small, the liquid film breaks out suddenly and the heated surface dries up very quickly.

In order to prevent interactions between liquid droplets on the plate we used relatively low flow rates of atomized liquid. As a consequence, in our experiments the amount of vapour formed per unit time was always equal to the flow rate of liquid impinging on the heated surface. Besides, optical observations showed that, practically, no coalescence of liquid droplets on the plate took place since, as we expected, only a fraction of the total heat transfer surface was wetted.

Therefore, the heat transfer process we were able to produce and maintain can be rightly identified as "dropwise evaporation," unlike other mist cooling processes described in [5, 6, 7] which are characterized by heat transfer surfaces that are constantly overflowed by unevaporated liquid.

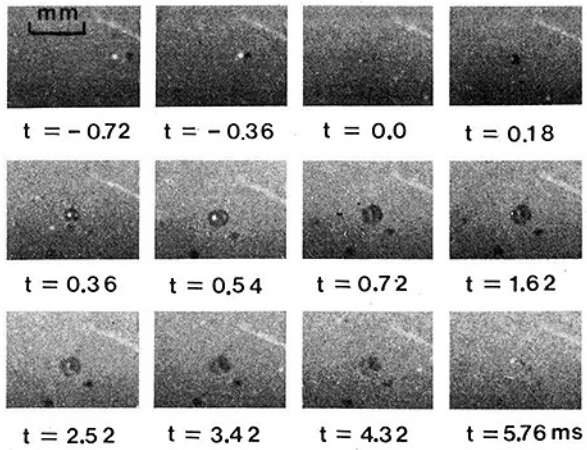

Fig. 2 Behavior of a liquid water droplet on an aluminum surface. Touch down takes place at $t = 0$. Measured values of physical parameters are: $T_w = 104.8$ °C, $T_{vs} = 100.0$ °C, $T_\ell = 20.5$ °C, $D = 95$ μm, $d = 395$ μm. Measured timelife is in good agreement with calculations based on equation (7).

The Model

The studies on the rate of evaporation from a single droplet make it possible to write the equations governing the evaporation from sprays by taking into account the distribution of droplet sizes.

Heat Transfer Analysis for a Single Droplet. Heat transfer analysis for a single droplet is based on the model shown in Fig. 4 and does not differ much from the corresponding analysis reported in [7]. The following assumptions are made:

1. No evaporation takes place before the droplet reaches the plate.
2. The time necessary for a droplet to spread from the spherical to the disk shaped form is negligible in comparison with the lifetime of the droplet on the plate.
3. The ratio between the diameter of a droplet in the spray and the diameter of the corresponding disk on the plate does not depend on the droplet size and does not change with time

$$D/d = 1/\beta_1 = \text{const} \tag{2}$$

4. The disk thickness is negligibly small when the liquid film breaks and the droplet dries up.
5. The temperature of the heated surface is constant with respect to time and position; i.e., the thermal resistance caused by constriction of heat flow lines in the plate near the evaporating droplets is negligible (see Appendix 1 for further discussion).

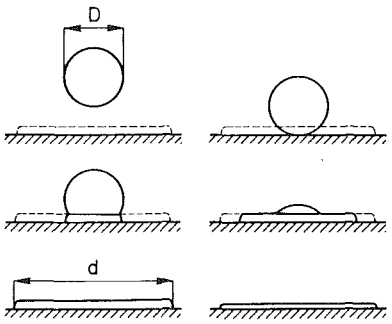

Fig. 3 Successive states of formation of a cylindrical disk like patch on the plate. This schematization is based on our own as well as on Toda's observations [7].

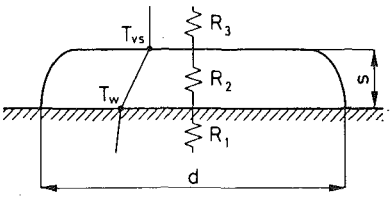

Fig. 4 Heat transfer through a disk shaped droplet from a heated surface to the atmosphere. R_1 is the constriction resistance, R_2 is the conduction resistance and R_3 is the thermal resistance corresponding to mass transfer. A linear one-dimensional temperature distribution is assumed in the droplet.

Nomenclature

A = heat transfer area
c = specific heat capacity
d = droplet diameter on the plate
D = droplet diameter in the spray
F_1, F_2 = shape factors defined in Appendix 1, dimensionless
h = heat transfer coefficient
H = distance defined in Fig. 6
k = thermal conductivity
m = mass
M = molecular mass
n = dispersion parameter in the Rosin-Rammler distribution, dimensionless
Nu = hD_m/k_l Nusselt number, dimensionless
p = pressure
q = heat flux density
Q = heat flux
R = universal gas constant
R_1, R_2, R_3 = heat transfer resistances defined in Fig. 4.
s = thickness of the droplet on the plate
t = time
T = temperature
v = specific volume
$w = W/A$ mass flux density
w = mass flux
$z = D/D_m = d/d_m$ dimensionless diameter
α = cone angle
$\beta_1, \beta_2, \beta_3$ = dimensionless constants, equations (2, 9) and (21)
γ = constant of evaporation, dimensionless
ϵ = fraction of heat transfer area covered by droplets, dimensionless
λ = latent heat
λ' = equivalent latent heat effect, equation (5)
ρ = density

Subscripts

d = droplet
e = equilibrium
ℓ = liquid
m = mass median
s = spray
vs = saturation
w = wall
ϕ = nozzle
0 = initial

6. The heat transfer resistance at the upper liquid-vapour interface is negligible (see Appendix 1).
7. In the cylindrical disk temperatures do not change in the radial direction, while the temperature distribution in the axial direction can be approximated by a straight line.
8. Nucleate and film boiling effects, if any exist, do not influence global heat transfer characteristics and, thus, can be neglected for the range of excess temperatures investigated here.

Under the above assumptions, the heat transfer rate through a droplet can be expressed as

$$q_d = Q_d/A_d \cong k_\ell\,(T_w - T_{vs})/s \tag{3}$$

Since heat transported through the droplet is used to evaporate liquid from the upper liquid-vapour interface, the following relationship holds good too

$$q_d \cong -\rho_\ell \lambda'\, ds/dt \tag{4}$$

where a modified latent heat of vaporization is introduced to account, in some way, for the sensible heat capacity:

$$\lambda' = \lambda + c_\ell\,(T_{vs} - T_\ell) \tag{5}$$

From expressions (3) and (4) the following differential equation is obtained:

$$k_\ell\,(T_w - T_{vs})dt = -\rho_\ell \lambda'\, s\, ds \tag{6}$$

which can be integrated to find the time necessary to evaporate completely the droplet

$$t_d = s_0^2\,\rho_\ell \lambda' \,[2k_\ell (T_w - T_{vs})]^{-1} \tag{7}$$

The initial thickness of the cylindrical disk can be expressed as a function of the droplet diameter on the plate. By equating the initial volume of the disk to the volume of the droplet in the spray we have:

$$s_0 = \beta_2 d \tag{8}$$

where

$$\beta_2 = 2/(3\beta_1^3) \tag{9}$$

Heat Transfer Analysis for a Spray of Droplets. In order to write the equations governing heat transfer from a spray of droplets, the following additional assumptions are needed:

9. Heat transfer from the dry area of the plate is negligible.
10. Since only a fraction of the heated surface is wetted, no coalescence of droplets takes place on the plate.
11. The distribution of droplet sizes in the spray can be described by a suitable frequency function such as, for example, the Rosin-Rammler distribution [3, 13]:

$$\varphi(z) = (\ln 2)\, n\, z^{n-1} \exp[-(\ln 2)\, z^n] \tag{10}$$

where n is the dispersion parameter whose value is generally in the range from 2 to 4, and

$$z = D/D_m = d/d_m \tag{11}$$

Under the above assumptions, the mass of droplets having diameters between d and $d+\Delta d$ that reaches the plate between the time instants t and $t+\Delta t$, is given by:

$$\Delta(\Delta m) = W_s\,[\varphi(\bar{z})\Delta z]\,\Delta t \tag{12}$$

where W_s is the flow rate of liquid impinging on the plate and $\bar{z}$ is a suitable value between d/d_m and $(d+\Delta d)/d_m$.

For any droplet the ratio between contact area and mass depends only on the diameter:

$$A_d/m_d = 1/(\rho_\ell s_0) = 1/(\beta_2 \rho_\ell d) \tag{13}$$

Therefore, the fraction of heat transfer area covered by the group of droplets referred to in equation (12), can be expressed as:

$$\frac{\Delta(\Delta A_s)}{A} = \frac{w_s}{\beta_2 \rho_\ell d_m}\,\frac{\varphi(\bar{z})}{\bar{z}}\,\Delta z\,\Delta t \tag{14}$$

The total fraction of heat transfer area covered by droplets is found letting $(\Delta t,\ \Delta z)$ tend to zero in equation (14). Then integration gives:

$$\epsilon = \frac{A_s}{A} = \int_0^\infty \left(\int_0^{t_a} \frac{w_s}{\beta_2 \rho_\ell dm}\,dt\right)\frac{\varphi(z)}{z}\,dz = \frac{\beta_2 w_s\, d_m\, \lambda'}{2\,k_\ell\,(T_w - T_{vs})}\,\frac{\Gamma[(n+1)/n]}{(1\ln 2)^{1/n}} \tag{15}$$

where $\Gamma[(n+1)/n]$ is the Gamma function defined as in [16]:

$$\Gamma(N) = \int_0^\infty z^{n-1} \exp(-z)\,dz \tag{16}$$

Since no overflow occurs, we have from assumption (9):

$$q = w_s\,\lambda' \tag{17}$$

Besides, for the values of the dispersion parameter n that are of interest here, it is[3]

$$\Gamma[(n+1)/n]/(\ln 2)^{1/n} \cong 1 \tag{18}$$

Equation (15) can be written in a simplified dimensionless form as

$$\epsilon \cong \beta_3\,\mathrm{Nu} \tag{19}$$

where

$$\mathrm{Nu} = hD_m/k_\ell \tag{20}$$

and

$$\beta_3 = 1/(3\beta_1^2) \tag{21}$$

Equation (19) correlates the fraction of the total heat transfer area covered by droplets to the dimensionless value of the heat transfer coefficient. Equations (19) and (20) imply that:

$$Q/[A(T_w - T_{vs})] = h = [k_\ell/(\beta_3 D_m)]\epsilon \tag{22}$$

Therefore our experimental data might be correlated as shown in Fig. 5. For the same excess temperature we can have different heat fluxes. Thus heat transfer measurements for Q/A and $(T_w - T_{vs})$ and optical observations for ϵ, taking place simultaneously, are required to test the model proposed here.

Experimental Apparatus and Measuring Techniques

The experimental apparatus built for this research is described in detail in [2]. Therefore, only essential information on the test section, represented in Fig. 6, is reported here.

Twice distilled water, at controlled pressure p_ℓ and temperature T_ℓ is supplied to the atomizing nozzle. Mean diameters and flow rates of liquid droplets depend mainly on the shape and size of the nozzle and on the feeding pressure. Specific flow rates of atomized liquid, in correspondance with the heated surface, depend also on the dis-

[3] Actually, equation (18) holds good to within 5 percent for n between 2 and ∞, while, as pointed out, typical n values for our sprays are in the range from 2 to 4.

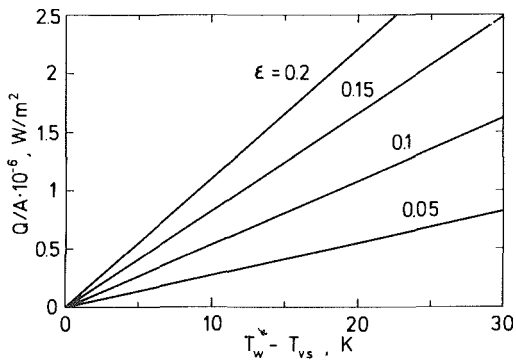

Fig. 5 Q/A **versus** $(T_w - T_{vs})$ **characteristic curves for dropwise evaporation computed from Equation (22) with** $d/D = 4.5$ **and** $D_m = 75\ \mu$**m.**

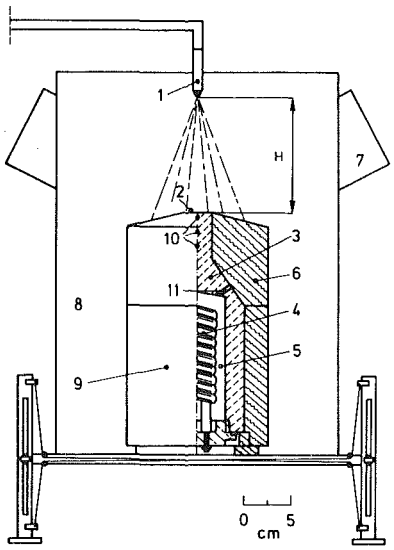

Fig. 6 Experimental test section. (1) nozzle, (2) heat transfer surface, (3) aluminum block, (4) electric resistance, (5) Wood metal, (6) Teflon ring, (7) plexiglas windows, (8) metallic container, (9) test section, (10) copper-constantan thermocouples, (11) vent

tance H from the nozzle which, in our apparatus, can be chosen in the range from 100 to 300 mm.

Several different nozzles, whose characteristics are listed in Table 1, have been utilized to create a wide range of fluodynamic conditions on the plate.

Mass median diameters in the sprays are evaluated from the empirical correlation [15]:

$$D_m/D_\Phi \cong 9.5\,[\Delta p^{.37} \sin(\alpha/2)]^{-1} \tag{23}$$

where D_Φ is the nozzle diameter, $\Delta p = p_\ell - p_{\text{atm}}$ is the acting pressure difference, *Pa*, and α is the cone angle. In [11], equation (22) was found to be in good agreement with the experimental measurements made on nozzles similar to the ones listed in Table 1.

No rebound of droplets on the heated surface was observed with impingment velocities in the range from 1 to 2 m/s, typical of our experiments. No attempt was made to measure accurately impingment velocities since this parameter does not seem to play an important role in a first approximation model for dropwise evaporation [8].

The heat transfer surface, at the top of the aluminum block, has a circular shape. This surface is carefully lapped, since a high surface roughness might not allow the droplets to assume stable configuration and might enhance nucleate boiling.

Heat is supplied by means of an electric resistance placed in a cavity of the block. The cavity is filled with Wood metal which, being liquid at operative temperatures, acts as a very effective heat transfer medium. An extended insulating ring and the shape of the block itself induce one-dimensional thermal fields in the vicinity of the test surface.

Two heating blocks of similar shape were used in the test section: the first one with a 25 mm dia heating plate and the second one with a 10 mm dia heating plate. Heat fluxes up to 600 W and up to 300 W have been generated in the first and in the second heating block respectively, these upper limits being imposed by limitations in the thermal design of the heating blocks. Heat fluxes are controlled by adjusting manually, through a variable transformer, potential differences across the electric resistance.

Pressures and temperatures at different points of the experimental circuit are accurately monitored to ensure that steady state conditions are mantained during each run.

Heat flux and temperature of the heated surface are measured by plugging several copper-constantan thermocouples into the one-dimensional heat flow zone of the aluminum block. The heat flux is calculated from values of temperature differences between measuring points and the knowledge of thermal conductivities of aluminum at

Table 1 Characteristics of atomizing nozzles. Nominal volumetric flow rates are referred to an inlet water pressure $p = 7$ bar and discharged into the atmosphere.

type	cone angle (degrees)	nozzle diameter (μm)	nominal volumetric flow rate (cm^3/s)
A	80	660	2.10
B	60	490	1.16
C	80	500	0.89
D	45	355	1.16
E	45	380	1.31
F	80	596	1.31
G	80	645	1.73
H	80	855	3.15
I	60	490	1.16
L	45	325	0.68
M	60	635	2.10
N	45	427	1.16
O	45	468	1.31
P	45	522	1.58

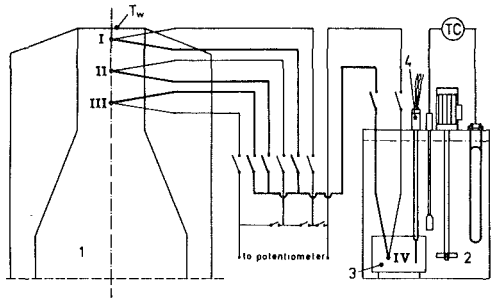

Fig. 7 Temperature measuring section. (1) heating section, (2) stirred oil bath, (3) temperature equalizer block, (4) precision resistance thermometer, TC automatic temperature controller, I, II, III, IV main measuring points.

operative temperatures. The temperature of the heated surface is calculated by extrapolation from temperature distribution measurements. The electric circuit utilized for these measurements is schematized in Fig. 7. The arrangement of electric connections is such that temperature differences between any two among the four measuring points can be evaluated directly.

Reference point IV is placed in a second aluminum block, immersed in a stirred oil bath, whose temperature does not differ much from the temperature of the test section and is maintained constant during each run. Therefore, an independent measurement of the bath temperature, by means of a precision resistance thermometer, allows a very accurate evaluation of the surface temperature T_w, without complicate calibrations of thermocouple signals.

The saturation temperature T_{vs} is evaluated from a measurement of the external atmospheric pressure. Since the metallic container where the test section is placed is not sealed, we assumed:

$$T_{vs} \equiv T_{vs}\,(p_{\text{atm}}) \tag{24}$$

Since we deal with a two degrees of freedom phenomenon, for the same $(T_w - T_{vs})$ we may have different ϵ's and different q's while, for the same ϵ we may have different $(T_w - T_{vs})$ and different q's. In the experiments we can control continuously the specific heat flux while we can change discontinuosly, for example by changing the nozzle, the specific mass flux of impinging droplets. We have to operate on these two parameters so as to reach equilibrium before making any measurement.

If, for a certain flow rate, we start with large heat fluxes $(q > w_s\lambda')$ and we progressively reduce them, we reach equilibrium in the high $(T_w - T_{vs})$-low ϵ zone of Fig. 5. Instead, if we start with a low heat flux and we increase it progressively, we reach equilibrium in the high ϵ-low $(T_w - T_{vs})$ zone of Fig. 5.

Two plexiglas windows in the metallic container allow visual, photographic and cinematographic observations of the test section.

In this research the behaviour of droplets on the 25 mm plate was observed with the aid of ultrafast cinematography. The Institute of Scientific Cinematography of the Technical University of Milan

supplied us with the optical bench, the high speed camera and the light sources [12].

Motion pictures, at an average rate of 6000 frames per second, were taken during the heat transfer experiments. From the photograms, magnified on a screen, fractions of heat transfer areas covered by droplets are easily measured. With the aid of reference dimensions and associated timers, also dimensions and timelifes of liquid droplets on the plate can be evaluated.

On the 10 mm plate, fractions of heat transfer area covered by droplets were evaluated for each run by means of photographic measurements. The same optical bench and experimental set up were used for both the cinematographic and the photographic observations. The only minor difference was the utilization of a flash-light instead of a flood-light source for the photographic observations.

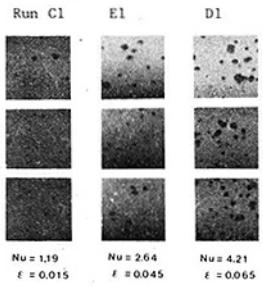

Fig. 8 Variation with the Nusselt number Nu ($=hD_m/k_\ell$) in the fraction of heat transfer area covered by droplets. Experimental conditions are reported in Table 2.

Results and Conclusions

A great number of high speed motion picture films, photographs and heat transfer measurements were obtained for sprays of atomized water evaporating at atmospheric pressure.

As is shown in Fig. 8, the pictures are sufficiently detailed to permit accurate measurements of the fraction of heat transfer area covered by droplets.

Typical experimental data are reported in Table 2.

As can be seen, values of the heat transfer coefficient up to 150 kW/m^{2}K are obtained with test surfaces which are safely away from flooded conditions.

The highest values of the heat transfer coefficient which have been obtained so far with a plate completely covered by a water film are of the order of 80 kW/m^{2}K [5, 6, 7]. Thus, from a thermodynamic point of view, dropwise evaporation is the most efficient among mist cooling processes.

In order to check the proposed model for dropwise evaporation, equation (19) was compared with the results of optical observations and thermal measurements. As can be seen from Fig. 9, with the assumption

$$d/D = \beta_1 \cong 4.5 \qquad (2')$$

the agreement between theory and experiments is impressive.

Specific heat fluxes up to 2.2 MW/m^2 have been maintained. This upper bound was imposed only by thermal limitations of the heating blocks. Hopefully, these limitations will be removed in the near future.

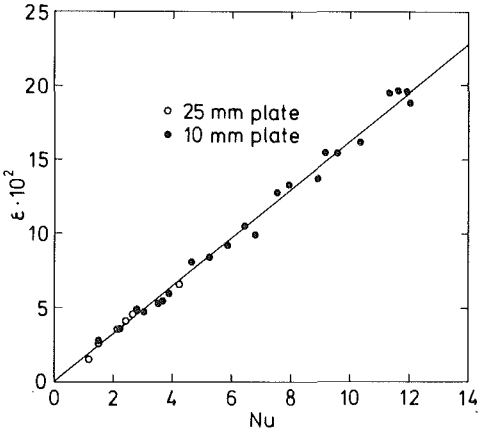

Fig. 9 Experimental data versus theoretical results. The continuous line is drawn from equation (19) assuming $d/D = 4.5$.

Table 2 Typical results and experimental conditions for dropwise evaporation. Wall temperatures have been corrected to take into account small variations from the conditions $T_{vs} = 100.0°C$ induced by atmospheric pressure variations. The characteristics of the atomizing nozzles, referred to in the first column, are reported in Table 1. The first set of results up to run E2 have been obtained using the 25 mm plate. All other results concern the 10 mm plate.

Run	p_ℓ (bar)	T_ℓ (°C)	H (cm)	T_w (°C)	Q/A (kW/m^2)	h (kW/m^{2}K)	D_m (μm)	Nu	ϵ Comp.	ϵ Meas.
A1	7	83.1	20	105.0	75.9	15.2	67	1.50	0.024	0.025
B1	7	82.3	25	104.3	96.6	22.5	64	2.12	0.034	0.035
C1	7	80.4	20	103.0	47.8	15.9	51	1.19	0.019	0.015
D1	7	80.3	20	103.1	148.	47.7	60	4.21	0.068	0.065
E1	7	82.3	18	118.0	497.	27.6	65	2.64	0.043	0.045
E2	7	81.6	20	117.7	446.	25.2	65	2.41	0.039	0.040
F1	5	23.0	25	105.3	78.4	14.8	69	1.50	0.024	0.028
G1	6	23.6	20	105.6	119.1	21.4	70	2.20	0.036	0.035
G2	6	24.2	20	104.0	116.6	29.2	70	3.03	0.049	0.047
H1	5	80.2	25	105.3	139.8	26.4	99	3.84	0.062	0.059
H2	5	78.2	15	106.4	298.9	46.7	99	6.80	0.111	0.099
H3	5	23.2	18	105.2	208.2	40.0	99	5.83	0.095	0.092
H4	5	22.4	14	107.3	321.9	44.1	99	6.42	0.104	0.105
I1	5	25.0	15	107.5	636.5	84.9	73	9.11	0.148	0.155
I2	5	25.0	20	106.4	530.6	82.9	73	8.90	0.145	0.137
L1	7	83.6	20	104.9	568.8	116.	56	9.53	0.155	0.154
L2	7	23.6	15	104.4	647.7	147.	56	12.0	0.195	0.188
L3	7	23.6	15	105.2	653.5	126.	56	10.3	0.167	0.162
M1	7	22.4	20	111.9	1099.	92.0	83	11.3	0.184	0.195
M2	7	22.4	18	112.0	1141.	95.0	83	11.6	0.189	0.196
N1	7	24.4	20	139.4	1420.	36.0	73	3.67	0.060	0.054
N2	7	24.4	20	143.5	1418.	32.6	73	3.50	0.057	0.053
N3	7	24.4	20	155.4	1419.	25.6	73	2.75	0.045	0.049
O1	7	25.3	20	137.9	1682.	44.4	80	5.22	0.085	0.084
O2	7	81.3	20	142.8	1685.	39.3	80	4.62	0.075	0.081
P1	7	21.6	20	135.8	2154.	57.0	89.5	7.92	0.129	0.133
P2	7	21.6	20	123.9	2153.	90.1	89.5	11.9	0.193	0.196
P3	7	80.6	20	136.7	2091.	57.0	89.5	7.50	0.122	0.128

Acknowledgment

The technical assistance of Dr. A. Berbenni and Mr. G. Ghezzi from the Istituto di Cinematografia Scientifica of the Politecnico di Milano, is gratefully acknowledged.

Mr. S. Barina, from the Laboratorio per la Tecnica del Freddo del C.N.R., Padova cooperated in the photographic observations.

References

1 Finlay, I. C., "Spray Flow as Heat-Transfer Media," *Chemical Processing,* Vol. 5, 1971, pp. 25–29.

2 Bonacina, C., Comini, G., and Del Giudice, S., "Evaporation of Atomized Liquids on Hot Surfaces (in Italian)," *La Termotecnica,* Vol. 32, 1978, pp. 472–481.

3 Hodgson, J. W., and Sunderland, J. E., "Heat Transfer from a Spray-Cooled Isothermal Cylinder," *Ind. Eng. Chem. Fundls.,* Vol. 7, 1968, pp. 567–571.

4 Wachters, L. H. J., Bonne, H., and Von Nouhis, H. J., "The Heat Transfer from a Horizontal Plate to Sessile Water Drops in the Spheroidal State," *Chem. Engng. Sci.,* Vol. 21, 1966, pp. 923–936.

5 Kopchikov, I. A., et al., "Liquid Boiling in a Thin Film," *Int. J. Heat Mass Transfer,* Vol. 12, 1969, pp. 791–796.

6 Toda, S., "A Study of Mist Cooling. 1st Report: Investigation of Mist Cooling," *Heat Transfer Japanese Research,* Vol. 1(3), 1972, pp. 39–50.

7 Toda, S., "A Study of Mist Cooling. 2nd Report: Theory of Mist Cooling and its Fundamental Experiments," *Heat Transfer Japanese Research,* Vol. 3 (1), 1974, pp. 1–44.

8 Bonacina, C., Comini, G., and Del Giudice, S., "Evaporation of Atomized Liquids on Hot Surfaces," *Letters in Heat and Mass Transfer,* Vol. 2, 1975, pp. 401–406.

9 Bonacina, C., Comini, G., and Del Giudice, S., "Evaporation from Cryogenic Liquids Sprayed on Flat Surfaces," *Proc. 5th Int. Heat Transfer Conf.,* Vol. IV, JSME-SCEJ, Tokyo, 1974, pp. 130–134.

10 Pedersen, C. O., "An Experimental Study of the Dynamic Behavior and Heat Transfer Characteristics of Water Droplets Impinging upon a Heated Surface," *Int. J. Heat Mass Transfer,* Vol. 13, 1970, pp. 369–381.

11 Del Giudice, S., and Barina, S., "Drop Size Analysis by Photographic Techniques," *Proc. 1st Heat Transfer Conf.,* Iasi, Rumania, 1973.

12 Berbenni, A., and Ghezzi, G., 1977, unpublished results.

13 Grassman, P., *Physical Principles of Chemical Engineering,* Pergamon, Oxford, 1971.

14 Abramowitz, M., and Segun, A., *Handbook of Mathematical Functions,* Dover, New York, 1972.

15 Longwell, J. P., "Combustion of Liquid Fuels," *Combustion Processes,* Vol. II, Lewis, B., and Pease, R. M., eds., Princeton Un. Press, 1956, pp. 407–415.

16 Mikic, B. B., "On Mechanisms of Dropwise Condensation," *Int. J. Heat Mass Transfer,* Vol. 12, 1969, pp. 1311–1323.

17 Glicksman, L. R., and Hunt, A. W., "Numerical Simulation of Dropwise Condensation," *Int. J. Heat Mass Transfer,* Vol. 15, 1972, pp. 2251–2269.

APPENDIX 1

Following [16] we can express in an approximate way: *the constriction resistance*

$$R_1 = (T_w - T_c)/Q_d = F_1/(\pi d\, k_w)$$

where T_w is the average wall temperature, T_c is the wall temperature in correspondence with the droplet and

$$F_1 \cong 0.5\, \pi\, (1 - \epsilon^{0.5})^{1.5}$$

is a shape factor [16]; *the conduction resistance*

$$R_2 = (T_c - T_i)/Q_d = F_2/(\pi\, d\, k_l)$$

where T_i is the interface temperature and

$$F_2 \cong 2\, s_0/d = 4/(3\beta_1{}^2)$$

is a time averaged shape factor.

Following [17] we can express the heat transfer resistance at the interface as

$$R_3 = (T_i - T_{vs})/Q_d = 4/(\pi\, d^2 h_i)$$

The heat transfer coefficient h_i due to the transfer of mass at the interface can be computed from the formula [17]

$$h_i \cong \frac{2\gamma}{2-\gamma}\left(\frac{M}{2\,\pi\, R\, T_{vs}}\right)^{0.5}\frac{\lambda}{T_{vs}\, v_{vs}}$$

where $\gamma = 1$ is the constant of evaporation [17].

With $p_{vs} = 1.013$ bar; $T_{vs} = 373.15$ K; $k_\ell = 0.68$ W/m·K $k_w = 182$ W/m·K; $\lambda = 2.25$ MJ/kg; $\epsilon = 0.1$; $d = 140$ μm we obtain:

$$h_i = 1.53 \times 10^7 \text{ W/m}^2\text{·K}$$

$$R_1/R_2 = (F_1 k_\ell)/(F_2 k_w) = 0.05$$

$$R_3/R_2 = (4k_\ell)/(dh_i F_2) = 0.01$$

Thus, as a first approximation, both constriction and interface resistances can be neglected in comparison with the conduction resistance.

G. R. Kubanek
Head, Process Engineering Division.

D. L. Miletti
Research Engineer,
Department of Process Technology.

Noranda Research Centre
Pointe Claire, Quebec
Canada H9R 1G5

Evaporative Heat Transfer and Pressure Drop Performance of Internally-Finned Tubes with Refrigerant 22

Heat transfer and pressure drop measurements were performed on three integral spiralled inner-fin tubes (12.7–15.9 mm OD, 30–32 fins, fin height 0.5–0.6 mm) with two-phase flow of refrigerant 22 under evaporating conditions. The data were compared with the performance of smooth tubes with and without a star-shaped insert. Based on the same length of heated test section (0.80 and 2.44 m), change in refrigerant quality (0.2 and 0.7) and mass velocity range (65,000 to 270,000 g/s · m²): (1) The enhancements in heat transfer coefficient for the internally-finned tubes over those for the smooth tubes ranged from 30 to 760 percent, and typically increased with mass velocity. Tighter fin spiralling significantly increased heat transfer. (2) The enhancements in heat transfer coefficient for the smooth tube with the star-shaped insert ranged from 40 to 370 percent, but decreased with mass velocity. (3) The increases in pressure drop for the internally-finned tubes over those for the smooth tubes ranged from 10 to 290 percent, while those for the smooth tube with the star-shaped insert were 300 to over 2000 percent. The factors enhancing the performance of the internally-finned tubes include the low fins which result in only a small reduction in cross-sectional flow area, and the tight spiral which increases the corner length per unit length of tube available for nucleation of vapor bubbles.

Introduction

This work is a continuation of the study of the heat transfer and pressure drop performance of Forge-Fin[1] tubes, made with integral internal fins. Previous reports [1–5] described the performance of Forge-Fin tubes in turbulent water and air flow, and in laminar oil flow. In this paper, performance data for the two-phase flow of refrigerant 22, whose properties are given in [6], are presented for evaporation inside smooth tubes, smooth tubes with star-shaped extruded aluminum inserts commonly employed in expansion water chillers, and three internally-finned tubes (Fig. 1 and Table 1) as a function of test section length, change in refrigerant quality, and mass velocity.

A large number of investigations have been carried out of two-phase evaporation under forced convection. However, Anderson, et al. [7] concluded, on the basis of a thorough experimental program with refrigerant 22 flowing in a 16.9 mm ID smooth tube (equivalent to tube 24A of this work) heated with warm water on the shell side, that none of the available correlations for calculating heat transfer and pressure drop were satisfactory for determining the performance of refrigerant evaporators in commercial equipment. Furthermore, they stated that, under the present state-of-the-art, experimental data suitable for design must be obtained from tests in which the tube circuiting arrangement, refrigerant, and operating conditions correspond closely to those in the proposed equipment.

The simplest and most commonly employed heat transfer correlation for evaporating refrigerants (incomplete evaporation) is that of Pierre [8]:

$$N_{\mathrm{Nu}} = 9.00 \times 10^{-4} N_{\mathrm{Re}} K_f^{0.5} \tag{1}$$

It should be noted that, when the two-phase heat transfer coefficient (h_{TP}) is plotted against the mass velocity (G), there is no dependency on the tube diameter (D_i) according to the Pierre correlation, while with the correlations of Gouse [9]. Dengler and Addoms [10], and Lavin and Young [11], h_{TP} is inversely proportionate to $(D_i)^{0.2}$. Thus when comparing tubes with inside diameters of 11.9 mm (tube 30) and 14.4 mm (tube 24B), this would result in a difference of only 4 percent, well within typical experimental error. A similar Pierre correlation is available for outlet superheat conditions. The major weakness of the Pierre correlations is that they consider only the average and not the local heat transfer coefficient [12]. There is thus no dependence on local refrigerant quality such as exists in other correlations [9–11] and those tabulated by Anderson et al. [7]. The latter, however, reported that the Pierre correlation gave the best agreement with their own results, but that it underestimated the heat transfer coefficient for short tubes when there was a large temperature difference between the refrigerant and the shell side water (i.e., high heat flux).

The most extensively used pressure drop correlation for evaporating refrigerants is that of Martinelli and Nelson [13], which consists of two terms, the first a frictional term to relate the pressure drop to that for single-phase flow, and the second an acceleration term to account for evaporation:

$$\Delta P_{TP} = r_1 \Delta P_L + r_2 \frac{G^2}{g_c} \tag{2}$$

Methods for determining the coefficients r_1 and r_2 are given by Anderson, et al. [7] and Altman, et al. [12]. Another suitable pressure drop correlation is given by Pierre [8]:

$$\frac{\Delta P_{TP}}{L} = \left[f_m + \frac{D_i \Delta x}{x_m L} \right] \frac{G^2 v_m}{g_c D_i} \tag{3}$$

where

$$f_m = 0.0185 \left[\frac{K_f}{N_{\mathrm{Re}}} \right]^{0.25} \text{ for } (N_{\mathrm{Re}}/K_f) > 1 \tag{4}$$

and

$$v_m = \frac{x_m}{\rho_G} + \frac{1 - x_m}{\rho_L} \tag{5}$$

Anderson, et al. [7] found that their pressure drop data fell consistently below the Martinelli and Nelson correlation and above that of Pierre.

Experimental

The heat transfer loop used for testing single tubes is shown in Fig. 2. Refrigerant 22 was passed from the five-ton compressor through an oil separator to minimize the oil content of the refrigerant. The quality of the refrigerant entering the horizontal evaporator test

[1] Registered trademark.

Contributed by the Heat Transfer Division for publication in the JOURNAL OF HEAT TRANSFER. Manuscript received by the Heat Transfer Division May 11, 1978.

section was controlled by mixing the vapor and liquid refrigerant streams at controlled flowrates. An ancillary evaporator was employed to prevent return of liquid refrigerant to the compressor. The loop was provided with a liquid stream bypass in order to obtain extra operational flexibility in terms of refrigerant flowrate.

Warm water (10–27°C) was employed as the shell-side heating medium and was pumped through a filter and a rotameter to the test section in concurrent flow with the refrigerant on the tube side. The temperature difference between the inlet and outlet water was measured with high sensitivity calibrated sensistors (7.92 mV/°C) located about 250 mm from the test section and checked with calibrated mercury-in-glass thermometers. The refrigerant temperature difference was measured with sensistors mounted in tees about 300 mm from the end of the heated length, and was checked with chromel/alumel thermocouples. All refrigerant lines were well insulated with asbestos wrapping tape. Pressure-tap rings with two taps were located about 130 mm from each end of the test section, and the pressure drop was measured with a mercury-filled or oil-filled U-tube manometer; the pressure drop data were therefore measured over a length of 1.07m for the short test sections (0.80m), and over 2.74m for the long test sections (2.44m). A minimum of 60 min. was generally required to reach steady state.

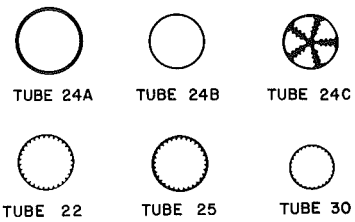

Fig. 1 Smooth and internally-finned tubes tested

The heat transfer coefficient for the refrigerant was calculated from its thermal resistance by subtracting the water-side and tube-wall resistances from the total resistance according to the method of Anderson, et al. [7]. The thermal resistance of the water-side was determined experimentally in a separate series of tests. The flow of water in the shell was varied over a wide range, while cold water or refrigerant was pumped through the inner tube at a fixed flowrate. The shell water-side resistance was then calculated from a modified Wilson plot. The constant representing the heat transfer resistance on the shell side was incorporated into the Sieder-Tate equation and was used to calculate the heat transfer coefficient on the shell side for each test. The tube-side heat transfer coefficient was then obtained from the overall coefficient. The heat transfer rate (Q), derived from the water flow rate and temperature drop, was used to calculate the change in

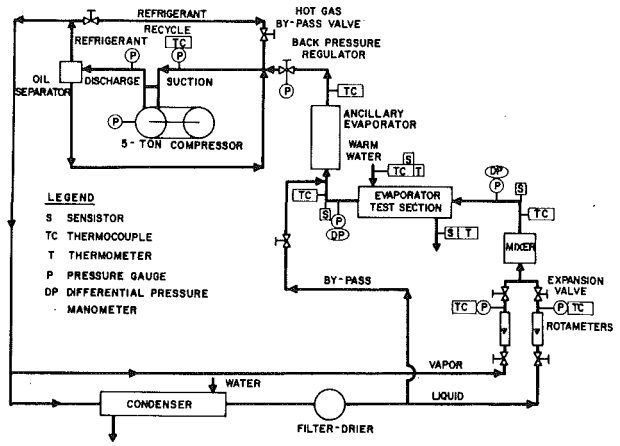

Fig. 2 Schematic diagram of two-phase evaporative heat transfer loop

Table 1 Dimensions of tubes tested

Tube Number Type	24A Smooth	24B Smooth	24C Star Insert	22 Inner-Fin	25 Inner-Fin	30 Inner-Fin
Number of Fins	0	0	5[4]	32	32	30
Outside diameter (D_0), mm	19.1	15.9	15.9	15.9	15.9	12.7
Inside diameter (D_i), mm	16.9	14.4	14.4	14.7	14.7	11.9
Fin height, mm	–	–	–	0.635	0.635	0.508
Fin pitch[1], mm	–	–	610	305	152	102
Inter-fin spacing, mm	–	–	–	1.14	1.14	0.76
Actual inside area (A_a), mm²/m × 10^{-3}	53.1	45.3	90.8	87.0	87.2	68.0
Nominal area[2] (A_n), mm²/m × 10^{-3}	53.1	45.3	45.2	46.2	46.2	37.4
A_a/A_n	1.00	1.00	2.00	1.88	1.89	1.82
Inside cross-sectional area (A_{xs}), mm²	224	163	92.9	163	163	107
Hydraulic diameter[3] (D_h), mm	16.9	14.4	4.09	7.57	7.57	6.30
Lengths of heated test section (L), m	2.44	0.80	0.80[5] 2.44[6]	0.80 2.44	0.80 2.44	0.80

[1] Length per full (360 deg) turn.
[2] $A_n = \pi D_i L$
[3] Hydraulic diameter $D_h = 4\ (A_{xs})/WP$
[4] Radial splines
[5] Insert length = 0.76 m
[6] Insert length = 2.44 m

Nomenclature

A = area
C_P = specific heat at constant pressure
D = diameter
f = friction factor
g_c = gravitational constant
G = mass velocity
h = heat transfer coefficient
J = mechanical equivalent of heat
k = thermal conductivity
K_f = load factor = $J\ \Delta x\ \lambda/L$
L = length
N_{Nu} = Nusselt number = $h_{TP}D_i/k_L$
N_{Pr} = Prandtl number = $C_p\ \mu/k$
N_{Re} = Reynolds number = D_iG/μ_L
N_{St} = Stanton number = $N_{Nu}/(N_{Re})(N_{Pr})$ = h/C_PG
P = pressure[2]
Q = heat transfer rate
r = Martinelli and Nelson coefficients
T = temperature
v = specific volume
w = mass flow rate
WP = wetted perimeter
x = refrigerant quality (fraction by weight in vapor form)
λ = heat of vaporization
μ = viscosity
ρ = density

Subscripts

a = actual
G = gas
h = hydraulic
i = inside
L = liquid
m = mean
n = nominal
o = outside
TP = two phase
w = wall to refrigerant
xs = cross-sectional

[2] Pressure drop ΔP_{TP} in equations (2) and (3) is in consistent units $lb_f/(ft^2)$ or Pa; pressure drop in figures is expressed for convenience as $\Delta P = \Delta P_{TP}/L$ in psi/ft or Pa/m.

refrigerant quality (Δx), and defined h_{TP} for all tubes as follows on the basis of inside diameter and nominal area: $Q = h_{TP} A_n \Delta T_w = w\lambda\Delta x$, where $A_n = \pi D_i L$. In most cases, Wilson plot data were generated at several shell-side inlet temperatures; an average value of the Sieder-Tate equation constant was then calculated.

The temperature of the refrigerant in the test section was about 4.4°C (or 40°F, corresponding to a saturation pressure of 68.5 psig). The shell-side water flowrate and temperature were varied to control the changes in refrigerant quality (0.2 or 0.7) reported for each tube. Further details of the heat transfer loop and procedure are given in [14].

Heat Transfer Results

Smooth Tubes. Two series of tests were carried out with smooth tubes. The first, with tube 24A in the 2.44 m test section, was conducted in order to compare the present data with those of Anderson, et al. [7] who employed an identical tube. The second, with tube 24B in the 0.80-m test section, was carried out in order to provide data for a smaller diameter tube (similar to tubes 22 and 25), as well as for a shorter length, i.e., higher heat flux for a given change in refrigerant quality.

The heat transfer results for smooth tube 24A in the long test section are shown in Fig. 3 for $\Delta x = 0.2$ and 0.7. In both cases, the data from the present investigation agreed closely with those of Anderson, et al. [7]. For $\Delta x = 0.2$ and 0.7, the present data were 4–11 percent and 3–6 percent, respectively, above the Pierre correlation, and the lines had essentially the same slope. On the other hand, in comparison with other available correlations, it was found that the data for $\Delta x = 0.7$ fell well below the correlation of Gouse [9], and well above the correlations of Dengler and Addoms [10], which were obtained for the evaporation of water in a vertical tube, and of Lavin and Young [11], whose correlation was extrapolated from the much higher mass velocity range employed in their tests. For $\Delta x = 0.2$, the anomalous data points at $x_1 = 0.8$ and $x_2 = 1.0$ in the mass velocity range (G) of 150×10^3 to 200×10^3 lb/(hr) (ft^2), were omitted in calculating the correlating equation. Similar anomalous data were obtained by Anderson, et al. [7] near the region of superheat, due to the lower rates of heat transfer obtainable by gas convection.

The heat transfer results for smooth tube 24B in the short test section are given in Fig. 4. The data for $\Delta x = 0.2$ and 0.7 all fell in the same range and were correlated by a single line which, however, fell between the Pierre correlations for $\Delta x = 0.2$ and $\Delta x = 0.7$. Comparison of the data for the short and long test sections shows that the heat flux is significantly higher for the former case, particularly for $\Delta x = 0.7$. However, while heat flux is represented as an independant variable in the Pierre correlation [8] within the load factor term as the ratio ($\Delta x/L$).

$$\text{heat flux} = \frac{Q}{\pi D_i L} = \frac{w\lambda\Delta x}{\pi D_i L} \tag{6}$$

it appears that the Pierre correlation does not adequately describe evaporative heat transfer in a short test section, particularly under conditions of high heat flux, as was also reported by Anderson, et al. [7].

It should be noted that the data for tube 24B (short test section) at $\Delta x = 0.2$ and 0.7 (Fig. 4) fell essentially on the same line as those for tube 24A (long test section) at $\Delta x = 0.7$ (Fig. 3). The ($\Delta x/L$) ratio for the three cases is about 0.1, 0.3, and 0.1, respectively, which values are comparable and proportional to the heat flux as shown above.

The oil content of the refrigerant in the heat transfer loop was determined using a similar procedure as that employed by Anderson, et al. A sample was taken in an evacuated copper tube 0.6 m downstream of the test section. The oil content averaged 0.125 percent, while that reported by Anderson et al. was 0.001 percent. Since their heat transfer data agree closely with the present data, it appears that the effect of oil content in the range 0.001 to 0.1 percent is insignificant.

Tubes with Star-Shaped Insert and with Internal Fins. The comparative heat transfer results for the smooth tubes (24A and 24B), the tube with the star-shaped insert (24C), and the internally-finned

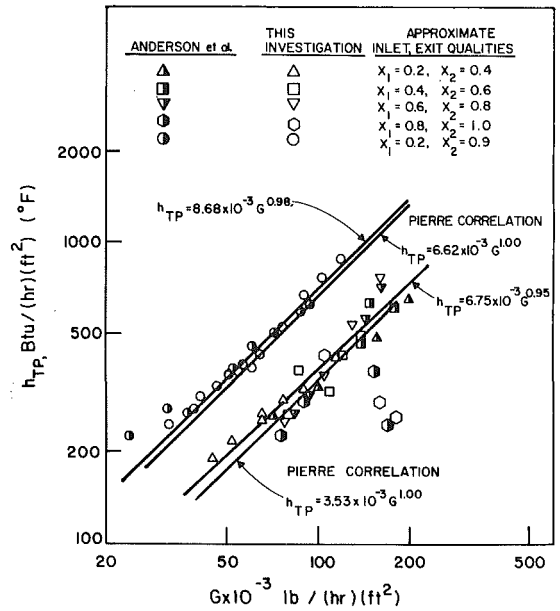

Fig. 3 Comparison of heat transfer data for smooth tube 24A in the 2.44-m test section for $\Delta x = 0.2$ and 0.7 with Anderson, et al. data [7] and Pierre correlation. Conversion factors: [g/s·m^2] = (1.356)[lb/(hr) (ft^2)]; [W/m^2·K] = (5.678) [Btu/(hr) (ft^2) (°F)]

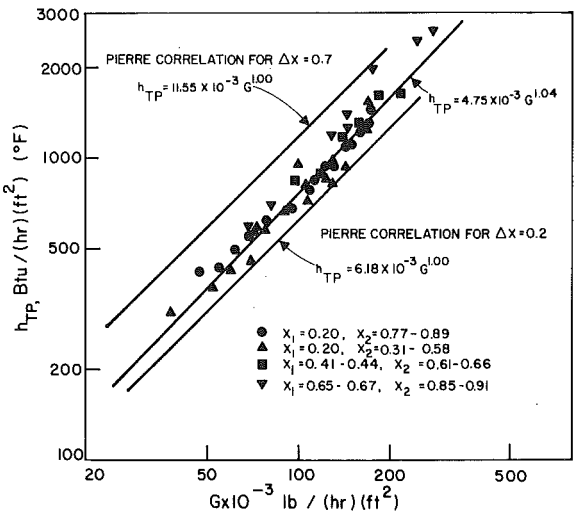

Fig. 4 Heat transfer data for smooth tube 24B in the 0.80-m test section. Conversion factors: [g/s·m^2] = (1.356) [lb/(hr) (ft^2)]; [W/m^2·K] = (5.678) [Btu/(hr) (ft^2) (°F)]

tubes (22, 25, and 30) are summarized in Figs. 5–7, showing the data points for tube 25, with the other data points omitted for the sake of clarity. The data for $\Delta x = 0.2$ all fell in the same range and were correlated by a single line for ease of comparison with data for the other tubes (Fig. 5).

Based on the same length of heated test section, change in refrigerant quality, and mass velocity range (65,000 to 270,000 g/s · m^2), it was determined that: (1) The highest enhancements in heat transfer coefficient over the smooth tube were generally obtained with internally-finned tube 25 (90 to 760 percent), and typically increased significantly with mass velocity. Tube 22 gave much lower enhancements (30 to 220 percent). The tighter spiralling in tube 25, resulting in increased turbulence effects, and the greater corner length per unit length of tube [11] providing more nucleation sites, would be expected to result in improved heat transfer performance well beyond the increase in surface area of about 90 percent (Table 1) due to the presence of the fins in these tubes. (2) The heat transfer coefficient enhancements for internally-finned tube 30 (120 to 160 percent) in the short test section were generally almost as high as those for tube 25 (90 to 460 percent) under similar conditions. (3) Significant heat transfer enhancements (40 to 370 percent) were achieved with tube 24C

(smooth tube with the star-shaped insert), but these decreased with increasing mass velocity. This may be due to the fact that the radial splines separate the tube into five separate compartments, and thus limit the degree of mixing which would normally occur with increased flow rate were the tube not compartmentalized. In addition, while the presence of the radial splines increased the surface area by about 100 percent and created more nucleation sites for evaporation (Fig. 1), the efficiency with which the splines transferred heat was probably reduced due to the presence of a temperature gradient along the splines, their base being at a higher temperature than their point of joining. (4) Because of the lower heat transfer coefficients obtained with the smooth tubes in comparison with the other tubes, higher water temperatures were required to obtain the same heat transfer rate, and this resulted in higher temperature differences between the wall and refrigerant (ΔT_w).

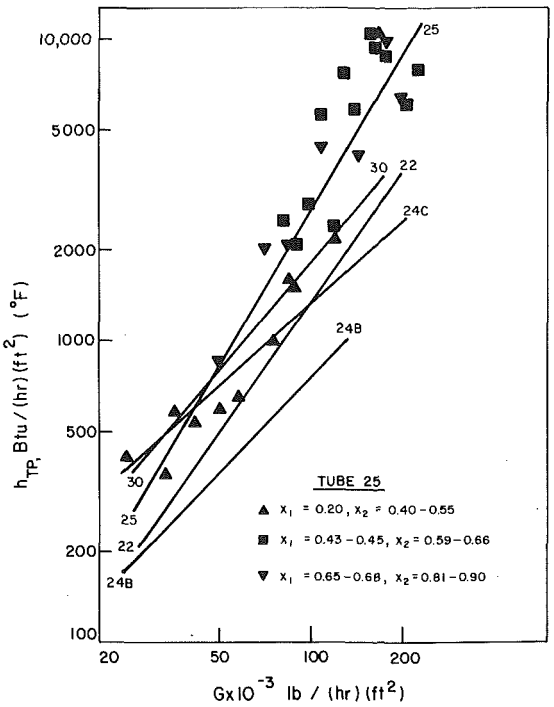

Fig. 5 Comparison of heat transfer data for tubes in the 0.80-m test section for Δx = 0.2. Conversion factors: [g/s·m^2] = (1.356) [lb/(hr) (ft^2)]; [W/m^2·K] = (5.678) [Btu/(hr) (ft^2) (°F)]

Discussion. In the Pierre correlation, the heat transfer coefficient h_{TP} is directly proportional to the mass velocity G, i.e., the exponent for G and the slope are equal to 1.00. The smooth tube data in Figs. 3 and 4 gave correlating lines with slopes of 0.95 to 1.04, essentially parallel to the Pierre correlation. However, the slope for tube 24C (smooth tube with star-shaped insert) was much lower (0.59 to 0.91), while the slopes for the internally-finned tubes were generally much higher than 1.00, up to 1.71 for tube 25. The relative slopes are evident in Figs. 5–7. Anderson has reported in the discussion section of [12] that the slope increases with increasing exit refrigerant quality from 1.0 at x_2 = 0.4 to 1.5 at x_2 = 0.8.

Based on the heat transfer data from this investigation, attempts were made to empirically correlate the two-phase evaporative heat transfer coefficient with the mass velocity (G), exit refrigerant quality (x_2) and the change in quality (Δx). The best fit was obtained by plotting h_{TP} versus $[Gx_2/(\Delta x)^{0.5}]$ or $[G(x_2/\Delta x)^{0.5}]$, and was independent of the test section length over the Δx range of 0.2 to 0.7 [14]. The correlation coefficients were higher than 0.9. The use of such groups would overcome the disadvantage of the Pierre correlation in that local, rather just average heat transfer coefficients could be calculated. These groups could also be incorporated into dimensionless numbers such as the Reynolds and Stanton numbers. Because this investigation was limited to tests with one refrigerant only, and its objective was primarily to compare the performance of the selected tubes rather than to study the effect of specific variables such as refrigerant quality, it is recommended that researchers working on the fundamentals of evaporative heat transfer investigate the further development of such correlations.

Pressure Drop Results

Smooth Tubes. Pressure drop data for smooth tube 24A in the 2.44-m test section (2.74m between the pressure taps) are shown in Fig. 8. The pressure drop (expressed as $\Delta P = \Delta P_{TP}/L$, i.e., pressure drop per unit length between pressure taps) increased significantly with the mass velocity, and with the exit refrigerant quality.

The present data for smooth tube 24A generally agreed closely in each case with the data of Anderson, et al. [7], and with the Pierre correlation [8], but were well below the Martinelli and Nelson correlation [13], as was the case for smooth tube 24B in the short test section [14]. It should be noted that the pressure drop (psi/ft) was higher

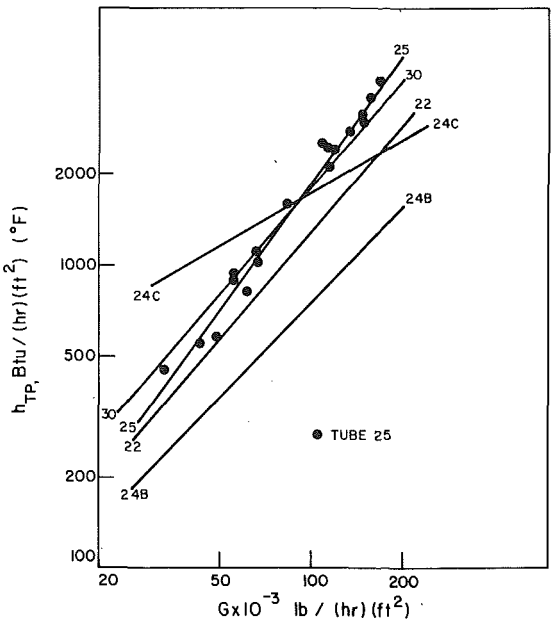

Fig. 6 Comparison of heat transfer data for tubes in the 0.80-m test section for Δx = 0.7. Conversion factors: [g/s·m^2] = (1.356) [lb/(hr) (ft^2)]; [W/m^2·K] = (5.678) [Btu/(hr) (ft^2) (°F)]

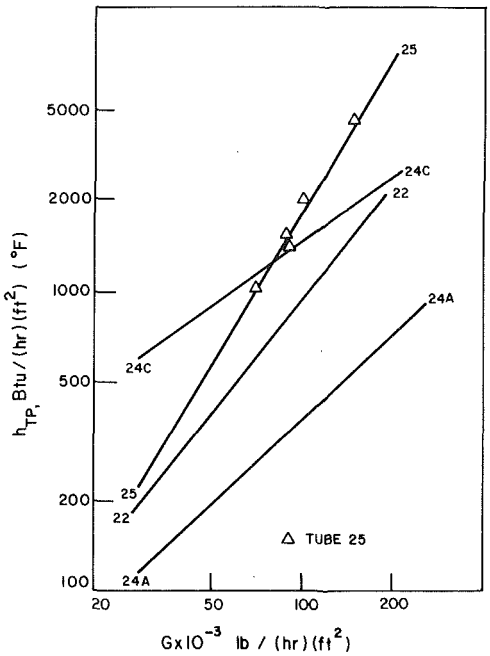

Fig. 7 Comparison of heat transfer data for tubes in the 2.44-m test section for Δx = 0.2. Conversion factors: [g/s·m^2] = (1.356) [lb/(hr) (ft^2)]; [W/m^2·K] = (5.678) [Btu/(hr) (ft^2) (°F)]

for the short test section (1.07m between pressure taps), mainly because the acceleration effect was much higher in this case per unit length of tube.

In the Pierre pressure drop correlation, equations (3–5), the frictional pressure drop term is strongly dependent on the inside diameter of the tube, (unlike the heat transfer case in which the dependence is small or non-existent), while the acceleration term is independent of the inside diameter. Because of the relatively wide range of inside tube diameters tested (11.9 to 16.9mm), and the close agreement of the present smooth tube data with the Pierre correlation, smooth tube pressure drops calculated using the Pierre correlation have been used as the basis for comparison of the performance of the other tubes [14].

Smooth Tube with Star-Shaped Insert. Pressure drop data for tube 24C are compared with calculated smooth tube data in Fig. 9. The data for tube 24C in the short and long test sections were correlated by the same line. The pressure drop increases over the corresponding smooth tube test section were very high, largely due to the reduced (by ~40 percent) cross-sectional flow area. The pressure drop increases over the corresponding smooth tube for the short test section ranged from 320 to 1500 percent, and for the long test section from 540 to over 2000 percent.

Internally-Finned Tubes. Pressure drop data for tube 22 in the short and long test sections were correlated by the same line, as shown in Fig. 10. The pressure drop increases over the smooth tube ranged from 10 to 290 percent. The pressure drop increases for tubes 22 and 25, which are identical except for pitch were generally similar (data for tube 25 also shown in Fig. 10). In contrast to the 40 percent reduction in cross-sectional flow area caused by the insert in tube 24C, the corresponding reduction for tubes 22, 25 and 30 was only 3.5 percent, which in part explains the much lower pressure drop increases. The pressure drop increase of tube 30 over the corresponding smooth tube ranged from 40 to 150 percent.

Discussion. The pressure drop data reported above include entrance and exit effects, frictional losses and the acceleration loss. Since there was a contraction in the cross-sectional flow area at the entrance to the test sections and an expansion at the outlet [14], their effects were estimated using standard techniques [15] involving contraction-loss and expansion-loss coefficients. The maximum pressure drop due to contraction and expansion (for tube 30) was found to be 7.5 percent of the measured total pressure drop which is well within experimental error, while with the other tubes, this loss was found to be negligible. Therefore, entrance and exit effects in the test section have been neglected.

The acceleration and frictional losses were calculated using the Pierre correlation given earlier. It should be noted that, in terms of pressure drop per unit length of tube, the frictional loss has a relatively low dependency on length (inversely proportional to $L^{0.25}$), while the acceleration loss has a high dependency (inversely proportional to L). Therefore, the acceleration loss is much greater for the short test section than for the long one. The relative magnitude of the frictional and acceleration losses for 14.5 and 11.9 mm ID smooth tubes is illustrated in Table 2.

The following conclusions may be made based on the data in Table 2. Relative to the frictional loss, the acceleration loss: (1) increases with mass velocity, (2) decreases with exit quality, (3) increases with quality change, (4) decreases with the test section length, and (5) increases with inside diameter.

For the short test section with the 14.5 mm ID tube, the acceleration loss ranged from 17 to 49 percent of the total pressure drop, and for the long test section from 9 to 32 percent. Since the acceleration loss should not vary much with or without small fins at a given inside diameter, it is the frictional loss which is the primary cause of increased pressure drop with the internally-finned tubes. This explains why the measured pressure drops per unit length of tube were relatively independent of the total test section length under given flow conditions.

The performance of the smooth tube with the star-shaped insert (tube 24C) is compared with that of internally-finned tubes 22, 25 and 30 in Table 3 at the intermediate mass velocity of 100,000 lb/(hr) (ft^2)

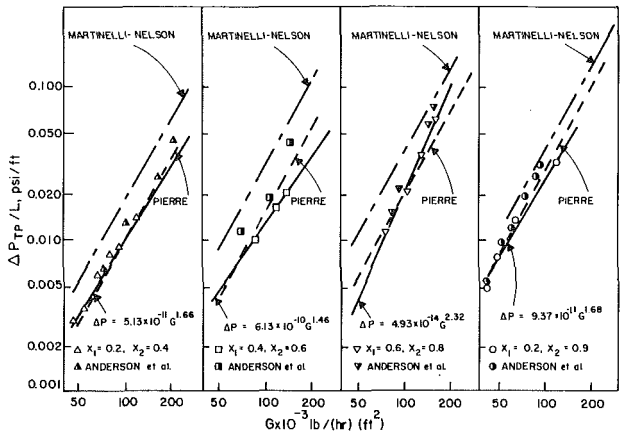

Fig. 8 Comparison of pressure drop data for smooth tube 24A in the long test section with data of Anderson, et al. [7] and the Pierre, and Martinelli and Nelson correlations. Conversion factors: [g/s·m^2] = (1.356) [lb/(hr) (ft^2)]; [Pa/m] = (2.262 × 10^4) [psi/ft]

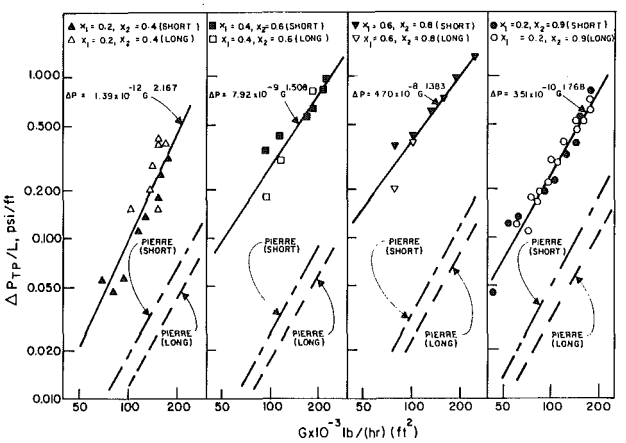

Fig. 9 Comparison of pressure drop data for smooth tube and tube 24C (smooth tube with star-shaped insert) in the short and long test sections. Conversion factors: [g/s·m^2] = (1.356) [lb/(hr) (ft^2)]; [Pa/m] = (2.262 × 10^4) [psi/ft]

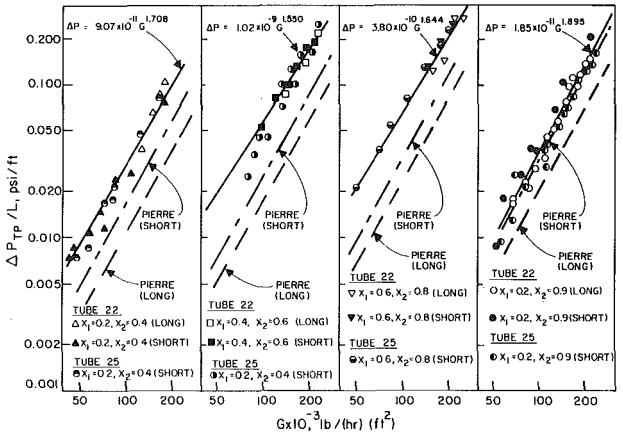

Fig. 10 Comparison of pressure drop data for smooth tube and tubes 22 and 25 in the short and long test sections. Conversion factors: [g/s·m^2] = (1.356) [lb/(hr) (ft^2)]; [Pa/m] = (2.262 × 10^4) [psi/ft]

using an enhanced performance ratio based simply on the ratio of the heat transfer enhancement to the pressure drop increase. It is clear that the heat transfer enhancement for tube 24C was significantly lower than the pressure drop increase (enhanced performance ratio of 0.14–0.48), while that of internally-finned tube 25 was much greater giving an enhanced performance ratio in the range of 1.23 to 2.29.

Table 2 Comparison of frictional and acceleration pressure drops for smooth tube[1] calculated using the Pierre correlation

Tube					Pressure Drop Distribution,[2] Percent at Mass Velocity, lb/(hr) (ft²)					
Inside Diameter, mm	Test Section Length,[1] m	Refrigerant Quality Inlet x_1	Outlet x_2	Change Δx	50,000 accel.	50,000 fric.	100,000 accel.	100,000 fric.	200,000 accel.	200,000 fric.
14.5	0.80	0.2	0.4	0.2	33	67	36	64	41	59
		0.4	0.6	0.2	23	77	26	74	29	71
		0.6	0.8	0.2	17	83	20	80	23	77
		0.2	0.9	0.7	40	60	45	55	49	51
14.5	2.44	0.2	0.4	0.2	19	81	22	78	25	75
		0.4	0.6	0.2	12	88	14	86	17	83
		0.6	0.8	0.2	9	91	11	89	13	87
		0.2	0.9	0.7	25	75	28	72	32	68
11.9	0.80	0.2	0.4	0.2	28	72	32	68	35	65
		0.4	0.6	0.2	19	81	21	79	24	76
		0.6	0.8	0.2	14	86	16	84	19	81
		0.2	0.9	0.7	35	65	39	61	43	57

Conversion factor: [g/s·m²] = (1.356) [lb/(hr) (ft²)].
[1] Length of heated test section; pressure drops measured over 1.07 and 2.74 m for short and long test sections, respectively.
[2] As a percentage of the total pressure drop

Table 3 Comparison of heat transfer enhancement and pressure drop increase

Test Section length, m	Refrigerant Quality Inlet x_1	Outlet x_2	Change Δx	Enhanced Performance Ratio[1] for Tube 24C	22	25	30
0.8	0.2	0.4	0.2	0.33	1.00	2.29	1.06
	0.4	0.6	0.2	0.16	0.76	1.89	0.80
	0.6	0.8	0.2	0.14	0.83	1.64	0.80
	0.2	0.9	0.7	0.48	1.53	2.11	1.54
2.44	0.2	0.4	0.2	0.48	0.95	–	–
	0.4	0.6	0.2	0.25	0.76	–	–
	0.6	0.8	0.2	0.23	0.92	–	–
	0.2	0.9	0.7	0.21	0.78	1.23	–

Basis: $G = 100 \times 10^3$ lb/(hr) (ft²)

[1] Enhanced performance ratio $= \dfrac{(h_{TP})_{\text{finned}}/(h_{TP})_{\text{unfinned}}}{(\Delta P)_{\text{finned}}/(\Delta P)_{\text{unfinned}}}$

Conclusions

1 On the basis of the heat transfer and pressure drop measurements, internally-finned tube 25 is clearly superior in performance to the smooth tube with a star-shaped insert.

2 The important factors which contribute to the high level of performance of tubes 25 and 30 include the low fins which cause only a small reduction in cross-sectional flow area, and the tight spiral which increases the corner length per unit length of tube available for nucleation of refrigerant vapor bubbles.

3 Based on the results of the present investigation, it is concluded that internally-finned tubes should prove beneficial in the design of compact direct expansion water chillers and other equipment in which the refrigerant is evaporated inside the tube to cool a fluid outside.

Acknowledgment

The authors wish to thank Mr. J. R. Russell for his co-operation in the program, Mr. T. C. Carnavos for his many helpful suggestions, and Noranda Metal Industries for their sponsorship of this investigation.

References

1 Watkinson, A. P., Miletti, D. L., and Tarassoff, P., "Turbulent Heat Transfer and Pressure Drop in Internally-Finned Tubes," *A.I.Ch.E. Symposium Series*, Vol. 69, No. 131, 1973, pp. 94–103.

2 Watkinson, A. P., Miletti, D. L., and Kubanek, G. R., "Heat Transfer and Pressure Drop of Internally-Finned Tubes in Turbulent Air Flow," *ASHRAE Trans.*, Vol. 81, Part I, 1975, pp. 330–349.

3 Watkinson, A. P., Miletti, D. L., and Kubanek, G. R., "Heat Transfer and Pressure Drop of Internally-Finned Tubes in Laminar Oil Flow," ASME Paper No. 75-HT-41, 1975.

4 Russell, J. J., and Carnavos, T. C., "Air Cooling of Internally-Finned Tubes," *Chemical Engineering Progress*, Vol. 73, No. 2, 1977, pp. 84–88.

5 Carnavos, T. C., "Cooling Air in Turbulent Flow with Internally-Finned Tubes," presented at the 12 National Heat Transfer Conference, Salt Lake City, Aug. 1977.

6 "Thermodynamic Properties of Freon 22 Refrigerant (Chlorodifluoromethane)," E. I. DuPont de Nemours and Company Bulletin, Nov. 1972.

7 Anderson, S. W., Rich, D. G., and Geary, D. F., "Evaporation of Refrigerant 22 in a Horizontal 3/4-in. o.d. Tube," *ASHRAE Trans.*, Vol. 72, Part I, 1966, pp. 22–36.

8 Pierre, B., *Kylteknisk Tidskrift*, No. 3, May 1957, p. 129; "Flow Resistance with Boiling Refrigerants," *ASHRAE J.*, Vol. 6, Sept. 1964, pp. 58 65, Vol. 6, Oct. 1964, pp. 73–77.

9 Gouse, W. S., and Dickson, A. J., Engineering Projects Laboratory Report DSR-8734-7, Massachusetts Institute of Technology, Dec. 1965.

10 Dengler, C. E., and Addoms, J. N., "Heat Transfer Mechanism for Vaporization of Water in a Vertical Tube," *Chem. Eng. Progress Symposium Series*, Vol. 52, No. 18, 1956, pp. 95–103.

11 Lavin, J. G., and Young, E. H., "Heat Transfer to Evaporating Refrigerants in Two-Phase Flow," *A.I.Ch.E. Journal*, Vol. 11, 1965, pp. 1124–31.

12 Altman, M., Norris, R. H., and Staub, F. W., "Local and Average Heat Transfer and Pressure Drop for Refrigerants Evaporating in Horizontal Tubes," ASME JOURNAL OF HEAT TRANSFER, Vol. 82, No. 3, 1960, pp. 189–198.

13 Martinelli, R. C., and Nelson, D. S., "Prediction of Pressure Drop during Forced-Circulation Boiling of Water," *Trans ASME*, Vol. 70, No. 6, 1948, pp. 695–702.

14 Kubanek, G. R., and Miletti, D. L., Noranda Research Centre Report 340, 1976.

15 McCabe, W. L., and Smith, J. C., *Unit Operations of Chemical Engineering*, McGraw-Hill, New York, 1956, pp. 74–83.

A. G. Bathelt
Graduate Research Assistant.

R. Viskanta
Professor.
Fellow ASME

W. Leidenfrost
Professor.

Heat Transfer Laboratory,
School of Mechanical Engineering,
Purdue University,
West Lafayette, Ind. 47907

Latent Heat-of-Fusion Energy Storage: Experiments on Heat Transfer from Cylinders During Melting

Melting from an array of three staggered, electrically heated cylinders imbedded in a paraffin (n-octadecane) has been studied. The shape of the melting front has been determined photographically, and the local heat transfer coefficients were measured using a shadowgraph technique. The experiments provide conclusive evidence of the important role played by natural convection on the timewise variation of the melt shape, the surface temperature and the instantaneous local as well as circumferentially averaged heat transfer coefficients around the imbedded heat sources. After a common solid-liquid interface is formed around the cylinders, natural convection circulation around each cylinder interacts strongly with the other two cylinders. The arrangement of heat sources affects significantly the melt shape but the circumferentially averaged instantaneous heat transfer coefficients differ only by about 10 percent for the two arrangements studied. The experimental findings indicate that natural convection effects are important and should be considered in analysis and design of systems involving phase change.

Introduction

In this paper, experiments are described which are aimed at providing quantitative data on heat transfer processes which occur when a solid is melted from multiple, horizontal heat sources. This study was motivated by the need to gain improved understanding of heat transfer during the charging phase of a thermal energy storage (TES) system which takes advantage of the latent heat-of-fusion of a phase change material (PCM) [1]. A relevant consideration in such systems is the effective utilization of the PCM by an optimum arrangement of tubes through which the working fluid is circulated. Good heat transfer characteristics between the transport fluid and the PCM for efficient thermal performance of a storage unit are also required. Data needed for the design of latent heat-of-fusion TES systems are not available.

The current standard analytical approach in treating heat transfer during melting is to assume that conduction is the only heat transport mechanism [2–4], and only recently [5, 6] has the presence of natural convection in the melt region been taken into account. As a result, the solid-liquid interfaces formed a succession of concentric circles surrounding a cylindrical heat source. However, temperature variations in the liquid are of necessity present during heat transfer, and the temperature differences may be sufficiently large to generate buoyancy forces for unstable situations which could produce natural convection motions. The circulation in the liquid could have an important bearing on the motion of the phase-change boundary and heat transfer. Recent experiments have provided conclusive evidence [6–8] that natural convection plays an important role in the melting of a solid surrounding an imbedded horizontal heat source. The augmentation or degradation of heat transfer that may occur as a result of melting around neighboring cylinders has not been studied.

Natural convection is an important process in problems involving melting, and it is the purpose of this paper to point out some of its characteristics. To this end, heat transfer processes which occur when a solid is melted from multiple cylindrical heat sources are studied. Quantitative experimental evidence is presented on the effects of natural convection in the melt region and heat source arrangement on the motion of the phase change boundary, the interference between plumes above adjacent cylinders and the local heat transfer when three horizontal cylinders were heated electrically. A paraffin (*n*-octadecane, $C_{18}H_{38}$; T_f = 301.15 K) was chosen as a test material because the liquid is transparent allowing for optical and photographic observation of the melt zone, and for the fact that paraffins have been suggested [9] as phase-change-materials for thermal energy storage systems which take advantage of the latent-heat-of-fusion of the storage medium. Another reason for using a paraffin, such as n-octadecane, is that it's physical and transport properties are well established [10] and thus facilitate the proper nondimensionalization which is necessary in generalizing the results. In addition, *n*-octadecane has a fusion temperature which is conducive for reducing the heat losses from the test cell to the ambient laboratory environment.

Experiments

Test Apparatus and Test Procedure. The main part of the test cell, a U-shaped aluminum frame 4.0 cm thick with inside dimensions of 16.2 × 13.2 × 4.0 cm, was attached to a rectangular base-plate which could be adjusted in vertical direction at its four corners for precise leveling. The front and back sides of the cell were made of plate glass, 0.6 cm thick, to allow for visualization, photographing and optical observation of the phenomena taking place during phase transformation. The sealing was accomplished by placing an o-ring between the aluminum frame and the glass plate. In order to press the glass plate uniformly against the U-shaped frame a collar was machined to the main frame on each side to accommodate an aluminum stress-relief strip which was pressed against the edges of the glass plate by screws.

To reduce natural convection from the test cell a second glass plate was installed on each side of the cell. The air gap between the two vertical glass plates was selected to minimize heat loss from the cell to the ambient environment. The top of the test cell was closed with a plexiglass cover. A screen was hinged to this cover which could be turned and placed parallel to the window facing the camera. This arrangement was used when the solid-liquid interface was photographed. For photographing the shadowgraphs the second screen was used. The first screen was removed from the optical path by turning it upwards, see Fig. 1.

Electrical cartridge heaters, 0.64 cm OD, were employed as heating elements. The heaters were inserted in snugly fitted brass tubes, 1.9 cm in outside diameter. The 4.0 cm long tubes with the heater inside were then installed in the test cell. Holes were drilled in one of the glass plates for bringing out the power leads of the heating elements

[1] Contributed by the Heat Transfer Division of the AMERICAN SOCIETY OF MECHANICAL ENGINEERS and presented at the AIAA/ASME Thermophysics and Heat Transfer Conference, Palo Alto, Calif., May 25–26, 1978. Revised manuscript received at ASME Headquarters July 19, 1978. Paper No. 78-HT-47.

and the thermocouple wires. The holes were then sealed to prevent the leaking of molten paraffin from the cell. A schematic diagram of the staggered, three cylinder arrangement used in the experiments is shown in Fig. 2.

The wall temperatures were measured by Chromel-Constantan thermocouples. Small diameter, 1.0 mm OD, holes were drilled axially and radially in the brass tube and then the thermocouple junctions were brought to the surface, soldered and the surface polished. The thermocouples were located at $\theta = 0, 90, 180$ and 270 deg. A shadowgraph system, shown schematically in Fig. 1, was employed for observing the melting front and for measuring the local heat transfer coefficient at the surface of the cylinder [11]. The system has been found to be satisfactory in preliminary experiments [6].

The test cell was filled with liquid n-octadecane (99 percent pure, Humphrey Chemical Co., North Haven, CT) and given sufficient time to solidify and reach uniform ambient temperature throughout in a temperature controlled laboratory environment. The initial temperature of the solid was maintained close to the melting temperature and was typically a maximum of only a couple degrees Kelvin lower than the melting temperature. Therefore, the small subcooling ($T_f - T_i$) is not expected to have much effect on the melting front motion. Each experiment was performed at constant electrical power input (constant heat flux) to the heater. Precautions were taken not to entrap any air as the liquid solidified. This was done by vibrating the test cell during freezing of the PCM. No entrapped air was observed to form a cavity. The maximum beam deflection and the motion of the melting front were recorded photographically.

Data Reduction. If a parallel light beam enters a uniform test section it remains so toward the screen. During the melting process, however, the material in the test section is nonuniform due to temperature gradients which cause a change of index of refraction of the PCM. Since the light beam remains deflected outside of the test cell, the displacement on the screen can be minimized by moving the screen as close as possible to the exit of the test section in contrast to studying heat transfer around the heat source where a large displacement is necessary for a quantitative evaluation of the photographs. In that case, a sufficient distance between test section and screen has to be maintained.

The path of light in a nonisothermal medium can be calculated from the geometrical optics theory [11]. For a system where changes in the index of refraction n and of the temperature in the axial direction are negligible in comparison to the radial direction, the geometrical optics theory yields the distance Y of the deflected light beam on the screen

$$Y = \frac{1}{n}\frac{dn}{dT}\frac{dT_\ell}{dr}\ell L \tag{1}$$

For a horizontal cylinder of radius R the local Nusselt number Nu defined by

$$\mathrm{Nu} = -\frac{2(\partial T_\ell/\partial r)_R R}{(T_w - T_f)} \tag{2}$$

can be expressed in terms of observed and known quantities as

$$\mathrm{Nu} = -n\frac{dT}{dn}\frac{2RY}{\ell L(T_w - T_f)} \tag{3}$$

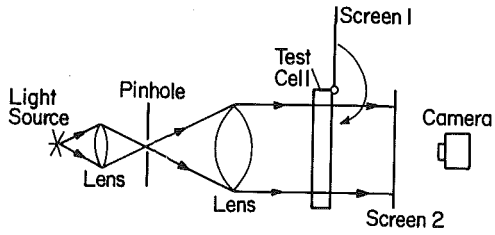

Fig. 1 Schematic diagram of shadowgraph system

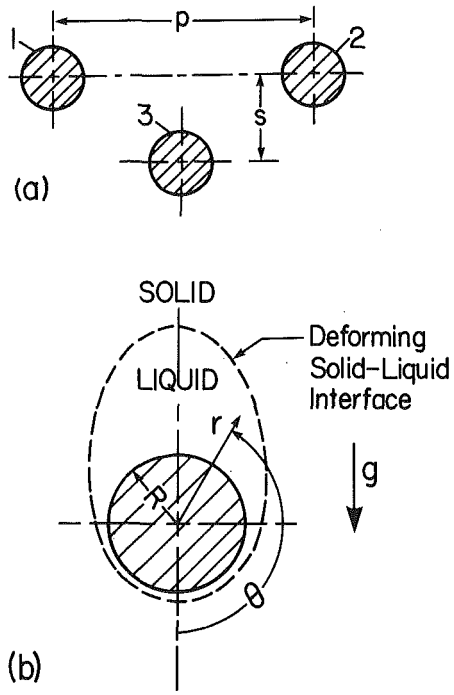

Fig 2 Schematic diagram of (*a*) three cylinder arrangement and (*b*) coordinate system

where T_w is the cylinder surface temperature. The distance Y is determined from the photographs made during the melting process. A more detailed discussion of the theoretical basis of the shadowgraph technique is given elsewhere [11].

There were unavoidable heat losses from the heating elements to the test cell walls. The length to diameter ratio of the heated cylinder was relatively small. A longer cylinder would have been preferrable. The choice was a compromise between the heat losses from the ends and the ability of the shadowgraph to give results at times when the melt layer is relatively thin. The shadowgraph technique only yields results when the tangent of the deflection angle is less than twice the thickness of the melt layer divided by the length of the cylinder. The heat losses from the ends of the heated cylinders were estimated from the heat input, heat transfer coefficient and temperatures measured along the cylinders. All of the heat transfer parameters containing heat input were corrected for these losses. The uncertainty in the heat

Nomenclature

c = specific heat
D = cylinder diameter
Fo = Fourier number, $\alpha t/R^2$
Gr = Grashof number, $g\beta(T_w - T_\infty)D^3/\nu^2$
Gr* = modified Grashof number based on heat flux, $g\beta qD^4/\nu^2 k$
g = acceleration of gravity
Δh_f = latent heat of fusion
k = thermal conductivity
L = length of the heat sources (cylinders)
ℓ = distance between test cell and screen
q = heat flux
n = index of refraction
R = radius of the cylinders
Ra = Rayleigh number, GrPr
Ra* = modified Rayleigh number, Gr*Pr
Ste = Stefan number, $cqR/k\Delta h_f$
T = temperature
t = time
α = thermal diffusivity, $k/\rho c$
β = thermal expansion coefficient
Θ = dimensionless temperature, $(T_w - T_f)/(qR/k)$
θ = polar angle, see Fig. 2
ν = kinematic viscosity
ρ = mass density
τ = dimensionless time, Ste·Fo

Subscripts

f = fusion (melting)
i = initial
ℓ = liquid
s = solid
w = wall
∞ = free stream

input, which is needed to evaluate the Stefan and Rayleigh numbers, is estimated to be about 5 percent and is due primarily to the lack of precise knowledge of the thermal conductivity of the electric cartridge heater and the thermal contact resistance between the ends of the brass sleeve heater and the test cell wall.

A number of experiments for different wall heat fluxes have been performed with three cylinders (in two rows) imbedded in a PCM. Three rows of cylinders were not considered because after a common solid-liquid interface is formed, the solid would lose support, descend down onto a lower row of cylinders and result in a totally different physical arrangement. Two different staggered arrangements have been considered to examine the effects of natural convection and plume interference on heat transfer and the melting front shape. The pitch and the spacing used are given in Table 1.

Results and Discussion

Melt Shape. A comparison of typical photographs illustrating the solid-liquid interface positions at selected times for arrangements A and B is given in Fig. 3. The shadows of the cylinders in the figure appear to be slightly out of round. This is not due to faulty imaging of the cylinders but due to the fact that the melting front was photographed off a screen attached to the test cell instead of photographing the cylinders directly. The actual contours of the cylinders in the photographs are indicated with dashed curves on the photographs. At early times (τ = 1.2 not shown in figure) the shape of the phase change boundary around an individual heat source is not influenced by the presence of other sources [6, 8]. However, the plumes are already developed at the top of the cylinders. The melt regions are no longer annular in shape because of natural convection. The effect of heat source arrangement on the melt shape is clearly seen at $\tau = 2.4$. For arrangement B a continuous solid-liquid interface has already been formed while for A the cylinders still have separate melt zones. This is due to closer spacing of the heat sources for arrangement B, see Table 1. The oscillation of the plumes above the cylinders is evident from the photographs. Observations revealed no definite period of plume oscillations. The dark lines visible in the photographs of arrangement A at θ = 270 deg and θ = 90 deg for cylinders 1 and 2, respectively, are the thermocouple and power leads.

Table 1 Cylindrical heat source arrangements used in tests: D = 1.905 cm

Arrangement	Pitch, p	Spacing, s
A	$3D$	$1.5D$
B	$3D$	D

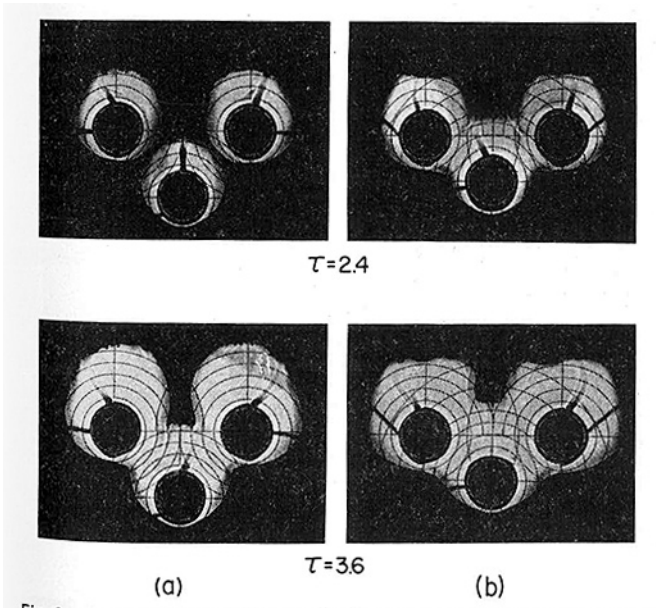

Fig. 3 Comparison of melt shapes for Ste = 1.25: (*a*) arrangement A and (*b*) arrangement B

The overall shapes of the melt zones are different for the two heat source arrangements at τ = 3.6. For arrangement A the melt zones extend into the vertical and for B into the horizontal directions. A prolonged plume activity in a given direction produces non-uniform local melting above the upper two cylinders. The very important role played by natural convection in forming the melt zone is evident from the photographs. Most of the melting occurs above and to the sides of the heat sources with very little below. The upward motion of the interface is driven at early times by the plume which rises from the top of the heated cylinder, and at later times by circulation which conveys the hot liquid to the upper part of the melt region. It appears that the presence of natural convection reduces the melting below the cylinders compared to that which would occur if heat transfer were by pure conduction.

The positions of the solid-liquid interface at a succession of times are plotted in Fig. 4(*a*). These melting front positions were taken directly from the photographs. Inspection of the figure reveals that at early times the melt regions are still separated. There is no detectable interaction, and the melting around the heat source occurs as if the solid were infinitely large and there were no other sources. At early times when heat transfer from the cylinder to the paraffin is dominated by conduction the melt region is symmetrical about the axis of the cylinder. As the heating continues and natural convection develops, the annular melt zone becomes increasingly distorted. The shapes of the molten regions shown in Fig. 4(*a*) for the cylinders at early times before interaction begins to take place are different for the same heat flux than those for SUNOCO P-116 wax [6]. The shapes for *n*-octadecane are similar to those obtained by Sparrow, et al. [7] for a eutectic of sodium nitrate and sodium hydroxide which has a melting temperature of ~517 K. The larger initial subcooling of the solid for the SUNOCO P-116 wax is considered to be the main reason for the somewhat more slender and sharper molten region near the top of the melt zone. The parameter $c_s(T_f - T_i)/\Delta h_f$ can be used as a measure of the importance of subcooling on the shape of the melt. For *n*-octadecane this parameter was a maximum of 0.03 while for SUNOCO P-116 wax it was 0.4. This clearly indicates that very little heat was required to bring n-octadecane to the fusion temperature while a substantial fraction of heat input was needed for SUNOCO P-116 wax.

As the Stefan number increases (see Fig. 4(*b*)) the solid above the cylinder melts faster which changes the overall shape of the melt. After

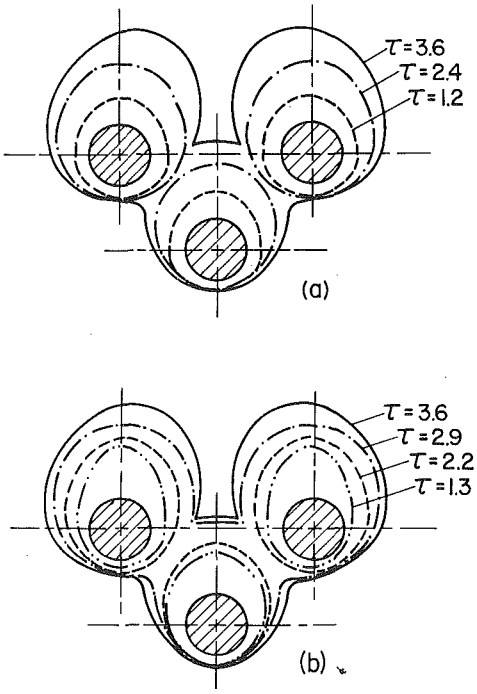

Fig. 4 Position of the solid-liquid interface for arrangement A: (*a*) effect of time (Ste = 1.25) and (*b*) effect of Stefan number (Fo = 2.88)

the liquid regions around the cylinders form a common boundary, the natural convection about the lower cylinder 3 supports melting in the region between and above cylinders 1 and 2. With increasing Stefan number the natural convection circulation in the liquid becomes more intense and influences the shape of the melt particularly in the region between and above the upper two cylinders. The interaction between the cylinders causes a shift of the symmetry from the axis of each cylinder to the vertical plane passing through the center of cylinder 3. Observations have shown that the melting was very uniform along the length of the heated cylinders. Only at very late times, after the melt thickness above the heated cylinder had reached about 5 cm, was there an observable (about 2 mm) difference in the melt layer thickness at the center of the test cell in comparison to the test cell wall. This suggests that even though natural convection circulation in the melt region is three-dimensional, the melting process is nearly two-dimensional.

The plumes which rose from the top of the heated cylinders were unstable, unpredictable and affected the shape of the solid-liquid interface. When the circulation was sufficiently intense, the plume above cylinder 3 was influenced by the circulation between cylinders 1 and 2 and originated on the upper $\frac{1}{3}$ (120 deg $< \theta <$ 240 deg) part of the cylinder. The plumes of cylinders 1 and 2 produced nonuniform, jagged melting shapes above the upper two cylinders.

Cylinder Surface Temperatures. The results obtained showed that there was relatively little variation in the surface temperature T_w along the entire length of the cylinder, but there was some variation of T_w with the angular position of θ. The maximum surface temperature typically occurred at θ = 180 deg, but the difference between the maximum and minimum temperatures never exceeded 0.5 Kelvin even for the largest wall heat flux (Ste = 1.25). There were also small temperature differences between the three cylinders. The surface temperature variations with time for cylinder 1 under different heating conditions are presented in nondimensional form in Fig. 5. The dimensionless variables for correlating the data are suggested by analysis [2] in which conduction was the only mode of heat transfer. Fig. 5 shows that for Ste = 0.76 and Ste = 0.46 distinct overshoots in the surface temperature are noted at approximately τ = 1.3 and τ = 0.8, respectively. The surface temperature decreases as creeping motion sets in and natural convection develops and intensifies. Similar type of overshoots have been observed during melting around a single electrically heated cylinder [6, 8] and in transient natural convection heat transfer from a vertical plate [12] and a small diameter wire [13]. At late times the surface temperatures reach constant values independent of time. The temperatures for the lower cylinder 3 showed similar trends with time but differed up to 1 K from those of the upper cylinders 1 and 2. The fact that the surface temperatures do not fall on a single curve for larger values of τ is a clear indication that conduction is not the only mechanism of heat transfer during melting of n-octadecane.

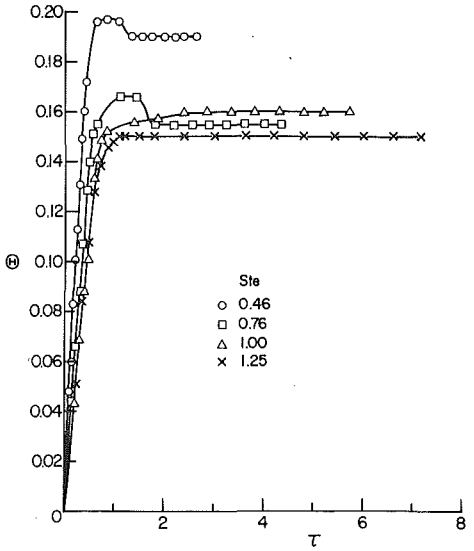

Fig. 5 Variation of dimensionless cylinder surface temperature for cylinder 1 with dimensionless time for arrangement A

The surface temperature of the cylinders for arrangement B were practically the same as those for arrangement A. At intermediate times ($\tau < 2.0$) the temperatures of the cylinders for Ste = 0.46 and for Ste = 0.76 were about 1 K larger for arrangement A than for B, while at later times ($\tau > 2.0$) lower constant temperatures were reached for Ste = 0.76 and 1.0. This difference was only about 0.5 K and is attributable to changed natural convection patterns between and above the upper two cylinders.

Shadowgraphs of the heated cylinders for arrangement B during the melting process are shown in Fig. 6. The dynamic process of developing natural convection is clearly evident from the photographs for Ste = 0.76. At early times (Fo = 0.578, Fig. 6(a)) the shadows are symmetrical about the cylinder axis indicating that heat transfer is solely by conduction. At a somewhat later time (Fo = 0.768, Fig. 6(b)) cells which have been formed at the upper part of cylinders are indicative of instability and initiation of natural convection. Study of the still and motion picture shadowgraphs which have been made revealed that the first indication of instability occured shortly before the cylinder surface temperatures reached their maximum. The occurance of the peak surface temperature is considered to be associated with the change from pseudo-conduction to fully developed natural convection regimes. The smoke pictures and Mach-Zehnder interferograms [14] for steady natural convection in a horizontal annulus indicate an onset of change in the flow pattern in form of three-dimensional vortices of unsteady oscillating kind in the transition regime between pseudo-conduction and fully developed natural convection. In the fully developed natural convection regime the motion

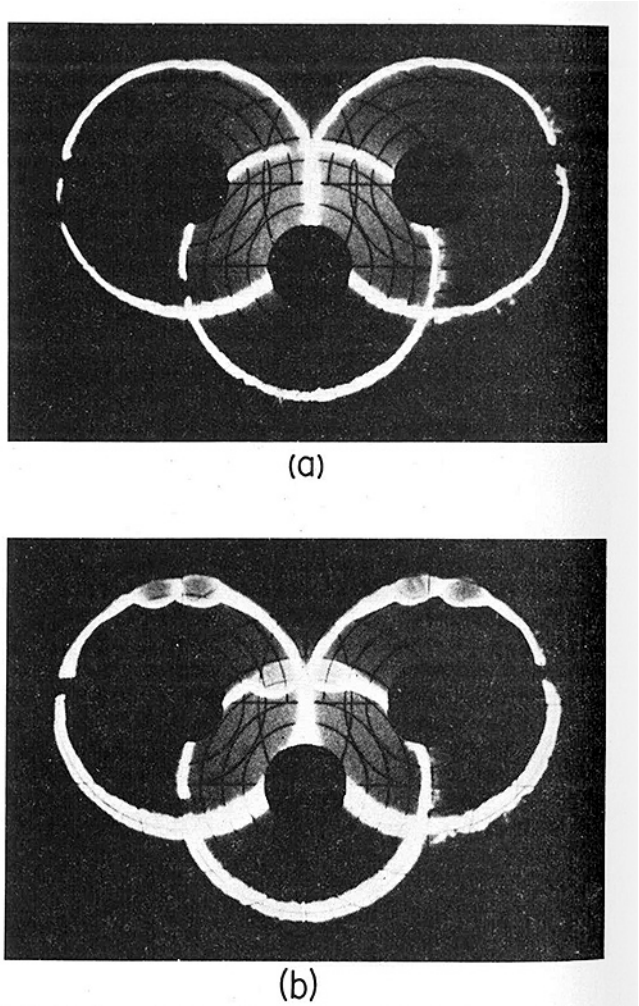

Fig. 6 Shadowgraphs illustrating development of natural convection during the melting process for arrangement B with Ste = 0.76: (a) τ = 0.44 and (b) τ = 0.58

returns to two-dimensional form. The shadowgraph pictures shown in Fig. 6 also appear to indicate the growth of longitudinal vortices, a process which is expected to follow a thermal instability at the top of the cylinders. The overshoot is considered to be associated with the change of flow motion in the melt region surrounding the cylinder.

Heat Transfer. The local Nusselt number can be deduced from the shadowgraphs of the type illustrated in Fig. 6. Since the light beams grazing the cylinder surface are deflected the most, they form the light zone around the dark shadow in the center. The distance on the screen from the cylinder surface to the light/dark boundary is directly proportional to the temperature gradient at the cylinder surface ($r = R$) and therefore to the local Nusselt number. It should be emphasized that the nature of the shadowgraph technique allows determination of only the average surface temperature gradient, $(dT/dr)_{r=R}$, over the entire length of the heated cylinder, see equation (1). Therefore, any nonuniformities in the gradient along the cylinder axis as a result of heat losses from the test cell walls are already accounted for, and the Nu numbers given in the paper should be considered as averaged values over the cylinder length. The diameter of the cylinder was used as the characteristic dimension in the parameters correlating the heat transfer data. However, since the melt (liquid) region is not infinite in volume but its shape and size change continuously with time the diameter may not be the appropriate characteristic dimension for correlating the data.

For small values of dimensionless time τ conduction is the only mechanism of heat transfer. During this phase of the melting process it may not even be entirely appropriate to use the concept of the heat transfer coefficient defined by equation (2) since there is no convection in the melt region, and because initially, at $\tau = 0$, $T_w - T_f$ could be negative or approach zero. As the heat input into the system (τ) increases the local heat transfer coefficient decreases monotonically and becomes circumferentially nonuniform as a result of natural convection [8, 10]. A comparison of local heat transfer results is presented in Fig. 7 in terms of standard parameters for correlating natural convection heat transfer of the data. The data points are joined by a solid line for the sake of clarity. The results shown are for the case when a common solid-liquid interface has been formed around the cylinders and a nearly time independent average heat transfer coefficient has been obtained. Only results for cylinders 1 and 3 are included because the local Nusselt numbers for cylinder 1 and cylinder 2 are antisymmetric about the vertical plane passing through the center of the arrangement, e.g., $\mathrm{Nu}(\theta)|_{cyl.1} = \mathrm{Nu}(-\theta)|_{cyl.2}$.

Inspection of Fig. 7 reveals that the local Nusselt number around cylinder 1 is influenced more by the arrangement than the lower cylinder 3. This is attributable primarily to the altered natural circulation flow patterns between and above the two cylinders as a result of the change in geometry and the melt shape. No general trends are discernible from the figure, with the exception that the Nusselt number around cylinder 1 is greater for arrangement A than for B. The heat transfer coefficient is higher at the bottom than at the top of the cylinder. This is consistent with the results for natural convection from a single uniformly heated horizontal cylinder [15], but the $\mathrm{Nu/Ra^{*1/5}}$ ratios during melting are about a factor of 1.5 lower than for natural convection in the liquid in the absence of phase change. This attributed to the changed natural convection flow field in a small, irregular melt region as compared to natural convection in an "infinite" volume of fluid.

A somewhat clearer indication of the effect of the melt shape on heat transfer is presented in Fig. 8 where a fractional departure of $\mathrm{Nu/Ra^{*1/5}}$ from that of a single cylinder at the same heat input rate are compared. The data could not be clearly interpreted around the upper stagnation point of the cylinder because of light interference from adjacent cylinders. The dashed curves shown in the figure represent estimated trends. The results clearly indicate that there is some degradation of heat transfer from that of a single cylinder for arrangement B but that there is somewhat more enhancement at the upper part of the cylinder for arrangement A. This is believed to be due to smaller interference with the flow field by the natural convection circulation around and between the upper two cylinders (see Fig. 3 for $\tau = 3.6$).

The circumferentially averaged instantaneous heat transfer coefficients are presented in Fig. 9 in dimensionless terms. The results available for melting from a single cylinder [8] and for natural convection heat transfer from a 0.953 cm outside radius circular heat exchanger approximating a constant wall temperature boundary

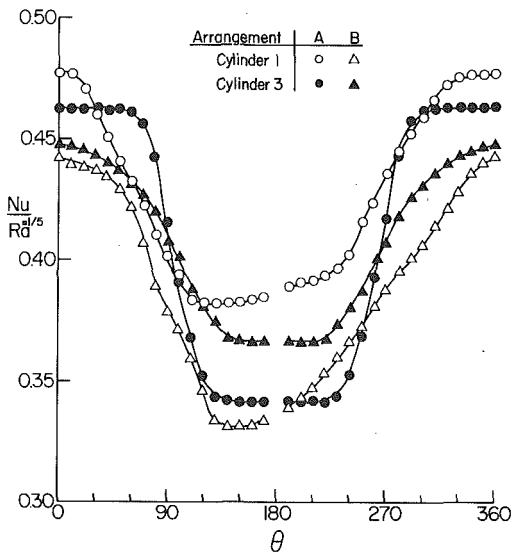

Fig. 7 Comparison of local Nusselt number variation around the cylinders 1 and 3 between arrangement A and B, Ste = 1.25

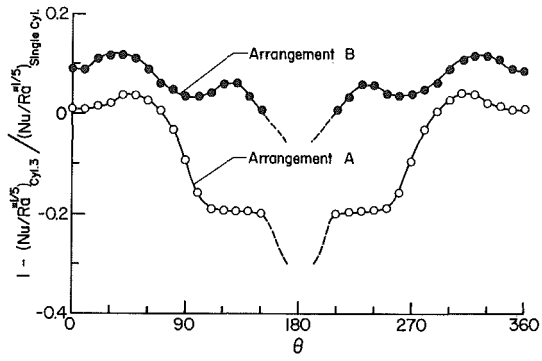

Fig. 8 Fractional departure of heat transfer results for cylinder 3 from those for a single cylinder: Ste = 1.0 and $\tau = 2.88$

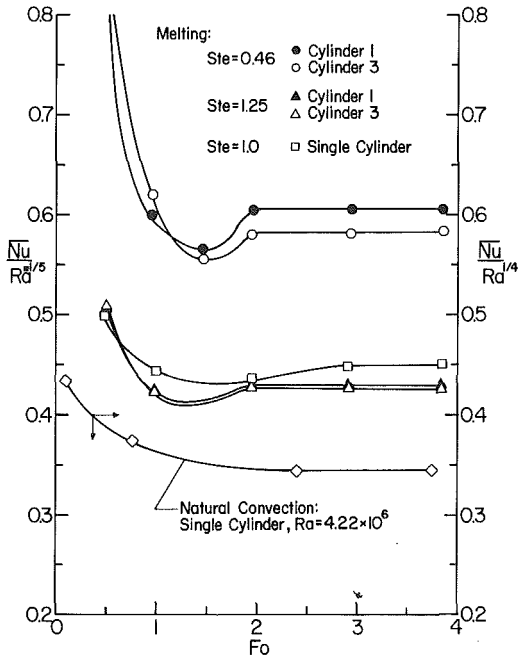

Fig. 9 Variation of instantaneous, circumferentially averaged heat transfer coefficients with Fourier number for arrangement A

condition are also included for the purpose of comparison. The results show that in a three cylinder arrangement the heat transfer coefficient during melting is only a little higher for cylinder 1 than for 3. Even plotting the results ($\overline{Nu}/Ra^{*1/5}$) versus τ (= Ste·Fo) did not collapse the data. This clearly indicates that the parameter τ is not unique for correlating heat transfer data during melting. The dimensionless time τ is appropriate only for correlating heat transfer results in conduction dominated processes [2].

The results of Fig. 9 show that the average Nusselt number reaches a constant quasi-steady-state value for Fo > 2 even though the solid-liquid interface continues to move as the melting progresses. This suggests that the processes which occur do not contribute significantly to the overall thermal resistance to heat transfer. This finding is in agreement with available results [7] and indicates that the presence of other cylinders does not prevent achieving a quasi-steady-state value for the average heat transfer coefficient. The minimum in $\overline{Nu}/Ra^{*1/5}$ corresponds to the overshoot in the cylinder surface temperature (see Fig. 5). The instantaneous spatially averaged heat transfer coefficients determined during melting of a salt eutectic also showed a minimum [7].

The effect of cylinder spacing on $\overline{Nu}$ is relatively small. As expected, when heat transfer by conduction (small τ) predominates $\overline{Nu}/Ra^{*1/5}$ is practically independent of the arrangement and the heating conditions. The results available [10] but not included in the figure show that for corresponding Ste and Fo the parameter $\overline{Nu}/Ra^{*1/5}$ is on the average less than 10 percent smaller for the tighter arrangement B than A.

Conclusions

The results obtained provide conclusive evidence of the role played by natural convection on the heat transfer during melting of a solid from multiple cylindrical heat sources. Not only the local but also the average heat transfer coefficients and their timewise variation are influenced by convection. After a common solid-liquid interface is formed around the cylinders, natural convection circulation around each cylinder interacts with the other cylinders to influence the melt shape.

In addition to natural convection, the heat source arrangement is an important factor in determining the melt shape. For the tighter spacing of the cylinders the overall melt zone is extended primarily in the horizontal direction, while for the wider spacing the melt shape extends primarily in the vertical direction. Unsteady and unpredictable thermal plume behavior above the heat sources influenced not only the melt shape locally but also the natural convection in the liquid between and above the heat sources.

The experimental investigation of heat transfer during melting of a solid from imbedded cylindrical heat sources provides quantitative description of the physical processes which occur during the transition from pure conduction heat transfer at the onset of melting to quasi-fully developed natural convection in the melt.

The findings of this study indicate that for an effective utilization of a PCM in a TES system the effects of natural convection and of tube arrangement are important and have to be accounted for in the design of such systems.

The theoretical prediction of the solid-liquid interface position is feasible during the early stages of melting when the melt zones are isolated but not after a common interface has been formed around the cylinders. The irregular shape of the melt region, the complexity of the natural circulation and mixing in the melt are some of the reasons for the difficulty in theoretical modeling. In practical systems, consisting of a large number of heat sources, the solid would lose support, descend onto a lower row of cylinders and create a totally different physical arrangement between the solid and the heat sources which would be extremely difficult to model analytically.

Acknowledgments

The work described in the paper was supported by the National Science Foundation under Grant No. ENG 75-15030.

References

1 Kovach, E. G., Editor, *Thermal Energy Storage,* Pergamon Press, Oxford, 1976.

2 Shamsundar, N., and Sparrow, E. M., "Storage of Thermal Energy by Solid-Liquid Phase Change—Temperature Drop and Heat Flux," ASME JOURNAL OF HEAT TRANSFER, Vol. 96, No. 4, Nov. 1974, pp. 541–544.

3 Horstemke, A., and Marschall, E., "Speicherung von Thermischer Energie in Salz-und Metallschmelzen," Bernnstoff-Wärme-Kraft, Band 28, Nr. 1, 1976, pp. 18–22.

4 Shamsundar, N., and Sparrow, E. M., "Effect of Density Change on Multidimensional Conduction Phase Change," ASME JOURNAL OF HEAT TRANSFER, Vol. 98, No. 4, Nov. 1976, pp. 550–557.

5 Sparrow, E. M., Patankar, S. V., and Ramdhyani, S., "Analysis of Melting in the Presence of Natural Convection in the Melt Region," ASME JOURNAL OF HEAT TRANSFER, Vol. 99, No. 4, Nov. 1978, pp. 520–526.

6 White, R. D., Bathelt, A. G., Leidenfrost, W., and Viskanta, R., "Study of Heat Transfer and Melting Front from a Cylinder Imbedded in a Phase Change Material," ASME Paper No. 77-HT-42, 1977.

7 Sparrow, E. M., Schmidt, R. R., and Ramsey, J. W., "Experiments on the Role of Natural Convection in the Melting of Solids," ASME JOURNAL OF HEAT TRANSFER, Vol. 100, No. 1, Feb. 1978, pp. 11–16.

8 Bathelt, A. G., Viskanta, R., and Leidenfrost, W., "An Experimental Investigation of Natural Convection in the Melted Region Around a Heated Horizontal Cylinder," *J. Fluid Mech.,* Vol. 90, Part 2, Jan. 1979, pp. 227–239.

9 Lorsch, H. G., Kauffman, K. W., and Denton, J. C., "Thermal Energy Storage for Heating and Off-Peak Air Conditioning," *Energy Conversion,* Vol. 15, Nos. 1/2, 1975, pp. 1–9.

10 Bathelt, A. G., Viskanta, R. and Leidenfrost, W., "Experiments on the Role of Natural Convection and Heat Source Arrangement in the Melting of a Solid", ASME Paper No. 78-HT-47.

11 Hauf, W., and Grigull, U., "Optical Methods in Heat Transfer," in *Advances in Heat Transfer,* Academic Press, New York, 1970, Vol. 6, pp. 133–366.

12 Goldstein, R. J., and Eckert, E. R. G., "The Steady and Transient Free Convection Boundary Layer on a Uniformly Heated Vertical Plate," *International Journal of Heat and Mass Transfer,* Vol. 1, Nos. 2/3, 1960, pp. 200–218.

13 Parsons, J. R., Jr. and Mulligan, J. C., "Transient Free Convection from a Suddenly Heated Horizontal Wire", ASME JOURNAL OF HEAT TRANSFER, Vol. 100, No. 3, Aug. 1978, pp. 423–428.

14 Grigull, U. and Hauf, W., "Natural Convection in Horizontal Annuli," *Proceedings of the Third International Heat Transfer Conference,* American Society of Chemical Engineers, New York, 1966, Volume 2, pp. 182–195.

15 Kim, C. B., Pontikes, T. J. and Wollersheim, D. E., "Free Convection from Horizontal Cylinders with Isothermal and Constant Heat Flux Surface Conditions," ASME, JOURNAL OF HEAT TRANSFER, Vol. 97, No. 1, Feb. 1975, pp. 129–130.

Y. Hayashi
Associate Professor.
Department of Mechanical Engineering

T. Komori
Professor.
Department of Construction and Environmental Engineering

Kanazawa University,
Kanazawa, Japan

Investigation of Freezing of Salt Solutions in Cells

Phenomena of salt rejection during freezing process of saline solutions included in cells were investigated analytically and experimentally as a problem of heat and mass transfer with phase change. By experiments of freezing of the aqueous solutions of 2.0–15.0 wt percent sodium chloride, three regions—a solid, a solid-liquid and a liquid—were recognized to coexist together in the freezing process. In the solid-liquid region, when freezing proceeds, freezing fronts were found to occur stepwise within several adjacent cells. This phenomenon was due to the depression of the freezing point which was caused by salt rejection in the cells. Furthermore, the mechanism of the freezing process was clarified in connection with the constitutional supercooling of the solution. The analytical solutions for the freezing problem of saline solutions were obtained by an approximation of using apparent heat capacity involving latent heat of fusion released in the solid-liquid region, and applying the procedure of Newmann's exact solutions for a semi-infinite body with phase change.

1 Introduction

Practical problems involving a phase change due to solidification are important in industrial processes such as casting of alloys, freezing of foodstuff, preservation of human blood, desalination of sea water, and many others.

Phenomena occurring during the freezing of aqueous solutions are quite similar to those found in the solidification of metal alloys. In the constitutional phase diagram, when the slope of the liquidus and solidus curves are negative, the equilibrium distribution coefficient takes a value in the region of zero to one. By solidification, therefore, solute is rejected at the solid-liquid interface and diffuses into the liquid region to form a solute-rich layer at the front of the interface. This phenomenon gives rise to depression of solidifying point, and sometimes it induces instabilities of the interface due to a constitutional supercooling. On freezing of aqueous solutions, solute is rejected almost completely, and the constitutional supercooling comes to appear more discernibly, compared with that in the case of solidification of alloys. This implies that the freezing front of an aqueous solution forms a rough surface by capturing the ice crystals at its surface and that there is the solid-liquid intermediate region, which contains the concentrated solutions in gaps among the ice crystals, between the solid and liquid regions. Therefore, freezing of aqueous solutions should be treated as a coupled heat and mass transfer problem with phase change.

Stephan, et al. [1] derived the numerical solution for the heat conduction problem in solidification coupled with the secondary transformation, supposing that the solidifying temperature at the solid-liquid interface was a function of the transformation speed, and illustrated the calculated results for the cases of solidification of a pure iron melt and freezing of an aqueous solution of sodium chloride. Comini, et al. [2] and Bonacina, et al. [3] presented a generally applicable numerical approach to transient heat conduction problems with non-linear physical properties and boundary conditions. For solidification of a binary eutectic semi-infinite body, Cho, et al. [4] and Tien, et al. [5] solved the conduction equations by treating latent heat of fusion liberated over a range of temperature as internal heat generation and proposed the exact solutions. Muehlbauer, et al. [6] used the heat-balance integral method to obtain approximate solutions to the solidification of binary eutectic. The energy liberated in the two phase region was treated as a pseudo specific heat. Terwilliger, et al. [7] and Grange, et al. [8] treated the salt rejection in the freezing of aqueous solutions of sodium chloride as a heat and mass transfer problem with phase change, assuming that there are the solid and liquid regions in the freezing process of the salt solution. They obtained the analytical solutions of the temperature and the solute concentration within the liquid region by solving the conduction and diffusion equations, introducing the apparent solute distribution coefficient.

The most troublesome points in this kind of problem with the solute rejection are in the complicated phenomena due to the constitutional supercooling. Instabilities at the interface caused by the constitutional supercooling lead to the formation of a rough surface and solute trapping, as already stated. Therefore, mass rejection at the freezing front which advances in the complicated state, is by no means determined solely by the equilibrium distribution coefficient, and is related with many factors. In the preceding papers [7, 8], these have been discussed, but reasonable conclusions have not been obtained.

This investigation uses cell walls which are impermeable. The two objectives of the study are as follows: First, we wish to clarify the mechanism of the freezing of aqueous solutions. By controlling the

Contributed by the Heat Transfer Division for publication in the JOURNAL OF HEAT TRANSFER. Manuscript received by the Heat Transfer Division December 31, 1978.

constitutional supercooling by the artificial means of using cell walls, the freezing process is simplified phenomenologically and is treated as a problem involved with secondary transformations within a certain temperature range. The second objective is to study, fundamentally, the freezing of foodstuff which consists of the cellular materials. Freezing problem of aqueous solutions is also important in foodstuff industry, in respect of the appearance of the freezing zone, destruction of cell membrane due to the expansion of volume, etc. These phenomena seem to be dominant features in freezing of intracellular solutions where the motion of solutions and of the rejected solute are interfered by membrane. Our investigation is performed at this standpoint, and the model presented here is not meant to simulate the living cell.

2 Theory

2.1 Freezing Process of Salt Solution in Cells. Fig. 1 shows the schematic representation of the freezing process of the salt solution included in cell groups. For simplicity, each cell is isolated by cell walls which are spaced equally perpendicular to the cooling surface.

When the temperature of the liquid at a cell wall descends to the equilibrium temperature T_i' corresponding to the initial solute concentration C_i by cooling, the freezing of the solution starts and the solidification front grows with time in the cell. Simultaneously, salt segregation occurs, and solute rejected at the solid-liquid interface diffuses into the liquid phase. Concentration gradient of solute is zero at the end of each cell, and the bulk concentration of solute in the liquid part of the cell increases with time by the diffused-in solute. On the other hand, there is the equilibrium correlation between the solute concentration and the temperature of the salt solution at the solid-liquid interface, as shown in Fig. 2. Then, the freezing of the salt solution in the cell is followed by depression of the freezing point until the temperature of solute-rich region reaches the eutectic point, as shown by the dotted line in Fig. 1.

These matters mentioned above suggest the following incidents: it seems probable that before freezing comes to an end in the foremost cell, freezing starts from next to next in the adjacent cells. Thus, the solid-liquid region, which is constituted by the partially frozen cells, appears between the solid or frozen region and the liquid region. This solid-liquid region, where freezing goes on, covers the temperature range extending from the equilibrium temperature corresponding to the initial solute concentration down to the eutectic point. In conclusion, the stepwise freezing is the most characteristic phenomenon for the freezing of the solution included in cells.

2.2 Distribution of Solid Fraction and Internal Heat Generation in Solid-Liquid Region. To facilitate the treatment of the complicated phenomena in the solid-liquid region, the following assumptions are made:

1 the gap of the cell is sufficiently small, and the distribution of the solid fraction within the solid-liquid region is considered to be continuous;

2 the equilibrium state is established locally between the solute concentration and the temperature in the solid-liquid region;

3 the equilibrium distribution coefficient is regarded as being approximately zero and the solute in the salt solution may be rejected completely by freezing.

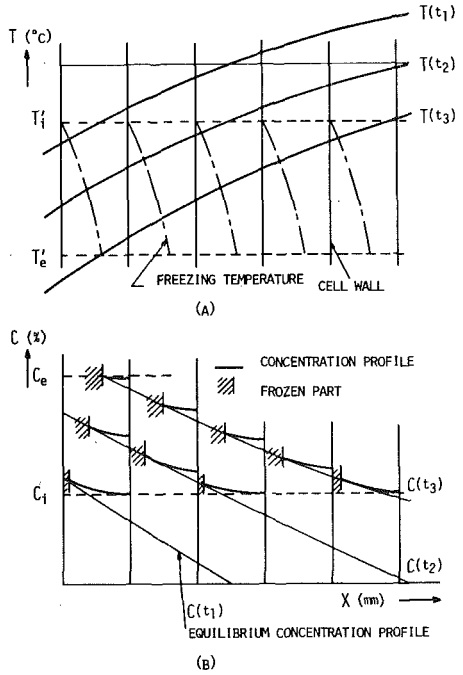

Fig. 1 Schematic representation of freezing process: (A) temperature profile (B) concentration profile

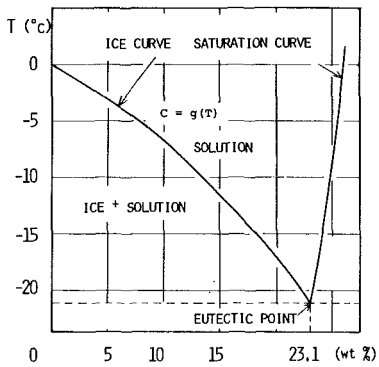

Fig. 2 Phase diagram of salt solution

Table 1 Properties of salt solution used for calculations

$f(T_e') = 1 - \frac{g(T_i')}{g(T_e')}$	$k = \frac{\partial}{\partial T}\left[\frac{g(T_i')}{g(T)}\right]$	λ_1	λ_2	λ_3 (w/mK)
		$c\rho_1$	$c\rho_2$	$c\rho_3$ (J/m^{3}K)
		κ_1	κ_2	κ_3 (m^2/s)
0.567	0.038	2.210	1.023	0.554
		$2.064 \cdot 10^6$	$3.872 \cdot 10^6$	$4.642 \cdot 10^6$
		$1.072 \cdot 10^{-6}$	$6.556 \cdot 10^{-8}$	$1.192 \cdot 10^{-7}$

Nomenclature

C = solute concentration
c = specific heat capacity
f = solid fraction
g = function defined by $C = g(T)$
$k = \frac{\partial}{\partial T}\left[\frac{g(T_i')}{g(T)}\right]$
L = latent heat of fusion
n_1 = constant defined by $\eta = n_1\sqrt{t}$
n_2 = constant defined by $\xi = n_2\sqrt{t}$
q = heat generation defined by equation (2)
T = temperature
T_i' = equilibrium temperature corresponding to the initial concentration of solute
T_e' = eutectic temperature
t = time
x = space co-ordinate
η = position of interface between the solid and the solid-liquid regions
κ = thermal diffusivity
λ = thermal conductivity
ρ = density
ξ = position of freezing front

Subscripts

1 = solid region
2 = solid-liquid region
3 = liquid region
0 = refers to $x = 0$
i = denotes the initial condition

According to the above assumptions, and paying attention to the equilibrium correlation, $C = g(T)$, between the solute concentration and temperature within the solid-liquid region, it may be reasoned that both the solid fraction, f, and the amount of internal heat generation, q, corresponding to the latent heat of fusion released in the freezing zone are functions of the temperature only.

Therefore, f and q are expressed as follows:

$$f(T) = 1 - \frac{C_i}{C} = 1 - \frac{g(T_i')}{g(T)} \tag{1}$$

$$q(T, t) = -\rho_3 L \frac{\partial}{\partial t}\{1 - f(T)\} = -\rho_3 L k \frac{\partial T}{\partial t} \tag{2}$$

where $k = \dfrac{\partial}{\partial T}\left\{\dfrac{g(T_i')}{g(T)}\right\}$

Fig. 3 shows the relations between $g(T_i')/g(T)$ and T for the various initial concentrations of the salt solutions. The values of k, which are obtained by the gradient of the solid line in this figure, change over a wide range. When the initial concentration of solute is comparatively high, it is assumed that k takes approximately a constant value, however here, the average values of k within a temperature range corresponding to the solid-liquid region are used for the calculations. Namely, internal heat generation in the freezing zone is a function of the cooling rate. This result has a significant meaning that the apparent heat capacity involving the term of internal heat generation may be substituted for the heat capacity in the conduction equation describing the energy balance of the solid-liquid region.

2.3 Analysis. An exact solution is presented in this section for a semi-infinite body which is divided into the three regions: the solid or frozen region, the solid-liquid region where freezing is taking place, and the liquid region. Fig. 4 shows the schematic physical system and coordinate.

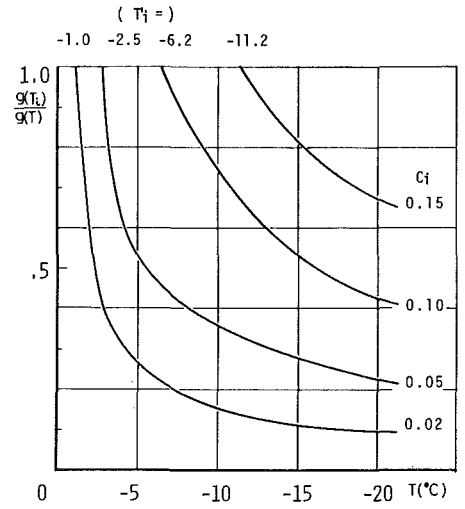

Fig. 3 Relations between $g(T_i')/g(T)$ and T for various initial concentrations

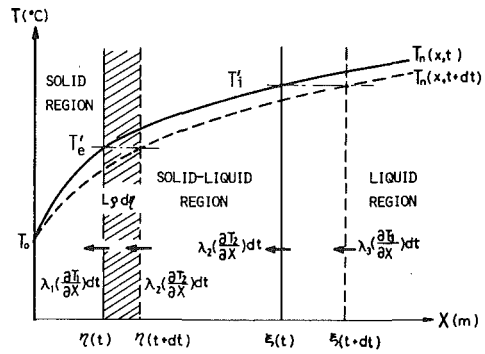

Fig. 4 Schematic physical system and coordinate

To simplify the mathematical manipulation for this problem, the following additional assumptions are made:

4 The temperature and the solute concentration of the salt solution are initially constant, moreover, the temperature of the cooling surface is fixed during the freezing process.

5 Heat flows along the x-direction only; i.e., a one-dimensional conduction problem is assumed.

6 Convection, which is due to the density difference or volume change by freezing, is not considered.

7 All physical properties of each region are assumed to remain constant, but may be different for different regions. For the solid-liquid region, the average values are available in taking account of the distribution of the solid fraction.

Upon these assumptions, the corresponding energy equations for the three regions are:

$$\frac{\partial T_n}{\partial t} = \kappa_n \frac{\partial^2 T_n}{\partial x^2} \quad (n = 1, 2, 3) \tag{3), (4), (5)}$$

where $\kappa_2 = \lambda_2/(C_2\rho_2 + k\rho_3 L)$

The initial and boundary conditions for this problem are

$$T_1(0, t) = T_0 \tag{6}$$

$$T_1(\eta, t) = T_2(\eta, t) = T_e' \tag{7}$$

$$T_2(\xi, t) = T_3(\xi, t) = T_i' \tag{8}$$

$$T_3(x, 0) = T_i \tag{9}$$

$$\lambda_1\left(\frac{\partial T_1}{\partial x}\right)_\eta - \lambda_2\left(\frac{\partial T_2}{\partial x}\right)_\eta = \rho_3 L\{1 - f(T_e')\} \tag{10}$$

$$\lambda_2\left(\frac{\partial T_2}{\partial x}\right)_\xi - \lambda_3\left(\frac{\partial T_3}{\partial X}\right)_\xi = \rho_3 L f(T_i') \tag{11}$$

To obtain the particular solutions for each region, the above conduction equations are solved on several proper conditions in addition to equations (6–9). Then, the general solutions for three regions may be obtained by applying to the boundary conditions at the interfaces.

Suppose that both η and ξ are proportional to the square root of time t, that is,

$$\eta = n_1\sqrt{t}\,, \quad \xi = n_2\sqrt{t} \tag{12), (13}$$

The solutions for this problem are

$$T_1 = \frac{(T_e' - T_0)\,erfc\dfrac{x}{2\sqrt{\kappa_1 t}} + T_0\,erfc\dfrac{n_1}{2\sqrt{\kappa_1}} - T_e'}{erfc\dfrac{n_1}{2\sqrt{\kappa_1}} - 1} \tag{14}$$

$$T2 = \frac{\left(T_i'\,erfc\dfrac{n_1}{2\sqrt{\kappa_2}} - T_e'\,erfc\dfrac{n_2}{2\sqrt{\kappa_2}}\right) - (T_i' - T_e')\,erfc\dfrac{x}{2\sqrt{\kappa_2 t}}}{erfc\dfrac{n_1}{2\sqrt{\kappa_2}} - erfc\dfrac{n_2}{2\sqrt{\kappa_2}}} \tag{15}$$

$$T_3 = T_i - (T_i - T_i')\frac{erfc\dfrac{x}{2\sqrt{\kappa_3 t}}}{erfc\dfrac{n_2}{2\sqrt{\kappa_3}}} \tag{16}$$

Furthermore, n_1 and n_2 are determined from the following simultaneous equations

$$\frac{\lambda_1(T_i' - T_0)e^{-(n_1/2\sqrt{\kappa_1})^2}}{\sqrt{\kappa_1}\,erf\dfrac{n_1}{2\sqrt{\kappa_1}}} + \frac{\lambda_2(T_e' - T_i)e^{-(n_2/2\sqrt{\kappa_2})^2}}{\left(erfc\dfrac{n_1}{2\sqrt{\kappa_2}} - erfc\dfrac{n_2}{2\sqrt{\kappa_2}}\right)\sqrt{\kappa_2}} = \frac{\sqrt{\pi}n_1\rho_3 L\{1 - f(T_e')\}}{2} \tag{17}$$

$$\frac{\lambda_2(T_i' - T_e')e^{-(n_2/2\sqrt{\kappa_2})^2}}{\left(erfc\frac{n_1}{2\sqrt{\kappa_2}} - erfc\frac{n_2}{2\sqrt{\kappa_2}}\right)\sqrt{\kappa_2}} + \frac{\lambda_3(T_i' - T_i)e^{-(n_2/2\sqrt{\kappa_3})^2}}{\sqrt{\kappa_3}\,erfc\frac{n_2}{2\sqrt{\kappa_3}}} = 0 \quad (18)$$

3 Experimental Apparatus and Experimental Method

A schematic diagram of the main part of the experimental installation is shown in Fig. 5. In the sample container, which was made from an acrylic resin hollow cylinder, 0.1 mm thick copper boards, serving as cell walls, were installed with an equal spacing between each other in the vertical direction. Between the wall of the container and the edges of the boards, small gaps were made in order to avoid the expansion of the sample due to freezing. A heat exchanger was mounted on a brass plate adjoining to the top of the sample container. The salt solution in the sample container was cooled downward by a coolant passing through the exchanger. By regulating the temperature of the coolant, the surface of the salt solution was instantaneously dropped and was maintained at constant temperature during a run. An air chamber was put in the bottom section of the sample container, so that the salt solution was ensured full contact with the heat exchanger. The outside of the sample container was insulated thermally by keeping at a vacuum of 2×10^{-3} mm Hg, using a vacuum pump.

The temperatures were measured at fixed positions along the height with copper-constantan thermocouples of 0.1 mm, which were inserted in contact with the cell walls. Furthermore, two thermocouples were located in the external coolant to regulate the temperature of the coolant.

The experiments were performed at the constant surface temperature which is lower than the eutectic temperature, for the aqueous solutions of the solute concentration of 2.0, 5.0, 10.0, and 15.0 wt percent, by using the cells with spacing 2.0, 4.0, 6.0, and 8.0 mm, respectively. In this experiment, the temperature profile and the growth of freezing front with time were measured, moreover, the progress of freezing of the salt solution was observed photographically. In addition, to investigate the effect of the cell wall on the freezing of the salt solution in the cells, the experiments on freezing of the salt solution were performed also with no cell wall inserted in the sample container.

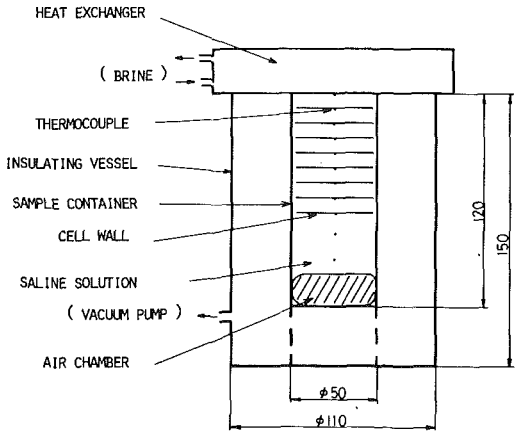

Fig. 5 Schematic diagram of main part of experimental installation

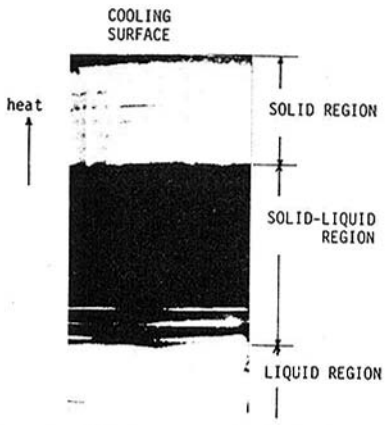

Fig. 6 Freezing state of 10 wt percent salt solution for length of cell gap, 2 mm

4 Experimental Results and Discussion

4.1 Observation of Freezing of Salt Solution. Fig. 6 shows a picture of the freezing process for the 10 wt percent salt solution as the typical result of the photographic observation. As is obvious from this photograph, it is found that there are three regions, the solid, the solid-liquid and the liquid regions in the freezing of the salt solution included in cells. The solid region, which is a complete segregation of ice and sodium, looks cloudy and can be easily distinguished from the solid-liquid region. On the other hand, the boundary between the solid-liquid region and the liquid region, is confirmed by the front of the freezing zone.

For the solid-liquid region, the stepwise freezing in each cell does not appear up to the expectation, but freezing fronts of the salt solution could be discerned only within several cells. However, other neighboring cells including no visible freezing front may be considered anyhow to be incompletely frozen, because if entirely frozen, they would turn to have a cloudy aspect. This suggests that the cell wall cannot suppress the diffusion of solute enough efficiently to prevent local constitutional supercooling of the salt solution, and it results in formation of a rough surface and captivation of solute on it on account of instabilities at the solid-liquid interface.

Fig. 7 shows a picture of the local discontinuous freezing of the salt solution in the cells within the solid-liquid region. By the photographic observations, the solid fraction in the cells declines in the opposite direction to heat flow and for the case of the cell gap of 2 mm, the formation of the solid-liquid interface is stable comparatively. However, when the gap of the cell is wide, the constitutional supercooling in the solid-liquid region has a tendency to lead to instabilities at the solid-liquid interface and the formation of a rough surface involving a lot of the needle-shaped crystals.

Fig. 8 shows a picture after the time elapse of 1.5 hr for the freezing of 10 wt percent NaCl solution in the sample container without the

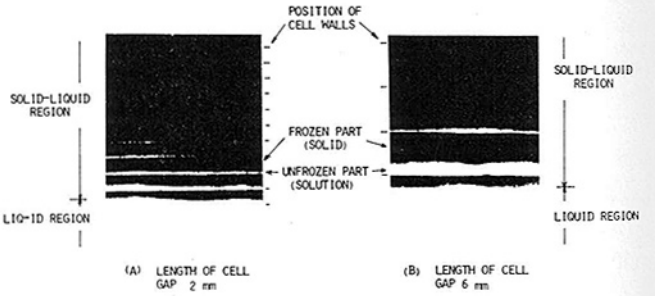

Fig. 7 State of local discontinuous freezing in solid-liquid region

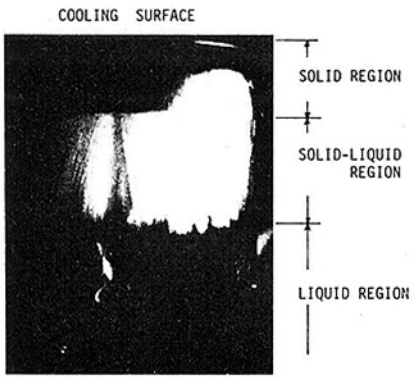

Fig. 8 Freezing state of 10 wt percent solution without cell walls

cells. In this case, at the very beginning of the freezing, a thin flat layer of ice was found at the surface of the cooling plate in the first period of few minutes. Then, small needle-shaped ice crystals generate at the interface, and grow gradually towards the liquid part to form the rough surface trapping the brine. As the time proceeds, the entrapped brine is further cooled and freezing continues until the brine temperature reaches the eutectic point. In this case also, the solid-liquid region appears between the solid and the liquid regions, but the mechanism of freezing is different from that in the presence of cells in the container. Furthermore, the front of the solid-liquid region does not advance with the constant equilibrium temperature corresponding to the initial solute concentration, but with the gradually depressing temperature due to appearance of a solute-rich boundary in the liquid region.

These results imply that when cell walls are absent, the freezing process of the solution cannot be treated as a heat conduction problem concerned with the temperature-dependent secondary transformations.

4.2 Analytical and Experimental Results. Comparisons of the experimentally measured and analytically predicted results for a typical run using the 10 wt percent NaCl solution are shown for the case of $T_s = -25.0°C$ and the length of cell gap, 2 mm.

Fig. 9 shows the experimental and analytical results of the growth of η and ξ with time. The temperature at the interface η is $-21.2°C$ and it is equivalent to the eutectic point of the salt solution. In this case, the experimental results for η were obtained by the visual observations, as was stated previously, assuming the cloudy portion of the sample to be the frozen region. On the other hand, the experimental results for the freezing front ξ were obtained by measuring the position of starting to freeze in the cell. Practically, ξ varies discontinuously with time, however, it is admissible that ξ in terms of cell gap changes continuously. According to the experimental results, both η and ξ were proportional to the square root of time. These experimental results agree approximately with the analytical results which are drawn with the solid lines in Fig. 9, except for the experimental results at the beginning of the freezing. These deviations are due to some difference in set-up of the constant surface temperature existing between the theory and the experiment.

In Fig. 10, the experimental results for the temperature profile of the salt solution are compared with the calculated results from the analytical solutions. Close agreement between the observed and calculated values was obtained except for the early stage of the freezing. The temperature at η is associated with the eutectic point T_e' and the temperature at ξ is equivalent to the equilibrium temperature T_i corresponding to the initial concentration of solute in the salt solution.

In this paper, the results are obtained for the case of $T_s = -25°C$ and $C_i = 0.1$. Generally, the experimental results obtained in the freezing under the other operating conditions also agree well with the calculated results from the analytical solutions. However, for the case of large cell spacing, the experimental results of both η and ξ become larger compared with the analytical values as shown in Fig. 9. It is considered that the discrepancy of the experimental results from the calculated results is due to dependency of the thermal conductivity on the structure of the composite solid-liquid phase in the freezing zone.

In practice, the freezing of the NaCl solution included in cells does not always appear stepwise, but takes place in formation of a layer consisting of pure ice and enclosures of the liquid brine. Moreover, the degree of the brine entrapment increases as the length of the cell gap increases, since the supercooling intensity is affected strongly by the length of cell gap. In spite of the difference of the freezing structure in the solid-liquid region, the values of the thermal conductivity used for calculation were estimated by assuming the solid-liquid parallel model with the stepwise freezing.

In conclusion, it is needed to adopt such thermal conductivities for calculation that the practical structure of the solid-liquid region is taken into accounts.

6 Conclusions

From the analytical and experimental investigations for the freezing

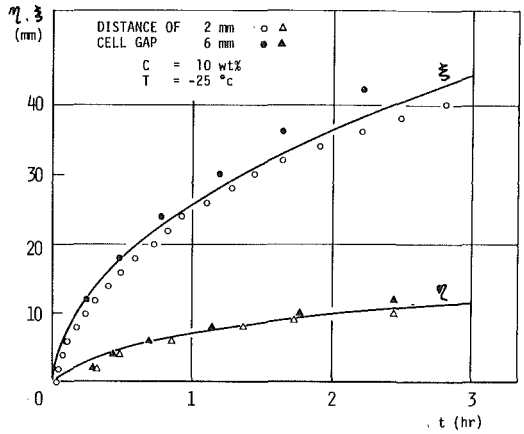

Fig. 9 Experimental and analytical results of η and ξ

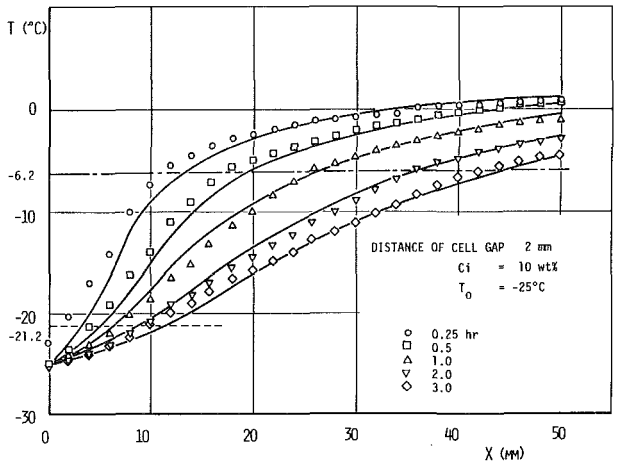

Fig. 10 Experimental and analytical temperature profiles

of the salt solutions included in cells, the following conclusions may be described.

1 Solute rejected by the frozen part leads to depression of the freezing point of the unfrozen part in the cell and instabilities at the solid-liquid interface due to the constitutional supercooling. Especially, instabilities at the interface give rise to the formation of a rough surface and occurrence of solute trapping on it.

2 The cell walls restrain or suppress the constitutional supercooling of the salt solution in freezing and promote the discontinuous freezing. In connection with this, the degree of suppression increases with decrease of the length of the cell gap.

3 It is found that there are three regions, the solid or frozen region, the solid-liquid region, and the liquid region. The two phases region, where freezing is taking place, extends over in the temperature range of the eutectic point to the equilibrium temperature corresponding to the initial solute concentration.

4 The analytical solutions for this problem may be obtained by an approximation of using apparent heat capacity involving latent heat of fusion released in the solid-liquid region, and applying the procedure of Neumann's exact solutions for a semi-infinite body with phase change.

References

1 Stephan, K., Genthner, K., and Holzknecht, B., "Heat Conduction in Solidification Coupled with Phase Transformations in the Solid," *Proceedings of the Fifth International Heat Transfer Conference*, Vol 1, 1974, p. 235.

2 Comini, G. and Guidice, S. D., "Finite Element Solution of Non-Linear Heat Conduction Problems with Special Reference to Phase Change," *International Journal for Numerical Methods in Engineering*, Vol. 8, 1974, pp. 613–624.

3 Bonacina, C., et al., "Numerical Solution of Phase-Change Problems," *Journal of Mechanical Engineering Science*, Vol. 14, 1972, pp. 19–24.

4 Cho, S. H. and Sunderland, J. E., "Heat-Conduction Problems with Melting or Freezing," ASME JOURNAL OF HEAT TRANSFER, Vol. 91, Aug.

1969, p. 421.
5 Tien, R. H. and Geiger, G. E., "The Unidimensional Solidification of a Binary Eutectic System," ASME JOURNAL OF HEAT TRANSFER, Vol. 89, 1967, p. 230.
6 Muehlbauer, J. C., et al., "Transient Heat Transfer Analysis of Alloy Solidification," ASME JOURNAL OF HEAT TRANSFER, Vol. 95, 1973, p. 324.
7 Terwilliger, J. P., et al., "Salt Rejection Phenomena in the Freezing of Saline Solutions," *Chemical Engineering Science,* Vol. 25, 1970, p. 1331.
8 Grange, B. W., et al., "Diffusion of Heat and Solute During Freezing of Salt Solutions," *Int. J. Heat and Mass Transfer,* Vol. 19, 1976, p. 373.

Chul Cho
M. N. Özişik

Department of Mechanical and Aerospace Engineering,
North Carolina State University,
Raleigh, N.C. 27650

Transient Freezing of Liquids in Turbulent Flow inside Tubes

The problem of freezing of a liquid in turbulent flow inside a circular tube whose wall is kept at a uniform temperature lower than the freezing temperature of the liquid is solved. The radius of the solid-liquid interface and the local wall heat flux are determined as a function of time and position along the tube for several different values of the Prandtl number and the freezing parameter.

Introduction

The problems of phase change involving melting and solidification have been of interest in numerous engineering applications. The exact solutions are available for only a few idealized situations. Purely numerical, electrical network analog, variational, perturbation and integral methods of solutions have all been applied to solve such problems. The analysis of phase change problems becomes more complicated when it involves freezing in internal flow; only a limited number investigation exists in this area. They include the works of Zerkle and Sunderland [1], Özişik and Mulligan [2], Bilenas and Jiji [3], Hwang and Sheu [4], which are for laminar or slug flow. The internal freezing for turbulent flow was studied only recently by Shibani and Özişik [5, 6] for the steady-state conditions. The transient freezing of liquids in internal turbulent flow is important in applications such as refrigeration system design, hydraulics, cryogenics, liquid metal technology, nuclear, mechanical and chemical engineering. Therefore, the purpose of this work is to investigate the freezing of liquids flowing in turbulent flow inside circular tubes under transient conditions.

Analysis

Consider a liquid flowing in turbulent flow inside a circular tube. Initially the liquid and the walls are at a uniform temperature T_0. At the time $t = 0$ the tube wall in the region $x \geq 0$ is suddenly lowered to a constant temperature T_w which is less than the freezing temperature, T_f, of the liquid, and maintained at that temperature for times $t > 0$. The tube wall in the region $x \leq 0$ is kept at the initial temperature T_0. As a result of this temperature change the liquid begins to freeze in the region $x \geq 0$ at the inside surface of the tube and forms a solid layer whose thickness increases with both time and position along the tube. The solid-liquid interface always remains at the freezing temperature, T_f, (i.e., $T_0 > T_f > T_w$).

Fig. 1 illustrates the problem under consideration. The following basic assumptions are employed in developing the formulation of the problem: (1) The flow is turbulent and fully developed. (2) The physical properties of liquid and solid phases phases are constant. (3) The thermal resistance of the tube wall is negligible. (4) The axial conduction, viscous dissipation and free convection are negligible (i.e., the axial conduction in the liquid phase is negligible for about Pe > 100). (5) The variation of the liquid-solid interface, $\delta(x,t)$, is a weak function of x and t.

The energy equation for the liquid phase is given in the dimensionless form as

$$\Delta^2 \frac{\partial \theta_\ell}{\partial \tau} + u^* \frac{\partial \theta_\ell}{\partial \xi} = \frac{1}{\eta} \frac{\partial}{\partial \eta} \left[\eta \epsilon(\eta) \frac{\partial \theta_\ell}{\partial \eta} \right] \text{ for } 0 \leq \eta \leq 1, \quad \xi \geq 0 \text{ and } \tau > 0. \quad (1)$$

The boundary and initial conditions are taken as

$$\theta_\ell = 0 \qquad \text{at } \eta = 1, \xi > 0, \tau > 0 \qquad (2a)$$

$$\frac{\partial \theta_\ell}{\partial \eta} = 0 \qquad \text{at } \eta = 0, \xi > 0, \tau > 0 \qquad (2b)$$

$$\theta_\ell = 1 \qquad \text{at } \xi = 0, 0 \leq \eta \leq 1, \tau > 0 \qquad (2c)$$

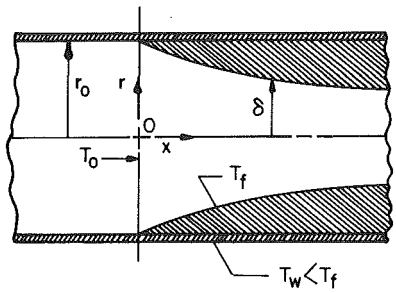

Fig. 1 The coordinate system for freezing of liquid inside tube

$$\theta_\ell = 1 \qquad \text{for } \tau = 0, \text{ in the region} \qquad (2d)$$

In equation (1) the term $v^* \partial\theta_\ell/\partial\eta$ is neglected because of the assumption (5). The eddy diffusivity model for the variation of $\epsilon(\eta)$ with the distance from the wall and the power law velocity profile u^* are the same as those described in [6].

The heat conduction equation for the solid phase is taken as

$$\Delta^2 \frac{\partial \theta_s}{\partial \tau} = \alpha^* \frac{1}{\eta} \frac{\partial}{\partial \eta} \left(\eta \frac{\partial \theta_s}{\partial \eta} \right) \quad \text{for } 1 \leq \eta \leq 1/\Delta, \quad \xi > 0 \text{ and } \tau > 0 \quad (3)$$

with boundary conditions,

$$\theta_s(1/\Delta, \xi, \tau) = \theta_w \quad \tau > 0 \qquad (4a)$$

$$\theta_s(1, \xi, \tau) = 0 \quad \tau > 0. \qquad (4b)$$

In equation (3) the axial conduction is neglected because both surfaces of the freeze layer are at uniform temperature and the solid-liquid interface varies slowly with x according to assumption (5).

Finally, the coupling condition at the solid-liquid interface is

$$\Delta \frac{d\Delta}{d\tau} = \text{Ste} \left[k^* \frac{\partial \theta_s}{\partial \eta} - \frac{\partial \theta_\ell}{\partial \eta} \right] \quad \text{at } \eta = \Delta, \tau > 0 \qquad (5a)$$

subject to the condition

$$\Delta = 1 \quad \text{for } \tau = 0. \qquad (5b)$$

The phase change problem described above by the system of equations (1–5) can be solved analytically as now described.

The temperatures of the liquid and solid phase, θ_ℓ and θ_s, are formally solved in terms of Δ from equations (1) and (3), respectively, by assuming Δ is a weak function of time and axial position. The expressions for θ_ℓ and θ_s obtained in this manner are introduced into the interface equation (5) to obtain an ordinary differential equation for Δ. When this ordinary differential equation is solved subject to the condition $\Delta(\tau = 0) = 1$ for each axial position, the location of the solid-liquid interface is determined as a function of time and position. The details of this procedure are as follows.

Analysis for Liquid Phase. The Laplace transform of equations (1) and (2), when the dependence of Δ on time is neglected under the assumption (5), gives

$$\frac{1}{\eta} \frac{\partial}{\partial \eta} \left[\eta \epsilon(\eta) \frac{\partial \bar{\theta}_\ell}{\partial \eta} \right] - \Delta^2 (p \bar{\theta}_\ell - 1) = u^* \frac{\partial \bar{\theta}_\ell}{\partial \xi} \qquad (6)$$

and

$$\bar{\theta}_\ell(1, \xi, p) = 0 \qquad (7a)$$

Contributed by The Heat Transfer Division for publication in THE JOURNAL OF HEAT TRANSFER. Manuscript received by the Heat Transfer Division October 3, 1979.

$$\frac{\partial \bar{\theta}_\ell}{\partial \eta}(0, \xi, p) = 0 \tag{7b}$$

$$\bar{\theta}_\ell(\eta, 0, p) = \frac{1}{p} \tag{7c}$$

where $\bar{\theta}_\ell \equiv \bar{\theta}_\ell(\eta,\xi,p)$ and p is the Laplace transform variable.

To remove the partial derivative with respect to the space variable, η, the finite integral transform pair is defined as

$$\text{Transform: } \tilde{F}(\lambda_m,\xi,p) = \int_0^1 \eta' u^* K_m(\lambda_m,\eta') F(\eta',\xi) d\eta' \tag{8a}$$

$$\text{Inversion: } F(\eta,\xi,p) = \sum_{\lambda_m} K_m(\lambda_m,\eta)\tilde{F}(\lambda_m,\xi) \tag{8b}$$

where the kernel $K_m(\lambda_m,\eta)$ is defined as

$$K_m(\lambda_m,\eta) \equiv \frac{\psi(\lambda_m,\eta)}{\sqrt{N}} \tag{9a}$$

$$N = \int_0^1 \eta'[\psi(\lambda_n,\eta')]^2 \, d\eta' \tag{9b}$$

and $\psi(\lambda_m,\eta)$ and λ_m are the eigenfunctions and eigenvalues of the following eigenvalue problem.

$$\frac{\partial}{\partial \eta}\left[\eta\epsilon(\eta)\frac{\partial \psi}{\partial \eta}\right] + \frac{\lambda_m^2}{2} u^* \eta \psi = 0 \quad \text{for } 0 \le \eta \le 1 \tag{10}$$

subject to

$$\psi(1,\xi) = 0 \tag{11a}$$

$$\frac{\partial \psi}{\partial \eta}(0,\xi) = 0. \tag{11b}$$

The eigenfunctions and eigenvalues of this eigenvalue problem are available in [6]; therefore, they are not reported here.

The integral transform of the system defined by equations (6) and (7), by the application of the transform (8a) gives

$$\frac{\partial \tilde{\bar{\theta}}_\ell}{\partial \xi} + \left(\frac{\lambda_m^2}{2} + \Delta^2 p\right)\tilde{\bar{\theta}}_\ell = \Delta^2 \tilde{1} \tag{12}$$

and

$$\tilde{\bar{\theta}}_\ell(\lambda_m,0,p) = \frac{1}{p}\tilde{1}. \tag{13}$$

To obtain this result the weight function u^* is approximated by $u^* \cong u^*_{\max} = 1$. The solution of equation (12) subject to the condition (13), when the dependence of Δ on ξ is neglected under the assumption (5), gives

$$\tilde{\bar{\theta}}_\ell = \tilde{1}\left\{\frac{1}{p} e^{-\left(\frac{\lambda_m^2}{2}+\Delta^2 p\right)\xi} + \frac{1}{\left(\frac{\lambda_m^2}{2\Delta^2} + p\right)}\left[1 - e^{-\left(\frac{\lambda_m^2}{2}+\lambda^2 p\right)\xi}\right]\right\} \tag{14}$$

where

$$\tilde{1} = \int_0^1 \eta u^* K_m(\lambda_m,\eta) d\eta = \frac{-2}{\lambda_m^2}\left.\frac{\partial K_m}{\partial \eta}^{(\lambda_m,\eta)}\right|_{\eta=1} \tag{15}$$

The double transform of temperature $\tilde{\bar{\theta}}_\ell$ given by equation (14) is inverted by the successive application of the integral transform and Laplace transform inversions to obtain the solution for the liquid-phase temperature $\theta_\ell(\eta,\xi,\tau)$ as

$$\theta_\ell = -2\sum_{\lambda_m}\frac{K_m}{\lambda_m^2}\left[\left.\frac{\partial K_m}{\partial \eta}\right|_{\eta=1}\right] \times \times \left[e^{-\lambda_m^2 \xi/2} h(\tau - \Delta^2\xi) + e^{-\lambda_m^2 \tau/2\Delta^2}\{1 - h(\tau - \Delta^2\xi)\}\right] \tag{16}$$

where h represents the unit step function, i.e.,

$$h(\tau - \Delta^2\xi) = \begin{cases} 1 \text{ for } \tau \ge \Delta^2\xi \\ 0 \text{ for } \tau \le \Delta^2\xi. \end{cases} \tag{17}$$

Analysis for Solid Phase. Assuming that $1/\Delta$ is a weak function of time, equation (3) subject to the boundary conditions (4) is solved by the application of the integral transform technique [7] to obtain the temperature $\theta_s(\eta\,\xi,\tau)$ for the solid phase as

$$\theta_s(\eta,\xi,\tau) = \frac{2\theta_w}{\pi}\sum_{\lambda_m}\frac{K_0(\beta_m,\eta)\,(1 - e^{-\alpha^*\beta_m^2\tau/\Delta^2})}{\beta_m^3\sqrt{N}\,J_0(\beta_m/\Delta)Y_0(\beta_m/\Delta)} \tag{18}$$

where

$$K_0(\beta_m,\eta) = \frac{\pi}{\sqrt{2}}\frac{\beta_m J_0(\beta_m/\Delta)Y_0(\beta_m/\Delta)}{\left[1 - \frac{J_0^2(\beta_m/\Delta)}{J_0^2(\beta_m)}\right]^{1/2}}\left[\frac{J_0(\beta_m\eta)}{J_0(\beta_m/\Delta)} - \frac{Y_0(\beta_m\eta)}{Y_0(\beta_m/\Delta)}\right]. \tag{19a}$$

$$N = \frac{(1/\Delta)^2}{2}R_0'^2(\beta_m,1/\Delta) - \frac{1}{2}R_0'(\beta_m,1) \tag{19b}$$

$$R(\beta_m,\eta) = \frac{J_0(\beta_m\eta)}{J_0(\beta_m/\Delta)} - \frac{Y_0(\beta_m\eta)}{Y_0(\beta_m/\Delta)}, \tag{19c}$$

β_m's are the positive roots of the transcendental equation

$$\frac{J_0(\beta)}{J_0(\beta/\Delta)} - \frac{Y_0(\beta)}{Y_0(\beta/\Delta)} = 0. \tag{19d}$$

Nomenclature

B = dimensionless freezing parameter defined by equation (21)
C_p = specific heat of liquid
$H(\tau,z)$ = dimensionless local heat flux as defined by equation (22)
k = thermal conductivity
k^* = dimensionless thermal conductivity, k_s/k_ℓ
L = latent heat of melting
Pr = Prandtl number
r = dimensional radial coordinate
r_0 = pipe radius
Re = Reynolds number, $\frac{Du_{o,m}}{\nu}$
Ste = Stefan number, $C_p(T_0 - T_f)/L$
T = temperature
T_0 = temperature at $x = 0$
u^* = dimensionless local velocity (local velocity/bulk mean velocity)
$u_{0,m}$ = mean velocity at $x = 0$
x = dimensional axial variable
α = thermal diffusivity
α^* = dimensionless thermal diffusivity, α_s/α
β_m = eigenvalues of solid phase
δ = radius of the liquid-solid interface
Δ = dimensionless radius of the liquid-solid interface, $\frac{\delta}{r_0}$
$\epsilon(\eta)$ = dimensionless total diffusivity, $1 + \frac{\epsilon_H}{\nu}\text{Pr} = \frac{\alpha+\epsilon_H}{\alpha}$
ϵ_H = eddy diffusivity of heat
η = dimensionless radial coordinate, $\frac{r}{\delta}$
τ = normalized time variable, $\alpha_\ell t/r_0^2$
θ = dimensionless temperature, $\frac{T-T_f}{T_0-T_f}$
λ_m = eigenvalues of liquid phase
ν = kinematic viscosity
ξ = dimensionless axial variable, $\frac{2x}{r_0\text{PrRe}}$

Subscripts

ℓ = liquid phase
s = solid phase
w = wall

and the prime denotes derivative with respect to η.

Liquid-Solid Coupling Condition. The partial derivatives $\partial\theta_\ell/\partial\eta$ and $\partial\theta_s/\partial\eta$ appearing in the coupling condition (5*a*) are determined from equations (16) and (18), respectively, by differentiation with respect to η and introduced into equation (5*a*) to obtain the following differential equation for the determination of $\Delta(\tau,\xi)$

$$\frac{d\Delta}{d\tau} = \frac{\text{Ste}}{\Delta}\left\{\frac{B}{\ell n\Delta} - 2B\sum_{\beta_m}\frac{J_0(\beta_m)J_0(\beta_m/\Delta)e^{-\alpha^*\beta_m^2\tau/\Delta^2}}{\beta^2[J_0^2(\beta_m) - J_0^2(\beta_m/\Delta)]} + 2\sum_{\lambda_m}\frac{1}{\lambda_m^2}\left(\left.\frac{\partial K_m}{\partial\eta}\right|_{\eta=1}\right)^2\left[e^{-\lambda_m^2\xi/2}h(\tau-z) + e^{-\lambda_m\tau/2\Delta^2}\{(1-h(\tau-z)\}\right]\right\} \quad (20)$$

where

$$B = -\frac{k_s}{k_\ell}\theta_w = \frac{k_s}{k_\ell}\frac{(T_0 - T_w)}{(T_0 - T_f)} \quad (21)$$

and λ_m's and β_m's are the eigenvalues for the liquid phase and solid phase, respectively.

The solution of equation (20), subject to the condition (5*b*), gives the dimensionless radius of the solid-liquid interface for each axial position ξ.

The dimensionless local transient heat flux, $H(\tau,\xi)$, at the wall is then related to $\Delta(\tau,\xi)$ by

$$H(\tau,\xi) = \frac{-B}{\ell n\Delta} + 2B\sum_{\beta_m}\frac{J_0^2(\beta_m)e^{-\alpha^*\beta_m^2\tau/\Delta^2}}{\beta_m^2\{J_0^2(\beta_m) - J_0^2(\beta_m/\Delta)\}} \quad (22)$$

where

$$H(\tau,\xi) = \frac{q(\tau,\xi)}{k_\ell(T_0 - T_f)/r_0} \quad (23a)$$

and

$$q(\tau,\xi) = -k_s\left.\frac{\partial T_s}{\partial r}\right|_{r=r_0} = -\frac{k_s(T_0 - T_f)}{r_0\Delta}\left.\frac{\partial\theta_s}{\partial\eta}\right|_{\eta=1/\Delta} \quad (23b)$$

Results

The location of the solid-liquid interface $\Delta(\tau,\xi)$ was determined from the Gaussian rules integration of equation (20) subject to the initial condition (5*b*) for each different value of ξ. The first few eigenvalues λ_m and the normalized eigenfunctions $K(\lambda_m,\eta)$ are determined numerically and the rest are calculated according to the asymptotic formula given in [6]. Once $\Delta(\tau,\xi)$ was known, the dimensionless local heat flux could be calculated from equation (22). Computations were performed for a fixed value of Reynolds Re = 10^4 since the variation of Reynolds number from 10^4 to 10^6 had negligible effect on the steady-state freezing problem studied in [6]. The effects of the Prandtl number on freezing was investigated over a wide range of the Prandtl number.

Fig. 2 shows the solid-liquid interface, $\Delta(\tau,\xi)$, as a function of the time variable, $(\tau - \xi)$ Ste, at the location, ξ = 0.001, near the inlet of the tube for several different values of the Prandtl numbers and the parameter B. The increase of the value of the Prandtl number moves the curves upward and the increase of the parameter B shifts the curves to the left. This implies that the solid-liquid interface attains a given thickness at a slower rate for large value of Prandtl numbers and at a much faster rate for large value of B. The steady state or asymptotic values of the solid-liquid interface profile are indicated by dotted lines. The dimensionless parameter B, defined by equation (21), is a measure of the ratio of the wall-to-freezing temperature difference for a given type of liquid. A large value of B corresponds either to a low wall temperature or a low inlet liquid temperature. The greater the value of B, the greater is the rate of freezing and the thicker is the freeze layer at any given position, ξ.

Fig. 3 shows the solid-liquid interface profile for the Prandtl number, $0 \le \text{Pr} \le 1000$, at the location, ξ = 0.001, near the inlet of the tube for the fixed value of the parameter, B = 10. As the Prandtl number increases, the thickness of the freeze layer becomes thinner. The reason for this is that the rate of heat removal from the liquid region is larger with higher Prandtl number than for lower Prandtl number at the given axial location.

Fig. 4 shows the profile of solid-liquid interface, $\Delta(\tau,\xi)$, as a function of the time variable at the various axial locations for the fixed value of low Prandtl number, Pr = 0.01, and the parameter B's. The increasing value of B shifts the curves to the left, which implies that at any position, ξ, the solid-liquid interface attains a given thickness at a much faster rate for large values of B.

Figs. 5 and 6 show a plot of the dimensionless local heat flux, $H(\tau,\xi)$, as a function of the time variable at different axial locations and for several different values of Prandtl number for the fixed value of the parameter B = 5. The steady-state values of the dimensionless local heat flux are also shown by dotted lines in these figures.

Because of the simplifying assumptions introduced in the analysis regarding Δ being a weak function of ξ, the solution may not be accurate for extremely fast rate of freezing, characterized with very large values of the parameter B (i.e., if the blockage is expected to occur, say within few diameters from the inlet). Therefore, results for very large values of B are not included in Figs. 2 to 4. The solution is also not applicable beyond a time when the flow passage opening at any position, ξ, reaches near closure.

References

1 Zerkle, R. D., and Sunderland, J. E., "The Effect of Liquid Solidification in a Tube upon the Laminar Flow Heat Transfer and Pressure Drop," ASME JOURNAL OF HEAT TRANSFER, 1968, pp. 183–190.

2 Özişik, M. N., and Mulligan, J. C., "Transient Freezing of Liquids in

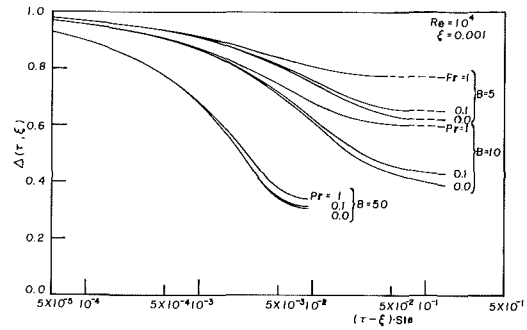

Fig. 2 Effects of Prandtl number and the parameter B on $\Delta(\tau,\xi)$ for ξ = 0.001, Re = 10^4

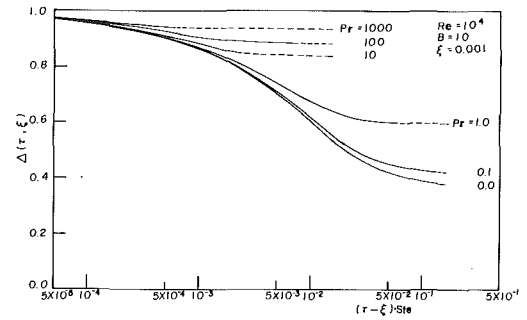

Fig. 3 Effects of Prandtl number on $\Delta(\tau,\xi)$ for B = 10, ξ = 0.001, Re = 10^4

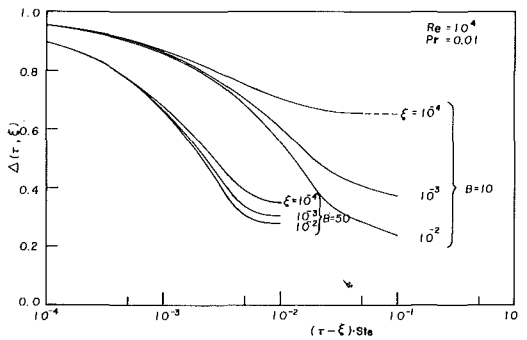

Fig. 4 Effects of the axial location and the parameter B on $\Delta(\tau,\xi)$ for Pr = 0.01, Re = 10^4

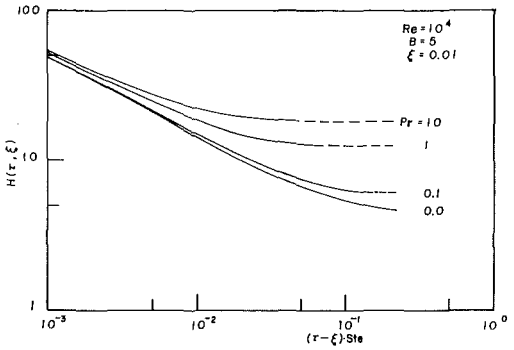

Fig. 5 Effects of Prandtl number on local heat flux $H(\tau,\xi)$ for $B = 5$, $\xi = 0.01$, $Re = 10^4$

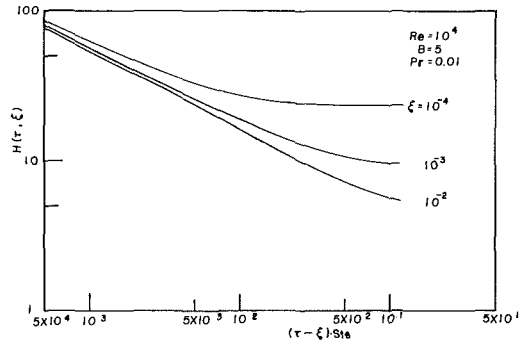

Fig. 6 Effects of the axial location ξ on local heat flux $H(\tau,\xi)$ for $B = 5$, $Pr = 0.01$, $Re = 10^4$

Forced Flow Inside Circular Tubes," ASME JOURNAL OF HEAT TRANSFER, 1969, pp. 385–390.

3. Bilenas, J. A., and Jiji, L. M., "Variational Solution of Axisymmetric Fluid Flow in Tubes with Surface Solidification," *Journal Franklin Inst.*, Vol. 289, 1970, pp. 265–275.

4. Hwang, G. J., and Sheu, J. P., "Liquid Solidification in Combined Hydrodynamic and Thermal Entrance Region of a Circular Tube," *Ca. J. Chem. Engr.*, Vol. 54, 1976, pp. 66–71.

5. Shibani, A. A., and Özişik, M. N., "A Solution of Freezing of Liquids of Low Prandtl Number in Turbulent Flow Between Parallel Plates," ASME JOURNAL OF HEAT TRANSFER, 1977, pp. 20–24.

6 Shibani, A. A., and Özişik, M. N., "Freezing of Liquids in Turbulent Flow inside Tubes," *Ca. J. Chem. Eng.*, Vol. 55, 1977, pp. 672–677.

7. Özişik, M. N., *Boundary Value Problems of Heat Conduction*, Int. Textbook, Scranton, PA, 1968.

Acknowledgment

This work was supported in part through the National Science Foundation Grant No. ENG. 77-12949.

A. T. Wassel
Science Applications, Inc.,
El Segundo, CA

A. F. Mills
Department of Chemical,
Nuclear and Thermal Engineering
University of California,
Los Angeles, CA 90024

Calculation of Variable Property Turbulent Friction and Heat Transfer in Rough Pipes

A numerical calculation method for turbulent flow in rough pipes is developed. A mixing length model is used in the turbulent core while a roughness element drag coefficient and a sub-layer Stanton number are used to characterize transport to the wall. Sample wall relations are developed for sandgrain roughness and transverse repeated rib roughness, and it is shown that large roughness heights require accounting for terms of order of roughness height divided by pipe radius. For gas flows with cooling, the effects of variable properties are investigated for smooth walls and both roughness patterns. For smooth walls, comparison with experiment is satisfactory; for rough walls experimental data is not available. Simple power law formulae representing variable property effects for fully rough flows are presented.

1 Introduction

Numerical calculation methods, primarily of the finite difference type, are nowadays widely used for the engineering prediction of turbulent flows over smooth walls. However, relatively little attention has been directed to extending such methods to rough walls and, as a result, many practically important rough wall turbulent flows cannot be adequately calculated at the present time. One example is prediction of the attenuation of an air blast wave in a duct reinforced with transverse ribs. Experiment [1] shows that the wall shear and heat transfer plays an important role, but skin friction and Stanton number correlations are unavailable for these flows which are characterized by large Reynolds numbers and highly cooled walls. Another example is found in gas cooled nuclear reactors, where artificial roughness is used to enhance heat transfer and an appropriate merit indicator (usually St^3/f) must be optimized. Such flows are characterized by complex geometries, e.g., annulus, shrouded rod bundle; also variable property effects are again important. A final example is the nose tip of a re-entry vehicle for which during peak heating on re-entry, the stagnation pressure is of the order of 100 atm and the boundary layer is, as a result, very thin. The roughness could be due to the carbon weave or erosion by dust and ice particle impact. Such boundary layers are characterized by large property variations (due to temperature and composition), pressure gradients, viscous dissipation, and blowing (due to carbon oxidation and sublimation). Finite difference methods have been developed to calculate such flows on smooth walls, e.g., the BLIMP code [2], but have not been extended to account for wall roughness.

In all the aforementioned examples the complexity of the problem suggests the use of finite difference methods to calculate the turbulent flow. Except in the region very close to the roughness elements, conventional modeling of turbulent transport, e.g., a mixing length model, leads to ordinary or parabolic partial governing differential equations which can be solved by standard methods. The remaining task is then to characterize the turbulent transport in the vicinity of the roughness elements. Recent practice, e.g., Heazler, et al. [3], Hatton and Walklate [4], has been to adapt smooth wall calculation methods by simply postulating a non-zero value of mixing length ℓ_0 at $y = 0$. However, such an approach is a poor representation of the physics since the drag on a fully rough wall is a form drag, not an eddy transport phenomenon. Also extension to include effects of variable properties, blowing, etc., must be highly empirical; in particular the turbulent Prandtl number required to match heat transfer data is not of order unity, and is physically meaningless.

Here we will follow an alternative approach in which the flow region is divided at $\bar{y} = h$, where h is of the order of the roughness elements height. Then for $\bar{y} \geq h$ smooth wall mixing length relations are used in the solution of the momentum equation. For $\bar{y} < h$ no attempt is made to solve the momentum equation; instead a drag coefficient is defined for the roughness elements via $\tau_w = C_d(\frac{1}{2}\rho u_h{}^2)$, and specification of C_d gives a third kind of boundary condition for the momentum equation in the domain $\bar{y} \geq h$. There is no analogy to form drag for heat transfer; some laminar sub-layer exists and constitutes a significant thermal resistance. Again, for the region $\bar{y} \geq h$ experiment shows that the smooth wall specification of Pr_t applies, and a "sub-layer Stanton number" is defined, $St_h = \dot{q}_w''/\rho v^*(h_w - h_h)$. A definition of St_h corresponding to that for C_d would be in terms of u_h instead of v^*; however v^* has been more widely used, and its continued use will avoid confusion. Specification of St_h provides a third kind boundary condition for the energy conservation equation in the domain $\bar{y} \geq h$. The concept of representing the near wall region by auxiliary wall relations C_d and St_h is certainly not new. For example, Goddard [5] used the concept to explain Mach number effects on rough wall skin friction: Dipprey and Sabersky [6] correlated and interpreted their sandgrain indentation roughness heat transfer data using a sub-layer Stanton number; Jayatilleke [7] made an extensive study of the effect of roughness pattern and Prandtl number on such wall relations. However it appears that this approach has not yet successfully been implemented in finite difference calculation procedures.

In the present paper we develop and apply a procedure for calculating turbulent skin friction and heat transfer in rough pipes for a variable property gas. Calculations are made for two types of roughness patterns: (1) sandgrain, or sandgrain indentation, and (2) repeated transverse rectangular ribs. In both cases there is experimental data for constant property flow which allow the establishment of appropriate wall relations. With the wall relations established, the effects of variable properties with wall cooling is demonstrated.

2 Analysis

2.1 Governing Equations. For constant fluid properties, low speed fully developed turbulent flow in a circular pipe is governed by

$$0 = -\frac{dP}{dx} + \frac{1}{r}\frac{\partial}{\partial r}\left(r\mu_{\text{eff}}\frac{\partial u}{\partial r}\right) \tag{1}$$

$$\rho u\frac{\partial h}{\partial x} = \frac{1}{r}\frac{\partial}{\partial r}\left(r\mu_{\text{eff}}\,\text{Pr}_{\text{eff}}{}^{-1}\frac{\partial h}{\partial r}\right) \tag{2}$$

for $r \leq R$ where turbulent transport has been modeled using an effective viscosity and effective Prandtl number. For variable properties we consider a quasi-developed flow for which the property variations in the x-direction are small compared to those in the r-direction, and

Contributed by the Heat Transfer Division for publication in the JOURNAL OF HEAT TRANSFER. Manuscript received by the Heat Transfer Division May 22, 1978.

take $\partial/\partial x(\rho u) \approx \rho \partial u/\partial x \approx 0$: the equation set remains unchanged, but then pressure P is more accurately interpreted as the total pressure $P + \rho u^2$ (see Petukhov [8]). McEligot, et al. [9] have shown that, for strongly heated flows in smooth pipes, neglect of the axial terms can lead to significant errors in the friction factor; however for the present purpose the added uncertainties in treating rough walls suggested that solution of the full governing partial differential equations was unwarranted.

Fig. 1 shows the coordinate system. The nominal radius of the pipe is $\overline{R}$ and $\overline{y}$ is measured from $r = \overline{R}$. At $\overline{y} = h$, a characteristic roughness height, the radius is R, and $y = \overline{y} - h$. For sandgrain roughness $h = k_s$, the sandgrain size, while for repeated ribs h is the height of the ribs. Then

$$G/A = \dot{m} \equiv \int_0^R \rho u 2\pi r dr = \text{constant} \tag{3}$$

$$\dot{q}_w'' 2\pi\overline{R} = \dot{m}\frac{dh_m}{dx} = \frac{d}{dx}\int_0^R \rho u h 2\pi r dr \tag{4}$$

i.e., it is assumed that the flow below $\overline{y} = h$ makes a negligible contribution to $\dot{m}$ and h_m.

Integration of the momentum equation with zero shear at the centerline gives the familiar linear shear distribution, so that equation (1) can be rewritten as

$$\mu_{\text{eff}}(\partial u/\partial y) = \tau = \tau_w(R - y)/\overline{R} \tag{5}$$

or

$$\epsilon^+ (du^+/dy^+) = (R^+ - y^+)/\overline{R}^+ \tag{6}$$

to be solved subject to $u = u_h$ at $y = 0$. With $\tau_w = C_d \tfrac{1}{2}\rho_h u_h^2$, the boundary condition becomes

$$u_h{}^{+2} = (2/C_d)(\rho_w/\rho_h) \tag{7}$$

Also,

$$\text{Re} \equiv 2G\overline{R}/\mu_m = (\mu_w/\mu_m)(4\overline{R}^+)\int_0^{R^+} (\rho/\rho_w)u^+(R^+ - y^+)dy^+ \tag{8}$$

$$C_f/2 \equiv \tau_w\rho_m/G^2 = (4\overline{R}^{+2}/Re^2)(\mu_w/\mu_m)^2(\rho_m/\rho_w) \tag{9}$$

With a constant wall heat flux $\partial h/\partial x = \partial h_w/\partial x = \partial h_m/\partial x$, equation (2) becomes

$$(2\pi\overline{R}\dot{q}_w''/\dot{m})\rho u = \frac{1}{(R-y)}\frac{\partial}{\partial y}\left[(R-y)\mu_{\text{eff}}\,\text{Pr}_{\text{eff}}^{-1}\frac{\partial h}{\partial y}\right] \tag{10}$$

or

$$2(\rho/\rho_w)u^+(y^+ - R^+)/\overline{R}^+ = (d/dy^+)[\epsilon^+\text{Pr}_{\text{eff}}^{-1}(R^+ - y^+)(dh^+/dy^+)] \tag{11}$$

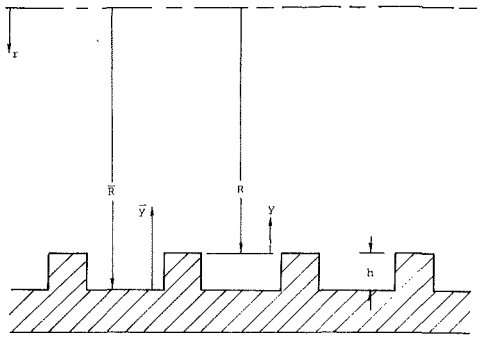

Fig. 1 Schematic of coordinate system

At $y^+ = R^+$, $\partial h^+/\partial y^+ = 0$, while at $y = 0$

$$-\mu_{\text{eff}}\text{Pr}_{\text{eff}}^{-1}(\partial h/\partial y) = \dot{q}_w''(\overline{R}/R) = \text{St}_h\rho_{sr}v^*(h_w - h)(\overline{R}/R) \tag{12}$$

or

$$\epsilon^+\text{Pr}_{\text{eff}}^{-1}(\partial h^+/\partial y^+) = \text{St}_h h^+(\overline{R}^+/R^+)(\rho_{sr}/\rho_w) \tag{13}$$

and the Stanton number $\text{St} = \dot{q}_w''/G(h_w - h_m) = 1/h_m{}^+$. An ideal gas was assumed such that $\rho\alpha h^{-1}$ and C_p = constant. With $\mu\alpha h^\omega$, $k\alpha h^\omega$, Pr = constant, and $\omega = 0.5, 0.7$ were used.

2.2 Turbulence Models. Experiment shows the Nikuradse mixing length expression [10] is valid for both smooth and rough walls,

$$(\ell/\overline{R}) = 0.14 - 0.08(1 - \overline{y}/\overline{R}) - 0.06(1 - \overline{y}/\overline{R})^2 \tag{14}$$

and $\mu_t \equiv \rho\ell^2(\partial u/\partial y)$. Experiment (e.g., [11]) has also shown that Pr_t in the turbulent core is unaffected by wall roughness; thus following common practice $\text{Pr}_t = 0.9$ is taken.

For the near wall region with a smooth wall the Van Driest damping factor based on local properties was applied,

$$(\mu_t/\mu_w) = (\rho/\rho_w)\ell^{+2}\{1 - \exp[-(y^+/26)(\rho/\rho_w)^{1/2} \times (\mu/\mu_w)^{-1}]\}^2(\partial u^+/\partial y^+) \tag{15}$$

Smooth wall calculations were made to check out the computer code, and in order to facilitate comparisons between rough wall and smooth wall behavior. For constant properties, calculated values of C_{f0} were generally between those given by the Prandtl-Schlicting formula and the Spalding law of the wall. Use of a constant mixing length in the core, with $\ell = 0.075\,\overline{R}$, had a negligible effect on C_{f0}. Calculated heat transfer agreed well with $\text{St}_0 = (C_{f0}/2)\text{Pr}^{-0.4}$.

2.3 Numerical Method. An implicit central differencing numerical technique was used in the solution procedure. The finite difference analogues to the conservation equations were first obtained and the resulting nonlinear algebraic equations were solved iteratively

Nomenclature

A = pipe cross-sectional area, $\pi\overline{R}^2$
B,B' = constants in logarithmic velocity profile
C_f = skin friction coefficient, $2\tau_w\rho_m/G^2$
C_d = roughness form drag coefficient, $2\tau_w/\rho_h u_h{}^2$
C_p = specific heat
$\overline{D}$ = nominal pipe diameter, $2\overline{R}$
f = friction factor, $(dP/dx)(4\overline{R}/\rho u_m{}^2) = 4C_f$
G = mass velocity, $(\rho u)_m$
h = enthalpy, $h^+ = (h_w - h)/(\dot{q}''_w/G)$
k_s = sandgrain roughness
ℓ = mixing length
$\dot{m}$ = mass flow rate, GA
p = pitch
P = pressure
Pr = Prandtl number
$\dot{q}_w''$ = wall heat flux
r = radial coordinate
R = radius of computational domain
$\overline{R}$ = nominal pipe radius
$\overline{R}^+$ = turbulent Reynolds number, $\rho_w v^*\overline{R}/\rho_w$
St = Stanton number
u = axial velocity
$u^+ = u/v^*$
v^* = friction velocity, $(\tau_w/\rho_w)^{1/2}$
x = axial coordinate
$y = R - r$
$y^+ = \rho_w v^* y/\mu_w$
$\overline{y} = \overline{R} - r$
$\overline{y}^+ = \rho_w v^*\overline{y}/\mu_w$
ϵ^+ = dimensionless total viscosity, $\left(\frac{\mu}{\mu_w} + \frac{\mu_t}{\mu_w}\right)$
κ = Prandtl's mixing length constant
μ = viscosity
ρ = density
τ = shear stress

Subscripts

eff = effective; laminar plus turbulent
h = at the characteristic roughness height
m = mean
0 = constant property
sr = sublayer reference enthalpy
t = turbulent
w = wall

Superscript

+ = dimensionless

using an efficient tridiagonal matrix inversion procedure. Convergence was assumed when successive iterates for the dependent variable distributions differed by less than .01 percent. A nonuniform exponential nodal point distribution and a relaxation scheme were used to ensure accuracy and avoid convergence problems.

3 Development of Wall Relations

In order to use the boundary conditions equations (7) and (13), appropriate expressions for C_d and St_h are required. In what follows we both discuss the general problem, and provide specific examples for sand grain roughness and transverse rectangular ribs.

3.1 Skin Friction for Fully Rough Walls. Correlations for C_d may be obtained by fitting experimental friction data, or directly from the velocity profile if available, since $C_d = 2/u_h{}^{+2}$. For example for sandgrain roughness with $h = k_s$, Nikuradse [10] represented the velocity profile as $u^+ = (1/\kappa)\ell n(y/h) + B$; thus $u_h{}^+ = B$ and $C_d = 2/B^2$. For $B = 8.5$, $C_d = 0.0277$. For an untested roughness pattern C_d may often be estimated using known data for the drag of individual protuberances, as was done by Lewis [12].

However, use of experimental pipe flow data requires closer examination, as there are a number of problems which must be resolved. In his pioneering work Nikuradse [10] presented (1) friction factor data, (2) a logarithmic velocity profile, and (3) a mixing length expression, all apparently obtained with considerable precision. Unfortunately Nikuradse did not clearly specify how his nominal diameter was measured, or the precise location of the coordinate origin in his mixing length expression: thus there are some difficulties in obtaining a consistent interpretation of the data, particularly at large roughness heights. For example, the measured friction factor was determined from $f = \Delta P/(L/\overline{D})\frac{1}{2}\rho u_m{}^2$; $u_m = 4\dot{m}/\pi\overline{D}^2$. Thus $f\alpha\overline{D}^5$, and precise specification of the nominal diameter is very important. The y-coordinate origin probably best chosen to be k_s below the location where $u^+ = 8.5$ so as to be consistent with the velocity profile, but this still doesn't fix the origin relative to the pipe. If we further assume that the origin is at the specified nominal radius $\overline{R}$ then we can derive a mixing length expression consistent with the logarithmic velocity profile. Using a linear shear distribution $\tau = \tau_w\ (1 - \overline{y}/\overline{R})$ there is obtained

$$\ell/\overline{R} = \kappa(\overline{y}/\overline{R})(1 - \overline{y}/\overline{R})^2 \tag{16}$$

As $\overline{y}/\overline{R} \to 1$, equation (16) is unacceptable, but then it is likewise impossible for the logarithmic profile to be valid as $\overline{y}/\overline{R} \to 1$. Thus Nikuradse's mixing length distribution is not consistent with the logarithmic velocity profile, and use of equation (14) in a numerical calculation procedure, will not give a logarithmic velocity profile of the extent shown by Nikuradse.

We now derive the friction factor consistent with a logarithmic velocity profile $u^+ = (1/\kappa)\ell n(y/h) + B$. From equation (3)

$$\frac{\dot{m}}{\rho v^*} = \int_h^{\overline{R}} u^+ 2\pi(\overline{R} - \overline{y})d\overline{y} = \frac{1}{\kappa}\pi\overline{R}^2\left[\ell n\frac{\overline{R}}{h} - \frac{3}{2} + \frac{2h}{\overline{R}}\right] + \pi R^2 B\left[1 - 2\frac{h}{\overline{R}}\right] \tag{17}$$

where terms of $O(h^2/\overline{R}^2)$ and higher have been dropped. Then

$$u_m{}^+ = \frac{1}{\kappa}\left[\ell n\frac{\overline{R}}{h} - \frac{3}{2} + \frac{2h}{\overline{R}}\right] + B\left[1 - 2\frac{h}{\overline{R}}\right] = \sqrt{\frac{2}{C_f}} = \sqrt{\frac{8}{f}} \tag{18}$$

with $\kappa = 2.5$, and solving for B,

$$B = \left(\sqrt{\frac{2}{C_f}} - 2.5\ \ell n\frac{\overline{R}}{h} + 3.75 - \frac{5h}{\overline{R}}\right)\Big/\left(1 - 2\frac{h}{\overline{R}}\right) \tag{19}$$

Also if terms of order $h/\overline{R}$ are ignored in equation (18) and we consider sandgrain roughness with $h = k_s$, $B = 8.5$,

$$f = (2.03\log(\overline{R}/k_s) + 1.682)^{-2} \tag{20}$$

a friction law first derived by Von Karman. Nikuradse's friction law

$$f = (2.0\log(\overline{R}/k_s) + 1.74)^{-2} \tag{21}$$

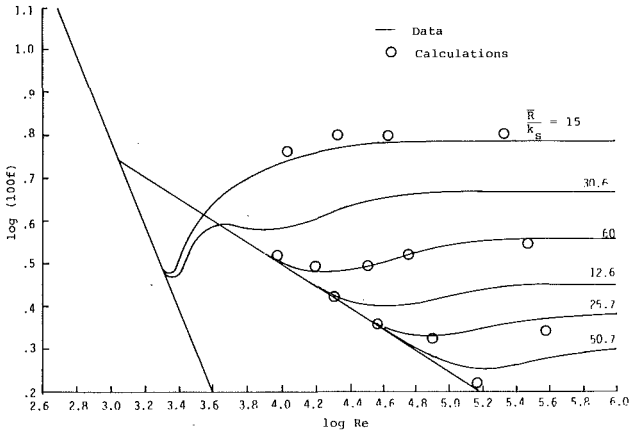

Fig. 2 Skin friction for sandgrain roughness: comparison with Nikuradse's data [10]

was obtained by slightly adjusting the constants in equation (20) in order to obtain better agreement with his experimental data for f. However at the largest roughness height tested, $\overline{R}/k_s = 15$, the discrepancy between equations (20) and (21) is only 1.1 percent.

The success of equation (20) in predicting Nikuradse's friction factor data has led most subsequent workers to use the corresponding form of equation (19), namely,

$$B = (2/C_f)^{1/2} - 2.5\ \ell n(\overline{R}/h) + 3.75 \tag{22}$$

to correlate their friction factor data, and to provide an expression for B, or equivalently, C_d. But for large roughness heights use of such values of B in a numerical calculation procedure will not recover the original friction factors. If equation (16) were used as the mixing length expression then the calculated friction factor for sandgrain roughness would agree with equation (18), which becomes

$$f = [2.03\log(\overline{R}/k_s) - 4.23(k_s/\overline{R}) + 1.582]^{-2} \tag{23}$$

For $\overline{R}/k_s = 15$, $C_f/2 = f/8 = 0.00871$, whereas Nikuradse's correlation gives $C_f/2 = 0.00746$, a 17 percent discrepancy. If, on the other hand, equation (14) is used for the mixing length, with $B = 8.5$, then the numerical calculation procedure gives $C_f/2 = 0.0081$. Fig. 2 compares the results of numerical calculations using equation (14) and $B = 8.5$ with Nikuradse's data (results are also shown for transitional roughness). Alternatively equation (19) can be used to deduce that for $\overline{R}/k_s = 15$, a value of $B = 10.2$ with $C_d = 1/B^2$ and equation (16) for the mixing length, the numerical calculation procedure will give an f in agreement with equation (21).

Dipprey and Sabersky [6] measured friction factors for sandgrain indentation roughness, and they were careful to specify their nominal diameter as a volumetric average, which proved equivalent to using the midpoint of the sandgrains. If u_m, and hence $C_f/2$ and f are defined in terms of this radius then numerical calculations using $B = 8.5$ and equation (14), also overpredict the experimental data at large roughness heights. For example, at $R/k_s = 10.3$, the predicted $C_f/2 = 0.0100$, while the experimental value is 0.00865.

It appears that the Nikuradse universal velocity profile for rough walls is not valid at large roughness heights, and perhaps B is not independent of R/k_s. However, there remains doubt as to the best location of the y-coordinate origin: Nikuradse did not give a precise specification, while Dipprey and Sabersky did not measure velocity profiles.

Webb, Eckert and Goldstein [13] measured friction and heat transfer for transverse rectangular ribs of height h and pitch p. Rib sizes and spacing were chosen to give $0.02 < h/\overline{R} < 0.08$, and $10 < p/h < 40$. The nominal pipe diameter was defined to correspond to the rib roots, and h was chosen as the characteristic roughness height. Equation (22) was used to determine the wall function B, which for fully rough conditions was correlated (rather poorly) as

$$B = 0.95(p/h)^{0.53} \text{ or } C_d = 2.22(p/h)^{-1.06};\quad h^+ \gtrsim 40 \tag{24}$$

For $p/h = 10$, $B = 3.22$. Now following our arguments for sandgrain

roughness this B function must be modified in order to properly recover the original friction data. Using equation (19) the required value of B is

$$B' = (3.22 - 5h/\overline{R})/(1 - 2h/\overline{R}) \tag{25}$$

which gives for $h/\overline{R} = 0.02$, 0.04 and 0.08 values of $B' = 3.36$, 3.29 and 3.25, respectively. However a closer look at the experimental data suggests that $B' \simeq 3.6$ for $h/\overline{R} = 0.04$ is more appropriate. The variation in B' is then about 10 percent which is no more than the scatter of the original data. Thus apparently B is not independent of $h/\overline{R}$. In order to be consistent it is preferable to use equation (14) in numerical calculations, thus a new expression for C_d for rib roughness was developed empirically by obtaining a best fit to all experimental friction data, as shown in Fig. 3: the resulting expression for C_d is dependent on $h/\overline{R}$

$$C_d = 2/(1 - h/\overline{R})^2(p/h) \tag{26}$$

More recently Dalle, Donne and Meyer [14] made an extensive study of repeated rib roughness, focusing mainly on annulus flow. They also found an effect of duct size, suggesting that for circular pipes B should be increased by 0.4 ℓn (100 $h/\overline{R}$). However these correlations are subject to similar criticism as those of Webb, et al. since the equivalent of equation (22) was used to derive the B function, and in addition, the empirical specification of the zero shear plane in annulus flow introduced a further possible source of error. Velocity profiles were not measured in these repeated rib studies so that the suitability of locating the coordinate origin at the rib roots cannot be evaluated.

3.2 Heat Transfer for Fully Rough Walls. The usual procedure to develop correlations for St_h has been to divide the flow into two regions with St_h characterizing transfer to the wall from the location $\overline{y} = h$. For pipe flow the thermal resistance of the turbulent core is found by applying Reynolds' analogy and assuming that the bulk enthalpy h_m and the bulk velocity u_m occur at the same value of y. Summing the two thermal resistances in series gives

$$1/\mathrm{St} = (2/C_f)^{1/2}[Pr_t(u_m{}^+ - u_h{}^+) + 1/\mathrm{St}_h] \tag{26}$$

Most workers have taken $\mathrm{Pr}_t = 1$, then since $u_h{}^+ = B$, and $u_m{}^+ = (2/C_f)^{1/2}$,

$$1/\mathrm{St}_h = (C_f/2)^{1/2}(1/\mathrm{St} - 2C_f) + u_h{}^+ \tag{27}$$

As was the case for C_d, correlations of St_h developed via equation (27) when used in a numerical calculation method will not exactly recover the heat transfer data due to the assumptions in the derivation of equation (27). Thus such correlations are best used as a guide, with adjustments made to give best agreement with the original heat transfer data. Figs. 4 and 5 show the results of such a procedure, for sandgrain and repeated rib roughness, respectively. The recommended St_h correlations are

$$\text{Sandgrain: } \mathrm{St}_h = (1/4.8)(k_s{}^+)^{-0.2}\mathrm{Pr}^{-0.44} \tag{28}$$

$$\text{Repeated rib: } \mathrm{St}_h = (1/4.3)(h^+)^{-0.28}\mathrm{Pr}^{-0.57} \tag{29}$$

3.3 Transitionally Rough Walls. For sandgrain roughness a numerical fit to Nikuradse's B function was used. For heat transfer the fully rough St_h correlation was extrapolated into the transitionally rough regime: the Dipprey and Sabersky data [6] show that such an extrapolation is a reasonable approximation for gases. For repeated rib roughness no attempt was made to model the transitionally rough walls, though some of the calculated results extend into this regime.

3.4 Summary of Recommended Fully Rough Wall Relations.

1 Sandgrain roughness: $C_d = 0.0277$ and equation (28) for St_h; $k_s{}^+ \gtrsim 75$; $15 < \overline{R}/k_s < \infty$.

2 Repeated rib roughness: equation (26) for C_d, and equation (29) for St_h; $h^+ \gtrsim 40$; $0.02 < h/\overline{R} < 0.08$ and $10 < p/h < 40$.

4 Results for Variable Properties

4.1 Cooling for Smooth Walls. Commencing with the pioneering work of Deissler and Eian [15], a number of workers have made numerical calculations of variable property turbulent gas flows

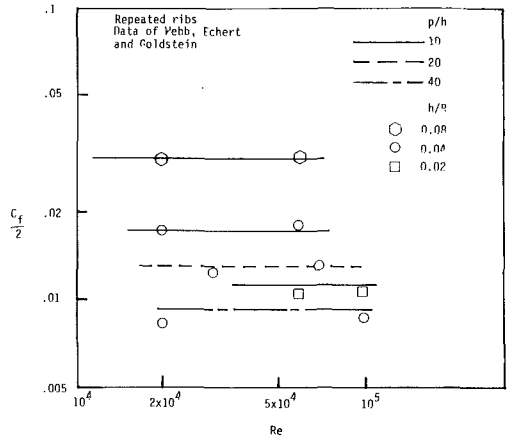

Fig. 3 Skin friction for repeated rib roughness: comparison with data of Webb, Eckert and Goldstein [13]

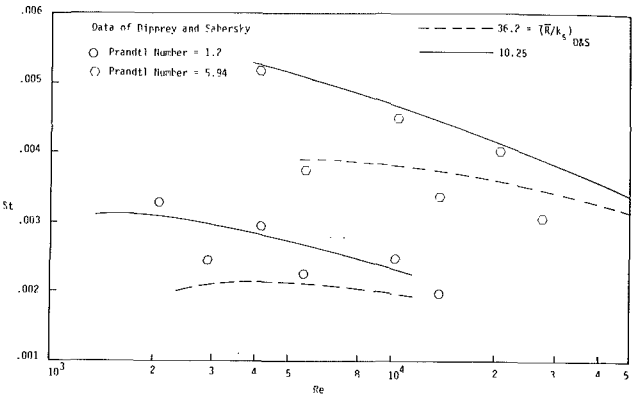

Fig. 4 Heat transfer for sandgrain indentation roughness: comparison with data of Dipprey and Sabersky [6]

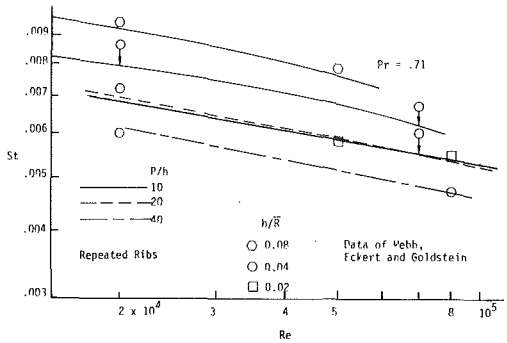

Fig. 5 Heat transfer for repeated rib roughness: comparison with data of Webb, Eckert and Goldstein [13]

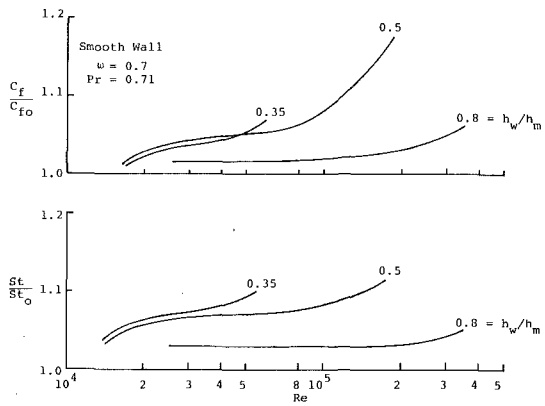

Fig. 6 Normalized skin friction and heat transfer for gas flow in smooth pipes with cooling

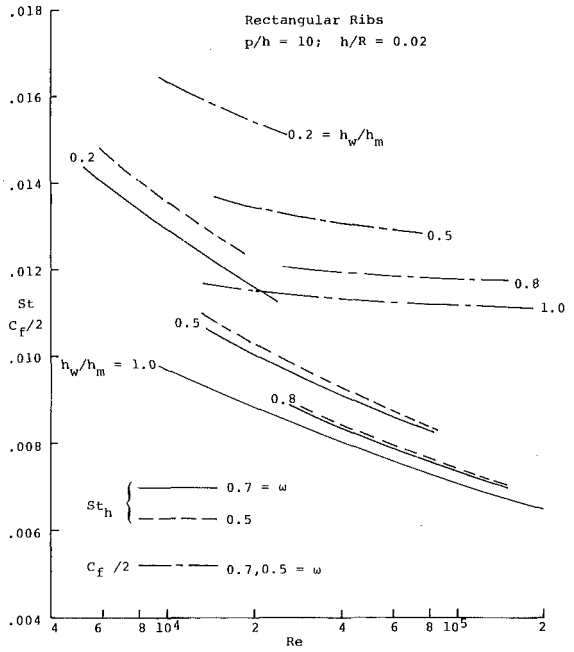

Fig. 7 Skin friction and heat transfer for repeated rib roughness: effect of wall cooling

in smooth pipes. Most attention has been directed to flows with heating because considerably more experimental data are available for heating as compared with cooling. McEligot, et al. [9] have shown that when there is strong heating, calculated skin friction and heat transfer are very sensitive to choice of mixing length model. Based on a single strong heating experimental run of Perkins and Worsoe-Schmidt [16], they chose the van Driest model with no wake component, and with properties evaluated at the wall condition. For our calculations of flows with cooling we have used the Nikuradse mixing length distribution and van Driest damping factor with locally evaluated properties, based on the success of a similar approach for external turbulent boundary layers [17]: Fig. 6 shows $C_f/2$ and St, both normalized with the constant property value, for various cooling ratios. Use of $\omega = 0.7$ gives a behavior which is a reasonable approximation for air at moderate temperature levels. The somewhat erratic dependence on Reynolds number is also in evidence in the heating calculations of McEligot. Petukhov [9] shows the experimental data of Il'in for $0.55 < h_w/h_m < 1.0$ as scattering between $C_f/C_{f0} = 1.0$ and 1.15. Humble, Lowdermilk and Desmon [18] with air for $0.46 < h_w/h_m < 1.0$ obtained values which, on an average, were marginally above unity. Wolf [19] obtained a limited amount of data for CO_2 with cooling and for Re > 40,000, found C_f/C_{f0} to vary between 1.05 and 1.08. Our calculations are clearly in line with the experimental data. For heat transfer the situation is similar. Petukhov shows the experimental data of Il'in for $0.55 < h_w/h_m < 0.9$ correlated as $St/St_0 = 1.10$. Humble, Lowdermilk and Desmon obtained $St/St_0 = 1.0$, but noted an effect of h_w/h_m would be obtained if a different temperature dependence of thermal conductivity were used. Wolf also obtained $St/St_0 = 1.0$. Again we suggest that our calculations are in line with experiment. On the other hand, Petukhov [8] using the Reichardt eddy diffusivity profile, calculated values of $C_f/C_{f0} \simeq 1.31$ and $St/St_0 \simeq 1.27$, for $h_w/h_m = 0.5$. These values are clearly not supported by experiment.

4.2 Cooling for Repeated Rib Rough Walls. Fig. 7 shows skin friction for repeated ribs with $p/h = 10$ and $h/R = 0.02$. Note that in using equation (7) for the wall relation we have assumed that the form drag scales with ρ_h in variable property flow: comparisons with experimental data when available may indicate a subsequent modification of this hypothesis. As expected there is negligible effect of ω for this fully rough situation. Fig. 7 also shows heat transfer for the same geometry: the curves for $\omega = 0.5$ should be viewed as a high temperature level asymptote for real gases. For the variable property

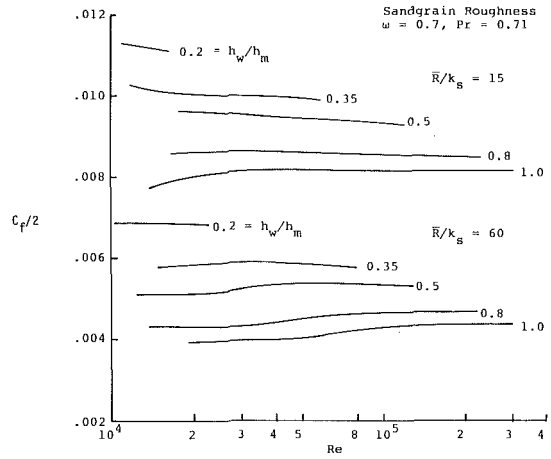

Fig. 8 Skin friction for sandgrain roughness: effect of wall cooling

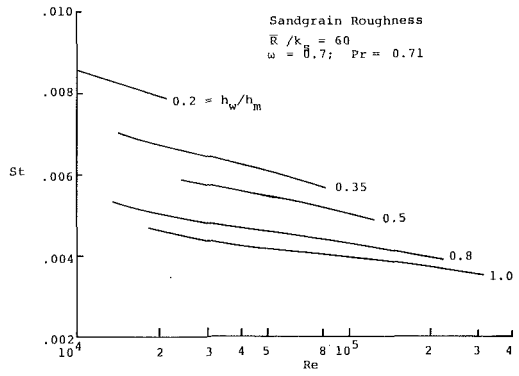

Fig. 9(*a*) Heat transfer for sandgrain roughness: effect of wall cooling for $\bar{R}/k_s = 60$

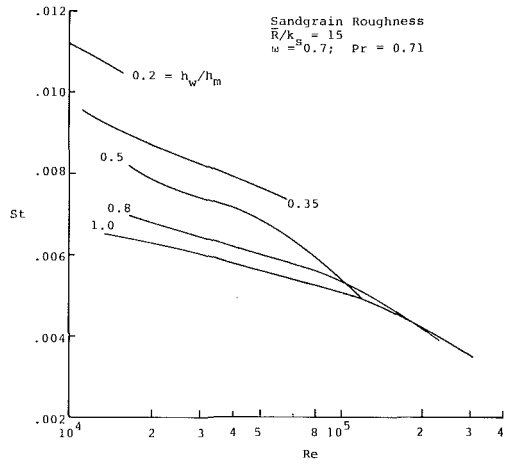

Fig. 9(*b*) Heat transfer for sandgrain roughness: effect of wall cooling for $\bar{R}/k_s = 15$

flow the properties in the sub-layer Stanton number have been evaluated at a mean film enthalpy, i.e., an average of h_w and h_h. The expected effect of ω through the sub-layer Stanton number correlation is in evidence. For both heat transfer and skin friction the calculated trends are quite regular, which is in marked contrast to the smooth wall case.

4.3 Cooling for Sandgrain Roughness. Fig. 8 shows skin friction for two sandgrain roughness sizes, $\bar{R}/k_s = 60$ and 15. For the smaller roughness the data at lower Reynolds numbers are in the transitionally rough regime. Figs. 9(*a*) and 9(*b*) show the heat transfer for $\bar{R}/k_s = 60$ and 15, respectively. In these calculations $\omega = 0.7$ and Pr = 0.71. The Stanton number behavior for $\bar{R}/k_s = 60$ is regular and similar to that for the repeated rib roughness; in contrast, for the larger sandgrain size of $\bar{R}/k_s = 15$, the Stanton number behavior is more

complex, exhibiting a tendency for the effect of wall cooling to disappear at high Reynolds numbers.

4.4 Correlation of C_f/C_{f0} and St/St_0. It is common practice to attempt a correlation of variable property effects in pipe flows as simple power laws, viz.,

$$C_f/C_{f0} = (h_w/h_m)^{-n};\ St/St_0 = (h_w/h_m)^{-m} \qquad (42\,a,b)$$

Fig. 10 shows plots of C_f/C_{f0} and St/St_0 versus h_w/h_m for all the roughnesses calculated. It is seen that C_f/C_{f0} depends on the roughness pattern and size, and there is a slight effect of Reynolds number. For the small sandgrain roughness $\overline{R}/k_s = 60$, the effect of Re is opposite to the other two cases, probably due to the fact that at Re = 25,000 the small sandgrain roughness gives transitionally, rather than fully rough flows. For the ribs $n = 0.2$ is a reasonable fit to the curves. The Re effect on St/St_0 is slight for the ribs and the small sandgrain size: for the large sandgrain size the Re effect cannot be ignored. For the repeated ribs with $\omega = 0.7$, $m = 0.22$; for general engineering use a value of $m = 0.25$ better represents the heat transfer results. Experimental data for rough pipes showing cooling effects are not available: however, for external boundary layers suitable data are available and could be used to evaluate the basic approach.

5 Conclusions

1 Turbulent flow in rough pipes may be satisfactorily calculated using smooth wall mixing length models in the turbulent core, with a roughness element drag coefficient and sub-layer Stanton number to characterize transport to the wall.

2 For large roughness heights proper comparison with experiment requires accounting for terms of the order of roughness height divided by pipe radius.

3 For smooth pipes the van Driest damping factor with locally evaluated properties gives predictions of variable property gas flows with cooling which are in accord with experiment.

4 Variable property effects are more pronounced for rough pipes as compared with smooth pipes, and Reynolds number trends are more regular.

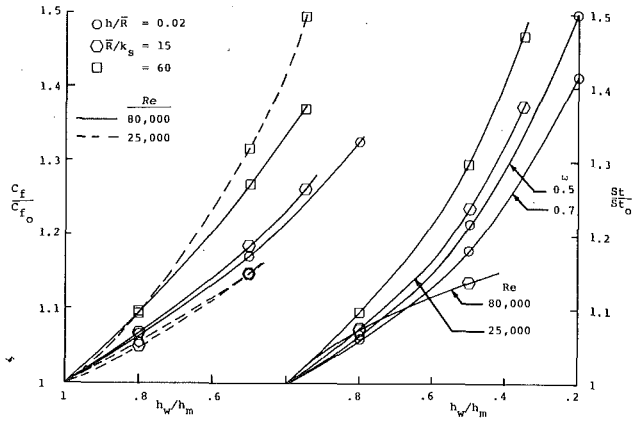

Fig. 10 Normalized skin friction and heat transfer versus enthalpy ratio for rough pipes

References

1 Hove, D. R., Craig, J. E., Issa, R., "Airblast Attenuation Experiments for the MX Trench," SAI-78-595-LA, *Science Applications*, El Segundo, CA, Oct. 1977

2 Anderson, L. W., and Morse, H. L., "Users Manual—Boundary Layer Integral Matrix Procedure—BLIMP," AFWL TR-69-114, Vol. I, Oct. 1971

3 Healzer, J. M., Moffat, R. J., and Kays, W. M., "The Turbulent Boundary Layer on a Rough Porous Plate: Experimental Heat Transfer with Uniform Blowing," Report No. HMT-18, Thermosciences Division, Dept. Mech. Eng., Stanford University, 1974.

4 Hatton, A. P., and Walklate, P., "A Mixing Length Model for Predicting Heat Transfer in Rough Pipes," *International Journal of Heat and Mass Transfer*, Vol. 19, 1976, pp. 1425–1432.

5 Goddard, F. E., Jr., "Effect of Uniformly Distributed Roughness on Turbulent Skin-Friction Drag at Supersonic Speeds," *Journal Aerospace Sciences*, Vol. 25, 1950, pp. 1–15.

6 Dipprey, D. F., and Sabersky, R. H., "Heat and Momentum Transfer in Smooth and Rough Tubes," *International Journal of Heat and Mass Transfer*, Vol. 6, 1963, pp. 329–353.

7 Jayatilleke, C. L. V., "The Influence of Pandtl Number and Surface Roughness on the Resistance of the Laminar Sub-Layer to Momentum and Heat Transfer," *Progress in Heat and Mass Transfer*, Vol. 1, Ed. U. Grigull and E. Hahne, Pergamon Press, 1969.

8 Petukhov, B. S., "Heat Transfer and Friction in Turbulent Pipe Flow with Variable Physical Properties," *Advances in Heat Transfer*, Vol. 6, Ed. J. P. Hartnett and T. F. Irvine, Jr., Academic Press, NY, 1970.

9 McEligot, E. M., Smith, S. B., and Bankston, C. A., "Quasi-Developed Turbulent Pipe Flow with Heat Transfer," ASME JOURNAL OF HEAT TRANSFER, Vol. 90, No. 4, Nov. 1970, pp. 641–650.

10. Nikuradse, J., "Laws of Flow in Rough Pipes," NACA TM 1292, 1950.

11. Pimenta, M. M., Moffat, R. J., and Kays, W. M., "The Turbulent Boundary Layer: An Experimental Study of the Transport of Momentum, and Heat with the Effect of Roughness," Report No. HMT-21, Thermosciences Division, Dept. Mech. Eng., Stanford University, May 1975.

12 Lewis, M. J., "An Elementary Analysis for Predicting the Momentum and Heat Transfer Characteristics of a Hydraulically Rough Surface," ASME JOURNAL OF HEAT TRANSFER, Vol. 97, No. 2, May 1975, pp. 249–254.

13 Webb, R. L., Eckert, E. R. G. and Goldstein, R. J., "Heat Transfer and Friction in Tubes with Repeated-Rib Roughness," *International Journal of Heat and Mass Transfer*, Vol. 14, 1971, pp. 601–618.

14 Dalle Donne, M., and Meyer, L., "Turbulent Convective Heat Transfer from Rough Surfaces with Two-Dimensional Rectangular Ribs," *International Journal of Heat and Mass Transfer*, Vol. 20, 1977, pp. 583–620.

15. Deissler, R. G., and Eian, C. S., "Analytical and Experimental Investigation of Fully Developed Turbulent Flow of Air in a Smooth Tube, with Heat Transfer with Variable Fluid Properties," NACA TN 2629, 1952.

16 Perkins, H. C. and Worsoe-Schmidt, D. M., "Turbulent Heat and Momentum Transfer for Gases in a Circular Tube at Wall-to-Bulk Temperatures Ratios to Seven," *International Journal of Heat and Mass Transfer*, Vol. 8, 1965, pp. 1011–1032.

17 Landis, R. B., and Mills, A. F., "The Calculation of Turbulent Boundary Layers with Foreign Gas Injection," *International Journal of Heat and Mass Transfer*, Vol. 15, 1972, pp. 1905–1932.

18 Humble, L. V., Lowdermilk, W. H., and Desmon, L. G., "Measurements of Average Heat Transfer and Friction Coefficients for Sub-sonic Flow of Air in Smooth Tubes at High Surface and Fluid Temperatures," NACA Report 1020, 1951.

19 Wolf, H., "The Experimental and Analytical Determination of the Heat Transfer Characteristics of Air and Carbon Dioxide in the Thermal Engrance Region of a Smooth Tube with Large Temperature Differences Between the Gas and the Tube Wall," Ph.D. Thesis, Purdue University, 1958.

H. Yamamoto
Associate Professor,
Department of Mechanical Engineering,
Asahikawa Technical College,
Asahikawa 070, Japan

N. Seki
Professor.

S. Fukusako
Associate Professor,
Department of Mechanical Engineering,
Hokkaido University,
Sapporo 060, Japan

Forced Convection Heat Transfer on Heated Bottom Surface of a Cavity

Experiments to measure the heat transfer characteristics for various cavities situated at a duct-wall were performed. Flow visualization, measurements of pressure and temperature distributions on the heated bottom surface of cavity were carried out. It was observed that the effects of main flow stream, reattachment of separated flow, and vortex flow in the cavity on heat transfer unexpectedly large. It was found that heat transfer did not always decrease monotonously with an increase of aspect (depth-width) ratio D/W, in the flow range of laminar to turbulent. Correlations between Nu_m and Re_w were made in laminar and turbulent heat transfer ranges.

Introduction

In recent years, considerable research on heat transfer and flow characteristics of separated flow have been done with its numerous applications. Convection heat transfer problems in a cavity or groove constructed in many types of structures is one such application.

Experimental studies by Roshko [1] and Tani, et al. [2] to obtain fundamental flow characteristics on the rectangular cavity exposed to flow field were early studies. Charwat, et al. [3, 4] mentioned aerodynamic and heat transfer characteristics in the cavity set up in subsonic and supersonic flow. Hagen and Dhanak [5] reported the experimental and theoretical results for a relation of heat transfer to turbulent boundary layer thickness over the cavity. Kurosaki, et al. [6] discussed heat transfer problems from a standpoint of mass transfer in a two-dimensional cavity with naphthalene walls.

Meanwhile, numerical calculations of heat transfer problems similar to those mentioned above were treated by many investigators [7–9]. Yamamoto, et al. [10] analyzed a laminar heat transfer problem in a two-dimensional cavity using the the finite difference method of alternative implicit direction, and discussed qualitatively the effects of free stream velocity, buoyancy force and depth of cavity on flow and temperature fields inside the cavity.

Heat transfer or flow characteristics in a cavity depend intricately on boundary layer thickness of flow, the shape of the cavity and thermal conditions at the walls. Therefore, it is rather difficult to clarify the aforementioned characteristics in detail. In the present work, experimental results concerned with the basic heat transfer characteristics on the bottom surface of a two-dimensional cavity situated at a duct-wall are reported.

Experimental Apparatus and Procedure

In the present experiments, observation was made of the flow pattern inside the cavity, and pressure and heat transfer distributions on the bottom surface of the cavity were measured.

The cavity is situated on the floor of an open-type wind tunnel which has a cross section of 30 cm (width) × 10 cm (height) and is operated up to the maximum speed of 15 meters per second, as shown in Fig. 1 (*a*). Free stream turbulence $\sqrt{\overline{u'^2}}/U_\infty$ measured by using hot wire anemometer was of about 0.7 percent, where $\overline{u'^2}$ was temporal mean of turbulent velocity. The cavity width W was held constant at 5 cm, while its depth D was varied from 0 to 5 cm changing the position of bottom.

For the observation of flow pattern inside the cavity, photographs of smoke starting to flow from the position of upstream top-corner parallel to free stream were taken under a free stream velocity U_∞ = 1.6 m/s.

The pressure distributions on the centerline of span on the bottom surface were sensed by 18 static holes of 0.5 mm dia drilled through the bottom wall and measured by a micromonometer.

In Fig. 1(*b*), a detailed view of the heating bottom of cavity is shown. A stainless steel foil of 50 μm in thickness is used as a main heater. The uniform heat flux on the surface thus obtained was evaluated by the supplied electric power.

The local temperature on the bottom surface was measured by means of 11 copper-constantan thermocouples of 0.2 mm in diameter. They were located on the centerline of span on the bottom surface and were attached to a mica leaf of 30 μm thickness sandwiched between the main heater and a bakelite plate under which a guard heater was mounted in order to minimize the heat loss to the environment. The inevitable heat loss was also checked by three measured values of temperature difference between the upper and lower faces of the bakelite plate.

For cases with nine cavities of aspect-ratio D/W = 0.0, 0.04, 0.08, 0.12, 0.16, 0.2, 0.3, 0.5 and 1.0, pressure and temperature distributions on the bottom surface were measured under several main stream velocities ranging from laminar boundary layer flow to turbulent one.

In Table 1, for three cavities including D/W = 0.0 and two free stream velocities, the approaching boundary layer flow characteristics are described with an indication of laminar or turbulent flow. The effective upstream length x_0 is evaluated from the displacement thickness δ^* which is obtained from the velocity profile at the upstream top-corner. In laminar flow range for D/W = 0.0, Re_w dependence of x_0 is expressed in the following relation:

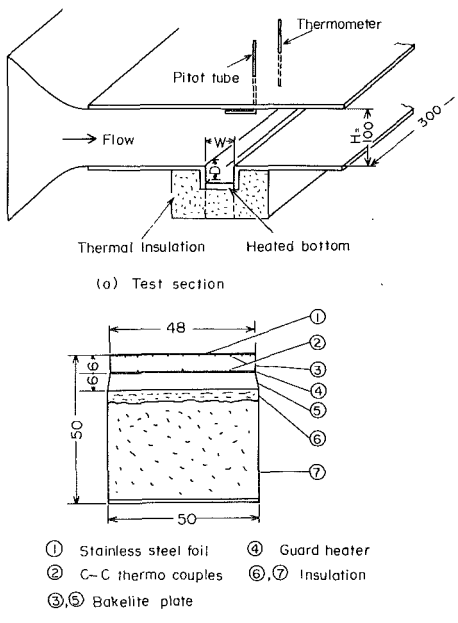

Fig. 1 Experimental apparatus

Contributed by the Heat Transfer Division for publication in the JOURNAL OF HEAT TRANSFER. Manuscript received by the Heat Transfer Division December 6, 1978.

Table 1 Approaching boundary layer characteristics at the upstream top-corner

D/W	U_∞ (m/s)	δ^* (mm)	x_0 (cm)	$U_\infty W/\nu$	x_0/W	$U_\infty x_0/\nu$	approaching boundary layer flow
0.0	1.1	2.1	10.5	3.6×10^3	2.1	7.6×10^3	laminar
	14.6	0.6	13.2	4.9×10^4	2.6	1.3×10^5	turbulent
0.2	1.3	2.2	12.4	4.2×10^3	2.5	1.0×10^4	laminar
	14.9	1.0	25.2	4.8×10^4	5.0	2.5×10^5	turbulent
1.0	1.1	1.9	8.6	3.7×10^3	1.7	6.3×10^3	laminar
	14.8	0.8	20.1	5.0×10^4	4.0	2.0×10^5	turbulent

$$x_0/W = A \cdot \mathrm{Re}_w{}^n$$

where $A = 33.2$, and $n = -0.345$.

Results and Discussion

Flow Visualization inside the Cavity. In Figs. 2(*a*)–2(*h*), photographs of the flow pattern inside the cavity at a free stream velocity $U_\infty = 1.6$ m/s are represented for the cavities of aspect-ratio $D/W \leqq 1.0$.

As shown in Fig. 2(*a*), in the case of a very shallow cavity, flow separated from the upstream top-corner reattaches on the bottom surface. With increasing depth, the reattachment point on the surface moves downward and the separated streamline reaches the downstream cavity wall (Fig. 2(*b*)). A recirculating vortex formed behind the upstream cavity wall moves its core down on the middle position of the bottom surface and increases the size.

In Fig. 2(*c*), an elliptic vortex which occupies the whole cavity is observed and with increasing depth, a small vortex appears in front of downstream cavity wall; this vortex is formed as a result of a part of the free stream impinging on the downstream cavity wall and then flowing toward the bottom surface. In Figs. 2(*d*) and 2(*e*), a vortex growing gradually in front of the downstream cavity wall is observed.

In Fig. 2(*f*), for the aspect-ratio $D/W = 0.4$, a vortex whose diameter equals approximately to the depth D is formed and a stagnant region of weak recirculating flow behind the upstream cavity wall is observed. With increasing depth, the core of the vortex moves up to the center of the bottom surface and (Fig. 2(*h*)) for the aspect-ratio $D/W = 1.0$, a large vortex which occupies the whole cavity is formed.

Similar observation using smoke flow was tried for higher free stream velocities corresponding to transient and turbulent flow regimes. Due to the strong diffusive nature of smoke flow, satisfactory flow patterns could not be obtained. In order to make the flow near the bottom surface of the cavity clear, another flow visualizing experiment was performed. In this experiment, the movement of small plastic particles distributed uniformly on the surface was observed. Fig. 3 shows the bottom surface on which plastic particles are distributed; the light parts on the surface are the places from where black-colored particles were blown away and the dark parts are the places where the particles were gathered up. The pictures of $U_\infty = 7.9$ m/s and $U_\infty = 14.6$ m/s correspond to transient and turbulent approaching boundary layer flow, respectively. From these observations and hot-wire anemometer measurement, the existence of unsteady flow near the surface and intermittent or three-dimensional flow (transverse flow to free stream one) may be understood. Thus, the flow patterns inside the cavity for transient or turbulent flow may significantly affect the heat transfer and flow characteristics in a different manner from those for laminar cavity flow.

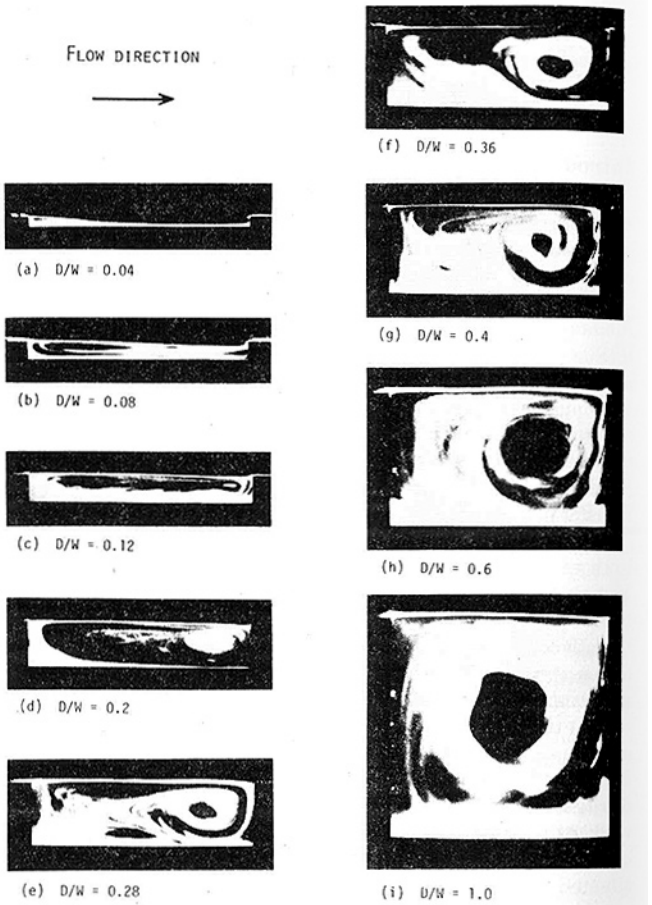

Fig. 2 Visualized flow pattern inside cavity

Pressure Distribution on the Bottom Surface. The measurement of pressure distribution on the bottom of cavity is fundamental from the standpoint of clarifying flow or heat transfer characteristics and many experimental results have been reported (e.g., [1, 2]).

In Figs. 4(*a*) and 4(*b*), pressure distributions on the bottom surface are shown in terms of pressure coefficient C_p for each cavity depth:

Nomenclature

C_p = surface pressure coefficient, equation (1)
D = depth of cavity
h_m = mean heat transfer coefficient, equation (2)
h_x = local heat transfer coefficient
Nu_m = mean Nusselt number
k_f = thermal conductivity of air
p = static pressure on bottom surface
p_0 = reference static pressure
q_w = heat flux rate from bottom to free stream
Re_w = Reynolds number, equation (3)
T_x = temperature at x position on bottom surface
T_∞ = temperature in free stream
U_∞ = free stream velocity
u = mean velocity parallel to bottom surface
W = width of cavity
x = distance along bottom surface
x_0 = effective upstream length
y = distance normal to bottom surface
δ^* = displacement thickness
ν_f = kinematic viscosity of air
ρ_∞ = density of air

Subscripts

f = evaluated at film temperature
∞ = evaluated at free stream temperature

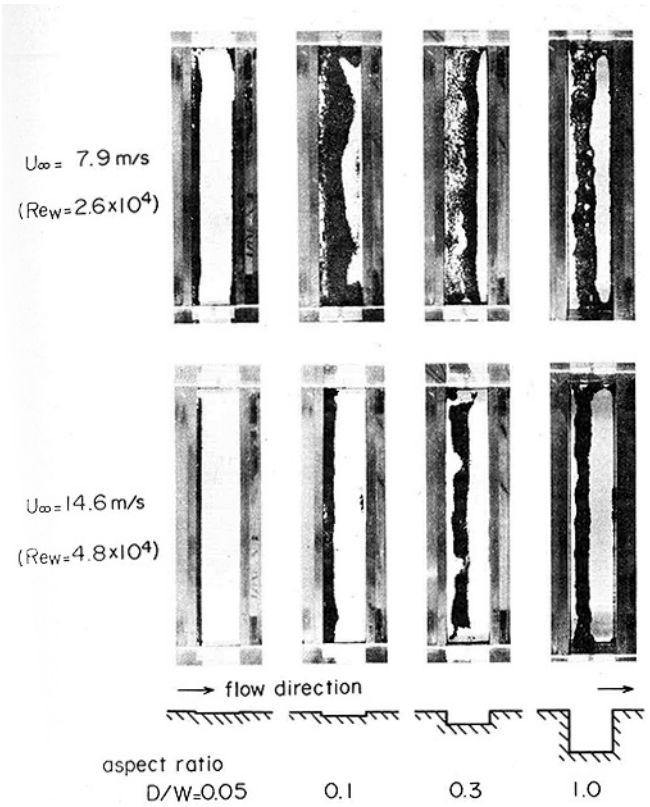

Fig. 3 **Flow visualization near the bottom surface of cavity**

$$C_p = \frac{p - p_0}{\frac{1}{2}\rho_\infty U_\infty^2} \tag{1}$$

where, p and p_0 are pressures on the bottom surface and at reference static hole on the duct wall 3 cm ahead of upstream top-corner of cavity, respectively.

In Fig. 4(a), for a lower free stream velocity of $U_\infty = 6.0$ m/s which corresponds to transient flow regime, a large variation in the pressure coefficient is seen downstream region of the bottom. For the cavities of lower aspect-ratio $D/W \leqq 0.12$, the coefficient increases gradually over the entire surface of the bottom and is positive on almost the entire surface of the bottom. For the other cavities, it is seen that each maximum point exists in these distributions, and the pressure coefficient C_p approaches to the value of $C_p = 0.0$, with increasing D/W.

For higher free stream velocity of $U_\infty = 13.5$ m/s which corresponds to turbulent flow regime (Fig. 4(b)) there is initially a rather rapid pressure rise in the upstream region of the bottom surface for the cavity of lower aspect-ratio, followed by a flat distribution of pressure. In addition, the trend of results indicates that the reattachment to the cavity floor occurs at greater x/W for greater D/W; moreover, with increasing depth, the separated flow from the upstream top-corner may reattach to the upstream facing wall.

Such behavior in pressure distribution on the bottom surface depends on the reattachment of separated flow and vortex flow inside the cavity, and may exert a significant effect on the heat transfer on the bottom surface.

Heat Transfer on the Bottom Surface. Heat transfer distribution on the bottom surface is expressed in terms of local heat transfer coefficient defined as follows:

$$h_x = \frac{q_w}{T_x - T_\infty} \tag{2}$$

where q_w is the heat transfer rate from the surface to the surroundings, and is evaluated from electrically supplied power, and $T_x - T_\infty$ is the difference between the bottom surface temperature and free stream temperature.

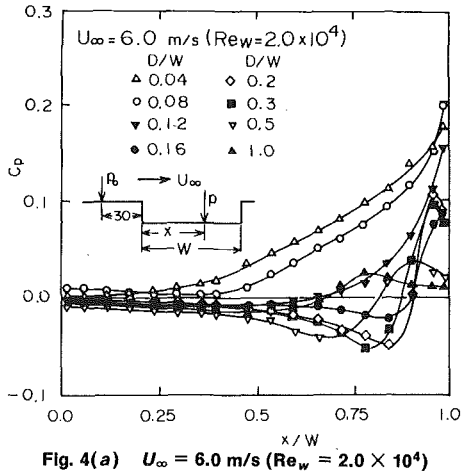

Fig. 4(a) $U_\infty = 6.0$ m/s ($Re_w = 2.0 \times 10^4$)

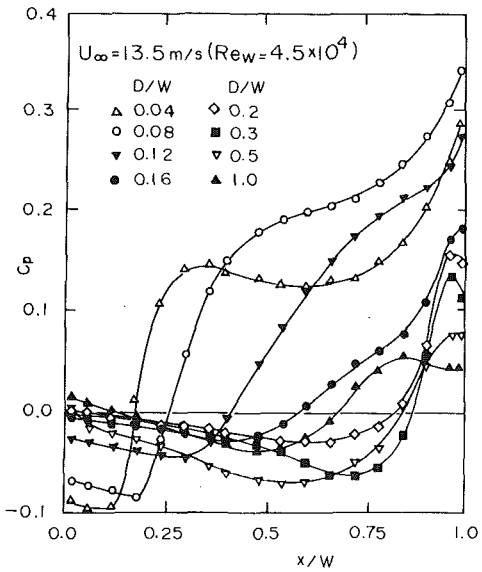

Fig. 4(b) $U_\infty = 13.5$ m/s ($Re_w = 4.5 \times 10^4$)

Fig. 4 **Pressure distribution on the bottom surface**

In Figs. 5(a)–5(d), ratios of h_x to h_m which is the numerically integrated value of h_x, are shown using Reynolds number Re_w as a parameter, which is defined as follows:

$$Re_w = \frac{U_\infty \cdot W}{\nu f} \tag{3}$$

The result in Fig. 5(a) for aspect-ratio $D/W = 0.0$ is the case of isolated surface heated under constant heat flux, which may not rigorously correspond to the heat transfer of a flat plate with an unheated starting section. In Fig. 5(a), the peculiar rise in heat transfer coefficient in region $x/W > 0.7$ is seen; this behavior may be considered to be due mainly to a little heat leakage to the side walls and to the lower part.

In Fig. 5(b), for shallow cavity, with increasing Reynolds number, maximum point is seen in heat transfer distributions. However, with decreasing Reynolds number they shift downstream. Such a maximum point appears as a result of reattachment of separated flow on the bottom surface, which starts from upstream top-corner.

With increasing aspect-ratio D/W, in Fig. 5(c), the contribution of the reattachment of the separated flow to the heat transfer decreases and then recirculating vortex flow formed in front of downstream cavity wall begin to affect the heat transfer on the bottom surface. For the deepest cavity of $D/W = 1.0$, in Fig. 5(d), variation of heat transfer coefficient is small over the entire bottom surface due to weak vortex flow near the surface.

For low Reynolds number, contributions of reattachment on the bottom in shallow cavity and of vortex flow in deeper one to heat

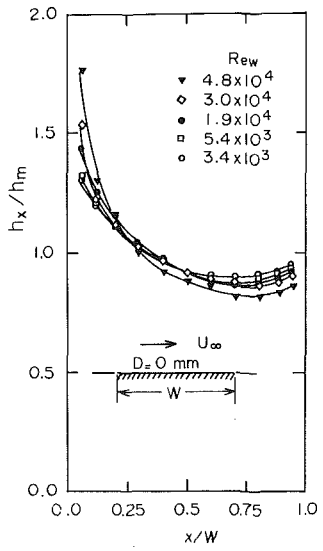

Fig. 5(*a*) *D/W* = 0.0 (isolated heating surface under uniform heat flux)

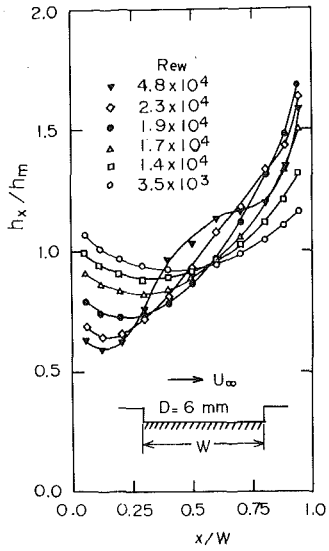

Fig. 5(*c*) *D/W* = 0.12

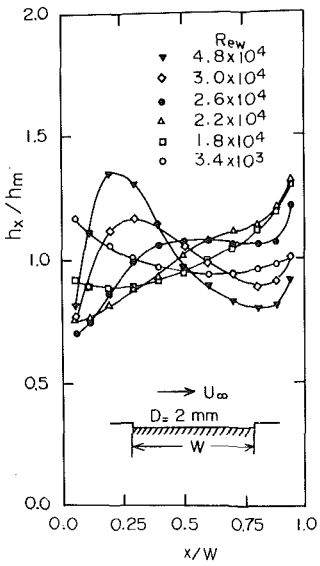

Fig. 5(*b*) *D/W* = 0.04

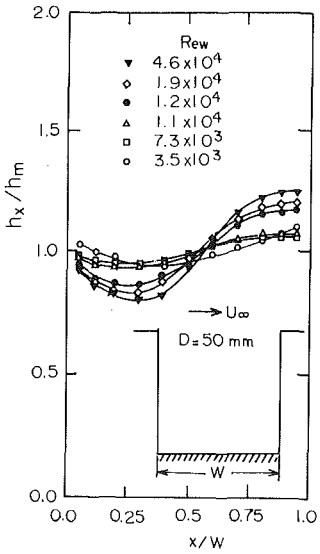

Fig. 5(*d*) *D/W* = 1.0

Fig. 5 Heat transfer distribution on the bottom surface

transfer are not so remarkable. And similar tendency of heat transfer distribution is observed in each figure except for Fig. 5(*a*). Thus, the heat transfer characteristics on the heated bottom surface of the cavities are greatly affected by the separated flow reattachment and vortex flow. Moreover, in discussing the overall heat transfer characteristics of the entire cavity which is practically important, the effects of the shear layer reattachment to the upstream facing wall should be taken into consideration.

In Fig. 6, the relation between mean Nusselt number Nu_m on the bottom surface and the Reynolds number Re_w is shown for several cavities, where Nu_m is defined as $Nu_m = h_m \cdot W/k_f$. The result for $D/W = 0.0$ is presented for comparison.

Heat transfer behavior in the cavity may be divided into approximately three regions: a laminar region for $Re_w \leqq (0.7 \sim 1.5) \times 10^4$, a turbulent region for $Re_w \geqq 2.8 \times 10^4$ and a middle, transient, region for $(0.7 \sim 1.5) \times 10^4 < Re_w < 2.8 \times 10^4$. However, for $D/W = 0.0$ laminar flow is $Re_w \leqq 1.7 \times 10^4$, turbulent flow is $Re_w \geqq 3.5 \times 10^4$ and the middle, transient, region is $1.7 \times 10^4 < Re_w < 3.5 \times 10^4$.

These distinctions are more remarkable for the cavities of lower aspect-ratio; and the transient region tends to extend its range with increasing aspect-ratio.

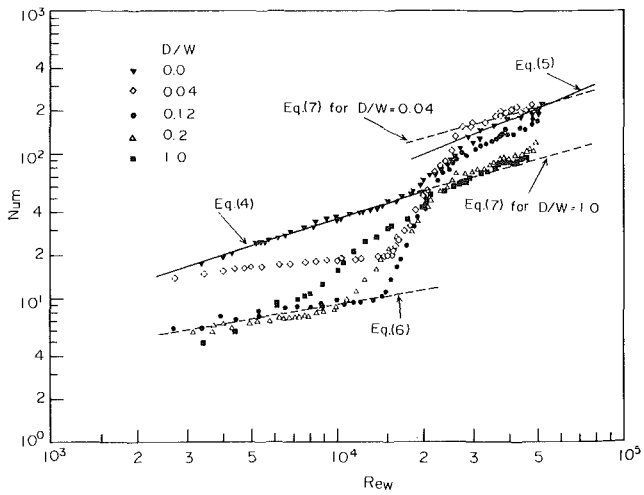

Fig. 6 Variation of mean Nusselt number with Reynolds number

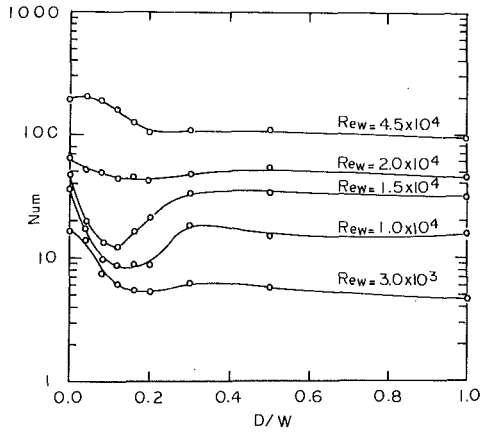

Fig. 7 Variation of mean Nusselt number with aspect-ratio

The correlations between Nu_m and Re_w for the case of isolated heating-surface of $D/W = 0.0$ can be made as follows: in laminar range, $Re_w \leqq 1.7 \times 10^4$,

$$Nu_m = 0.0772 \times Re_w^{2/3} \tag{4}$$

This expression might correspond to the prediction for laminar flow having an unheated starting section with a Reynolds number dependence of $x_0 \propto Re_w^{-0.345}$ ($\fallingdotseq Re_w^{-1/3}$) obtained experimentally in the present study. Comparison with the previous result obtained from heated flat plate without unheated starting section under constant heat flux (e.g., [12]), might reveal that the distance from the leading edge is usually used as a representative length of Nusselt number and Reynolds number, while the cavity width, W, is used as the representative length in equation (4).

In the turbulent range, $Re_w \geqq 3.0 \times 10^4$,

$$Nu_m = 0.0363 \times Re_w^{0.8} \tag{5}$$

may be written, and are shown in Fig. 6. equation (5) agrees considerably with Colburn's equation [11] for turbulent flow over an isolated heating-surface under uniform temperature:

$$\left(\frac{h \cdot W}{k}\right)_{avg} = 0.034 \left(\frac{W \cdot U_\infty}{\nu}\right)^{0.8}, \text{ by Colburn.}$$

On the other hand, in the case of heat transfer in the cavity, the following correlations can be written: in laminar ranges of $Re_w \leqq 1.5 \times 10^4$ for $D/W = 0.08$, $Re_w \leqq 1.4 \times 10^4$ for $D/W = 0.12$, $Re_w \leqq 1.2 \times 10^4$ for $D/W = 0.16$, $Re_w \leqq 1.0 \times 10^4$ for $D = 0.2$, $Re_w \leqq 0.9 \times 10^4$ for $D/W = 0.3$ and 0.5, and $Re_w \leqq 0.7 \times 10^4$ for $D/W = 1.0$, excepting $D/W = 0.04$,

$$Nu_m = 0.427 \times Re_w^{1/3} \tag{6}$$

In this range, Nu_m for all cavities are smaller than that of $D/W = 0.0$; and in equation (6) the term including the aspect-ratio D/W does not appear since the effect of depth on heat transfer is not so remarkable.

In turbulent ranges of $Re_w \geqq 2.8 \times 10^4$ for $D/W \leqq 0.08$, and of $Re_w \geqq 2.5 \times 10^4$ for $D/W \geqq 0.12$, correlation may be written as

$$Nu_m = 0.390 \times Re_w^{1/2} \times (D/W)^{-0.27} \tag{7}$$

In this range, Nu_m for $D/W = 0.04$ shows a somewhat larger value than those for $D/W = 0.0$. This may result because a large effect on heat transfer is experienced due to reattachment of separated flow from the upstream top-corner on the bottom surface. At this point, it might be noted that most of previously reported results are concerned with the flow characteristics in a cavity [1, 2] or numerical method of solution of governing equation [7–9], or the heat transfer of an entirely heated cavity [4, 5, 11].

These correlations in laminar and turbulent ranges for a cavity are indicated by dotted lines in Fig. 6. In these correlations for the cavity, it may be noticed that the exponents proposed differ from those of empirical equations previously reported and are the result of the difference of representative length in the Reynolds number used in the present correlations.

Heat transfer behavior associated with a variation of D/W in laminar, transient and turbulent regions is shown in Fig. 7. On the whole, a considerable change in mean Nusselt number Nu_m is generally seen in the range of $D/W \leqq 0.3$, and Nu_m decreases monotonously with increasing depth in the range of $D/W \geqq 0.3$. For the very shallow cavities, reattachment of separated flow to the bottom surface from upstream top-corner greater affects the heat transfer behavior on the surface. With increasing D/W, a vortex flow occurring in front of the upstream facing wall contribute considerably to the heat transfer on the bottom surface; moreover, the one developing inside the cavity affects the heat transfer on the bottom surface and experiences rather low heat transfer. For each Re_w in Fig. 7, the heat transfer behavior may be understood as follows: For $Re_w = 3.0 \times 10^3$ in laminar flow region, the Nu_m for all aspect-ratio is smaller than the Nu_m for $D/W = 0.0$, while the Nu_m for $D/W = 0.3$ and 0.5 tends to show a somewhat larger value than that for $D/W = 0.12 \sim 0.2$. For $Re_w = 4.5 \times 10^4$ in turbulent flow region, the Nu_m for $D/W = 0.04$ shows a somewhat larger value than that for $D/W = 0.0$. However, for the other D/W, the Nu_m decreases monotonously toward the value for $D/W = 1.0$ with increasing D/W. For $Re_w = (1.0, 1.5 \text{ and } 2.0) \times 10^4$ in the transient flow region, the Nu_m varies, a little complicatedly, depending on the flow patterns inside the cavity. Thus it might be said that the variation of Nu_m on the bottom surface does not always decrease monotonously with increasing D/W.

Summary

Flow patterns inside the cavity at low main flow velocity have been observed by flow visualization using smoke. Heat transfer characteristics on the heated bottom surface have been discussed in relation to the distributions of pressure and heat transfer coefficients. Reattachment of separated flow for shallow cavities and vortex flow for deeper ones had a large effect on the heat transfer behavior on the heated bottom surface. Moreover it was found that, in each cavity, laminar, transient, and turbulent heat transfer regions could be classified. In addition, for both cases of partially heated flat plate and cavities, correlations between Nu_m and Re_w in laminar and turbulent regions were made.

References

1 Roshko, A., "Some Measurements of Flow in a Rectangular Cutout," N.A.C.A. Tech. Note No. 3488, 1955.

2 Tani, I., Iuchi, M., and Komoda, H., "Experimental Investigation of Flow Separation Associated with a Step or Groove," Aeronautical Research Institute, University of Tokyo, Report No. 364, April 1961, pp. 119–136.

3 Charwat, A. F., Roos, J. N., Dewey, F. C., and Hitz, J. A., "An Investigation of Separated Flows—Part 1: The pressure Field," *Journal of the Aerospace Sciences*, Vol. 28, No. 6, June 1961, pp. 457–470.

4 Charwat, A. F., Dewey, F. C., Roos, J. N., and Hitz, J. A., "An Investigation of Separated Flows—Part 2: Flow in Cavity and Heat Transfer," *Journal of the Aerospace Sciences*, Vol. 28, No. 7, July 1961, pp. 513–527.

5 Haugen, R. L., and Dhanak, A. M., "Heat Transfer in Turbulent Boundary-Layer Separation Over a Surface Cavity," ASME JOURNAL OF HEAT TRANSFER, Vol. 89, No. 4, November 1967, pp. 335–340.

6 Kurosaki, Y., Sasada, N., and Nakazawa, S., "Heat Transfer of Separated Flow in Two-Dimensional Cavity," Seventh Annual Symposium of the Heat Transfer Society of Japan, 1968, pp. 49–52.

7 Kawaguti, M., "Numerical Solution of the Navier-Stokes Equations for the Flow in a Two-Dimensional Cavity," *Journal of Physical Society of Japan*, Vol. 16, No. 12, November 1961, pp. 2307–2315.

8 Gosman, A. D., Pun, W. M., Runchal, A. K., Spalding, D. B., and Wolfshtein, M., *Heat and Mass Transfer in Recirculating Flows*, Academic Press, New York, 1969.

9 Torrance, K., Davis, R., Eike, K., Gill, P., Gutman, D., Hsui, A., Lyons, S., and Zien, H., "Cavity Flows Driven by Buoyancy and Shear," *Journal of Fluid Mechanics*, Vol. 51, part 2, 1972, pp. 221–231.

10 Yamamoto, H., Seki, N., and Fukusako, S., "Heat Transfer in a Rectangular Groove with Heated Bottom Surface in Laminar Forced Flow Field," *Trans. JSME*, Vol. 43, No. 371, July 1977, pp. 2662–2669.

11 Seban, R. A., "Heat Transfer and Flow in a Shallow Rectangular Cavity with Subsonic Turbulent Air Flow," *Int. Journal of Heat and Mass Transfer*, Vol. 8, 1965, pp. 1353–1368.

12 Kays, W. M. *Convective Heat and Mass Transfer*, McGraw-Hill, New York, 1966, p. 222.

Shi-chune Yao
Assistant Professor,
Department of Mechanical Engineering,
Carnegie-Mellon University,
Pittsburgh, PA 15213

Convective Heat Transfer of Laminar Droplet Flow in Thermal Entrance Region of Circular Tubes

Convective heat transfer of laminar droplet flow is calculated numerically for the thermal entrance region of circular tube with constant wall temperature. The heat transfer contribution of saturated droplets in the superheated vapor stream is considered as distributed heat sink. In the thermal entrance region, the size and the population density of the droplets are considered as constants. The heat transfer of droplet flow is found to be considerably higher than that of single phase flow. The effects of the droplet characteristics and the wall superheat to the convective heat transfer are studied. Fundamental differences of heat transfers in single phase flow and droplet flow are revealed.

Introduction

In many engineering systems liquid droplets are entrained or introduced into the heated vapor stream. The presence of the saturated droplets in the stream augments the vapor heat transfer from the wall. The heat is transferred from the superheated vapor to the droplets. Additionally the generated vapor from droplets cools the hot vapor stream. The radial temperature gradient near the wall is therefore increased which augments the convective heat transfer.

The emergency core cooling system of a water reactor refloods the dried core from the bottom and induces droplet flow. The droplet flow cools the hot core and prevents the fuel rods from melt down before the reflood quench front arrives. The steam generator of a conventional power plant also encounters droplet flow at the inlet of its superheater. The understanding of the heat transfer behavior of nonequilibrium droplet flow is important to the analyses of the above systems and many other industrial equipments.

Generally, the droplet flow heat transfer are analyzed in one of two approaches. The heat transfer of a droplet moving in vapor stream is first calculated in detail, and then the heat transfer effects of collective droplets to the continuous phase are evaluated. Along this approach, Habib [1] studied the cooling of a hot gas stream in adiabatic ducts by evaporating drops, and Bhatti [2] analyzed the droplet heat transfer in a laminar boundary layer.

On the other hand, when the heat transfer in the continuous phase is of the primary concern the heat transfer effect of the droplets can be regarded as equivalent heat sink distributed in the continuous phase. Sun, Gonzalez, and Tien [3] successfully calculated the laminar droplet flow heat transfer at fully developed condition where the axial temperature gradient of the vapor is assumed to be zero. Their results were further analyzed for parabolic velocity profile by Dix and Anderson [4]. It was found that when the droplet density is low the Nusselt number does not approach 3.65. In the absence of proper explanation, empirical equation was suggested to fit the single phase result when droplet density is low. In applying this result to practical conditions, however, question arises as to the applicability of the fully developed heat transfer result to the entire tube length because both the heat transfer behavior and the length of the thermal entrance region are not known for droplet flow.

The present analysis follows the latter approach to study the convective heat transfer in thermal entrance region of laminar droplet flow. The entrance region convective heat transfer of single phase laminar tube flow has been calculated numerically by Kays [5]. With droplets present in the vapor, the heat transfer in entrance region can be analyzed in the similar manner as in [5] but considering the effect of droplets as distributed heat sink in the vapor stream.

Contributed by the Heat Transfer Division for publication in the JOURNAL OF HEAT TRANSFER. Manuscript received by the Heat Transfer Division July 24, 1979.

Model

In a convective boiling system the droplets are entrained into the vapor stream from the annular flow regime where the vapor is at the saturation state. At downstream of the dryout point of the annular film the vapor flow may be assumed to be parabolic profile. Due to the relatively low heat transfer rate of the droplet flow the wall temperature is likely to be at a level higher than the Leidenfrost temperature of the droplets. It has been reported by the author that in film boiling the direct contact heat transfer between the liquid and the wall at this temperature is insignificant as compared with the vapor convective heat transfer [6]. For the same reason, the direct contact heat transfer between droplets and wall can be neglected for droplet flow at this condition. In addition, the radiative heat transfer can also be neglected if the wall temperature is assumed to be not too high. Finally, the droplet-vapor heat transfer will be the only significant means the droplets remove heat from the wall.

At the tube inlet, all the droplets are assumed to be the same size. In laminar flow a droplet may move radially due to the presence of radial temperature or velocity gradients [7]. A droplet will be pushed away from the wall due to its nonuniform evaporation near the wall. A rotating droplet will move either toward or away from the wall depending upon the relative velocity between the droplet and the surrounding vapor. These radial mixings make each droplet to evaporate at a same rate so that the droplets are of uniform size at each tube cross-section. If it is assumed that the droplets are not very small or their latent heat of vaporization is high, the size of droplets can be considered as a constant over the entire entrance region. In addition, if the droplet density is not very high, the fully developed vapor flow may not be seriously affected by the generated vapor from droplets or by the motion of droplets.

This model can be applied to some special problems with proper assumptions. For example, during the bottom reflooding of a nuclear reactor core the droplet flow heat transfer occurs above the quench front. The droplets are ejected from the quench front at a speed different from the local vapor velocity. However, the relative velocities of small droplets with respect to the vapor will reach their terminal velocities in a short distance. Therefore the hydrodynamic condition can be assumed to be fully developed near the quench front such that the present model for thermal entrance region can be applied as a first approximation to this problem.

If the chemical composition of the vapor and the droplet are identical the mass transfer due to concentration difference will not occur. Heat is transferred from the superheated vapor to the saturated droplets, and the subsequently generated vapor will be heated up to the vapor stream temperature.

As a result, the equivalent heat sink per unit volume is

$$n\,\pi d^2 h_d(T - T_s) + n\pi d^2 h_d(T - T_s)C_p(T - T_s)/h_{fg} \qquad (1)$$

where

$$h_d = \frac{k}{d}(2.0 + 0.74\mathrm{Re}_d^{0.5}P_r^{0.33}) \quad (2)$$

is the heat transfer coefficient from superheated vapor to a saturated droplet [8].

Another way of interpreting the heat sink per unit volume is to recognize that the quality of the superheated vapor is

$$x_v = 1 + C_p(T - T_s)/h_{fg} \quad (3)$$

Therefore, the heat sink per unit volume becomes

$$n\pi d^2 h_d (T - T_s) x_v \quad (4)$$

which is the heat transferred from the superheated vapor to the saturated droplets multiplying the quality of the vapor. If the vapor is at saturation state, the generated vapor due to droplet evaporation will not cool the vapor stream. This is the case when x_v equals 1.0 in equation (4).

The droplet Reynolds number in equation (2) is based on the relative velocity between droplet and vapor, which will be different for vertical and horizontal tube flows. In general, the droplets will undergo terminal falling in the vapor. However, droplets may also have radial motion due to the various mechanisms as pointed out in [7]. Since the detailed dynamics of evaporating droplets is not well reported in the open literature, the accurate calculation of the relative velocity will not be emphasized in this paper.

For the purpose of illustration, vertical tube flows will be considered specifically and the terminal falling velocity can be considered as the dominant contribution to the relative velocity.

Formulations

With the fully developed parabolic velocity profile and the equivalent heat sink described in equation (1), the energy equation for the vapor phase can be written as

$$2\rho_v C_p V\left(1 - \left(\frac{r}{r_0}\right)^2\right)\frac{\partial T}{\partial x} = \frac{k}{r}\frac{\partial}{\partial r}\left(r\frac{\partial T}{\partial r}\right) - \beta(T - T_s)\left[1 + \frac{C_p(T - T_s)}{h_{fg}}\right] \quad (5)$$

where the droplet-vapor heat transfer constant is defined as

$$\beta = n\pi d^2 h_d \quad (6)$$

with the initial and boundary onditions

$$T = T_s \text{ at } x = 0 \quad (7)$$

$$T = T_w \text{ at } r = r_0 \quad (8)$$

and

$$\frac{\partial T}{\partial r} = 0 \text{ at } r = 0 \quad (9)$$

With the vapor temperature profile available, the Nusselt number is evaluated from the temperature gradient at the wall. That is

$$\mathrm{Nu}_x = 2r_0\left(\frac{\partial T}{\partial r}\right)_{r=r_0} \Big/ (T_w - T_m) \quad (10)$$

where T_m is the bulk mean temperature of the vapor

$$T_m = \frac{4}{r_0^2}\int_0^{r_0} T\left(1 - \left(\frac{r}{r_0}\right)^2\right) rdr \quad (11)$$

The above equations can be nondimensionalized and presented in terms of

$$R = r/r_0 \quad (12)$$

$$X = \frac{(x/r_0)}{\mathrm{RePr}} = \frac{x\alpha}{2Vr_0^2} \quad (13)$$

and

$$\theta = (T_w - T)/(T_w - T_s) \quad (14)$$

$$\theta_m = (T_w - T_m)/(T_w - T_s) \quad (15)$$

where the $\mathrm{R_e}$ is the vapor flow Reynolds number. Finally the set of equations become

$$(1 - R^2)\frac{\partial\theta}{\partial X} = \frac{1}{R}\frac{\partial}{\partial R}\left(R\frac{\partial\theta}{\partial R}\right) + B(1 - \theta)[1 + (1 - \theta_m)C] \quad (16)$$

where the droplet parameter B and the wall superheat parameter C are defined as

$$B = \beta \mathrm{r_0}^2/\mathrm{k} \quad (17)$$

$$C = C_p(T_w - T_s)/h_{fg} \quad (18)$$

with the initial and boundary conditions

$$\theta = 1 \text{ at } X = 0 \quad (19)$$

$$\theta = 0 \text{ at } R = 1 \quad (20)$$

$$\frac{\partial\theta}{\partial R} = 0 \text{ at } R = 0 \quad (21)$$

and

$$\mathrm{Nu}_x = \frac{2}{\theta_m}\left(\frac{\partial\theta}{\partial R}\right)_{R=1} \quad (22)$$

with

$$\theta_m = 4\int_0^1 \theta(1 - R^2)\, RdR \quad (23)$$

In equation (16) the heat sink term has been linearized by substituting θ_m for θ in the term of C. The error introduced by this linearization is small, which will be illustrated in a later section.

Nomenclature

B = droplet parameter, defined in equation (17)
C = wall superheat parameter, defined in equation (18)
C_p = specific heat of vapor
d = droplet diameter
d_0 = original droplet diameter
h_d = heat transfer coefficient between the vapor and the droplet
h_{fg} = latent heat of vaporization
k = thermal conductivity of vapor
n = droplet number density
Nu_x = local Nusselt number
Nu_s = local Nusselt number defined in terms of T_s
Nu_∞ = Nusselt number at fully developed condition
Pr = Prandtl number of the vapor
q_w = wall heat flux
r = radial position
r_0 = radius of the circular tube
R = nondimensional radial position, defined in equation (12)
$\mathrm{R_e}$ = Reynolds number of vapor flow in tubes
Re_d = droplet Reynolds number, based upon droplet size and its relative velocity to vapor
T = temperature of the vapor
T_s = saturation temperature
T_w = wall temperature
T_m = bulk mean temperature of the vapor
V = average vapor velocity
w = heat sink parameter, defined in equation (34)
x = axial position
x_v = quality of vapor phase
X = nondimensional axial position, defined in equation (13)
α = thermal diffusivity of the vapor $k/\rho_v C_p$
β = droplet-vapor heat transfer constant, defined in equation (6)
ϵ_ℓ = emissivity of droplets
θ = nondimensional temperature, defined in equation (14)
θ_m = nondimensional bulk mean temperature, defined in equation (15)
λ = a heat transfer dependent parameter, used in equation (27)
ρ_v = vapor density
σ = Stefan-Boltzmann constant

In the present study the values of B and C are constants. The quantity of the droplet parameter B is determined by the droplet size, number density, and the droplet-vapor heat transfer coefficient. Its value varies in a relatively wide range. In the present study the range of B covers 0 to 120. Of course the larger the value of B the more the assumptions of constant droplet size and fixed velocity profile deviate from practical situation. The quantity of the wall superheat parameter C depends upon the wall temperature and the latent heat of vaporization of the droplet, and varies in a relatively narrow range. For water in steam at atmospheric pressure the value of C varies from 0.1 to 0.5 for wall temperatures between 220 and 700°C.

Equations (16–23) are solved numerically by finite difference method using a DEC-20 computer. All the variables are put into double precision to reduce the truncation error. The numerical stability is achieved by using implicit scheme for the differential equation (16). A tridiagnol matrix is generated in this scheme and the Gaussian elimination method is used to solve it [9]. In order to reduce the discretization error, the radial increment of R is selected as 0.05 and the axial increment of X is set at 0.0005.

The radial temperature profile near the wall is constructed as a second order polynomial with its constants determined from calculated temperatures at three discrete radial locations near the wall. The temperature profile is then used to evaluate the wall temperature gradient in equation (22) for the local Nusselt number. The θ_m is integrated from the equation (23) using trapezoidal rule.

Limitations of this Model

In the present analysis of droplet flow the radiative heat transfer is considered to be negligible as compared with the convective heat transfer. The droplets participate in the convection as heat sinks and in the radiative transfer as absorbing medium. Using an order of magnitude analysis, the heat sink per unit length of tube can be presented as

$$\beta(T_m - T_s)\pi r_0^2 \tag{24}$$

The radiative transfer from the wall to droplets can be evaluated from

$$\epsilon_\ell 2\pi r_0\, \sigma(T_w{}^4 - T_s{}^4) \tag{25}$$

where ϵ_ℓ is the emissivity of droplets given in [3]. Here the radiative absorption of vapor is neglected. Therefore, the radiative heat transfer can be neglected if

$$\frac{\beta(T_w - T_s)r_0}{2\epsilon_\ell \sigma(T_w{}^4 - T_s{}^4)} \gg 1 \tag{26}$$

where T_w is used instead of T_m for the simplicity of the evaluation.

In the model of this analysis it is assumed that droplets are well dispersed in the stream and having a constant size. This assumption is not true at locations far downstream of the entrance because the droplet size will diminish. The range, where the present analysis is valid, can be determined from the variation of the heat sink along the stream.

As a simple approach, the heat sink decreases along the stream due to both the decreasing of the droplet size and the reduction of the droplet density. Generally, the droplet size diminishes according to

$$d^2 = d_0{}^2 - 2\,\lambda\, t \tag{27}$$

where the λ is a heat transfer dependent value [1, 2] which can be regarded as a constant in the present consideration. If the original droplet size is not very small the variation of droplet size at entrance region can be considered negligible. Thus, the decreasing of droplet density due to the evaporation will be the only important factor to the variation of heat sink. The vapor generation per unit volume of mixture for unit length of flow is

$$\frac{n\pi d^2 h_d(T_m - T_s)}{\rho_v h_{fg}} \frac{1}{V} \tag{28}$$

If 20 percent dilution of droplets is allowed in present model, the present analysis will be applicable to a range of entrance region

$$X_0 = \left(\frac{0.2\,\rho_v h_{fg} V}{n\pi d^2 h_d(T_m - T_s)}\right)\frac{\alpha}{2Vr_0{}^2} \tag{29}$$

or

$$X_0 = \frac{0.1}{BC} \tag{30}$$

Results and Discussion

The calculated local Nusselt numbers for the thermal entrance region of laminar droplet flow in a circular tube are shown in Fig. 1 at various axial locations with the droplet parameter B and wall superheat parameter C as indices. The limitation of present analysis is up to the X_0 which is evaluated from equation (30) with a typical value of $C = 0.25$. When there are no droplets present in the vapor stream the value of B equals zero. At this condition the calculated local Nusselt numbers should equal the values reported by Kays [5] for single phase heat transfer. Comparisons between the present result to that in reference [5] show differences which are less than 0.5 percent, and the fully developed Nusselt number is 3.65.

Fig. 1 indicates that the local Nusselt number is sensitive to the variation of the droplet parameter B in the range of present consideration. The larger the value of B the higher the local Nusselt number. However, the local Nusselt number appears to be less sensitive to the variation of the wall superheat parameter C which is in the range of 0 to 1.0. For the same reason, the error introduced by substituting the θ_m for θ in linearizing the energy equation can be considered as small, because the effect of this approximation will be of the same order of magnitude as that of the variation of C in present study.

The Nusselt number can also be presented in a form of

$$\mathrm{Nu}_x = \left[\frac{2q_w r_0}{k(T_w - T_s)}\right] \Big/ \theta_m \tag{31}$$

$$= \mathrm{Nu}_s/\theta_m \tag{32}$$

The Nusselt number is essentially the ratio of a newly defined Nusselt number Nu_s and the nondimensional bulk mean temperature of the vapor. This Nu_s is defined in terms of saturation temperature of the fluid instead of the bulk mean temperature. The Nu_s and the θ_m along the axial locations are presented in Figs. 2 and 3, respectively. Both of these sets of curves show monotonic variations. For very diluted droplet flow (for example, $B = 0.05$) these curves are very close to that of single phase flow, which is consistent with what would be expected.

The fully developed Nusselt number of laminar droplet flow with parabolic velocity profile has been reported by Dix and Anderson [4]. That is

$$\mathrm{Nu}_\infty = \frac{2wI_1(w)}{I_0(w) - 8I_2(w)/w^2} \tag{33}$$

where

$$w = [B(1 + (1 - \theta_{m\infty})C)]^{1/2}, \tag{34}$$

and I is the modified Bessel function of the first kind.

The comparison of the equation (33) and the calculated fully developed Nusselt number of present study is shown in Fig. 4. It is in-

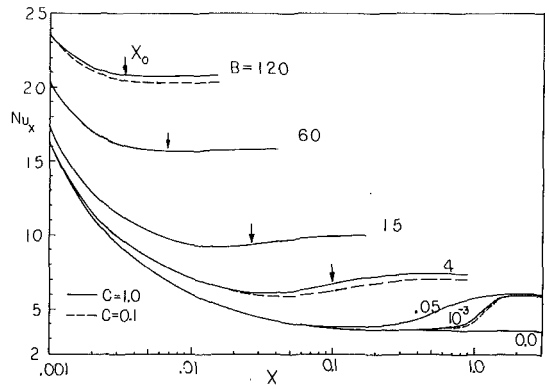

Fig. 1 The variation of local Nusselt number Nu_x with axial locations

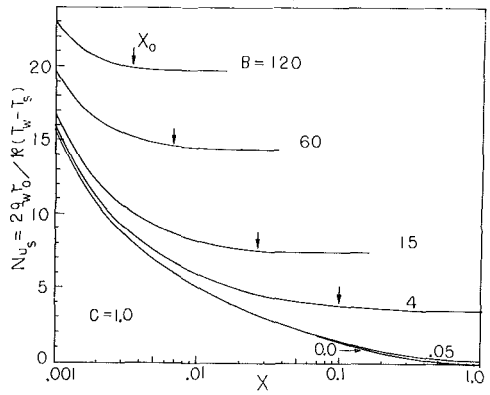

Fig. 2 The variation of Nu_s with axial locations

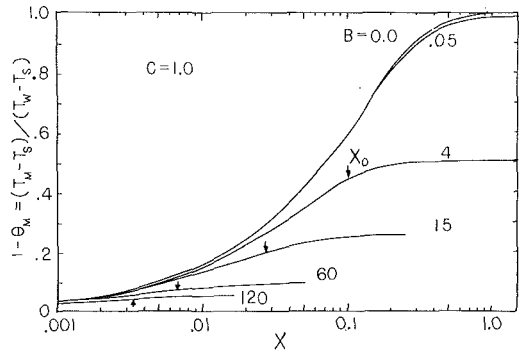

Fig. 3 The variation of bulk mean temperature with axial locations

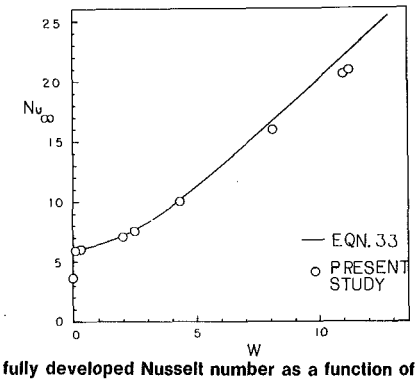

Fig. 4 The fully developed Nusselt number as a function of the heat sink parameter w

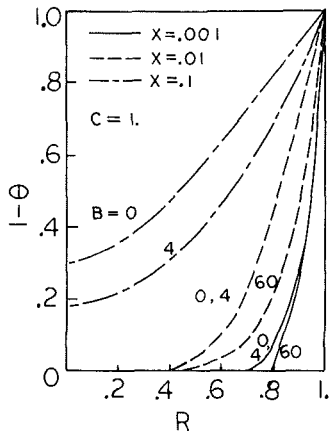

Fig. 5 The comparisons of radial temperature profiles for different droplet parameters B at locations

teresting to find from both results that when the value of w approaches zero the Nu_∞ approaches 6.0 instead of 3.65. This feature also appears clearly in Fig. 1. Regardless of the smallness of B values the fully developed Nusselt number of droplet flow is always about 6. In fact, the fully developed behavior occurs mostly beyond the position of X_0; therefore the above discussion is subject to the accuracy of present model.

When the value of B is very small the X_0 can be very large. However, the small B would imply very low droplet density if the droplet size is assumed to be not too fine. Here the present analysis is also not accurate because the assumption of well dispersed droplets is not adequate when droplet density is very low. As a result, the deviation of the fully developed Nusselt number at low B's from the single phase result is not a critical point of the discussions.

Along the flow direction of a tube which has constant wall temperature, the wall heat flux decreases while the effective heat sink increases because the thermal field gradually penetrates toward the centerline of the tube. This unique feature of droplet flow is further elaborated in Fig. 5 where the radial temperature profiles are presented for different values of B at axial locations. Without droplets the vapor temperature profiles are similar after they reach the tube centerline. When droplets are present in the vapor stream, the temperature profile also penetrates toward the tube center line, however, with a much slower rate. The stronger the heat sink the less the penetration at a same axial location. In other words, the central core of the vapor stream is less influenced by the heated wall for droplet flow with higher droplet parameter B.

In practical application, it is interesting to know that, unlike the single phase heat transfer, the energy balance equation does not give the explicit quantitative relationship between the wall heat flux and the bulk mean temperature. The energy balance equation for the vapor in droplet flow can be written as

$$2\pi r_0 q_w = \pi r_0^2 V \rho_v C_p \frac{dT_m}{dX} + \int_0^{r_0} n\pi d^2 h_d (T - T_s)\left[1 + \frac{C_p(T - T_s)}{h_{fg}}\right] 2\pi r dr \quad (35)$$

Without knowing the vapor temperature profile the heat sink term can not be evaluated. Therefore, Figs. 2 and 3 are recommended for the direct evaluation of the wall heat flux and the bulk mean temperature of the vapor.

Conclusion

The present analysis revealed some unique heat transfer behaviors of laminar non-equilibrium droplet flow. The approximation of droplet heat transfer contribution by equivalent heat sink in the continuous phase is demonstrated to be very effective in handling complicated problems.

Acknowledgment

The author is grateful for the assistance of Mr. J. Zerpa, Mechanical Engineering Student, Carnegie-Mellon University.

References

1 Habib, I. S., "The Interaction of a Hot Gas Flow and a Cold Liquid Spray in Chennels," ASME JOURNAL OF HEAT TRANSFER, Vol. 98, 1976, pp. 421–426.

2 Bhatti, M. S., "Dynamics of a Vaporizing Droplet in Laminar Entry Region of a Straight Channel," ASME JOURNAL OF HEAT TRANSFER, Vol. 99, 1977, pp. 574–579.

3 Sun, K. H., Gonzalez-Santalo, J. M., and Tien, C. L., "Calculations of Combined Radiation and Convection Heat Transfer in Rod Bundles Under Emergency Cooling Conditions," ASME JOURNAL OF HEAT TRANSFER, Vol. 98. 1976, pp. 414–420.

4 Dix. G. E., and Andersen, J. G. M., "Spray Cooling Heat Transfer for a BWR Fuel Bundle," *Thermal and Hydraulic Aspects of Nuclear Reactor Safety*, Vol. 1., *Light Water Reactor*, Ed. O. C. Jones and S. G. Bankoff, ASME, 1977, p. 236.

5 Kays, W. M., "Numerical Solutions for Laminar-Flow Heat Transfer in Circular Tubes," *Trans. ASME*, Vol. 77, 1955, pp. 1265–1274.

6 Yao, S. C., and Henry, R. E., "An Investigation of the Minimum Film Boiling Temperature on Horizontal Surfaces," ASME JOURNAL OF HEAT TRANSFER, Vol. 100, 1978, pp. 260–267.

7 Ganic, E. N., and Rohsenow, W. M., "On the Mechanisms of Liquid Drop Deposition in Two Phase Flow," ASME Paper No. 76-WA/HT-18.

8 Lee, K., and Ryley, D. J., "The Evaporation of Water Droplets in Superheated Steam," ASME JOURNAL OF HEAT TRANSFER, Vol. 90, 1968, pp. 445–451.

9 Carnahan, B., Luther, H., and Wilkes, J., *Applied Numerical Methods* John Wiley & Sons, Inc., 1969, p. 270.

S. K. Griffiths
NSF Graduate Fellow,
Department of Mechanical and Industrial Engineering,
University of Illinois at Urbana-Champaign
Urbana, IL 61801
Student Mem. ASME
F. A. Morrison, Jr.
University of California,
Lawrence Livermore Laboratory,
Livermore, CA 94550
Mem. ASME

Low Peclet Number Heat and Mass Transfer from a Drop in an Electric Field

An electric field, when applied to a dielectric drop suspended in another such fluid, generates a circulating motion. The low Peclet number transport from the drop is investigated analytically using a regular perturbation expansion. A digital computer is used to obtain exact solutions to the resulting equations. These solutions yield accurate results up to a Peclet number of at least 60.

Introduction

When a uniform electric field is applied to a dielectric fluid in which a drop of another dielectric fluid is suspended, a charge buildup occurs at the drop/continuous phase interface. The field, acting on this charge distribution, produces stresses on the drop surface. The tangential stress component is balanced by fluid motion in the neighborhood of the interface. Such flow will increase the heat or mass transfer rate between the drop and the continuous phase. Consequently, the flow generated by an electric field is of practical interest for direct contact exchange between immiscible liquids.

Taylor [1] analyzed the creeping motion generated by an electric field imposed on a spherical drop. It was found that either of two directions of circulating flow are produced. For either type, the streamlines describing such flow inside and outside a drop are shown in Fig. 1.

Transient heat and mass transfer for high Peclet number flow generated by an electric field was analyzed by Morrison [2]. It was found that the Nusselt number is proportional to the magnitude of the applied field. Experimental studies by Thornton [3], and Kozhukhar and Bologa [4] indicate remarkable increases in heat transfer and chemical extraction rates.

The purpose of this study is to examine the low Peclet number transfer in this electroconvective, creeping flow. Creeping fluid motion is characterized by negligibly small Reynolds number. Since dielectric fluids possess high Prandtl or Schmidt numbers, transport can occur over the full range of Peclet number.

Governing Equations

The flow generated by an electric field, outside a spherical drop of radius a is given by the Stokes stream function

$$\psi = Ua^2[(a/r)^2 - 1](1 - Z^2)Z \tag{1}$$

where $Z = \cos(\theta)$. As shown in Fig. 1, r is the radial distance from the drop center and θ is the polar angle measured from the axis of symmetry. The scalar U is the maximum fluid speed produced by the electric field. This maximum occurs at the interface $r = a$, and $\theta = \pi/4$ and $3\pi/4$. Taylor [1] found that

$$U = \frac{-9\,E^2 a\kappa_2}{8\pi(2 + \sigma_2/\sigma_1)^2} \frac{(\sigma_2\kappa_1)/(\sigma_1\kappa_2) - 1}{5(\mu_1 + \mu_2)} \tag{2}$$

E is the magnitude of the applied field. κ, σ, and μ are the dielectric constant, electrical conductivity, and viscosity, respectively. The subscript 1 refers to the surrounding fluid. The subscript 2 refers to the drop.

It is observed that when the ratio $(\sigma_2\kappa_1)/(\sigma_1\kappa_2)$ is greater than unity, circulation is from the equator to the poles and vice versa when $(\sigma_2\kappa_1)/(\sigma_1\kappa_2)$ is less than unity. It is further observed that the speed of circulation is dependent on the sum of the viscosities, but not on their ratio.

The individual velocity components are related to the stream function by the equations

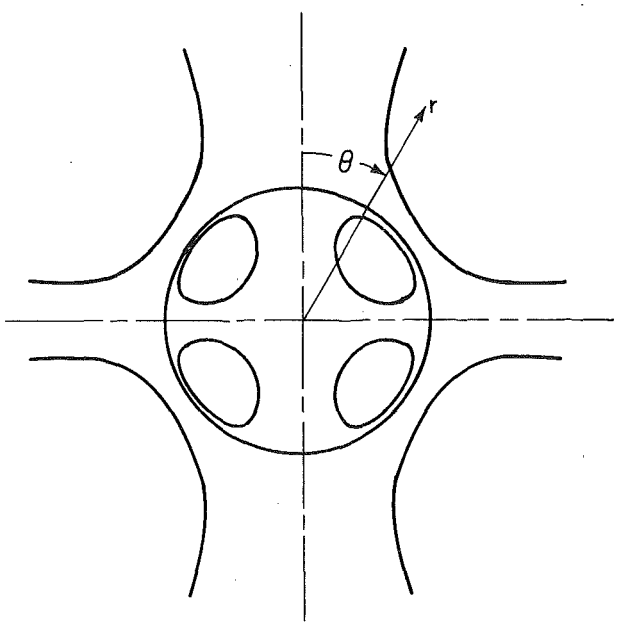

Fig. 1 Streamlines of the electrically driven circulating flow

$$v_r = -\frac{1}{r^2}\frac{\partial\psi}{\partial Z} \tag{3}$$

and

$$v_\theta = -\frac{1}{r(1 - Z^2)^{1/2}}\frac{\partial\psi}{\partial r} \tag{4}$$

The steady-state temperature distribution is governed by the energy equation

$$\alpha\nabla_r{}^2 t = \vec{V} \cdot \nabla_r t \tag{5}$$

where t is the local temperature, α is the thermal diffusivity, and $\vec{V}$ is the local fluid velocity. Subscripts are used on the vector operators to denote the appropriate radial variable.

The governing equations for mass transfer are analogous to those for heat transfer and need not be written separately. The corresponding expressions for mass transfer are obtained by replacing temperature by concentration and thermal diffusivity by molecular diffusivity. The analysis of mass transfer additionally requires the introduction of a distribution coefficient for the interface boundary condition.

Restricting our attention to the case where the dominant thermal resistance is found outside the drop, we seek to solve the energy equation in that region.

Dimensionless Formulation

The dimensionless distance from the drop center is taken to be

$$R = \frac{r}{a} \tag{6}$$

Contributed by the Heat Transfer Division for publication in the JOURNAL OF HEAT TRANSFER. Manuscript received by the Heat Transfer Division July 31, 1978.

which is everywhere positive. The dimensionless temperature T is defined by

$$T = (t - t_\infty)/(t_s - t_\infty) \tag{7}$$

where t_∞ is the fluid temperature far from the drop and t_s is the drop surface temperature. The Peclet number associated with the flow generated by an electric field is defined in terms of the maximum circulation speed U and the thermal diffusivity of the fluid outisde the drop.

$$\mathrm{Pe} = \frac{2Ua}{\alpha_1} \tag{8}$$

For convenience, the parameter

$$\epsilon = \frac{1}{2}\mathrm{Pe} \tag{9}$$

is introduced. The dimensionless velocity components are

$$u_r = \frac{v_r}{U} \tag{10}$$

and

$$u_\theta = \frac{v_\theta}{U} \tag{11}$$

Applying these definitions, the steady-state energy equation reduces to

$$\frac{1}{R^2}\frac{\partial}{\partial R}\left(R^2\frac{\partial T}{\partial R}\right) + \frac{1}{R^2}\frac{\partial}{\partial Z}\left[(1-Z^2)\frac{\partial T}{\partial Z}\right] = \epsilon\left[u_r\frac{\partial T}{\partial R} - \frac{u_\theta}{R}(1-Z^2)^{1/2}\frac{\partial T}{\partial Z}\right] \tag{12}$$

In dimensionless form, the boundary conditions for equation (12) are

$$T = 1 \quad \text{at} \quad R = 1 \tag{13}$$

and

$$T \to 0 \quad \text{as} \quad R \to \infty \tag{14}$$

Zeroth Order Solution

Substituting velocities found from the stream function (1) into the dimensionless energy equation (12) yields

$$\nabla_R{}^2 T = \epsilon\left[(R^{-4} - R^{-2})(3Z^2-1)\frac{\partial T}{\partial R} + 2R^{-5}(Z^2-1)Z\frac{\partial T}{\partial Z}\right] \tag{15}$$

Again, a subscript is used on the vector operator to denote the appropriate radial variable. The solution of equation (15), for small ϵ, is sought in the form of a regular perturbation expansion about the conduction solution.

It is noted that a regular expansion fails when used in an attempt to analyze transport from a translating sphere in Stokes flow [5]. The reason for this failure is that the fluid velocity does not approach zero as r increases without bound. Therefore, in some region far from the sphere, the convection and conduction contributions to transport will be of the same order of magnitude. More graphically, the fluid velocity associated with a translating sphere is $0(U)$ far from the body. The conduction temperature distribution, however, falls off inversely with distance from the sphere center. Hence, as r increases without bound, the ratio of the convection to the conduction flux is

$$\frac{\vec{V}\cdot\nabla T}{\alpha\nabla^2 T} = 0[(r/a)\mathrm{Pe}] \tag{16}$$

Conduction clearly cannot be the dominant mode of transport far from the body, regardless of how small Pe may be. This constitutes a contradiction of assumption and demonstrates that the conduction solution is not everywhere a valid approximation for undertaking a perturbation analysis of transfer from a translating body.

Examining the circulating flow generated by an electric field, it is observed that the fluid velocity far from the drop is $0(Ua^2/r^2)$. In this instance, the ratio of the convection to the conduction flux far from the body becomes

$$\frac{\vec{V}\cdot\nabla T}{\alpha\nabla^2 T} = 0[(a/r)\mathrm{Pe}] \tag{17}$$

Equation (17) indicates that throughout the fluid, conduction will be the dominant mode of transfer provided that Pe is sufficiently small. Therefore, a regular perturbation is appropriate and a solution of the energy equation (15) may be written in the form

$$T = T_0 + \epsilon T_1 + \epsilon^2 T_2 + \ldots \tag{18}$$

Satisfying the boundary conditions given in equation (13) and equation (14) for all ϵ requires that

$$T_0 = 1 \quad \text{at} \quad R = 1 \tag{19}$$

$$T_0 \to 0 \quad \text{as} \quad R \to \infty \tag{20}$$

and that

$$T_i = 0 \quad \text{at} \quad R = 1 \tag{21}$$

$$T_i \to 0 \quad \text{as} \quad R \to \infty \tag{22}$$

for higher order terms.

Corresponding to the form of equation (18), an expression for the heat or mass transfer coefficient will be sought in the form

$$\mathrm{Nu} = \mathrm{Nu}_0 + \epsilon\mathrm{Nu}_1 + \epsilon^2\mathrm{Nu}_2 + \ldots \tag{23}$$

Substituting equation (18) into equation (15) and grouping like powers of ϵ leads to the recursive expression

$$\nabla_R{}^2 T_i = (R^{-4} - R^{-2})(3Z^2-1)\frac{\partial T_{i-1}}{\partial R} + 2R^{-5}(Z^2-1)Z\frac{\partial T_{i-1}}{\partial Z} \qquad i = 1, 2, 3, \ldots \tag{24}$$

As the entire right-hand side of equation (24) is known, it is a Poisson equation. T_0 describes the temperature distribution for transfer by conduction only and is given by

$$\nabla_R{}^2 T_0 = 0 \tag{25}$$

Nomenclature

a = sphere radius
$A(N)$ = function defined by equation (36)
$B(N)$ = function defined by equation (37)
$C(N)$ = function defined by equation (38)
$D(N)$ = function defined by equation (40)
E = magnitude of applied field
$E(N)$ = function defined by equation (41)
$f(R)$ = function defined by equation (28)
$G(N)$ = function defined by equation (42)
Nu = Nusselt number
Pe = Peclet number
$P_N(Z)$ = Legendre polynomial
r = spherical radial position
R = dimensionless spherical radial position
t = temperature
T = dimensionless temperature
u_r = dimensionless radial velocity component
u_θ = dimensionless tangenital velocity component
U = maximum circulation speed
v_r = radial velocity component
v_θ = tangential velocity component
$\vec{V}$ = velocity vector
Z = cos (θ)
α = thermal diffusivity
ϵ = variable defined by equation (9)
κ = dielectric constant
θ = polar angle
μ = viscosity
σ = electrical conductivity
ψ = Stokes stream function

Subscripts

1 = outside drop
2 = inside drop
i = order of solution
N = variable defined by equation (28)

Superscript

i = order of solution

The well known solution to equation (25) which satisfies the specified boundary conditions is

$$T_0 = \frac{1}{R} \tag{26}$$

The zeroth order contribution to heat transfer is also well known.

$$\mathrm{Nu}_0 = 2 \tag{27}$$

Higher Order Terms

To solve for higher order terms, the solution to equation (24) is sought in the form

$$T_i = \sum_N f_N{}^i(R) P_N(Z) \tag{28}$$

where $P_N(Z)$ is the Nth order Legendre polynomial. To satisfy the boundary conditions given in equation (21) and equation (22) for all Z, we must have

$$f_N{}^i(R) = 0 \quad \text{at} \quad R = 1 \tag{29}$$

and

$$f_N{}^i(R) \to 0 \quad \text{as} \quad R \to \infty \tag{30}$$

By making the substitution indicated in equation (28), equation (24) may be rewritten as

$$\sum_N \left\{ P_N(Z) \frac{1}{R^2} \frac{d}{dR}\left[R^2 \frac{df_N{}^i(R)}{dR}\right] + \frac{1}{R^2} f_N{}^i(R) \frac{d}{dZ} \cdot \left[(1 - Z^2) \frac{dP_N(Z)}{dZ}\right]\right\} =$$

$$\sum_N \left\{ P_N(Z)(R^{-4} - R^{-2})(3Z^2 - 1) \frac{df_N{}^{i-1}(R)}{dR} + 2R^{-5} f_N{}^{i-1}(R)(Z^2 - 1) Z \frac{dP_N(Z)}{dZ}\right\} \tag{31}$$

It is observed that a portion of equation (31) may be simplified using Legendre's equation.

$$\frac{d}{dZ}\left[(1 - Z^2) \frac{dP_N(Z)}{dZ}\right] = -N(N+1) P_N(Z) \tag{32}$$

If the identities

$$(Z^2 - 1) \frac{dP_N(Z)}{dZ} = NZP_N(Z) - NP_{N-1}(Z) \tag{33}$$

and

$$ZP_N(Z) = \frac{(N+1)P_{N+1}(Z) + NP_{N-1}(Z)}{2N+1} \tag{34}$$

are appropriately applied, equation (31) may be further simplified.

$$(3Z^2 - 1)P_N(Z) = A(N)P_{N+2}(Z) + B(N)P_N(Z) + C(N)P_{N-2}(Z) \tag{35}$$

where

$$A(N) = 3(N+1)(N+2)/(2N+3)(2N+1) \tag{36}$$

$$B(N) = \frac{3(N+1)^2}{(2N+3)(2N+1)} + \frac{3N^2}{(2N-1)(2N+1)} - 1 \tag{37}$$

and

$$C(N) = 3N(N-1)/(2N-1)(2N+1) \tag{38}$$

$$(Z^2 - 1)Z \frac{dP_N(Z)}{dZ} = D(N)P_{N+2}(Z) + E(N)P_N(Z) + G(N)P_{N-2}(Z) \tag{39}$$

where

$$D(N) = N(N+1)(N+2)/(2N+3)(2N+1) \tag{40}$$

$$E(N) = \frac{N(N+1)^2}{(2N+3)(2N+1)} - \frac{N^2(N+1)}{(2N-1)(2N+1)} \tag{41}$$

and

$$G(N) = -N(N-1)(N+1)/(2N-1)(2N+1) \tag{42}$$

At this point it is clear that equation (31) may be solved termwise. The Nth term of the left-hand side is comprised of expressions involving $P_N(Z)$ only. The Nth term of the right-hand side will, however, contain expressions involving $P_{N+2}(Z)$, $P_N(Z)$, and $P_{N-2}(Z)$. If the right-hand side is expanded and terms containing like order Legendre polynomials are equated, equation (31) may be written as

$$\frac{1}{R^2}\frac{d}{dR}\left[R^2 \frac{df_N{}^i(R)}{dR}\right] - \frac{1}{R^2} N(N+1) f_N{}^i(R) = (R^{-4} - R^{-2}) \cdot \left[A(N-2) \frac{df_{N-2}{}^{i-1}(R)}{dR} + B(N) \frac{df_N{}^{i-1}(R)}{dR} + C(N+2) \cdot \frac{df_{N+2}{}^{i-1}(R)}{dR}\right] + 2R^{-5}[D(N-2) f_{N-2}{}^{i-1}(R) + E(N) f_N{}^{i-1}(R) + G(N+2) f_{N+2}{}^{i-1}(R)] \tag{43}$$

Equation (43) is an Euler equation and is readily solved using the method of variation of parameters.

Inspection of equation (43) yields several useful results. Firstly, the values of N for which $f_N{}^i(R)$ is not necessarily zero will lie in the interval

$$0 \le N \le 2i \tag{44}$$

Secondly,

$$f_N{}^i(R) = 0 \quad \text{when } N \text{ is odd} \tag{45}$$

satisfies the governing equation and the boundary conditions. Lastly, the undefined functions $f_{-2}{}^i(R)$ and $f_{-1}{}^i(R)$ will not appear in equation (43) since

$$A(-2) = A(-1) = D(-2) = D(-1) = 0 \tag{46}$$

T_1 is found by taking i equal to one. By equation (44) and (45), the values of N are limited to 0 and 2. Noting that $f_2{}^0(R) = 0$ and that $A(-2) = B(0) = D(-2) = E(0) = 0$, equation (43) for $N = 0$ becomes

$$\frac{1}{R^2}\frac{d}{dR}\left[R^2 \frac{df_0{}^1(R)}{dR}\right] = 0 \tag{47}$$

whose solution satisfying equation (29) and equation (30) is zero.

Calculating coefficients for N equal to 2, substituting $f_0{}^0(R) = 1/R$ into equation (43) and noting that $f_2{}^0(R)$ and $f_4{}^0(R)$ are zero yields

$$\frac{1}{R^2}\frac{d}{dR}\left[R^2 \frac{df_2{}^1(R)}{dR}\right] - \frac{6}{R^2} f_2{}^1(R) = 2(R^{-4} - R^{-6}) \tag{48}$$

whose solution, which satisifes the boundary conditions, is

$$f_2{}^1(R) = -\frac{1}{3}R^{-4} + \frac{5}{6}R^{-3} - \frac{1}{2}R^{-2} \tag{49}$$

Combining these results yields

$$T_1 = \left(-\frac{1}{3}R^{-4} + \frac{5}{6}R^{-3} - \frac{1}{2}R^{-2}\right)P_2(Z) \tag{50}$$

T_2 may be computed in a similar manner, yielding

$$T_2 = \left(\frac{2}{105}R^{-7} - \frac{1}{18}R^{-6} + \frac{1}{75}R^{-5} + \frac{1}{12}R^{-4} - \frac{1}{15}R^{-3} + \frac{41}{6300}R^{-1}\right)P_0(Z) + \left(\frac{4}{35}\ln(R)R^{-3} + \frac{5}{189}R^{-7} - \frac{5}{63}R^{-6} + \frac{1}{147}R^{-5} + \frac{5}{21}R^{-4} - \frac{254}{1323}R^{-3}\right)P_2(Z) + \left(\frac{4}{35}\ln(R)R^{-5} + \frac{16}{385}R^{-7} - \frac{1}{7}R^{-6}\right)$$

$$+\frac{753}{2156}R^{-5}-\frac{9}{28}R^{-4}+\frac{18}{245}R^{-3}\Big)P_4(Z) \quad (51)$$

Heat Transfer

The first, and all higher order contributions to transfer may be found by integrating the normal flux over the drop surface.

$$\mathrm{Nu}_i = -\int_{-1}^{1}\frac{\partial T_i}{\partial R}\Big|_{R=1}dZ \quad (52)$$

The Legendre polynomials are, however, an orthogonal set over the interval -1 to 1 with respect to a weight function of unity.

$$\int_{-1}^{1}P_N(Z)dZ = 0 \quad \text{for} \quad N \neq 0 \quad (53)$$

Hence, each term of equation (23) yields a contribution

$$\mathrm{Nu}_i = -2\frac{df_0^i(R)}{dR}\Big|_{R=1} \quad (54)$$

Accordingly, the first order contribution is

$$\mathrm{Nu}_1 = 0 \quad (55)$$

This result is not, as might appear, happenstance. It has been shown [6] that the average heat transfer coefficient of convection heat transfer from any isothermal body, to a fluid of uniform temperature, is invariant to flow reversal. Although flow reversal may result in large differences in local fluxes, and although the two flux distributions may not mirror one another, the overall steady-state transfer rate is independent of the direction of flow.

The invariance of the transfer rate is not trivial. Flow reversal does not constitute mere rotation of the coordinate axis. In the case of flow generated by an electric field, one direction of flow has a contacting stream surface approaching the drop on a line, the axis, and leaving on the equatorial plane. The contacting stream surface in the reverse direction of flow does precisely the opposite. The characteristics of two such flows are quite different and the fact that the average transfer rate is the same in both cases does not result from symmetry.

Noting that ϵ in equation (23) may be either positive or negative, it follows that the first order result (55) holds for all odd order contributions to the Nusselt number.

$$\mathrm{Nu}_i = 0 \quad \text{when } i \text{ is odd} \quad (56)$$

Since the odd order terms in the series solution of the energy equation make no contribution to heat or mass transfer, an unusually large number of temperature terms must be computed to obtain nonvanishing, higher order results. Beyond the third order term this task becomes unreasonable to perform by hand. To overcome this impediment a computer solution was sought. The result is a PL/I FORMAC [7,8] implemented program which analytically solves equation (43) and can more generally solve equation (12) using a regular perturbation expansion (18) for a wide range of velocity distributions. The program source utilizes the same algorithm used to compute T_1 and T_2 by hand.

FORMAC was chosen as the programming language for its capacities in symbolically manipulating mathematical expressions. FORMAC expressions may contain variables, constants to 2295 digits, the symbolic constants, e, π, and i, and a variety of common functions such as $\sin(x)$, $\ln(x)$, $\mathrm{erf}(x)$, etc. Provisions are also made for the use of user defined functions. Mathematical expressions may be compared and evaluated. FORMAC's built-in operations include differentiation, rational arithmetic, extraction of polynomial coefficients and exponents, and extraction of common denominators. Key operators can also be discerned so that expressions may be parsed. As the PL/I-FORMAC Interpreter is an extension of the IBM OS/360 PL/I (F) compiler, the entire PL/I capability is available to the FORMAC user.

In addition to the direct use of FORMAC's indigenous operations, it was necessary to devise a routine to perform variation of parameters. This routine includes a user developed integration package capable of integrating any expression of the form

$$\sum_m\sum_n C_{mn}R^m\ln^n(R) \quad (57)$$

All integration procedures are verified using the FORMAC symbolic differentiation capability. Failure of positive verification would result in terminating program execution.

Following variation of parameters, the program evaluates the resulting general solutions in order to satisfy the boundary conditions specified in equations (29) and (30). Each term of the energy equation solution is then analyzed using equation (54) to yield its contribution to heat transfer.

To date, the first six terms of the energy equation solution have been computed. No effort has been made to obtain the seventh term. As an observation on the necessity of employing computer techniques, it is noted that the sixth order solution contains 239 terms and constants to 37 digits.

The computer results agree identically with the first and second-order solutions obtained by hand. Additionally, it was found that equation (56) is satisfied through the fifth-order term.

The following expression for low Peclet number transfer was obtained.

$$\mathrm{Nu} = 2+\frac{41}{3150}\epsilon^2-\frac{66245909}{1376633758500}\epsilon^4 + \frac{256775989847862459773}{886183941117771846049500000}\epsilon^6+0(\epsilon^8) \quad (58)$$

It is again noted that the value of the Nusselt number is independent of the sign of ϵ. Convective contributions to transport for the two directions of flow are identical.

The valid range of equation (58) is not known precisely. A comparison of the coefficients in equation (58) indicates that the expression is valid, and accurate to within 2 percent at a Peclet number of 15. This corresponds to a Nusselt number of 2.61. At a Peclet number of 30, the terms in equation (58) become about equal in magnitude. Beyond this value, the series appears to diverge badly.

Simple failure of the series to converge should not automatically be taken to mean that the useful range has been exceeded. Many divergent or slowly convergent series may be successfully summed employing a variety of special methods [9]. A method which seems especially well suited to summing oscillating series, both convergent and divergent, has been proposed by Shanks [10] and Lubkin [11].

The nonlinear, nonregular, first-order Shanks transform is given by

$$e(S_n) = \frac{S_{n-1}S_{n+1}-S_n{}^2}{S_{n-1}+S_{n+1}-2S_n} \quad (59)$$

where, in our case, the partial sums are given by

$$S_n = \sum_{i=0}^{n}\mathrm{Nu}_{2i}\epsilon^{2i} \quad n = 0, 1, 2, \ldots \quad (60)$$

It has been shown [11] that if S_n and $e(S_n)$ converge, then their limits are equal. That is

$$\lim_{n\to\infty}S_n = \lim_{n\to\infty}e(S_n) \quad (61)$$

The advantage in utilizing such a transform is that $e(S_n)$ may converge more rapidly than S_n. Additionally, in some instances where S_n does not converge, $e(S_n)$ may converge to the analytical continuation of the sums of convergent series (60).

Applying the transform (59) to the partial sums S_1 and S_2 of equation (58) yields $e(S_1)$ and $e(S_2)$. A comparison of these two terms indicates that convergence under the transform is very good up to a Peclet number of about 30. This value corresponds to a Nusselt number of 3.89.

Up to and beyond a Peclet number of 30, the results obtained here have been compared with those of a preliminary numerical analysis of the problem [12]. This revealed that the arithmetic mean

$$\mathrm{Nu} \sim \frac{e(S_1)+e(S_2)}{2} \quad (62)$$

(equivalent to the first-order Cesaro sum of the transformed series) is accurate to within 2 percent up to a Peclet number of 60. The Nusselt number corresponding to a Peclet number of 60 is 6.17. Convective effects are, of course, quite significant in this range.

Conclusions

Unlike the case of a translating sphere, it was found that a perturbation about the zero flow solution is everywhere valid for analysis of transport due to the low Peclet number creeping flow generated by an electric field. A computer program was developed to perform the perturbation expansion by analytically solving a recursive set of Poisson equations in spherical coordinates with axial symmetry. Employing this program, the average transport rate, expressed as the Nusselt number, was determined as a power series in Peclet number having rational coefficients. The useful range of the series was found to extend at least to a Peclet number of 60. In this regime, the electroconvective contribution to heat or mass transport becomes very significant. As anticipated, it was also observed that the Nusselt number is invariant to flow reversal.

References

1 Taylor, G. I., "Studies in Electrohydrodynamics I. The Circulation Produced in a Drop by an Electric Field," *Proceedings of The Royal Society*, Vol. 291, 1966, pp. 159–166.

2 Morrison F. A., "Transient Heat and Mass Transfer to a Drop in an Electric Field," ASME JOURNAL OF HEAT TRANSFER, Vol. 99, 1977, pp. 269–273.

3 Thornton, J. D., "The Applications of Electrical Energy to Chemical and Physical Rate Processes," *Reviews of Pure and Applied Chemistry*, Vol. 18, 1968, pp. 197–218.

4 Kozhukhar, I. A., and Bologa, M. K., "Heat Transfer in Dielectric Emulsions in the Electric Field," *Elektonnaia Obrabotka Materialov*, No. 1, 1968, (in Russian), pp. 51–55.

5 Kronig, R., and Bruijsten, J., "On the Theory of Heat and Mass Transfer from a Sphere in a Flowing Medium at Low Values of Reynolds' Number," *Applied Scientific Research*, Vol. A2, 1951, pp. 439–446.

6 Brenner, H., "On the Invariance of the Heat Transfer Coefficients to Flow Reversal in Stokes and Potential Streaming Flows Past Particles of Arbitrary Shape," *Journal of Mathematical and Physical Sciences*, Vol. 1, 1967, pp. 173–179.

7 Tobey, R., et al., *PL/I-FORMAC Interpreter*, IBM Federal Systems Division, 1967.

8 Fike, C. T., *PL/I for Scientific Programmers*, Prentice-Hall, Inc., Englewood Cliffs, N. J., 1970.

9 Van Dyke, M., "Analysis and Improvement of Perturbation Series," *Q. J. of Mechanics and Applied Mathematics*, Vol. 27, Pt. 4, 1974, pp. 423–450.

10 Shanks, D., "Non-Linear Transformations of Divergent and Slowly Convergent Sequences," *Journal of Mathematics and Physics*, Vol. 34, 1955, pp. 1–42.

11 Lubkin, S., "A Method of Summing Infinite Series," *Journal of Research of the National Bureau of Standards*, Vol. 48, 1952, pp. 228–254.

12 Sharpe, L., Jr., and Morrison, F. A., Jr., (in progress).

A. Balakrishnan[1]
D. K. Edwards
Professor.
Mem. ASME

School of Engineering and Applied Science
University of California, Los Angeles
Los Angeles, Calif. 90024

Molecular Gas Radiation in the Thermal Entrance Region of a Duct

The effect of molecular gas radiation upon the thermal development downstream from a step change in wall temperature is examined for both laminar and turbulent flow in a black-walled flat-plate duct. The exponential-tailed band model is used to represent spectral variations in gas absorption and emission. Values of total and radiative Nusselt numbers, cold-wall-layer transmission factors, and dimensionless bulk temperatures are reported for several dimensionless axial locations and for various sets of the dimensionless controlling parameters. Even in the entrance region, self absorption by wall layer gas blocks significantly the radiation exchange between the gas core and wall. An approximate correlation is proposed for both plane-duct and pipe turbulent entrance flows.

Introduction

While much progress has been made in treating simultaneous radiation and convection in detail for some specific duct flow situations [1–15], engineering analysis is usually carried out using one of two alternative approximations. One is the zone method [16–18] which is often used for convenience, because uncertainties in radiant properties [19] generally outweigh those introduced by simplicity in modeling. The other is the multiflux method in which a differential formulation is employed for finite-difference calculations carried on to solve for the temperature and flow fields [20]. The objective of this paper is twofold. On the one hand, the paper shows how the thermal entrance region of a parallel plate duct may be treated in detail with account taken of the spectral variations in molecular gas properties without invoking either of the two common approximate methods. In this respect it is a contribution to the detailed literature represented by references [1–13]. On the other hand, the paper derives values of wall layer transmittance, a convenient factor to introduce into either a zone or multiflux model in order to correct for the shielding effect of the wall boundary layer. In this respect the paper adds to the literature on the wall layer effect [4–6, 19].

Turbulent entrance flow in an annulus was treated by Nichols [1] who used a perturbation series expansion and neglected gas-to-gas radiation in evaluating the coefficient integrals. The assumption was made that the temperature profile was not much affected by the optically thin radiation. Comparison was made with an experiment at 3.2 atm in an annulus with radius ratio 0.2 at a Reynolds number of 20000. A seven percent increase in heat transfer due to radiation was observed in agreement with predictions. Landram, Grief, and Habib [2] treated hydrodynamically and thermally established turbulent flow of an optically thin fluid in a tube with constant wall heat flux. Nusselt number was found to vary as $C(\xi)\mathrm{Re}^n$ (for Pr = 0.73) with an exponent n of approximately 0.7 independent of a radiation interaction parameter ξ, and $C(\xi)$ was nearly linear in ξ, with ξ itself a function of Reynolds number, Nusselt number, and a radiation-conduction parameter based on Planck mean absorption coefficient. Habib and Greif [3] measured wall temperature and gas temperature profiles in a 48.3 mm ID tube containing turbulently flowing carbon dioxide and, for comparison, air. Balakrishnan and Edwards [4] treated thermally and hydrodynamically established turbulent flow in a flat plate duct with isothermal wall. Previously Edwards and Balakrishnan [5, 6] had treated such flow for a constant volume heat source. The difference in solutions was found to be small, suggesting that the results were valid for constant wall heat flux under thermally established conditions. Wassel and Edwards [7] treated thermally and hydrodynamically established flow with constant wall heat flux for the circular pipe. Tabulated results and interpolation rules were presented to facilitate practical calculations.

In the case of established laminar flow, Viskanta [8] treated the problem of a gray gas in a parallel plate channel. Edwards, et al. [9] developed an approximate solution for a nongray radiating gas. A simple relation for a radiative Nusselt number was found in terms of an exponential-band-radiation-to-conduction parameter. Balakrishnan and Edwards [4], in addition to treating turbulent established flow, developed appropriate band expressions needed for the approximate laminar solution and compared it with detailed numerical calculations. Agreement was within 7 percent. Wassel and Edwards [7] treated the laminar case as well for established pipe flow.

Laminar entrance flow in a pipe was treated numerically by deSoto [10]. Results in dimensional form were particular to a 1.83 m long 50.8 mm ID black pipe at 1389 K having 4.54 kg/hr of CO_2 gas enter at 1 atm and 294 K. Comparison of the numerical results was made with a "crude approach" in which the local wall heat flux was equated to the uncoupled local heat transfer coefficient from the Graetz solution times wall-to-bulk temperature difference, plus the gas-total-absorptivity-wall-radiosity product, and minus the gas total emissivity multiplying the black body radiosity at the gas bulk temperature. Agreement with the crude approach was very poor for laminar flow, because, as was shown earlier by deSoto and Edwards [11], isothermal gas radiation at the bulk temperature does not correspond at all well to the true gas radiation incident upon the wall, particularly for a hot wall and cold gas.

Pearce and Emery [12] treated the thermal entrance problem and the simultaneous hydrodynamic and thermal entrance problem for a black circular tube in laminar flow. A gray gas and a gray-band gas were considered. Kurosaki [13] examined the laminar entrance flow of a gray radiating fluid in the parallel plate duct. Grief and McEligot [14] treated the thermal entrance region of a parallel-plate duct for hydrodynamically established laminar flow (and slug flow) of an optically thin gas. An analytical series was obtained in the linearized radiation limit, and successive substitution was used for the nonlinear case. In the linearized limit, superposition of the conduction and radiation wall heat fluxes computed independently was exact, but when the wall-to-bulk temperature ratio differed markedly from unity the conduction contribution was found to be quite sensitive to radiation. Later a nongray, non-optically-thin gas was treated, and results particular to carbon monoxide were calculated [15].

While what deSoto termed the "crude approach" is not appropriate to laminar duct flow, for turbulent flow a zone or well-stirred reactor approach is often appropriate to engineering. What has been found for established flows, however, is that a wall-layer transmittance must be introduced to account for self-absorption by the wall layer [6]. It is of interest to know how close to the inlet one must be for this quantity to be substantially equal to unity, how rapidly it falls to its established value, and what is an appropriate mean value. In this paper both the laminar and turbulent thermal entry problem are treated, and the solutions tabulated in dimensionless form. For turbulent flow, a simple Dittus-Boelter type correlation is proposed.

[1] Presently member of the technical staff, Aerospace Systems Division, Acurex Corporation, Mountain View, California.

Contributed by the Heat Transfer Division for publication in the JOURNAL OF HEAT TRANSFER. Manuscript received by the Heat Transfer Division November 29, 1978.

Formulation

Assumptions. Fluid enters the heated or cooled section of a parallel plate duct of thickness 2δ with uniform inlet temperature T_0 and hydrodynamically established velocity profile. The walls have equal and uniform temperature T_w and are black. Streamwise conduction and radiation are assumed negligible, and properties are assumed constant at a reference state temperature. In the case of turbulent flow, the eddy diffusivity for momentum is modeled by the Van Driest expression [21] near the wall, and the Mei and Squire correction [22] is applied for the channel center. Eddy diffusivity for heat is taken to be that for momentum divided by a turbulent Prandtl number equal to 0.9 [23, 24]. For laminar flow the eddy diffusivities are, of course, zero.

The spectral absorption coefficient k_ν for wavenumber ν is prescribed by the exponential-tailed band model [20]. At wavenumbers near the origin ν_k of the kth absorption band,

$$k_k(\nu) = \frac{\alpha_k}{\omega_k} \exp[-(\nu_k - \nu)/\omega_k], \quad \nu > \nu_k \tag{1}$$

where α_k is the integrated intensity and ω_k is the band wing decay width. The representation here is for an asymmetric band with overlapped lines, but a symmetrical band is represented by a mathematically equivalent expression. Thus the results hold for either shape.

In formulating the radiant flux, the assumption is made that the partial derivative of the Planck function with temperature is evaluated at a reference temperature and at wavenumber ν_k for wavenumbers near the kth band. The bands are thus assumed to be nonoverlapped, and the temperature difference $|T_0 - T_w|$ is assumed small compared to the absolute temperature level.

Governing Equations. In dimensionless form the governing equations are the momentum equation

$$0 = \mathrm{R}_t + \frac{d}{dy^*}\left(\epsilon^+ \frac{du^+}{dy^*}\right) \tag{2}$$

subject to

$$y^* = 0, u^+ = 0; y^* = 1, du^+/dy^* = 0 \tag{3}$$

and the energy equation

$$u^+ \frac{\partial\theta}{\partial x^*} = \frac{\partial}{\partial y^*}\left[\epsilon_H{}^+ \frac{\partial\theta}{\partial y^*}\right] + R_{dm} \frac{\partial}{\partial y^*}[q_R{}^*(y^*)] \tag{4}$$

subject to

$$x^* = 0, \theta = 1; y^* = 0, \theta = 0; y^* = 1, \partial\theta/\partial y^* = 0 \tag{5}$$

where, following references [4] and [5],

$$\mathrm{R}_t = \delta^+ = \upsilon_\tau \delta/\nu_m, \upsilon_\tau = u_b\sqrt{c_f/2}$$

$$y^* = y/\delta = y^+/\delta^+, u^+ = u/\upsilon_\tau$$

$$\epsilon^+ - 1 = (\epsilon_{VD}/\nu_m)/(1 + 3.4y^*)$$

$$\epsilon_{VD}/\nu_m = -(1/2) + (1/2)\{1 + 4(\mathrm{K}y^+)^2[1 - \exp(-y^+/A^+)]^2\}^{1/2}$$

$$\mathrm{K} = 0.4, A^+ = 26$$

$$\theta = (T - T_w)/(T_0 - T_w), x^* = x/(\delta \mathrm{R}_t \mathrm{Pr}_m)$$

$$\epsilon_H{}^+ = 1 + (\mathrm{Pr}_m/\mathrm{Pr}_t)(\epsilon^+ - 1)$$

$$R_{dm} = \sum_{k=1}^{n} \omega_k[\partial B(\nu_k, T)/\partial T]A_k{}^*/(k_m/\delta)$$

$$B(\nu, T) = 2\pi hc^2\nu^3/[\exp(hc\nu/kT) - 1]$$

$$A_k{}^* = A_s{}^*(2\tau_{H,k}), A_s{}^*(z) = \ln(z) + E_1(z) + \gamma + (1/2) - E_3(z)$$

$$\tau_{H,k} = \alpha_k \rho\delta/\omega_k, \gamma = 0.5772156\ldots$$

$$E_n(t) = \int_0^1 \exp[-t/\mu]\mu^{n-2}d\mu \ (\mu = \cos\theta)$$

$$q_R{}^* = \sum_{k=1}^{n} W_k \int_0^1 \mathrm{K}_k{}^*(y^*, y^{*\prime})[\partial\theta/\partial y^{*\prime}]dy^{*\prime}$$

$$W_k = \omega_k[\partial B(\nu_k, T)/\partial T]A_k{}^* \Big/ \sum_{k=1}^{n} \omega_k[\partial B(\nu_k, T)/\partial T]A_k{}^*$$

$$\mathrm{K}_k{}^* = [A_s{}^*(\tau_{H,k}(2 - y^* - y^{*\prime})) - A_s{}^*(\tau_{H,k}|y^* - y^{*\prime}|)]/A_k{}^*$$

Nomenclature

A_k = band absorption of kth band, cm^{-1}
A_s = slab band absorptance, cm^{-1}
A^+ = van Driest parameter, $A^+ = 26$
B = Planck radiosity of black body, $\mathrm{W/m^2\ cm^{-1}}$
B' = derivative of B with respect to T, $\mathrm{W/m^2\ cm^{-1}\ K}$
c = speed of light, $c = 2.998 \times 10^8$ m/s
c_f = skin friction coefficient
c_p = specific heat at constant pressure, J/kg K
D = hydraulic diameter, m
E_n = exponential integral of order n
h = Planck's constant, $h = 6.626 \times 10^{-34}$ J s
k = Boltzmann constant, $k = 1.3805 \times 10^{-23}$ J/K
k_k = absorption coefficient of kth band, $(\mathrm{kg\ m^{-2}})^{-1}$
k_m = molecular conductivity, W/m K
K = von Karman constant, K = 0.4
K_k = radiant flux kernel for kth band
n = total number of gas bands
N_{rm} = radiation to molecular conduction ratio
Nu = Nusselt number based on D
P = pressure, $\mathrm{N/m^2}$
Pr = Prandtl number
q = heat flux, $\mathrm{W/m^2}$
$\bar{r}_{WL}$ = wall layer thickness to beam length ratio
Re = Reynolds number based on D
R_{dm} = dimensionless radiation conduction parameter
R_t = turbulent Reynolds number
t = optical depth (dummy variable)
T = temperature, K
u = axial velocity, m/s
υ_τ = friction velocity, m/s
V_0 = transformation constant
W_k = weighting factor for kth band
x = axial distance, m; also mole fraction
y = distance from wall, m
α = integrated band intensity, $\mathrm{cm^{-1}/kg\ m^{-2}}$
α_{slab} = slab absorptivity of gas
γ = Euler constant, $\gamma = 0.5772156\ldots$
δ = channel half width, m
ϵ_H = eddy diffusivity for heat, $\mathrm{m^2/s}$
ϵ_M = eddy diffusivity for momentum, $\mathrm{m^2/s}$
ϵ_{slab} = slab emissivity of gas
θ = dimensionless temperature $(T - T_w)/(T_0 - T_w)$; also angle from wall normal
μ = micron, 10^{-4} cm or 10^{-6} m
μ_m = molecular (dynamic) viscosity, N s/$\mathrm{m^2}$
ν = wavenumber, $\mathrm{cm^{-1}}$
ν_k = wavenumber location of kth band, $\mathrm{cm^{-1}}$
ν_m = molecular kinematic viscosity, $\mathrm{m^2/s}$
π = mathematical constant, $\pi = 3.1415927\ldots$
ρ = density of gas, $\mathrm{kg/m^3}$
σ = Stefan-Boltzmann constant, $\sigma = 5.67 \times 10^{-8}\ \mathrm{W/m^2\ K^4}$
τ = optical depth
τ_H = optical depth at the head of the kth band
τ_{WL} = wall layer transmissivity
ω_k = band wing decay width, $\mathrm{cm^{-1}}$

Subscripts

b = bulk
C = convective
0 = inlet
R = radiative
t = turbulent
T = total
w = wall
δ = center of channel
ν = spectral

Superscripts

* = dimensionless quantity
+ = turbulent dimensionless quantity
– = averaged over x

The parameters are seen to be Reynolds number (which fixes c_f and hence R_t), the molecular Prandtl number Pr_m and turbulent Prandtl number Pr_t, the radiation-conduction interaction parameter R_{dm}, and the optical depths $\tau_{H,k}$.

Method of Solution. Because of the assumption of constant properties and hydrodynamically established flow, the momentum equation is an uncoupled ordinary differential equation and may be solved at the outset by numerical integration. The integro-partial-differential energy equation is solved by using a modified form of the Patankar-Spalding [25] implicit finite difference technique. A transformation is first made from y^* to z^*,

$$y^* = \frac{1}{V_0}[e^{z^*} - 1],\ z^* = \ln[1 + V_0 y^*] \tag{6}$$

This transformation, with V_0 set equal to $0.4\mathrm{R}_t$, stretches the wall region when equal differences in z^* are used [4, 5]. Details of the numerics are contained in a Ph.D. thesis by Balakrishnan [25].

Engineering Parameters. The temperature profiles [25] obtained cannot be presented here in full, nor are they easy to use for engineering purposes. Of interest to engineers are Nusselt number, cold-wall-layer transmission factor, and bulk temperature. Local Nusselt number is defined as local heat flux times hydraulic diameter divided by molecular conductivity and wall-to-bulk temperature difference

$$\mathrm{Nu}_T = \frac{q(x, y = 0)D}{k_m(T_w - T_b)} = \mathrm{Nu}_C + \mathrm{Nu}_R \tag{7}$$

where $D = 4\delta$ is hydraulic diameter. In terms of the dimensionless variables, the convective Nusselt number

$$\mathrm{Nu}_C = \frac{4}{\theta_b(x^*)} \left.\frac{\partial\theta(x^*, y^*)}{\partial y^*}\right|_{y^*=0} \tag{8}$$

and the radiative Nusselt number is

$$\mathrm{Nu}_R = \frac{4}{\theta_b(x^*)} R_{dm} q_R^*(x^*, y^* = 0) \tag{9}$$

Table 1 Thermal development in laminar flow

a) $N_{rm} = R_{dm}/A_s^*(2\tau_H) = 1.0$

	Nonradiating gas		$\tau_H = 0.1$, $A_s^*(2\tau_H) = 0.3385$			$\tau_H = 1.0$, $A_s^*(2\tau_H) = 1.789$		
x^*	Nu_T	θ_b	Nu_T	τ_{WL}	θ_b	Nu_T	τ_{WL}	θ_b
0.001	31.6	0.9888	32.20	0.934	0.9880	34.77	0.914	0.9866
0.002	24.8	0.9818	26.01	0.920	0.9812	31.15	0.897	0.9786
0.004	19.8	0.9713	20.99	0.904	0.9701	26.01	0.876	0.9651
0.01	14.77	0.9469	15.91	0.880	0.9440	20.78	0.845	0.9321
0.02	12.02	0.9163	13.14	0.860	0.9110	17.89	0.821	0.8887
0.04	9.96	0.8681	11.04	0.841	0.8584	15.72	0.798	0.8177
0.10	8.12	0.7604	9.26	0.820	0.7399	13.90	0.774	0.6572
0.20	7.64	0.6260	8.69	0.813	0.5908	13.37	0.766	0.4691
0.40	7.54	0.4278	8.59	0.812	0.3846	13.30	0.765	0.2399
1.0	7.54	0.1394	8.59	0.812	0.1073	13.30	0.765	0.0333

	$\tau_H = 10$, $A_s^*(2\tau_H) = 4.073$			$\tau_H = 100$, $A_2^*(2\tau_H) = 6.376$		
x^*	Nu_T	τ_{WL}	θ_b	Nu_T	τ_{WL}	θ_b
0.001	43.61	0.773	0.9842	45.16	0.559	0.9842
0.002	36.96	0.742	0.9754	38.26	0.526	0.9743
0.004	31.45	0.705	0.9591	32.53	0.492	0.9574
0.01	25.74	0.654	0.9188	26.59	0.449	0.9155
0.02	22.57	0.618	0.8652	23.30	0.421	0.8601
0.04	20.23	0.587	0.7775	20.90	0.397	0.7697
0.10	18.48	0.561	0.5827	19.18	0.379	0.5700
0.20	18.13	0.556	0.3691	18.86	0.376	0.3536
0.40	18.10	0.556	0.1476	18.85	0.376	0.1355
1.0	18.10	0.556	0.0095	18.85	0.376	0.0081

b) $N_{rm} = R_{dm}/A_s^*(2\tau_H) = 10$

	$\tau_H = 0.1$, $A_s^*(2\tau_H) = 0.3385$			$\tau_H = 1.0$, $A_s^*(2\tau_H) = 1.789$		
x^*	Nu_T	τ_{WL}	θ_b	Nu_T	τ_{WL}	θ_b
0.001	43.97	0.934	0.9857	96.13	0.910	0.9727
0.002	36.91	0.919	0.9757	87.88	0.889	0.9502
0.004	31.64	0.903	0.9595	81.35	0.866	0.9113
0.01	26.19	0.877	0.9190	74.20	0.832	0.8100
0.02	23.13	0.857	0.8648	70.08	0.806	0.6770
0.04	20.78	0.836	0.7756	67.13	0.787	0.4804
0.10	18.75	0.815	0.5793	65.27	0.771	0.1791
0.20	18.14	0.808	0.3675	65.02	0.769	0.0359
0.40	18.04	0.807	0.1485	65.01	0.769	0.0014
1.0	18.04	0.807	0.0104	65.01	0.769	0.0000

	$\tau_H = 10$, $A_s^*(2\tau_H) = 4.073$			$\tau_H = 100$, $A_s^*(2\tau_H) = 6.376$		
x^*	Nu_T	τ_{WL}	θ_b	Nu_T	τ_{WL}	θ_b
0.001	154.5	0.751	0.9572	166.7	0.528	0.9523
0.002	141.5	0.708	0.9210	151.0	0.490	0.9132
0.004	130.7	0.667	0.8604	138.5	0.457	0.8487
0.01	119.4	0.620	0.7104	126.1	0.422	0.6915
0.02	114.3	0.598	0.5293	121.0	0.407	0.5049
0.04	112.2	0.588	0.2988	119.2	0.402	0.2735
0.10	111.8	0.587	0.0552	118.9	0.401	0.0446
0.20	111.8	0.587	0.0035	118.4	0.400	0.0023
0.40	111.6	0.586	0.0001	118.4	0.400	0.0000

where

$$\theta_b(x^*) = \frac{\int_0^1 \theta(x^*, y^*)u^+(y^*)dy^*}{\int_0^1 u^+(y^*)dy^*} = \frac{T_b - T_w}{T_0 - T_w} \tag{10}$$

Wall-layer transmittance is defined as the ratio of the radiative flux at the wall to that expected based upon an isothermal gas at the bulk temperature

$$\tau_{WL} = \frac{-q_R(x, y = 0)}{\epsilon_{\text{slab}}(T_b)\sigma T_b{}^4 - \alpha_{\text{slab}}(T_b, T_w)\sigma T_w{}^4} \tag{11}$$

Here ϵ_{slab} and α_{slab} are the gas emissivity and absorptivity, respectively. With the approximations invoked in formulating the radiation, the denominator in equation (11) is the numerator of R_{dm}, so that

$$\tau_{WL} = \frac{1}{4}\frac{\text{Nu}_R}{R_{dm}} \tag{12}$$

Average Nusselt number is defined such that

$$\theta_b = \exp\left[-\frac{4(x/D)}{\text{RePr}_m}\overline{\text{Nu}}_T\right] \tag{13a}$$

$$\overline{\text{Nu}}_T = \frac{\text{RePr}_m}{4(x/D)}\ln(1/\theta_b) \; (= (4/x^*)\ln(1/\theta_b) \text{ for laminar flow}) \tag{13b}$$

where Re is Reynolds number based upon hydraulic diameter D.

Results and Discussion

Laminar Flow. Table 1 gives results for four optical depths ($\tau_{H,k}$ = 0.1, 1, 10, and 100) and two values of $N_{rm} = R_{dm}/A_k{}^*$ (0.1 and 10) versus dimensionless distance from inlet x^*. For laminar flow R_t was taken to be 3, and thus x^* is understood to be $(x/\delta)/[(u_b\delta/\nu_m)\text{Pr}_m]$. Also shown for comparison are results for a nonradiating gas. The results in Table 1 apply to a gas with a single band or to a gas with a number of identical bands.

The nonradiating gas results are in excellent agreement with those of Schade and McEligot [26], and the correct result is obtained for thermally established conditions. With the addition of some molecular gaseous absorption and emission, the radiation heat transfer increases rapidly at first and then more slowly with increasing τ_H. In contrast, a gray gas has a maximum radiation contribution at $\tau_H \doteq 2$, and further increases in τ_H cause a decrease in radiation heat flux, eventually as $1/\tau_H$ [8].

In laminar flow, a value of wall layer transmittance τ_{WL} less than one arises from two factors, (1) the self-absorption by the wall layer, as expected, but also (2) the temperature distribution for which the bulk and volumetric temperatures differ. Table 1 shows that even for small optical depth, the value of τ_{WL} drops below unity as the flow develops because of the latter factor, and at larger values of optical depth the former factor contributes strongly to reducing τ_{WL}. Even in the inlet region, values of τ_{WL} considerably below unity are seen to exist.

Turbulent Flow. Table 2 gives results for turbulent flow for a gas with a single band (or several identical ones) for R_t = 1000. Optical depths of 1, 10, 100 and 1000 are examined. Table 3 shows the effect of R_t for values of 100, 300, 1000, and 3000 at τ_H = 50 and N_{rm} = 10. The Reynolds number value based on hydraulic diameter is shown for each corresponding value of R_t. Turbulence causes a blunter temperature profile in the channel, a sharper temperature gradient at the wall, and more rapid thermal development. For laminar flow and τ_H = 50, a value of τ_{WL} = 0.4 is approached at large x^*. Asymptotic values of 0.53 and 0.76 are seen in Table 3, depending upon turbulence level. While the values are significantly higher than for laminar flow, they are still considerably less than one. Again, even in the thermal inlet region values are seen to be significantly below unity. The radiation heat flux grows nearly in proportion to $R_{dm}/A_s{}^*(2\tau_H)$ as has been observed previously [5]. A rapid increase in heat transfer occurs with increasing τ_H at first, but with further increase an asymptotic value is approached. Figs. 1 and 2 show graphs of Nu_T, $\overline{\text{Nu}}_T$, and τ_{WL} for N_{rm} = 1.

As the radiative interaction increases, the convective heat flux increases at low turbulence but decreases at high turbulence, as shown in Table 4. At low turbulence, radiation in the wall layer transfers energy to increase the temperature gradient, but at high turbulence radiation acts to thicken the entire thermal boundary layer, and convective transfer at the wall is reduced.

Results for multiband gases (H_2O and CO_2) are shown in Table 5. The H_2O is seen to have a larger value of R_{dm} because of its wider and more numerous bands. However, the bands have considerably less optical depth, 12.01 and 5.97 for the strongest two H_2O bands vs 447.8 and 11.97 for the strongest two CO_2 bands. The more intense CO_2 bands give rise to a smaller value of wall layer transmittance. With both R_{dm} and τ_{WL} smaller for CO_2 than for H_2O, the values of Nu_R

Table 2 Thermal development in turbulent flow. Effect of optical depth at band head

Pr_m = 0.7, Pr_t = 0.9, $N_{rm} = R_{dm}/A_s{}^*(2\tau_H)$ = 10.0
R_t = 1000, Re = 85717, c_f = 0.00436

	Nonradiating Gas		τ_H = 1.0, $A_s{}^*(2\tau_H)$ = 1.789			τ_H = 10.0, $A_s{}^*(2\tau_H)$ = 4.073		
x^*	Nu_C	θ_b	Nu_T	τ_{WL}	θ_b	Nu_T	τ_{WL}	θ_b
0.001	293	0.9958	363.8	0.991	0.9950	448.0	0.954	0.9940
0.002	255	0.9928	325.9	0.987	0.9911	407.4	0.940	0.9892
0.004	229	0.9874	298.6	0.983	0.9844	376.6	0.923	0.9806
0.01	201	0.9737	269.9	0.975	0.9657	342.0	0.894	0.9569
0.02	184	0.9535	252.8	0.967	0.9381	320.2	0.869	0.9220
0.04	171	0.9171	239.0	0.960	0.8880	302.5	0.847	0.8596
0.1	161	0.8230	228.8	0.953	0.7601	290.1	0.830	0.7044
0.2	160	0.6912	227.2	0.952	0.5901	288.6	0.828	0.5093
0.4	160	0.4858	227.1	0.952	0.3540	288.5	0.827	0.2644
1.0	160	0.1714	227.1	0.952	0.0783	288.5	0.827	0.0383

	τ_H = 100, $A_s{}^*(2\tau_H)$ = 6.376			τ_H = 1000, $A_s{}^*(2\tau_H)$ = 8.678		
x^*	Nu_T	τ_{WL}	θ_b	Nu_T	τ_{WL}	θ_b
0.001	501.2	0.823	0.9934	514.3	0.643	0.9935
0.002	453.7	0.794	0.9879	464.2	0.616	0.9875
0.004	416.5	0.763	0.9784	424.9	0.589	0.9778
0.01	374.0	0.721	0.9523	380.2	0.553	0.9512
0.02	347.3	0.690	0.9144	352.4	0.527	0.9127
0.04	326.0	0.663	0.8474	330.4	0.506	0.8448
0.1	311.7	0.644	0.6835	315.6	0.491	0.6792
0.2	310.1	0.642	0.4817	314.0	0.489	0.4762
0.4	310.0	0.642	0.2375	313.9	0.489	0.2325
1.0	310.0	0.642	0.0296	313.9	0.489	0.0281

Table 3 Thermal development in turbulent flow. Effect of turbulence

$\tau_H = 50$, $A_s^* = 5.6824$, $N_{rm} = R_{dm}/A_s^*(2\tau_H) = 10.0$, $\mathrm{Pr}_m = 0.7$, $\mathrm{Pr}_t = 0.9$

	$R_t = 100$, Re = 5685			$R_t = 300$, Re = 21676		
x^*	Nu_T	τ_{WL}	θ_b	Nu_T	τ_{WL}	θ_b
0.001	287.3	0.786	0.9941	351.4	0.834	0.9943
0.002	257.2	0.751	0.9893	313.8	0.804	0.9898
0.004	232.9	0.715	0.9810	284.5	0.772	0.9819
0.01	205.2	0.665	0.9587	252.0	0.726	0.9605
0.02	187.7	0.628	0.9266	231.8	0.692	0.9295
0.04	172.7	0.592	0.8702	214.8	0.658	0.8747
0.1	157.7	0.553	0.7328	198.6	0.624	0.7396
0.2	151.3	0.536	0.5606	193.0	0.611	0.5673
0.4	149.2	0.530	0.3303	192.0	0.609	0.3341
1.0	149.0	0.530	0.0699	191.9	0.609	0.0702
	$R_t = 1000$, Re = 85717			$R_t = 3000$, Re = 291480		
x^*	Nu_T	τ_{WL}	θ_b	Nu_T	τ_{WL}	θ_b
0.001	490.2	0.874	0.9935	824.7	0.892	0.9909
0.002	444.7	0.847	0.9882	759.4	0.865	0.9831
0.004	409.1	0.819	0.9788	704.5	0.837	0.9693
0.01	368.3	0.777	0.9532	641.3	0.798	0.9315
0.02	342.6	0.746	0.9158	606.2	0.774	0.8767
0.04	322.0	0.719	0.8496	587.4	0.761	0.7805
0.1	308.1	0.700	0.6871	583.3	0.758	0.5545
0.2	306.5	0.698	0.4864	583.3	0.758	0.3150
0.4	306.4	0.697	0.2420	583.3	0.758	0.1005
1.0	306.4	0.697	0.0310	583.3	0.758	0.0035

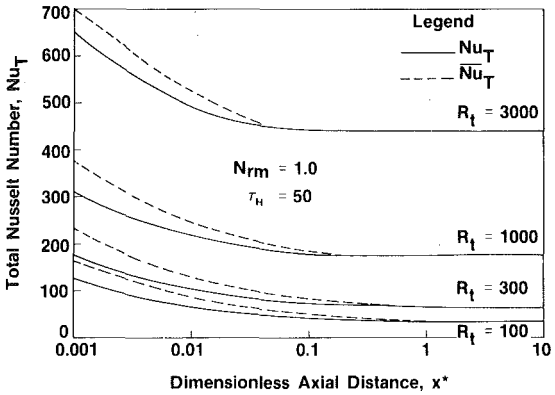

Fig. 1 Local and average total Nusselt number for turbulent flow

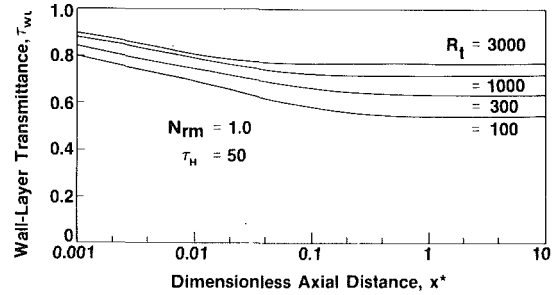

Fig. 2 Local wall-layer transmittance for turbulent flow

Table 4 Effect of radiation heat transfer on convective heat flux at the wall ($\tau_H = 50$)

	Nu_C			
N_{rm}	$R_t = 100$	$R_t = 300$	$R_t = 1000$	$R_t = 3000$
0.0	21.94	55.1	159.6	428.9
0.1	22.0	55.1	159.5	428.8
1.0	22.5	55.0	158.2	427.0
10.0	28.6	53.5	147.9	411.0
100.0	50.0	77.0	129.0	324.0

Table 5 Results for multi-band gases (constant property, linearized radiation, and turbulent flow)

Reference temperature, $T_0 = 1000$ K
Half thickness, $\delta = 0.50$ m
Total pressure, $P_{\mathrm{Tot}} = 3$ atm
Turbulent Reynolds number, $R_t = 160$
Reynolds number, Re = 10,253
Turbulent Prandtl number, $\mathrm{Pr}_t = 0.90$
Skin friction coefficient, $c_f = 0.00779$

a) Gas: Water Vapor
Mole fraction, $x_{H_2O} = 0.180$
Molecular Prandtl number, $\mathrm{Pr}_m = 0.875$
Molecular thermal conductivity, $k_m = 0.069$ W/m^2 K (nitrogen diluent)

Band No.	Wave Number ν_k, cm^{-1}	Maximum Optical Depth $\tau_{H,k}$	Band Decay Width ω_k, cm^{-1}	Slab Band Absorption $A_s^*(2\tau_{H,k})$	Planck Function Derivative $B'(\nu_{k,T})$
1	500	11.92	109.4	4.249	0.002
2	1600	12.01	225.1	4.256	0.014
3	3760	5.97	283.3	3.557	0.015
4	5350	1.29	172.3	2.030	0.006
5	7250	0.91	155.0	1.699	0.001

Radiation to conduction parameter $R_{dm} = 673.37$

x^*	Nu_T	Nu_R	τ_{WL}	θ_b
0.001	2566	2423	0.900	0.9597
0.002	2458	2336	0.867	0.9218
0.004	2346	2241	0.832	0.8561
0.01	2201	2113	0.784	0.6906
0.02	2122	2039	0.757	0.4942
0.04	2083	2004	0.744	0.2573
0.10	2075	1996	0.741	0.0376
0.20	2075	1996	0.741	0.0016

b) Gas: Carbon Dioxide
Mole fraction, $x_{CO_2} = 0.20$
Molecular Prandtl number, $\mathrm{Pr}_m = 0.72$
Molecular thermal conductivity, $k_m = 0.0660$ W/m^2 K (nitrogen diluent)

Band No.	Wave Number ν_k, cm^{-1}	Maximum Optical Depth $\tau_{H,k}$	Band Decay Width ω_k, cm^{-1}	Slab Band Absorption $A_s^*(2\tau_{H,k})$	Planck Function Derivative $B'(\nu_{k,T})$
1	667	66.68	45.85	5.970	0.003
2	960	0.14	98.03	0.454	0.006
3	1060	0.43	36.37	1.070	0.008
4	2410	447.80	39.53	7.875	0.019
5	3660	11.97	80.64	4.253	0.016
6	5200	0.11	158.11	0.364	0.007

Radiation to conduction parameter $R_{dm} = 414.79$

x^*	Nu_T	Nu_R	τ_{WL}	θ_b
0.001	1302	1161	0.700	0.9784
0.002	1218	1102	0.664	0.9588
0.004	1140	1043	0.629	0.9246
0.01	1041	964.1	0.581	0.8341
0.02	979.2	912.8	0.550	0.7132
0.04	935.6	875.8	0.528	0.5295
0.10	913.0	856.4	0.516	0.2243
0.20	909.6	854.0	0.515	0.0703

for the CO_2 are approximately one-half of those for the H_2O. As channel width δ is reduced below the 0.5 m value assumed for this comparison, however, the Nu_R values for H_2O would fall more rapidly than those for CO_2, because of the optical depth effect.

Application of Results to Pipe Flow. The present results can be applied approximately to flow in a circular pipe simply by basing the convective parameters on hydraulic diameter and the radiation parameters on mean beam length. In pipe flow the radius R is used in place of the channel half width δ, but the hydraulic diameter is $2R$

for a pipe and 4δ for parallel plates. Similarly the geometric mean beam length is $2R$ for a pipe and 4δ for the flat-plate channel. (Geometric mean beam length equals hydraulic dimeter for a long duct.) The parameters used by Wassel and Edwards [7] for pipe flow were N_{rm}, τ_R defined as τ_H here, and R_t, all with radius R replacing δ. The rules for converting flat plate results to pipe results are as follows

$$R_{t,\text{plate}} = \frac{1}{2} R_{t,\text{tube}}$$

$$\tau_{H,\text{plate}} = \frac{1}{2} \tau_R$$

$$N_{rm,\text{plate}} = \frac{1}{2} N_{rm,\text{tube}}$$

The Nusselt numbers are based upon hydraulic diameter in both cases and are directly comparable. Comparison with [7] can be made only for established flow (large x^*), because only established results are presented there, but one would think that the same reasoning would apply to the entrance region. Table 6 shows the comparison. A maximum error on only 2.2 percent in Nu_R is encountered for turbulent flow. The difference in Nu_T is somewhat larger, up to 7 percent.

An Approximate General Correlation. An approximate general correlation for $\overline{\text{Nu}}_T$ can be put forward based upon the observations that Nu_C is little affected until Nu_R becomes large and that Nu_R is linear in $R_{dm}\tau_{WL}$. With an approximate value of $\overline{\text{Nu}}_T$, the bulk temperature development downstream of the thermal entrance is given by equation (13*a*). The correlation is as follows:

$$\overline{\text{Nu}}_T = \overline{\text{Nu}}_C + \overline{\text{Nu}}_R \tag{14}$$

For convection we use

$$\overline{\text{Nu}}_C = 0.020\text{Re}^{0.8}\text{Pr}^{0.33}\bar{F} \tag{15}$$

$$\bar{F} = 1 + \frac{0.88}{1 + 0.4(x/D)} \tag{16}$$

We may note in passing that $\bar{F}$ derived from the calculated results for the nonradiating gas is in good agreement with the experimental results of Mills [27]. For radiation we use

$$\overline{\text{Nu}}_R = \frac{D}{k} \sum_{k=1}^{n} \omega_k [\partial B(\nu_k, T)/\partial T] A_k^* \bar{\tau}_{WL,k} \tag{17}$$

$$\bar{\tau}_{WL,k} = \frac{\ln(1 + 4\tau_{H,k}) - \ln(1 + 4\tau_{H,k}\bar{r}_{WL})}{\ln(1 + 4\tau_{H,k})} \tag{18}$$

$$\bar{r}_{WL} = \frac{1.37}{\text{Re}^{0.37}}\{1 - \exp[-(x/10D)^{0.6}]\} \tag{19}$$

Note that $4\tau_{H,k}$ is the band-head optical depth based upon geometric mean beam length or hydraulic diameter. The correlation yields values for average total Nusselt number within approximately 6 percent of the values calculated with the detailed numerical program.

Table 6 Comparison of turbulent channel flow with pipe flow

	$N_{rm,\text{tube}} = 20$, $N_{rm,\text{plate}} = 10$					
Result	Parallel Plate $\tau_H = 5$	Pipe [7] $\tau_R = 10$	Parallel Plate $\tau_H = 25$	Pipe [7] $\tau_R = 50$	Parallel Plate $\tau_H = 100$	Pipe [7] $\tau_R = 200$
	$R_{t,\text{tube}} = 500$, $R_{t,\text{parallel plate}} = 250$ ($\text{Re}_{\text{tube}} = 16901$)					
Nu_T	158.7	154.2	178.9	173.2	184.1	179.2
Nu_R	111.0	109.3	131.7	128.9	137.1	134.5
τ_{WL}	0.821	0.790	0.660	0.636	0.537	0.521
	$R_{t,\text{tube}} = 1000$, $R_{t,\text{parallel plate}} = 500$ ($\text{Re}_{\text{tube}} = 37185$)					
Nu_T	200.0	194.6	223.0	217.1	230.0	225.1
Nu_R	115.5	114.6	141.8	140.3	150.5	149 2
τ_{WL}	0.854	0.828	0.711	0.692	0.590	0.578
	$R_{t,\text{tube}} = 2000$, $R_{t,\text{parallel plate}} = 1000$ ($\text{Re}_{\text{tube}} = 80650$)					
Nu_T	274.9	256.5	300.6	292.4	310.0	303.3
Nu_R	118.7	118.5	150.5	150.2	163.8	164.0
τ_{WL}	0.878	0.857	0.754	0.741	0.642	0.635

Summary and Conclusions

Molecular gas radiation causes an increased radiative coupling to the wall of the inlet region so that Nu_R is nearly linear in $\tau_{WL}R_{dm}$. With increasing optical depth, R_{dm} increases as $A_s^*(2\tau_{H,k})$, but the wall layer transmittance τ_{WL} falls with increasing τ_H in such a way that Nu_R approaches a constant at high τ_H. The increased radiative coupling affects the convective Nusselt number, but not greatly except where Nu_R dominates anyway. With increased radiative coupling, thermal development is much more rapid. During the thermal development both convective and radiative Nusselt numbers fall, the latter due to self-absorption in the developing wall thermal layer. The results obtained for turbulent flow in the parallel-plate duct apply approximately to the circular pipe as well. A correlation for average total Nusselt number in turbulent duct flow of a radiating and conducting molecular gas agrees sufficiently well with detailed calculations to be useful for engineering calculations.

References

1 Nichols, L. D., "Temperature Profile in the Entrance Region of an Annular Passage Considering the Effects of Turbulent Convection and Radiation," *Int. J. Heat Mass Transfer*, Vol. 8, 1965, pp. 589–607.

2 Habib, I. S., and Greif, R., "Heat Transfer to a Flowing Nongray Radiating Gas: An Experimental and Theoretical Study," *Int. J. Heat Mass Transfer*, Vol. 13, 1970, pp. 1571–1582.

3 Landram, C. S., Greif, R., and Habib, I. S., "Heat Transfer in Turbulent Pipe Flow with Optically Thin Radiation," ASME JOURNAL OF HEAT TRANSFER, Vol. 91, 1969, pp. 330–336.

4 Balakrishnan, A., and Edwards, D. K., "Established Laminar and Turbulent Channel Flow of a Radiating Molecular Gas," *Heat Transfer 1974*, Vol. I, Fifth International Heat Transfer Conference, Tokyo, Sept. 1974, pp. 93–97.

5 Edwards, D. K., and Balakrishnan, A., "Nongray Radiative Transfer in a Turbulent Gas Layer," *Int. J. Heat Mass Transfer*, Vol. 16, 1973, pp. 1003–1015.

6 Edwards, D. K., and Balakrishnan, A., "Self-Absorption of Radiation in Turbulent Molecular Gases," *Combustion and Flame*, Vol. 20. 1973, pp. 401–417.

7 Wassel, A. T., and Edwards, D. K., "Molecular Gas Radiation in a Laminar or Turbulent Pipe Flow," ASME JOURNAL OF HEAT TRANSFER, Vol. 98, 1976, pp. 101–107.

8 Viskanta, R., "Interaction of Heat Transfer by Conduction, Convection and Radiation in a Radiating Fluid," ASME JOURNAL OF HEAT TRANSFER, Vol. 85, 1963, pp. 318–328.

9 Edwards, D. K., Glassen, L. K., Hauser, W. C., and Tuchscher, J. S., "Radiation Heat Transfer in Nonisothermal Nongray Gases," ASME JOURNAL OF HEAT TRANSFER, Vol. 89, 1967, pp. 219–229.

10 deSoto, S., "Coupled Radiation, Conduction, and Convection in Entrance Region Flow," *Int. J. Heat Mass Transfer*, Vol. 11, 1968, pp. 39–53.

11 deSoto, S., and Edwards, D. K., "Radiative Emission and Absorption in Nonisothermal Nongray Gases in Tubes," *Proceedings of the 1965 Heat Transfer and Fluid Mechanics Institute*, Stanford University Press, 1965, pp. 358–372.

12 Pearce, B. E., and Emery, A. F., "Heat Transfer by Thermal Radiation and Laminar Forced Convection to an Absorbing Fluid in the Entry Region of a Pipe," ASME JOURNAL OF HEAT TRANSFER, Vol. 92, 1970, pp. 221–230.

13 Kurosaki, Y., "Heat Transfer by Simultaneous Radiation and Convection in an Absorbing and Emitting Medium in a Flow Between Parallel Plates," *Heat Transfer 1970*, Vol. III, paper R2.5, Fourth International Heat Transfer Conference, Paris-Versailles, 1970.

14 Greif, R., and McEligot, D. M., "Influence of Optically Thin Radiation on Heat Transfer in the Thermal Entrance Region of a Narrow Duct," ASME JOURNAL OF HEAT TRANSFER, Vol. 93, 1971, pp. 473–475.

15 Greif, R., and McEligot, D. M., "Thermally Developing Laminar Flows with Radiative Interaction Using the Total Band Absorptance Model," *Appl. Sci. Res.*, Vol. 25, 1971, pp. 234–244.

16 Hottel, H. C., and Sarofim, A. F., *Radiative Transfer*, McGraw-Hill Book Co., New York, 1967, pp. 450–487.

17 Nakra, N. K., and Smith, T. F., "Combined Radiation-Convection for a Real Gas," ASME JOURNAL OF HEAT TRANSFER, Vol. 99, 1977, pp. 60–65.

18 Becker, H. B., "A Mathematical Solution for Gas-to-Surface Radiative Exchange Area for a Rectangular Parallelepiped Enclosure Containing a Gray Medium," ASME JOURNAL OF HEAT TRANSFER, Vol. 99, 1977, pp. 203–211.

19 Sarofim, A. F., and Hottel, H. C., "Radiative Transfer in Combustion Chambers: Influence of Alternative Fuels," *Sixth International Heat Transfer Conference*, Toronto, Canada, Aug. 7–11, 1978, Vol. 6, pp. 199–217.

20 Edwards, D. K., and Menard, W. A., "Comparison of Models for Correlation of Total Band Absorption," *Applied Optics*, Vol. 3, 1964, pp. 621–625.

21 Van Driest, E. R., "On Turbulent Flow Near a Wall," *J. Aeronautical Sciences*, Vol. 23, 1956, pp. 1007–1011.

22 Mei, J., and Squire, W., "A Simple Eddy Viscosity Model for Turbulent Pipe and Channel Flow," *AIAA Journal,* Vol. 10, 1972, pp. 350–352.
23 Hatton, A. P., and Quarmby, A., "The Effect of Axially Varying and Unsymmetrical Boundary Conditions on Heat Transfer with Turbulent Flow Between Parallel Plates," *Int. J. Heat Mass Transfer,* Vol. 6, 1963, pp. 903–914.
24 Kestin, J., and Richardson, P. D., "Heat Transfer Across Turbulent, Incompressible Boundary Layers," *Int. J. Heat Mass Transfer,* Vol. 6, 1963, pp. 147–189.
25 Balakrishnan, A., "Nongray Radiative and Convective Transfer in the Entrance Region of a Parallel-Plate Duct," Ph.D. Dissertation, UCLA School of Engineering, 1974.
26 Schade, K. W., and McEligot, D. M., "Cartesian Graetz Problems with Air Property Variation," *Int. J. Heat Mass Transfer,* Vol. 14, 1971, pp. 653–666.
27 Mills, A. F., "Experimental Investigation of Turbulent Heat Transfer in the Entrance Region of a Circular Conduit," *J. Mechanical Engr. Sci.,* Vol. 4, 1962, pp. 63–77.

F. P. Incropera
Professor of Mechanical Engineering, Mem. ASME

W. G. Houf
Graduate Research Assistant,

Heat Transfer Laboratory
School of Mechanical Engineering
Purdue University
West Lafayette, Ind. 47907

A Three-Flux Method for Predicting Radiative Transfer in Aqueous Suspensions

A three-flux method is formulated for predicting radiative transfer in aqueous suspensions. The radiation field is resolved into three components, and the physical effects which are considered include refraction at the air-water interface, highly anisotropic scattering in the suspension, and diffuse reflection at the bottom. Calculations are performed for wide ranges of the scattering albedo, bottom reflectance, optical depth and irradiation, and results obtained for the local radiation flux and volumetric absorption, as well as for the overall suspension absorptance and the reflectance of the suspension-bottom complex, are in good agreement with those obtained from the more detailed method of discrete ordinates. Excellent agreement is also obtained between predictions of the net radiative flux in the suspension and measurements obtained for a suspension of unicellular algae.

Introduction

Interest in the problem of visible radiation transfer in aqueous suspensions has been stimulated by the need to better understand the effects of solar radiation on various environmental and engineering systems. Solar radiation transfer strongly influences thermal structure and photosynthetic activity in natural water impoundments, as well as the performance of liquid solar collectors. The problem typically involves one-dimensional transfer in a planar, scattering-absorbing suspension (Fig. 1). The incident solar radiation is comprised of diffuse and collimated components which experience reflection and refraction at the air-water interface. Radiation absorption and anisotropic scattering occur within the suspension, and reflection may occur at the bottom.

The radiation field within the water is specified in terms of the monochromatic intensity, I_λ, which may be determined by solving the following form of the equation of transfer [1]

$$\mu \frac{dI_\lambda(\tau_\lambda, \mu, \phi)}{d\tau_\lambda} = -I_\lambda(\tau_\lambda, \mu, \phi) + \frac{\omega_\lambda}{4\pi}\int_0^{2\pi}\int_{-1}^{+1} p_\lambda(\mu', \phi' \to \mu, \phi) I_\lambda(\tau_\lambda, \mu', \phi') d\mu' d\phi' \quad (1)$$

where $\mu \equiv \cos\theta$ and τ_λ, ω_λ and p_λ are the monochromatic optical depth, scattering albedo and phase function of the suspension. From knowledge of I_λ the downward (+) and upward (−) components of the local radiation flux may be determined from expressions of the form

$$F_\lambda^+(\tau_\lambda) = \int_0^{2\pi}\int_0^{+1} I_\lambda(\tau_\lambda, \mu, \phi)\mu d\mu d\phi \quad (2)$$

$$F_\lambda^-(\tau_\lambda) = \int_0^{2\pi}\int_{-1}^{0} I_\lambda(\tau_\lambda, \mu, \phi)\mu d\mu d\phi \quad (3)$$

A normalized form of the net radiation flux may then be expressed as

$$\overline{F}_\lambda(\tau_\lambda) = [F_\lambda^+(\tau_\lambda) + F_\lambda^-(\tau_\lambda)]/F_\lambda^*(0) \quad (4)$$

where $F_\lambda^*(0)$ is the combined irradiance at the air-water interface. From knowledge of $\overline{F}_\lambda(\tau_\lambda)$ the expression

$$\overline{H}_\lambda(\tau_\lambda) = -\frac{d\overline{F}_\lambda(\tau_\lambda)}{d\tau_\lambda} \quad (5)$$

may then be used to obtain the normalized local volumetric radiation absorption rate.

The foregoing expressions provide useful information concerning local characteristics of the radiation field. Results which are also useful relate to overall suspension properties and include the overall absorptance of the suspension, A_λ^M, the fraction of $F_\lambda^*(0)$ absorbed by the bottom, A_λ^B, and the reflectance, R_λ^M, of the suspension-bottom complex. These quantities are defined as

$$A_\lambda^M = \overline{F}_\lambda(0) - \overline{F}_\lambda(\tau_{\lambda,d}) \quad (6)$$

$$A_\lambda^B = (1-\rho_d)\overline{F}_\lambda^+(\tau_{\lambda,d}) \quad (7)$$

$$R_\lambda^M = [\overline{F}^-(0)]^* \quad (8)$$

where ρ_d is the bottom reflectance and $\tau_{\lambda,d}$ is the optical depth of the suspension.

The many efforts which have been made to solve equation (1) and to determine one or more of the quantities defined by equations (2–8) vary according to the manner in which air-water interface conditions, multiple scattering effects and bottom reflection were considered. Early efforts typically involved a Beer's law solution for which multiple scattering effects and internal surface reflections were neglected [2–4]. A variation of this method which has been somewhat successful is the forward scattering approximation [5]. It accounts for all internal reflections but essentially neglects the effects of multiple scattering.

Two-flux models have been used to treat scattering effects, but such models typically fail to account for interface reflection and refraction [6, 7] or assume isotropic scattering [8]. Two-flux models are, in fact, ill-suited for treating the highly anisotropic scattering associated with aqueous suspensions [9, 10]. A recent two-flux model [11], which attempted to account for the anisotropic nature of the phase function but assumed that all scattered radiation became diffuse, significantly overpredicted radiation absorption, $\overline{H}_\lambda$, in the upper layers of the suspension.

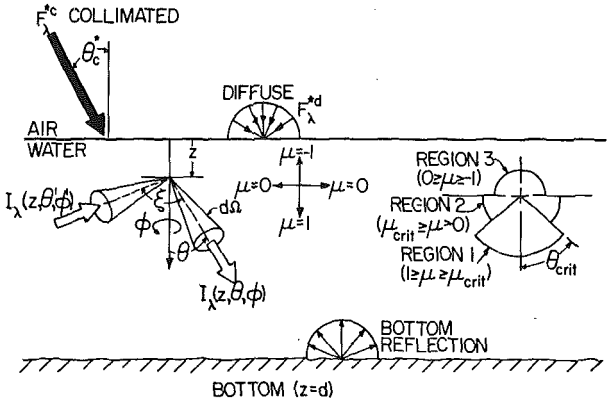

Fig. 1 Coordinate systems for radiation absorption and scattering in an aqueous suspension

Contributed by the Heat Transfer Division for publication in the JOURNAL OF HEAT TRANSFER. Manuscript received by the Heat Transfer Division January 24, 1979.

A six-flux model [12] has been applied to a highly anisotropic scattering suspension, and results compared well with those obtained from the more rigorous method of discrete ordinates [11]. However, in another study [13] this method was found to significantly overpredict the overall suspension absorptance, $A_\lambda{}^M$, for nonisotropic phase functions.

There exist a variety of more rigorous models, the most versatile of which are the methods of discrete ordinates, spherical harmonics and adding-doubling. Each of these methods can accommodate any phase function, scattering albedo and optical depth. Moreover, each method assumes that in solving equation (1) the integrand of the scattering integral can be closely approximated by a polynomial expression. However, for the strongly asymmetric phase functions which characterize liquids, polynomials of especially high degree are generally needed, thereby requiring large amounts of computer time and storage. Despite this difficulty the method of discrete ordinates has been successfully used to predict radiative transfer in aqueous media [5, 11, 14].

The primary objective of this study has been to develop a solution method which minimizes computational requirements, yet adequately treats all physical features relevant to radiative transfer in water layers, particularly the anisotropic nature of the phase function. The method was suggested by measurements of the angular variation of the radiance in a diffusely irradiated suspension [14]. The measurements showed that a large fraction of the downward propagating radiation is confined to angles less than the critical angle, θ_{crit}, associated with refraction at the air-water interface, while only a small portion of this radiation is located in the outer region of the downward hemisphere ($\theta_{crit} < \theta \leq \pi/2$). Accordingly, it is reasonable to separate the noncollimated portion of the radiation field into three isotropic components corresponding to the three regions shown in Fig. 1. Region 1 consists of that portion of the lower hemisphere bounded by θ_{crit}, while region 2 comprises the remaining portion of the lower hemisphere and region 3 comprises the entire upward hemisphere.

The Three-Flux Solution

The first step in the development of this solution is to separate the radiation field into collimated and noncollimated components. Dropping the subscript λ for convenience, the equation of transfer for the noncollimated intensity, I_n, is then of the form

$$\mu \frac{dI_n(\tau,\mu,\phi)}{d\tau} = -I_n(\tau,\mu,\phi) + \frac{\omega}{4\pi}\int_0^{2\pi}\int_{-1}^{+1} I_n(\tau,\mu',\phi')p(\mu',\phi'\rightarrow\mu,\phi)d\mu'd\phi' + \frac{\omega[1-\rho^*(\mu_c{}^*)]}{4\pi} F^{*c}{}_{exp}(-\tau/\mu_c)(\mu_c{}^*/\mu_c)p(\mu_c,\phi_c\rightarrow\mu,\phi) \quad (9)$$

Averaging this equation over each of the three regions by using operators of the form

$$\underline{\text{Region 1}}\quad \int_0^{2\pi}\int_{\mu_{crit}}^{1} d\mu d\phi \qquad \underline{\text{Region 2}}\quad \int_0^{2\pi}\int_0^{\mu_{crit}} d\mu d\phi \qquad \underline{\text{Region 3}}\quad \int_0^{2\pi}\int_{-1}^{0} d\mu d\phi$$

the following differential equations may be obtained for the contributions of the three regions to the noncollimated flux

$$\frac{dF_1}{d\tau} = \frac{[\omega S_{1,1} - 2(1-\mu_{crit})]}{(1-\mu^2_{crit})}F_1 + \frac{\omega S_{1,2}}{\mu^2_{crit}}F_2 - \omega S_{1,3}F_3 + (\omega/2)[1-\rho^*(\mu_c{}^*)](\mu_c{}^*/\mu_c)F^{*c}S_{1,c}\exp(-\tau/\mu_c) \quad (10)$$

$$\frac{dF_2}{d\tau} = \frac{\omega S_{2,1}}{(1-\mu_{crit}{}^2)}F_1 + \frac{(\omega S_{2,2} - 2\mu_{crit})}{\mu_{crit}{}^2}F_2 - \omega S_{2,3}F_3 + (\omega/2)[1-\rho^*(\mu_c{}^*)](\mu_c{}^*/\mu_c)F^{*c}S_{2,c}\exp(-\tau/\mu_c) \quad (11)$$

$$\frac{dF_3}{d\tau} = \frac{\omega S_{3,1}}{(1-\mu_{crit}{}^2)}F_1 + \frac{\omega S_{3,2}}{\mu_{crit}{}^2}F_2 + (2-\omega S_{3,3})F_3 + (\omega/2)[1-\rho^*(\mu_c{}^*)](\mu_c{}^*/\mu_c)F^{*c}S_{3,c}\exp(-\tau/\mu_c) \quad (12)$$

The flux components associated with each of the three regions may be defined in terms of average intensities, $I_{1,a}$, $I_{2,a}$ and $I_{3,a}$, by expressions of the form

$$F_1 = \int_0^{2\pi}\int_{\mu_{crit}}^{1} I_1\mu d\mu d\phi = \pi I_{1,a}[1-\mu_{crit}{}^2] \quad (13)$$

$$F_2 = \int_0^{2\pi}\int_0^{\mu_{crit}} I_2\mu d\mu d\phi = \pi I_{2,a}\mu_{crit}{}^2 \quad (14)$$

$$F_3 = \int_0^{2\pi}\int_{-1}^{0} I_3\mu d\mu d\phi = -\pi I_{3,a} \quad (15)$$

The $S_{i,j}$ and $S_{i,c}$ quantities appearing in equations (10–12) are scattering parameters which represent the fractions of the noncollimated radiation in region j and the collimated radiation, respectively, which are scattered into region i. If the phase function is expanded in a Legendre series about the scattering angle and the theorem of spherical harmonics is applied [15], the fractions may be expressed as

$$S_{i,1} = \int_i\int_{\mu_{crit}}^{1}\sum_{k=1}^{N}\tilde{\omega}_k P_k(\mu)P_k(\mu')d\mu d\mu' \quad (16)$$

$$S_{i,2} = \int_i\int_{0}^{\mu_{crit}}\sum_{k=1}^{N}\tilde{\omega}_k P_k(\mu)P_k(\mu')d\mu d\mu' \quad (17)$$

$$S_{i,3} = \int_i\int_{-1}^{0}\sum_{k=1}^{N}\tilde{\omega}_k P_k(\mu)P_k(\mu')d\mu d\mu' \quad (18)$$

$$S_{i,c} = \int_i\sum_{k=1}^{N}\tilde{\omega}_k P_k(\mu_c)P_k(\mu')d\mu' \quad (19)$$

Nomenclature

A^B = fraction of $F_\lambda{}^*$ (0) absorbed by the bottom
A^M = overall absorptance of the suspension
C_i = coefficients of the homogeneous solution
d = depth of the suspension, m
F = net radiative flux, W/m^2
F_c = collimated radiative flux in the suspension, W/m^2
F^{*c} = collimated radiative flux incident on the air-water interface, W/m^2
F^{*d} = diffuse radiative flux incident on the air-water interface, W/m^2
H = volumetric radiation absorption rate, W/m^3
I = intensity, W/m^2-sr
K_i = coefficients of the particular solution
n = refractive index of water
p = phase function
P_k = Legendre polynomial of order K
R^M = reflectance of the suspension-bottom complex
$R_{i,j}$ = eigenvectors
$S_{i,j}$ = noncollimated radiance scattering fractions
$S_{i,c}$ = collimated radiance scattering fractions
$T_N[x]$ = transmission integral
z = vertical coordinate, m
γ_i = eigenvalues
θ = declination angle, rad
θ_{crit} = critical angle for internal reflection, rad
$\mu = \cos\theta$
ξ = relative scattering angle, rad
ρ = surface reflectance
ρ_d = bottom reflectance
τ = optical depth
ϕ = azimuthal angle, rad
Ω = solid angle, sr
ω = single scattering albedo
$\tilde{\omega}_k$ = weights of Legendre polynomials

Subscripts

a = average
c = collimated radiation
d = bottom ($z = d$) condition
n = noncollimated radiation
λ = monochromatic condition
1, 2, 3 = regions of the three-flux method

Superscripts

+ = downward (positive z) direction
− = upward (negative z) direction
* = air side of air-water interface
A bar over a symbol (i.e., $\bar{H}$) indicates a normalized quantity

where integration over i implies application of the limits (μ_{crit} to 1), (0 to μ_{crit}) and (−1 to 0) for regions 1, 2 and 3, respectively.

Complete solutions to equations (10–12) may be expressed in terms of the sum of homogeneous and particular solutions

$$F_1(\tau) = \sum_{i=1}^{3} C_i R_{1,i} \exp(\gamma_i \tau) + K_1 \exp(-\tau/\mu_c) \quad (20)$$

$$F_2(\tau) = \sum_{i=1}^{3} C_i R_{2,i} \exp(\gamma_i \tau) + K_2 \exp(-\tau/\mu_c) \quad (21)$$

$$F_3(\tau) = \sum_{i=1}^{3} C_i R_{3,i} \exp(\gamma_i \tau) + K_3 \exp(-\tau/\mu_c) \quad (22)$$

where the eigenvalues and eigenvectors of the homogeneous solution are denoted by γ_i and $R_{j,i}$, respectively. The values of K_j are determined from the particular solution, while the constants C_i are determined from appropriate energy balances at the air-water interface and the bottom. These balances are of the form

$$F_1(0) = 2T_3[0]F^{*d} - 2F_3(0) \int_{\mu_{crit}}^{1} \mu\rho(\mu)d\mu \quad (23)$$

$$F_2(0) = -\mu_{crit}^2 F_3(0) \quad (24)$$

$$F_3(\tau_d) = -\rho_d \mu_c^* [1 - \rho^*(\mu_c^*)]F^{*c} \exp(-\tau_d/\mu_c) - \rho_d[F_1(\tau_d) + F_2(\tau_d)] \quad (25)$$

where the transmission integral, $T_N[x]$, is defined as

$$T_N[x] = n^2 \int_{\mu_{crit}}^{1} [1 - \rho^*(\mu)] \exp(-x/\mu)\mu^{N-2}d\mu \quad (26)$$

The foregoing model may be used to solve for the noncollimated flux components $F_1(\tau)$, $F_2(\tau)$ and $F_3(\tau)$. The net radiative flux may then be expressed as

$$F(\tau) = F_1(\tau) + F_2(\tau) + F_3(\tau) + \mu_c F_c(\tau) \quad (27)$$

where the collimated flux is

$$F_c(\tau) = [1 - \rho^*(\mu_c^*)](\mu_c^*/\mu_c)F^{*c} \exp(-\tau/\mu_c) \quad (28)$$

The net flux may be used to determine the volumetric absorption and the suspension absorptance from equations (5) and (6), respectively, and the component fluxes may be used to determine the fraction of F^* (0) absorbed by the bottom and the reflectance of the suspension-bottom complex from equations (7) and (8), respectively.

Numerics

Calculations based on the three-flux method have been performed for a wide range of conditions, and results are compared with those obtained from the more detailed method of discrete ordinates. The phase function used for all of the calculations was approximated by a 150 term Legendre polynomial of the form

$$p(\xi) = \sum_{n=0}^{150} (2n + 1)(0.89)^{n/2} P_n(\cos\xi) \quad (29)$$

This expression provides a highly forward peaked phase function which is independent of wavelength in the visible region of the spectrum [10] and is representative of measurements obtained for typical aqueous suspensions (Fig. 2). It should be noted, however, that the discrete ordinate method yields spurious results if more than twenty-five ordinates are used and if the number of terms in the phase function expansion exceeds the number of ordinates by more than a factor of two. Although this problem was resolved by using 20 ordinates and a 30 term Legendre polynomial in a previous study [11], the phase function was poorly approximated by the polynomial. In contrast the 150 term polynomial was used in this study to more accurately represent the highly asymmetric phase function, and 24 ordinates were used for the method of discrete ordinates. The numerical problems resulting from use of such a high degree polynomial were resolved by using a phase function renormalization procedure for radiation scattered from the noncollimated field [16].

The solution to the three simultaneous, linear, differential equations (10–12) was obtained in two steps. The homogeneous solution

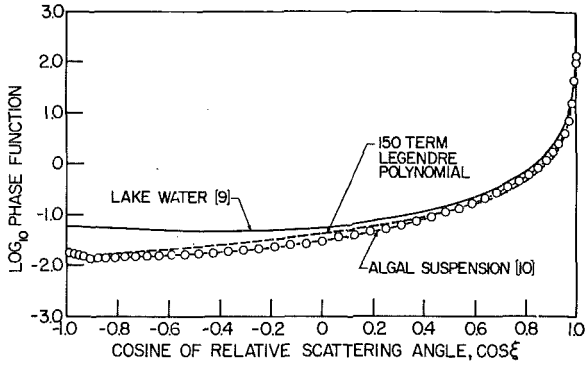

Fig. 2 Representative phase function distributions for aqueous media

was found by substituting an assumed solution, consisting of the sum of three exponentials, into the homogeneous form of the equations. This procedure resulted in an eigenvalue problem that was solved using a matrix routine from the EISPACK library [17] to compute the eigenvalues and eigenvectors. The particular solution was found by substituting an assumed exponential solution into the complete nonhomogeneous equations. The resulting set of linear, algebraic equations was then solved using LU decomposition [18] to find the undetermined coefficients of the assumed solution. The noncollimated scattering parameters defined by equations (16–18) are needed to effect this solution. These parameters were computed by dividing the rectangular region associated with the limits of the double integration into an 80 by 80 rectangular grid. An interpolating, natural, bicubic spline [19] was used to approximate the integrand in each rectangle, and the double integral associated with each rectangle was determined by integrating the bicubic spline exactly. The collimated scattering fraction defined by equation (19) was also computed by using an interpolating cubic spline to approximate the integrand and integrating exactly.

The general solution to the system of differential equations is given by equations (20–22). Once the eigenvalues, γ_i, eigenvectors, $R_{j,i}$, and coefficients, K_j, associated with the particular solution have been found, the boundary conditions given by equations (23–25) may be applied. The resulting set of three linear algebraic equations is then solved by LU decomposition to determine the unknown coefficients C_i and hence to complete the solution.

It should be noted that the numerical features of the three-flux method are similar to those of both the discrete ordinate method and a six-flux method considered in a previous study [11]. In each case the solution to a system of nonhomogeneous, linear differential equations, of varying number, must be obtained, and the same procedures are used to compute the eigenvalues and eigenvectors and to calculate the constant coefficients from the boundary conditions. The major difference is related to the manner in which multiple scattering effects are treated. In the discrete ordinate method the phase function must be approximated by a continuous Legendre polynomial, while in the three-flux and six-flux techniques, simple quadrature rules may be used to integrate the phase function without first approximating it by a continuous function. It is principally the need of a Legendre polynomial expansion of the phase function that causes the computer time required by the discrete ordinate method to exceed that of the three-flux method by approximately a factor of five. In addition, computational difficulties, which are attributed to round-off errors resulting from small eigenvalues, arise when the discrete ordinate method is used for large optical depths and/or large scattering albedos. While the amount of computer time required by the six-flux method exceeds that of the three-flux method by only 15 percent, the six-flux method is limited in its ability to accurately treat refraction at the air-water interface and diffuse reflection at the bottom.

Most of the calculations of this study were performed for standard conditions corresponding to collimated and diffuse irradiation components of $F^{*c} = 500$ W/m^2 and $F^{*d} = 200$ W/m^2, respectively, a collimated incidence angle of $\theta_c^* = 30°$, a scattering albedo and suspension optical depth of $\omega = 0.75$ and $\tau_d = 2.0$, respectively, and a bottom reflectance of $\rho_d = 0.5$. These conditions provide a baseline

for the parametic calculations and are more representative of shallow water layers in the natural environment than those used in a previous study [11].

Results

Variations of the collimated and noncollimated fluxes with optical depth are shown in Fig. 3 for the discrete ordinate and three-flux methods, and there is good agreement between results. Since the collimated flux is modeled in the same way for both methods, equation (28), a single distribution is obtained. The noncollimated flux increases from its initial value at the air-water interface because scattering from the collimated field into the noncollimated field exceeds the rate at which the noncollimated field is absorbed. As the collimated field is attenuated, however, a point is reached where the rate of scattering from the field does not exceed the rate at which the noncollimated field is absorbed, and there is a maximim in the noncollimated flux distribution.

Appropriate components of the noncollimated flux are shown in Fig. 4. The maximum in the optical depth distribution of the downward (+) flux predicted by the discrete ordinate method is due to the absorption rate eventually exceeding the rate of scattering from the collimated field into the forward hemisphere. However, since the upward (−) component consists of radiation scattered from both the collimated and noncollimated downward fluxes, as well as radiation reflected off the bottom, it increases with optical depth throughout the suspension. The same trend characterizes the upward component, $\overline{F}_3$, predicted by the three-flux method. The sum of $\overline{F}_1$ and $\overline{F}_2$ represents the downward flux for the three-flux method, with the dominant contribution coming from region 1, and the distribution with respect to optical depth is in good agreement with that obtained for $\overline{F}^+$ from the discrete ordinate method.

The normalized volumetric absorption predicted by the two methods is plotted as a function of optical depth in Fig. 5 for different values of the scattering albedo, ω, and in all cases there is good agreement between results. In suspensions characterized by a small value of ω and a highly forward peaked phase function, the radiation field retains nearly the same directional distribution as that which is transmitted across the air-water interface and conditions are dominated by absorption. In such suspensions the effect which bottom reflection has on increasing the absorption rate near the bottom is significant. In contrast, with increasing ω scattering effects become more significant, and more of the radiation experiences a directional redistribution rather than absorption. Volumetric absorption is reduced throughout the suspension, and the distribution of $\overline{H}$ with respect to τ becomes more uniform, with the effect of bottom reflection on absorption near the bottom becoming less pronounced. Note that the scattering albedo for aqueous suspensions is typically in the range from 0.85–0.95 [10, 20].

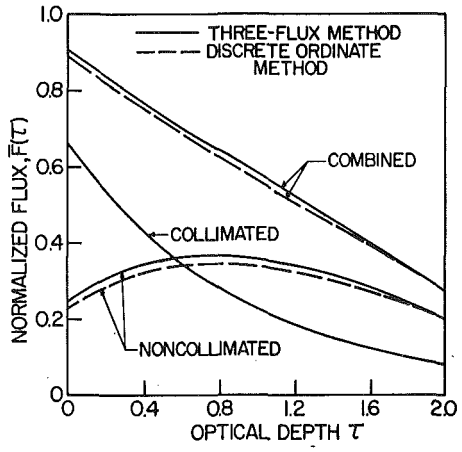

Fig. 3 Collimated and noncollimated flux distributions with respect to optical depth for $F^{*c} = 500$ W/m², $F^{*d} = 200$ W/m², $\theta_c{}^* = 30$ deg, $\omega = 0.75$, $\rho_d = 0.5$, $\tau_d = 2.0$

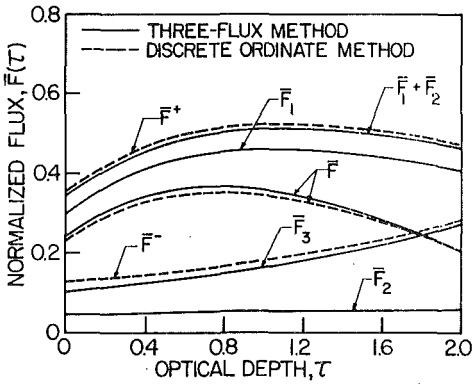

Fig. 4 Noncollimated flux components corresponding to $F^{*c} = 500$ W/m², $F^{*d} = 200$ W/m², $\theta_c{}^* = 30$ deg, $\omega = 0.75$, $\rho_d = 0.5$, $\tau_d = 2.0$

Fig. 6 and 7, respectively. With decreasing ρ_d and/or increasing τ_d, there is a diminishing effect of bottom reflection on conditions within the suspension. There is a general reduction in the magnitude of the absorption and its decay with optical distance from the air-water interface becomes more pronounced. In contrast, for large ρ_d and/or small τ_d, there is greater absorption throughout the suspension and the decay is less pronounced. Agreement between the three-flux and discrete ordinate results is generally good, although differences become more pronounced with increasing ρ_d and decreasing τ_d. To determine whether the accuracy of the three-flux method is significantly reduced under such conditions, additional calculations were performed for the extreme case of $\rho_d = 1.0$ and $\tau_d = 0.5$ (with $F^{*c} = 500$ W/m², $F^{*d} = 200$ W/m², $\theta_c{}^* = 30$ deg, $\omega = 0.75$). The results revealed that, although the three-flux predictions exceed those based on the discrete ordinate method throughout the suspension, differences remain less than 10 percent.

The effect of varying the angular distribution of the incident radiation was studied by holding the combined incident flux constant, while changing the relative magnitudes of the collimated and diffuse irradiances. Three cases were considered. They include a pure diffuse field of $F^{*d} = 700$ W/m², a pure collimated field of $F^{*c} = 700$ W/m², and the combined field of $F^{*c} = 500$ W/m² and $F^{*d} = 200$ W/m². For the two additional cases there is little variation from the results corresponding to the standard conditions (the middle distributions of Figs. 5–7), and the agreement between the three-flux and discrete ordinate results is good.

Equations (6–8) were also used to determine the overall suspension

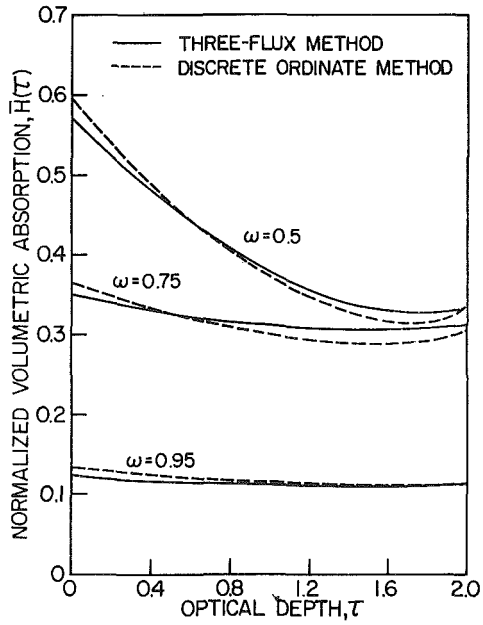

Fig. 5 Normalized volumetric absorption as a function of optical depth and scattering albedo for $F^{*c} = 500$ W/m², $F^{*d} = 200$ W/m², $\theta_c{}^* = 30$ deg, $\rho_d = 0.5$, $\tau_d = 2.0$

absorptance, A^M, the fraction of F^* (0) absorbed by the bottom, A^B, and the reflectance, R^M, of the suspension-bottom complex. The results are summarized in Table 1, and the agreement between methods is good, with differences of less than five percent characterizing the overall suspension absorptance. Note that A^M decreases and A^B and R^M increase with increasing ω, which is consistent with the requirement that the probability of absorption within the suspension decrease with increasing albedo. Similarly, A^M and R^M increase and A^B decreases with increasing ρ_d, while A^M increases and R^M and A^B decrease with increasing τ_d. In contrast there is little effect of the relative contributions of the diffuse and collimated radiation on these properties.

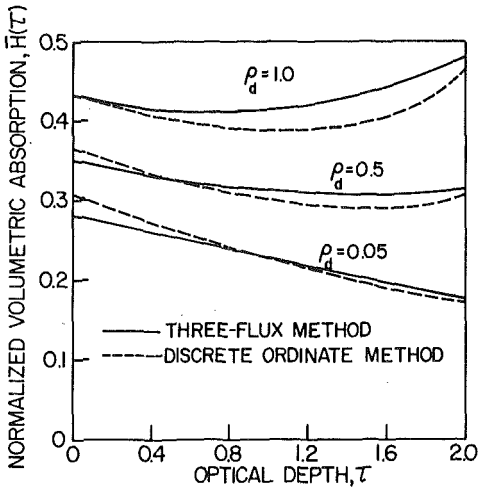

Fig. 6 Normalized volumetric absorption as a function of optical depth and bottom reflectance for F^{*c} = 500 W/m², F^{*d} = 200 W/m², $\theta_c{}^*$ = 30 deg, ω = 0.75, τ_d = 2.0

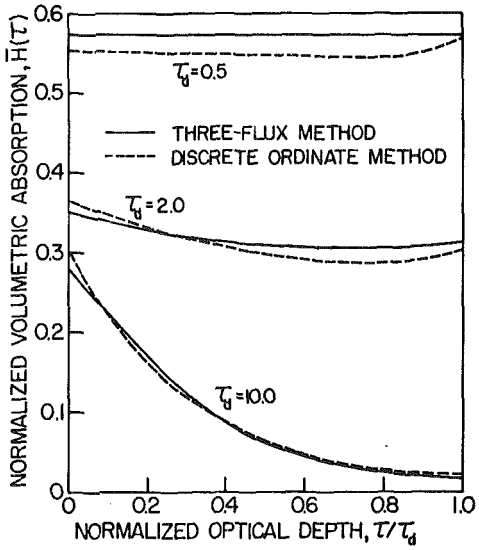

Fig. 7 Normalized volumetric absorption as a function of normalized and overall optical depth for F^{*c} = 500 W/m², F^{*d} = 200 W/m², $\theta_c{}^*$ = 30 deg, ρ_d = 0.5, ω = 0.75

Although the foregoing comparisons indicate that the three-flux predictions are consistent with those obtained from the more detailed discrete ordinate method, the validity of the three-flux method may only be confirmed by comparisons with experiment. Such a comparison is made in Fig. 8, where predictions of the normalized flux are compared with measurements made for a dense algal culture at λ = 513 nm. The results verify the accuracy of the three-flux method for aqueous suspensions of large albedo ($\omega \gtrsim 0.85$) and optical depth ($\tau_d \approx 10$). Confirmation for large values of ρ_d and small values of τ_d must await the acquisition of measured results for such conditions.

For all the conditions of this study, calculations were also performed using a six-flux method previously described [11], and the agreement with the three-flux and discrete ordinate results was generally good. The only significant differences occurred near the bottom of the suspension, where the six-flux method consistently underpredicted results from the other methods by 10–20 percent. This difference may be attributed to the fact that the six-flux method does not separately allow for propagation of collimated and noncollimated radiation fields in the suspension and cannot properly account for directional changes in the radiation field which result from bottom reflection.

The number of fluxes appropriate for calculating radiative transfer in an aqueous suspension may be selected. Two-flux methods have been shown to be inadequate [11] because they approximate the radiation intensity by a single value over the entire forward hemisphere. Both three-flux and six-flux methods yield satisfactory results for the local radiative flux and volumetric absorption, but the three-flux method requires slightly less computer time and is better able to treat the effects of bottom reflection. While the discrete ordinate method has the advantages of superior accuracy and the ability to resolve the directional nature of the radiation, its computer time requirements significantly exceed those of the three and six-flux methods. Accordingly, the three-flux method offers a good compromise between accuracy, operational convenience and computation time.

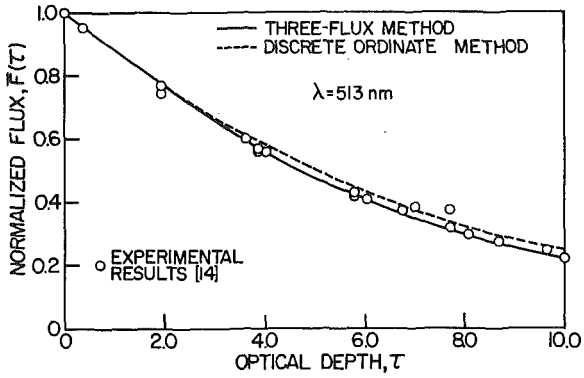

Fig. 8 Comparison of predicted and measured fluxes for an algal culture with diffuse irradiation at the air-water interface (Fluxes are normalized with respect to measured and predicted values at τ = 0).

Table 1 Absorption and reflection calculations for the standard conditions (F^{*c} = 500 W/m², F^{*d} = 200 W/m², $\theta_c{}^*$ = 30 deg, ω = 0.75, ρ_d = 0.5, τ_d = 2.0) and selected variations

	Three-Flux			Discrete Ordinate		
	A^M	A^B	R^M	A^M	A^B	R^M
Standard Conditions	0.637	0.272	0.091	0.623	0.273	0.104
ω = 0.50	0.803	0.149	0.048	0.800	0.153	0.047
ω = 0.95	0.229	0.508	0.263	0.237	0.496	0.267
ρ_d = 0.05	0.456	0.495	0.049	0.463	0.502	0.035
ρ_d = 1.00	0.857	0.000	0.143	0.814	0.000	0.186
τ_d = 0.5	0.286	0.481	0.233	0.277	0.481	0.242
τ_d = 10.0	0.937	0.015	0.048	0.950	0.021	0.029
F^{*d} = 700 W/m² F^{*c} = 0 W/m²	0.622	0.257	0.121	0.626	0.265	0.109
F^{*d} = 0 W/m² F^{*c} = 700 W/m²	0.643	0.279	0.078	0.622	0.277	0.101

Summary

The objective of this study has been to develop a solution method which considers all physical features pertinent to radiative transfer in aqueous suspensions, yet minimizes computational requirements. The method resolves the radiative field into three isotropic components. The components include that portion of the lower hemisphere bounded by the critical angle associated with refraction at the air-water interface, the remaining portion of the lower hemisphere, and the upper hemisphere. The method is judged on the basis of its ability to predict the local radiative flux and volumetric absorption, as well as the overall suspension absorptance and the reflectance of the suspension-bottom complex. These predictions are in good agreement with results obtained from the more detailed method of discrete ordinates for a wide range of suspension properties. This agreement suggests that the three-flux method is able to satisfactorily account for refraction at the air-water interface, anisotropic scattering within the medium, and diffuse reflection at the bottom. The credibility of the method is further confirmed by excellent agreement between predictions of the net radiative flux and measurements obtained for a dense algal culture.

Acknowledgments

Support of this work by the National Science Foundation under Grant No. ENG 75-17370 is gratefully acknowledged.

References

1 Siegel, S., and Howell, J. R., *Thermal Radiation Heat Transfer,* McGraw-Hill, New York, 1972.

2 Kraus, E. B., and C. Rooth, "Temperature and Steady State Vertical Heat Flux in the Ocean Surface Layers," *Tellus,* Vol. 13, No. 2, 1961, pp. 231–238.

3 Dake, J. M. K., and Harleman, D. R. F., "Thermal Stratification in Lakes: Analytical and Laboratory Studies," *Water Resour. Res.,* Vol. 5, No. 2, 1969, pp. 488–495.

4 Foster, T. D., "A Convective Model for the Diurnal Cycle in the Upper Ocean," *J. Geophys. Res.,* Vol. 76, No. 3, 1971, pp. 666–675.

5 Viskanta, R., and Toor, J. S., "Effect of Multiple Scattering of Radiant Energy Transfer in Waters," *J. Geophys. Res.,* Vol. 78, No. 18, 1973, pp. 3538–3551.

6 Bergquam, J. B., and Seban, R. A., "Heat Transfer by Conduction and Radiation in Absorbing and Scattering Materials," ASME JOURNAL OF HEAT TRANSFER, Vol. 93, No. 1, 1971, pp. 236–241.

7 Sanders, C. F., and Lenoir, J. M., "Radiative Transfer through a Cloud of Absorbing-Scattering Particles," *AIChE J.,* Vol. 18, No. 1, 1972, pp. 155–160.

8 Armaly, B. F., and Lam, T. T., "Influence of Refractive Index on Reflectance from a Semi-Infinite Absorbing-Scattering Medium with Collimated Incident Radiation," *Int. J. Heat Mass Transfer,* Vol. 18, No. 4, 1975, pp. 893–899.

9 Duntely, S. Q., "Light in the Sea," *J. Opt. Soc. Amer.,* Vol. 53, No. 1, 1963, pp. 214–220.

10 Privoznik, K. G., Daniel, K. J., and Incropera, F. P., "Absorption, Extinction and Phase Function Measurements for Algal Suspensions of Chlorella Pyrenoidosa," *J. Quan. Spectrosc. Radiat. Transfer,* Vol. 20, 1978, pp. 345–352.

11 Daniel, K. J., Laurendeau, N. M., and Incropera, F. P., "Prediction of Radiation Absorption and Scattering in Turbid Water Bodies," ASME JOURNAL OF HEAT TRANSFER, Vol. 101, No. 1, 1979, pp. 63–67.

12 Chu, C. M., and Churchill, S. W., "Numerical Solution of Problems in Multiple Scattering of Electromagnetic Radiation," *J. Phys. Chem.,* Vol. 59, No. 3, 1955, pp. 855–863.

13 Meador, W. E., and Weaver, W. R., "Six-Beam Models in Radiative Transfer Theory," *Appl. Opt.,* Vol. 15, No. 12, 1976, pp. 3155–3160.

14 Daniel, K. J., Laurendeau, N. M., and Incropera, F. P., "Comparison of Predictions with Measurements for Radiative Transfer in an Algal Suspension," *Int. J. Heat Mass Transfer,* Vol. 21, No. 11, 1978, pp. 1379–1384.

15 Korn, G. A., and Korn, T. M., *Mathematical Handbook for Scientists and Engineers,* McGraw-Hill, 1961.

16 Wiscombe, W. J., "On Initialization, Error, and Flux Conservation in the Doubling Method," *J. Quan. Spectrosc. Radiat. Transfer,* Vol. 18, 1976, pp. 637–658.

17 Smith, B. T., Boyle, J. M., Garbow, B. S., Ikebe, Y., Klema, V. C., and Moler, C. B., *Matrix Eigensystem Routines—EISPACK Guide,* Vol. 6, *Lecture Notes in Computer Science,* Springer-Verlag, 1974.

18 Gerald, C. F., *Applied Numerical Analysis,* Addison-Wesley, 1978.

19 Ahlberg, J. H., Nilson, E. N., and Walsh, J. L., *The Theory of Splines and Their Applications,* Academic Press, 1967.

20 Incropera, F. P., and Privoznik, K. G., "Radiative Property Measurements for Selected Water Suspensions," *Water Resour. Res.,* Vol. 15, No. 1, 1979, pp. 85–89.

T. F. Smith
Associate Professor.
Mem. ASME

P. H. Paul[1]
Research Assistant.
Student Mem. ASME

Division of Energy Engineering,
The University of Iowa,
Iowa City, Iowa 52242

Radiative Transfer in Hartmann MHD Flow

The high temperatures and gaseous products resulting from combustion of hydrocarbon fuels in magnetohydrodynamic generators have provided an impetus to develop more accurate methods for prediction of gas temperature profiles and heat fluxes at the generator walls. One area where an improvement may be realized is in the evaluation of radiative transfer between the gas and surrounding walls. Analyses and results are presented to examine the importance of the radiative transfer term appearing in the gas energy balance for classical Hartmann MHD flow. Results for both real (nongray) and gray gas radiative properties are presented. Inclusion of radiation is found to increase the surface heat flux as well as to alter gas temperature profiles. Furthermore, real gas results differ significantly from those for a gray gas.

Introduction

Increasingly higher temperatures of gaseous products resulting from combustion of hydrocarbon fuels have resulted in a need to develop more accurate techniques for evaluation of gas temperature profiles and wall heat fluxes in energy systems. The magnetohydrodynamic generator (MHD) represents an energy system which has been undergoing extensive development and is designed to operate at temperatures significantly higher than found in existing systems. Information concerned with gas temperature profiles particularly near the generator walls is needed in order to evaluate the gas electrical conductivity and associated wall heat fluxes. Successful design of a wall cooling system and selection of materials for the generator walls also require estimates for wall heat fluxes. At the higher temperatures and with the presence of combustion products of carbon dioxide and water vapor as well as particles, radiative transfer is expected to become an important factor. The overall objective of this research is an examination of radiative transfer in MHD flows.

Viskanta [1], Cramer and Pai [2] and Wilson and Haji-Sheikh [3] examined radiative effects for MHD flow between infinite parallel plates for gray gas properties where the absorption coefficient is independent of frequency. The results demonstrated that the gas temperature in the central region of the flow becomes more uniform as a result of radiative effects. The discussion of Edwards [4] concerning the application of gray results to real (nongray) gas results suggests that these studies may not be applicable in evaluation of real gas temperature profiles and heat fluxes. Datta and Jana [5] examined the effects of radiation for an optically thin gas. Other investigations [6, 7] employed the mean beam length concept and total gas properties [8] to partially account for radiative transfer. In view of these studies, there is lacking adequate information to evaluate the influence of radiative transfer for real gases in MHD flows.

The system selected for study as depicted in Fig. 1 consists of Hartmann MHD flow [9]. This system was chosen for convenience of including MHD effects and enabling radiative contribution to be studied. Analyses and results presented here, however, are expected to be applicable to more comprehensive models of MHD flow. Classical Hartmann flow consists of hydrodynamically and thermally established laminar steady flow of an electrically conducting fluid between two infinite parallel walls with an imposed uniform and constant magnetic field applied in the positive z-direction. An electric field is applied in the positive y-direction. The walls are isothermal and black. With the exception of gas radiative properties, all other gas properties are constant. The gas is assumed to emit and absorb thermal radiation and scattering effects are negligible. Gas radiative properties are taken as real where a band absorption model is employed or gray where the absorption coefficient is a constant. Results are sought for gas temperature profiles and wall heat fluxes as a function of the system variables.

Analysis

For fully developed laminar flow between infinite parallel plates, the energy equation for a radiatively participating gas where viscous dissipation and Joule heating effects are considered but axial components of conductive, convective and radiative transfer are neglected is [9, 10]

$$k\frac{d^2T}{dz^2} = -\mu\left(\frac{dv}{dz}\right)^2 - \frac{j^2}{\sigma_e} + \frac{dq_r}{dz} \tag{1}$$

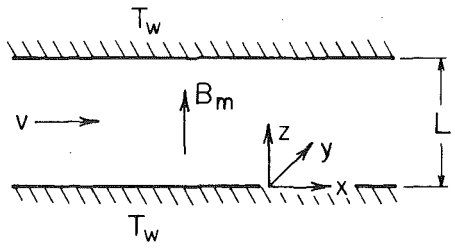

Fig. 1 Schematic diagram of MHD channel

[1] Presently, Graduate Student, Stanford University, Stanford, CA.

Contributed by the Heat Transfer Division of THE AMERICAN SOCIETY OF MECHANICAL ENGINEERS and presented at the AIAA/ASME Thermophysics and Heat Transfer Conference, Palo Alto, Calif., May 25–26, 1978. Manuscript received by the Heat Transfer Division July 6, 1978. Paper No. 78-HT-18.

where in the Joule heating term j is the total current and the last term denotes the divergence of the transverse component of the radiative flux. The boundary conditions for the temperature distribution are $T(0) = T(L) = T_w$. The role of the various energy terms may be conveniently examined by expressing equation (1) in dimensionless form as follows

$$\frac{d^2\theta}{d\eta^2} = -\mathrm{PrEc}\left[\left(\frac{dV}{d\eta}\right)^2 + 4\mathrm{Ha}^2J^2\right] - \frac{\tau_0^2}{N}\frac{dQ_r}{d\eta} \tag{2}$$

with boundary conditions of $\theta(0) = \theta(1) = 1$. In this equation, N represents the ratio of conduction to radiation for a gas with mean absorption coefficient κ and optical thickness τ_0. Since Q_r is an integral term, equation (2) constitutes a second-order, nonlinear integrodifferential equation for the gas temperature distribution.

Derivation of expressions for gas velocity profile for Hartmann MHD flow are available elsewhere [9] and only the final results are presented here. The gas velocity normalized with the mean velocity is given as

$$V(\eta) = \frac{\mathrm{Ha}[\cosh \mathrm{Ha} - \cosh \mathrm{Ha}(2\eta - 1)]}{\mathrm{Ha}\cosh \mathrm{Ha} - \sinh \mathrm{Ha}} \tag{3}$$

The Hartmann number, Ha, relates the magnetic forces to viscous dissipation and is based on the half-channel width. Representative velocity profiles have been presented in [9] and show a flattening and steeper gradient near the channel wall as the Hartmann number increases. The electrically conducting gas moving through the imposed magnetic field produces an induced current flowing in the negative y-direction. In dimensionless form, the total current is

$$J(\eta) = K - V(\eta) \tag{4}$$

where K is the power factor. If $K = 1$, an open circuit exists and the net current given by the integration of equation (4) across the channel is zero. A short circuit results in $K = 0$. Values of $K < 1$ and $K > 1$ apply to a MHD generator and pump or accelerator, respectively.

The formulation of the radiative heat flux for the real (nongray) gas was based on the band model correlation method. Utilizing the technique presented by Cess and Tiwari [11], the radiative heat flux for a multiple band gas in local thermodynamic equilibrium is expressed as

$$q_r(\eta) = b\sum_{i=1}^{M} A_{0i}U_{0i}\int_0^1 [B_i(T) - B_i(T_w)] \times \overline{A}'_i[bU_{0i}(|\eta - \zeta|)]\,\mathrm{sgn}\,(\eta - \zeta)d\zeta \tag{5}$$

where the exponential integral approximations given by $E_3(t) = (1/2)\exp(-bt)$ were utilized with b denoting a constant whose value ranges from 1.5 to 2.0 [12, 13]. In equation (5), $\overline{A}'(u)$ is the derivative of the dimensionless band absorptance $\overline{A}(u)$ with respect to u. Values for these parameters are obtained from the band absorptance correlation as discussed later. $B_i(T)$ is the Planck black body emissive power evaluated at the band center and temperature, T. For the real gas, the mean absorption coefficient is evaluated from

$$\kappa = \frac{1}{\sigma T_w{}^4 L}\sum_{i=1}^{M} A_{0i}U_{0i}B_i(T_w) \tag{6}$$

This definition for κ is similar to that for the Planck mean absorption coefficient [10]. Utilizing this expression for κ dimensionless wall radiative flux may be expressed as

$$Q_r(0) = \frac{b}{4}\sum_{i=1}^{M} W_i\int_0^1 [\phi_i(\theta) - 1]\overline{A}'_i(bU_{0i}\eta)d\eta \tag{7}$$

where, for convenience, W_i is defined by

$$W_i = A_{0i}U_{0i}B_i(T_w)\Big/\sum_{j=1}^{M} A_{0j}U_{0j}B_j(T_w) \tag{8}$$

In equation (7), $\phi_i(\theta)$ denotes the ratio of the Planck function evaluated at a temperature of $\theta(\eta)$ to that for the wall temperature.

The divergence of the radiative heat flux is found by differentiation of equation (5) with respect to η and then performing an integration by parts on the remaining integral. The resultant expression may be expressed in terms of dimensionless quantities as follows

$$\frac{dQ_r(\eta)}{d\eta} = -\frac{b}{4}\sum_{i=1}^{M} W_i\int_0^1 \overline{A}'_i[bU_{0i}(|\eta - \zeta|)]\frac{d\phi_i}{d\theta}\frac{d\theta}{d\zeta}\,\mathrm{sgn}\,(\eta - \zeta)d\zeta \tag{9}$$

A second integration by parts of equation (9) would yield the band absorptance $\overline{A}$ and second derivative of ϕ_i. However, in view of results presented by Nelson [13], the first derivative of the band absorptance is still adequately described by the band correlations.

In the preceding expressions for the radiative transfer terms, the temperature dependency of the band parameters has been neglected and the band parameters are to be evaluated at some convenient temperature as defined later.

For a gray gas, κ corresponds to the frequency independent absorption coefficient and the radiative heat flux is evaluated from [10]

$$q_r(\eta) = \sigma T_w{}^4\{\exp(-b\tau_0\eta) - \exp[-b\tau_0(1 - \eta)]\} + b\tau_0\sigma\int_0^1 T^4(\zeta)\exp[-b\tau_0(|\eta - \zeta|)]\,\mathrm{sgn}\,(\eta - \zeta)d\zeta \tag{10}$$

where the exponential integral approximations have also been employed. At the channel wall, equation (10) may be written as

$$Q_r(0) = \frac{b}{4}\int_0^1 [\theta^4(\eta) - 1]\exp(-b\tau_0\eta)d\eta \tag{11}$$

The divergence of the radiative flux is derived from equation (10) and acquires the form

Nomenclature

$\overline{A}$ = dimensionless band absorptance
A_0 = band width parameter, l/m
b = exponential integral approximation parameter
B = Planck black body function, $W - m/m^2$
B_m = magnetic field, Webers/m^2
c_p = constant pressure specific heat, J/kg − K
E = electric field, V/m
Ec = Eckert number, $\overline{v}^2/c_pT_w$
f = function in equation (18)
Ha = Hartmann number, $LB_m\sqrt{\sigma_e/\mu}/2$
j = current density, amp/m^2
J = dimensionless current density, $j/\sigma_e\overline{v}B_m$
k = thermal conductivity, W/m − C
K = power factor, $E/\overline{v}B_m$
L = channel width, m
M = number of gas bands
N = conduction-radiation parameter, $k\kappa/4\sigma T_w{}^3$
Nu = Nusselt number, $2Lq_w/k(T_w - T_b)$
p = partial pressure, atm
P = total pressure, atm
Pr = Prandtl number, $c_p\mu/k$
q = heat flux, W/m^2
Q = dimensionless heat flux, $-q/4\tau_0\sigma T_w{}^4$
S = integrated band intensity, l/atm-m^2
t = parameter
T = temperature, K
u = path length, Spz/A_0
U_0 = dimensionless pressure-path length, SpL/A_0
v = velocity, m/s
$\overline{v}$ = mean velocity, m/s
V = normalized velocity, $v/\overline{v}$
W = function in equation (8)
x, y, z = coordinates, m
β = line structure parameter
η, ζ = dimensionless coordinates, z/L
θ = dimensionless temperature, T/T_w
κ = absorption coefficient, l/m
μ = viscosity, kg/m-s
σ = Stefan-Boltzmann constant, W/m^2-K^4
σ_e = electrical conductivity, mho/m
τ_0 = optical thickness, κL
ϕ = dimensionless Planck function, $B(T)/B(T_w)$

Subscripts

b = bulk
c = convective
r = radiative
w = wall

$$\frac{dQ_r(\eta)}{d\eta} = \frac{b^2\tau_0}{4}\int_0^1 [\theta^4(\zeta) - 1]\exp[-b\tau_0(|\eta - \zeta|)]d\zeta - \left[\theta^4(\eta) - \frac{b}{2}\right] \quad (12)$$

The wall heat flux is the sum of the conductive and radiative heat fluxes evaluated at the wall and is given by

$$Q_w = \frac{N}{\tau_0^2}\frac{d\theta}{d\eta}\bigg|_{\eta=0} + Q_r(0) \quad (13)$$

Another quantity of interest is the Nusselt number which when combined with equation (13) is expressed as

$$\mathrm{Nu} = \mathrm{Nu}_c + \mathrm{Nu}_r \quad (14)$$

where convective and radiative Nusselt numbers are defined, respectively, as

$$\mathrm{Nu}_c = \frac{2}{\theta_b - 1}\frac{d\theta}{d\eta}\bigg|_{\eta=0};\ \mathrm{Nu}_r = \frac{2\tau_0^2}{(\theta_b - 1)N}Q_r(0) \quad (15)$$

The above definition of the convective Nusselt number includes effects attributed to radiative transfer since the temperature gradient at the wall is partially governed by the radiant exchange process. The bulk fluid temperature is found from

$$\theta_b = \int_0^1 \theta V d\eta \quad (16)$$

Hence, the only quantities remaining are the band correlation parameters.

Gas Radiative Properties

In several MHD generators under development, the combustion of hydrocarbon fuels (natural gas and coal) is planned to occur at pressures slightly above atmospheric pressures. The gas temperature is around 2800 K and wall temperatures range from 1000 to 1800 K depending on the wall material and cooling system. The gas contains in decreasing amounts, water vapor, and carbon dioxide as well as several other species which are expected not to be significant contributors to the radiative transfer processes. In addition, a seed material and soot particles are expected to be present but these are not considered. Therefore, the infrared bands of water vapor and carbon dioxide will be significant contributors and the band correlations developed for these gases [4, 11, 14] may be applied here. Applicability of these correlations particularly at the higher temperatures requires further investigation.

Several continuous correlations which extend over the pressure-path length range have been proposed. Nelson [13] as well as Tiwari [15] have examined radiative heat transfer results based on various band correlations. The correlation utilized in this study to obtain gas properties for a particular band is attributed to Tien and Lowder [16] and is of the form

$$\overline{A}(u, \beta) = \ln\left\{uf(\beta)\left[\frac{u+2}{u+2f(\beta)}\right] + 1\right\} \quad (17)$$

where

$$f(\beta) = 2.94\,[1 - \exp(-2.60\beta)] \quad (18)$$

and β is the line structure parameter. The band absorptance is characterized by three parameters, namely, A_0, U_0 and β. Correlations quantities are available for the bands of carbon dioxide and water vapor [11, 14, 17] and are expressed in terms of temperature, partial pressure and total pressure as well as the band center. The wall temperature was employed to evaluate the correlation parameters for the results presented in this study.

Method of Solution

The energy equation is a second order, nonlinear integrodifferential equation whose solution is arrived at by a finite difference scheme yielding a set of nonlinear algebraic equation. An iterative procedure was devised wherein an initial temperature distribution is calculated from the energy equation without the radiation term. The radiative terms are evaluated utilizing this temperature distribution. Integrals appearing in the divergence of radiative flux equations were evaluated by employment of a Simpson integration scheme. With the radiative term known, the algebraic equations are reduced to a linear form and solved by a maximum pivot strategy. For the real gas case, the spatial derivative of temperature was evaluated by fitting a third order Chebyshev polynomial to the gas temperature distribution. If the new solution, upon comparison with the initial guess, has not converged within an error tolerance of one-tenth percent, the calculated temperature distribution is used as a new guess and the iterative process repeated. For the real gas solution, it was necessary to suppress initially the radiative term and then to increase successively this term as convergence was approached. The rate of convergence was increased by utilizing the temperatures from successive iterations to evaluate a new convergence constant for adjustment of temperatures in each iteration. Temperature profiles for the nonradiating case compared favorably with those presented in [9]. For the gray case with MHD effects, results were compared to those of Wilson and Haji-Sheikh [3] where excellent agreement was found when a numerical integration error in [3] was corrected.

Results and Discussion

Nonradiating MHD Flow. Temperature distributions for a nonradiating MHD gas are presented in Fig. 2 for one-half of the channel width and for Hartmann numbers of 4 and 10. Values for the other governing parameters are $K = 0.5$, $\mathrm{Pr} = 0.7$ and $\mathrm{Ec} = 0.2$. Values for these parameters are also applicable to all other results presented in this study. The Prandtl and Eckert numbers were selected to be representative of those for MHD channels [7]. The temperature distributions illustrated in Fig. 2 serve as reference values for the radiating gas results. For $\mathrm{Ha} = 4$, the Joule heating produces a gas centerline temperature approximately 1.6 times higher than the wall temperature. This factor is increased to 3.5 for $\mathrm{Ha} = 10$.

Radiating MHD Flow. Representative temperature profiles for a radiating MHD gas are illustrated in Fig. 3 where the values for the partial pressure of carbon dioxide and water vapor as well as total gas pressure are provided. The results are applicable for $\mathrm{Ha} = 4$. The gas thermal conductivity was taken from [7]. The values for the channel width, wall temperature and pressures are typical of those for the U-25 MHD generator [18]. The radiating gas results were calculated utilizing five bands corresponding to the 4.3 μm band of CO_2 and 1.38, 1.87, 2.7 and 6.3 μm bands of H_2O. The long wavelength bands were

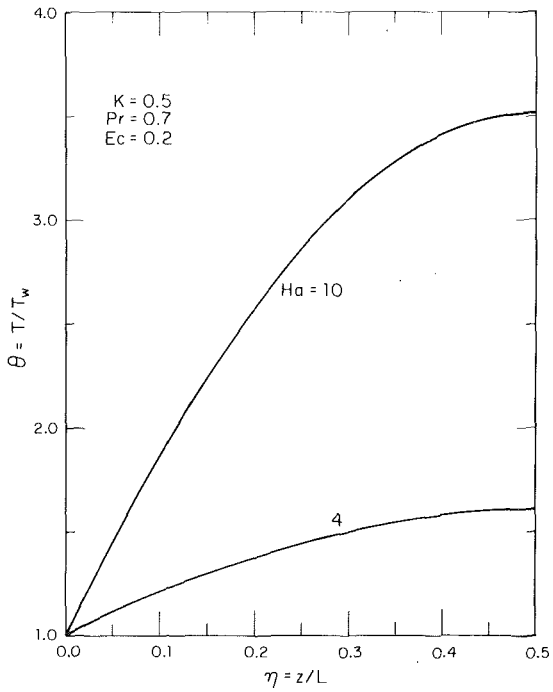

Fig. 2 Temperature distributions for a nonradiating gas

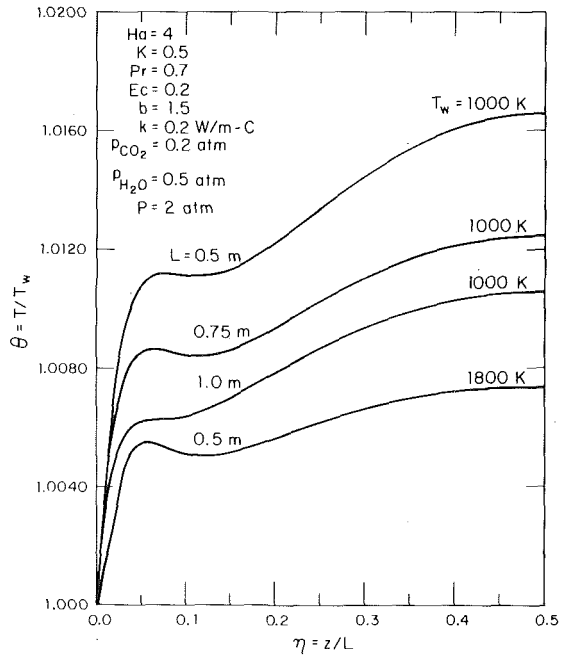

Fig. 3 Temperature distributions for a radiating gas with Ha = 4

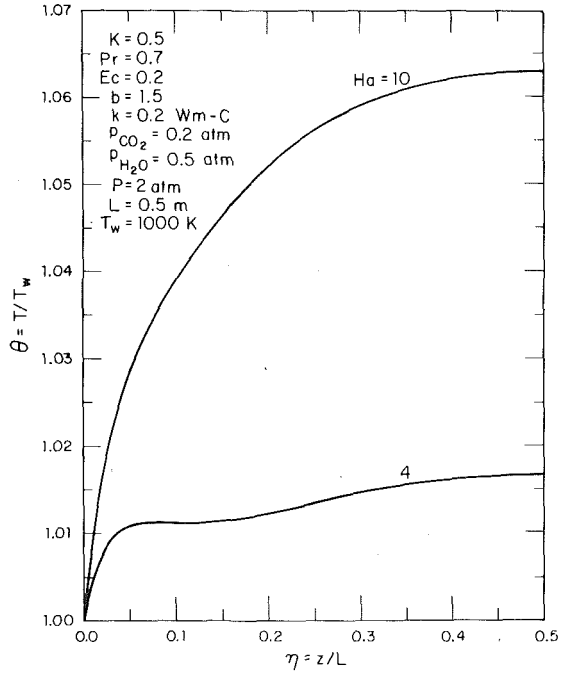

Fig. 4 Temperature distributions for a radiating gas with Ha = 4 and 10

neglected in view of the high temperatures. Furthermore, the overlapped band of 2.7 μm of CO_2 was neglected in comparison with the 2.7 μm band of H_2O [19].

The first observation is that the temperatures for the radiating gas are significantly lower than those for the nonradiating gas as presented in Fig. 2. The general trend of gas temperatures is to increase followed by a leveling off or in some cases a slight decrease and then increase to some centerline value. For these results, the shape of the temperature curves is governed by the behavior of the viscous dissipation and Joule heating terms in the energy balance. As a result of the assumed value for the power factor and recognizing that the current density is evaluated from equation (4), the viscous dissipation dominates near the wall and decreases as the distance from the wall increases. On the other hand, the Joule heating is small near the wall but dominates over the viscous term in the center of the channel. The cross over between viscous dissipation and Joule heating occurs near $\eta = 0.15$. This behavior of the "energy source" term of the energy balance becomes important since the "energy sink" term attributed to the radiative term is significant. Temperature profiles presented by Cramer and Pai [2] for Couette flow of a gray gas also display a similar characteristic.

The behavior of the temperature profiles with channel width is as expected. A wider channel results in larger path lengths and increased absorption of radiant energy. The centerline temperatures are more sensitive to a change in channel width from 0.5 to 0.75 m than from 0.75 to 1.0 m. This trend is attributed to the logarithmic behavior of the band absorptance at large path lengths.

Several proposed designs of MHD channels are to be operated at wall temperatures near 1800 K to increase the gas electrical conductivity near the channel wall and to prevent condensation of the seed material. The influence of wall temperature may be examined by reference to Fig. 3 where results for wall temperatures of 1000 and 1800 K with a channel length of 0.5 m are also displayed. Dimensionless gas temperatures are found to decrease as the wall temperature increases resulting in more uniform temperature profiles. Although the dimensionless path length parameter U_0 decreases with increasing wall temperature yielding a more transparent gas, the radiant energy shifts to shorter wavelengths as a result of the behavior of the black body spectral emission. Thus, the shorter wavelength bands of water vapor become more participating causing an increase in the gas absorption. The magnitudes of gas temperatures displayed in Fig. 3 support the utilization of the molecular gas band correlations.

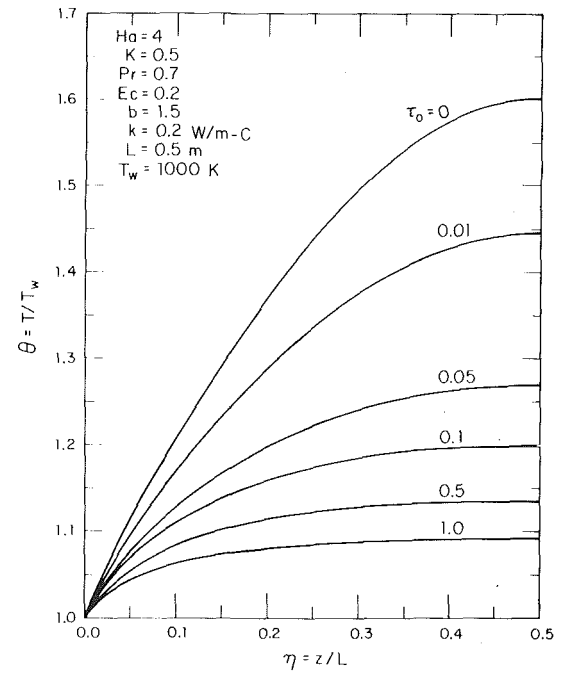

Fig. 5 Temperature distributions for a gray gas

The effect of the Hartmann number is demonstrated by results presented in Fig. 4 for Ha = 4 and 10 with $L \doteq 0.5$ m and $T_w = 1000$ K. At the higher Hartmann number, the Joule heating dominates the "energy source" term and the gas temperatures increase monotonically to the channel centerline. For the U-25 channel, a Hartmann number of 350 is expected. However, this order of magnitude of the Hartmann number would produce very high gas temperatures for a non-radiating gas. Thus, gas radiation would appear to lower these high temperatures to values observed in experimental studies.

Gray gas temperature profiles are presented in Fig. 5 for Ha = 4 and values of optical thickness τ_0 from 0 to 1.0 where the lower limit would correspond to a nonradiating gas. It was found more convenient for this study to express these results in terms of values for L, T_w and k although the gray gas results may be expressed in terms of the con-

duction to radiation parameter N and optical thickness τ_0. As the optical thickness increases, gas temperatures decrease and are expected to increase and eventually reach the non-radiating gas results for an opaque gas. As a result of the emphasis in this study on real gas results, an effort to obtain results for larger optical thicknesses was not made. Larger optical depths, however, are expected to produce temperature profiles with characteristics similar to those in Fig. 3 and reported in [2]. It was stated in [3] that an absorption coefficient of 0.0001 m^{-1} or $\tau_0 = 0.00005$ for the channel length in Fig. 5 is typical of that encountered in MHD channels. In view of results presented for the real gas, a much higher absorption coefficient appears to exist. Further investigation is required to identify the source of this discrepancy.

Nusselt Numbers. In Table 1, results are presented for the bulk temperature, convective, radiative and total Nusselt numbers, conduction to radiation parameter as well as optical thickness for a real gas and a nonradiating gas. In view of the gas temperature gradients at the wall, the convective Nusselt numbers are dominated by the radiative Nusselt numbers. The radiative Nusselt numbers increase with increasing channel width and wall temperature but are nearly identical for Ha = 4 and 10. Although the gas temperature gradient at the wall increases as the Hartmann number increases from 4 to 10, the bulk temperature also increases yielding a lower convective Nusselt number at the higher Hartmann number value. The values for the conduction to radiation parameter are found to be relatively small implying that radiative transfer dominates over conductive transfer. The optical thicknesses for the real gas are also large again demonstrating the importance of radiation. For the nonradiating gas $\tau_0 = 0$, the convective Nusselt numbers are smaller than those for the radiating gas as a result of the higher bulk temperatures. Nusselt number results for the gray gas exhibit a similar behavior as those for the real gas.

Table 1 Nusselt Numbers

Real Gas*

Ha	L, m	T_w, K	θ_b	Nu_c	Nu_r	Nu	$N \times 10^3$	τ_0
4	0.5	1000	1.014	57.7	200	258	8.47	4.8
4	0.75	1000	1.011	69.2	347	416	8.47	7.2
4	1.0	1000	1.009	67.6	490	558	8.47	9.6
4	0.5	1800	1.006	1.6	502	504	0.40	1.3
10	0.5	1000	1.052	34.4	200	234	8.47	4.8
4			1.45	11.0		11.0		0
10			2.78	10.7		10.7		0

* $K = 0.5$, Pr = 0.7, Ec = 0.2, $b = 1.5$, $k = 0.2$ W/m-C, $p_{CO_2} = 0.2$ atm, $p_{H_2O} = 0.5$ atm, $P = 2$ atm

Gray Gas*

θ_b	Nu_c	Nu_r	Nu	$N \times 10^4$	τ_0
1.34	12.5	18.7	31.2	0.176	0.01
1.22	16.1	76.2	92.3	0.882	0.05
1.17	19.2	137	156	1.76	0.1
1.12	23.1	239	262	8.82	0.5
1.08	27.2	320	347	17.6	1.0

* Ha = 4, $K = 0.5$, Pr = 0.7, Ec = 0.2, $b = 1.5$, $k = 0.2$ W/m-C, $T_w = 1000$ K, $L = 0.5$ m

Conclusions

Analysis and results have been presented to examine the influence of gas radiation on temperature profiles for classical Hartmann MHD flow. Real gas radiative properties are described by a band correlation model with parameters for carbon dioxide and water vapor. Results for gas temperature distributions as well as convective, radiative and total Nusselt numbers were obtained for several values of the Hartmann number, channel width and wall temperature for nonradiating, real and gray gas properties. The results demonstrated that gas temperature profiles were significantly reduced as a result of radiative transfer from the gas to the channel walls. Furthermore, the radiative Nusselt number was found to be significantly higher than the convective Nusselt number. The conduction-radiation parameter reflected the findings that radiative transfer was significant. The analysis and results suggested that higher Hartmann numbers should be investigated and that additional information regarding gas radiative properties particularly at higher temperatues is required. Additionally, the radiation portion of the analysis should be combined with a more realistic description of MHD flow with possible inclusion of turbulence.

References

1 Viskanta, R., "Some Considerations of Radiation in Magnetohydrodynamic Couette Flow," *ZAMP*, Vol. 15, 1964, pp. 227–236.

2 Cramer, K. R. and Pai, S., *Magnetofluid Dynamics for Engineers and Applied Physicists*, McGraw-Hill, 1973.

3 Wilson, D. R. and Haji-Sheikh, A., "Effect of Radiative Cooling on the Temperature Distribution in MHD Channel Flows," ASME JOURNAL OF HEAT TRANSFER, Vol. 97, 1975, pp. 151–152.

4 Edwards, D. K., "Molecular Gas Band Radiation," *Advances in Heat Transfer*, Vol. 12, Academic Press, 1976, pp. 115–193.

5 Datta, N. and Janta, R. N., "Effect of Wall Conductances on Hydromagnetic Convection of a Radiating Gas in a Vertical Channel," *Int. Journal Heat and Mass Transfer*, Vol. 19, 1976, pp. 1015–1019.

6 Heywood, J. B. and Womack, G. J., *Open-Cycle MHD Power Generation*, Pergamon, 1969.

7 Bunde, R., et al., *MHD Power Generation*, Springer-Verlag, 1975.

8 Hottel, H. C. and Sarofim, A. F., *Radiative Transfer*, McGraw-Hill, 1967.

9 Sutton, G. W. and Sherman, A., *Engineering Magnetohydrodynamics*, McGraw-Hill, 1965.

10 Sparrow, E. M. and Cess, R. D., *Radiation Heat Transfer*, Brookes/Cole, 1966.

11 Cess, R. D. and Tiwari, S. N., "Infrared Radiative Energy Transfer in Gases," *Advances in Heat Transfer*, Vol. 8, Academic Press, 1971, pp. 229–283.

12 Greif, R. and Habib, I. S., "Infrared Radiation Transport: Exact and Approximate Results," ASME JOURNAL OF HEAT TRANSFER, Vol. 91, 1969, pp. 282–284.

13 Nelson, D. A., "A Study of Band Absorption Equations for Infrared Radiative Transfer in Gases—I. Transmission and Absorption Functions for Planar Media," *Journal Quant. Spectrosc. Radiat. Transfer*, Vol. 14, 1974, pp. 69–80.

14 Tien, C. L., "Thermal Radiation Properties of Gases," *Advances in Heat Transfer*, Vol. 5, Academic Press, 1969, pp. 253–324.

15 Tiwari, S. N., "Applications of Infrared Band Model Correlations to Nongray Radiation," *Int. Journal Heat Mass Transfer*, Vol. 20, 1977, pp. 741–751.

16 Tien, C. L. and Lowder, J. E., "A Correlation for Total Band Absorptance of Radiating Gases," *Int. Journal Heat Mass Transfer*, Vol. 9, 1966, pp. 698–701.

17 Edwards, D. K., Glassen, L. K., Hauser, W. C. and Tuchscher, J. S., "Radiation Heat Transfer in Nonisothermal Nongray Gases," ASME JOURNAL OF HEAT TRANSFER, Vol. 89, 1967, pp. 219–229.

18 Brogan, T. R., Aframe, A. M. and Hill, J., "Preliminary Design of a Magnetohydrodynamic Channel for the USSR U-25 Facility," Final Report, MEPPSCO Inc., Nov. 1974.

19 James, R. K. and Edwards, D. K., "Effect of Molecular Gas Radiation on a Planar, Two-Dimensional Turbulent-Jet-Diffusion Flame," ASME JOURNAL OF HEAT TRANSFER, Vol. 99, 1977, pp. 221–226.

Ali Montakhab
Assoc. Mem. ASME

Convective Heat Transfer in Porous Media

Convective heating or cooling of granular solids or porous media is of interest in the design of thermal energy storage systems. The solutions to the energy initial boundary value problems governing convective heat transfer between a fixed bed of granular solids and a steady flow of heating or cooling fluid are presented. The storage system is considered to be initially in thermal equilibrium at a uniform temperature, a step change in the inlet temperature of the working fluid is imposed, and the thermal response of the system predicted. The results are valid for gases and liquids when the temperature gradient in the solid material is small and axial conduction effect is negligible in comparison with the convective heat transfer. Unlike the previously available solutions to this problem, the results presented are in closed form. This greatly simplifies evaluation and design of thermal energy storage systems of this general type.

Introduction

Convective heating or cooling of granular solids and/or porous materials is of interest in the design of thermal storage systems [1–3]. This paper presents solutions to the energy equations governing convective heat transfer between a fixed bed of granular solids and a steady flow (constant mass velocity) of heating or cooling fluid. The results are closed-form solutions for finding the temperatures of the fluid and granular solids as a function of time and axial position in the direction of the flow.

This problem was first solved by Anzelius [4] and later by Schumann [5]. Locke [6] extended the solution to include a distributed heat source and performed experimental investigations to measure the friction factor and convective heat transfer coefficient. Other investigators [7–13] extended the problem to compact heat exchanger experiments, gas turbine regenerator design, and adsorption in granular solids.

Previous work resulted in either a series solution involving the nth-order derivative of a zero-order Bessel function [5, 6] or double integration of a zero-order Bessel function [4, 7–11]. Hung, et al. [12] and Rao, et al. [13] presented improved solutions based on Laplace transform techniques.

The analysis presented in this paper is based on a different approach which yields closed-form solutions and drastically reduces the amount of computation for convergence.

Idealizations and Assumptions

The analysis is based on a one-dimensional treatment with uniform bulk fluid velocities and temperatures at any cross section normal to direction of the flow. Heat transfer due to radiation or axial conduction is neglected, the temperature gradient in the solid materials is assumed to be small, and the fluid and granular solids are assumed to undergo no phase change. The initial temperature of the granular solids is assumed to be uniform, and internal heat generation and chemical and/or nuclear reactions are assumed to be nonexistent. The change in the kinetic energy of the fluid across any section is negligible compared with changes in specific enthalpy, and external force fields are not considered. The convective heat transfer coefficients and density and specific heat of the granular solids are treated as constants. The governing equations are initially derived for liquids as well as gases to indicate the basic differences. The final solution, however, is based on a simplified case which applies to liquids as well as gases, when the idealizations involved in the analysis are justified.

Mathematical Model

Energy Equations. The energy equations for the fluid and porous media can be derived using the idealizations stated above, together with an appropriate equation of state for the working fluid.

1 *Fluid Side.* Because of the basic differences, in the equation of state, the final form of the energy equation for gases is slightly different from that of liquids. Thus,

$$\left.\begin{aligned}\text{(gases)}\quad & \frac{\partial}{\partial z}(GT)+\frac{1-\beta}{\gamma\sigma R}\frac{\partial p}{\partial t}=\frac{h\alpha}{c\sigma}(T_s-T)\\ \text{(liquids)}\quad & \frac{\partial}{\partial z}(GT)+\frac{(1-\beta)\rho}{\sigma}\frac{\partial T}{\partial t}=\frac{h\alpha}{c\sigma}(T_s-T)\end{aligned}\right\} \tag{1}$$

2 *Solid Side.* When the temperature gradient in the solid materials is small and the axial conduction effect is negligible, the energy equation for the solid materials can be written in the following form:

$$\text{(solids)}\quad \frac{\partial T_s}{\partial t}+\frac{h\alpha}{\rho_s\beta c_s}(T_s-T)=0 \tag{2}$$

These equations can be written in nondimensional form by introducing the following variable changes:[1]

$$\left.\begin{aligned}\zeta &\equiv \frac{h\alpha z}{G\sigma c}\\ \tau &\equiv \frac{h\alpha t}{\rho_s\beta c_s}\end{aligned}\right\} \tag{3}$$

$$\left.\begin{aligned}\theta &\equiv \frac{T-T_1}{T_{so}-T_1}e^{\zeta+\tau}\\ \theta_s &\equiv \frac{T_s-T_1}{T_{so}-T_1}e^{\zeta+\tau}\end{aligned}\right\} \tag{4}$$

For steady flow conditions, the mass velocity of the fluid (G in equations (1)) is constant in the z direction. In many practical situations, the second term on the left-hand side of equations (1) is quite small compared with the first term and may be neglected.[2] For example, Schmidt and Szego [1] calculate the magnitude of the coefficient of the second differential in equations (1) for water and air as the working fluid and Feolite as the storage material. It is concluded that these coefficients are sufficiently small so that a negligible error is introduced in the analysis if the second terms on the left-hand sides of equations (1) are neglected. If this is done and equations (3) and (4) are introduced into equations (1),

$$\frac{\partial\theta}{\partial\zeta}=\theta_s \tag{5}$$

Contributed by the Heat Transfer Division and presented at the AIAA/ASME Thermophysics and Heat Transfer Conference, Palo Alto, California, May 25–26, 1978. Manuscript received by the Heat Transfer Division June 22, 1978. Paper No. 78-HT-45.

[1] The analysis which led to the choice of these non-dimensional groupings is based on the Buckingham π-theorem, although other approaches (e.g., Garabedian [14]) lead to the same groupings.

[2] If this is done, the solution is valid for gases and liquids.

and equation (2) reduces to

$$\frac{\partial \theta_s}{\partial \tau} = \theta \tag{6}$$

Equations (5) and (6) are coupled by the temperatures of the solids and the fluid. Taking the derivative of both sides of equation (5) with respect to τ and adding the result to equation (6) yields

$$\frac{\partial^2 \theta}{\partial \tau \partial \zeta} = \theta \tag{7}$$

Taking the derivative of θ_s for both sides of equation (6) with respect to τ and adding the results to equation (5) yields

$$\frac{\partial^2 \theta_s}{\partial \tau \partial \zeta} = \theta_s \tag{8}$$

Equations (7) and (8) can be solved together with a set of auxiliary conditions, given in the following section.

Auxiliary Conditions. The temperature of the fluid at the entrance to the granular solids region (at $z = 0$) and the initial temperature of the granular solids are known values and are referred to as T_1 and T_{so}, respectively. Introducing the definitions of θ and θ_s from equation (4) enables these conditions to be written in the following form:

$$\theta(0, \tau) = 0 \tag{9}$$

$$\theta_s(\zeta, 0) = e^{\zeta} \tag{10}$$

Another set of initial and boundary conditions can be obtained from equations (5) and (6). Introducing the condition given by equation (10) into equation (5) at $\tau = 0$ yields

$$\frac{\partial}{\partial \zeta}\theta(\zeta, 0) = e^{\zeta} \tag{11}$$

Similarly, if the condition of equation (9) is introduced into equation (6) at $\zeta = 0$,

$$\frac{\partial}{\partial \tau}\theta_s(0, \tau) = 0 \tag{12}$$

Solution

Two sets of initial boundary value problems for the temperatures of the fluid and granular solids have been derived. Equation (7) is the governing equation for the fluid temperature, and equations (9) and (11) provide the required auxiliary conditions. Equation (8) together with equations (10) and (12) provide the initial boundary value problem for the temperature of the solids.

The solution to the characteristic initial boundary value problem on the fluid side is obtained in the Appendix. The final result is

$$\theta(\zeta, \tau) = e^{\zeta+\tau} - \sum_{n=0}^{\infty} \psi_n(\zeta) \frac{\tau^n}{n!} \tag{13}$$

where

$$\psi_n(\zeta) \equiv \sum_{k=0}^{n} \frac{\zeta^k}{k!} \tag{14}$$

Substituting the expression for θ in equations (4) yields the final expression for the fluid temperature in terms of time and axial distance through the granular solids:

$$\frac{T - T_1}{T_{so} - T_1} = 1 - e^{-(\zeta+\tau)} \sum_{n=0}^{\infty} \psi_n(\zeta) \frac{\tau^n}{n!} \tag{15}$$

A similar procedure can be used to obtain the solution for the temperature of the granular solids with respect to time and axial position. It is simpler, however, to use equation (5), noting that the fluid temperature given by equation (13) can be differentiated with respect to ζ to find an expression for $\theta_s(\zeta, \tau)$:[3]

$$\theta_s(\zeta, \tau) = e^{\zeta+\tau} - \sum_{n=1}^{\infty} \psi_{n-1}(\zeta) \frac{\tau^n}{n!} \tag{16}$$

Substituting the expression for θ_s in equations (4) yields the final expression for the granular solids temperature:

$$\frac{T_s - T_1}{T_{so} - T_1} = 1 - e^{-(\zeta+\tau)} \sum_{n=1}^{\infty} \psi_{n-1}(\zeta) \frac{\tau^n}{n!} \tag{17}$$

Equations (15) and (17) are plotted in Figs. 1 and 2. An expression for

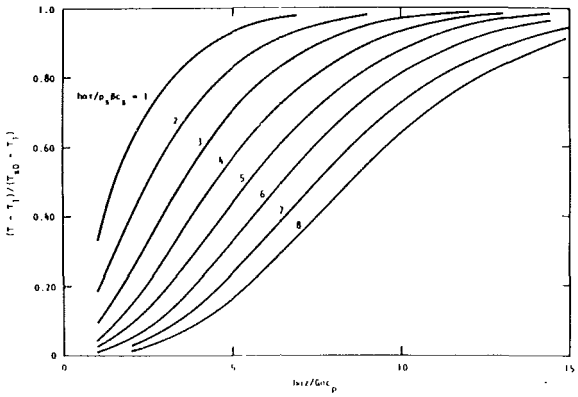

Fig. 1 Temperature of fluid as a function of time and position

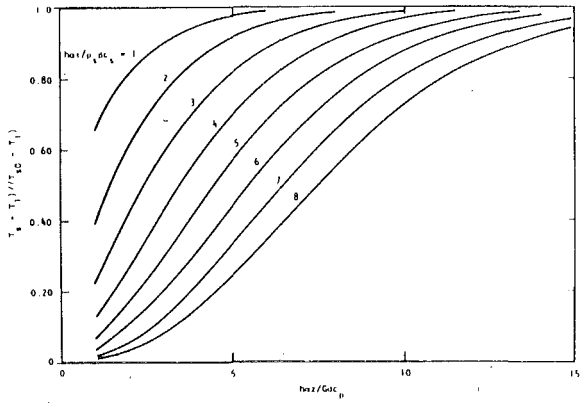

Fig. 2 Temperature of solid materials as a function of time and position

[3] Note that $\psi_n'(\zeta) = \psi_{n-1}(\zeta)$.

Nomenclature

Bi = Biot number
c = specific heat of liquid or of gas at constant pressure
c_s = specific heat of solid materials
G = mass velocity of the fluid
h = convective heat transfer coefficient
k_s = thermal conductivity of solid materials
p = pressure
R = gas constant
T = temperature of fluid
t = time
T_s = temperature of solid materials
T_1 = fluid inlet temperature
T_{so} = initial temperature of solid materials
w = semithickness of solid materials
z = vertical coordinate
α = heat transfer area per unit total volume
β = volume fraction of granular solids
γ = ratio of specific heats for gas
ζ = nondimensional coordinate defined by equation (3)
θ = nondimensional fluid temperature defined by equation (4)
θ_s = nondimensional solids temperature defined by equation (4)
ρ_s = density of solid materials
σ = minimum free-flow area per unit frontal area
τ = nondimensional time defined by equation (3)
ψ_n = function defined by equation (14)

the fluid-solids temperature differences can be obtained by subtracting both sides of equation (15) from equation (17), noting that $\psi_0(\zeta) = 1$:

$$\frac{T_s - T}{T_{so} - T_1} = e^{-(\zeta+\tau)} \sum_{n=0}^{\infty} \frac{(\zeta\tau)^n}{(n!)^2} \tag{18}$$

Discussion of Results

Equations (15) and (17) are solutions to the energy initial boundary value problems governing convective heat transfer between a fixed bed of granular solids (or porous media) and a steady flow of heating or cooling fluid. These solutions are useful for the design or performance evaluation of thermal energy storage systems of this general type. The storage system is initially in thermal equilibrium at a uniform temperature T_{so}, the fluid inlet temperature is held at a constant value T_1, and the temperature of the working fluid T and solid materials T_s are predicted. The thermal response of the storage system depends on two independent variables: a nondimensional time τ and a nondimensional axial position in the direction of the flow ζ. The maximum amount of thermal energy which can be stored by the unit can be determined from equation (18) or results similar to those plotted in Figs. 1 and 2.

A comparison of the results given by equations (15) and (17) with the results presented by London, et al. [3] indicates excellent agreement. The nondimensional variables used are related to those used in this paper by the following expressions:

$$N_{tu} = \zeta, \qquad \tau^* = \tau$$

$$\epsilon_f^* = \frac{T_{so} - T}{T_{so} - T_1}, \qquad \epsilon_w^* = \frac{T_{so} - T_s}{T_{so} - T_1}$$

Equations (15) and (17) are valid for gases and liquids when the temperature gradient in the solid materials is small ($\mathrm{Bi} \equiv hw/k_s < 0.01$) and the axial conduction effect in the solids is negligible in comparison with the convective heat transfer. These equations are based on a one-dimensional treatment of the problem with uniform bulk fluid velocities and temperatures at any cross section normal to the direction of the flow. Thus uniform flow distribution and proper insulation of the storage unit are important considerations if the one-dimensional treatment is to be applied. Furthermore, internal heat generation and chemical or nuclear reactions are assumed to be non-existent and the fluid and granular solids are assumed to undergo no phase change.

The solutions presented by equations (15) and (17) do not account for the events that take place from the instant the fluid is allowed to flow in the unit to the moment the first particles of the fluid leave the unit. Typically this time interval is of an order of magnitude smaller than the characteristic time scale of the process, but care must be taken when results for small times are required.

When the temperature gradient within the solid material is no longer small, a lumped parameter analysis of the solid materials may no longer be valid for the accurate determination of the transient response of the storage system. The solution to this case is presented by Schmidt and Szego [1] for a storage unit composed of rectangular solid materials. A comparison of these results with those presented in this paper indicates excellent agreement with the parameters are selected so that the internal temperature gradients in the solids are negligible. It can be concluded that the conduction effect is negligible when the Biot number ($\mathrm{Bi} \equiv hw/k_s$) is less than 0.01.

Equations (15) and (17) provide excellent means for the design, evaluation, or prediction of storage system performance, especially when a digital computer is used. The infinite series which appear in these equations are rapidly convergent, and excellent accuracy can be obtained with the inclusion of only a few terms. This is not the case with the previously available solutions to this problem because of the time and difficulties involved in computing the integral or the nth order derivative of the zero-order Bessel function.

Summary

An improved solution for heat transfer between a fixed bed of granular solids and a steady flow of heating or cooling fluid is presented. The results are closed-form solutions for the temperatures of the fluid and granular solids as a function of two independent variables: nondimensional time and nondimensional axial position. The results are valid for gases and liquids when the temperature gradient in the solid materials is small and the axial conduction in the flow direction is negligible. Unlike the previously available solutions to this problem, the results presented are in closed form. This greatly simplifies the computations involved in the evaluation and design of thermal energy storage systems of this general type.

Acknowledgments

The encouragement and technical guidance of Professor A. L. London of Stanford University is gratefully acknowledged. General Atomic Company provided partial funding for the preparation of this paper.

References

1 Schmidt, F. W., and Szego, J., "Transient Response of Solid Sensible Heat Thermal Storage Units—Single Fluid," ASME JOURNAL OF HEAT TRANSFER, Aug. 1976, pp. 471–476.

2 Coppage, J. E., and London, A. L., "Heat Transfer and Flow Friction Characteristics of Porous Media," *Chem. Engrg. Progress*, Vol. 52, No. 2, pp. 57–63.

3 London, A. L., Lampsell, D. F., and McGowan, J. G., "The Transient Response of Gas Turbine Plant Heat Exchangers—Additional Solutions for Regenerators of the Periodic Flow and Direct Transfer Types," ASME *Journal of Engineering for Power*, Vol. 86, 1964, pp. 127–135.

4 Anzelius, A., "Über Erwärmung Vermittels Durchströmender Medien," *Z. Angew. Math. Mech.*, Vol. 6, 1926, pp. 291–294.

5 Schumann, T. E. W., "Heat Transfer: A Liquid Flowing through a Porous Prism," *Franklin Institute Journal*, Vol. 208, 1929, pp. 405–416.

6 Locke, G. L., "Heat Transfer and Flow Friction Characteristics of Porous Solids," Stanford Univ., Dept. of Mech. Engrg., Technical Report No. 10.

7 Dang Dihn Heip, "Transient Heat Transfer in Porous Media," U. S. Naval Postgraduate School, Mech. Engrg. Dept., 1965.

8 Kohlmayr, G. F., "Analytical Solution of the Single-Blow Problem by a Double Laplace Transform Method," Pratt & Whitney Aircraft, Report PWA-3158, 1967.

9 Moreland, F. E., "Solution of the Single Blow Problem with Longitudinal Conductivity by Numerical Inversion of Laplace Transform," MS thesis, U. S. Naval Postgraduate School. 1964.

10 Howard, C. P., "Heat Transfer and Flow Friction Characteristics of Skewed Passages and Glass Ceramic Heat Transfer Surfaces," Stanford Univ., Dept. of Mech. Engrg., Report TR-59, Oct. 1963.

11 Hougen, O. A., and Marshall, Jr., W. R., "Adsorption from a Fluid Stream Flowing through a Stationary Granular Bed," *Chemical Engrg. Progress, Trans. Section*, Vol. 43, No. 4, pp. 197–208, April 1947.

12 Hung, F. T., and Nevins, R. G., "Unsteady-State Heat Transfer with a Flowing Fluid through Porous Solids," ASME Paper 65-HT-10, 1965.

13 Rao, S. K., and Suri, R. K., "Thermal Characteristics of Homogeneous Packed Beds with Steady Fluid Flow," *I.E.(I) Journal*—ME, Vol. 50, Nov. 1969, pp. 63–69.

14 Garabedian, P. R., *Partial Differential Equations*, John Wiley & Sons, 1964.

Appendix

Solution to the Energy Initial Boundary Value Problem

The solution to the linear, homogeneous differential equation

$$\theta_{xy} - \Omega\theta = 0 \tag{19}$$

with a set of auxiliary conditions

$$\theta(a, y) = \psi(y)$$

$$\theta(x, b) = \Phi(x) \tag{20}$$

subject to

$$\psi(b) = \Phi(a)$$

is [14]

$$\theta(x, y) = A(S, R)\theta(S) + \int_S^P \theta_y A d\eta + \int_S^0 \theta_x A d\mu \tag{21}$$

where the quantity $A(R, S) = A(x, y; \mu, \eta)$ is known as the Riemann function associated with the linear partial differential equation

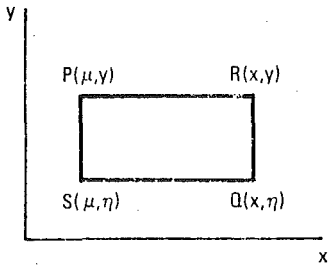

Fig. 3 Coordinates and characteristic lines

(equation (19)). The points P and Q in Fig. 3 represent the pairs of coordinates (μ, y) and (x, ν), respectively, when they occur as arguments of A. The line integral between P and Q in equation (21) must be evaluated along a segment of the vertical characteristic through P and a segment of the horizontal characteristic through Q. These characteristics intersect at a point denoted by S.

The Riemann function for equation (19) is [14]

$$A(x, y;\mu, \eta) = I_0[2\sqrt{\Omega(x-\mu)(y-\eta)}] \tag{22}$$

where I_0 is a Bessel function with the following infinite series representation:

$$I_0(r) = \sum_{n=0}^{\infty} \left[\frac{(r/2)^n}{n!}\right]^2 \tag{23}$$

The solution to equations (7, 9), and (11) can be obtained by using equations (21–23) and introducing the following changes of variables: $\Omega = 1, a = b = 0, x = \zeta, y = \tau, \psi(\tau) = 0, \Phi'(\mu) = e^{\mu}$. This yields

$$\theta(\zeta, \tau) = \int_0^{\zeta} e^{\mu} I_0[2\sqrt{\tau(\zeta-\mu)}]\, d\mu \tag{24}$$

Substituting the series form of I_0 from equation (23) results in

$$\theta(\zeta, \tau) = \sum_{n=0}^{\infty} \frac{\tau^n}{(n!)^2} \int_0^{\zeta} e^{\mu}(\zeta-\mu)^n\, d\mu \tag{25}$$

and using a successive series of integration by parts results in

$$\int_0^{\zeta} e^{\mu}(\zeta-\mu)^n\, d\mu = \left(e^{\zeta} - \sum_{k=0}^{n} \frac{\zeta^k}{k!}\right) n! \tag{26}$$

Substituting equation (26) into equation (25) and noting that

$$e^{\tau} = \sum_{n=0}^{\infty} \frac{\tau^n}{n!}$$

yields

$$\theta(\zeta, \tau) = e^{\zeta+\tau} - \sum_{n=0}^{\infty} \psi_n(\zeta) \frac{\tau^n}{n!} \tag{27}$$

where

$$\psi_n(\zeta) \equiv \sum_{k=0}^{n} \frac{\zeta^k}{k!} \tag{28}$$

W. Roetzel
Prof. Dr.-Ing.

J. Neubert
Dipl.-Ing.

Institut für Thermodynamik,
Hochschule der Bundeswehr Hamburg,
Holstenhofweg 85 / Postfach 700 822,
2000 Hamburg 70
Germany

Calculation of Mean Temperature Difference in Air-Cooled Cross-Flow Heat Exchangers

An approximate explicit equation together with empirical coefficients is presented for the fast calculation of the mean temperature difference of eight cross-flow arrangements. The mean temperature difference is calculated from the effectiveness of the process stream and the number of transfer units on the air side.

1 Introduction

In computerized heat exchanger design, the mean temperature difference can be calculated using a generally valid approximate equation with a different set of coefficients for each flow arrangement [1, 2]. The mean temperature difference is calculated from the inlet and outlet temperatures of both streams. The following equations are applied.

First the effectivenesses of both streams are calculated according to

$$p = \frac{T_1 - T_2}{T_1 - t_1} \tag{1}$$

and

$$q = \frac{t_2 - t_1}{T_1 - t_1} \tag{2}$$

Then the dimensionless logarithmic mean temperature difference for countercurrent flow is determined using

$$r_{l.m.} = \frac{p - q}{\ln \dfrac{1 - q}{1 - p}} \tag{3}$$

The actual dimensionless mean temperature difference

$$r = \frac{\Delta T_m}{T_1 - t_1} \tag{4}$$

is found by correcting the dimensionless logarithmic mean temperature difference according to

$$r = F_T \cdot r_{l.m.} \tag{5}$$

The correction factor F_T is calculated from the following equation

$$F_T = 1 - \sum_{i=1}^{m} \sum_{k=1}^{n} a_{i,k} \cdot (1 - r_{l.m.})^k \cdot \sin\left(2 \cdot i \cdot \arctan \frac{p}{q}\right) \tag{6}$$

with a different set of coefficients $a_{i,k}$ for each flow arrangement.

The procedure [1] described above is very convenient if the inlet and outlet temperatures of both streams are given. However, when designing air-cooled cross-flow heat exchangers, usually the inlet and outlet temperatures and the mass flow rate of the process fluid are prescribed; while on the air side, only the inlet temperature is fixed. The air outlet temperature or the air mass flow rate is subject to an optimization process.

Depending on the optimization method applied, it might be of advantage if the mean temperature difference could be calculated without knowing the air outlet temperature.

Experience in the design of air-cooled cross-flow heat exchangers has shown that the number of transfer units (NTU = s), defined by

$$s = \frac{K \cdot A}{\dot{c}} = \frac{t_2 - t_1}{\Delta T_m} = \frac{q}{r} \tag{7}$$

is a suitable design variable in that one knows the approximate values of $s = K \cdot A/\dot{c}$ for different types of fin-tube bundles. In this paper a general approximate explicit equation is presented for the calculation of the mean temperature difference in air-cooled cross-flow heat exchangers from the effectiveness p of the process stream and the number of transfer units s on the air side.

2 General Equation

As with equation (6), the idea is to use a generally valid type of empirical equation with a different set of coefficients for each cross-flow arrangement.

Considering equation (3) reveals that it cannot be solved for r as function of p and $s = q/r$. Therefore the new equation is not based on the correction of $r_{l.m.}$, but on the correction of the mean temperature difference for one-row cross-flow.

The well-known equation (see e.g., [3]) for this flow arrangement

$$r_I = \frac{-q}{\ln\left[1 + \dfrac{q}{p} \ln (1 - p)\right]} \tag{8}$$

can also be given in the form

$$r_I = \frac{e^{-s} - 1}{s} \cdot \frac{p}{\ln (1 - p)} \tag{9}$$

This dimensionless mean temperature difference is the smallest which occurs in cross-flow arrangements (for fixed values of p and s). Thus a correction must be added to r_I to get the dimensionless mean temperature difference of a cross-flow arrangement with more than one row. The correction must revert to zero if $p = 0$ or $s = 0$ ($q = 0$) because in these limiting cases the mean temperature difference of any flow arrangement (as r_I) assumes the logarithmic mean temperature difference (one stream isothermal).

The following function (r_I from equation (9)) was found to be suitable:

$$r = r_I + \sum_{i=1}^{m} \sum_{k=1}^{n} b_{i,k} \cdot p^i \cdot \left(\frac{s}{1 + s}\right)^k \tag{10}$$

The coefficients $b_{i,k}$ were determined by a least squares estimation. The absolute error of the dimensionless mean temperature difference was minimized. The exact values were calculated according to the references shown below:

1 one to four rows in a single pass [3]
2 two rows with a single row per pass [4]
3 three rows with a single row per pass [5]
4 four rows with two rows per pass and with a single row per pass [6]

The limiting case of an infinite number of rows with a single row per pass is countercurrent flow according to equation (3).

For the least squares estimation, 1036 to 1191 points were used in the range $0.25 \le s \le 2.5$ and $r/r_{l.m.} > 0.5$. 16 coefficients ($m = n = 4$) were found to be sufficient. The absolute standard error is in all cases less than $1.4 \cdot 10^{-4}$. In the flow arrangement with four rows and two rows per pass, the process fluid is assumed to be completely mixed in box-type headers between passes. Two other variants with no

Contributed by the Heat Transfer Division for publication in the JOURNAL OF HEAT TRANSFER. Manuscript received by the Heat Transfer Division March 26, 1978.

mixing between passes (Fig. 1) are possible and were investigated through an incremental calculation [7]. It was found that variant *a* yields slightly higher and variant *b* slightly lower mean temperature differences than the variant of complete mixing between passes. However, the absolute differences of r are smaller than 0.001 and can be neglected. Thus the coefficients of Table 4 are valid for mixing and no mixing between passes.

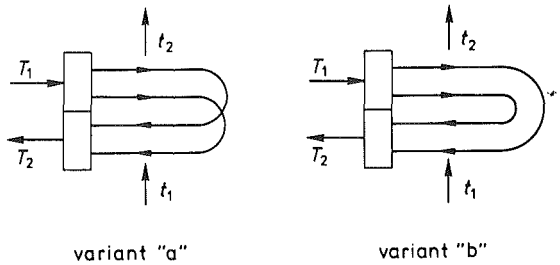

Fig. 1 Cross-flow with four rows and two passes—two variants with no mixing of process fluid between passes

3 Conclusion

As an alternative to equation (6) [1], the new equation (9, 10) together with the coefficients given in Tables 1–8 can be recommended for computerized design of air-cooled cross-flow heat exchangers when the effectiveness of the process fluid is given and the number of transfer units on the air side can be estimated.

References

1 Roetzel, W., and Nicole, F. J. L., "Mean Temperature Difference for Heat Exchanger Design—A General Approximate Explicit Equation," *Trans ASME*, Vol. 97, Feb. 1975, pp. 5–8.

2 Jarzebski, A. B., Lachowski, A. J., Szponarski, T. and Gasior, S., "Approximate Mean Temperature Difference for Calculation of Heat Exchangers," *The Canadian Journal of Chemical Engineering*, Vol. 55, Dec. 1977, pp. 741–743.

3 Schedwill, H., "Thermische Auslegung von Kreuzstromwärmeaus-tauschern," *Fortschr.-Ber.* VDI-Z. Reihe 6, Nr. 19 (1968).

4 Bowman, R. A., Mueller, A. C., and Nagle, W. M., "Mean Temperature Difference in Design," *Trans ASME*, Vol. 62, May 1940, pp. 283–294.

5 Stevens, R. A., Fernandez, J., and Woolf, J. R., "Mean Temperature Difference in One, Two, and Three-Pass Cross-Flow Heat Exchangers," *Trans ASME*, Vol. 79, Feb. 1957, pp. 287–297.

6 Nicole, F. J. L., "Mean Temperature Difference in Cross-Flow Heat Exchange, Applied to Multipass Air-Cooled Fin-Tube Units with a Finite Number of Rows," MSc (Engng.) thesis, University of Pretoria, CSIR Special Report CHEM 223, Nov. 1972.

7 The numerical calculations were carried out by Olt D. Hellfeier at the Institute for Thermodynamics of the Hochschule der Bundeswehr (German Armed Forces University,) Hamburg.

Table 1

Values of $b_{i,k}$ for 2 row, 1 pass

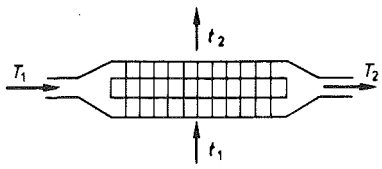

	i = 1	2	3	4
k = 1	1,078587 10^{-2}	1,795548 10^{-2}	-1,055502 10^{-2}	-6,755819 10^{-3}
2	-4,814754 10^{-2}	-1,551399 10^{-1}	6,967073 10^{-2}	7,109024 10^{-2}
3	2,165124 10^{-1}	4,281138 10^{-1}	-1,122809 10^{-1}	-2,497038 10^{-1}
4	-1,408721 10^{-2}	-5,021447 10^{-1}	1,828372 10^{-1}	1,198928 10^{-1}

Table 2

Values of $b_{i,k}$ for 3 row, 1 pass

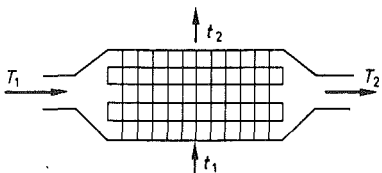

	i = 1	2	3	4
k = 1	1,367766 10^{-2}	1,898826 10^{-2}	-2,248502 10^{-2}	1,562070 10^{-3}
2	-6,745581 10^{-2}	-1,506259 10^{-1}	1,403442 10^{-1}	1,963323 10^{-2}
3	2,917225 10^{-1}	3,874476 10^{-1}	-2,320301 10^{-1}	-1,586416 10^{-1}
4	-5,399342 10^{-2}	-4,674339 10^{-1}	2,610630 10^{-1}	5,421831 10^{-2}

Table 3

Values of $b_{i,k}$ for 4 row, 1 pass

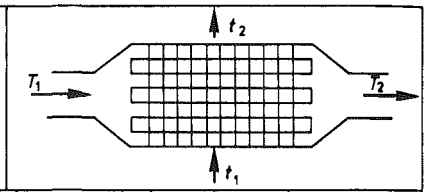

	i = 1	2	3	4
k = 1	1,464745 10^{-2}	1,956024 10^{-2}	-3,117082 10^{-2}	9,394464 10^{-3}
2	-7,208576 10^{-2}	-1,594945 10^{-1}	2,203055 10^{-1}	-4,986404 10^{-2}
3	3,091601 10^{-1}	4,131215 10^{-1}	-4,498517 10^{-1}	2,853396 10^{-2}
4	-5,897784 10^{-2}	-4,883689 10^{-1}	4,481267 10^{-1}	-1,078078 10^{-1}

Table 4

Values of $b_{i,k}$ for 4 row, 2 pass

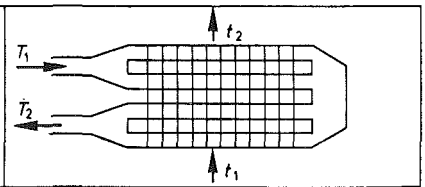

	i = 1	2	3	4
k = 1	1,307011 10^{-1}	6,992744 10^{-2}	-2,278923 10^{-1}	9,311681 10^{-2}
2	8,850189 10^{-3}	-9,936248 10^{-1}	2,085591 10^{0}	-1,220000 10^{0}
3	2,976786 10^{-1}	1,918493 10^{0}	-4,319479 10^{0}	2,481958 10^{0}
4	-3,597806 10^{-1}	-1,213912 10^{0}	2,901783 10^{0}	-1,633085 10^{0}

Nomenclature

A = heat transfer area
$a_{i,k}$ = coefficients in equation (6)
$b_{i,k}$ = coefficients in equation (10)
$\dot{c}$ = heat capacity stream of the air (flow rate times specific heat)
F_T = logarithmic mean temperature difference correction factor
$i;k$ = summation counters in equations (6) and (10)
K = overall heat transfer coefficient
$m;n$ = maximum value of i and k, respectively
$p;q$ = effectivenesses defined by equations (1) and (2)
r = dimensionless mean temperature difference
$r_{l.m.}$ = dimensionless logarithmic mean temperature difference (countercurrent flow)
s = number of tranfer units (NTU) on the air side
T = temperature of process stream
t = temperature of air
ΔT_m = mean temperature difference

Subscripts

I = one row
1 = inlet conditions
2 = outlet conditions

Table 5

Values of $b_{i,k}$ for 2 row, 2 pass

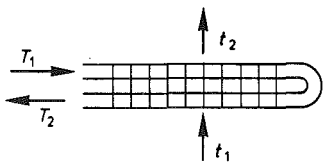

	i = 1	2	3	4
k = 1	1,352164 10^{-1}	3,022285 10^{-2}	-1,446582 10^{-1}	4,929542 10^{-2}
2	-2,146670 10^{-2}	-7,378003 10^{-1}	1,525232 10^{0}	-8,786464 10^{-1}
3	3,378088 10^{-1}	1,415703 10^{0}	-3,143227 10^{0}	1,748077 10^{0}
4	-3,933261 10^{-1}	-9,123792 10^{-1}	2,108533 10^{0}	-1,120026 10^{0}

Table 6

Values of $b_{i,k}$ for 3 row, 3 pass

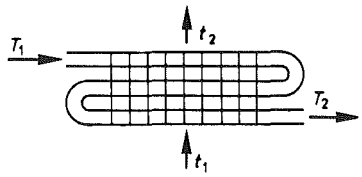

	i = 1	2	3	4
k = 1	1,790271 10^{-1}	-6,875258 10^{-2}	4,852566 10^{-2}	-7,308333 10^{-2}
2	-1,569109 10^{-1}	-1,058458 10^{-1}	3,466809 10^{-1}	-1,837218 10^{-1}
3	7,012144 10^{-1}	1,316315 10^{-2}	-5,420772 10^{-1}	2,021705 10^{-1}
4	-6,967973 10^{-1}	1,161698 10^{-1}	2,877119 10^{-1}	-4,482438 10^{-2}

Table 7

Values of $b_{i,k}$ for 4 row, 4 pass

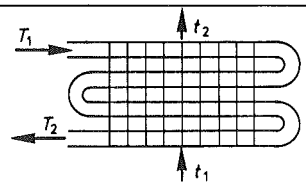

	i = 1	2	3	4
k = 1	1.711282 10^{-1}	5,004573 10^{-2}	-1,790643 10^{-1}	5,747072 10^{-2}
2	-4,722645 10^{-2}	-9,271206 10^{-1}	1,928328 10^{0}	-1,097924 10^{0}
3	4,930444.10^{-1}	1,754712.10^{0}	-3,907875.10^{0}	2,146092 10^{0}
4	-5,765170 10^{-1}	-1,046178 10^{0}	2,577633 10^{0}	-1,367120 10^{0}

Table 8

Values of $b_{i,k}$ for ∞ row, ∞ pass countercurrent flow

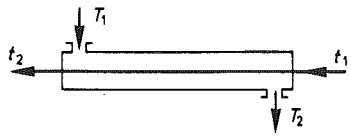

	i = 1	2	3	4
k = 1	1,686934 10^{-1}	1,550887 10^{-1}	-3,746646 10^{-1}	1,651076 10^{-1}
2	3,441903 10^{-2}	-1,609212 10^{0}	3,207463 10^{0}	-1,799140 10^{0}
3	3,651848 10^{-1}	3,124173 10^{0}	-6,480088 10^{0}	3,539501 10^{0}
4	-5,279530 10^{-1}	-1,887773 10^{0}	4,201879 10^{0}	-2,226954 10^{0}

S. W. Mandel[1]
Manager of Advanced Technology,
Rockwell International—Admiral Group
Chicago, IL

M. A. Townsend
Department of Mechanical Engineering and
Materials Science,
Vanderbilt University,
Nashville, TN

T. F. Parrish, Jr.[1]
U.S. Army

Optimal Fin-Side Design of Compact Tube-in-Fin Heat Exchangers with Rippled Fins

The optimal design of rippled fins found in the common compact heat exchanger is addressed to maximize the heat transferred per unit pressure drop (pumping power). Ripples are common for structural integrity and to facilitate handling and manufacture. Typical designs operate at Reynolds numbers below about 1200. Because a complex flow with heat transfer process is involved, the optimal design synthesis approach—modeling, objective function definition and optimization—coupled with the desire to efficiently verify the results leads to a highly effective hybrid design technique and substantially less experimentation than might be expected. The model uses a finite difference marching procedure and variable fluid properties. General results for ripple designs and spacings are obtained and corroborated experimentally. In general a short ripple of about 25 deg and height/fin spacing of 0.25 are optimum. Distance between ripples is shown to be a simple function of Reynolds numbers. The final discussion addresses aspects of this approach, its strengths and limitations.

Introduction

The modeling and optimal design synthesis of heat exchange systems has received considerable attention in recent years [1, 2] although often for relatively exotic applications such as space flight. To reflect terrestrial concerns for energy conservation and more efficient energy conversion and materials utilization, this paper addresses some practical design considerations of a widely-used and "homely" device—the so-called compact heat exchanger of the forced-convection tube-in-fin type such as is found in automotive and air conditioning radiators.

This is an established, time-proven and widely-used design whose continued development and application seems assured. The basic construction has multiple parallel tubes which are mechanically or hydraulically expanded into many identical plate fins. However, in the actual design often the fins are rippled or corrugated, as suggested by Fig. 1, for improved rigidity and overall structural integrity. Furthermore, manufacturing experience has shown that an unrippled fin is virtually impossible to handle: the final shearing process tends to generate internal stresses in the fin which cause it to roll up or spiral.

Satisfactory performance is usually accomplished through adjustments in heat exchanger geometry. Rippling will affect the through-flow characteristics, possibly deleteriously. However, it is often possible to disturb a flow situation to improve the heat transfer coefficient [3], although there may be other penalties incurred—most commonly in the form of pumping power (increased pressure drop). Since presumably some geometries will be better than others or will at least minimize the deterioration of heat exchanger performance, the present study investigates as a problem in optimal design the effect of ripple design on compact heat exchanger performance. We shall consider practical and manufacturing considerations such as number and patterns of ripples, fin spacing and length, pumping power, etc. vis-a-vis the wide variety of applications. Although we shall largely neglect the tube side, it is clear that any improvement of the fin side will improve overall performance, and in many instances, the fin side is the limiting and more costly aspect of these designs [4, 5]. Because of the nature of the system model and design criterion, the results will be applicable to different tube-side capacities.

As motivation for this study, we would observe that to a large extent, most designs are based upon accumulated in-house knowledge and extensive experimental investigations such as Kays and London [4]. Our purpose is to indicate an alternative to their observation [4, p. 5] that ". . . the basic characteristics can be reliably established only by experiments and by model laws to extend the range of applicability of the results." As a design (synthesis) procedure, a trial-and-error approach with extensive experimentation can be very costly, time consuming and possibly inconclusive; we intend to show that a good design model and design criterion can greatly improve the effectiveness of the design and experimental efforts. That is, the mathematical model treats a fairly complex flow with heat transfer problem, and experimental verification of the model is desirable.

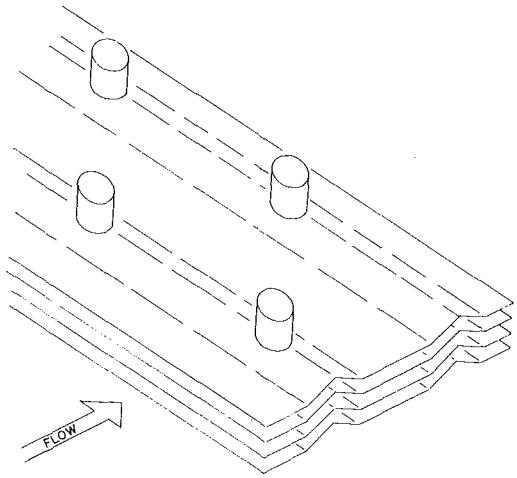

Fig. 1 Tube-in-fin heat exchanger with rippled fins

Hence, what we shall demonstrate is a hybrid design synthesis methodology built upon a mixture of (1) concepts of optimal design—mathematical modeling and optimization to reduce the drudgery of repeated analysis and to indicate better designs and (2) judicious experimentation based on these findings. Additionally, some relatively purposeful analysis of the system model and numerical experiments allowed for computational simplifications and generalizations of the results. As a consequence, an effective design model and results are confirmed with relative economy of experimental effort. These results are from a companion experimental study [6], which actually was developed as a consequence of this design study.

The Design Synthesis Problem

The critical stages of any such study are:

1 development of a suitable model, no more complex than necessary,

2 identification of design variables affecting performance and constraints (limits) upon them,

3 defining a mathematical objective function which quantifies

---

[1] Formerly Graduate Student, Mechanical Engineering, Vanderbilt University, Nashville, TN.

Contributed by the Heat Transfer Division for publication in the JOURNAL OF HEAT TRANSFER. Manuscript received by the Heat Transfer Division February 9, 1979.

the performance in terms of the design variables and provides a relevant comparison between feasible designs,

4 implementation of an optimization algorithm and any other computational procedures,

5 evaluation of results.

These are developed in the following sections:

1 **Mathematical Model.** Most compact heat exchanger operate in the laminar flow region on the fin side, typically between Reynolds Numbers of 400 and 800. Accordingly, and following conventional practice [7], the mathematical analysis (model) is based upon laminar boundary layer flow between two infinite flat plates. The applicable equations are momentum in the direction of flow (x-direction), continuity, and energy. In their dimensionless forms these are, respectively

$$U\frac{\partial U}{\partial X}+V\frac{\partial U}{\partial Y}=-A\frac{dP}{dX}+B\frac{\partial^2 U}{\partial Y^2} \tag{1}$$

$$\phi\frac{\partial U}{\partial X}+\phi\frac{\partial V}{\partial Y}+U\frac{\partial \phi}{\partial X}=0 \tag{2}$$

$$U\frac{\partial T}{\partial X}+V\frac{\partial T}{\partial Y}=C\frac{\partial^2 T}{\partial Y^2} \tag{3}$$

The boundary conditions are

$$U=V=0 \text{ @ } Y=0;\ U=V=0 \text{ @ } Y=1;$$
$$T=1 \text{ @ } Y=0 \text{ and } Y=1. \tag{4}$$

For solution by digital computer, finite difference forms of equations (1 − 3) are employed. In the numerical solution, it was convenient to use a slightly modified dimensionless continuity expression in conjunction with equations (1) and (3) to facilitate inclusion of variable fluid properties (necessary for large temperature differences), viz.

$$\int_0^1 U dY = 1/\phi. \tag{5}$$

Equation (2) is then used to evaluate the transverse velocity components.

The development of the grid network follows in part from the choice of geometry. There are numerous possible ripple and louver (slot) configurations. Louvers are considered extensively by Kays and London [4] and can produce an effective heat transfer surface. They are typically multiple staggered fins or a sheared plate, and involve substantial shearing and/or smaller continuous sections (than a ripple). The former pose somewhat more complex manufacturing and assembly processes; the latter may induce internal stresses and a tendency to warp. In both cases, louvers may not substantially improve the structural rigidity of an assembly. Ripples offer some advantages and appear to have been less extensively investigated. Of the ripples possible, probably a symmetric crimp as suggested in Figs. 1 and 2 is the most common due to ease of manufacture and assembly.

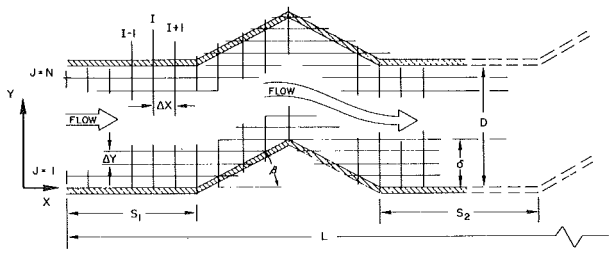

Fig. 2 Grid Structure for finite difference solution and characterization of ripple design and parameters

Accordingly and possibly slightly arbitrarily we shall consider single and multiple ripples of this type.

In Fig. 2 the kth ripple may be completely located and characterized within the chosen coordinate system by defining the location of its leading edge (spacing of ripples) s_k, $k = 1, \ldots K$ for K ripples, the ramp angle β_k, and the maximum height δ_k. The length of such a ripple is

$$\ell_k = 2\delta_k \cot \beta_k \tag{6}$$

As will be shown (and might be expected) optimal multiple ripples will be identical.

The grid network is developed as follows. In the through-flow direction, the ΔX can be somewhat arbitrary in the straight (non-rippled) sections, chosen to yield a good compromise between speed of computation and accuracy and then "adjusted" depending upon the rate of change in the x-direction dependent variables: high rate of change, small ΔX and vice versa. The dimensionless ΔY spacing is $1/(N+1)$ where N is specified from consideration of the ripple geometry, and boundary conditions, as follows.

In treating the nonlinearities of equations (1–5) in the *straight* sections, unknown coefficients of the derivatives are approximated by the previous (I-1) values of the given quantity at the I location. This gives acceptable accuracy for a sufficiently fine grid spacing in the direction of flow, as discussed below and subsequently verified experimentally [6]. Using this approach, all of the $U(X)$, $T(X)$ and $P(X)$ at a given coordinate X can be solved in a matrix solution as the solution "marches" downstream.

Up to this point the analysis follows that of classic Poiseuille flow, and the approach is similar to Bodoia [8]. With the ripple, it is not possible to use symmetry as in [8], and the problem is to manipulate the numerical solution so that all the basic equations and boundary conditions remain unchanged while the coordinate frame is adjusted to simulate flow through a rippled section. This is done by choice of N and ΔY. To retain the original coordinate frame, it is seen that if nodal locations occur naturally at the points where the vertical grid spacing intersects with the surface of the ripple, the boundary conditions can be handled and the solution can proceed much as in straight sections. That is, in Fig. 2, in a rippled section the boundaries and zero velocity conditions now occur at an interior node on one side and an exterior node on the other side. If this were not the case—if

Nomenclature

* = optimum
D = distance between plates
D_h = hydraulic diameter (= 2D)
g_c = gravitational constant
I = index in x-direction
J = index in y-direction
K = number of ripples
ℓ, ℓ_k = length of a ripple
L = length of fin
p = local static pressure
p_0 = total pressure at inlet
N = number of grid points in y-direction
Nu = Nusselt number
p_ℓ = penalty parameter, equation (12)
Pr = Prandtl number
Q = number of constraints
$\boldsymbol{r}$ = vector of design variables
Re = Reynolds number
s_E = theoretical entry length
s_1 = distance from inlet to first ripple
s_k, $k = 2, \ldots K$ = distance between ripples
t = local temperature
t_0 = average entering fluid temperature
t_w = wall temperature
u = local velocity (x-direction)
u_0 = average inlet velocity (x-direction)
v = local velocity (y-direction)
x = coordinate parallel to plate fin
y = coordinate normal to plate fin
Z, $Z(\boldsymbol{r}, p_\ell)$ = design criterion
α = thermal diffusivity
β, β_k = ripple angle
δ, δ_k = ripple height
ν = kinematic viscosity
ρ = local mass density of fluid
ρ = fluid mass density at STP
ψ_q = inequality form of constraints, equation (9) $q = 1, \ldots Q$
$A = g_c p_0 (p\, u_0^2)$
$B = \nu/(u_0 D)$
$C = \alpha/(u_0 D)$
$P = (p_0 - p)/p_0$
$T = (t - t_0)/(t_w - t_0)$
$U = u/u_0$
$V = v/v_0$
$X = 2(x/D_h)/(\mathrm{Re\ Pr})$
$Y = y/D$
ΔX, ΔY = grid spacings
$\phi = \rho/\rho_0$

no node occurred on a surface at a solution point—there could be unknown or incorrect boundary conditions. To assure known boundary conditions, there must be a node on the fin (ripple) surface at each ΔX. Furthermore, in order that each ΔY remain constant throughout the solution, there must be a fixed relationship between ΔX and ΔY in a rippled section, i.e.,

$$\Delta X = \Delta Y \cot \beta \tag{7}$$

such that N is an integer.

Thus, the model comprises a finite difference marching procedure to solve the combined laminar flow with heat transfer problems with variable fluid and heat transfer properties. In all fin segments, the solution of the numerical equations is carried out as in the flat plate case except that the boundary and zero-velocity boundary conditions can now occur at interior and exterior nodes. As the problem solution marches downstream in the channel, the size of the step in the direction of flow ΔX is arbitrary and may be chosen to yield the best compromise between accuracy, speed of solution and compatibility with an impending rippled section. The various adjustments to accommodate different ripple geometries and flows are inherent in the model. A certain amount of numerical experimentation (not really extensive) is involved in selecting the number of nodes required usually aimed at achieving reasonable accuracy with the least computational effort (CPU time), particularly in large problems like this and when multiple iterative solutions are involved. It was found that in the y-direction $N \geq 24$ was satisfactory. In the horizontal sections ΔX varied from .01 to equal to the vertical plate spacing, depending upon $\partial U/\partial X$ and approach of a ripple. In the rippled section, the ΔX was determined according to ripple geometry, satisfaction of modal boundary conditions, and N. These were based on favorable comparison of this model's solution with published results for laminar flow between flat plates [8]. Maximum differences between solutions of no more than seven percent were found for the heat transfer and pressure drop values. After incorporating some streamlining features in the program (discussion in (4)), each complete model solution (design) entailed about five *minutes* CPU time on a Xerox XDS-7 Computer.

As a final comment on this model, its relation to other approaches, and subsequent presentation of results, this computational procedure enables direct treatment of variable properties and solves for the temperature and flow variations directly on a step-by-step basis. Thus, approximate variable properties treatment (as in [4], chapter 4) using empirical coefficients offers no advantages and is unnecessary. Similarly, a priori parameterization by friction factors, etc. is not required, since the flow conditions are solved explicitly. Thus, we have "constructed" a nonlinear problem solution whose explicit behavior is relatively insensitive to the usual problems of nonlinearities because of the embedding within an optimization procedure (3, below). The choice of a finite difference technique (versus finite element) provides some advantage in this way and averts an interior iteration—i.e., a double iteration when the optimization is superimposed.

2 Design Variables and Constraints. The design variables in this model could be all of the variables identified above equation (6) for each segment of fin plus length of fin L and spacing D. Fin thickness is not an explicit consideration in the present problem.

In any problem it is usually advantageous to treat explicitly no more variables than necessary, for ease of visualization of results and less computational time and cost. In view of the very long computation times for each design and the iterative nature of optimization algorithms, it became worthwhile to investigate the effect of the various design variables upon the objective function.

By the nondimensionalization and characterizing the flow in terms of Re, one of the variables, D, can be eliminated, the remaining length variables now being per unit fin spacing. Hence, the complete vector of design variables $\boldsymbol{r}$ could be

$$\boldsymbol{r} = \left\{\frac{L}{D}, \mathrm{Re}, \beta_k, \frac{\delta_k}{D}, \frac{s_k}{D}, \quad k = 1, \ldots, K, \text{ and } K\right\} \tag{8}$$

All of the variables are constrained to be nonnegative and by upper limits, as may be feasible. Typically

$$0 \leq \beta_i \leq 60 \text{ deg}; 0 \leq \frac{\delta_k}{D} \leq 0.9; \bar{s}_1(\min) \leq \frac{s_1}{D}$$

$$\bar{s}_k(\min) \leq \frac{s_k}{D} - \left(\frac{s_{k-1}}{D} + \frac{\ell}{D}\right), \quad k = 2, \ldots K; 0 \leq \frac{L}{D} - \left(\frac{s_k}{D} + \frac{\ell}{D}\right) \tag{9}$$

and K is a specified parameter, several values being considered. The last two constraints insure that all ripples are suitably spaced and lie completely within the fin length. As it turns out, it will be possible to simplify these constraints and to determine a suitable $\bar{s}_k(\min)$. Also as indicated earlier, under most conditions (and certainly as a practical consideration) the ripples will be identical and symmetrically spaced with respect to the fin center, thereby reducing the number of variables in $\boldsymbol{r}$.

Accordingly, this problem has several inequality constraints and no equality constraints, the model being solved explicitly for each function evaluation.

3 Design Objective Function. Optimal design involves finding the best feasible combination of the design parameters for an objective function which is representative of the application. In a common device such as this, the interpretation of optimum design and performance may well vary from application to application, or an application may dictate a design objective. Thus, it is possible for conflicting designs to result if, in one instance a reliable continuous level of performance of a system is required over a long period of time, and in the second instance a variable level (output) is required on an intermittent basis—even though both situations may require basically the same device. This particular conflict is not explicit in the present model, although such considerations could conceivably be superimposed, possibly by choice of objective function.

In this model, there may exist a conflict between heat transfer and acceptable pressure drop. Thus, there may be numerous optimum solutions which could be achieved for the general case described up to this point. Since maximum heat transfer and minimum pressure drop are typically desirable, a reasonable function to minimize (following conventional practice) would be of the form total pressure drop/average heat transfer or equivalently, minimize

$$Z = Z(\boldsymbol{r}) = \frac{P}{\mathrm{Nu}} \tag{10}$$

while maintaining Reynolds number similarity. Obviously, this is one of many possible design criteria. In another situation, the objective might be to maximize the average heat transfer, subject only to an upper limit on total pressure drop, or equation (10) might be a constraint. Investigation of multiple criteria is reasonably straightforward once one has a suitable model and solution algorithm.

4 Optimization Algorithm and Computational Aspects. Having done (1–3), in principle the problem may be solved by a general purpose optimization algorithm. However, because of special attributes or difficulties inherent in a problem, solutions may be more effectively obtained by certain algorithms or some ad hoc technique. With a complex model and the iterative nature of the optimal design procedure involving multiple evaluations of the model, computational interaction of the model and algorithm may be important. Such is the case here.

Each objective function evaluation requires solution of the entire flow model, including the internal grid adjustments to accommodate characterization of the ripple(s) and to ensure numerical stability. Initially we experienced enormous CPU times in the iterative optimization mode. To assist in debugging the combination and selecting a suitable algorithm, the problem (model) was temporarily simplified to treat fixed properties (valid for about 20°F (12°C) temperature difference), and response surfaces were generated by curve fitting and linear interpolation.[2] The inclusion of variable properties intensified

[2] The mathematical model is used to generate a series of values for the objective function using a matrix of values for the independent variables. Once sufficient data is obtained, the results are curve fitted; a least squares polynomial fit was used. The maximum error between the actual values of the objective function and the values calculated from the polynomial fits was less than one percent. Linear interpolation was used between fitted curves to produce a "surface".

the variability of the design contours and precise location and values of the optima, although the general character was similar. The fixed-property solutions were not considered sufficiently accurate in general when compared to variable-property model results, and as subsequently verified experimentally. However, this approach did facilitate debugging the variable properties model, particularly when other problems appeared.

At this point, it was known that independently the models worked, and that algorithms under consideration would reliably solve test problems and would identify optima using the fixed-properties model curve-fit equations. Hence, it became imperative to select an algorithm which could be expected to reach optima with as few as possible function evaluations or other difficulties, to streamline the model treatment, and to effect any possible further reduction of the number of design variables.

Problems were identified with interactions of the model and algorithm and influenced the algorithm choice. One (now obvious) conclusion was that algorithms which computed gradients could lead to long run times simply due to number of function evaluations; however, even traditionally efficient gradient-calculating algorithms could (and did) have difficulties due to the quasi-discrete nature of characterizing the ripple(s) and the necessary adjustments of the flow grid—which also might be different for each variable. Therefore, a direct-search algorithm was indicated—preferably one which would be tunable to capitalize upon previous favorable moves and the design-space topography.

To streamline the model solution in the iterative mode, all calculated quantities which might be recalculated for subsequent trial designs. were stored whenever the time consumed in recalculation was greater than the time to access the stored information. This technique was highly effective in reducing CPU time by more than 50 percent—to the aforemention average of about five min per complete solution (value of objective function).

As a consequence of all this activity, the algorithm selected was a direct-search variable polyhedron of the Nelder-Mead type [9]. (We also developed some feel for good starting points.) After a number of trials and some tuning, this algorithm appeared to be reasonably robust for the type of region encountered. This algorithm is generally used with a penalty function for constrained problems. The constraint equations (9) were reformulated to provide a feasible region defined by

$$\psi_q(\boldsymbol{r}) \leq 0, \quad q = 1, \ldots, Q. \tag{11}$$

which were appended to the objective function in the form of an exterior-barrier type parametric penalty function of the form

$$F(\boldsymbol{r}, p_\ell) = Z(\boldsymbol{r}) + \frac{1}{p_\ell} \sum_{q=1}^{Q} \{\max[\psi_q(\mathbf{x}), 0]\}^2 \tag{12}$$

where $F(r, p)$ is to be minimized for a specified decreasing sequence of p_ℓ's > 0. Typically p decreases from 1 to 10^{-6} in increments of 10^{-2}, with values for $\mathbf{r}^*$ found for each value. There are no equality constraints in this problem.

Interestingly, all of the optima turned out to be interior, although close to the upper limits of β_i and δ_i/D, so it was not necessary to be concerned with the explicit character of the sequence p_ℓ.

Reduction of the number of variables is discussed separately in the following because it involved almost a complete independent study.

Testing the Model, Effects of Design Variables. Solution of the defining equations shows that both the heat transfer and the pressure increase with fin length L, the rate of increase being greater for the pressure drop. Accordingly, L will always tend to a minimum for this objective function, and the value of L is a sizing parameter based upon capacity requirements of a specific application. Actually, for this objective function in the Re range of interest, L drops out of the problem in favor of spacing D.

As a function of through flow in the typical operating range of between Re of 100 and 1200, the optimal Re, is always at the minimum possible for this design objective function: Z decreases monotonically with decreasing Re since P decreases more rapidly than Nu. Hence, the optimal Re is either known a priori (based on capacity requirements) or is determined by some other objective. In either case Re can be specified as an independent parameter of the solution.

Only a few ripples are practical (under 3) and K must be an integer. Typically, variables which can only take on integral values are more conveniently treated as parameters which take on specified values.

The numerical experiments indicated that design for ripple location and number of ripples design could be expedited. As corroborated experimentally, it was observed that for one ripple

(a) the objective function is virtually insensitive to the specified value of entry length s_1 as long as s_1 is relatively well into (preferably greater than) an entry length s_E, empirically defined by Olson [10] as

$$S_E = 0.0059 D_h R_e \tag{13}$$

where D_h = hydraulic diameter, two-dimensional, so that

$$\frac{s_E}{D} = 0.0118 \mathrm{R}_e \tag{14}$$

(b) the objective function increases markedly if s_1 is less than, say,

$$\frac{1}{2} s_E.$$

Experimental verification was with a "worst case" flow condition of high Re (Re = 1200), since these effects tend to be more pronounced with increasing Re.

Similar observations were made regarding spacing between multiple ripples: as long as the ripples which occur in the fin length are sufficiently far apart such that the flow disturbance caused by any given ripple does not affect its downstream neighbor, the exact ripple locations are irrelevant to the value of $Z(\boldsymbol{r})$. Practically, one would expect that ripples would be spaced equally and symmetrically; consequently there are two predominant cases for design synthesis:

- the spacing *between* multiple ripples can be made greater than s_e, and $\bar{s}_1(\min) \geq 1/2 s_E$, or
- location of the ripple(s) is chosen (fixed) for other reasons, e.g. symmetry, manufacturing ease, die design, etc.

(15)

These define the $\bar{s}_k(\min)$, $k = 1, \ldots, K$ in the constraint equations (9).

Under these conditions, it is necessary to consider the optimal design of a single ripple: multiple ripples will be identical, and the value of the objective function is a function of the number of ripples. As shown in Table 1 the value of Z depends only upon the number of ripples, all other variables being fixed and spacing requirements being satisfied: the nearly linear behavior of P, Nu and Z are seen in the three right columns. The flat plate case ($N = 0$) probably should not be considered as an extrapolation, but is included for completeness.

Results

As indicated in selecting the objective function, this problem has a large number of design options, so a completely general investigation is virtually impossible. Nevertheless, the design synthesis approach has already yielded several general results as a consequence of the judicious and systematic studies of the foregoing sections, thereby reducing the actual algorithmic effort. Thus, it is necessary to treat the optimal design of a single ripple, multiple ripples being identical, and the value of the objective function increases with the number of ripples for such optimally designed ripples. (Also, the case of a single ripple probably is of greatest practical interest.) Next, optimal spacing has been determined as a function of Re in equations (15), and the objective function is minimized by minimizing fin length L. Fin length and spacing (hence $(L/D)^*$) are determined by for capacity, requirements and the application and only relate secondarily to relative performance with a ripple as defined by Z. Only the feasible number of optimal ripples remain to be determined, as a function of Re. Generally, the number will be the minimum compatible with structural and manufacturing requirements, and they will be symmetrically placed.

Table 1 Effect on number of ripples on values of pressure drop, heat transfer and design function

All Ripples: $\beta = 30$ deg, $\frac{\delta}{D} = .5$, $\frac{\ell}{D} = .866$

$$\text{Re} = 1225\frac{s_E}{D} = 14.44, \frac{L}{D} = 120$$

No. of Ripples, K	Location from leading edge	$P(10^{-4})$	Nu	$Z(10^{-5})$	$\frac{P_{(N \text{ ripples})}}{P_{(\text{channel})}}$	$\frac{\text{Nu}_{(\text{ ripples})}}{\text{Nu}_{(\text{channel})}}$	$\frac{Z(N)}{Z(0)}$
0	—	3.365	7.928	4.244	1.0000	1.0000	1.0
1	60	4.021	8.517	4.721	1.2354	1.0743	1.15
2	30, 90	4.594	9.076	5.062	1.4409	1.1448	1.259
3	30, 60, 90	5.172	9.686	5.340	1.6481	1.2217	1.349

Experimental Hardware Date: $L = 15$ in., $D = .122$, $L/D = 120$

Accordingly, the remaining design variables are 1) Re, flow Reynolds Number and s_k/D accordingly, 2) δ, ripple height, and 3) β, ripple angle.

Since Re may be specified (in conjunction with an application or capacity) the variation of the design parameters and $(s_i/D)^*$ are evaluated as functions Re.

Optimal Design. Table 2 shows the effect of different Reynolds numbers on the values of the optimum ripple angle (β^*), height (δ^*/D) and s_i^*/D (minimum) and values of the objective function. There is virtually no dependence of β^* and $(\delta/D)^*$ on Re—being essentially 25.56 deg and 0.234 for all cases—although the value of the objective function is seen to be strongly Reynolds number dependent. That is, pressure drop (pumping power) increases more rapidly than heat transfer, the latter being temperature-limited. Although these results are independent of the specific size, the numerical values are presented here in terms of an example design typical of many such compact heat exchangers (and which illustrates most of the important points): fin length of 2 in. (5.08 cm), fin spacing of .0773 (0.2 cm), equivalent to 12 fins/in. (approximately 5 fins/cm).

The ripple is symmetrically located, for obvious practical reasons. Design is considered for Re of 100, 750 and 1200, with Re = 750 being typical of many applications. All results are for variable properties.

Ripple location has no effect on results as long as the ripple does not occur close enough to the leading edge to penetrate the entry region. However, as Re increases the length of the entry region also increases so that a ripple which is located "out" of the entry region for Re = 100 could easily be "in" the entry region at a Re = 1200. In Table 2, this is seen to be the case: Re = 750 is approximately the borderline. Hence for Re = 1200; the ripple actually lies within an entry length defined by equation (15). This may account for slightly different values of δ^* and β^*. However, is easily shown that Z^* versus Re for all designs are essentially in a fixed logarithmic relationship. As to whether the Re = 1200 design might be slightly suboptimal, further investigation did not so indicate.

Some optimal design studies were made an Re = 2000, where the entry length is essentially the total fin length. The model solution showed a tendency to diverge for some of the trial points; the model predicts flow separation in the region following the ripple—a contingency which the model adaptive grid structure was not developed to accommodate easily. As flow separation in this range of Re tends to lead to lower overall heat transferred due to quiescent regions, it was not felt worthwhile to extend the model further nor to intercede too strongly in "guiding" the solutions.

Fig. 3 is a topographic map of the design surface.[3] Upon evaluation of Fig. 3 and Table 1 it is seen that the flat plate case provides the minimum value of Z, i.e. minimum pressure drop per unit heat transfer coefficient. However, the optimal ripple is only slightly higher. This result might suggest that the use of any ripple would be undesirable, but manufacturing experience and structural properties described earlier strongly encourage some geometric alteration of the fin.[4] Thus, by proper ripple design one can take advantage of this geometric change or at least to prevent the change from causing any appreciable deterioration of the heat exchanger performance.

Table 2 Effect of Reynolds' Number on optimal ripple design ($L = .0489$)

Re	$\frac{s_E}{D}$	$\frac{\delta^*}{D}$	β^*	$Z^*(10^{-5})$	$P^*(10^{-4})$	Nu*
100	1.18	.234	25.56°	.248	.1912	7.71
750	8.85	.234	25.56°	2.500	2.5566	10.23
1200	14.16	.232	27.90°	4.024	4.7838	11.89

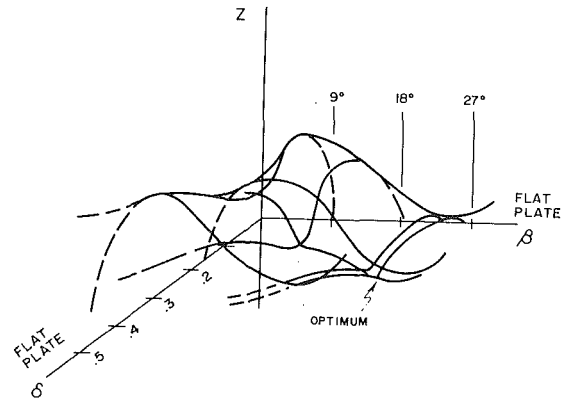

Fig. 3 Topographic map of design region (Re = 750)

A few other comments on the optimization procedure may be of value. First, the topographic plot shows the objective function to be unimodal. However, the exact value for ripple angle at the optimum design was found to be slightly starting-point sensitive, due to the narrow valley of the design region and partly due to the "waviness" of the solutions due to varying grids. The value for the ripple height at the design optimum did not change.

By altering the convergence criterion for the Nelder and Mead algorithm, it was found that after about ten iterations the solution was established (using a relatively conventional design as a starting point).

The implication of the optimized solution is interesting in that it tends to suggest that a small and very "sudden" flow disturbance yields the best performance. The most important question of all is, of course, unanswered (at least for the present): is the solution obtained here physically accurate? This is addressed in the next section.

Experimental Corroboration. Because a fairly complex flow with heat transfer model has been developed from which several observations on design have been made, some experimental verification is highly desirable. (As stated earlier this study [6] actually was instigated by this study.) The purpose here is to substantiate the optimal design approach by presenting representative comparisons of the experiment and model. Full results of the experimental study will appear elsewhere.

[3] This would normally not be done, since it rather defeats the general premise of this approach (see Discussion). It is presented here mainly for interest.

[4] Actually, another relative optimum seems to occur as $K \to \infty$, the ripple becoming very small so as to cause minimal flow disturbance; this is impractical and excluded here.

Figs. 4 and 5 show comparisons for fins with two identical ripples located at $X = 0.04, 0.11$ for two different designs and the flat plate. The case for $\delta/D = .5, \beta = 10$ deg are representative of some practice. The cases for $\beta = 30$ deg and $\delta/D = 0.25$ were selected as a consequence of this study for experimental verification. Also shown is one case with the fixed properties model (Fig. 4).

In Fig. 4, it is seen that the model very accurately predicts the pressure development. The consistently slightly lower predicted curves are attributed to the use of an empirical constant associated with entrance pressure drop taken from published data [10] and the vicissitudes of hardware construction.[5] Obviously, the character of the curves is identical.

The pressure curves s_E downstream of the ripples parallel the flat plate case. Thus, the effect on the numerator of Z, i.e. P, is that K optimally designed ripples will be the same as a single optimal ripple, since the flow conditions approaching each ripple are identical if the ripples are adequately spaced per previous discussion. For constant Nu, the value of Z will increase with number of ripples and Re.

Fig. 5 shows the model predicted temperature development and a few measured values. With the ripples, the temperature rise appears to be logarithmic between ripples, as in the flat plate case, but is no longer overall logarithmic. While the general values predicted are quite good, it is known there may be some corrections for location of thermocouples, shielding and convection to the thermocouples, etc. These and other error considerations are addressed in [6]; their consideration is not really germane to this study.

The solution was substantially complicated by the inclusion of variable properties. However, it is seen that fixed fluid properties quite noticeably affects the predicted pressure development in Fig. 4—although in an essentially linear fashion for the flat plate case. The fixed property assumption has a much smaller effect on Nu (under 4 percent). The discrepancy on pressure prediction was nevertheless unsuitable since it could modify location of the optimal design and significantly vary the value of the design objective function.

With regard to the optimal design, it is seen that the smaller ripple has a much higher pressure drop with slightly higher heat transfer, and that the 30 deg ripple with $\delta/D = .25$ is very close to the flat plate case.

Discussion

The mechanism of heat transfer enhancement is due mainly to effecting a flow profile with transverse velocity components conducting heat away from the surfaces and to a lesser extent slightly increased the surface area. The latter alone does not account for the improvement. This can be viewed as identifying an equilibrium "trade-off" point between the increased pressure drop which accompanies the transverse flow causing the improved heat transfer for this design criterion.

It has been our main purpose to indicate that such design can take place in the absence of an existing well-stocked data bank. The precise purpose of such approaches is to overcome the limitations, expense, and time of developing empirical hardware-bound relations. It has been shown that the modeling allowed cheap, fast numerical experiments and indicated both a number of simple generalizations and a few full-scale experiments necessary to validate the results without a comprehensive program. Obviously one must be careful, but usually it is apparent when limitations are being encountered. These results can be extended through similarity modeling or more computer runs.

The limitations lie in the model and choice of objective function and constraints. Usually, a change of Z is easy; using the penalty function approach, additional constraints are easily added. We have suggested a robust, direct search algorithm for reasons already noted. The solutions were not particularly sensitive to tuning the algorithm, although penalty function approaches occasionally give problems. Again, these are easily diagnosed. Here, for example, the topographic

[5] With a slightly higher value for this coefficient, the curves can be made to coincide. However it was decided not to arbitrarily modify this coefficient in the model to be consistent with accepted values.

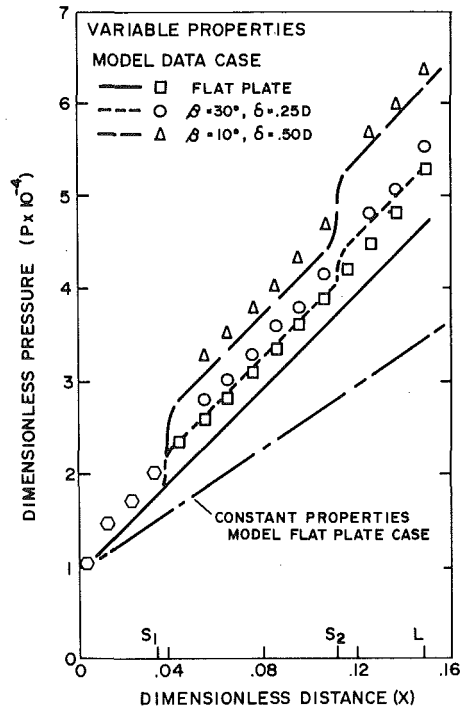

Fig. 4 Comparison of model and experiment: pressure development

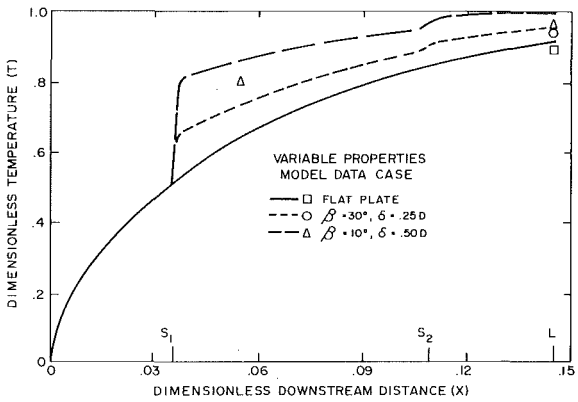

Fig. 5 Comparison of model and experiment: temperature development

plot shows the objective function to be unimodal. However, the exact value for ripple angle at the optimum design was found to be slightly starting-point sensitive, due to the narrow valley of the design region and partly due to the waviness of the solutions due to varying grids. The value for the ripple height at the design optimum did not change. By altering the convergence criterion for the Nelder-Mead algorithm, it was found that after about ten iterations the solution was established (using a relatively conventional design as a starting point).

As to the model and utilization of these results, the principal caveat relates to the neglect of the tubes. Strictly speaking, these results apply to widely-spaced tubes, say rank/file spacings greater than 1 and regions more than ½ to 1 dia away from the tubes. The former is suggested by [4, p.127] and the latter from classical solutions to flow around a cylinder. However, for close spacings—up to the point where it is irrelevant what is between the tubes—we expect very close to the same results for the designs, but higher values of Z. Regardless, many practical designs satisfy the above spacing conditions.

Conclusions

The optimum ripples have been identified for the common compact heat exchanger operating below about Re = 1200. The hybrid optimal design synthesis technique developed greatly eases the computational burden, provides greater generality of results and allows great economy in the experimental effort required to affirm the design model and synthesis technique. The results with variable fluid properties are found to differ significantly from constant properties.

Because of the discrete nature of the finite difference marching procedure used in solving this problem, the choice of algorithm can also effect the ability to achieve solutions with reasonable computational effort. The experimental results reflect a fairly common design and very close to the optimal design; clearly the optimal ripple shows greater heat transfer per unit pressure drop (pumping power).

Using this approach reduces the need to develop a comprehensive data bank, most of which by definition would be nonoptimal designs. Presumably, all approaches will lead to the same design, but this approach may well speed up the progress and save time and money.

References

1 Hu, M. H. and Chang, Y. P., "Optimization of Finned Tubes for Heat Transfer in Laminar Flow," ASME JOURNAL OF HEAT TRANSFER, Vol. 95, No. 3, Aug. 1973, Paper No. 73-HT-M.

2 Demetri, E. P. and Ellis, W. E., "Surface Selection in Optimization of Compact Heat Exchangers for Space Applications," ASME *Aviation and Space Progress and Prospects,* Annual Aviation and Space Conference, Beverly Hills, Calif., June 1968.

3 Kays, W., *Convective Heat and Mass Transfer,* McGraw-Hill, New York, N.Y., 1966.

4 Kays, W. M. and London, A. L., *Compact Heat Exchangers,* 2nd Ed. McGraw-Hill, New York, N.Y., 1964.

5 McAdams, J. L., *Heat Transmission,* McGraw-Hill, New York, N.Y., 1954.

6 Parrish, T. F., "Laminar Flow and Heat Transfer in Rippled Fins," M.S. Thesis, Vanderbilt Univ., Nashville, TN, 1977.

7 Schlichting, H., *Boundary Layer Theory,* McGraw-Hill, New York, N.Y., 1968.

8 Bodoia, J. R., "The Finite Difference Solution of Confined Viscous Flows," Ph.D. Thesis, Carnegie Institute of Technology, Pittsburgh, Pa., 1959.

9 Nelder, J. A. and Mead, R., "A Simplex Method for Function Minimization," *Computer Journal,* Vol. 7, p. 308, 1965.

10 Olson, R. M., *Essentials of Engineering Fluid Mechanics,* Intext, New York, N.Y., 1973.

R. E. Mayle[1]
Associate Professor.
Department of Mechanical Engineering,
Rensselaer Polytechnic Institute, Troy, NY 12181
Mem. ASME

M. F. Blair
Research Engineer,
United Technologies Research Center,
East Hartford, Conn.
Mem. ASME

F. C. Kopper
Research Engineer,
Pratt and Whitney Aircraft
East Hartford, Conn.
Mem. ASME

Turbulent Boundary Layer Heat Transfer on Curved Surfaces

Heat transfer measurements for a turbulent boundary layer on a convex and concave, constant-temperature surface are presented. The heat transferred on the convex surface was found to be less than that for a flat surface, while the heat transferred to the boundary layer on the concave surface was greater. It was also found that the heat transferred on the convex surface could be determined by using an existing two-dimensional finite difference boundary layer program modified to take into account the effect of streamline curvature on the turbulent shear stress and heat flux, but that the heat transferred on the concave surface could not be calculated. The latter result is attributed to the transition from a two-dimensional flow to one which contained streamwise, Taylor-Görtler type vortices.

Introduction

The prediction of turbine blade heat loads is critical to a successful gas turbine design. The prediction process, however, is hampered by insufficient information on a number of "special effects" which significantly influence the viscous and thermal boundary layer development along the blades. The term special effects is used in the same context as Bradshaw's [1] and refers to the effects on a turbulent boundary layer caused by three-dimensionality, streamline curvature, Reynolds number and free-stream turbulence and unsteadiness. For turbine blades these effects commonly occur simultaneously and in regions of large (relaminarizing) streamwise pressure gradients, which generally give the designer an uneasy feeling about the accuracy of his heat load prediction and, hence, his blade life estimate. In an effort to understand one of these special effects, so that eventually a designer may routinely take it into account, the present work on the influence of curvature on heat transfer in a turbulent boundary layer was undertaken.

The recent upsurge in experiments on curved surfaces [2–6] has provided much information on the effect of streamline curvature on turbulent boundary layer growth, Reynolds stresses and wall shear stress. In general, the results show that the Reynolds stresses and wall shear stress are reduced on the convex surface and increased on the concave when compared to those for flow on a flat surface. In one case [2] the convex curvature was sufficiently strong to reduce the turbulent shear stress to zero. And in each case, the effect of streamline curvature on the Reynolds stresses was at least an order of magnitude greater than that expressed explicitly in the turbulent stress transport equations. The measurements also indicate that the flow on the concave surface may not be two dimensional, but exhibit steady (in the time-averaged sense) Taylor-Gortler type vortices within the boundary layer. Tani [7] was the first to study this phenomenon and since then additional information has been provided by Meroney [3] and So and Mellor [4]. For an extensive review of the work done previous to 1973 on turbulent boundary layers with streamline curvature see Bradshaw [8].

There is no reason to expect that the turbulent heat flux in curved flows should behave qualitatively different than the turbulent shear stress. Thomann [9] inferred this from his measurements of surface heat flux which showed a decrease on the convex surface and an increase on the concave when compared to the heat flux from a flat plate. This trend was also shown to be unaffected by the heat flux direction and streamwise pressure gradients. However, his experiments were conducted with a free-stream Mach number of 2.5 and, as pointed out by Bradshaw (either [8] or [10]), curvature effects can be much larger at high supersonic velocities. The present work was performed at a low speed so that the curvature effect unaugmented by compressibility effects could be evaluated.

If the boundary layer thickness is very much less than the radius of curvature, i.e., $\delta/R \ll 1$, as in the turbine blade application, the curvature terms in the equations of motion and energy can be neglected compared to the usual convective terms and the only way curvature can affect the mean motion and thermal field is through the turbulent shear stress and heat flux. An examination of the Reynolds stress transport equations for $\delta/R \ll 1$ reveal that only the production of $(\overline{v'^2})$ and $(-\overline{uv})$ are explicitly affected by curvature. If the free-stream and surface temperature difference is small compared to the free-stream temperature and again $\delta/R \ll 1$, the transport equation for the turbulent heat flux may be written (in the usual notation) as

$$D(\overline{v'T'})/Dt = \overline{-v'^2}\frac{\partial \overline{T}}{\partial y} - \frac{1}{\rho}\overline{T'\frac{\partial p'}{\partial y}} - \frac{\partial}{\partial y}\overline{v'^2T'} + \alpha\overline{v'\frac{\partial^2 T'}{\partial y^2}} + \nu\overline{T'\frac{\partial^2 v'}{\partial y^2}}$$

which is identical to that without curvature. Thus, the advection, production, diffusion and dissipation of turbulent heat flux are not explicitly dependent on mean-streamline curvature and, in particular, the production depends only on the effect curvature has on the Reynolds stress $\overline{v'^2}$ and mean temperature gradient.

This set of circumstances has made the calculation of curvature effects for turbulent boundary layer flow difficult and at best correlative in nature. The favored method at present is that proposed by Bradshaw [10] where a curvature correction is applied to either the dissipation or mixing length, and hence the local turbulent shear stress, in a Spalding-Patankar type calculation procedure. The correction generally has the form

$$\ell/\ell_0 = 1 - \beta\,\mathrm{Ri} = 1 - \beta\left(2\frac{u}{R}\right)\Big/\left(\frac{\partial u}{\partial y}\right)$$

where ℓ_0 is the length scale without curvature, Ri is the Richardson number, u is the mean velocity, R is the surface radius taken positive for a convex surface and negative for a concave, and β is a correlation constant. The Richardson number has been defined for incompressible flow and represents the ratio of centrifugal to inertia forces. Values for β of 7 to 10 for a convex surface and 4.5 for a concave have been suggested by Bradshaw [10] while Eide and Johnston [11] propose a value of 6 for both surfaces. In order to calculate the mean temperature distribution, the Prandtl number is assumed unaffected by curvature. This assumption, which was shown to be good at least in the outer region of the boundary layer by Mayle, et al. [12], and the length correction above are the basic assumptions used in the boundary layer calculations presented herein for comparison with the measurements.

Description of Experiment

The experiment was conducted in a closed-circuit wind tunnel with the curved surface test section forming one of the bends in the circuit. Air from a centrifugal blower passed through a honeycomb section,

[1] Consultant, Pratt and Whitney Aircraft, East Hartford, Conn.

Contributed by the Heat Transfer Division for Publication in the JOURNAL OF HEAT TRANSFER. Manuscript received by the Heat Transfer Division July 14, 1978.

screens and a nozzle into a 51 cm by 20 cm by 74 cm long approach duct which directly preceded the curved surface test section. The flow from the test section was then diffused and entered a return duct which contained a heat exchanger that was used to maintain a steady thermal testing condition. Make-up air to compensate for air leakage and bleeds was drawn in upstream of the blower and mixed with the return flow.

The nozzle and approach duct boundary layers were bled off before the flow entered the test section. The boundary layers on the upper and lower walls were bled through adjustable scoop-like gaps as shown in Fig. 1. The sidewall boundary layers were bled through a series of adjustable flush slots in the approach duct sidewalls. This bleeding was necessary to reduce the secondary flow in the curved test section which normally migrates along the sidewalls from the concave to convex surface and eventually onto the convex surface. The effect of this flow (converging flow on the convex surface and diverging flow on the concave) is in the same direction as that caused by streamline curvature and therefore should be reduced to a small percentage of the curvature effect. In the present experiment, yaw measurements at the most downstream position and 10 cm on each side of the test section centerline showed that the secondary flow was mainly confined to the boundary layers and that the maximum convergence on the convex surface and divergence on the concave was about 2 deg. This secondary flow produces an error in Stanton number of about 2 percent which, at the same streamwise position, amounts to about 7 percent of the curvature effect.

The test section, shown in Fig. 1, was 51 cm wide and 12 cm high at its entrance. The curved test surfaces formed 90 deg portions of a cylindrical surface 51 cm wide with a radius of 61 cm attached to a 20.3 cm long flat leading edge section. Only one test surface at a time was installed in the test section. The opposite wall was made of a flexible steel sheet reinforced by bars across its width in order to maintain a rectangular cross-section passage at any streamwise position. The bars were spaced at 14 cm intervals and were connected to rigid tunnel structural members by means of adjustable turnbuckles. This wall was adjusted to provide a negligible streamwise pressure gradient along the test surface.

The curved test walls were constructed by casting a 2.5 cm thick layer of rigid urethane foam, having a thermal conductivity two to three times that of air, in aluminum molds which had been formed to produce the 61 cm radius. A flat 2.5 cm-thick foam section was then attached to form the leading edge. Heater elements consisting of a thin etched foil with a Kapton substrate (0.20 mm thick) were attached to the foam walls. Copper plates (0.81 mm thick and rolled to a 61 cm radius for the curved section) were attached to the heater elements to provide the surface in direct contact with the airstream. These plates measured 5.0 cm in the streamwise direction on the curved portion, 2.5 cm on the flat, and were about 17 cm long. Three rows of plates across the width of the foam wall covered the surface. The heat transfer measurements were taken along the center row; the other rows served as guard heaters. The plates were thermally isolated from each other using a low thermal conductivity filler and the heaters below each plate electrically isolated so that the electrical power input to each heater-plate unit could be related directly to the local convective heat transfer. Chromel-Alumel thermocouples were soldered into small holes drilled in the copper plates from the back to measure the surface temperature. During the test the power to each heater was adjusted to obtain a uniform value of this temperature over the entire

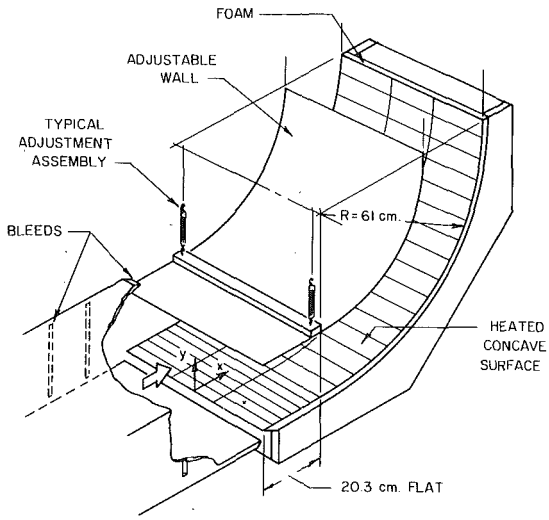

Fig. 1 Curved surface test section

surface. The entire test surface was painted with several thin coats of varnish to produce a hydraulically smooth surface and then sprayed with a carbon black paint to provide a surface with an emissivity of nearly unity. A 1.5 mm thick Micarta sheet was attached to the backside of the foam wall for strength and an additional 10 cm of fiberglass building insulation was fitted against the Micarta sheet.

The convective heat flux from the test surface was obtained from the measured power dissipated in the heaters after correcting for heat losses. The corrections included those for surface radiation which took into account the curved wall view factor and for back losses attributed to conduction through the foam, heater leads and thermocouple leads. These corrections amounted to about 10 and 3 percent of the measured power, respectively.

The velocity measurements were obtained with a DISA 55D01 constant-temperature anemometer using a 0.05 mm dia hot-film boundary layer probe. Temperature measurements were taken almost simultaneously at a given point by switching the unit from a constant-temperature operating mode to a resistance-thermometer mode. With this arrangement the velocities and temperatures could be determined to within 0.5 m/s and 0.5°C, respectively.

At the test section entrance, the free-stream velocity and temperature were found to be uniform and were nominally maintained at 21 m/s and 18°C, respectively. On the flat portion of the test surface, 7.5 cm downstream from the leading edge, a 0.64 mm dia trip wire was attached to provide a turbulent boundary layer over the curved surface. For an unheated surface (see [12])[2] the momentum thickness Reynolds number and shape factor at $x/R = 0.29$, which was slightly before the curved portion, were found to be 835 and 1.48, respectively, and a comparison with Coles' correlations [13] revealed it to be in equilibrium.

Results and Discussion

In contrast to the well-behaved, two-dimensional flow on the convex surface, the flow on the concave surface was found to be quite complex. Spanwise traverses of a 1.6 mm dia pitot tube near the surface

[2] The trip wire diameter was 0.64 mm for that experiment also, and not the value reported.

Nomenclature

c_p = specific heat at constant pressure
d = pitot tube diameter
G_t = turbulent Görtler number
ℓ = turbulent length scale
M = Mach number
p_s = static pressure
p_t = total pressure
Pr = Prandtl number
q = surface convective heat flux
R = radius of curvature of surface
Re_x = Reynolds number based on distance from leading edge
Ri = incompressible Richardson number
St = Stanton number
T = absolute temperature
u, v = velocity components in x and y direction, respectively
x, y, z = spatial coordinate system with x and y coordinates parallel and normal to the surface, respectively
γ = ratio of specific heats
δ = boundary layer thickness
δ^{**} = momentum thickness
λ = wavelength
ν = molecular kinematic viscosity
ρ = density

Subscripts

∞ = free-stream state
w = evaluated at wall

revealed lateral variations in the total pressure within the boundary layer which can be attributed to Taylor-Gortler type vortices. The results of the measurements for the tube touching the surface are shown in Fig. 2 where the ordinate, a dimensionless dynamic pressure, is proportional to the wall shear stress [14]. The momentum thickness at the start of curvature, δ_0^{**}, (measured without surface heating) and the radius, R, has been used to scale the lateral and streamwise distance, respectively, where $\delta_0^{**}/R = 1.05(10)^{-3}$. With the streamwise distance, x, measured from the leading edge of the test surface, curvature started at $x/R = 0.33$. Two items are immediately apparent from Fig. 2. The first is that the three-dimensional disturbances, which are initially barely detectable, grow in the streamwise direction and second they become more regular downstream. These two observations indicate that a regular system of vortices was evolving within the boundary layer. The same measurements taken without heating revealed an identical situation which in turn indicates that the inertia forces dominated the buoyancy forces in the process. As will be seen shortly, the growth of the vortices is particularly important since it affects the heat transfer dramatically.

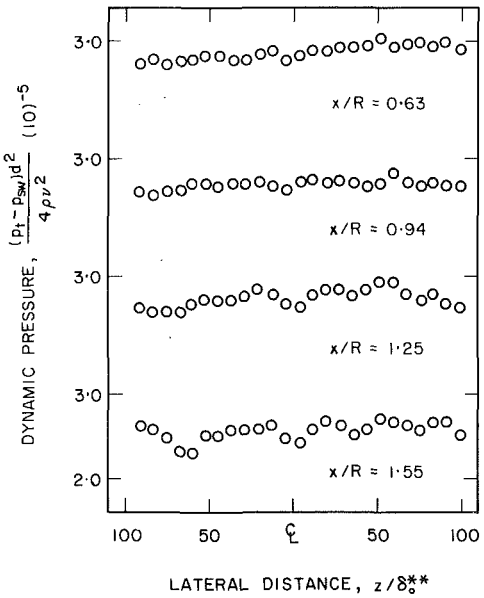

Fig. 2 Lateral dynamic pressure variation near concave surface

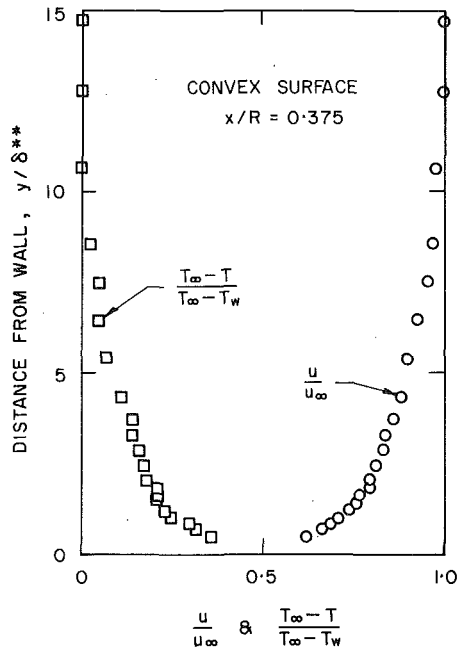

Fig. 3 Initial velocity and temperature profiles on convex surface

The likelihood of vortices being formed within a turbulent boundary layer on a concave surface can be determined from Tani's work. If the wavelength, λ, of the disturbance at $x/R = 1.55$ and the initial momentum thickness are used, a turbulent Gortler number, $G_t = 43\,(\delta_0^{**}/R)^{1/2}$, and a dimensionless wave number, $2\pi\,\delta_0^{**}/\lambda$, of 1.39 and 0.11 are found, respectively. This result, when plotted on Tani's graph for stability of a turbulent boundary layer on a concave surface lies well within the unstable region. Hence, a disturbance should amplify and a system of streamwise vortices should form as found.

Boundary layer velocity and temperature measurements were made at $x/R = 0.375$ which was slightly downstream of the point where curvature began. At this location the flow on the concave surface was still two-dimensional. The resulting profiles for both the convex and concave surfaces are shown in Figs. 3 and 4, and exhibit only slight differences. The momentum and enthalpy Reynolds numbers are 907 and 797, respectively, for the convex surface and 981 and 979 for the concave. The shape factors for both surfaces are identical and equal to 1.52. The enthalpy Reynolds numbers obtained by integrating the measured surface heat flux up to the profile measurement location are 917 for the convex surface and 937 for the concave. The discrepancies between these values and the profile values are attributed to the inaccuracies in the profile temperature measurements. For comparison, the momentum and enthalpy Reynolds numbers for a turbulent boundary layer on a flat surface developing over the same length are about 913 and 1022, respectively.

The curved surface heat transfer results are presented in Fig. 5. The Stanton number, St, defined as

$$\mathrm{St} = \frac{q}{\rho u_\infty c_p (T_w - T_\infty)}$$

with q the surface convective heat flux, is plotted against the Reynolds number based on the inlet mainstream conditions and distance from the leading edge. Although there is a fair amount of scatter in the data, particularly for the concave surface, the effect of surface curvature is unmistakable. Again, as found by Thomann, the heat transfer is much greater on the concave surface than on the convex; in this case, by almost a factor of two at the most downstream position. The correlation of Reynolds, et al. [15] for heat transfer in a turbulent boundary layer on a flat plate, i.e.

$$\mathrm{St}\left(\frac{T_w}{T_\infty}\right)^{0.4} = 0.0296\,\mathrm{Pr}^{-0.4}\,\mathrm{Re}_x^{-0.2}$$

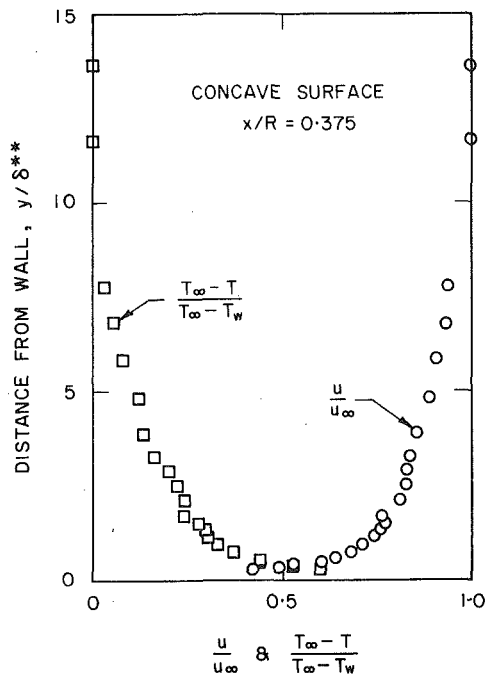

Fig. 4 Initial velocity and temperature profiles on concave surface

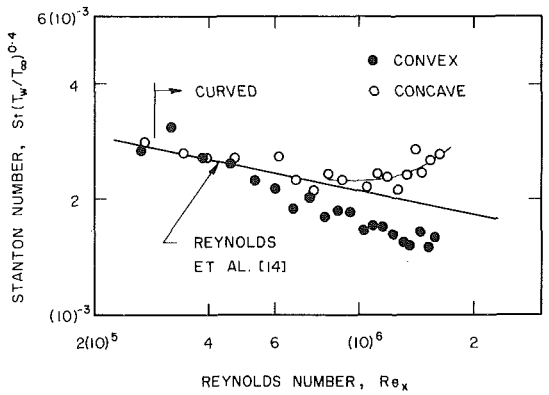

Fig. 5 Stanton number measurements on curved surfaces and comparison with flat plate correlation

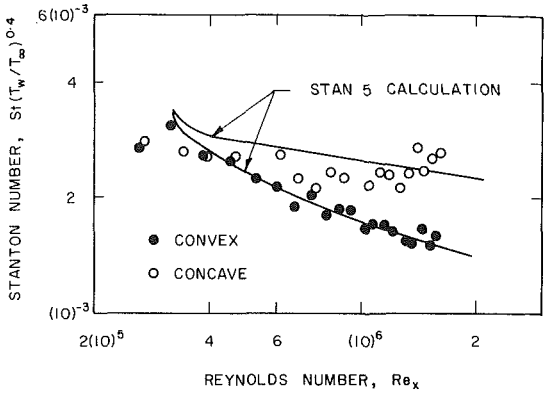

Fig. 6 Comparison of measured Stanton numbers with boundary layer calculations

is also shown in Fig. 5. A comparison of the data with this indicates an increasing departure as the viscous and thermal boundary layers develop along the curved surfaces. At the most downstream position, which is about 120 boundary layer thicknesses from the start of curvature, the heat transfer on the convex surface is about 20 percent less than the correlation while on the concave surface it is about 33 percent greater. The deviation of the concave surface data is particularly interesting since it occurs mostly on the downstream half of the surface and is still changing rapidly (compared to the data on the convex surface) at the most downstream position. This does not appear to be caused by curvature modifying the turbulent heat flux in a two-dimensional sense, as on the convex surface, and is most likely a result of the observed streamwise growth of vortices.

A comparison of the present results to Thomann's at the same number of boundary layer thicknesses downstream from the start of curvature reveals that curvature had much less of an effect in the present experiment even though the Richardson number, as defined earlier and averaged through the boundary layer, was virtually identical for both. Apparently, this is a consequence of the different Reynolds numbers and Mach numbers. The present experiment was carried out at Reynolds numbers based on the momentum thickness (1000 to 2000) about four times smaller than Thomann's and at a Mach number of about 0.06 compared to Thomann's value of 2.5. At the lower momentum thickness Reynolds numbers, viscous effects are more important and reduce curvature's influence. Therefore, curvature will have a smaller effect in the present situation. The effect of compressibility as shown in [10] is to increase the ratio of centrifugal to inertia forces by a factor of $[1 + (\gamma - 1)M^2/2]$. Accordingly, the appropriate Richardson number for Thomann's experiment is not as defined earlier but $[1 + (\gamma - 1)M^2/2]$ larger or slightly more than twice that for the present experiment. As a result, curvature will have a greater effect in the supersonic flow examined by Thomann.

Comparison with a Calculation Method

The calculation of two-dimensional turbulent boundary layer flow for a variety of mainstream and surface conditions has been made practical in recent years through the use of the digital computer. As a result, a number of boundary layer programs, both integral and finite difference types, have been developed. One of these programs called STAN 5, a finite difference type developed at Stanford University [16] using basically the Patankar-Spalding scheme [17], was modified to include streamline curvature. The modification was essentially that proposed by Bradshaw and is identical in form to that used by Eide and Johnston. That is, the mixing length without curvature was altered according to

$$\ell/\ell_0 = 1 - \beta\left(2\frac{u}{R}\right)\Big/\left(\frac{\partial u}{\partial y}\right)$$

for $(\partial u/\partial y) > 0.3\,(u_\infty/\delta)$ and

$$\ell/\ell_0 = 1 - \beta\left(2\frac{u}{R}\right)\Big/\left(0.3\frac{u_\infty}{\delta}\right)$$

for $(\partial u/\partial y) < 0.3\,u_\infty/\delta$. The restriction on $(\partial u/\partial y)$ is an artifice to prevent the mixing length from becoming infinitely large in the outer region of the boundary layer where $(\partial u/\partial y)$ becomes zero. The value of β used in the calculations was 6 for both the convex and concave surfaces. Also, the turbulent Prandtl number was assumed to be unaffected by curvature but the option was used in STAN 5 which allowed for its variation through the boundary layer. The wake value of the turbulent Prandtl number was taken as 0.86. Finally, in each case the velocity and temperature profiles shown in Figs. 3 and 4 were used to start the calculation.

The results of the calculations and the data are presented in Fig. 6 where again the distance from the leading edge of the test surface has been used in the Rynolds number. On the convex surface the calculation agrees reasonably well with the measurements which indicates that the heat load on a convex surface may be determined satisfactorily by using an appropriately modified two-dimensional boundary layer program. But on the concave surface the agreement is poor. In light of the transition from a two-dimensional to a three-dimensional flow which took place on the concave surface, this result is not unexpected and indicates rather clearly the area in which further work must be done before accurate heat transfer calculations for a turbulent boundary layer on a concave surface become feasible.

Concluding Remarks

As found by Thomann, the heat transferred to a turbulent boundary layer on a convex surface is less than that on a flat surface, while the heat transferred to a turbulent boundary layer on a concave surface is greater. However, the difference is much less for the present experiment than that reported by Thomann. This is attributed in part to the effects of compressibility in curved flows and indicates that curvatures effects become more important at higher Mach numbers.

The good agreement between the heat transfer results on the convex surface and the boundary layer calculation appears to indicate that only a modification to the turbulent shear stress (and turbulent heat flux via the turbulent Prandtl number) is required to successfully calculate the heat load on a convex surface. However, for flow on a concave surface, a two-dimensional calculation can only be expected to provide a reasonable average value of the heat load over the whole surface. The term "reasonable," of course, depends on whether or not the presently accepted value of β is appropriate for all flow situations over a concave surface. At that, the streamwise distribution of heat flux cannot be satisfactorily calculated and, eventually, the three-dimensional nature of the flow will have to be investigated and modeled.

References

1 Bradshaw, P., "Prediction of Turbulent Shear Layers in Turbomachines," *Fluid Mechanics, Acoustics, Design of Turbomachinery,* NASA SP-304, Part I, pp. 251–264.

2 So, R. M. C., and Mellor, G. L., "Experiment on Convex Curvature Effects in Turbulent Boundary Layers," *Journal of Fluid Mechanics,* Vol. 60, No. 1, 1973, pp. 43–62.

3 Meroney, R. N., "Measurements of Turbulent Boundary Layer Growth Over a Longitudinally Curved Surface," Project THEMIS Technology Report 25, 1974.

4 So, R. M. C., and Mellor, G. L., "Experiment on Turbulent Boundary

Layers on a Concave Wall," *Aero. Quart.*, Vol. 26, No. 1, 1975, pp. 35–40.
5 Ellis, L. B., and Joubert, P. N., "Turbulent Shear Flow in a Curved Duct," *Journal of Fluid Mechanics*, Vol. 62, 1974, pp. 65–84.
6 Ramaprian, B. R., and Shivaprasad, B. G., "Mean Flow Measurements in Turbulent Boundary Layers along Mildly Curved Surfaces," *AIAA Journal*, Vol. 15, No. 2, 1977, pp. 189–196.
7 Tani, I., "Production of Longitudinal Vortices in the Boundary Layer Along a Concave Wall," *Jour. Geophys. Res.*, Vol. 67, No. 8, 1962, pp. 3075–3080.
8 Bradshaw, P., "Effects of Streamline Curvature on Turbulent Flow," *AGARD-ograph*, Vol. 169, 1973.
9 Thomann, H., "Effect of Streamwise Curvature on Heat Transfer in Turbulent Boundary Layer," *Journal Fluid Mechanics*, Vol. 33, No. 2, 1968, pp. 283–292.
10 Bradshaw, P., "The Analogy between Streamline Curvature and Buoyancy in Turbulent Shear Flow," *Journal of Fluid Mechanics*, Vol. 36, No. 1, 1969, pp. 177–191.
11 Eide, S. A., and Johnston, J. P., "Prediction of the Effects of Longitudinal Wall Curvature and System Rotation on Turbulent Boundary Layers," Thermosciences Div. Rept. PD-19, Stanford University, 1974.
12 Mayle, R. E., Kopper, F. C., Blair, M. F., and Bailey, D. A., "Effect of Streamline Curvature on Film Cooling," *Trans. ASME*, Vol. 99, No. 1, 1977, pp. 77–82.
13 Coles, D., "The Turbulent Boundary Layer in a Compressible Fluid," Rand Report R-403-PR, Appendix A, 1962.
14 Preston, J. H., "The Determination of Turbulent Skin Friction by Means of Pitot Tubes," *J. Royal Aero. Soc.*, Vol. 58, 1954, pp. 109–121.
15 Reynolds, W. C., Kays, W. M., and Kline, S. J., "Heat Transfer in a Turbulent Incompressible Boundary Layer, I-Constant Wall Temperature," NASA Memo 12-1-58W, 1958.
16 Crawford, M. E., and Kays, W. M., "STAN 5—A Program for Numerical Computation of Two-Dimensional Internal and External Boundary Layer Flows," NASA Contractor Report, NASA CR-2742, 1976.
17 Patankar, S. V., and Spalding, D. B., *Heat and Mass Transfer in Boundary Layers*, 1st ed., Morgan-Grampian, London, 1967 or 2nd ed., International Textbook Company, London, 1970.

D. E. Metzger
Professor.
Mem. ASME

L. W. Florschuetz
Professor.
Mem. ASME

D. I. Takeuchi
Graduate Student.

R. D. Behee
Graduate Student.
Assoc. Mem. ASME

R. A. Berry
Graduate Student.
Student Mem. ASME

Department of Mechanical Engineering
Arizona State University
Tempe, Ariz. 85281

Heat Transfer Characteristics for Inline and Staggered Arrays of Circular Jets with Crossflow of Spent Air

Heat transfer characteristics were measured for two-dimensional arrays of jets impinging on a surface parallel to the jet orifice plate. The impinging flow was constrained to exit in a single direction along the channel formed by the jet plate and the heat transfer surface. Both mean Nusselt numbers and streamwise Nusselt number profiles are presented as a function of Reynolds number and geometric parameters. The results show that significant periodic variations occur in the streamwise Nusselt number profiles, persisting downstream for at least ten rows of jet holes. Both channel height and hole spacing can have a significant effect on the streamwise profiles, smoothed across the periodic variations. Where significant differences exist, inline hole patterns provide better heat transfer than staggered ones, particularly downstream. These and other effects of the geometric parameters are presented and discussed.

Introduction

Impingement with high velocity gas jets has become an established method of convectively cooling or heating surfaces in a wide variety of process and thermal control applications. In gas turbine airfoils a significant application is the cooling of the midchord region with a two-dimensional array of jets with a trailing edge discharge. In this configuration all of the jet air is constrained to flow toward the rear of the airfoil so that the exhaust from the upstream jets imposes a crossflow on the downstream jets.

At the present time, knowledge of the effect of array configuration on heat transfer characteristics is inadequate for achievement of optimal designs, even for uniformly spaced arrays. [1–5] are typical of those currently in use for predicting heat transfer with multiple jet impingement. Gauntner, et al, [6] recently reported results of measurements made on an impingement cooled gas turbine vane which demonstrate the inadequacy of existing correlations. In particular, the question of the effect of crossflow on the downstream heat transfer performance is not adequately resolved.

A NASA sponsored investigation was initiated with the primary objective of determining heat transfer behavior for a variety of uniformly spaced impingement array configurations which model those of interest in current and future gas turbine airfoil cooling. This paper provides a description of the basic experimental facility, presents representative results drawn from the data obtained thus far, and discusses the significant trends observed. Chordwise profiles of spanwise averaged, as well as overall averaged, Nusselt numbers are presented as a function of Reynolds number and the geometric parameters. Results are given for chordwise jet hole spacings of 5 and 10 hole diameters, spanwise spacings of 4 to 8 diameters, channel heights from 1 to 3 diameters with some data at 6, both inline and staggered hole patterns, and mean jet Reynolds numbers from 5 to 20×10^3. Additional details and results will be available in [7].

Experimental Facility

The test facility consists basically of a compressed air supply, an air flow metering section, and interchangeable plenum/jet plate assemblies which produce arrays of jets impinging on an instrumented heat transfer test surface. Chordwise and spanwise cross-sectional views of the assembly of the major components are shown in Fig. 1 for one plenum size. A single test plate unit consisting of a segmented copper test plate with individual segment heaters, the necessary thermal insulation, and the test plate support structure, is utilized for all tests. The segmented design provides for control of the chordwise thermal boundary condition at the heat transfer test surface, as well as for determination of spatially resolved heat transfer coefficients in the chordwise direction. The jet plate under test, positioned by the jet plate holder, is bolted to the lower flange of the plenum, which in turn, is bolted to the test plate unit. The jet plate lower surface is positioned relative to the heat transfer surface via interchangeable spacers to permit covering the desired range of z/d.

Laboratory compressed air is piped to the plenum and passed through the plenum packing to provide a uniform flow upstream of the jet plate. After passing through the jet plate the air exhausts to atmospheric pressure by flowing along the channel formed by the jet plate, the test surface, and the spacer.

There are four interchangeable plenums, each of a different chordwise length. Thus, the channel length varies depending on the size of the particular plenum/jet plate assembly being utilized. The thermally active length of the test plate consists, for a given test, of

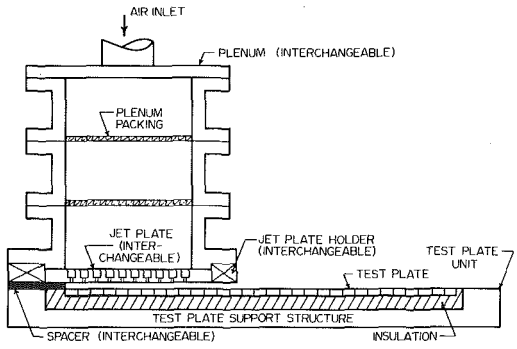

Fig. 1 Test unit assembly

Contributed by the Heat Transfer Division for publication in the JOURNAL OF HEAT TRANSFER. Manuscript received by the Heat Transfer Division July 27, 1978.

those test plate segments which are immediately opposite the jet plate. The maximum active chordwise length is 38.1 cm (15 in.) (30 segments by 1.27 cm (0.5 in.) per segment), with an additional segment at the downstream end to serve as a guard element. For tests in which only a fraction of the test plate was thermally active the segment immediately downstream of the active portion served as a guard element.

The spanwise width of the test plate and the channel were fixed at 12.2 cm (4.8 in.) and 18.3 cm (7.2 in.), respectively. The excess width of the channel permitted the jet hole pattern to extend beyond the edges of the heat transfer surface, thus minimizing flow pattern edge effects on the heat transfer characteristics (see Fig. 1, spanwise view).

The significant dimensions and geometric characteristics unique to the interchangeable plenums and matching jet plates for which data is reported here are summarized in Table 1. The smallest jet hole diameter is near prototype size for the gas turbine application, while the larger sizes provide for improved chordwise resolution of heat transfer coefficients. Note that the number of holes across the channel span always exceeds the number across the test surface by three or more. The number of spanwise rows of holes was fixed at 10 for all jet plates. Each jet plate with a staggered hole pattern was identical to its inline counterpart, except that alternating spanwise rows were offset by one-half of the spanwise spacing. In what follows a given size and hole spacing configuration will, where convenient, be referred to in abbreviated form such as A (10, 6), indicating size A with $x_n/d = 10$, $y_n/d = 6$.

The jet plate thickness, b, at each hole location is equal to the jet hole diameter. This was achieved by appropriately counterboring plates of larger overall thickness (Fig. 1). This design feature was dictated primarily by the need to insure accurate channel heights during test runs, a particularly critical requirement for the narrowest channel heights. The counterbore was three jet hole diameters, except for the narrowest hole spacings where two jet hole diameters was used. In one test with $z/d = 1$, a $2d$ counterbore plate was used with the counterbored holes subsequently bored out to $3d$, and the test repeated. The results were identical to within experimental uncertainty.

Qualification tests for each jet plate prior to mounting on the test plate unit included both pressure and flow uniformity measurements across the hole pattern with the plate mounted on the matching plenum.

The relationship between the chordwise hole spacing and the test plate segments for each plenum size is represented in Fig. 2. This relation determines the maximum possible chordwise resolution as listed in Table 1.

The copper test plate segments were 0.635 cm (1/4 in.) thick and 1.19 cm (15/32 in.) wide with 0.079 cm (1/32 in.) balsa wood insulation bonded between adjacent segments to minimize heat leak. The individual heaters were foil-type bonded to the underside of each segment, each with power input controlled by a separate variac. The edges and undersides of the segment/heater assemblies were bonded to basswood, selected for the combination of structural and insulating qualities it provided. Those insulation surfaces which would have formed part of the channel and been exposed to the air flow were surfaced with 0.079 cm (1/32 in.) Lexan plastic to provide a smooth aerodynamic surface and prevent possible erosion of the wood insulation materials. The primary temperature instrumentation in the test plate consisted of copper-constantan thermocouples mounted in the center of each copper segment, with a redundant thermocouple in each segment offset 1.52 cm (0.6 in.) in the spanwise direction. Several segments at intervals along the plate had additional thermocouples mounted out to the edge to verify that the spanwise temperature distributions during testing were essentially uniform.

Table 1 Summary of significant geometric characteristics of plenum/jet plate assemblies for which data is reported

Plenum Size Designation	ℓ cm (in.)	Jet Plates: d and b cm (in.)	x_n/d	y_n/d	N_s	N_s'	Maximum Chordwise Resolution
A	6.35 (2.5)	0.0635 (.025)	10	6	32	48	$2x_n$
				8	24	36	
B	12.7 (5)	0.127 (.050)	10	4	24	36	x_n
				8	12	18	
		0.254 (0.100)	5	4	12	18	
				8	6	9	
C	25.4 (10)	0.254 (0.100)	10	6	8	12	$\frac{1}{2}x_n$
				8	6	9	
D	38.1 (15)	0.381 (0.150)	10	4	8	12	$\frac{1}{3}x_n$

Note: $N_c = \ell/x_n$ fixed at 10 for all tests.

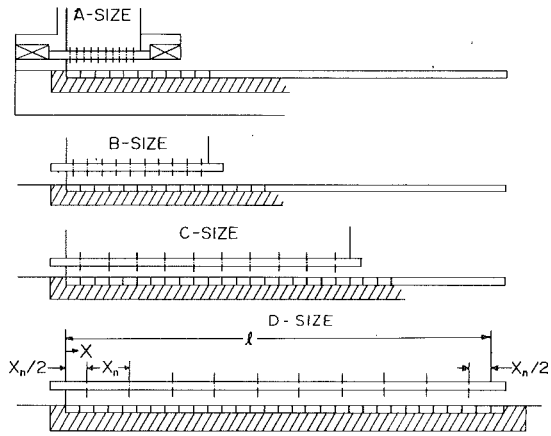

Fig. 2 Chordwise relation of jet hole rows to test plate segments

Experimental Procedures and Data Reduction

A typical test run was defined by setting up a selected geometric configuration and setting a constant air flow rate to the plenum. When

Nomenclature

A = heat transfer surface area of individual test plate segment
$A_0{}^*$ = ratio of jet hole area to opposing heat transfer surface area (open area ratio)
b = thickness of jet plate
d = jet hole diameter
$\overline{G}$ = mean mass flux based on jet hole area
$\overline{G}^*$ = mean mass flux based on heat transfer surface area
h = convective heat transfer coefficient
$\overline{h}$ = convective heat transfer coefficient averaged over entire heat transfer surface
k = thermal conductivity of air
ℓ = chordwise length of heat transfer surface
N_c = number of spanwise rows in chordwise direction
N_s = number of jet holes across span of heat transfer surface
N_s' = number of jet holes across span of channel
Nu = Nusselt number resolved in chordwise direction, averaged across span, hd/k
$\overline{\text{Nu}}$ = Nusselt number averaged over entire heat transfer surface, $\overline{h}d/k$
Q = heat rate from individual test plate segment
$\overline{\text{Re}}$ = mean jet Reynolds number, $\overline{G}d/\mu$
$\overline{\text{Re}}^*$ = mean superficial Reynolds number, $\overline{G}^*d/\mu$
T_p = plenum air temperature
T_r = fluid reference temperature
T_s = heat transfer surface temperature
x = chordwise location along heat transfer surface measured from upstream end of channel
x_n = chordwise jet hole spacing
y_n = spanwise jet hole spacing
z = channel height or jet plate-to-impingement surface spacing
μ = dynamic viscosity

steady state was achieved with zero power input to the test plate segment heaters, the segment temperatures were recorded. These temperatures closely approximated the adiabatic wall temperature profile along the test surface. The adiabatic wall condition was not precisely achieved primarily because of small but unavoidable heat leaks. Next, power inputs to segment heaters were individually adjusted to maximum values, under the constraint that the test surface was essentially isothermal. Maximum power input was limited, depending on flow conditions, either by temperature limitations of materials in the test plate unit or by current limitations in the switching circuit used for recording the individual power inputs to the heaters. Finally, the power input was adjusted to nominally half of the maximum value, but again with individual heaters adjusted so as to maintain an isothermal surface. Under each power input level, individual segment power inputs and temperatures were recorded. This completed a heat transfer test run.

For each geometric setup, heat transfer data was typically obtained by the above technique for three different flow rates corresponding to nominal mean jet Reynolds numbers of 5, 10, and 20×10^3. The maximum Reynolds numbers were limited only by the laboratory air capacity available at the time these tests were run.

At the maximum power inputs the segment temperature rise above the zero power case ranged from about 15 to 35 K, depending on flow conditions. Surface temperature variations during isothermal tests were normally within 0.25 K, while during zero power tests surface temperatures varied up to 4 K, the maximum variations occurring for $z/d = 1$ at the maximum flow rates ($\overline{\mathrm{Re}} = 20 \times 10^3$).

Segment heat transfer coefficients were determined based on the defining equation

$$h = (Q/A)/(T_s - T_r)$$

Q is the segment heat rate determined from the measured power input to the segment heater suitably corrected for heat leaks (typically less than 5 percent); A is the segment surface area; T_s is the segment surface temperature as determined from the thermocouple imbedded at the center of the copper segment suitably corrected for temperature drop from thermocouple to surface (always less than 0.2 K); and T_r is a reference temperature. At the outset it is assumed only that a suitable reference temperature exists, but it is not explicitly defined. With three sets of test plate segment data (Q/A, T_s) available for a given flow condition (corresponding to the zero, maximum and one-half maximum power input levels) one can use any combination of two sets to give two equations of the above form in the two unknowns h and T_r. Since there are three such combinations of the three data sets, one can compute three values of h for a given flow condition. If the assumption that a suitable reference temperature exists for defining the heat transfer coefficient is correct then these three values should be consistent to within experimental uncertainty. The results indeed show that this is the case. Once this was demonstrated, a minimum of just two data sets at two different power levels for a given flow condition would be necessary. However, the experimental procedure described above was retained for all test runs to serve as a constant check on the self-consistency and repeatability of the reduced data. For a 95 percent confidence level the results are typically self-consistent to within about ±3 percent, the larger inconsistencies normally occurring for the low Reynolds number cases. Overall experimental uncertainties on heat transfer coefficients are estimated to be about ±4 percent.

The closest possible experimental condition to an adiabatic wall measurement in the present study was for the zero power input measurements. Comparison of T_r values computed by combining data sets for maximum and one-half maximum power levels with segment surface temperatures measured for the corresponding zero power input case show that these values agree to within 1 percent of the ($T_s - T_r$) differences which occurred during the measurements with power inputs. This verifies that T_r may be correctly identified as the adiabatic wall temperature. The segment heat rates which occurred during zero power measurements due to heat leaks were also less than 1 percent of the heat rates which existed during power input.

The largest differences between T_r and T_p in these tests were about 6 K occurring downstream for the largest Reynolds numbers at the smallest channel heights ($z/d = 1$). These differences are significant relative to the corresponding ($T_s - T_r$) differences. Thus, for such tests the assumption that $T_r = T_p$ would lead to invalid results for heat transfer coefficients. Space limitations do not permit a presentation here of the reference (adiabatic wall) temperatures in a generally useful form. These results will be reported at a later date in conjunction with flow distribution data which is currently being analyzed. In applications where one may, to a reasonable approximation, take $(T_s - T_p)/(T_s - T_r) = 1$ knowledge of the heat transfer coefficients and plenum temperature is adequate for determination of heat fluxes. Such is the case, for example, in the turbine cooling application, which motivated the present study.

Results and Discussion

Presentation Variables and Parameters. Heat transfer characteristics are presented here in terms of Nusselt numbers based on jet hole diameter. It is emphasized that all Nusselt numbers presented are spanwise averaged values; i.e., the experiments were not designed to provide any degree of spatial resolution across the span of the heat transfer surface. Though a major objective of the experiments was to determine chordwise variations of heat transfer coefficients, it must be kept in mind that the chordwise resolution is limited by the width of the individual segments of the test plate (1.27 cm). The maximum possible resolution ranges from $2x_n$ for the A-size to $x_n/3$ for the D-size as was indicated in Table 1. Data from any size configuration can, of course, be averaged over as many segments as desired.

It is useful to organize the Nusselt number data in three categories: (1) mean values, $\overline{\mathrm{Nu}}$, averaged over the entire active heat transfer surface, (2) low-resolution values averaged over x_n or $2x_n$, (3) higher-resolution values averaged over $x_n/3$ or $x_n/2$. As will be seen, the higher resolution results show significant periodic variations of heat transfer coefficients superimposed on the overall chordwise trend, while the low-resolution results show more clearly the overall chordwise trend smoothed across the periodic variations. Both the low and higher-resolution Nusselt numbers are denoted by Nu. These values are plotted against x/x_n. The spacing of the data points along the abscissa directly reflects the chordwise resolution involved. Nusselt numbers are presented as a function of four geometric parameters; channel height (z/d), chordwise and spanwise hole spacings (x_n/d and y_n/d), and hole pattern (inline or staggered).

A mean Reynolds number based on jet hole diameter is utilized as the flow parameter. Two definitions of Reynolds number are employed. One is the mean jet Reynolds number, $\overline{\mathrm{Re}}$, based on the mass velocity at the jet holes, while the second, $\overline{\mathrm{Re}}^*$, is based on the mass flow rate per unit heat transfer surface area. They are related simply through the ratio of the open or flow area of the jet plate to the opposing heat transfer surface area; i.e.,

$$\overline{\mathrm{Re}}^* = \overline{\mathrm{Re}} \cdot A_0^*$$

where for the present jet plate design configurations,

$$A_0^* = \frac{\pi}{4} \frac{1}{(x_n/d)(y_n/d)}$$

It is well to keep in mind that Nusselt numbers compared for the same $\overline{\mathrm{Re}}$ reflect the relative magnitude of heat transfer coefficients for the same pressure drop across the jet plate, while those Nusselt numbers compared for the same $\overline{\mathrm{Re}}^*$ reflect the relative magnitude of heat transfer coefficients compared for the same mass flow per unit heat transfer surface area.

Mean Nusselt Numbers. Values of $\overline{\mathrm{Nu}}$ as a function of $\overline{\mathrm{Re}}$ are shown in Fig. 3 for the inline pattern with $x_n/d = 10$. The three plots on the left hand side of the figure are for $y_n/d = 6$, each for a different z/d as indicated. The plots on the right are for $y_n/d = 8$, for the same set of z/d's as those on the left. The plots are arranged so as to directly compare results for geometrically similar configurations of several different sizes. While most of these results for geometrically similar cases are essentially coincident, differences exist which exceed experimental uncertainties. For example, the results for B (10, 8) and C (10, 8) are essentially coincident, but differ from the results for the

corresponding smallest size, A (10, 8), by at most, about 20 percent. The most plausible explanation for these differences will be discussed shortly, after the low-resolution chordwise Nusselt number profiles are presented.

It is also apparent from Fig. 3 that there is little effect of channel height on these mean Nusselt numbers. Results for several cases at $z/d = 6$ were also obtained, but are not shown to conserve space. These values were only a few percent lower than the corresponding results for $z/d = 3$. The magnitudes of these mean values, to the extent that they can be compared given differences in values and combinations of geometric parameters, are consistent with several recently published results for configurations of similar types [8, 9].

Low-Resolution Chordwise Profiles. Chordwise profiles of Nu, resolved to $2x_n$, are plotted in Fig. 4 for the same cases shown in Fig. 3, with $\overline{\text{Re}}$ as a parameter in each plot. The corresponding values of $\overline{\text{Nu}}$ are shown at the right hand side of each graph. The plots are again arranged so as to directly compare results for geometrically similar configurations of different sizes. In these plots, the spanwise jet hole row locations relative to the heat transfer surface are indicated by the vertical arrows. As in the case of the mean Nusselt numbers, the chordwise profiles are fairly coincident for the various sizes of a given geometric configuration, yet differences do exist which exceed experimental uncertainties. An additional point that comes to light is that even though the mean results may be coincident, the chordwise profiles may show some differences. This is readily apparent from the comparisons for A (10, 6) and C (10, 6) at $z/d \approx 1$. Here the chordwise profiles for these two sizes differ somewhat, but cross each other in such a way that the mean values are essentially coincident. The same trend is detectable for $z/d = 2$, but is less significant. For the (10, 8) configuration it appears that the profiles for the B and C size data are in somewhat better agreement with each other than they are with the A size profiles.

The possibility exists that an effect similar to that reported by Gardon and Akfirat [10] may be, in some measure, a contributing factor. They reported the detection of a slot width dependence for slot jet stagnation point heat transfer at slot width-to-spacing ratios less than eight, which was attributed to turbulence effects. However, it appears at this time that in the present case the observed differences are primarily the result of differences in flow characteristics related to compressibility effects. Plenum pressure measurements in conjunction with static pressure traverses along the channel indicate that for the A-size configurations jet Mach numbers equal unity for the larger Reynolds numbers, at least for the downstream rows. In addition, cross flow velocities for a given jet Reynolds number are largest for the A-size configuration; and for $z/d = 1$ they too are choked for the largest $\overline{\text{Re}}$.

These compressibility effects are significant in the A-size configuration because of the low laboratory pressure levels and the resulting relatively large pressure drop required to achieve the large jet Reynolds numbers with the small jet diameters. The pressure levels in the anticipated turbine application are much higher, with correspondingly lower Mach numbers. Therefore, it is expected that the present data for sizes larger than A-size best models the prototype heat transfer characteristics for the gas turbine engine application, at least over the present range of jet Reynolds numbers.

Four graphs showing chordwise Nusselt number profiles resolved to one chordwise hole spacing are presented in Fig. 5, drawn from the inline pattern B-size data. Corresponding mean values are again indicated at the right hand margins. Each graph is for a different set $(x_n/d, y_n/d)$, but all are plotted for the same value of jet Reynolds number, $\overline{\text{Re}} = 10^4$. Here the effect of z/d can be visualized directly in each graph. The differences in the profiles are in every case greater between $z/d = 1$ and 2, than between $z/d = 2$ and 3, the effect being most pronounced for the closest spanwise spacing, $y_n/d = 4$, shown in the two graphs at the top of the figure. The lower left hand graph includes results for $z/d = 6$ which differ only slightly from the results for $z/d = 2$ and 3, primarily at the upstream locations. These graphs show clearly that although the chordwise profiles of heat transfer coefficients can vary significantly with z/d, especially with close spanwise spacings, the mean values remain relatively insensitive to

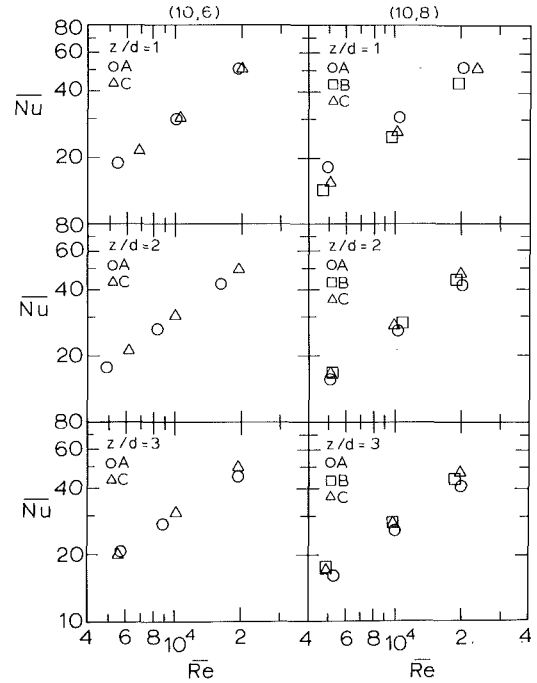

Fig. 3 Comparison of mean Nusselt numbers for geometrically similar configurations—inline hole pattern

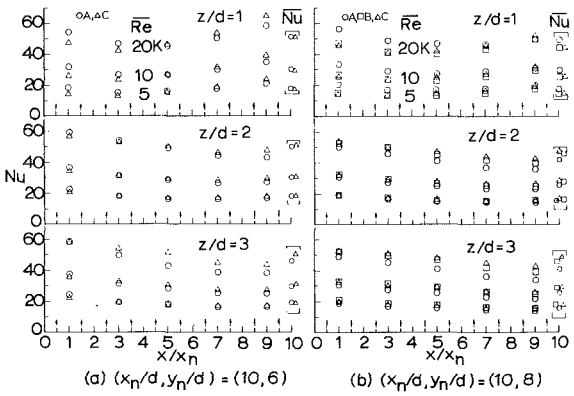

Fig. 4 Comparison of chordwise Nusselt number profiles for geometrically similar configurations—inline hole pattern

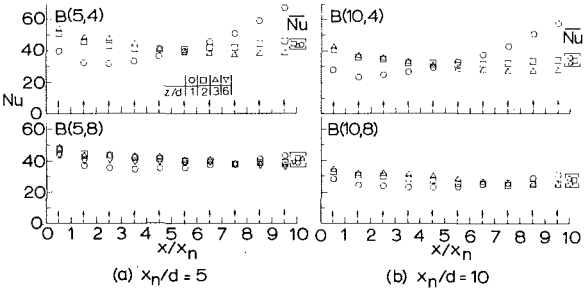

Fig. 5 Effect of channel height (z/d) on chordwise Nusselt number profiles—inline hole pattern, Re = 10^4

z/d over the range covered. In particular, what occurs over the range $1 \leq z/d \leq 3$ for every set $(x_n/d, y_n/d)$ shown is that the upstream cooling rate is higher for the larger z/d, but the difference decreases until at some point downstream all z/d result in the same cooling rate, while further downstream the smaller values of z/d give the higher cooling rates. These effects are undoubtedly related, at least in part, to the fact that for this range of z/d, jet impingement cooling with minimal crossflow, which is the upstream condition, increases with z/d, while cooling rates due to channel-type flows, which here arise downstream as a crossflow, typically vary inversely with channel height.

Additional chordwise Nusselt number profiles drawn from the B-size tests are presented in the series of graphs of Fig. 6. The open points represent data for the specified inline hole patterns, while the solid points represent data for the corresponding staggered hole patterns. For the moment attention is focused on the inline hole pattern data only (open points). Discussion of the effect of inline versus staggered hole patterns will be taken up in the next section. The individual graphs directly compare profiles for $y_n/d = 4$ with those for $y_n/d = 8$, all for the same $\overline{\mathrm{Re}}^*$, at specified values of x_n/d and z/d. Such a comparison directly reflects the effect of spanwise hole spacing, y_n, for a fixed $\overline{G}^*$, and otherwise fixed geometry (i.e., d, x_n, z, and ℓ). It is apparent that, compared in this way the mean heat transfer coefficients for $y_n/d = 8$ are significantly larger than those for $y_n/d = 4$ irrespective of the values of the other geometric parameters, x_n/d and z/d. However, the chordwise profiles show that for $z/d = 1$ and 2 the differences are largest upstream and, for $z/d = 1$, in particular, almost disappear downstream. For $z/d = 3$ the differences are fairly uniform along the channel. This behavior lends support to the view that for the smaller channel heights there is a significant contribution to the downstream heat transfer due to the crossflow.

The effect of varying the chordwise hole spacing for a fixed cooled surface length cannot be determined directly from the present data base since the ratio ℓ/x_n was fixed at ten for all tests. In Fig. 6, increasing x_n/d from 5 to 10 does show the effect of spreading ten spanwise rows of holes over twice the cooled surface length while maintaining a fixed $\overline{G}^*$ and otherwise fixed geometry (i.e., d, y_n, and z). Such an increase in x_n increases the mean heat transfer coefficients regardless of the values of the other geometric parameters.

It will subsequently be possible to determine the effect of varying N_c (i.e., x_n independently of ℓ) utilizing the present data base. One could, of course, calculate $\overline{\mathrm{Nu}}$ over any number of upstream rows less than ten. To properly interpret and compare such results the mean jet Reynolds number over the corresponding number of rows must be determined. Such a procedure requires accurate knowledge of the chordwise jet flow distribution, and should be checked experimentally by selected tests utilizing jet plates with varying numbers of spanwise rows. The necessary data is currently being generated in order to extend the present results, as well as attempt to correlate the Nusselt number profiles with the chordwise flow distributions.

Inline Versus Staggered Jet Hole Patterns. Attention is now turned to the comparison between heat transfer coefficients for the corresponding inline and staggered hole patterns. A major result obtained from these comparative tests is that the mean heat transfer coefficients for the inline patterns were in every case equal to (within experimental uncertainty) or larger than those for the corresponding staggered patterns. This is illustrated in Fig. 6 for the B-size data, where it is apparent that the largest differences occurred for the highest hole density B (5, 4) at the largest channel heights, $z/d = 2$ and 3. For these cases the inline mean heat transfer coefficients exceeded the staggered values by 18 percent. Little or no effect is apparent for the largest spanwise spacing, $y_n/d = 8$, regardless of the values of the other parameters. For B (10, 4) the inline mean values exceed the staggered values by about 10 percent. The chordwise profiles clearly show that the hole pattern effect increases in significance in the downstream direction. For B (5, 4), $z/d = 3$, the downstream ($x/x_n = 9.5$) value of Nu for the inline pattern exceeds the staggered value by about 60 percent, indicating that the local effects can be quite significant. It seems reasonable that these hole pattern effects would tend to be most significant at the downstream locations, and for the highest hole density at the largest channel height since all of these conditions presumably enhance the possible degree of interaction of adjacent jets. With the complex jet and crossflow interactions which occur in these flow configurations it is not immediately obvious, however, why it is the inline pattern which produces the highest heat transfer rate.

Higher-Resolution Profiles. As has already been indicated, the low resolution results clearly show the overall chordwise trends, but do not detect the significant periodic variations which are observed when the resolution is increased to better than one chordwise hole spacing, as is possible for the C and D-size data. These variations are most clearly shown by the D-size data with a resolution of $x_n/3$ as illustrated in Fig. 7. Upstream the peak values occurring opposite the jet holes exceed the minimum values between holes by a factor of at least three. Downstream the peaks diminish while the valleys increase in magnitude, but the variations clearly persist even at the tenth row location. It may also be observed that downstream the peaks have shifted to locations between the jet holes, while the valleys now occur opposite the holes. This behavior is undoubtedly due to the deflection of the jets by the increasing magnitude of the crossflow. The dashed line joining the data points is added for clarity only. It does not precisely reflect the infinitely resolved chordwise variation which would be even greater. In this connection the recent work of Sparrow, et al. [11] is relevant. Their measurements were for a single jet in a crossflow rather than for a two-dimensional array of jets. However, their chordwise resolution was comparable to the jet orifice diameter. Their results show impingement point values exceeding upstream and downstream values by large factors. Prior studies of two-dimensional array configurations with crossflow similar to those investigated here have apparently been limited to resolutions of at best one chordwise hole spacing, so that the periodic variations were not observed. The implications of the characteristics of these periodic variations for the designer should be quite significant, particularly from the thermal stress standpoint in applications such as the cooling of gas turbine airfoils. The acquisition of higher resolution data for additional channel heights, hole spacings, and flow rates, as well as for staggered hole patterns is currently underway in order to further characterize the effect of the crossflow on the nature of the observed periodic variations as a function of these parameters. These results will be reported in a subsequent paper.

Concluding Remarks

The final set of data presented here (Fig. 7) indicates that a periodic variation in the chordwise Nusselt number profile can persist for at least ten rows downstream. The period of this variation is equal to the chordwise hole spacing. The emphasis in this paper, however, has been

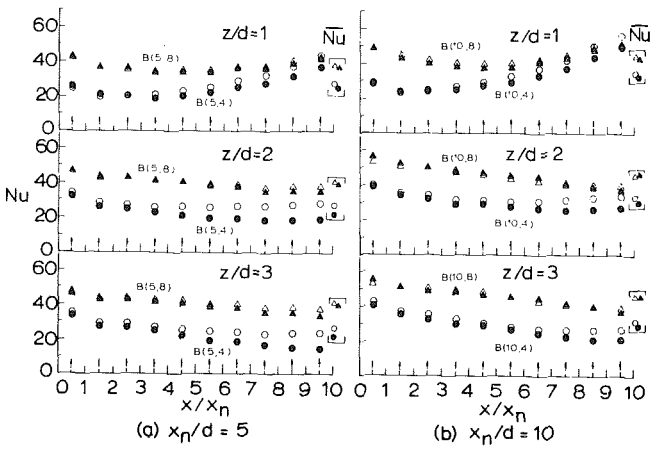

Fig. 6 Effect of hole spacing and hole pattern on chordwise Nusselt number profiles. Open points are inline patterns. Solid points are corresponding staggered patterns. Re* = 196

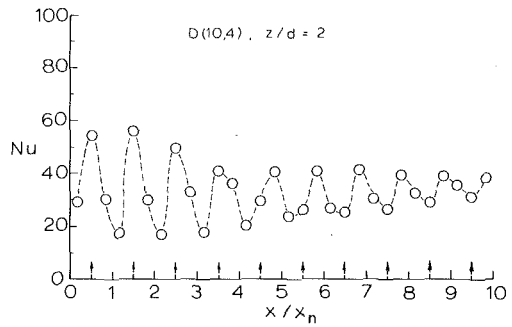

Fig. 7 Higher-resolution chordwise Nusselt number profile—inline hole pattern, Re = 10^4. Dashed line used for clarity only

placed on the chordwise trend smoothed across the periodic variations—i.e., data averaged over one or two chordwise spacings, referred to as low-resolution results. These results show that for $1 \leq z/d \leq 3$, upstream Nusselt numbers compared for the same $\overline{\text{Re}}$ increase with channel height, while downstream the reverse is true. The effect is most pronounced for the narrowest spanwise hole spacing. In addition it is found that for $z/d = 1$ and $y_n/d = 4$ the Nusselt numbers reach a minimum as far upstream as the second or third row of holes after which the values increase continuously, more than doubling by the tenth row. The possibility of such behavior is significant for the designer to keep in mind, particularly since the implication of several prior studies of similar flow configurations is that increasing crossflow always tends to degrade the heat transfer performance [4, 8]. For $z/d \geq 2$, the present results show that the heat transfer coefficient either decreases continuously downstream or shows only a slight upturn after exhibiting a broad minimum. The strong effect on the chordwise profiles as z/d approaches unity is not reflected in the mean Nusselt numbers, which vary with z/d by no more than about 10 percent.

Over the open area ratio range covered (1 to 4 percent), the denser hole patterns result in the highest heat transfer coefficients when compared for the same $\overline{\text{Re}}$ (Fig. 5), but when compared for the same $\overline{\text{Re}}^*$ the reverse is true (Fig. 6). Hole pattern effects may be quite significant in their effect on mean Nusselt numbers as well as on the chordwise profiles. Some prior studies have reported results in terms of open area ratios only rather than in terms of hole spacings for specific hole patterns [1, 8, 12] with one recent paper reporting a correlation equation in terms of open area ratio [8]. The present data demonstrate that neither chordwise Nusselt number profiles nor mean values can be characterized solely in terms of the open area ratio, but that specific hole patterns and spacings must be considered, particularly for the denser arrays.

Acknowledgments

The support of the National Aeronautics and Space Administration, Lewis Research Center, under Grant NSG 3075 is hereby gratefully acknowledged.

References

1 Daane, R. A., and Han, S. T., "An Analysis of Air Impingement Drying," *Tappi*, Vol. 44, 1961, pp. 73–80.

2 Gardon, R., and Cobonpue, J., "Heat Transfer Between a Flat Plate and Jets of Air Impinging on It," International Developments in Heat Transfer, *Proceedings of 2nd International Heat Transfer Conference*, ASME, New York, N.Y., 1962, pp. 454–460.

3 Huang, G. C., "Investigations of Heat Transfer Coefficients for Air Flow Through Round Jets Impinging Normal to a Heat Transfer Surface," ASME JOURNAL OF HEAT TRANSFER, Vol. 85, pp. 237–243.

4 Kercher, D. M., and Tabakoff, W., "Heat Transfer by a Square Array of Round Air Jets Impinging Perpendicular to a Flat Surface Including the Effect of Spent Air," ASME *Journal of Engineering for Power*, Vol. 92, No. 1, Jan. 1970, pp. 73–82.

5 Metzger, D. E., and Korstad, R. J., "Effects of Cross Flow in Impingement Heat Transfer, "ASME *Journal of Engineering for Power*, Vol. 94, 1972, pp. 35–41.

6 Gauntner, J. W., Gladden, H. J., Gauntner, D. J., and Yeh, F. C., "Crossflow Effects on Impingement Cooling of a Turbine Vane," NASA TM X-3029, March 1974.

7 NASA Contractor Report, Arizona State University, Tempe, in preparation.

8 Chance, J. L., "Experimental Investigation of Air Impingement Heat Transfer Under an Array of Round Jets," *Tappi*, Vol. 57, No. 6, 1974, pp. 108–112.

9 Hollworth, B. R. and Berry, R. D., "Heat Transfer from Arrays of Impinging Jets with Large Jet-to-Jet Spacing," ASME Paper 78-GT-117, Gas Turbine Conference, London, April 1978.

10 Gardon, R., and Akfirat, J. C., "The Role of Turbulence in Determining the Heat Transfer Characteristics of Impinging Jets," *International Journal of Heat and Mass Transfer*, Vol. 8, 1965, pp. 1261–1272.

11 Sparrow, E. M., Goldstein, R. J., and Rouf, M. A., "Effect of Nozzle-Surface Separation Distance on Impingement Heat Transfer for a Jet in a Crossflow," ASME JOURNAL OF HEAT TRANSFER, Vol. 97, 1975, pp. 528–533.

12 Friedman, S. J., and Mueller, A. C., "Heat Transfer to Flat Surfaces," *Proceedings, General Discussion on Heat Transfer*, The Institute of Mechanical Engineers, London, England, 1951, pp. 138–142.

C. J. Chen
Professor.
Mem. ASME

C. H. Chen
Graduate Assistant.

Energy Division,
College of Engineering,
The University of Iowa,
Iowa City, Iowa 52242

On Prediction and Unified Correlation for Decay of Vertical Buoyant Jets

A differential turbulence model is used to predict the decay behavior of turbulent buoyant jets in a uniform environment at rest. The turbulent stresses and heat fluxes are modeled by the algebraic expressions while the differential transport equations are solved for the kinetic energy of turbulence, k, the rate of dissipation of turbulence kinetic energy, ϵ, and the fluctuating temperature $\overline{T'^2}$. The numerical result correlated with a unified scaling law was shown to fall into a single curve for the flows beyond the zone of flow establishment. The flow characteristics are then classified into a non-buoyant region, an intermediate region and a plume region. The predicted results show that the buoyant jets is accelerated in the zone of flow establishment. Equations for decay of velocity, density, and turbulent quantities are given from the non-buoyant region to the plume region for both plane and round buoyant jets.

1 Introduction

Many problems associated with environmental pollution require the buoyant jet characteristics such as entrainment rate of surrounding fluid, dispersion of thermal or waste pollutants and the decay of buoyant jet velocity, density and temperature. This paper presents a mathematical model for predicting buoyant jet flow in a uniform environment at rest and correlates the predicted result in a uniform way so that the properties and behaviors of the buoyant jets are elucidated. Particular attention is given to the decay behavior of buoyant jets from the near source field or the zone of flow establishment to the far field where buoyant jets are evolved to become plumes.

Although the differential method of solution for turbulent buoyant jets is more complex and requires elaborate computation, it has potentially wider applications and provides an accurate prediction of the buoyant jet behavior. The differential method needs a turbulence closure model for turbulence transport quantities. A mixing length closure model was adapted by Madni and Plecther [1]. Several closure models for the turbulent transport equations were proposed by Launder [2], Lumley [3] and many others. They are reviewed by Hossain and Rodi [4]. Gibson and Launder [5] have tested the Launder's model by application of the model to a horizontal surface jet and mixing layer. Chen and Rodi [6] showed that the turbulence model based on Launder's model predicted satisfactory results for the far field behavior of vertical buoyant jets.

In this study we use Chen and Rodi's [6] turbulence model to predict further detail of the decay phenomena from the exit of a buoyant jet to the far field behavior where the buoyant jet becomes a plume. Further, a new scaling law is used to present the results in a unified way. This new scaling law permits one to observe clearly how a buoyant jet evolves from the exit to the zone of flow establishment and to a non-buoyant region, intermediate region or plume region.

2 Analysis

Fig. 1 depicts a vertical buoyant jet discharging into a uniform environment at rest. U and V, respectively, denote the mean velocity components in the axial, x, and normal, y, directions. The flow is assumed to be steady and of the boundary-layer type (i.e., $U \gg V$, $\partial/\partial y \gg \partial/\partial x$). With Boussineq approximation, the governing equations for velocity and temperature are [6]

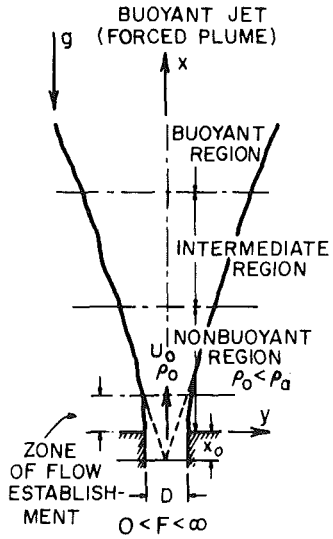

Fig. 1 Zone and regions of buoyant jet

Continuity:

$$\frac{\partial U}{\partial x} + \frac{1}{y^i}\frac{\partial}{\partial y}(y^i V) = 0 \tag{1}$$

Momentum:

$$U\frac{\partial U}{\partial x} + V\frac{\partial U}{\partial y} = \frac{1}{y^i}\frac{\partial}{\partial y}(-y^i \overline{uv}) + \frac{g(T - T_a)}{T_a} \tag{2}$$

Energy:

$$U\frac{\partial T}{\partial x} + V\frac{\partial T}{\partial y} = \frac{1}{y^i}\frac{\partial}{\partial y}(-y^i \overline{vT'}) \tag{3}$$

Here T_a is the local ambient temperature and the superscript i is equal to zero for the plane buoyant jet and to unity for the round buoyant jet. $\overline{uv}$ and $\overline{vT'}$ are, respectively, the turbulent shear stress and heat flux. In order to solve equations (1–3) one must solve the problem by adapting a turbulence model. We will consider here a turbulence model proposed by Chen and Rodi [6] based on Launder's modelling. Briefly, this model is based on closure approximations made in the turbulent transport equations for Reynolds Stresses $\overline{u_i u_j}$, the dissipation rate of turbulent kinetic energy ($k = 1/2\,\overline{u_i u_i}$), $\epsilon = \nu\,\overline{\partial u_i/\partial x_k}\,\partial u_i/\partial x_k$ turbulent heta flux $\overline{u_i T'}$, and the $\overline{T'^2}$. The subscript i and j stand for 1, 2, 3 denoting x, y and z components of fluctuating velocity u_i. In case of the repeated subscripts the Cartesian tensor summation convention applies. The differential equations for $k - \epsilon - \overline{T'^2}$ model under boundary layer approximation are given as [6]

Contributed by the Heat Transfer Division of The American Society of Mechanical Engineers and presented at the AIAA-ASME Thermophysics and Heat Transfer Conference, Palo Alto, Calif., May 24–26, 1978. Revised manuscript received by the Heat Transfer Division July 14, 1978. Paper No. 78-HT-21.

Convection		Diffusion		Production		Dissipation	
$U\frac{\partial k}{\partial x}+V\frac{\partial k}{\partial y}$	=	$\frac{1}{y^i}\frac{\partial}{\partial y}\left(y^i c_k \frac{k\overline{v^2}}{\epsilon}\frac{\partial k}{\partial y}\right)$	−	$\overline{uv}\frac{\partial U}{\partial y}+\frac{\overline{guT'}}{T_a}$	−	ϵ	(4)
$U\frac{\partial \epsilon}{\partial x}+V\frac{\partial \epsilon}{\partial y}$	=	$\frac{1}{y^i}\frac{\partial}{\partial y}\left(y^i c_\epsilon \frac{k\overline{v^2}}{\epsilon}\frac{\partial \epsilon}{\partial y}\right)$	+	$c_{\epsilon 1}\frac{\epsilon}{k}\left(-\overline{uv}\frac{\partial U}{\partial y}+\frac{\overline{guT'}}{T_a}\right)$	−	$c_{\epsilon 2}\frac{\epsilon^2}{k}$	(5)
$U\frac{\partial \overline{T'^2}}{\partial x}+V\frac{\partial \overline{T'^2}}{\partial y}$	=	$\frac{1}{y^i}\frac{\partial}{\partial y}\left(y^i c_T \frac{k^2}{\epsilon}\frac{\partial \overline{T'^2}}{\partial y}\right)$	−	$2\,\overline{VT'}\frac{\partial T}{\partial y}$	−	$c_{T1}\frac{\epsilon \overline{T'^2}}{k}$	(6)

The differential equations for $\overline{u_i u_j}$ and $\overline{u_i T'}$ terms which include $\overline{uv}$ and $\overline{vT'}$ terms in equations (2) and (3) are given by Hossain and Rodi [4]. These equations are further simplified by neglecting, respectively, the convective and diffusive transport terms of $\overline{u_i u_j}$ and $\overline{u_i T'}$. This leads to the following approximated algebraic relation for $\overline{uv}$, $\overline{v^2}$, $\overline{vT'}$

$$-\overline{uv}=\frac{1-c_0\frac{\overline{v^2}}{k}}{c_1}\left(1+\frac{kg\left(\frac{\partial T}{\partial y}\right)}{c_h\,\epsilon\,T_a\left(\frac{\partial U}{\partial y}\right)}\right)\frac{k^2}{\epsilon}\frac{\partial U}{\partial y} \tag{7}$$

$$\overline{v^2}=c_2 k \tag{8}$$

$$-\overline{vT'}=\frac{1}{c_h}\frac{\overline{v^2}}{k}\frac{k^2}{\epsilon}\frac{\partial T}{\partial y} \tag{9}$$

$$\overline{uT'}=\frac{k}{c_h\epsilon}\left[-\overline{uv}\frac{\partial T}{\partial y}-\overline{uT'}\,(1-c_{h1})\frac{\partial U}{\partial y}+\frac{g(1-c_{h1})}{T_a}\overline{T'^2}\right] \tag{10}$$

Equations (1–10) form a closed set as a $k-\epsilon-\overline{T'^2}$ turbulence model containing 11 emperical constants. Unlike the determination of molecular viscosity or thermal conductivity, these constants are determined and calibrated with many turbulent flows and are shown for example, by Hanjalic and Launder [7] to be approximately constants. We adapted the same constant values proposed by Chen and Rodi [6] which are mostly suggested by Launder [2]. They are:

c_0 .55	$c_{\epsilon 1}$ 1.43	c_{T1} 1.25
c_1 2.2	$c_{\epsilon 2}$ 1.92	c_h 3.2
c_2 0.53	c_k 0.225	c_{h1} 0.5
c_ϵ 0.15	c_T 0.13	

We also adapt a correction function as suggested by Chen and Rodi [6] that for the round jet only the right hand side of equation (7) is multiplied by $(1-.465G)$ and $c_{\epsilon 2}$ is multiplied by $(1-0.035G)$ where

$$G=\left|\frac{\Delta y}{2U_\phi}\left(\frac{dU_\phi}{dx}-\left|\frac{dU_\phi}{dx}\right|\right)\right|^{0.2} \tag{11}$$

Here Δy is half jet width and subscript ϕ denotes the centerline value. The above equations are a parabolic system and can be solved by Patankar and Spalding's [8] finite difference program with some modifications to adapt the $k-\epsilon-\overline{T'^2}$ differential equations. We specify boundary conditions at the edge of the buoyant jet.

$$x>0,\quad y\to\infty,\quad T=T_a,\quad U=k=\epsilon=\overline{T'^2}=0 \tag{12}$$

The condition at the exit is assumed to be a flat profile such as a flow passed through a grid screen or

$$x=0,\quad T=T_0,\quad U=U_0$$
$$k=k_0,\quad \epsilon=\epsilon_0 \tag{13}$$
$$\overline{T'^2}=\overline{T'^2_0}$$

The initial kinetic energy k_0 and temperature fluctuation T'^2_0 are given a 5 percent intensity of the mean value U_0^2 and $(T_0-T_a)^2$. The initial dissipation, ϵ_0, is taken to be 2 percent of U_0^3/D where D is the jet exit width when $i=0$ and the diameter when $i=1$.

3 Scaling Law

In general, the data of buoyant jets cannot be correlated into a single curve from the near field where it behaves like a jet to the far field where it behaves like a plume. Recently, Chen and Rodi [9] proposed a universal scaling law and showed that the decay of vertical buoyant jets in a uniform, stagnant environment can indeed be correlated into a single curve beyond the zone of establishment. This scaling law is obtained by reasoning that the local character of a turbulent buoyant jet at some distance from the exit is determined by the initial momentum $M_0=\rho_0 U_0^2 D(\pi D/4)^i$, the initial buoyant strength $W_0=g(\rho_a-\rho_0)U_0 D(\pi D/4)^i$ and the ambient density ρ_a. From the dimensional analysis of these three quantities they obtained the following scaling quantities for length, velocity and buoyant force for plane ($i=0$) and round ($i=1$) buoyant jets

$$x_r=D\mathrm{F}^{2/(3+i)}(\rho_0/\rho_a)^{1/(3+i)} \tag{14}$$

$$U_r=U_0\mathrm{F}^{-(1+i)/(3+i)}(\rho_0/\rho_a)^{1/(3+i)} \tag{15}$$

$$(\rho_a-\rho_r)=(\rho_a-\rho_0)\,\mathrm{F}^{-(1+i)/(3+i)}(\rho_0/\rho_a)^{-(2+i)/(3+i)} \tag{16}$$

A Froude number F is defined as $\rho_0 U_0^2/gD(\rho_a-\rho_0)$.
We shall use these equations to normalize the calculated results to make a comparison between the prediction and experiment.

4 Results and Discussion

Equations (1–10) with boundary and initial conditions are solved on IBM 360. Froude number is varied from 0.1 to 1232. Each flow takes about 3.5 minutes of the computer time to cover a sufficient distance from the exit to the zone of established flow in 600 steps.

Nomenclature

D = diameter or width of buoyant jet
F = Froude number $\rho_0 U_0^2/gD(\rho_a-\rho_0)$
G = correction function see equation (11)
g = gravitational constant
k = turbulent kinetic energy $=\frac{1}{2}\overline{u_i u_i}$
T = mean temperature
$\overline{T'^2}$ = fluctuating temperature
U, V = mean velocity component in x and y direction
$\overline{uv}$ = turbulent shear stress
$\overline{v^2}$ = turbulent normal stress in y direction
x, y = direction along and normal to the buoyant jet axis
$\bar{x}$ = dimensionless quantity $=\frac{x}{x_r}$
x_r = reference length scale
Δy = half jet width where $\mathrm{U}=\frac{1}{2}U_\phi$
ρ = density
$c^*=\left(\frac{\rho_a-\rho_\phi}{\rho_a-\rho_0}\right)$

Subscripts

a = ambient
i, j, k = cartesian tensor notation
0 = exit condition
ϕ = centerline
ρ = density
1 = dimensionless quantity along centerline
r = reference scale from scaling law
u = velocity

Superscripts

i = 0 for plane flows i = 1 for round flows

Gradual changes from the jetlike behavior to the plume-like behavior are calculated. We present here only the decays of center-line value for both plane and round buoyant jets in Figs. 2–9. In presenting the results we shall concentrate on four center-line quantities, namely, velocity, U_ℓ, density, $(\rho_a - \rho_\ell)$, turbulent kinetic energy, k, and dissipation of a turbulent kinetic energy, ϵ.

Plane Buoyant Jets. Figs. 2–5 show the plane buoyant jet behavior. Predicted data are plotted according to the scaling law (14–16) for six different values of Froude number 0.1, 1, 6.3, 39.3, 245.6, 1232. Figs. 2 and 3 show the decay of the center-line velocity and density. It is interesting to observe that except in the zone of flow establishment all data in the zone of established flow fall into a single line. The zone of flow establishment is the zone where the flow undergoes a change from the flat exit profile to a self preserving profile which normally is approximated well by Gaussian distribution function. The fact that all data in the established zone merge into a single curve demonstrates the validity of the universal scaling law derived by Chen and Rodi [9]. We consider now, for example, the calculation for F = 1232 in Figs. 2 and 3. Since the value of the Froude number is large one would expect that the flow at the beginning of the established zone will behave like a nonbuoyant jet. A comparison of the result calculated for all six Froude numbers in the zone of established flow and the decay similarity law for jet [10] shows that the buoyant jet behaves like a jet up to $\bar{x} = 0.5$. Beyond $\bar{x} = 0.5$ the center-line decay starts to deviate from the jet behavior. However the flow does not behave like a plume, until $\bar{x}$ reaches approximately a value of 5. For a plane buoyant jet to become a plane plume ($i = 0$) according to the decay similarity law [10] the centerline velocity U_1 should become constant and the density decay should be proportional to $\bar{x}^{-1}$. From the above observation one may classify the zone of established flow for buoyant jets into three regions, nonbuoyant region ($\bar{x} < .5$), intermediate ($.5 < \bar{x} < 5$), and plume region ($\bar{x} > 5$). Where $\bar{x} = F^{-2/3}(\rho_0/\rho_a)^{-1/3}(\frac{x}{D})$. The predicted value of $\bar{x}$ for the demarcation of three regions agrees with the values suggested by Chen and Rodi [9] from analysis of available experimental data [10]. Froude numbers covered in the experiments are from 1.4 to ∞. From Figs. 2 and 3 we may derive the following theoretical decay laws for flows in the zone of established flow.

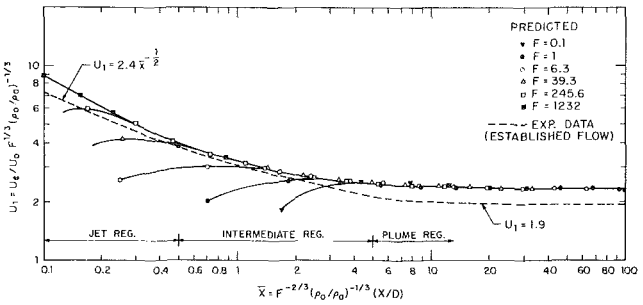

Fig. 2 Centerline velocity in plane buoyant jets

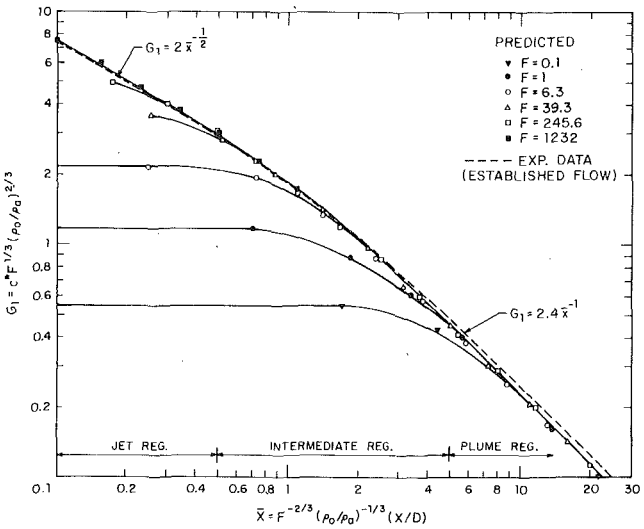

Fig. 3 Centerline density in plane buoyant jets

Nonbuoyant region:

$$U_1 = 2.7\,\bar{x}^{-1/2}, \quad G_1 = 2.15\,\bar{x}^{-1/2}, \quad x \le 0.5 \tag{17}$$

Intermediate region:

$$U_1 = 3.9\,\bar{x}^{-1/3}, \quad G_1 = 1.72\,\bar{x}^{-4/5}, \quad 0.5 \le \bar{x} \le 5 \tag{18}$$

Plume region:

$$U_1 = 2.28, \quad G_1 = 2.15\,\bar{x}^{-1}, \quad 5 \le \bar{x} \tag{19}$$

Here

$$U_1 = \frac{U_\ell}{U_0} F^{1/3}\left(\frac{\rho_0}{\rho_a}\right)^{-1/3}, \quad G_1 = \frac{\rho_a - \rho_\ell}{\rho_a - \rho_0} F^{1/3}\left(\frac{\rho_0}{\rho_a}\right)^{2/3}.$$

We consider now the centerline value of the turbulent kinetic energy k_1 and its dissipation ϵ_1 as shown in Figs. 4 and 5. Here k_1 is the center-line turbulent kinetic energy normalized by U_r^2 and ϵ_1 is the center-line dissipation function divided by U_r^3/x_r. These two quantities are the two fundamental variables characterizing the turbulent behavior of any turbulent buoyant jets. The kinetic energy, k, denotes the energy content of the flow and the dissipation of the kinetic energy, ϵ, controls the growth of turbulent energy. From Figs. 4 and 5 we observe that respectively k_1 and ϵ_1 for all ranges of the Froude number calculated merges into a single curve when the flow becomes established. In the zone of establishment both turbulent kinetic energy and its dissipation function first decay and then increase. After the flow is established both quantities then decay again. The initial decay of k_1 and ϵ_1 in the zone of establishment is due to the fact that the flow at the exit is uniformly flat and is being accelerated by a buoyant force. Under this condition there will be no turbulence generation and the flow decays. As the potential core of this buoyant jet is quickly mixed with the surrounding fluid to form a sharp shear layer, turbulent energy is now produced in the layer and diffused to the centerline. Thus the turbulent kinetic energy in Fig. 4 shows a sharp increase. Experimental data of the turbulent kinetic energy in non-buoyant jet regions given by Bradbury [11] is included in Fig. 4 to show the agreement of the predicted result. No data in plume regions are available. The dissipation function follows with the increase of turbulent kinetic energy to maintain a proper balance as shown in Fig. 5. When the flow becomes established the mixing shear layer flow gradually transforms into a smooth Gaussian-like jet profile and becomes similar. In the jet region both k_1 and ϵ_1 start to decay again.

In the established zone one may perform a similarity transformation analysis, say, one parameter group transformation by Morgan [12] for equations (1–10). For example, one can show that all Reynolds stresses and turbulent kinetic energy of a turbulent plume under present turbulence model possess a decay relation of $\bar{x}^{-2i/3}$ and the dissipation ϵ_1 is proportional to $\bar{x}^{-(1+i)}$. Therefore, we determine from Figs. 4 and 5 the far field behavior for any plane buoyant jets should behave

$$k_1 = 0.44, \qquad \bar{x} > 5$$
$$\epsilon_1 = 1.2\,\bar{x}^{-1}, \quad \bar{x} > 5$$

Round Buoyant Jets. We now examine the predicted results for round buoyant jets. The results are presented in Figs. 6–9. Again all results are normalized by the scaling law (14–16). All figures show the convergence of data into a single curve beyond the zone of flow establishment which is approximately beyond a distance of 10 diameters or widths from the exit. Figs. 6 and 7 give the centerline value of velocity and density showing a gradual change from the nonbuoyant behavior to the plume-like behavior. The demarcation is gradual but one may approximately divide the total zone of established flow into three regions again. Within each region we find the decay of centerline velocity and density approximation as follows:

Nonbuoyant region:

$$U_1 = A_u\bar{x}^{-1} \quad G_1 = A_\rho\bar{x}^{-1} \quad \bar{x} \le 0.5 \tag{21}$$

$$A_u = 7, \quad A_\rho = 5$$

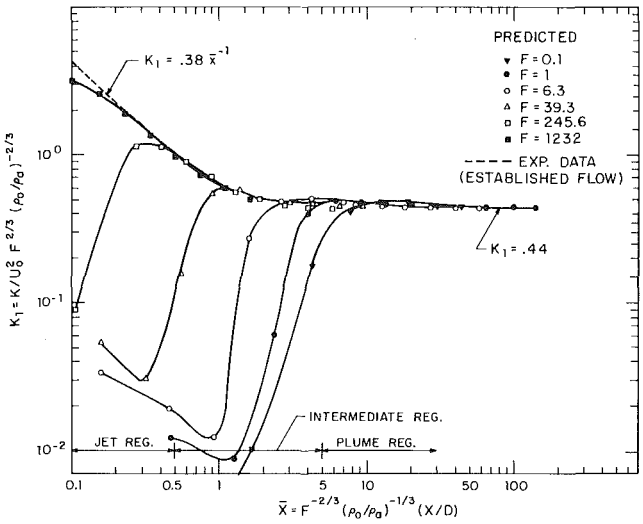

Fig. 4 Centerline turbulent kinetic energy in plane buoyant jets

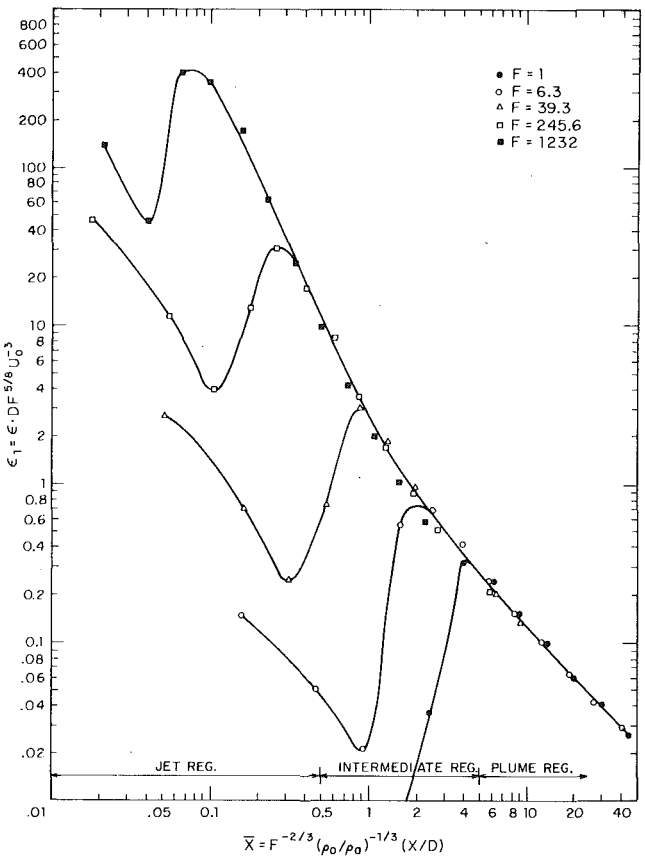

Fig. 5 Centerline dissipation function in plane buoyant jets

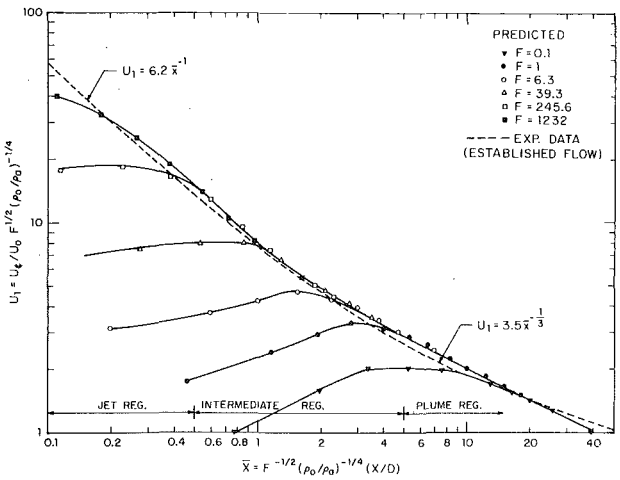

Fig. 6 Centerline velocity in round buoyant jets

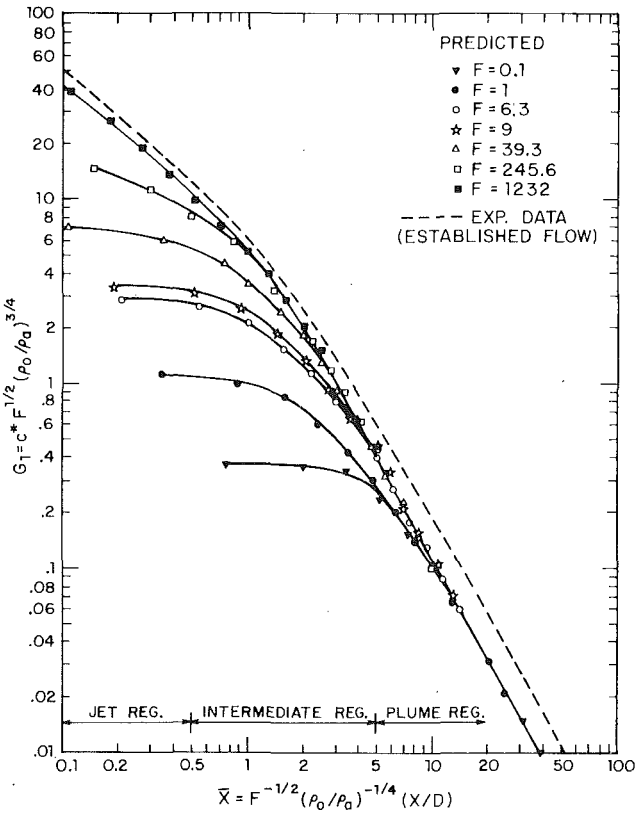

Fig. 7 Centerline density in round buoyant jets

Intermediate region:

$$U_1 = 0.2\,\bar{x}^{-4/5}, \quad G_1 = 4\bar{x}^{-10/7}, \quad 0.5 \le \bar{x} \le 5 \tag{22}$$

Plume region:

$$U_1 = B_u\,\bar{x}^{-1/3}, \quad G_1 = B_\rho\,\bar{x}^{-5/3}, \quad 5 < \bar{x} \tag{23}$$

Here

$$B_u = 4.4, \quad B_\rho = 5.69$$

$$U_1 = \frac{U_\ell}{U_0} F^{1/2} \left(\frac{\rho_0}{\rho_a}\right)^{-1/4},$$

$$G_1 = \frac{(\rho_a - \rho_\ell)}{(\rho_a - \rho_0)} F^{1/2} \left(\frac{\rho_0}{\rho_a}\right)^{3/4}$$

and

$$\bar{x} = \frac{x}{x_r} = F^{-1/2} \left(\frac{\rho_0}{\rho_a}\right)^{-1/4} \left(\frac{x}{D}\right).$$

Comparison of predicted results with experimental data shows in general a fair agreement. The experimental data reviewed by Chen and Rodi [10] gives $A_u = 6.2$, $A_\rho = 5$ for the nonbuoyant region while the present prediction gives $A_u = 7$ and $A_\rho = 5$. For plume region the experimental value based on George's [13] measurement gives $B_u = 3.4$ and $B_\rho = 7.735$. The theoretical prediction gives approximately $B_u = 4.4$ and $B_\rho = 5.69$. The comparison shows the predicted velocity decay constant B_u to fall between the two experimental values while the predicted decay constant B_ρ is below the experimental value.

We now turn to the flow in the zone of flow establishment. First we find from Fig. 6 that the velocity of the round buoyant jets at the beginning is accelerated far more strongly than that in the plane buoyant jets (see Fig. 2). Secondly, for a round buoyant jet to have a nonbuoyant behavior in the near field Froude number should have a value

greater than 245. For buoyant jets with Froude number less that 245 its decay characteristics in the zone of established flow starts with intermediate behavior. For a buoyant jet with Froude number equal or less than one, its characteristic in the entire flow is plume like behavior, as expected, because the buoyant force is dominant.

Turbulent kinetic energy and dissipation function normalized by the scaling law are shown in Figs. 8 and 9 with dimensionless variables $k_1 = k/Ur^2$, $\epsilon_1 = \epsilon x_r/Ur^3$. We find that the axial variation of the turbulent kinetic energy k_1 and the dissipation function, ϵ, all converge to a single curve under the scaling law. The similarity law in the plume region, i.e., far field, for round buoyant jets, gives the turbulent kinetic energy k_1 to be proportional to $\bar{x}^{-2/3}$ and the dissipation ϵ_1 to $\bar{x}^{-2}$. The present analysis predicts that

$$k_1 = 1.5\,\bar{x}^{2/3}, \quad \epsilon_1 = 10.5\,\bar{x}^{-2}, \quad \bar{x} > 5 \tag{24}$$

The experimental data given by Rodi [14] for the nonbuoyant region is also shown in Fig. 6 showing a fair agreement between the predicted results with the experiment. In the zone of establishment, both k_1 and ϵ_1 first decrease and increase again. Then when the buoyant jet flow is established both k_1 and ϵ_1 decay again and eventually behave as given by equation (24). The reason for the decreasing and increasing phenomenon is similar to that of plane buoyant jets in that the positive buoyant force accelerates the flow with an initial flat profile. In this condition there will be no generation of turbulent kinetic energy and hence dissipation function. Therefore, the turbulent kinetic energy k_1 and the dissipation function ϵ_1 first decreases. When the diffusion of the turbulent kinetic energy generated in the mixing layer reaches the center-line both the turbulent kinetic energy and dissipation function increases again. We note from Figs. 3 and 9 that a buoyant jet with a smaller Froude number has a much stronger effect on the magnitude of decrease and increase for both turbulent kinetic energy k_1 and dissipation ϵ_1. However, this phenomenon is shown to persist even for buoyant jets with a larger Froude number of 1232.

5 Conclusion

The decay phenomenon of a buoyant jet from its exit in the zone of flow establishment to the zone of established flow is predicted from a differential $k - \epsilon - T'^2$ turbulence model. The decay of center-line values for velocity, density, turbulent kinetic energy, and the dissipation of turbulent kinetic energy are predicted for Froude number of 0.1 to 1232. The results are normalized with a proper scaling law. The correlation of calculated results for the range of Froude number enables us to subdivide the entire flow into a nonbuoyant, an intermediate, and a plume region. In the zone of flow establishment the theoretical prediction reveals that with a flat initial profile and the acceleration of a flow by the buoyant force the flow in this region has a dampening effect on the turbulent kinetic energy and its dissipation. This effect, although small, persists even at a large Froude number of 1232. The predicted data are compared with the experimental data with fair agreement. The similarity laws are verified. In addition, an approximated but simple equation is devised for each region of a buoyant jet so that the result is ready for application. Unlike other buoyant jet model the present model includes the buoyant effect not only in the mean flow equation but also in the second order correlation equations. The model is shown capable of predicting the buoyant jet flow characteristic from the exit to the far field for a large range of Froude numbers. The model can be applied to other vertical buoyant flows such as buoyant jets in a nonlinearly stratified ambient where integral methods may be difficult to apply.

Since the unified correlation is demonstrated for buoyant jets in the entire zone of established flow, it has more wider applications than the existing correlation which is valid either in the jet region or the plume region.

References

1 Madni, I. K. and Pletcher, R. H., "Prediction of Turbulent Forced Plumes Issuing Vertically into Stratified or Uniform Ambients," ASME JOURNAL OF HEAT TRANSFER, Vol. 99, No. 1, Feb. 1976, p. 99–104.

2 Launder, B. E., "Turbulence Model and Their Experimental Verification," Imperial College, Dept. of Mech. Eng. Report HTS/73/26, 1973.

3 Lumley, J. L., "A Model for Computation of Stratified Turbulent Flows,"

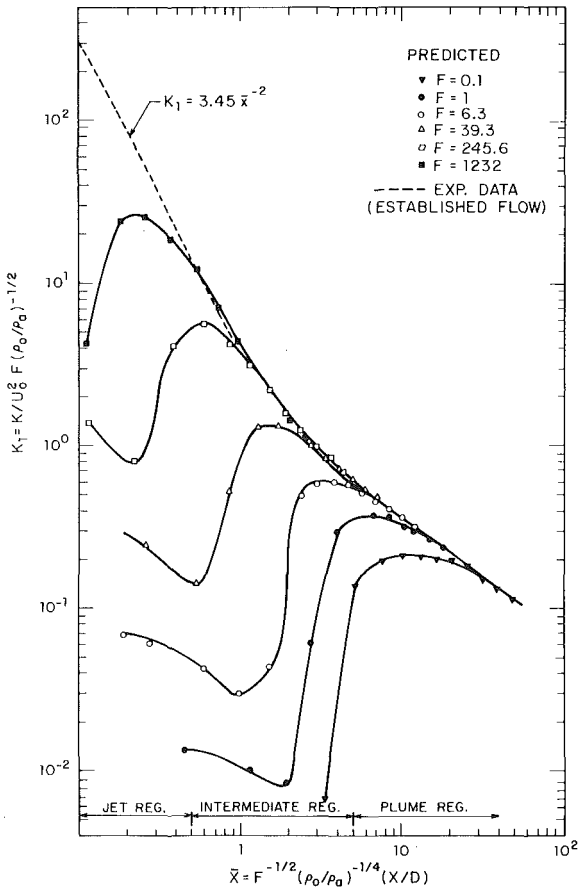

Fig. 8 Centerline turbulent kinetic energy in round buoyant jets

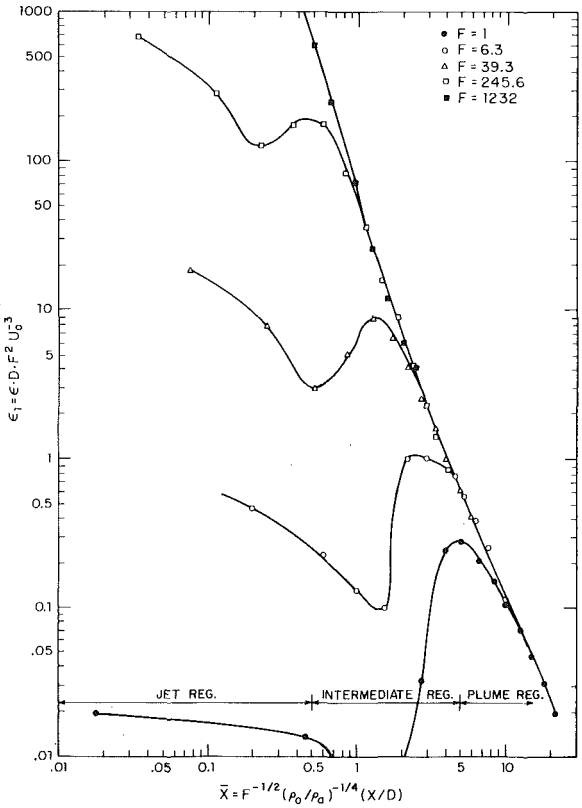

Fig. 9 Centerline dissipation function in round buoyant jets

Int. Symposium on Stratified Flows, Novosibirsk, 1972.

4 Hossain, M. S. and Rodi, W., "Equations for Turbulent Buoyant Flows and Their Modelling," Report SFB 80/T 146, University of Karlsrube, 1974.

5 Gibson, M. M. and Launder, B. E., "On the Calculation of Horizontal Nonequilibrium Turbulent Shear Flows Under Gravitational Influence," ASME JOURNAL OF HEAT TRANSFER, Feb. 1976, p. 81–87.

6 Chen, C. J. and Rodi, W., "A Mathematical Model for Stratified Turbulent Flow and Its Application to Buoyant Jets," 11th IAHR Congress, Sao Paulo, Brazil, 1975.

7 Hanjalic, K. and Launder, B. E., "A Reynolds Stress Model of Turbulence and Its Application to Thin Shear Flows," *J. Fluid Mech.*, Vol. 52, 1972, p. 609–638.

8 Patankar, S. V., and Spalding, D. B., "Heat and Mass Transfer in Boundary Layers," Intext, London, 1970.

9 Chen, C. J. and Roid, W., "On Decay of Vertical Buoyant Jets in Uniform Environment," 6th International Heat Transfer Conference, Toronto, Ontario, Canada, Aug. 7–11, 1978.

10 Chen, C. J. and Rodi, W., *A Review of Experimental Data of Vertical Turbulent Buoyant Jets*, Pergamon Press, 1978; also IIHR Report No. 193, Iowa Institute of Hydraulic Research, Univ. of Iowa, Iowa City, Iowa.

11 Bradbury, L. J. S., "The Structure of Self-Preserving Turbulent Plane Jet," *J. Fluid Mech.*, Vol. 23, 1965, p. 31–64.

12 Morgan, A. J. A., "The Reduction by One of the Number of Independent Variables in Some Systems of Partial Differential Equation," *Quarterly Journal of Mathematics*, Oxford (2), 3, 1952, p. 250–259.

13 George, W. K., Alpert, R. L., and Tamanini, F., "Turbulence Measurements in an Axisymmetric Plume," Factor Mutual Research Rept. No. 22359-2, 1976.

14 Rodi, W., "The Prediction of Free Turbulent Boundary Layer by Use of a 2-Equation Model of Turbulence," Ph.D. Thesis, University of London, 1972.

J. J. Lorenz
P. A. Howard

Argonne National Laboratory
Argonne, Il 60439

Entrainment by a Jet at a Density Interface in a Thermally Stratified Vessel

A study was conducted to determine the thermal behavior and upward movement of the density interface resulting from entrainment by an impinging jet in a thermally stratified vessel. Experiments were performed using a cylindrical vessel with water as the test fluid. The upward movement of the interface was detected by vertical strings of closely spaced thermocouples. As the interface passed a given thermocouple location, the temperature was observed to drop abruptly while oscillating in the process. It was found that vigorous entrainment and mixing maintain a relatively sharp temperature "step" in the impingement region. Using the theory of free submerged jets, a correlation was developed for the rise rate of the interface in terms of the Froude number based on local jet impingement parameters.

Introduction

Nearly all published work on entrainment at density interfaces has dealt with geophysical phenomena in atmospheric and ocean layers, e.g., [1–3]. In these investigations, the entrainment process was artificially driven by mechanical agitation or stirring of one layer. In a recent study, Baines [4] considered the problem of entrainment by a plume, such as one containing industrial pollutants, at a density interface, which may be formed by an atmospheric inversion boundary. Baines experimentally simulated the inversion boundary using layers of fresh and salt water. An analogous problem is that of entrainment by an impinging jet at a density interface in a thermally stratified vessel, see Fig. 1. This situation can occur in many practical instances, such as in the upper plenum of a Liquid Metal Fast Breeder Reactor (LMFBR) during certain transient conditions. The density interface, or hot-cold interface, constitutes a boundary between two distinct regions: a warm (light) quiescent region above and a cooler (heavy) active region below. Entrainment of the warm fluid by the cool impinging jet causes an upward movement of the interface. It is important to predict the behavior of the hot-cold interface since structural components located in the neighborhood of the interface can be adversely affected by thermal discontinuity stresses and cycle fatigue.

The present work considers the thermal behavior and upward movement of a density interface resulting from entrainment by an impinging jet in a thermally stratified vessel. Previous studies shed some light on this problem but, by themselves, are insufficient to provide a complete analysis. In the present study experiments are performed using a cylindrical vessel with water as the test fluid. The upward movement of the interface is detected by vertical strings of closely spaced thermocouples. Using the theory of free submerged jets, a correlation is developed for the rise rate of the interface in terms of local jet impingement parameters.

Analytical Modeling

Based on entrainment studies of jets and plumes at brine interfaces, Baines [4] found that the volumetric entrainment flux can be described in terms of the local Froude number at impingement. Experimental results indicated that Reynolds number was an unimportant parameter. He also found that entrainment was limited to a region about the size of the jet cross section at impingement. Baines correlated entrainment data for jets and plumes with a relatively simple expression, which in a modified form is given as:

$$\frac{Q}{V_j d_j{}^2} = \frac{\pi}{4} a(\mathrm{Fr}_j)^{-b} \tag{1}$$

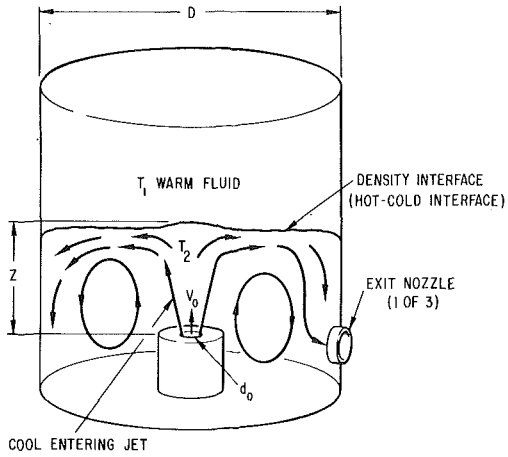

Fig. 1 Density interface in a thermally stratified cylindrical vessel

Equation (1) represents a departure from Baines who employed the centerline velocity $V_{\mathfrak{e}}$, instead of V_j. If, as in the study of Baines, impingement at the density interface occurred at a great distance from inlet (i.e., where the jet velocity profiles are fully developed and similar), the use of $V_{\mathfrak{e}}$ would be appropriate. However in a stratified vessel, impingement may occur within a few diameters of the inlet (i.e., in the region where the jet profiles are developing and non-similar); consequently, an average velocity V_j over the impingement area was deemed necessary. Another departure is in the definition of the Froude number: the modified Froude number, Fr_j, as defined herein is often referred to in the literature as the Richardson number, Ri. Physically, the modified Froude number represents the ratio of buoyant to inertial forces.

It is reasonable to expect that entrainment at a hot-cold interface in a stratified vessel can be described by a relation similar to equation (1). An important requirement is that the vessel cross section be large compared to the jet cross section at impingement; otherwise the entrainment process may be influenced by the vessel walls.

For the case of a cylindrical vessel, the volumetric entrainment flux, Q, is related to the interfacial rise rate, $\epsilon = dZ/dt$, as follows:

$$Q = \frac{\pi D^2}{4} \epsilon \tag{2}$$

Equations (1) and (2) can be combined to yield:

$$\frac{\epsilon}{V_j}\left(\frac{D}{d_j}\right)^2 = a(\mathrm{Fr}_j)^{-b} \tag{3}$$

Equation (3) will provide the basis for correlating the data of the present study. When applying the results to cases where the vessel cross section is non-cylindrical, it is necessary to obtain Q from equation (1) and relate this to the rise rate, ϵ, by the appropriate geometrical expression.

Contributed by the Heat Transfer division of THE AMERICAN SOCIETY OF MECHANICAL ENGINEERS and presented at the AIChE/ASME Heat Transfer Conference, Salt Lake City, Utah, August 15–17, 1977. Revised manuscript received by the Heat Transfer Division September 20, 1979. Paper No. 77-HT-23.

The value of d_j and V_j required in equation (3) can readily be determined from the theory of free submerged jets. It will be shown that the values of d_j and V_j are uniquely determined for given values of d_0, V_0, and Z. Albertson, et al. [5] give the following expressions for the velocity profiles of free submerged turbulent jets: (refer to Fig. 2)

Zone of Flow Establishment $(0 \le Z \le Z_0)$

$$\frac{V_{rz}}{V_0} = \exp\left[-\frac{(r + C_1 Z - d_0/2)^2}{2(C_1 Z)^2}\right], \text{ for } r > d_c/2 \tag{4}$$

and

$$\frac{V_{rz}}{V_0} = 1, \text{ for } r \le d_c/2 \tag{5}$$

where

$$\frac{d_c}{d_0} = 1 - Z/Z_0 \text{ and } \frac{Z_0}{d_0} = \frac{1}{2C_1}$$

Zone of Established Flow $(Z_0 < Z)$

$$\frac{V_{rz}}{V_\ell} = \exp\left[-\frac{1}{2(C_2)^2}\left(\frac{r}{Z}\right)^2\right] \tag{6}$$

where

$$V_\ell = \frac{V_0 d_0}{2C_2 Z} \tag{7}$$

Albertson, et al. [5] recommended a value of $C_1 = 0.111$ within the zone of flow establishment and $C_2 = 0.083$ within the zone of established flow. In most cases considered in this study, impingement occurred within the zone of flow establishment. For a limited number of cases, impingement occurred just a short distance within the zone of established flow. In view of this and to avoid a discontinuity within the transition region, it was decided to let $C_2 = C_1 = 0.111$.

Let the effective jet diameter, d_j, be defined as the locus of points where the local jet velocity is a specified fraction, ζ, of the maximum velocity; i.e., $\zeta = V_{rz}/V_0$ in the zone of flow establishment and $\zeta = V_{rz}/V_\ell$ in the zone of established flow. Also let the average jet velocity over d_j be defined as follows:

$$V_j = \frac{4}{\pi d_j^2}\int_0^{d_j/2} 2\pi r V_{rz}\, dr \tag{8}$$

Employing the foregoing definitions in conjunction with equations (4–7), the following equations are obtained for d_j and V_j:

Zone of Flow Establishment $(0 \le Z \le Z_0)$

$$\frac{d_j}{d_0} = 2\alpha(Z/d_0) + 1 \tag{9}$$

and

$$\frac{V_j}{V_0} = 2\left[(Z/d_0)^2 C_1^2\left(\frac{3}{2} - e^{-\beta^2} - \frac{\sqrt{2\pi}}{2}\operatorname{erf}\beta\right) + \frac{C_1}{2}(Z/d_0)\left(-1 + \frac{\sqrt{2\pi}}{2}\operatorname{erf}\beta\right) + \frac{1}{8}\right] \times \left[\alpha(Z/d_0) + \frac{1}{2}\right]^{-2} \tag{10}$$

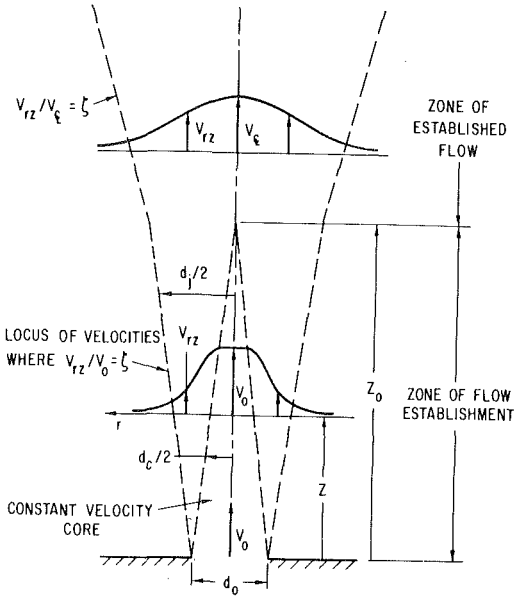

Fig. 2 Sketch of free submerged jet

where

$$\alpha = C_1[(-2\ln\zeta)^{1/2} - 1] \text{ and } \beta = \frac{1}{\sqrt{2}}(-2\ln\zeta)^{1/2}$$

Zone of Established Flow $(Z_0 < Z)$

$$\frac{d_j}{d_0} = 2(-2C_2^2\ln\zeta)^{1/2}(Z/d_0) \tag{11}$$

and

$$\frac{V_j}{V_0} = \frac{1}{(Z/d_0)2C_2}\left(\frac{\zeta - 1}{\ln\zeta}\right) \tag{12}$$

Equations (9–12) provide the effective jet diameter, d_j, and velocity, V_j, as functions of d_0, V_0, Z, and ζ. The value of ζ will be chosen to provide the best correlation of the data. When calculating d_j and V_j for use in equation (3), the value of Z is taken as the instantaneous coordinate of the density interface. The values of d_j and V_j obtained thereby are, of course, not exact because in reality the jet profile is influenced by the presence of the interface.

Experimental Apparatus and Procedure

Fig. 3 shows the basic cylindrical test section. The principal geometric variable was the inlet diameter, d_0, which could readily be changed by adding inserts of the desired diameter. Temperatures were recorded by two vertical strings of thermocouples: one located along the vessel centerline and the other 12.7 cm radially outward. With this configuration the hot-cold interface could easily be detected as it advanced upward. A total of 45 thermocouples were employed, only a small portion of which are shown in Fig. 3. The thermocouples were bare chromel-constantan (0.25 mm wire) couples with a response time of 10 μs.

Referring to Fig. 4, the test procedure was as follows: Initially warm water at T_1 was pumped through the test section from the primary

Nomenclature

a, b = constants in equation (1)
D = vessel diameter, cm
d_c = diameter of constant velocity jet core, cm
d_j = effective jet diameter at impingement, cm
d_0 = inlet diameter, cm
Fr_j = modified Froude number, $\Delta\rho d_j g/\rho V_j^2$
g = gravitational acceleration, m/s^2
Pe = Peclet number, $V_j d_j/\alpha$
Q = volumetric entrainment flux at interface, m^3/s
r = radial jet coordinate, cm
Re = Reynolds number, $V_j d_j/\nu$
T_1 = temperature above interface, °C
T_2 = temperature below interface, °C
V_j = average jet velocity at impingement, m/s
V_0 = inlet jet velocity, m/s
V_{rz} = local jet velocity, m/s
Z = vertical coordinate of interface, cm
α = diffusivity of heat, m^2/s
ϵ = rise rate of interface (dZ/dt), m/s
ζ = fraction of maximum jet velocity
ν = kinematic viscosity, m^2/s
ρ = fluid density, kg/m^3
$\Delta\rho/\rho$ = fractional density difference across interface based on $(T_1 - T_2)$

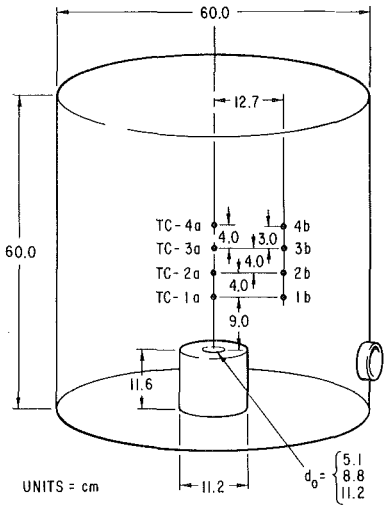

Fig. 3 Test section geometry and thermocouple locations

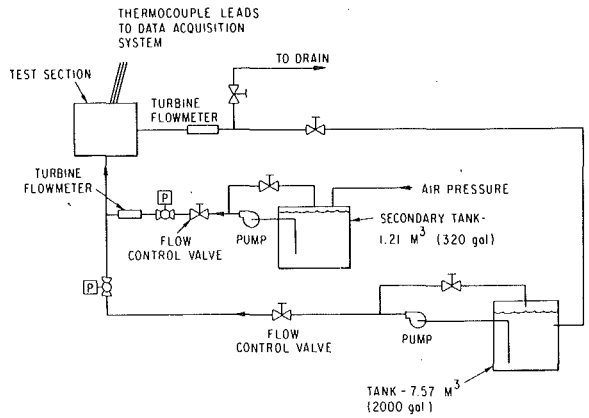

Fig. 4 Schematic of water flow loop

tank (7.57 m^3). When steady state conditions were established, the warm water supply was shut off and cool water at T_2, and the desired flowrate, introduced from the secondary tank (1.21 m^3). Subsequently the inlet temperature, T_2 and flowrate were held constant at these values for the duration of the run. Data taking was initiated when a well defined interface was visually observed. The run was terminated when the hot-cold interface advanced a sufficient distance to obtain meaningful rise rate data. A total of 20 runs were conducted, encompassing a sufficiently wide range of temperature differences ($T_1 - T_2$), flowrates, and orifice diameters to cover all cases of practical interest. The following ranges were covered: flowrates = 0.11 kg/s to 1.26 kg/s; ($T_1 - T_2$) = 11.1°C to 33.3°C; and d_0 = 5.1 cm, 8.8 cm, and 11.2 cm. These conditions yielded Froude numbers in the range 1.5 to 42 and Reynolds numbers in the range 3000 to 15,000.

Each channel of data was recorded at 50 samples/s by an HP 2112 minicomputer and permanently stored on magnetic tape. Measured temperatures were accurate to ±0.55°C and flowrates to ±2 percent (of reading).

Results and Discussion

Flow visualization tests revealed that the incoming jet of fluid impinges on the density interface, forming a slight bulge, and then spreads radially outward along the interface. In most cases the bulge was small, and the "nominal" interface appeared remarkably flat over the entire vessel cross section. The interface appeared to be a wavy unsteady boundary with bursts of fluid penetrating above and below the nominal interface. Periodically, large eddies of cooler fluid would engulf and entrain warmer stagnant fluid above, which resulted in an upward movement of the interface. The temperature gradient at the interface remained fairly sharp because the warmer fluid was engulfed and rapidly incorporated by turbulent mixing into the cooler region. Entrainment occurred primarily in the region of the impingement where relatively large waves and eddies were observed. At positions further removed from the vessel centerline, interfacial unsteadiness was relatively small. These observations are consistent with those of Baines [4].

Fig. 5 shows the temperature response as the interface advances upward. The data were obtained for the following conditions: inlet flowrate = 0.39 kg/s; T_1 = 54.4°C; T_2 = 24°C; d_0 = 8.8 cm. It is interesting to observe that the temperature at given thermocouple locations remains constant at T_1 = 54.4°C until the influence of the advancing interface is felt. As the interface passes a particular thermocouple location, the temperature drops abruptly from T_1 = 54.4°F to T_2 = 24°C while oscillating during the process. These oscillations are clear evidence of wave motion and turbulent eddies at interface. Since temperature fluctuations can produce thermal fatigue damage, these oscillations may have an important impact on the design of structural components. The vigorous entrainment and mixing maintain a relatively sharp interfacial temperature "step" in the impingement region, Fig. 5(a). At locations further outward from the vessel centerline, reduced turbulence and possible molecular effects cause a more gradual temperature decay, Fig. 5(b).

A close-up of the temperature response at TC-2a is plotted in Fig. 6. While the interface is approaching TC-2a, pulses of cool fluid are felt from t = 4.9 minutes to t = 5.45 min. These cool pulses are produced by crests of interfacial waves and by eddies of cool fluid penetrating above the nominal interface. From t = 5.45 minutes to t = 6.2 minutes, the interface is advancing beyond TC-2a and the reverse occurs. Warm pulses are produced by valleys of interfacial waves and by entrainment of warm fluid "packets". For $t > 6.2$ minutes the jet has advanced sufficiently far beyond TC-2a that thermal pulses are no longer felt. The effective "thickness" of the density interface was estimated to be about 1 cm.

Fig. 7 shows a plot of interfacial position versus time, constructed from the data of Fig. 5(a) along with data at additional locations which were not plotted in Fig. 5(a). The time at which the interface reached a given thermocouple location was defined as the instant when the first abrupt temperature response was observed. Since the response at locations along the centerline was relatively sharp and well defined, the data of Fig. 5(a) was used in preference to that of Fig. 5(b). In principle, the height of the bulge in the impingement region could be determined by the difference between the interfacial position as determined from the thermocouple string at the vessel centerline and the one further outward. However, under most conditions, the height of the bulge was too small to permit meaningful measurements. In Fig. 7 it can be seen that the rise rate is not constant, but decreases with time. This is due to spreading of the jet with increasing distance from the inlet, causing the average jet velocity at impingement to decrease; consequently the degree of entrainment (and hence the rise rate) is correspondingly reduced. The instantaneous rise rate, $\epsilon = dZ/dt$, of the interface at a given position, Z, is given by the local derivative of the position versus time curve. For each of the 20 runs in this study, a position-time curve was constructed. From each curve, rise rates were determined at two or three different Z values. In several of the runs with d_0 = 11.2 cm the position-time curve was constructed from a visual determination rather than from the thermocouples.

The experimental data obtained in the study was used in conjunction with equations (3, 9–12) to develop a correlation for the rise rate of the hot-cold interface. Employing equations (9–12), values of d_j/d_0 and V_j/V_0 are calculated for a given Z. In all but a couple of cases, the Z values fell within the zone of flow establishment; therefore, equations (9) and (10) were used predominantly. The local Froude number, Fr_j, is readily calculated, along with the quantity on the left-hand side of equation (3). Fig. 8 is a log-log plot of the data for all runs conducted in this study. Although exhibiting some scatter, the data are reasonably well correlated by equation (3) with a = 0.8 and b = 1.1. (A similar degree of scatter was apparent in the results of Baines [4].) For this correlation, a value of ζ = 0.15 was employed. Other values in the range $0.1 < \zeta < 0.5$ were tried but ζ = 0.15 provided the best correlation of the data. The scatter of the data in Fig. 8 is more than would be expected on the basis of experimental uncertainty alone and perhaps reflects a Peclet number dependence not included in the

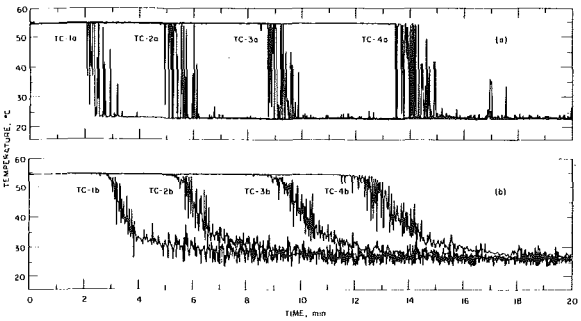

Fig. 5 Temperature response: a) TC locations along vessel centerline; and b) TC locations 12.7 cm radially outward

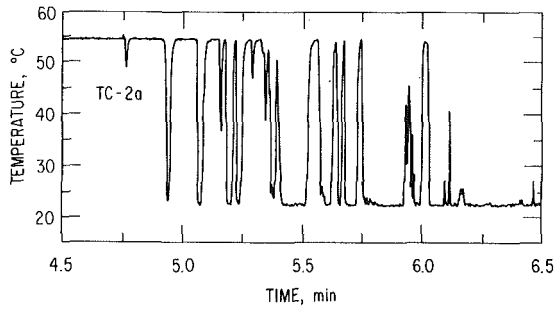

Fig. 6 Close-up of temperature response at TC-2a along vessel centerline

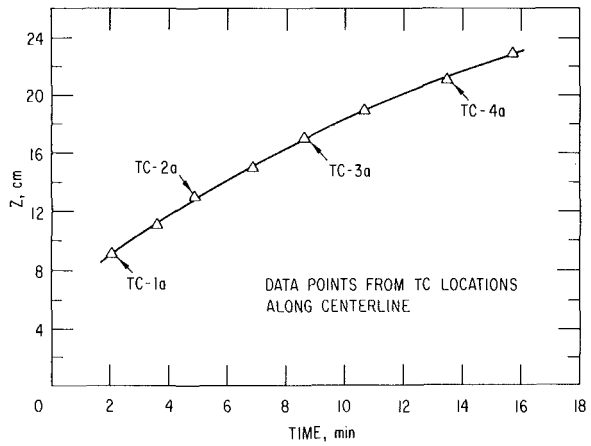

Fig. 7 Position of density interface versus time

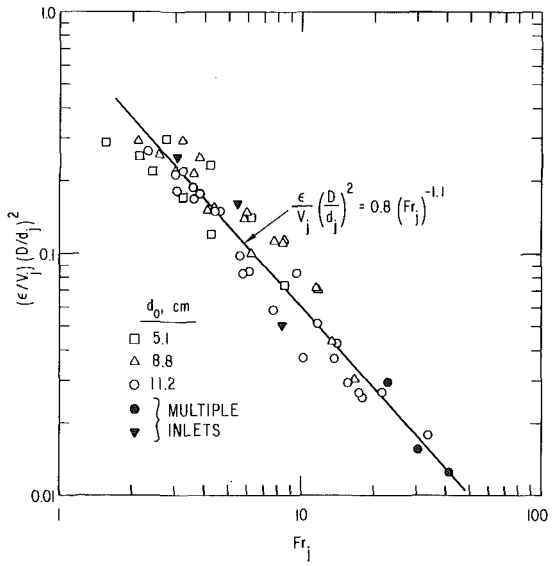

Fig. 8 Correlation of rise rate data

modelling. Further remarks concerning this possibility will be given shortly. The results of the present study should be applicable to other fluids, besides water, over the same range of Froude numbers, i.e., $1.5 < Fr_j < 42$. Also the requirement that D be large compared to d_j does not appear to be as important as expected initially. In some of the runs, the jet diameter was nearly 30 percent of the vessel diameter. Nevertheless caution should be exercised when applying the present model to situations where d_j/D is significantly greater than 0.3.

The present correlation for interfacial rise rate can be applied to vessels having a more complicated inlet geometry than shown in Fig. 1. A number of runs were conducted with the fluid entering the vessel via a cluster of smaller tubes rather than via a single large tube. The cluster of smaller tubes could possibly represent the exit region of a reactor core. In applying the present correlation to this geometry, a single effective inlet diameter was defined such as to circumscribe the entire cluster of tubes. The flow issuing from these multiple inlets was assumed to be spread uniformly over the effective inlet diameter. As shown in Fig. 8, the data for cases with multiple inlets are adequately correlated.

It is interesting to compare the results of the present study with those of Baines [4]. Baines correlated his data for jets and plumes in terms of the centerline velocity, V_ℓ, and with $\zeta = 0.368$; consequently to facilitate comparison it was necessary to perform a conversion into the parameters of the present study. The data of Baines fell entirely within the zone of the established flow; thus only equations (7, 11), and (12) were required for the transformation. This conversion procedure is only approximate since the exact form of the velocity profiles at impingement employed by Baines may be slightly different from the profiles used herein. Applying this conversion procedure to the best-fit of Baines' data yielded values of $a = 0.93$ and $b = 1.5$ in equation (3). Thus the results of Baines and of the present study indicate that entrainment is proportional to $(Fr_j)^{-1.5}$ and $(Fr_j)^{-1.1}$, respectively. At relatively small values of Fr_j, both correlations agree fairly well; but for larger Fr_j, the correlation of Baines falls below that of the present study. This observation is significant because density differences were produced by salt in the work of Baines and by temperatures in the present study. Variances in the results of these two studies suggest that molecular effects may play an important role in the entrainment process.

Turner [1] observed similar variances for entrainment at density interfaces created by salinity and temperature differences. He found that entrainment was proportional to $(Fr_j)^{-1.5}$ and $(Fr_j)^{-1}$ for salinity and temperature, respectively. In his work the agitation was produced by stirring rather than impingement by a jet. Although the mechanism responsible for the difference is not well understood, one explanation offered by Turner is that entrainment at temperature interfaces is increased relative to that at brine interface due to the more rapid incorporation of entrained fluid into its surroundings by diffusion. This latter observation recognizes the fact that the diffusivity of heat is greater than the diffusivity of mass. Turner's work suggests that the parameter Fr_jPe may be important in determining entrainment at a density interface. This quantity expresses a balance between buoyancy, which tends to return a fluid element to the interface, and diffusion, which causes the element to merge with the turbulent region. An attempt was made to correlate the data of the present study using Fr_jPe in conjunction with Fr_j. With these two parameters it was found that certain subsets of data correlated better than with Fr_j alone, but other subsets did not correlate as well. On the basis of the limited amount of data obtained in the present study, the importance of Fr_jPe could neither be confirmed nor denied. It is evident that a broader data base will be required to adequately assess molecular effects.

Further evidence of molecular effects was observed with liquid metals. A limited number of tests with liquid sodium were performed in the present study to compare the behavior of the hot-cold interface. It was found that the temperature step across the interface was more abrupt in water than in sodium. Apparently the high thermal conductivity of sodium tends to "smear" the temperature gradient. Furthermore, this smearing was found to lessen the magnitude of thermal oscillations at the interface.

Conclusions

Flow visualization tests revealed considerable wave motion and unsteadiness at the density interface. In addition the nominal interface was found to be remarkably flat over the entire vessel cross section.

The density interface moves upward as a result of entrainment by the impinging jet. As the interface passed a given thermocouple location, the temperature dropped abruptly while oscillating in the process. Vigorous entrainment and mixing maintain a relatively sharp interfacial temperature step in the impingement region. At locations further outward from the vessel centerline, reduced turbulence lessens the gradient.

Molecular effects may play an important role as suggested by the fact that entrainment at temperature interfaces is greater than entrainment at brine interfaces. Molecular effects were also observed with liquid metals.

A correlation was developed for the rise rate of the interface in terms of the Froude number based on local jet impingement parameters. This correlation has important practical application such as in predicting the behavior of the density interface in a stratified LMFBR upper plenum.

Acknowledgments

The authors are indebted to R. A. Morris for assisting in the operation of the facility and to J. Tomac for programming associated with the data acquisition system.

All work was conducted under funding provided by the U.S. Department of Energy.

References

1 Turner, J. S., *Buoyancy Effects in Fluids,* Cambridge University Press 1973, pp. 288–299.

2 Rouse, H. and Dodu, J., "Turbulent Diffusion Across a Density Discontinuity," La Houille Blanche, 1955, 10, pp. 522–32.

3 Turner, J. S., "The Influence of Molecular Diffusivity on Turbulent Entrainment Across a Density Interface," *J. Fluid Mech.,* 1968, 33, pp. 639–656.

4 Baines, W. D., "Entrainment by a Plume or Jet at a Density Interface," *J. Fluid Mech,* 1975, 68, pp. 309–320.

5 Albertson, M. L., Dai, Y. B., Jensen, R. A., and Rouse, H., "Diffusion of Submerged Jets," *Proceedings ASCE,* Paper No. 2409, 1948.

Dr. F. W. Holm
Assoc. Professor.

Dr. S. P. Goplen
Instructor.

Texas A&M University,
Department of Mechanical Engineering,
College Station, TX 77843

Heat Transfer in the Meniscus Thin-Film Transition Region

Capillary surface wetting is a passive phenomenon that depends on free surface energies. As heat transfer rates increase, within limits, more liquid flows onto the surface and evaporates. The differential equations describing mass and heat transfer mechanisms have been solved simultaneously for several capillary groove configurations. Further, by methods outlined in this paper, the effects of solid-liquid-vapor interline heat transfer phenomena can be isolated and evaluated. Not only does this provide a method for predicting surface heat transfer coefficients for surfaces wetted through capillary grooves, it also provides basic information about heat transfer in the vicinity of the meniscus attachment region.

Introduction

Very high heat transfer rates have been observed near a triple interline, the junction of the vapor, the evaporating thin film, and the non-evaporating adsorbed thin film [5, 9, 13]. Dropwise condensation, as an example, exhibits surface heat transfer coefficients that are approximately one order of magnitude greater than the coefficients resulting from film condensation.

The formation of interlines in dropwise condensation is a useful means of augmenting heat transfer, however in practice, the extent of interline dispersion at any time is not easily controlled or predicted. Maximizing the heat transfer associated with this phenomena is difficult unless some control over formation of the interlines is achieved.

The use of capillary grooves partially filled with a liquid as a means of forming the triple interline region achieves this objective since the number and length of the interlines can easily be controlled by the number and length of the grooves. The heat transfer is augmented by the flow of the liquid into the groove under the action of capillary forces, a passive process.

The use of capillary grooves for augmenting heat transfer introduces a number of factors to investigate. The portion of the meniscus on the groove wall that constitutes the meniscus attachment region must be identified and the effectiveness of this region for enhancing heat transfer must be analyzed. In addition, it is expected that the rest of the meniscus will also serve to enhance heat transfer and its role in the overall heat transfer process must be determined. The primary flow up the meniscus forms a hydrodynamic problem that is coupled with the heat transfer problem.

Because of the small physical dimensions associated with a meniscus, any probes to measure temperature gradients, flow velocities, liquid pressures, and liquid film thickness essentially destroy the flow field. Consequently, experimental information on any of the local characteristics of the meniscus, especially near the interline region, are extremely difficult to obtain and only overall characteristics are detectable.

In this paper we intend to show that the local characteristics of the combined heat and mass transfer process can be deduced from overall characteristics such as:

- total heat transferred from a grooved plate,
- overall temperature drops (top-to-bottom) in the walls separating the grooves,
- the temperature difference between the top of the wall and the surrounding vapor.

By decreasing the width of the walls and thereby forcing an increase in the temperature gradients in the wall, the three overall characteristics listed above can be controlled in a systematic manner. Further, by restricting the thermal conduction path to the triple interline, we are able to deduce basic information about local heat and mass transfer mechanisms. The main contribution provided in this paper is an approximate method for predicting and verifying the heat transfer in the vicinity of the meniscus thin-film transition region.

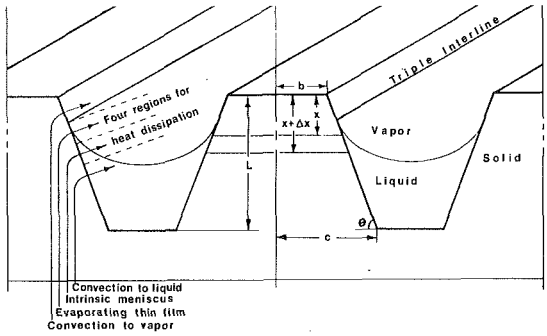

Fig. 1 Liquid-filled capillary grooves on a plate

Analysis

The analytical model developed in this paper is intended to represent capillary grooves machined on a metal plate as shown in Fig. 1. The groove dimensions are small so capillary forces will cause the primary flow of liquid along the groove, partially filling each groove. A meniscus is formeed extending up each side of the groove. As the plate is heated, heat travels by conduction in a direction transverse to primary flow and up the groove walls to be dissipated by evaporation. A secondary liquid flow up the groove wall surface occurs and supplies liquid to the extended meniscus, replacing that lost by evaporation.

The extended meniscus formed on the heated wall is characterized by three regions:

1) *Equilibrium Thin Film Region*—formed at the upper extent of the extended meniscus. In this region the short range adhesion forces prevent evaporation and there is no heat transfer from the wall.

2) *Evaporating Thin Film Region*—formed just below the equilibrium thin film. The film thickness in this region has increased and the adhesion forces are diminished causing evaporation and heat transfer. The disjoining pressure gradient is the forcing function for the secondary flow in this region.

3) *Intrinsic Meniscus Region*—formed at the bottom of the extended meniscus. In this region the thin film adhesion forces produce a negligible effect on the evaporation rate. The film thickness is sufficiently large to introduce significant increases in thermal resistance due to conduction. The decrease in the surface curvature provides the forcing function for the secondary flow.

The heat conducted up the solid walls is dissipated in four ways (see Fig. 1): convection to the liquid below the intrinsic meniscus region, heat conduction through the intrinsic meniscus to the liquid-vapor interface where evaporation takes place, evaporation of the liquid in the evaporating thin film portion of the extended meniscus, and convection to the vapor above the extended meniscus region.

The heat transfer is influenced both by the adhesion forces and the film thickness. At the top of the evaporating film region where the

Contributed by the Heat Transfer Division for publication in the JOURNAL OF HEAT TRANSFER. Manuscript received by the Heat Transfer Division July 21, 1978.

adhesion forces are large the heat transfer is small. As the film thickness increases, the adhesion forces decrease and the heat transfer increases to a maximum at the base of the evaporating film. The heat transfer then decreases, due to the conduction resistance, as the film thickness increases towards the base of the extended meniscus. The transition region between the evaporating film and the intrinsic meniscus, where the maximum heat transfer occurs, is sometimes referred to as the triple interline region.

The Conduction in the Wall. The configuration and the dimensions of the wall and the adjacent liquid layer are shown in Fig. 1. A one-dimensional temperature distribution is assumed for conduction calculations inside the wall. In support of this assumption, our calculations indicate that more than 80 percent of the total heat dissipation occurs in a region that is 0.005 in. (0.127 mm) to 0.006 in. (0.152 mm) high in the meniscus thin-film transition region. The Biot number for this region is 0.08 for a wall thickness (c) of 0.008 in. (0.203 mm) and decreases linearly with wall thickness. Heat transfer in the direction of the groove is neglected and steady state conditions are assumed.

A heat balance, written for an element in the wall of thickness Δx (Fig. 1) takes the form

$$Q_{x+\Delta x} = Q_x + Q_{\mathrm{DIS}} \tag{1}$$

where Q_x and $Q_{x+\Delta x}$ are the heat transfer rates across the x and $x + \Delta x$ surfaces respectively and Q_{DIS} is the heat transfer rate from the wall to the liquid. Combining this heat balance with Fourier's conduction equation leads to

$$Q_{\mathrm{DIS}} + \frac{d}{dx}\left[KA(x)\frac{dT(x)}{dx}\right]\Delta x = 0 \tag{2}$$

where K is the conduction coefficient for the wall, $T(x)$ is the wall temperature, and $A(x)$ is the horizontal cross-sectional area. Substituting the expression $A(x) = 2(b + x \cot\theta)$, into equation (2) and rearranging gives

$$(b + x\cot\theta)\frac{d^2T(x)}{dx^2} + \cot\theta\frac{dT(x)}{dx} = \frac{Q_{\mathrm{DIS}}}{2K\Delta x}. \tag{3}$$

This is the basic conduction equation for the wall and the form of Q_{DIS} depends on which of the heat dissipation regions along the wall is being considered.

The Evaporating Film Region. The evaporating liquid film region is a very thin layer partially adsorbed onto the wall, thus the temperature of the liquid-vapor interface, T_{1v}, is assumed to be the same as that of the wall and is higher than the temperature of the surrounding vapor, T_v. The saturation pressure, $P_{v1v}{}^0$, corresponding to the temperature T_{1v} is higher than the surrounding vapor pressure, P_v, and evaporation would be expected. However, in the equilibrium film the adhesion forces reduce the saturation pressure to a value in equilibrium with the vapor pressure and evaporation does not occur. The adhesion forces also reduce the saturation pressure P_{v1v} in the evaporating film region to a value in the range $P_v < P_{v1v} \leq P_{v1v}{}^0$. Therefore, evaporation can occur but at a reduced rate compared to that for a thick film where the saturation pressure would be $P_{v1v}{}^0$. The effects of the adhesion forces are represented as a negative pressure called the "disjoining pressure" denoted by P_d. This disjoining pressure for water, polar fluid, has been characterized for a two-dimensional extended meniscus [9] by the equation

$$P_d = \rho_1 R T_{1v} \ln(P_{v1v}/P_{v1v}{}^0), \tag{4}$$

where ρ_1 is the liquid density, R is the gas constant, P_{v1v} is the reduced saturation pressure of the film, and $P_{v1v}{}^0$ is the saturation pressure corresponding to T_{1v}.

In the thin film region, P_{v1v} is always less than $P_{v1v}{}^0$ and it is evident that equation (4) yields a negative value for P_d. For later calculations it is convenient to rewrite equation (4) as

$$P_{v1v} = P_{v1v}{}^0 \exp[P_d/\rho_1 R T_{1v}]. \tag{5}$$

Deryagin and Zorin [11] have experimentally studied adsorption pressures as a function of film thickness. It is possible, from their work, to express P_{v1v} as a function of film thickness in the form

$$P_{v1v}/P_{v1v}{}^0 = at^b, \tag{6}$$

where t is the film thickness and a and b are constants. Combining equations (4) and (6) gives

$$P_d = \rho_1 R T_{1v} \ln(at^b), \tag{7}$$

where P_d goes to zero as the quantity (at^b) approaches one.

At the base of the equilibrium film there is no evaporation since $P_{v1v} = P_v$ and the disjoining pressure at this point, $P_d{}^0$, is given by

$$P_d{}^0 = \rho_1 R T_c 1v \ln(P_v/P_{v1v}{}^0). \tag{8}$$

The film thickness at the point, t^0, can also be found using the equation

$$t^0 = (P_v/aP_{v1v}{}^0)^{1/b}. \tag{9}$$

As the evaporating film increases in thickness, P_d increases from $P_d{}^0$ to zero. This allows the reduced saturation pressure, P_{v1v}, to increase from P_v to $P_{v1v}{}^0$ and the pressure difference $(P_{v1v} - P_v)$, which causes the evaporation, increases from zero to a maximum value $(P_{v1v}{}^0 - P_v)$.

The heat transfer mechanism for the evaporating film region is represented by a modified form of the equation presented by Sukhatme and Rohsenow [12]

$$\tilde{Q} = \left(\frac{2\sigma_a H}{2-\sigma_a}\right)\left(\frac{g_c}{2\pi R\overline{T}}\right)^{1/2}(P_{v1v} - P_v), \tag{10}$$

where $\tilde{Q}$ is the heat flux, σ_a is the accommodation coefficient, H is the enthalpy of evaporation, g_c is the gravitational constant, and $\overline{T} = 1/2(T_v + T_{1v})$.

Neglecting the effects of the small change in T_{1v} on the heat transfer, it appears that $\tilde{Q}$ depends primarily upon the difference $(P_{v1v} - P_v)$. Thus in the evaporating film, the heat transfer is zero at the top and increases to a maximum at the base of the film.

The heat transfer rate, Q_{DIS}, in equation (3) can be found from the heat flux $\tilde{Q}$. The area on one side of the wall for a given heat flux value is Δy per unit length of wall, where $\Delta y = \Delta x/\sin\theta$. Thus $Q_{\mathrm{DIS}} = 2Q\Delta y$ for each unit length of wall.

The mass of the liquid evaporated by this heat transfer is given as

$$M_{ev} = Q\Delta y/H \tag{11}$$

where M_{ev} is the mass rate of evaporation of the liquid. The mass flow rate, M_i, of the fluix flowing into a region of the film is found from the mass balance

$$M_i = M_{ev} + M_0 \tag{12}$$

where M_0 is the mass flow rate of the liquid flowing out of the region into the region above. Liquid flow in the meniscus is shown in Fig. 2.

The average flow velocity, U_a, of the liquid entering any region is given by

$$U_a = M_i/\rho_1 t \tag{13}$$

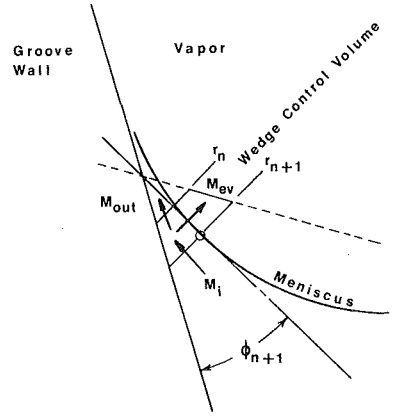

Fig. 2 Description of the flow field up the meniscus

where t is the film thickness at the height corresponding to U_a. A wedge flow model can be used to determine the pressure gradient, $dP/dr|_f$, required for the flow [13]. The flow field has a wedge angle formed by the tangent to the meniscus and the solid wall. Sparrow's [14] solution to the wedge flow problem can be expressed as

$$dP/dr|_f = \frac{U_a \rho_1 \nu \cos^2 \phi[(\xi R_e/2\phi) \cos \lambda + 4]}{\Delta z^2[\cos \lambda - (1/\lambda) \sin \lambda] g_c} \tag{14}$$

where $R_e = U_a 2\phi r/\nu$, $\lambda = (|4 + \xi R_e/2\phi|^{1/2})\phi$, ϕ is the wedge angle, ν is the kinematic viscosity, ξ is a constant, $r = t/\sin \phi$, and $\lambda z = t \cot \phi$.

In the evaporating film the wedge angle is very small and the pressure gradient $dP/dr|_f$ is approximated by the limiting case of equation (14) as ϕ goes to zero which is given by

$$dP/dr|_f = 3\nu U_a \rho_1 / g_c t^2 \tag{15}$$

The total pressure gradient, dP_1/dr, forcing the liquid up the wall must include the elevation head as well as $dP/dr|_f$ thus,

$$dP_1/dr = dP/dr|_f + \rho_1 g \cos (90 \text{ deg} - \theta), \tag{16}$$

where $\cos (90 \text{ deg} - \theta)$ is a correction term for wall angles other than 90 deg. Equation (16) can be rewritten as

$$dP_1/dt = [dP/dr|_f + \rho_1 g \cos (90 \text{ deg} - \theta)]/\phi, \tag{17}$$

since $dP_1/dr = dP_1/dt(dt/dr) = (\sin \phi) dP_1/dt$, and $\sin \phi \approx \phi$.

The dominant pressure in the evaporating film is the disjoining pressure and the pressure gradient dP_1/dt is equal to dP_d/dt and,

$$\phi = \frac{[dP/dr|_f + \rho_1 g \cos (90 \text{ deg} - \theta)]}{dP_d/dt}. \tag{18}$$

The pressure gradient dP_d/dt can be found by differentiating equation (7) to give, $dP_d/dt = \rho_1 R[(\ln at^b)(dT_{1v}/dt) + T_{1v} ab(t^{b-1})/at^b]$, which reduces to $dP_d/dt = \rho_1 R \ln at^b (dT_{1v}/dt) + (\rho_1 R T_{1v} b)/t$.

Calculations, using water as the liquid, have shown that the first term on the right is at least two orders of magnitude smaller than the second and is negligible so that

$$dP_d/dt = (\rho_1 R T_{1v} b)/t \tag{19}$$

and

$$\phi = [dP/dr|_f + \rho_1 g \cos (90 \text{ deg} - \theta)]t/\rho_1 R T_{1v} b \tag{20}$$

Equation (20) will be used to calculate the wedge angles for the flow field. The initial wedge angle, ϕ^0, at the top of the evaporating film can be found from equation (20) if $dP/dr|_f$ is set equal to zero, resulting in

$$\phi^0 = g \cos (90 \text{ deg} - \theta) t^0 / R T_{1v} b \tag{21}$$

The thickness of the film at any point $n + 1$ is found from, $t_{n+1} = t_n + (\Delta x \phi_n / \sin \theta)$ where ϕ_n has replaced $\tan \phi_n$ since ϕ_n is very small.

The Intrinsic Meniscus Region. The basic heat transfer mechanism in this region is still evaporation from the liquid-vapor interface, but the film thickness is larger so that equations will account for conduction effects through the film. The evaporation heat transfer process is represented by Newton's law of cooling

$$\tilde{Q} = h_{evf}(T_{1v} - T_v), \tag{22}$$

where

$$h_{evf} = \left(\frac{2\sigma_a H^2}{2 - \sigma_a}\right)\left(\frac{g_c}{2\pi}\right)^{1/2}\left(\frac{1}{R}\right)^{3/2}\left(\frac{1}{T}\right)^{5/2} P_v,$$

and the conduction contribution is

$$\tilde{Q} = K_1(T(x) - T_{1v})/t, \tag{23}$$

where K_1 is the conduction coefficient for the liquid. Combining equations (22) and (23) to eliminate T_{1v} gives

$$\tilde{Q} = \frac{h_{evf} K_1}{K_1 + h_{evf} t}(T(x) - T_v). \tag{24}$$

The expression for the heat transfer rate, Q_{DIS}, used in equation (3) is $Q_{\text{DIS}} = 2\tilde{Q}\Delta y$.

The mass of liquid evaporated, the average velocity and the pressure gradient for the liquid flow, can be calculated using equations (11–14). The total pressure gradient in the liquid to cause the flow is

$$dP_1/dr = dP/dr|_f + \rho_1 g \cos (90 \text{ deg} - \theta) \tag{25}$$

The forcing function for the flow is the decrease in curvature of the meniscus.

The capillarity equation for a wetting film is given as

$$P_1 = P_v - \sigma K_{cr} \tag{26}$$

where σ is the surface tension and K_{cr} is the curvature of the meniscus. Differentiating equation (26), assuming P_v and σ are constants, gives $dP_1/dr = -\sigma(dK_{cr}/dr)$, or

$$dK_{cr}/dr = -\frac{1}{\sigma}[dP/dr|_f + \rho_1 g \cos (90 \text{ deg} - \theta)]. \tag{27}$$

A finite difference form of equation (27) is used to calculate the curvature at points down the meniscus. A value for the curvature is assumed at the top of the intrinsic meniscus and the assumed value checked by requiring that $1/K_{cr}$ at the base of the intrinsic meniscus equal one half the groove width.

The thickness of the film at any point down the meniscus is calculated from the finite difference form of the curvature equation,

$$K_{cr} = \frac{d^2t/dy^2}{[1 + (dt/dy)^2]^{3/2}}. \tag{28}$$

The wedge angle ϕ, needed for equation (14), can be found from the equation

$$\phi_n = \arctan (\Delta t/\Delta y) \tag{29}$$

where Δt is the change in thickness for distance Δy along the wall. A check on the location of the base of the intrinsic meniscus is obtained by requiring that the wedge angle equal the wall angle when the thickness is equal to one half the groove width. Below the base of the intrinsic meniscus heat transfer is represented by a convection process to the liquid.

Convection to the Liquid. The portion of the wall below the extended meniscus is surrounded by liquid at bulk temperature, T_L. Newton's law of cooling applies

$$\tilde{Q} = h_1[T(x) - T_L], \tag{30}$$

where the value $h_1 = 50$ Btu/hr-ft^2-°F (283W/m^2-°C) was used. This value is at the low end of the range for forced convection heat transfer coefficients for water. The heat transfer rate, Q_{DIS}, in equation (3) is found from the heat flux, $\tilde{Q}$, using $Q_{\text{DIS}} = 2\tilde{Q}\Delta y$.

Meniscus Curvature. The equations presented for the four regions are solved using finite difference techniques. The solution starts at the top of the evaporating film region and integrates toward the base. Coming down the meniscus, the equilibrium non-evaporating thin film (Region I) ends when the film thickness is t^0 (predicted by equation (9)) and the meniscus continues in the direction ϕ^0 (specified by equation (21)) into the evaporating thin film region (Region II).

In Region II the best way to model the combined effects of a pressure gradient resulting from a curvature gradient with one resulting from a thickness gradient is not known. Kamotani [15] points out that a rigorous analysis for a perfectly flat wall surface may not be valid for an actual surface, roughness of order 10^{-7} m.

In our model, the evaporating film is joined to the intrinsic meniscus (Region III) by matching the pressure from the thickness gradient to the pressure resulting from the curvature gradient and also by smoothly connecting the meniscus profiles, or first derivatives, in each region. The second derivatives (curvature) were not matched.

It is difficult to say how much error is introduced by not matching curvatures between these regions and also by not superimposing two pressure gradients by a linear or nonlinear combination in the evaporating film region. However, both Wayner [16], Kamotani [15] and

this paper agree that less than 10 percent of the total heat dissipation occurs in the evaporating film region. This low fraction of the total heat dissipation would indicate some flexibility for making approximations in this thin region. Additionally, the dimensions of this thin region are 10^{-7} m which are the same order of magnitude as surface roughness, making any analytical solution very complex and uncertain.

The intrinsic meniscus, Region III, continues to zero slope at the middle of the groove. Region IV accounts for heat transfer by convection below the meniscus.

Results

Calculations are presented for a grooved plate with dimensions 0.020 in. (0.508 mm) wide grooves separated by walls 0.050 in. (1.27 mm) high. The width of the walls was one of the independent parameters and varied from 0.001 in. (0.0254 mm) to 0.010 in. (0.254 mm). A wall angle of 90 deg (1.57 rad) was used. All calculations are based on 1 ft (0.304 m) of groove length.

The temperature of the vapor, T_v, and that of the liquid, T_l, surrounding the wall was set at 500°R (277.57 K). The heat transfer rate from the wall was controlled by choosing a value for the temperature at the top of the wall, T_{end}. Values used for T_{end} were 500.25°R (277.72K), 500.5°R (277.86K), and 500.75°R (278.0K).

Setting a value for $T_{end} - T_v$ does not establish a constant heat flux from the wall, since changing either the wall thickness or the conductivity of the wall will change the temperature distribution in the wall. This in turn changes both the heat transfer rate in the intrinsic meniscus region and the convection rate to the liquid.

The constants a and b used in equation (6) were assigned the values of 1.5336 and 0.0243, respectively, for film thickness, t, in feet. Those values were obtained by fitting a curve of the form at^b to the data Deryagin and Zorin [11] have obtained for a water film on glass. It is expected that these data apply only at low temperatures on the order of 40 to 60°F (4.4 to 15.5°C).

The heat flux from the wall as a function of the height above the base is shown in Fig. 3. In all cases the heat flux increases in the evaporating film region, reaches a maximum in the transition region and then decreases in the intrinsic meniscus region.

The size of the evaporating film region depends on the amount of heat dissipated in that region. Table 1 gives the representative values for the height of the regions for each of the values of $(T_{end} - T_v)$.

The total heat transfer for the evaporating film region accounts for a maximum of only about 8 percent of the heat transfer from the wall (see Fig. 3). The heat flux as well as the total heat transfer rate in this region depends primarily upon the values of $(T_{end} - T_v)$. Table 1 lists the overall heat transfer rates for the evaporating film region for the values of $(T_{end} - T_v)$.

The temperature increases in the wall associated with these heat transfer rates are very small, on the order of 10^{-3}°F (5.55×10^{-4}°C), and the effect of this temperature increase on T_{lv} is negligible. Thus P_{vlv} is a function only of the film thickness and the heat flux is essentially dependent upon the disjoining pressure. The highest heat flux in the evaporating film region is at the very base where the magnitude of the disjoining pressure is decreasing the fastest.

The development of equation (19) was dependent upon the term $\ln (at^b) dT_{lv}/dt$ being less than bT_{lv}/t. A typical value of dT_{lv}/dt for the tests run was on the order of 10^5°F/ft whereas a typical value of $T_{lv}(b/t)$ is on the order of 10^9°F/ft. This would seem to substantiate the assumption that $\rho_l R \ln (at^b) dT_{lv}/dt$ is negligible.

The maximum heat flux from the wall occurs in the transition region between the evaporating film and the intrinsic meniscus. At this point the heat flux is still primarily determined by the pressure drop $(P_{vlv}{}^0 - P_v)$ which is essentially dependent upon the temperature difference $(T_{end} - T_v)$. Table 1 lists the maximum heat flux for the different values of $(T_{end} - T_v)$.

The equation for the heat flux in the intrinsic meniscus region is

$$Q = \frac{h_{evf} K_1}{K_1 + h_{evf} t} (T(x) - T_v),$$

Thus, in this region, the decrease in the heat flux as the film thickness increases is partially offset by the increase in wall temperature. Fig. 3 shows that the heat flux from the wall at any given location in the intrinsic meniscus region increases as the wall thickness decreases. As the wall thickness decreases there is a tendency for the film thickness at a given location to decrease also. This decrease in film thickness as well as the increasing temperature gradients are the forcing functions for the increased heat flux.

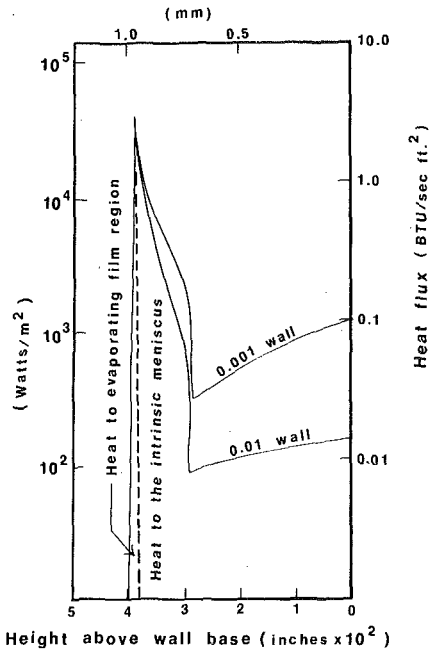

Fig. 3 Heat flux from walls of different thickness maintaining $T_{end} - T_v \approx$ 0.25°F (0.14°C) and K = 25 Btu/hr-ft-°F (43.3 Watts/m-°C) for the wall

Table 1 Heat transfer data and meniscus configuration in the evaporating film region for a single groove surface and liquid interface. Calculations are based on 1 ft. (0.304 m) of groove length and for a single interline

$T_{end} - T_v$	Fahrenheit 0.25		0.50	0.75
	Centigrade 0.14		0.28	0.42
Rate of heat dissipation	Btu/hr	0.134	0.245	0.323
	Watts	0.0393	0.0718	0.0946
Maximum heat flux	Btu/hr-ft^2	1.51×10^4	3.08×10^4	4.62×10^4
	Watts/m^2	4.67×10^4	9.53×10^4	14.29×10^4
Evaporating film height	in.	17.28×10^{-4}	8.16×10^{-4}	4.56×10^{-4}
	mm	0.044	0.021	0.012
Intrinsic meniscus height	in.	9.24×10^{-3}	9.24×10^{-3}	9.10×10^{-3}
	mm	0.235	0.235	0.231

The increase in the temperature gradients in the wall, corresponding to a decrease in wall thickness, causes an increase in the convective heat transfer rate to the liquid. In all tests the liquid temperature was considered the same throughout the liquid and so the temperature difference $(T(x) - T_L)$ increased towards the base of the wall. Thus, it is evident that the convective heat flux increases both towards the base of the wall and as the wall thickness decreases.

Fig. 4 illustrates some interesting conclusions concerning where the heat is leaving the wall. Except for very closely spaced grooves or very thin walls, more than 80 percent of the heat is transferred in the intrinsic meniscus region and most of this heat is transferred in the top half of this region. It appears the triple interline, that forms the large heat sink, is in reality a region some 0.005 in. (0.127 mm) to 0.006 in. (0.152 mm) high at the top of the intrinsic meniscus for the materials and dimensions used in our study.

The rapid increase in the portion of the heat transferred to the liquid as the wall thickness decreases is somewhat misleading. These

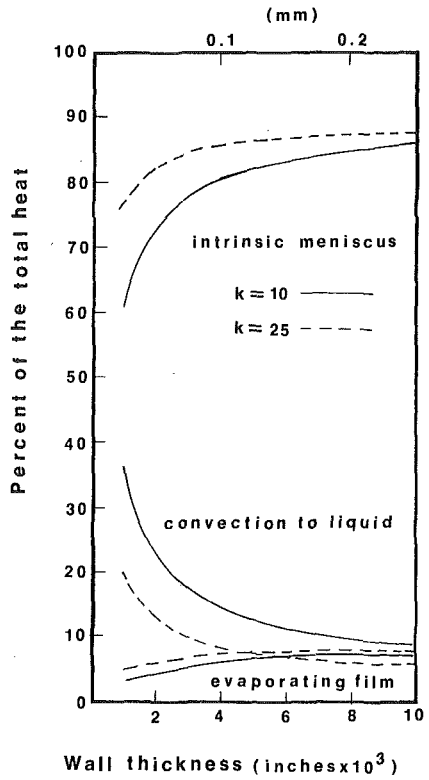

Fig. 4 Percent of the total heat dissipated in each region for $l_{end} - T_v$ = 0.25°F (0.14°C), K = 10 Btu/hr-ft-°F (17.3 Watts/m-°C) and K = 25 Btu/hr-ft-°F (43.3 Watts/m-°C) for the wall

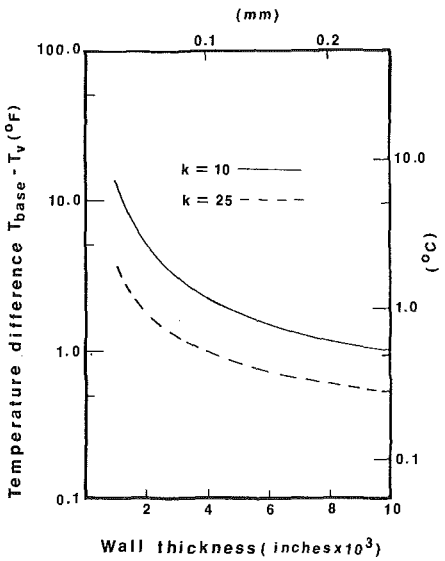

Fig. 5 Temperature difference $T_{base} - T_v$ giving an indication of wall superheat maintaining $T_{end} - T_v$ = 0.25°F (0.14°C), K = 10 Btu/hr-ft-°F (17.3 Watts/m-°C), and K = 25 Btu/hr-ft-°F (43.3 Watts/m-°C) for the wall

high heat transfer rates are the result of values for $T(x)$ that are much higher than could be achieved without boiling.

If it is assumed that the difference $(T_{base} - T_v)$, as shown in Fig. 5, is analogous to the excess temperature for pool boiling, then it would be expected that $(T_{base} - T_v)$ has some maximum value above which boiling would occur at the bottom of the groove. This boiling, which would destroy the capillary flow patterns, would be one possible form of failure for the heat transfer mechanisms.

Conclusions

The model developed in this study is recommended for describing the heat and mass transfer from a surface wetted through capillary grooves. The presence of a region of high heat transfer rates is demonstrated by the model. For the conditions used in our calculations, this region, called the thin-film transition region, is approximately 0.005 in. (0.127 mm) to 0.006 in. (0.152 mm) high and is located at the top of the intrinsic meniscus. This region accounts for approximately 80 percent of the heat dissipation from the wall.

The heat transfer from the evaporating film region is of significantly less importance since, for the conditions used in these calculations, this region was responsible for only about 8 percent of the total heat transfer. It should be recognized that a change in the adsorption characteristics in the thin liquid film could increase the importance of the heat transfer in the evaporating film region. This would require a film for which the magnitude of the disjoining pressure decreases rapidly allowing significant evaporation to occur.

The major limitation on this model is a lack of published data on the adsorption characteristics of thin liquid films on metals. Film thickness versus saturation pressure data as found in [11, 17] are needed for commonly used metals such as steel, brass, aluminum and copper.

Finally, the most important finding presented in this paper is a conceptual experimental method for detecting the heat and mass transfer effects that occur in the vicinity of a liquid-solid-vapor interline. By controlling the groove spacing and shape, and by measuring the vapor temperature T_v, the base temperature T_b, the tip temperature T_e, and the heat dissipated by the wall Q_{DIS}, one is able to isolate and quantify the effects of interline heat transfer.

References

1 Shea, Jr., F. L., and Drase, N. W., "Drop-wise and Film Condensation of Steam," *Trans. AIChE*, Vol. 36, 1940, pp. 463–487.

2 Kreith, F., *Principles of Heat Transfer*, International Text Book Company, Scranton, PA., 1965.

3 El-Wakil, M. M., *Nuclear Heat Transport*, International Text Book Company, Scranton, Penn., 1971.

4 Kosson, R., Hembach, R., Edelsein, F., and Tawil, M., "A Tunnel Wick 100,000 watt-inch Heat Pipe," AIAA 7th Thermophysics Conference, AIAA Paper No. 72-273, April, 1972.

5 Wayner, Jr., P. C., and Coccio, C. L., "Heat Transfer in the Vicinity of the Triple Interline of a Meniscus," *AIChE Journal*, Vol. 17, No. 3, 1971, pp. 569–574.

6 Bressler, R. G., and Wyatt, P. W., "Surface Wetting Through Capillary Grooves," ASME JOURNAL OF HEAT TRANSFER, Vol. 92, 1970, pp. 126–132.

7 Ayyaswamy, P. S., Catton, I., and Edwards, D. K., "Capillary Flow in Triangular Grooves, "ASME *Journal of Applied Mechanics*, Vol. 41, 1974, pp. 332–336.

8 Edwards, D. K., Gier, K. D., Ayyaswamy, P. S., and Catton, I., "Evaporation and Condensation in Circumferential Grooves on Horizontal Tubes," paper presented at ASME-AIChE Heat Transfer Conference, Atlanta, Ga., August 5–8, 1973.

9 Potash, Jr., M., and Wayner, Jr., P. C., "Evaporation from a Two-Dimensional Extended Meniscus," *Int. J. Heat and Mass Transfer*, Vol. 15, 1972, pp, 1851–1863.

10 Harper, W. P., and Brown, D. R., "Mathematical Equations for Heat Conduction in the Fins of Air-Cooled Engines," NACA Report 158, 1922.

11 Deryagin, B. V., and Zorin, A. M., "Optical Study of the Absorption and Surface Condensation of Vapors in the Vicinity of Saturation on a Smooth Surface," *Proc. 2nd Int. Congr. Surface Activity*, London, 2, 1957, pp. 145–152.

12 Sukhatme, S. P., and Rohsenow, W. M., "Heat Transfer During Film Condensation of a Liquid Metal Vapor," ASME JOURNAL OF HEAT TRANSFER, Vol. 88, No. 1, 1966, pp. 19–27.

13 Wayner, Jr., P. C., and Potash, Jr., M., "Fluid Flow in an Evaporating Meniscus," Pre-print No. 30.b, 63rd annual meeting AIChE, Chicago, Ill., 29 Nov.–3 Dec. 1970.

14 Sparrow, E. M., and Starr, J. B., "Heat Transfer to Laminar Flow in Tapered Passages," *J. Appl. Mech.* 32 E, 684–689 (1965).

15 Kamotani, Y., "Evaporator Film Coefficients of Grooved Heat Pipes," *Proc. of 3rd International Heat Pipe Conference*, 1978.

16 Wayner, P. C., "Effect of Interline Heat Transfer or Meniscus Profile and Capillary Pressure," *Proc of 3rd International Heat Pipe Conference*, 1978.

17 Wayner, P. C., "Effect of the London-Van der Waals Dispersion Force on Interline Heat Transfer," ASME JOURNAL OF HEAT TRANSFER, Vol. 100, Feb. 1978, pp. 155–159.

Y. P. Chang
K. C. Poon

Department of Mechanical Engineering,
State University of New York at Buffalo,
Amherst, New York 14260

Three-Dimensional, Steady-State Heat Conduction in Cylinders of General Anisotropic-Media[1]

This paper provides the analytical solution of three-dimensional steady-state heat conduction in solid and hollow cylinders of general anisotropic-media. By the use of Fourier transforms and a change of variables the partial differential equation is reduced to Kummer's equation. Some calculated results for a solid cylinder are shown and discussed. A parameter γ is found to represent the coupling effect of three-dimensional anisotropy. For small values of γ, an approximate solution is recommended. The inequality $\sigma > 0$ which was found in an earlier paper is further discussed.

1 Introduction

In an earlier paper [1] we have shown that a number of the first-class problems of heat conduction in anisotropic media can be transformed into corresponding problems in isotropic media. Such transformations were conceived from results in [2–4] which were obtained by the use of integral transforms and also from the separation of variables [4, 5].

In the case of three-dimensional heat conduction in a general anisotropic-medium which is homogeneous in circular cylinder coordinates, however it is no longer possible to transform an anisotropic problem into the corresponding isotropic one, except for the special case: $\nu_{23} = \nu_{12}\nu_{13}$ [1]. Nonetheless, such problems as well as their Green's functions can still be handled by the technique of Fourier transforms as well as the classical method, as was pointed out in [4]. In this paper only the solution of two simpler problems is reported: steady-state heat conduction in solid and hollow cylinders of infinite length with the boundary condition or conditions of the first kind (Dirichlet) and without distributed heat source in the medium. Obviously, these problems are of the first class defined in [1–3].

2 Statement of Problems

The steady state heat conduction in an anisotropic medium which is homogeneous in circular cylinder coordinates (r, θ, z) may be stated as:

$$T_{rr} + \frac{1}{r}T_r + 2\nu_{12}\frac{1}{r}T_{r\theta} + \nu_{22}\frac{1}{r^2}T_{\theta\theta} + 2\nu_{13}T_{rz} + 2\nu_{23}\frac{1}{r}T_{\theta z} + \nu_{13}\frac{1}{r}T_z + \nu_{33}T_{zz} = 0 \quad (2.1)$$

where ν_{ij} denotes the ratios of thermal conductivity coefficients with $i, j = 1\,2, 3$ designating r, θ and z, respectively; T is the temperature; and subscripts r, θ and z of T represent the differentiation with respect to these spatial variables. The boundary conditions may be written in the general form, although only the solution of (2.1) subject to boundary conditions of the first kind are shown. For the solid cylinder, $0 \le r < r_0$,

$$C_0\left(T_r + \nu_{12}\frac{1}{r}T_\theta + \nu_{13}T_z\right) + hT = \begin{matrix} f_0(\theta,z) \\ 0 \end{matrix} \quad \text{for } r = r_0,\ -\pi < \theta \le \pi,\ \begin{matrix} -\ell \le z \le \ell \\ \ell < z < -\ell \end{matrix} \quad (2.2)$$

$$T = \text{finite for } r = 0,\ |z| < \infty \quad (2.3)$$

and for the hollow cylinder, $r_1 < r < r_2$,

$$C_1\left(T_r + \nu_{12}\frac{1}{r}T_\theta + \nu_{13}T_z\right) - h_1T = \begin{matrix} f_1(\theta, z) \\ 0 \end{matrix} \quad \text{for } r = r_1,\ -\pi < \theta \le \pi,\ \begin{matrix} -\ell_1 \le z \le \ell_1 \\ \ell_1 < z < -\ell_1 \end{matrix} \quad (2.4)$$

$$C_2\left(T_r + \nu_{12}\frac{1}{r}T_\theta + \nu_{13}T_z\right) + h_2T = \begin{matrix} f_2(\theta, z) \\ 0 \end{matrix} \quad \text{for } r = r_2,\ -\pi \le \theta \le \pi,\ \begin{matrix} -\ell_2 \le z \le \ell_2 \\ \ell_2 < z < -\ell_2 \end{matrix} \quad (2.5)$$

where either c's may be equal to zero or unity and h is a known constant including zero so that boundary conditions of the first and second kinds are included.

In order to obtain unique solutions for all cases, we impose also the condition

$$T = 0, \quad |z| = \infty \quad (2.6)$$

This requires that all prescribed nonvanishing data are to be confined in finite interval or intervals of z.

3 Reduction of Governing Equations

We now try to reduce (2.1) to an ordinary differential equation involving the independent variable r only by the application of the complex Fourier and the periodic transforms defined by:

$$\bar{g}(r, n, \omega) = \int_0^{2\pi}\int_{-\infty}^{\infty} g(r, \theta, z)e^{-in\theta - i\omega z}d\theta dz \quad (3.1)$$

$$g(r, \theta, z) = \frac{1}{4\pi^2}\sum_{n=-\infty}^{\infty} e^{in\theta}\int_{-\infty}^{\infty}\bar{g}(r, n, \omega)e^{i\omega z}d\omega \quad (3.2)$$

where the function $g(r, \theta, z)$ is assumed to be absolutely integrable. Applying the transform (3.1) to (2.1), we obtain

$$r^2\overline{T}_{rr} + (1 + 2in\nu_{12} + 2i\omega\nu_{13}r)r\overline{T}_r + (-n^2\nu_{22} - 2n\omega\nu_{23}r + i\omega\nu_{13}r - \nu_{33}\omega^2r^2)\,\overline{T} = 0 \quad (3.3)$$

If we let

$$\overline{T} = \phi(r)r^{-in\nu_{12} + |n|\beta_{12}}e^{-r\omega(i\nu_{13} + \beta_{13})} \quad (3.4)$$

where $\beta_{13} = (\nu_{33} - \nu_{13}^2)^{1/2}$, and $\beta_{12} = (\nu_{22} - \nu_{12}^2)^{1/2}$ then (3.3) can be further transformed into the standard form of the confluent hypergeometric equation [5]:

$$r\phi_{rr} + (1 + 2|n|\beta_{12} - 2\omega\beta_{13}r)\phi_r - (\beta_{13}\omega + 2|n|\beta_{12}\beta_{13}\omega + 2n\omega\gamma)\,\phi = 0 \quad (3.5)$$

Now we apply the transform (3.1) followed by (3.4) to boundary conditions (2.2–2.5) and (2.7) to obtain for the solid cylinder

[1] This study was supported in part by the National Science Foundation, ENG 76-83367.

Contributed by the Heat Transfer Division for publication in the JOURNAL OF HEAT TRANSFER. Manuscript received by the Heat Transfer Division October 11, 1978.

$$C_0\phi_r + \left(C_0\frac{|n|\beta_{12}}{r_0} - C_0\omega\beta_{13} + h\right)\phi = \bar{f}_0(n,\omega)r_0{}^{in\nu_{12}-|n|\beta_{13}}e^{r_0\omega(i\nu_{13}+\beta_{13})},\ r = r_0 \quad (3.6)$$

where

$$\bar{f}_0(n,\omega) = \int_{\infty}^{2\pi}\int_{-\infty}^{\infty} f_0(\theta,z)e^{-in\theta-i\omega z}d\theta dz \quad (3.7)$$

and for the hollow cylinder

$$C_1\phi_r + \left(C_1\frac{n}{r_1} - C_1\omega\beta_{13} - h_1\right)\phi = \bar{f}_1(n,\omega)r_1{}^{in\nu_{12}-|n|\beta_{13}}e^{r_1\omega(i\nu_{13}+\beta_{13})},\ r = r_1 \quad (3.8)$$

$$C_2\phi_r + \left(C_2\frac{n}{r_2} - C_2\omega\beta_{13} + h_2\right)\phi = \bar{f}_2(n,\omega)r_2{}^{in\nu_{12}-|n|\beta_{13}}e^{r_2\omega(i\nu_{13}+\beta_{13})},\ r = r_2 \quad (3.9)$$

where $\bar{f}_1$ and $\bar{f}_2$ are the transforms of f_1 and f_2, respectively.

It is seen from (3.5–3.9) that we have achieved our attempt of using transform (3.1).

4 Solid Cylinder

Equation (3.5) is also known as Kummer's equation whose solution involves in general Kummer's functions of the first and second forms [7]. By the condition that T is finite at $r = 0$, we have to discard the second form, so that

$$\phi = A_1F_1(a;\ b;\ 2\omega\beta_{13}r) \quad (4.1)$$

where ${}_1F_1$ denotes Kummer's function of the first form [5];

$$a = \frac{1}{2} + |n|\beta_{12} + \frac{n}{\beta_{13}}\gamma;\ b = 1 + 2|n|\beta_{12} \quad (4.2)$$

and A, an arbitrary constant, is determined by the boundary condition:

$$\phi(r_0) = \bar{f}_0(n,\omega)r_0{}^{in\nu_{12}-|n|\beta_{12}}e^{\omega r_0(i\nu_{13}+\beta_{13})},\ r = r_0 \quad (4.3)$$

to yield

$$A = \frac{\bar{f}_0(n,\omega)r_0{}^{in\nu_{12}-|n|\beta_{12}}e^{i\omega\nu_{13}r_0+\beta_{13}\omega r_0}}{{}_1F_1(a_0;\ b_0;\ 2\omega\beta_{13}r_0)} \quad (4.4)$$

where

$$a_0 = \frac{1}{2} + |n|\left(\beta_{12} + \frac{\gamma}{\beta_{13}}\right);\ b_0 = b \quad (4.5)$$

Substituting (4.4) into (4.1) and the result into (3.4), we obtain

$$\bar{T}(r,n,\omega) = \bar{f}_0(n,\omega)\frac{{}_1F_1(a_0;\ b_0;\ 2\omega\beta_{13}r)}{{}_1F_1(a_0;\ b_0;\ 2\omega\beta_{13}r_0)} \times r_0{}^{in\nu_{12}-|n|\beta_{12}}e^{\omega r_0(i\nu_{13}+\beta_{13})} \quad (4.6)$$

The inverse of $\bar{T}(r,\eta,\omega)$ gives the temperature field:

$$T(r,\theta,z) = \frac{1}{2\pi^2}\int_{-\pi}^{\pi}\int_{-\ell}^{\ell}\int_{\omega=0}^{\infty} f(\theta',z')\left\{\frac{I_0(\omega\beta_{13}r)}{I_0(\omega\beta_{13}r_0)}\cos\varphi_0 + \sum_{n=1}^{\infty}\left(\frac{r}{r_0}\right)^{n\beta_{12}}e^{-\omega\beta_{13}(r_0-r)}\left[\frac{{}_1F_1(b_0-a_0;\ b_0;\ -2\omega\beta_{13}r)}{{}_1F_1(b_0-a_0;\ b_0;\ -2\omega\beta_{13}r_0)}\cos\varphi_1 + \frac{{}_1F_1(a_0;\ b_0;\ -2\omega\beta_{13}r)}{{}_1F_1(a_0;\ b_0;\ -2\omega\beta_{13}r_0)}\cos\varphi_2\right]\right\}d\omega\,dz'd\theta' \quad (4.7)$$

where

$$\varphi_0 = \omega[(z-z') + \nu_{13}(r_0-r)]$$

$$\varphi_1 = n\left[(\theta-\theta') - \nu_{12}\ln\frac{r}{r_0}\right] + \varphi_0$$

$$\varphi_2 = n\left[(\theta-\theta') - \nu_{12}\ln\frac{r}{r_0}\right] - \varphi_0$$

The integral with kernel involving Bessel function can be evaluated with respect to ω by the residue theorem so that

$$T(r,\theta,z) = \frac{1}{2\pi\beta_{13}r_0}\sum_{m=1}^{\infty}\frac{J_0(\mu_m\beta_{13}r)}{J_1(\mu_m\beta_{13}r_0)} \times \int_{-\pi}^{\pi}\int_{-\ell}^{\ell} f(\theta',z')\,e^{-\mu_m|z-z'+\nu_{13}(r_0-r)|}\,dz'd\theta' + \frac{1}{2\pi^2}\sum_{n=1}^{\infty}\left(\frac{r}{r_0}\right)^{n\beta_{12}}\int_{-\pi}^{\pi}\int_{-\ell}^{\ell}\int_{\omega=0}^{\infty} f(\theta',z')e^{-\omega\beta_{13}(r_0-r)}\cdot\left[\frac{{}_1F_1(b_0-a_0;\ b_0;\ -2\omega\beta_{13}r)}{{}_1F_1(b_0-a_0;\ b_0;\ -2\omega\beta_{13}r_0)}\cos\varphi_1 + \frac{{}_1F_1(a_0;\ b_0;\ 2\omega\beta_{13}r)}{{}_1F_1(a_0;\ b_0;\ 2\omega\beta_{13}r_0)}\cos\varphi_2\right]d\theta'dz'd\omega \quad (4.8)$$

The second integral in (4.8) can also be evaluated with respect to ω, but the result involves nonorthogonal eigenfunctions with complex eigenvalues and therefore more time is required in the numerical computation of $T(r,\theta,z)$ [6].

5 Hollow Cylinder

For the hollow cylinder $r_1 < r < r_2$, the general solution of (3.5) is in the form [8]:

$$\phi(r,\omega,n) = A_1F_1(a;\ b;\ 2\omega\beta_{13}r) + BU(a;\ b;\ 2\omega\beta_{13}r) \quad (5.1)$$

where a and b have been defined in (4.2); and the function $U(a;\ b;\ 2\omega\beta_{13}r)$ is a linear combination of ${}_1F_1(a;\ b;\ 2\omega\beta_{13}r)$ and $(2\omega\beta_{13}r)^{1-b}$ ${}_1F_1(1+a-b;\ 2-b;\ 2\omega\beta_{13}r)$ which is usually called Kummer's function of the second form and has been partially tabulated [8, 9]:

$$U(a;\ b;\ 2\omega\beta_{13}r) = \frac{\pi}{\sin\pi b}\left\{\frac{{}_1F_1(a;\ b;\ 2\omega\beta_{13}r)}{\Gamma(1+a-b)\Gamma(b)} - \frac{(2\omega\beta_{13}r)^{1-b}{}_1F_1(1+a-b;\ 2-b;\ 2\omega\beta_{13}r)}{\Gamma(a)\Gamma(2-b)}\right\} \quad (5.2)$$

where the principal branch has been taken and a, b remain the same as defined in (4.2); and Γ denotes Gamma function.

The arbitrary constants A and B in (5.1) are determined by the boundary conditions. We consider first the case:

$$T(r_1,\theta,z) = 0, \quad -\pi < \theta \leqslant \pi, \quad |z| < \infty$$
$$T(r_2,\theta,z) = \begin{cases} f_2(\theta,z), & -\pi < \theta \leqslant \pi, \quad -\ell_2 \leqslant z \leqslant \ell_2 \\ 0, & \ell_2 < z < -\ell_2 \end{cases} \quad (5.3)$$

Nomenclature

$a = \frac{1}{2} + |n|\beta_{12} + \frac{n\gamma}{\beta_{13}}$
$b = 1 + 2|n|\beta_{12}$
f = boundary data
${}_1F_1(a;\ b;\ x)$ = first form of Kummer's function
h = heat transfer coefficient/k_{11}
$I_0(x)$ = modified Bessel's function of first kind, order zero
$J_\alpha(x)$ = Bessel's function of first kind, order α
$K_0(x)$ = modified Bessel's function of second kind, order zero
k_{ij} = thermal conductivity coefficients
r = radial coordinate
$\bar{r} = \frac{r}{r_0}$
r_0 = radius of solid cylinder
r_1, r_2 = radii of hollow cylinder
T = temperature
$U(a;\ b;\ x)$ = second form of Kummer function
$Y_0(x)$ = Bessel's function of second kind, order zero
z = axial coordinates; $\bar{z} = \frac{z}{r_0}$
$\beta_{12} = (\nu_{22} - \nu_{12}{}^2)^{1/2}$
$\beta_{13} = (\nu_{33} - \nu_{13}{}^2)^{1/2}$
$\Gamma(x)$ = gamma function
$\gamma = \nu_{23} - \nu_{12}\nu_{13}$
θ = angular coordinate
$\nu_{ij} = k_{ij}/k_{11}$
ω,η = transformation parameter
$\bar{\omega} = \omega\beta_{13}r_0$

which gives for $-\pi < \theta \leq \pi$

$$\varphi = 0, \quad r = r_1, \quad |z| < \infty \tag{5.4}$$

$$\phi = \begin{matrix} \bar{f}_2(n,\omega) r_2^{i n \nu_{12} - |n|\beta_{12}} e^{(i\nu_{13}-\beta_{13})\omega r_2}, & r = r_2, \quad -\ell \leq z \leq \ell \\ 0, & \qquad\qquad \ell < z < -\ell \end{matrix} \tag{5.5}$$

After the determination of A and B, we obtain

$$\phi(r,0,\omega) = \bar{f}_2(\omega) e^{i\nu_{13}\omega r} \cdot \left[\frac{I_0(\omega\beta_{13}r_1)K_0(\omega\beta_{13}r) - I_0(\omega\beta_{13}r)K_0(\omega\beta_{13}r_1)}{I_0(\omega\beta_{13}r_1)K_0(\omega\beta_{13}r_2) - I_0(\omega\beta_{13}r_2)K_0(\omega\beta_{13}r_1)} \right] \tag{5.6}$$

$$\phi(r,n,\omega) = \bar{f}_2(n,\omega) r_2^{i n \nu_{12} - n\beta_{12}} \cdot \left[\frac{{}_1F_1(a;b;2\omega\beta_{13}r_1)U(a;b;2\omega\beta_{13}r) - {}_1F_1(a;b;2\omega\beta_{13}r)U(a;b;2\omega\beta_{13}r_1)}{{}_1F_1(a;b;2\omega\beta_{13}r_1)U(a;b;2\omega\beta_{13}r_2) - {}_1F_1(a;b;2\omega\beta_{13}r_2)U(a;b;2\omega\beta_{13}r_1)} \right] \tag{5.7}$$

Substituting (5.6) and (5.7) into (3.4) and taking the inverse, we obtain the temperature distribution:

$$T(r,\theta,z) = \frac{1}{2\pi^2} \int_{-\pi}^{\pi} \int_{-\ell_2}^{\ell_2} \int_{\omega=0}^{\infty} f_2(\theta', z') \cdot \left\{ \frac{I_0(\omega\beta_{13}r_1)K_0(\omega\beta_{13}r) - I_0(\omega\beta_{13}r)K_0(\omega\beta_{13}r_1)}{I_0(\omega\beta_{13}r_1)K_0(\omega\beta_{13}r_2) - I_0(\omega\beta_{13}r_2)K_0(\omega\beta_{13}r_1)} \cos\varphi_0 + \sum_{n=1}^{\infty} \left(\frac{r}{r_2}\right)^{n\beta_{12}} e^{-\omega\beta_{13}(r_2-r)} \right.$$

$$\left[\frac{{}_1F_1(b_0-a_0;b_0;-2\omega\beta_{13}r){}_1F_1(1-a_0;2-b_0;-2\omega\beta_{13}r_1) - \left(\frac{r_1}{r}\right)^{2n\beta_{12}} {}_1F_1(b_0-a_0;b_0;-2\omega\beta_{13}r_1){}_1F_1(1-a_0;2-b_0;-2\omega\beta_{13}r)}{{}_1F_1(b_0-a_0;b_0;-2\omega\beta_{13}r_2){}_1F_1(1-a_0;2-b_0;-2\omega\beta_{13}r_1) - \left(\frac{r_1}{r_2}\right)^{2n\beta_{12}} {}_1F_1(b_0-a_0;b_0;-2\omega\beta_{13}r_1){}_1F_1(1-a_0;2b_0;-2\omega\beta_{13}r_2)} \right.$$

$$\cdot \cos\varphi_1 - \frac{{}_1F_1(a_0;b_0;-2\omega\beta_{13}r){}_1F_1(1+a_0;b_0-2-b_0;-2\omega\beta_{13}r_1) - \left(\frac{r_1}{r}\right)^{2n\beta_{12}} {}_1F_1(a_0;b_0;-2\omega\beta_{13}r_1({}_1F_1(1+a_0-b_02-b_0;-2\omega\beta_{13}r)}{{}_1F_1(a_0;b_0;-2\omega\beta_{13}r_2){}_1F_1(1+a_0-b_0;2-b_0;-2\omega\beta_{13}r_1) - \left(\frac{r_1}{r_2}\right)^{2n\beta_{12}} {}_1F_1(a_0;b_0;-2\omega\beta_{13}r_1F_1(1+a_0-b_02-b_0;-2\omega\beta_{13}r_2)} \right.$$

$$\left. \left. \cdot \cos\varphi_2 \right] \right\} d\omega\, dz'\, d\theta' \tag{5.8}$$

where (5.2) has been used and

$$\varphi_0 = \omega[z - z' + \nu_{13}(r_2 - r)]$$

$$\varphi_1 = n\left[\theta - \theta' - \nu_{12}\ln\left(\frac{r}{r_2}\right)\right] + \varphi_0$$

$$\varphi_2 = n\left[\theta - \theta' - \nu_{12}\ln\left(\frac{r}{r_2}\right)\right] - \varphi_0 \tag{5.9}$$

If the outer surface condition is homogeneous while the inner surface is prescribed as:

$$T(r,\theta,z) = \begin{matrix} f_1(\theta,z), & -\ell_1 < z \leq \ell_1 \\ 0, & -\pi < \theta \leq \pi, \quad \ell_1 < z < -\ell_1 \end{matrix}$$

$$T(r_2,\theta,z) = 0, \qquad -\pi < \theta < \pi, \quad |z| < \infty \tag{5.10}$$

the temperature field can be obtained by the same way. The result is:

$$T(r,\theta,z) = \frac{1}{2\pi^2} \int_{-\pi}^{\pi} \int_{-\ell_1}^{\ell_1} \int_{\omega=0}^{\infty} f_1(\theta', z') \left\{ \frac{I_0(\omega\beta_{13}r_2)K_0(\omega\beta_{13}r) - I_0(\omega\beta_{13}r)K_0(\omega\beta_{13}r_2)}{I_0(\omega\beta_{13}r_2)K_0(\omega\beta_{13}r_1) - I_0(\omega\beta_{13}r_1)K_0(\omega\beta_{13}r_2)} \cos\varphi_0' + \sum_{n=1}^{\infty} \left(\frac{r_1}{r}\right)^{n\beta_{12}} e^{-\omega\beta_{13}(r-r_1)} \right.$$

$$\cdot \left[\frac{{}_1F_1(b_0-a_0;b_0;-2\omega\beta_{13}r_2){}_1F_1(1-a_0;2-b_0;-2\omega\beta_{13}r) - \left(\frac{r}{r_2}\right)^{2n\beta_{12}} {}_1F_1(b_0-a_0;b_0;-2\omega\beta_{13}r){}_1F_1(1-a_0;2-b_0;-2\omega\beta_{13}r_2)}{{}_1F_1(b_0-a_0;b_0;-2\omega\beta_{13}r_2){}_1F_1(1-a_0;2-b_0;-2\omega\beta_{13}r_1) - \left(\frac{r_1}{r_2}\right)^{2n\beta_{12}} {}_1F_1(b_0-a_0;b_0;-2\omega\beta_{13}r\,1){}_1F_1(1-a_0;2-b_0;-2\omega\beta_{13}r_2)} \cos\varphi_1' \right.$$

$$+ \frac{{}_1F_1(a_0;b_0;-2\omega\beta_{13}r_2){}_1F_1(1+a_0-bn0;2-b_0;-2\omega\beta_{13}r) - \left(\frac{r}{r_2}\right)^{2n\beta_{12}} {}_1F_1(a_0;b_0;-2\omega\beta_{13}r){}_1F_1(1+a_0-b_0;2-b_0;-2\omega\beta_{13}r_2)}{{}_1F_1(a_0;b_0;-2\omega\beta_{13}r_2){}_1F_1(1+a_0-b_0;2-b_0;-2\omega\beta_{13}r_1) - \left(\frac{r_1}{r_2}\right)^{2n\beta_{12}} {}_1F_1(a_0;b_0;-2\omega\beta_{13}r_1){}_1F_1(1+a_0-b_0;2-b_0;-2\omega\beta_{13}r_2)}$$

$$\left. \left. \cos\varphi_2' \right] \right\} d\omega\, dz'\, d\theta' \tag{5.11}$$

where

$$\varphi_0' = \omega[z - z' + \nu_{13}(r_1 - r)]$$

$$\varphi_1' = n\left[\theta - \theta' - \nu_{12}\ln\left(\frac{r}{r_1}\right)\right] + \varphi_0'$$

$$\varphi_2' = n\left[\theta - \theta' - \nu_{12}\ln\left(\frac{r}{r_1}\right)\right] - \varphi_0' \qquad (5.12)$$

Thus the solution of the general Dirichlet problem can be obtained by the simple superposition of (5.8) and (5.11).

6 Special Cases

In Sections 3 and 4 many detailed steps of derivation cannot be shown due to the limited space available here. One way to verify the correctness of (4.7) or (4.8) and (5.8) or (5.11) is to inspect whether they would reduce to simpler cases and those for isotropic media.

If we put $\nu_{13} = \nu_{23} = \nu_{33} = 0$, (4.7) and (5.8) reduce to those reported in [4]. Setting $\nu_{12} = \nu_{22} = 0$, (4.7) simplifies to

$$T(r, z) = \frac{1}{\beta_{13} r_0}\sum_{n=1}^{\infty}\frac{J_0(\lambda_n r)}{J_1(\lambda_n r_0)} \int_{-\ell}^{\ell} f(z')e^{-\lambda n/\beta_{13}|z-z'+\nu_{13}(r_0-r|}\, dz' \qquad (61.1)$$

where λ_n are the positive roots of

$$J_0(\lambda_n r_0) = 0 \qquad (6.2)$$

and (5.8) reduces to

$$T(r, z) = \frac{1}{\beta_{13}}\sum_{n=1}^{\infty}\frac{X_n(r)X_n'(r_2)}{N_n} \times \int_{-\ell}^{\ell} f_2(z')e^{-\lambda n/\beta_{13}|z-z'+\nu_{13}(r_2-r)|}\, dz' \qquad (6.3)$$

where

$$X_n = \frac{J_0(\lambda_n r)}{J_0(\lambda_n r_2)} - \frac{Y_0(\lambda_n r)}{Y_0(\lambda_n r_2)};\ N_n = r_2^2 X_n'^2(r_2) - r_1^2 X_n'^2(r_1)$$

and λ_n are the positive roots of

$$\frac{J_0(\lambda_n r_1)}{J_0(\lambda_n r_2)} - \frac{Y_0(\lambda_n r_1)}{Y_0(\lambda_n r_2)} = 0 \qquad (6.4)$$

Results (6.1) and (6.3) could have been readily written down from results for the corresponding isotropic medium according to [1].

We now consider a very special anisotropic medium with $\gamma = \nu_{23} - \nu_{12}\nu_{13} = 0$. For this case, (3.5) reduces to:

$$r\phi_{rr} + (1 + 2|n|\beta_{12} - 2\omega\beta_{13}r)\phi_r - (\beta_{13}\omega + 2|n|\beta_{12}\beta_{13}\omega)\,\phi = 0, \quad 0 \leqslant r < r_0 \qquad (6.5)$$

and (4.7) simplifies to

$$T(r, \theta, z) = \frac{1}{2\pi r_0}\sum_{n=0}^{\infty}\sum_{m=1}^{\infty}\frac{\epsilon J_n(\lambda_{nm}r)}{J_{n+1}(\lambda_{nm}r_0)} \times \int_{-\pi}^{\pi}\int_{-\ell}^{\ell} f(\theta', z')e^{-\lambda nm|z-z'+\nu_{13}(r_0-r)\theta|}\cos n \times \left[\theta - \theta' - \nu_{12}\ln\frac{r}{r_0}\right] dz'd\theta' \qquad (6.6)$$

where $\epsilon = 1$ if $n = 0$ and $\epsilon = 2$ otherwise; and λ_{nm} are the psoitive roots of

$$J_n(\lambda r_0) = 0 \qquad (6.7)$$

Again the result (6.6) can be readily written down from that for the corresponding isotropic problem [1] and also be obtained from the inverse of (3.4) where ϕ is the solution of (6.5) satisfying boundary condition (4.3).

7 Calculated Results for Solid Cylinder

Both (4.7) and (4.8) had been used for calculation, but (4.8) was found more convenient. Some calculated results of the temperature distribution are shown in Figs. 1–4 for the following data

$$\nu_{12} = 0.40; \quad \nu_{13} = 0.25; \quad \nu_{23} = 0.30$$
$$\beta_{12} = 1.0; \quad \beta_{13} = 1.0$$
$$f_0 = \begin{cases} T_0\cos\dfrac{\theta}{2}, & -\pi < \theta \leqslant \pi, \quad -r_0 \leqslant z \leqslant r_0 \\ 0, & \qquad\qquad\quad r_0 < z < -r_0 \end{cases}$$

where T_0 is a constant. In this case, the temperature field is given by the following expression:

$$\frac{T}{T_0} = \frac{2}{\pi}\left\{\sum_{n=1}^{\infty}\Lambda_n(\bar{z})\frac{J_0(\mu_n\bar{r})}{J_0(\mu_n)} + \frac{2}{\pi}\sum_{n=1}^{\infty}\frac{(-1)^{n+1}(\bar{r})^{n\beta_{12}}}{(4n^2-1)}\int_0^{\infty}\frac{e^{\bar{\omega}(\bar{r}-1)}}{\bar{\omega}}$$

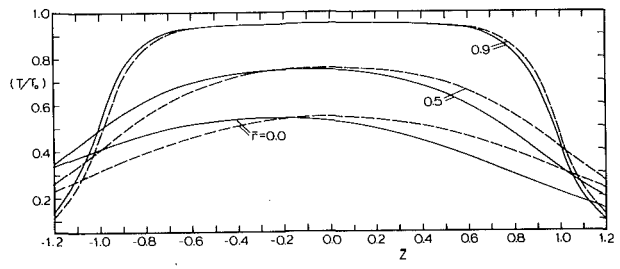

Fig. 1 Axial temperature variation of isotropic and anisotropic medium with radial position. —— anisotropic; - - - isotropic ($\beta_{12} = \beta_{13} = 1.0$, $\nu_{12} = 0.4$, $\nu_{13} = 0.25$, $\nu_{23} = 0.3$)

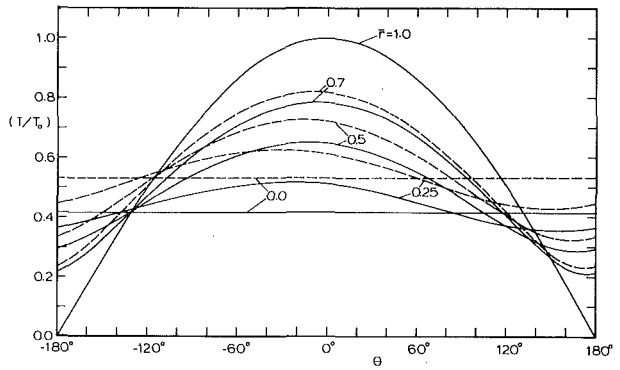

Fig. 2 Azimuthal (angular) temperature variation at different axial positions; $\bar{r} = 0.7$. —— anisotropic; - - - isotropic

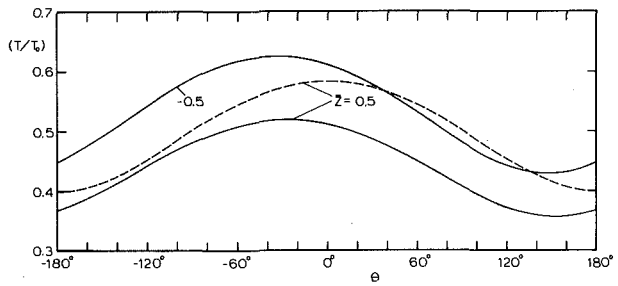

Fig. 3 Azimuthal (angular) temperature variation at different axial positions; $\bar{r} = 0.25$. —— anisotropic; - - - isotropic

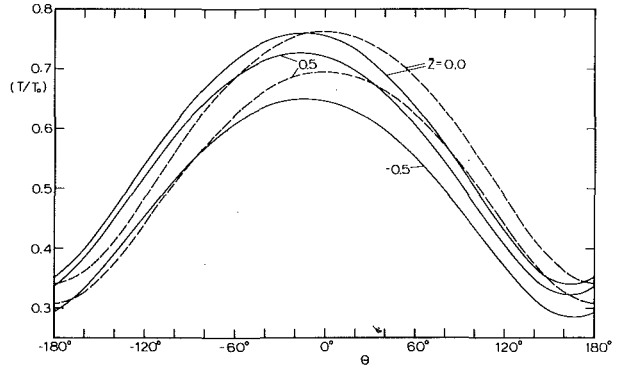

Fig. 4 Azimuthal (angular) temperature variation at different radial positions; - - - $\bar{z} = -0.5$; —— $\bar{z} = 0.5$

$$\cdot \sin\left(\frac{\bar{\omega}}{\beta_{13}}\right)\left[\frac{{}_1F_1(b_0-a_0;\,b_0;\,-2\bar{\omega}\bar{r})}{{}_1F_1(b_0-a_0;\,b_0;\,-2\bar{\omega})}\cos\bar{\varphi}_1 - \frac{{}_1F_1(a_0;\,b_0;\,-2\bar{\omega}\bar{r})}{{}_1F_1(a_0;\,b_0;\,-2\bar{\omega})}\cos\bar{\varphi}_2\right] d\bar{\omega}\Bigg\} \quad (7.1)$$

where μ_n are the positive roots of

$$J_0(\mu_n) = 0 \quad (7.2)$$

and

$$\Lambda_n(\bar{z}) = \begin{cases} \dfrac{1}{\mu_n}\{e^{-\mu_n[\bar{z}-1-\nu_{13}(\bar{r}-1)]} - e^{-\mu_n[\bar{z}+1-\nu_{13}(\bar{r}-1)]}\}; & \hat{z}_1, \hat{z}_2 \geq 0 \\ \dfrac{1}{\mu_n}\{2 - e^{-\mu_n|\bar{z}-1-\nu_{13}(\bar{r}-1)|} - e^{-\mu_n[\bar{z}-1-\nu_{13}(\bar{r}-1)]}\}; & \hat{z}_1 < 0, \hat{z}_2 > 0 \\ \dfrac{1}{\mu_n}\{e^{-\mu_n|\bar{z}+1-\nu_{13}(r-1)|} - e^{-\mu_n|\bar{z}-1-\nu_{13}(\bar{r}-1)|}\}; & \hat{z}_1, \hat{z}_2 \leq 0 \end{cases} \quad (7.3)$$

with

$$\hat{z}_1 = (\bar{z}-1) - \nu_{13}(\bar{r}-1);\ \hat{z}_2 = (\bar{z}+1) - \nu_{13}(\bar{r}-1)$$

$$\bar{z} = \frac{z}{r_0};\quad \bar{\omega} = \omega\beta_{13}r_0;\quad \bar{r} = \frac{r}{r_0}$$

$$\bar{\varphi}_1 = n[\theta - \nu_{12}\ln\bar{r}] + \frac{\bar{\omega}}{\beta_{13}}[\bar{z} - \nu_{13}(\bar{r}-1)]$$

$$\bar{\varphi}_2 = n[\theta - \nu_{12}\ln\bar{r}] - \frac{\bar{\omega}}{\beta_{13}}[\bar{z} - \nu_{13}(\bar{r}-1)] \quad (7.4)$$

In order to gain more insight into the role of parameter $\gamma(=\nu_{23}-\nu_{12}\nu_{13})$, some calculated results of the temperature distribution are shown in Tables 1 and 2. In each row of Table 1, the upper-level data are calculated for $\gamma = 0.2$ from (4.8) which is exact whereas the lower-level data are calculated by setting $\gamma = 0$ no matter whether it is actually zero or not, i.e., from (6.6) which is approximate. The lower-level data in each row of Table 2 represent the temperature distribution at $r = 0.7$ for an isotropic medium while the upper level data are for an anisotropic medium with $\gamma = 0.8$.

8 Discussions and Concluding Remarks

Calculated results in Figs. 1–4 have revealed what we have discussed on the effect of anisotropy in early papers [1–4]: The main role of ν_{12}, ν_{13} and γ is to shift the temperature profile from symmetric to asymmetric while that of β_{12} and β_{13} is to change the magnitude of temperature. Therefore $\nu_{ij}(i \neq j)$ and γ have been called shifting factors and β_{ij} scale factors. The shifting is in a spiral manner instead of rectilinear in an anisotropic medium homogeneous in rectangular coordinates [3].

The choice of values of β_{ij} and ν_{ij} in the calculation of Table 2 was made to isolate the effect of $\gamma(=0.8)$. It is seen that γ produces rotational and axial shifts as well as the change of magnitude of the temperature profile in comparison with that for an isotropic medium. However, even for such an unusually large value of γ, the shifting and scaling effects are not substantial.

For small values of $\gamma/(\beta_{12}\beta_{13})$ say <0.5, we may use (6.6) for the calculation of temperature distribution in the region not too much beyond that where non-vanishing data are prescribed, for instance $|\bar{z}| < 1.5$ in cases that have been calculated. The maximum error is 2 percent for $\gamma = 0.2$ and 20 percent for $\gamma = 0.8$, as can be seen from Tables 1 and 2. The error reduces for other values of r (not shown in this paper). Though the percentage of error increases rapidly as $|z|$ increases, yet the magnitude of temperature becomes vanishingly small for $|z| > 1.5$.

Consequently, though an isotropic material with $\nu_{23} = \nu_{12}\nu_{13}$ can be seldom found in nature or made artificially, the solution (6.6) may be employed for the approximate calculation of three-dimensional heat conduction in the general anisotropic medium for small values of $\gamma/(\beta_{12}\beta_{13})$.

It is interesting to note from the solution of (4.8) as well as (5.8) that $\beta_{23} = (\nu_{33} - \nu_{23}^2)^{1/2}$ does not appear as a parameter and ν_{23} enters the solution only through γ. Therefore γ may be considered as a parameter representing the coupling effect of three-dimensional anisotropy. Since ν_{ij} are usually small, γ cannot be large unless $\nu_{23} > 0$ and either one of ν_{12} and ν_{13} is negative.

Table 1 Nondimensional temperature distribution. $\beta_{12} = \beta_{13} = 1$, $\nu_{12} = 0.4$, $\nu_{13} = 0.125$, $\nu_{23} = 0.3$, $\gamma = 0.2$, $r = 0.7$. Data in lower level of each row are for $\gamma = 0$.

θ \ $\bar{z}$	-1.5	-1.3	-1.1	-0.9	-0.7	-0.5	-0.1	0.1	0.5	0.7	0.9	1.1	1.3	1.5
-180°	0.060	0.092	0.119	0.181	0.212	0.238	0.248	0.248	0.217	0.186	0.164	0.095	0.065	0.039
	0.058	0.089	0.116	0.179	0.212	0.238	0.249	0.249	0.219	0.189	0.167	0.098	0.065	0.040
-150°	0.072	0.120	0.181	0.278	0.328	0.356	0.369	0.367	0.327	0.279	0.222	0.119	0.071	0.042
	0.067	0.112	0.171	0.270	0.323	0.353	0.369	0.368	0.332	0.287	0.232	0.127	0.076	0.045
-120°	0.086	0.154	0.256	0.398	0.473	0.508	0.528	0.523	0.473	0.405	0.306	0.159	0.086	0.049
	0.080	0.145	0.245	0.388	0.467	0.505	0.528	0.525	0.479	0.414	0.317	0.169	0.093	0.053
-90°	0.099	0.185	0.322	0.503	0.603	0.646	0.672	0.666	0.607	0.520	0.385	0.199	0.104	0.057
	0.094	0.177	0.312	0.494	0.597	0.643	0.672	0.667	0.612	0.528	0.395	0.208	0.110	0.061
-60°	0.109	0.207	0.370	0.581	0.699	0.750	0.782	0.775	0.709	0.609	0.447	0.232	0.119	0.065
	0.105	0.202	0.363	0.575	0.695	0.747	0.782	0.775	0.713	0.615	0.454	0.238	0.123	0.068
-30°	0.113	0.218	0.396	0.625	0.754	0.809	0.846	0.838	0.770	0.663	0.486	0.253	0.129	0.070
	0.112	0.216	0.393	0.622	0.752	0.808	0.845	0.838	0.771	0.665	0.489	0.256	0.131	0.072
0°	0.112	0.218	0.398	0.630	0.763	0.819	0.858	0.851	0.783	0.676	0.496	0.260	0.133	0.073
	0.113	0.219	0.399	0.631	0.763	0.819	0.857	0.850	0.782	0.674	0.495	0.259	0.132	0.073
30°	0.106	0.205	0.375	0.596	0.724	0.779	0.817	0.811	0.748	0.647	0.478	0.253	0.130	0.072
	0.109	0.210	0.380	0.601	0.727	0.780	0.817	0.810	0.745	0.642	0.473	0.248	0.127	0.070
60°	0.095	0.182	0.329	0.527	0.641	0.692	0.727	0.723	0.667	0.579	0.434	0.231	0.121	0.068
	0.100	0.189	0.338	0.535	0.646	0.695	0.727	0.722	0.662	0.572	0.425	0.223	0.116	0.065
90°	0.081	0.151	0.266	0.429	0.523	0.567	0.597	0.594	0.548	0.478	0.366	0.197	0.107	0.061
	0.087	0.160	0.277	0.439	0.529	0.571	0.597	0.593	0.543	0.469	0.355	0.188	0.101	0.057
120°	0.067	0.118	0.193	0.314	0.382	0.419	0.441	0.440	0.404	0.354	0.282	0.156	0.090	0.052
	0.073	0.127	0.204	0.323	0.388	0.422	0.441	0.439	0.399	0.345	0.271	0.146	0.083	0.048
150°	0.058	0.091	0.128	0.205	0.248	0.277	0.291	0.292	0.262	0.230	0.198	0.114	0.073	0.044
	0.061	0.097	0.136	0.212	0.252	0.279	0.292	0.292	0.260	0.225	0.191	0.108	0.069	0.041
180°	0.060	0.092	0.119	0.181	0.212	0.238	0.248	0.248	0.217	0.186	0.164	0.095	0.064	0.039
	0.058	0.089	0.116	0.179	0.212	0.238	0.249	0.249	0.219	0.189	0.167	0.098	0.065	0.040

$\beta_{12} = \beta_{13} = 1.0$, $\nu_{12} = 0.4$, $\nu_{13} = 0.25$, $\nu_{23} = 0.3$, $\gamma = 0.2$, $r = 0.7$

Table 2 Nondimensional temperature distribution. $\beta_{12} = \beta_{13} = 1$, $\nu_{12} = \nu_{13} = 0$, $\nu_{23} = 0.8$, $\gamma = 0.8$, $r = 0.7$. Date in lower level of each row are for $\gamma = 0$.

θ \ z	-0.5	-0.3	-0.1	0.1	0.3	0.5	0.7	0.9	1.1	1.3	1.5
-180°	0.209	0.230	0.232	0.232	0.230	0.209	0.181	0.156	0.118	0.088	0.058
	0.221	0.239	0.241	0.241	0.239	0.221	0.194	0.162	0.112	0.076	0.048
-150°	0.309	0.323	0.324	0.319	0.311	0.285	0.240	0.179	0.107	0.068	0.047
	0.299	0.319	0.323	0.323	0.319	0.299	0.267	0.216	0.140	0.086	0.052
-120°	0.469	0.483	0.484	0.478	0.464	0.433	0.373	0.273	0.151	0.077	0.045
	0.453	0.476	0.484	0.484	0.476	0.453	0.408	0.321	0.197	0.109	0.062
-90°	0.616	0.634	0.639	0.632	0.614	0.579	0.507	0.376	0.208	0.099	0.052
	0.599	0.626	0.638	0.638	0.626	0.599	0.541	0.421	0.253	0.133	0.073
-60°	0.727	0.751	0.761	0.755	0.736	0.699	0.620	0.465	0.262	0.125	0.063
	0.708	0.739	0.754	0.754	0.739	0.708	0.640	0.496	0.296	0.153	0.082
-30°	0.795	0.824	0.838	0.835	0.816	0.779	0.698	0.530	0.305	0.148	0.075
	0.780	0.812	0.829	0.829	0.812	0.780	0.705	0.545	0.324	0.165	0.088
0°	0.812	0.846	0.864	0.864	0.846	0.812	0.734	0.565	0.332	0.165	0.840
	0.805	0.839	0.857	0.857	0.839	0.805	0.728	0.562	0.334	0.170	0.090
30°	0.779	0.816	0.835	0.838	0.824	0.795	0.724	0.565	0.339	0.173	0.091
	0.780	0.812	0.829	0.829	0.812	0.780	0.705	0.545	0.324	0.165	0.088
60°	0.699	0.736	0.755	0.761	0.751	0.727	0.668	0.530	0.327	0.173	0.093
	0.708	0.739	0.754	0.754	0.739	0.708	0.640	0.496	0.296	0.153	0.082
90°	0.579	0.614	0.632	0.639	0.634	0.616	0.571	0.463	0.294	0.162	0.090
	0.599	0.626	0.638	0.638	0.626	0.599	0.541	0.421	0.253	0.133	0.073
120°	0.433	0.464	0.478	0.484	0.483	0.469	0.440	0.368	0.245	0.143	0.083
	0.453	0.476	0.484	0.484	0.476	0.453	0.408	0.321	0.196	0.109	0.062
150°	0.285	0.311	0.319	0.324	0.323	0.309	0.291	0.256	0.182	0.117	0.072
	0.299	0.319	0.323	0.323	0.319	0.299	0.267	0.216	0.140	0.086	0.052
180°	0.209	0.230	0.232	0.232	0.230	0.209	0.181	0.156	0.118	0.088	0.058
	0.221	0.239	0.241	0.241	0.239	0.221	0.194	0.162	0.112	0.076	0.048

According to irreversible thermodynamics [10] and theory of integral equations [11, 12], k_{ii} and β_{ij} must be real and positive and $\nu_{ij} (i \neq j)$ can be either positive or negative, but no discussion has been made about the inequality: $\sigma \equiv (\beta_{12}\beta_{13} - \gamma^2)^{1/2} > 0$. It was found in an earlier paper [3] that if $\sigma \leq 0$ then Green's function does not exist and hence there is no solution of heat conduction problems. In fact, it can be shown that the inequality $\sigma > 0$ represents another limitation of the second law of thermodynamics [6]; the determinant of k_{ij} is positive and definite. This, however, does not rule out the existence of a solution of the field equations for $\sigma \leq 0$. Calculations had been done for $\sigma \gtrless 0$ with nonperiodical prescribed-data. A wave-like temperature profile was found for $\sigma < 0$ which obviously violates the second law.

In this paper, we have considered only the solution of the homogeneous differential equation with boundary condition or conditions of the first kind. Problems with boundary conditions of the second and third kinds can be solved by very much the same way as shown in Sections 2 and 3 [13]. For the solution of inhomogeneous differential equations, however, we had better use Green's functions.

References

1 Poon, K. C., and Chang, Y. P., "Transformation of Heat Conduction Problems from Anisotropic to Isotropic," Intern. Letters of Heat Mass Transfer, Vol. 5, No. 3, 1978 pp. 215–222; also "Solution of Anisotropic Problems of the First Class by Coordinate Transformation," ASME JOURNAL OF HEAT TRANSFER, May, 1979, pp. 340–345

2 Chang, Y. P., and Tsou, R. C. H., "Heat Conduction in an Anisotropic Medium Homogeneous in Cylindrical Regions—Unsteady State," ASME JOURNAL OF HEAT TRANSFER, Vol. 99, No. 1, 1977, pp. 41–46.

3 Chang, Y. P., "Analytical Solution for Heat Conduction in Anisotropic Media in Infinite, Semi-infinite and Two-plane-bounded Regions," *Intern. Journal Heat Mass Transfer*, Vol. 20, 1977, pp. 1019–1028.

4 Chang, Y. P. and Tsou, R. C. H., "Heat Conduction in an Anisotropic Medium Homogeneous in Cylindrical Regions—Steady State," ASME JOURNAL OF HEAT TRANSFER, Vol. 99, No. 1, pp. 132–134.

5 Chang, Y. P., "Heat Conduction in Isotropic and Anisotropic Media," Lecture Notes, Dept. Mech. Engg., SUNY, Buffalo.

6 Poon, K. C. and Chang, Y. P., "Three-dimensional Unsteady-state Heat Conduction in General Anisotropic Media," submitted for publication.

7 Sommerfield, A., *Partial Differential Equations in Physics*, Academic Press, 1949.

8 Slater, L. J., *Confluent Hypergeometric Functions*, Cambridge University Press, 1960.

9 Abramowitz, M. and Stegun, I. A., *Handbook of Mathematical Function*, National Bureau of Standards, 1970.

10 Prigogine, I., *Thermodynamics of Irreversible Processes*, Charles C. Thomas, Springfield, Ill., 1955.

11 Friedman, A., *Partial Differential Equations of Parabolic Type*, Prentice Hall, 1964.

12 Pogorzelski, W., *Integral Equations*, Pergamon Press, 1966.

13 Poon, K. C., "Analytical Solutions for Heat Conduction in Anisotropic Media Homogeneous in Cylindrical Coordinates at Rest and in Motion," Dept. of Mechanical Engineering. SUNY at Buffalo, Feb. 1979.

journal of heat transfer

technical notes

This section contains shorter technical papers. These shorter papers will be subjected to the same review process as that for full papers.

Flow through Successive Enlargement, Turning, and Contraction—Pressure and Fluid Flow Characteristics

E. M. Sparrow[1] and M. Charmchi[1]

Introduction

In heat exchange devices and in associated piping systems, it is not uncommon for a flowing fluid to pass consecutively through an enlargement and a contraction—with a possible turning of the flow between the two area changes. Such a sequence of events may occur, for example, in the header of a heat exchanger. In this paper, experiments on the enlargement-turning-contraction sequence are described.

In the experiments, a fully developed turbulent pipe flow was ducted to a spherical chamber as shown schematically in the inset of Fig. 1. The fluid exited the chamber through an outlet port whose position, defined by the angle ϕ, fixed the degree of turning of the flow. The exit port led into a tube of diameter equal to that of the delivery tube, the diameter purposefully being chosen to be small compared with that of the sphere. From the measurements, results were obtained for the net pressure loss due to the expansion-turning-contraction sequence and for the pressure distribution in the sphere. A flow visualization study was also performed to provide information on the flow pattern within the spherical chamber.

The experiments were carried out for pipe Reynolds numbers Re in the delivery and extraction tubes ranging from 10,000 to 60,000, and the turning angle ϕ was assigned values of 0, 90, and 150 deg. Air was the working fluid in the pressure-related experiments, whereas water was employed in the flow visualization studies.

The Experiments

The key component of the experimental apparatus was a hollow sphere, 24 cm (9.45 in.) in diameter, machined inside a plexiglass cube. Four openings were bored radially through the wall of the sphere. One of these served as the fluid inlet port. The others were employed, one at a time, as the fluid exit port. In terms of the angle ϕ defined in the inset of Fig. 1, the exit ports were situated at $\phi = 0$ (colinear inlet and exit), 90, and 150 deg. During any given data run, only one exit port was open; the others were sealed with plugs whose surfaces were machined to match precisely with the contour of the surface of the sphere.

In order to determine the pressure distribution around the circumference of the sphere, a total of 46 taps were installed. Twenty-four of these taps were deployed around the circumference in a vertical plane that passed through the center of the sphere and included the fluid inlet port; the other 22 were situated in the corresponding horizontal plane. For the flow visualization studies, the pressure taps served as dye injection ports.

Fluid was ducted to the spherical chamber via a 60-diameters-long seamless brass tube with an internal diameter of 1.27 cm (0.50 in.). An identical tube was employed to extract the fluid from the chamber. Each of these tubes was fitted with ten pressure taps distributed axially at intervals of 5.08 cm (2 in.).

As was noted earlier, air was employed as the working fluid in the pressure-related experiments. The air was supplied by a central compressor. A precision pressure regulator effectively suppressed flow fluctuations, as witnessed by the complete absence of tremors of the float of the rotameter used to meter the flow rate. One of two calibrated rotameters was used for the metering task, depending on the extent of the flow. The pressure distributions along the delivery and extraction tubes and around the circumference of the sphere were sensed by a Baratron capacitance-type pressure meter.

Water, supplied from a constant head tank, was the working fluid in the flow visualization experiments. The tank, in turn, was fed with both hot and cold water from the city mains. The temperature of the water at the inlet to the sphere was measured with a calibrated thermocouple, and flow metering was accomplished by a weigh tank situated at the downstream end of the extraction tube.

Visualization was facilitated by injection of dye into the spherical chamber. The dye was conveyed via plastic tubing from a reservoir suspended about 3½ m (~12 ft) above the test section to an 11-tap manifold. In turn, the taps of the manifold were connected to a selection of 11 taps on the sphere. By opening or closing clamps on the interconnecting lines, dye could be injected into the sphere either individually or simultaneously through the selected taps.

Results and Discussion

Pressure Losses. The net pressure loss due to the expansion, turning, and contraction processes was determined by utilizing the axial pressure distributions along the delivery and extraction tubes.

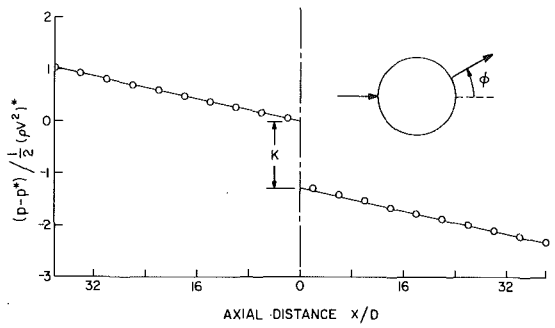

Fig. 1 Representative pressure distributions along the fluid delivery and extraction tubes, Re = 20,000 and $\phi = 0$ deg. The inset shows a schematic of the physical situation under study.

[1] Department of Mechanical Engineering, University of Minnesota, Minneapolis, Minn. 55455

Contributed by the Heat Transfer division for publication in the JOURNAL OF HEAT TRANSFER. Manuscript received by the Heat Transfer Division January 9, 1979.

For each case (defined by the pipe Reynolds number Re and the turning angle ϕ), the axial pressure distributions were plotted as shown in Fig. 1. This figure, which is typical of the others, is for Re = 20,000 and ϕ = 0 deg. The pressure data for the delivery tube are plotted in the left-hand portion of the figure, while those for the extraction tube are plotted in the right-hand portion.

The pressure distributions are in dimensionless form in terms of the quantity

$$(p - p^*)/\tfrac{1}{2}(\rho V^2)^* \tag{1}$$

In this expression, p^* is a reference pressure determined by extrapolating the linear pressure distribution in the delivery tube to the inlet cross section of the spherical chamber. Furthermore, $(\rho V^2)^* = \dot{m}^2/\rho^* A^2$, where ρ^* is the density at p^* and T^* (the entire system was isothermal), A is the cross-sectional area of the delivery tube, and $\dot{m}$ is the rate of mass flow. The abscissa of the figure is the dimensionless axial distance along the respective tubes, with x denoting the axial coordinate and D denoting the internal diameter of the tube.

The figure shows that the pressure distribution in the delivery tube is precisely linear and also that a linear distribution is re-established in the extraction tube downstream of the hydrodynamic redevelopment region. The straight lines shown in the figure are least-squares fits of the data in the aforementioned linear regions. As seen in the figure, the respective lines have been extrapolated to the inlet and exit cross sections of the spherical chamber. In the absence of the chamber, the lines would be continuous. Therefore, their vertical separation gives the net pressure loss Δp_{net} due to all processes related to its presence. A dimensionless loss coefficient K may then be defined as

$$K = \Delta p_{net}/\tfrac{1}{2}(\rho V^2)^* \tag{2}$$

The magnitude of K is indicated in Fig. 1 for the case in question.

A listing of the K values for the three turning angles ϕ = 0 (no turning), 90, and 150 deg is presented in Table 1. Inspection of the table indicates that the pressure loss for the turned flows (ϕ = 90 and 150 deg) is somewhat greater than that for the unturned flows (ϕ = 0 deg), but the increment due to turning is only about 0.2 of a velocity head. Thus, the turning loss is substantially smaller than the head loss for the abrupt expansion which, as will be documented shortly, is about one velocity head. Furthermore, the turning loss appears to be independent of the turning angle, at least for angles greater than 90 deg. This finding takes on added significance when note is taken of the fact that the ϕ = 150 deg case represents a situation where the flow exits in a direction that is very close to the direction in which it entered.

The K values are quite insensitive to the Reynolds number, as is consistent with the fact that the losses in question are inertial. The largest variation of K with Re (about six percent) is for the unturned flows.

Distributions of Pressure in the Chamber. Pressure distributions around the circumference of the spherical chamber were measured for six cases, encompassing Reynolds numbers of 10,000, 30,000, and 60,000 and turning angles ϕ of 0 and 150 deg. Only illustrative results can be presented here owing to space limitations, but all of the data are available in [1].

For a dimensionless presentation, the pressure data are reported in the form

$$(p - p_{min})/\tfrac{1}{2}(\rho V^2)^* \tag{3}$$

Table 1 Pressure Loss Coefficient, K

	K		
Re	ϕ = 0 deg	90 deg	150 deg
10,000	1.25	1.48	1.45
20,000	1.28	1.46	1.46
30,000	1.31	1.48	1.47
40,000	1.31	1.49	1.48
60,000	1.33	1.48	1.47
Average	1.30	1.48	1.47

where p is the local pressure and p_{min} is the lowest of the pressures measured in the chamber. Figure 2 shows the distribution of this dimensionless pressure variable around the circumference in a vertical plane passing through the center of the sphere and intercepting the inlet port. The given information is for ϕ = 0 deg. At each indicated circumferential location, two numbers are listed, one above the other. The bottom number corresponds to Re = 10,000, whereas the top number is for Re = 30,000. The results for Re = 60,000 are so close to those for Re = 30,000 that a separate listing is not warranted. It is noteworthy that the illustrated pressure distributions are also an accurate representation for those measured around the circumference in a horizontal plane. They are also representative of measurements made for the ϕ = 150 deg turning angle.

From Fig. 2, it can be seen that aside from a narrow region affected by the jet-like impingement of the incoming flow, the pressures on the surface of the sphere are nearly uniform. This suggests that, aside from a core flow which issues from the inlet and impinges on the opposite wall, most of the chamber is filled with slow moving fluid.

If the impingement-affected taps are excluded, an average chamber pressure can be evaluated from the data at the other taps. For each case, this average may be compared with p^* (the pressure at the inlet of the sphere). Such a comparison yields the head loss due to the abrupt expansion. For the six cases for which data were available, the abrupt-expansion head loss was in the range from 0.975 to 0.989 × $\tfrac{1}{2}(\rho V^2)^*$. This finding is consistent with the available predictions for abrupt expansions with large area ratios [2].

Flow Patterns within the Chamber. The patterns of fluid flow within the chamber were determined by extensive visual observations of the motions of injected dye streams. Photographs of the dye stream patterns are available in [1].

In general, aside from the jet-like core, the main feature of the flow field is a recirculation which carries fluid circumferentially along the walls toward the inlet. Since this flow direction is opposite to that of the core, it may be termed a backflow. At selected circumferential locations, the fraction of time at which backflow prevailed was determined by observations extending over three to five minute intervals. Illustrations of these findings are presented here, and the remainder are recorded in [1].

Figures 3 and 4 convey information about the backflow as it was observed in a horizontal plane passing through the center of the sphere. These figures correspond respectively to turning angles ϕ of 0 and 150 deg. In the figures, the number adjacent to each selected circumferential location indicates the time percentage when there is backflow. The Reynolds number for both cases is about 40,000.

It is seen from these figures that backflow fully predominates in the portion of the chamber where the jet-like core impinges. This backflow is, in essence, a wall jet which is driven by momentum supplied by the impingement of the core flow and its subsequent deflection. As the wall jet streams backward along the surface of the sphere, its momentum is dissipated both by wall friction and by entrainment processes along its outer boundary. The entrainment effects become increasingly important as the wall jet broadens and the proximity of the strong (forward flowing) core is felt. It is these processes which bring about the diminished backflow percentages that are in evidence in the figures. As seen in Fig. 4, the presence of the ϕ = 150 deg exit port tends to renew the backflow on its adjacent surface and deplete the backflow on the opposite part of the surface.

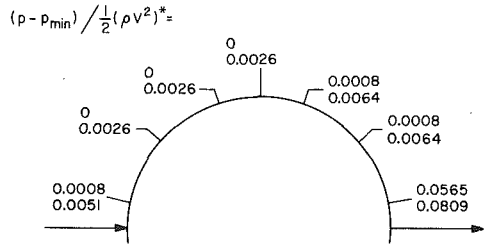

Fig. 2 Representative distributions of pressure around the circumference of the spherical chamber, Re = 10,000 to 60,000 and ϕ = 0 deg

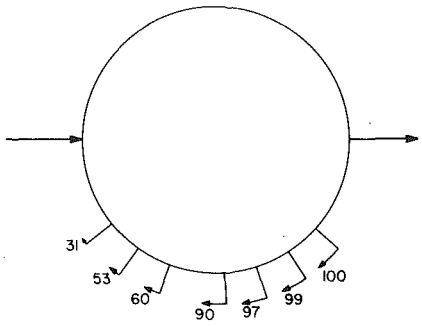

Fig. 3 Time percentages indicating when backflow prevails along the wall of the chamber, Re ~ 40,000 and $\phi = 0$ deg

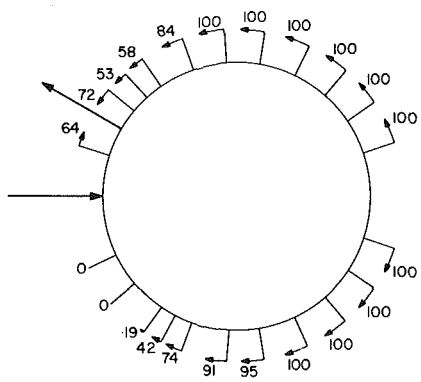

Fig. 4 Time percentages indicating when backflow prevails along the wall of the chamber, Re ~ 40,000 and $\phi = 150$ deg

Acknowledgment

This research was performed under the auspices of NSF grant ENG77-06762.

References

1 Charmchi, M., "Pressure Drop Characteristics of Partially Blocked Pipe Flows and Expansion Chambers," Thesis, Department of Mechanical Engineering, University of Minnesota, Minneapolis, Minn., 1979.

2 Streeter, V. L. and Wylie, E. B., *Fluid Mechanics*, Seventh Edition, McGraw-Hill, New York, 1979.

Two-Dimensional Scattering from a Medium of Finite Thickness[1]

D. C. Look[2]

Nomenclature

C_{sca} = scattering cross section
c = scattering cross section divided by the effective particle volume
I_{exp} = experimental intensity leaving the medium normal to the irradiated surface
I_i = incident flux at $r = 0$
L = depth of distilled water (medium) in tank
N = particle number density
r = radial distance from center of incident (laser) beam
r_0 = effective radius of incident (laser) beam
V_p = volume of paint
V_{sp} = effective volume of a scatterer
V_w = volume of water
ξ = volume of latex paint per unit volume of water plus latex paint
ξ^1 = volume of scattering centers in the paint per unit volume of water plus latex paint
τ_0 = optical depth ($= NC_{sca}L$)
τ_r = radial optical coordinate ($= NC_{sca}r$)
τ_{r_0} = effective optical radius of the incident laser beam ($= NC_{sca}r_0$)

Introduction

The basic assumption of most reported experimental investigations of two-dimensional scattering is that the scattering medium is one of essentially infinite optical depth (e.g., [1, 2]). A few studies have included the finite optical depth as an indirect parameter [3–5].

The objectives of this note are to present (1) the effects of a finite depth on the power escaping normal to the irradiated surface of a scattering volume with a flat black bottom and (2) correct a previously published definition.

[1] The work was supported in part by a grant from the National Science Foundation (ENG 74-22107)

[2] Professor, Thermal Radiative Transfer Group, Mechanical and Aerospace Engineering, University of Missouri—Rolla, Rolla, MO 65401. Mem. ASME.

Contributed by the Heat Transfer Division for publication in the JOURNAL OF HEAT TRANSFER. Manuscript received by the Heat Transfer Division November 7, 1978.

Investigation

Experiment. The apparatus used in this experimental investigation has been discussed in detail in [2, 6], and [7]. In the works previously reported, the depth was chosen so that the power received as a result of reflection from the bottom was negligible (an approximate model of a semi-infinite volume). A depth of approximately 21.6 cm was quite adequate when the substrate was black and diffuse [7]. In the case of the work reported here, the depth was decreased. In all instances, the medium was distilled and filtered water with latex paint serving as the scattering centers. The working procedure of this investigation was exactly like that of [2, 6], and [7].

Theory. The optical coordinate, τ, was presented in [2] as

$$\tau = \xi c x.$$

The word definitions of ξ and c are, however, incompatible; thus a slight revision is required. To understand this required revision notice that

$$\begin{aligned}\tau &\equiv \sigma x \\ &\equiv NC_{sca}x \\ &= NV_{sp}\left(\frac{C_{sca}}{V_{sp}}\right)x \\ &= NV_{sp}cx \\ &= \frac{n}{V_p + V_w}V_{sp}cx \\ &= \frac{nV_{sp}}{V_p + V_w}cx \\ &= \xi^1 cx\end{aligned}$$

Thus, in order for c to be consistent with its word definition, ξ^1 must be used instead of ξ to evaluate the optical coordinate. Notice that the c is unaffected by this correction.

This inadvertant confusion of the definitions resulted in an error in the optical coordinates τ_r, τ_0 and τ_{r_0} of [2]. By using this consistent pair, $\xi^1 C$, only a slight correction of the resultants of [2] is required.

In the illustrations that follow, theoretical curves are designated by the solid lines. In Figs. 1 and 2, the theory responsible has been presented in [2]. The theory of Fig. 3 will be published in the open literature later by different authors [8] and is presented here only as an aid for comparison. This upcoming publication will present the back scattered intensity from a finite two-dimensional medium exposed to a Gaussian beam of radiation. The parameters of importance will be the optical thicknesses (used here) and the single scattering

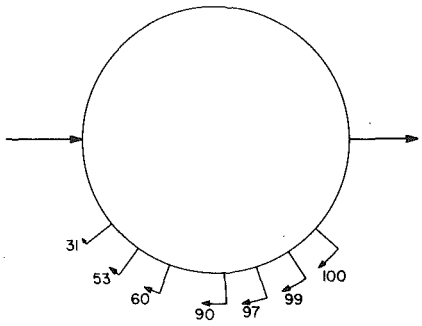

Fig. 3 Time percentages indicating when backflow prevails along the wall of the chamber, Re ~ 40,000 and $\phi = 0$ deg

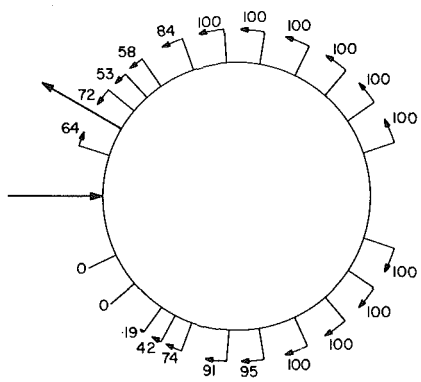

Fig. 4 Time percentages indicating when backflow prevails along the wall of the chamber, Re ~ 40,000 and $\phi = 150$ deg

Acknowledgment

This research was performed under the auspices of NSF grant ENG77-06762.

References

1 Charmchi, M., "Pressure Drop Characteristics of Partially Blocked Pipe Flows and Expansion Chambers," Thesis, Department of Mechanical Engineering, University of Minnesota, Minneapolis, Minn., 1979.

2 Streeter, V. L. and Wylie, E. B., *Fluid Mechanics*, Seventh Edition, McGraw-Hill, New York, 1979.

Two-Dimensional Scattering from a Medium of Finite Thickness[1]

D. C. Look[2]

Nomenclature

C_{sca} = scattering cross section
c = scattering cross section divided by the effective particle volume
I_{exp} = experimental intensity leaving the medium normal to the irradiated surface
I_i = incident flux at $r = 0$
L = depth of distilled water (medium) in tank
N = particle number density
r = radial distance from center of incident (laser) beam
r_0 = effective radius of incident (laser) beam
V_p = volume of paint
V_{sp} = effective volume of a scatterer
V_w = volume of water
ξ = volume of latex paint per unit volume of water plus latex paint
ξ^1 = volume of scattering centers in the paint per unit volume of water plus latex paint
τ_0 = optical depth ($= NC_{sca}L$)
τ_r = radial optical coordinate ($= NC_{sca}r$)
τ_{r_0} = effective optical radius of the incident laser beam ($= NC_{sca}r_0$)

Introduction

The basic assumption of most reported experimental investigations of two-dimensional scattering is that the scattering medium is one of essentially infinite optical depth (e.g., [1, 2]). A few studies have included the finite optical depth as an indirect parameter [3–5].

The objectives of this note are to present (1) the effects of a finite depth on the power escaping normal to the irradiated surface of a scattering volume with a flat black bottom and (2) correct a previously published definition.

[1] The work was supported in part by a grant from the National Science Foundation (ENG 74-22107)

[2] Professor, Thermal Radiative Transfer Group, Mechanical and Aerospace Engineering, University of Missouri—Rolla, Rolla, MO 65401. Mem. ASME.

Contributed by the Heat Transfer Division for publication in the JOURNAL OF HEAT TRANSFER. Manuscript received by the Heat Transfer Division November 7, 1978.

Investigation

Experiment. The apparatus used in this experimental investigation has been discussed in detail in [2, 6], and [7]. In the works previously reported, the depth was chosen so that the power received as a result of reflection from the bottom was negligible (an approximate model of a semi-infinite volume). A depth of approximately 21.6 cm was quite adequate when the substrate was black and diffuse [7]. In the case of the work reported here, the depth was decreased. In all instances, the medium was distilled and filtered water with latex paint serving as the scattering centers. The working procedure of this investigation was exactly like that of [2, 6], and [7].

Theory. The optical coordinate, τ, was presented in [2] as

$$\tau = \xi c x.$$

The word definitions of ξ and c are, however, incompatible; thus a slight revision is required. To understand this required revision notice that

$$\begin{aligned}\tau &\equiv \sigma x \\ &\equiv NC_{sca}x \\ &= NV_{sp}\left(\frac{C_{sca}}{V_{sp}}\right)x \\ &= NV_{sp}cx \\ &= \frac{n}{V_p + V_w}V_{sp}cx \\ &= \frac{nV_{sp}}{V_p + V_w}cx \\ &= \xi^1 cx\end{aligned}$$

Thus, in order for c to be consistent with its word definition, ξ^1 must be used instead of ξ to evaluate the optical coordinate. Notice that the c is unaffected by this correction.

This inadvertant confusion of the definitions resulted in an error in the optical coordinates τ_r, τ_0 and τ_{r_0} of [2]. By using this consistent pair, $\xi^1 C$, only a slight correction of the resultants of [2] is required.

In the illustrations that follow, theoretical curves are designated by the solid lines. In Figs. 1 and 2, the theory responsible has been presented in [2]. The theory of Fig. 3 will be published in the open literature later by different authors [8] and is presented here only as an aid for comparison. This upcoming publication will present the back scattered intensity from a finite two-dimensional medium exposed to a Gaussian beam of radiation. The parameters of importance will be the optical thicknesses (used here) and the single scattering

albedo (ω of approximately unity used here). The other assumptions of the theoretical point of view are that the medium is infinite in the radial direction, homogeneous, non-emitting and scatters isotropically while the bottom surface is black.

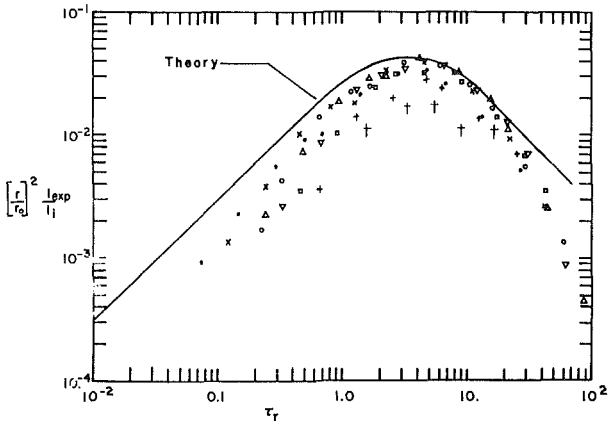

Fig. 1 The weighted ratio of the normal emergent intensity to the flux incident normally upon the scattering volume $(r/r_0)^2(I_{exp}/I_i)$ versus τ_r for a 10.8 cm deep medium with a flat black, diffuse substrate: ● $r/r_0 = 15$, x $r/r_0 = 25$, ○ $r/r_0 = 35$, △ $r/r_0 = 50$, ▽ $r/r_0 = 70$, □ $r/r_0 = 100$, + $r/r_0 = 140$, and † $r/r_0 = 180$

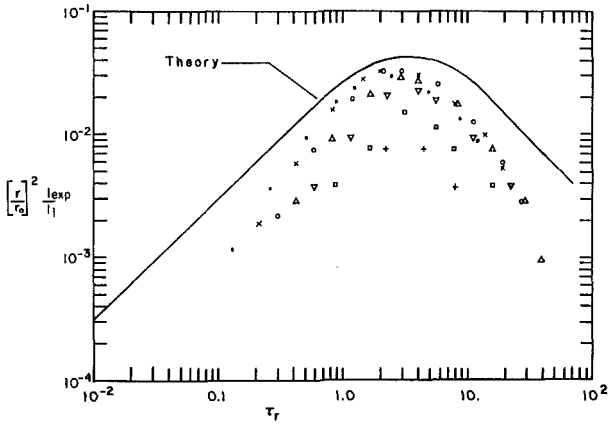

Fig. 2 The weighted ratio of the normal emergent intensity received to the flux incident normally upon the scattering volume $(r/r_0)^2(I_{exp}/I_i)$ versus τ_r for a 5.4 cm deep medium with a flat black diffuse substrate (Same legend as Fig. 1 except no $r/r_0 = 180$)

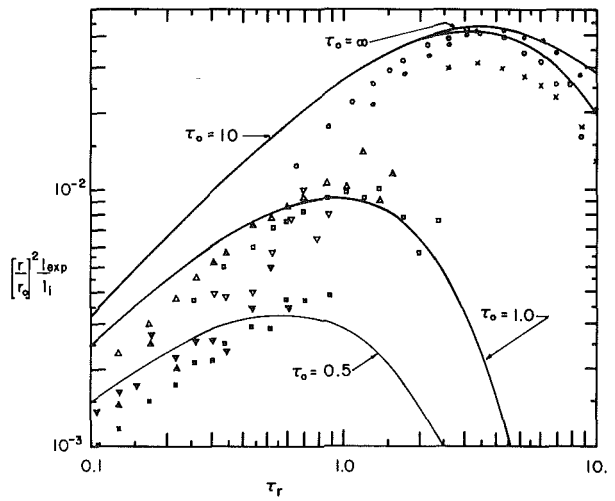

Fig. 3 The weighted ratio of normal emergent intensity received to the flux incident normally upon the scattering volume $(r/r)^2(I_{exp}/I_i)$ versus τ_r for a flat black, diffuse substrate: $\tau_0 = 9.4$ and depths of ● (21.6 cm), ○ (10.8 cm), and x (5.4 cm); $\tau_0 = 0.94$ and depths of ▽ (21.6 cm), △ (10.8 cm), and □ (5.4 cm); and $\tau_0 = 0.47$ and depths of ▼ (21.6 cm), ▲ (10.8 cm) and ■ (5.4 cm)

Results

The results of this investigation are presented in Figs. 1–3. Figs 1 and 2 present $(r/r_0)^2$ (I_{exp}/I_i) versus τ_r with the radial coordinate of the detector as the parameter. The solid curves (theory) come directly from Fig. 8 of [2]. These are typical of the data presented in [2, 6], and [7], with the slight exceptions that the finite depth effects are noticeable. The theory curves of these two figures are for an infinite depth (i.e., $\tau_0 \to \infty$) and are presented here to emphasize the effect of a finite depth. Thus, as for Fig. 1, the water depth of 10.8 cm provides a medium whose scattering characteristics are noticeably different than that of a semi-infinite medium. The peak and general shape of the experimental points are similar to those of the theoretical curve. As the depth of the scattering medium decreases (Fig. 2) the spread of the experimental data points depart significantly from the semi-infinite case (theory). Neither shape or peak position may be pin-pointed. Thus, the received energy is uncharacteristic of the semi-infinite theory.

Fig. 3 illustrates the experimental data of Figs. 1 and 2, but it is regrouped according to the parameter $\tau_0(=NC_{sca}L)$. The theoretical curves are developed for a model more characteristic of this experimental situation [9]. The theoretical curves and the experimental data are in general agreement. That is, though dispersed, the data points follow the general increasing-to-a-peak-and-decreasing characteristic of the theory curves.

Conclusion

An investigation of the effects of finite depth on the two-dimensional scattering from a planar medium with a highly absorbing (flat black) bottom has been carried out. Data representative of the power emerging normally from the top surface of the scattering medium are included. Ordinary flat white latex paint was used as the source of scattering centers in a medium of distilled water. The agreement between theory and experiment using only one empirically determined coefficient (c) is at least fair. That is, the results of the experimental data and the values from the theory are in fair agreement in magnitude, shape, and position. Careful measurement of the volume of scattering centers has been used to correct the optical dimension in the presentation of data.

Acknowledgment

This work has been supported in part by the National Science Foundation Grant (ENG 74-22107). Thanks are given to Mr. R. Dewhurst and Mr. K. Merrill for their assistance in this laboratory effort and to Drs. A. L. Crosbie and H. F. Nelson for helpful suggestions and discussions.

References

1 Il'ich, G. K. and Ivanov, A. P., "Diffuse Reflection of Light from The Optically Thick Layers of Scattering Media," *Atm. and Ocean Phys.*, Vol. 1, 1965, pp. 343–347.

2 Look, D. C., Nelson, H. F., Crosbie, A. L., and Dougherty, R. L., "Two-Dimensional Multiple Scattering: Comparison of Theory and Experiment," ASME JOURNAL OF HEAT TRANSFER, Vol. 100, No. 9, Aug. 1978, pp. 480–485.

3 Ivanov, A. P. and Sherbaf, I. D., "Optical Conditions in a Turbid Medium Illuminated by a Narrow Light Beam," *Opt. and Spect.*, Vol. 18, 1965, pp. 391–394.

4 Ivanov, A. P. and Sherbaf, I. D., "Attenuation of a Narrow Beam in a Turbid Medium," *J. Appl. Spect.*, Vol. 5, 1966, pp. 147–151.

5 Ivanov, A. P. and Sherbaf, I. D., "Influence of the Angular Dispersion of a Beam of Light on its Penetration into a Scattering Medium," *Atm. and Ocean*, Vol. 2, 1966, pp. 188–190.

6 Look, D. C. and Tripses, J. G., "Preliminary Study of Two-Dimensional Multiple Scattering," *Letters in Heat and Mass Transfer*, Vol. 4, No. 2, 1977, pp. 129–139.

7 Look, D. C., "Exhibit of Unwanted Effects in a Two-Dimensional Multiple Scattering Experiment," *Letters in Heat and Mass Transfer*, Vol. 5, No. 3, 1978, pp. 175–186.

8 Crosbie, A. L. and Dougherty, R. L., personal communication, University of Missouri-Rolla, Rolla, MO.

9 Dougherty, R. L., "Two-Dimensional Isotropic Scattering in a Semi-Infinite Cylindrical Medium," Ph.D. Dissertation, May 1978, University of Missouri-Rolla, Rolla, Mo. (In preparation for open literature publication).

Diffuse Radiation View Factors from Differential Plane Sources to Spheres

N. H. Juul[1]

Nomenclature

XYZ = cartesian coordinates
A = area
F = diffuse radiation view factor
IN = integrand
H = perpendicular distance from center of sphere 2 to plane of dA_1
L = distance from H-axis to dA_1 in the plane of dA_1
x = distance from dA_1 to center of sphere 2
r = radius of sphere 1 or cylinder 1
ℓ = distance between dA_1 and dA_2
s = separation between sphere 2 and sphere 1 or cylinder 1
R = radius of sphere 2
$\vec{n}$ = unit vector normal to dA
θ = angle between normal to dA and direction of line ℓ
λ = angular orientation angle between normal $\vec{n}_1$ and X-axis

Subscripts

1 and 2 = surfaces
L = limit of angle

Introduction

The diffuse radiation view factor, F_{dA_1-2}, from a differential plane source, dA_1, to a sphere, 2, is derived by using a new integration scheme. In this scheme the sphere is replaced by that part of a concave spherical surface, A_2, which intercepts the same amount of radiant energy and lies on a spherical enclosure, the center of which is at dA_1. The advantage of this configuration is that the expression of the integrand is obtained in a form which is readily integrated over A_2 in closed form. The results agree with the ones derived by Cunningham [1], Hottel [2], and Chung and Sumitra [3] using different schemes or techniques. Interesting results are obtained by letting the differential plane source traverse two and three dimensional surfaces of simple geometry which are of interest in current design applications. Finally, the limitations for using F_{dA_1-2} to synthesize the view factor from a finite surface to the sphere are set forth here.

Analysis

The diffuse radiation view factor from a differential plane source, dA_1, to a sphere 2 is determined by

$$F_{dA_1-2} = \int_{A_2} \cos\theta_1 \cos\theta_2/(\pi\ell^2) dA_2 \tag{1}$$

The integration over the surface of the sphere can be replaced by the integration over any arbitrary surface, A_2, the solid angle of which is equal to that subtended by the sphere as viewed from dA_1.

Selecting A_2 as the concave spherical surface abd, lying on the spherical enclosure with radius $\ell = |\vec{\ell}| = \sqrt{x^2 - R^2}$, shown in Fig. 1($b$), the integrand of equation (1) is obtained directly as a function of ϵ_1, λ and β_2 in a form which is suitable for closed form integration. ϵ_1 is the angle from the X-axis to $\vec{\ell}$. β_2 is the angle from the plane of $Z = 0$ to dA_2, in planes of X-constant. $\cos\theta_1 = \vec{\ell}\cdot\vec{n}_1/|\vec{n}_1\cdot\vec{\ell}| = \cos\epsilon_1 \cos\lambda + \sin\epsilon_1 \sin\lambda \cos\beta_2$, $\cos\theta_2 = 1$ and $dA_2 = (\ell d\epsilon_1)(\ell \sin\epsilon_1 d\beta_2)$ the integrand becomes

$$IN = 1/\pi(\cos\epsilon_1 \cos\lambda + \sin\epsilon_1 \sin\lambda \cos\beta_2) \sin\epsilon_1$$

Fig. 1 shows the geometry for the integration scheme and the limits of integration when the plane of dA_1 intersects the sphere. Utilizing the symmetry in respect to plane $Z = 0$, IN is first integrated with respect to β_2 and then ϵ_1. The integration over ϵ_1 is carried out in two steps. In the first step the integration is carried out over the spherical segment of A_2 where $\epsilon_{1L} \le \epsilon_1 \le \epsilon_{1L1}$ and $0 \le \beta_2 \le \pi$. The second is over the remainder of A_2 where $\epsilon_{1L1} \le \epsilon_1 \le \sin^{-1}(R/x)$ and $0 \le \beta_2 \le \beta_{2L}$ as shown in Fig. 1. The limits of ϵ_{1L}, ϵ_{1L1} and β_{2L} depend on λ. Thus equation (1) becomes

$$F_{dA_1-2} = 2\left(\int_{\epsilon_{1L}}^{\epsilon_{1L1}} \int_0^{\pi} IN\, d\epsilon_1 d\beta_2 + \int_{\epsilon_{1L1}}^{\sin^{-1}(R/x)} \int_0^{\beta_{2L}} IN\, d\epsilon_1 d\beta_2\right) \tag{2}$$

The integration of the first double integral of equation(2) yields

$$\sin^2\epsilon_1 \cos\lambda\Big]_{\epsilon_{1L}}^{\epsilon_{1L1}}$$

The limit of integration β_{2L} shown in Fig. 1(a) is given by

$$\beta_{2L} = \pi - \cos^{-1}\frac{\ell\cos\epsilon_1 \tan(\pi/2 - \lambda)}{\ell \sin\epsilon_1} = \cos^{-1}(-\cot\epsilon_1 \cot\lambda)$$

Performing the integration of the second term in equation (2) with respect to β_2 and upon substituting the limits, one obtains

$$\frac{2}{\pi}\int_{\epsilon_{1L1}}^{\sin^{-1}(R/x)} [\sin\epsilon_1 \cos\epsilon_1 \cos\lambda \cos^{-1}(-\cot\epsilon_1 \cot\lambda) + \sin^2\epsilon_1 \sin\lambda \sin(\cos^{-1}(-\cot\epsilon_1 \cot\lambda))] d\epsilon_1 \tag{2a}$$

The first term is integrated by parts and becomes

$$\frac{1}{\pi}\left(\left[\sin^2\epsilon_1 \cos\lambda \cos^{-1}(-\cot\epsilon_1 \cot\lambda) + \cos^2\lambda \sin^{-1}\left(\frac{\cos\epsilon_1}{\sin\lambda}\right)\right]_{\epsilon_{1L1}}^{\sin^{-1}(R/x)}\right.$$

The second term of equation (2a) becomes

$$\frac{2}{\pi}\int_{\epsilon_{1L1}}^{\sin^{-1}(R/x)} -\sqrt{\sin^2\lambda - \cos^2\epsilon_1}\, d(\cos\epsilon_1) = -\frac{1}{\pi}\left[\cos\epsilon_1 \sqrt{\sin^2\lambda - \cos^2\epsilon_1} + \sin^2\lambda \sin^{-1}\left(\frac{\cos\epsilon_1}{\sin\lambda}\right)\right]_{\epsilon_{1L1}}^{\sin^{-1}(R/x)}$$

Finally, upon substituting the results of the integrations above, we obtain the general expression for the view factor as

$$F_{dA_1-2} = \sin^2\epsilon_1 \cos\lambda\Big]_{\epsilon_{1L}}^{\epsilon_{1L1}} + \frac{1}{\pi}[\cos\lambda \sin^2\epsilon_1 \cos^{-1}(-\cot\lambda \cot\epsilon_1) - \cos\epsilon_1 \sqrt{\sin^2\epsilon_1 - \cos^2\lambda} - \sin^{-1}(\cos\epsilon_1/\sin\lambda)]_{\epsilon_{1L1}}^{\sin^{-1}(R/x)} \tag{3}$$

The integral limits for ϵ_1 depend upon λ. There are three cases.

For $0 \le \lambda \le \pi/2 - \sin^{-1}(R/x)$ the plane of dA_1 does not intersect the sphere. The disk of the sphere is fully visible. The integral limits are $\epsilon_{1L} = 0$ and $\epsilon_{1L1} = \sin^{-1}(R/x)$. Equation (3) yields

$$F_{dA_1-2} = (R/x)^2 \cos\lambda \tag{4}$$

For $\pi/2 - \sin^{-1}(R/x) \le \lambda \le \pi/2$ the plane of dA_1 intersects the sphere and more than one half of the disk is visible. The limits are $\epsilon_{1L} = 0$ and $\epsilon_{1L1} = \pi/2 - \lambda$. Equation (3) becomes

$$F_{dA_1-2} = \frac{1}{\pi}[(R/x)^2 \cos\lambda \cos^{-1}(-\cot\lambda \sqrt{(x/R)^2 - 1}) - \sqrt{1 - (R/x)^2}\sqrt{(R/x)^2 - \cos^2\lambda} - \sin^{-1}(\sqrt{1 - (R/x)^2}/\sin\lambda) + \pi/2] \tag{5}$$

For $\pi/2 \le \lambda \le \pi/2 + \sin^{-1}(R/x)$ less than one half of the disk of the sphere is visible. $\epsilon_{1L} = \epsilon_{1L1} = \lambda - \pi/2$ is substituted into equation (3). The first term is zero but the second yields equation (5).

Expressions (4) and (5) are identical to the ones obtained by Cun-

[1] Associate Professor of Mechanical Engineering, SUNY at Buffalo, Amherst, NY 14260.

Contributed by the Heat Transfer Division for publication in the JOURNAL OF HEAT TRANSFER. Manuscript received by the Heat Transfer Division August 4, 1978.

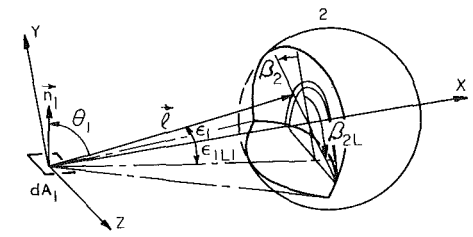

Fig. 1(*a*) Isometric view

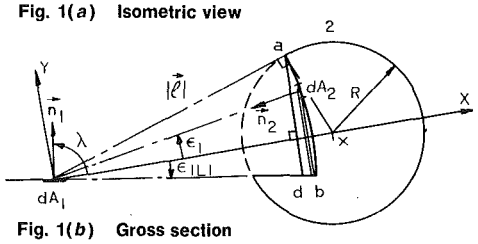

Fig. 1(*b*) Gross section

Fig. 1 Geometry for view factor analysis from a differential plane source dA_1 to sphere 2

ningham [1] who replaced the sphere with a disk and Hottel [2] who used the contour integral method. For $\lambda = 0$ and $\pi/2$ they agree with Chung and Sumitra's [3] solution for a coaxial and orthogonal sphere, respectively.

When dA_1 touches the surface of the sphere, $x = R$, and equation (5) is reduced to

$$F_{dA_1-2} = (\cos\lambda + 1)/2 \tag{6}$$

Equation (6) also expresses the view factor from dA_1 touching an infinite flat plane A_2 if λ is the angle between planes of dA_1 and A_2 [4]. This suggests that the surface of the sphere when touched by dA_1 can be replaced by the tangential plane at the point of contact with dA_1. Thus, the view factor, from a differential plane source touching any arbitrary convex surface, is given by equation (6) which may then be used to verify, in the limit, the expressions or values of F_{dA_1-2} obtained by either closed form or numerical integration.

Applications

1 The behavior of F_{dA_1-2} will be illustrated as dA_1 moves over the surface of a (a) flat plate, (b) sphere, and (c) cylinder (the mid-plane of which goes through the center of the sphere).

Case a. In Fig. 2 the location of dA_1 is defined by the cylindrical coordinate system H, L, γ. The axis, H, which is normal to the plane of dA_1, has its origin at the center of sphere 2. L is the distance from dA_1 to H. γ is the angular position of dA_1 in the plane of dA_1. By symmetry, F_{dA_1-2} is independent of γ.

The parameters λ and x are related to L and H by: $\lambda = \cos^{-1}(H/\sqrt{H^2+L^2}) = \sin^{-1}(L/\sqrt{H^2+L^2})$ and $x/R = \sqrt{(L/R)^2 + (H/R)^2}$. Equations (4) and (5) become

$$F_{dA_1-2} = HR^2/(L^2+H^2)^{3/2} \text{ for } H/R \geq 1 \tag{7}$$

and

$$F_{dA_1-2} = 1/\pi\,[HR^2/(L^2+H^2)^{3/2}\cos^{-1}(-H/(LR)\sqrt{L^2+H^2-R^2}) - \sqrt{(L^2+H^2-R^2)(R^2-H^2)}/(L^2+H^2) - \sin^{-1}\times(\sqrt{(H^2+L^2-R^2)}/L^2) + \pi/2] \text{ for } -1 \leq H/R \leq 1 \tag{8}$$

The results are presented graphically in Fig. 2 as a function of H/R and with L/R as a parameter. For $0 \leq L/R \leq 1$, the curves end on the broken curve which represents the view factor for dA_1 touching the surface of the sphere. For $L/R > 1$, the curves shown a maximum, the location of which shifts to the right as L/R increases. When the plane of dA_1 does not intersect the sphere, the maximum value is given by $F_{dA_1-2} = 2/((\sqrt{3})^3(L/R)^2)$ and occurs at $H/R = L/R\sqrt{2}$ for $L/R \geq \sqrt{2}$. This behavior is interesting and may be used to determine, for example, the H/R location of a coaxial ring with given radius for which the view factor is maximum.

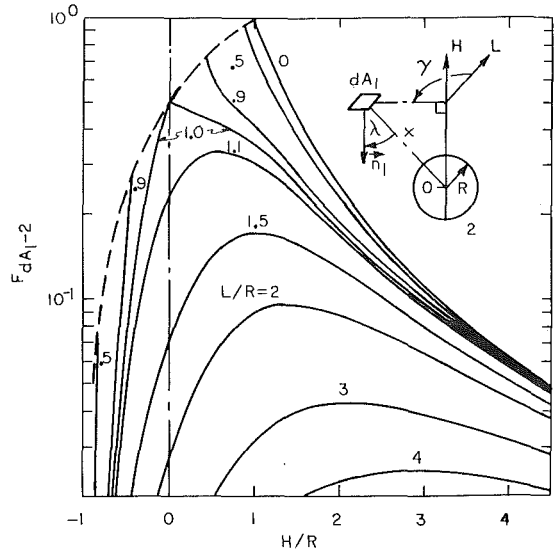

Fig. 2 View factor from a differential plane source dA_1, lying in planes perpendicular to the H axis, to sphere 2

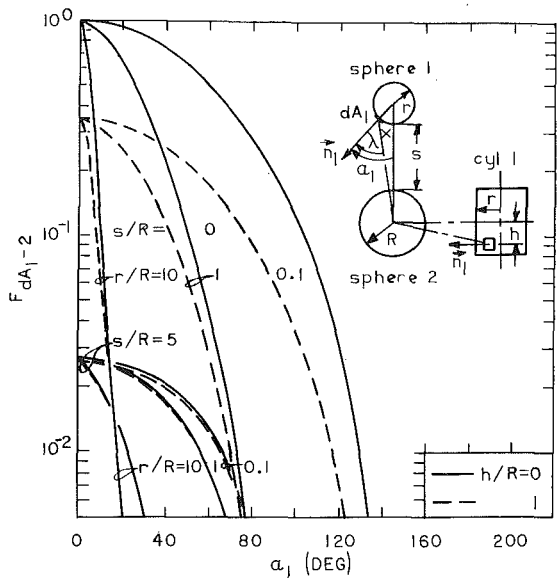

Fig. 3 View factor from a differential plane source dA_1, located on sphere 1 ($h/R = 0$) or cylinder 1 ($0 \leq h/R \leq 1$) at latitude α_1, to sphere 2 for r/R = 0.1, 1 and 10

Since F_{dA_1-2} is independent of γ, the view factor from an infinitesimal coaxial ring or ring sector is expressed by either equations (7) or (8). For $H/R \geq 1$, the result is given by equation (7) and it agrees with the one obtained by Fiengold and Gupta [5].

Case b. In Fig. 3 the location of dA_1 on sphere 1 is defined by the coordinates, s/R, r/R, α_1. s/R is the separation ratio, r/R is the radius ratio and α_1 is the latitude. λ and x/R are expressed by $\lambda = \tan^{-1}(\sin\alpha_1/(\cos\alpha_1 - r/(s+r+R)))$ and $x/R = ((s/R + r/R + 1)^2 + (r/R)^2 - 2(s/R + r/R + 1)\, r/R\cos\alpha_1)^{1/2}$. Substituting into equations (4) and (5) $F_{dA_1-2} = f(\alpha_1, r/R, s/R)$ is obtained. Equation (4) is valid for $0 \leq \alpha_1 \leq \cos^{-1}((r/R+1)/(s/R+r/R+1)) = \alpha_{1L1}$ and equation (5) is valid for $\alpha_{1L1} \leq \alpha_1 \leq \cos^{-1}((r/R-1)/(s/R+r/R+1)) = \alpha_{1L}$.

The solid curves ($h/R = 0$) in Fig. 3 present the behavior of the view factor from a differential plane source located on sphere 1 to sphere 2 as a function of α_1 for r/R and s/R as parameters. Equation (4) is valid in the region between the ordinate and the curves defined by α_{1L1} which are not shown in order to avoid confusion. But the expression for α_{1L1} shows that for a given r/R the range of α_1 for which equation (4) is valid, goes from 0 deg for $s/R = 0$ to 90 deg for $s/R \to \infty$. Consequently the range of α_1 for which equation (5) is valid is maximum for $s/R = 0$ and 0 deg for $s/R \to \infty$. The behavior of the limiting angles α_{1L1} and α_{1L} as a function of r/R and s/R is discussed

in [6]. The results obtained here are in agreement with [7] which only presents values for $r/R = 1$ using numerical integration.

Case c. The location of dA_1 on the curved surface of a cylinder is determined by s/R, r/R, α_1 and the distance ratio from the symmetry plane, h/R, as shown in Fig. 3.

For this coordinate system x/R and λ are given by

$$x/R = ((1 + s/R + r/R(1 - \cos\alpha_1))^2 + (h/R)^2 + (r/R(1 - \cos\alpha_1))^2)^{1/2}$$

and

$$\lambda = \cos^{-1}(((1 + s/R + r/R(1 - \cos\alpha_1))\cos\alpha_1 - r/R\sin^2\alpha_1)/(x/R))$$

When substituted into equations (4) and (5), the view factor from a differential plane source lying on the curved surface of a cylinder to the sphere is obtained.

The limits of α_1 for application of equations (4) and (5) are identical to case b. Fig. 3 presents the curves of the view factor for $r/R = 0.1$, 1, 10 as a function α_1 and with s/R as a parameter. The solid curves are for $h/R = 0$ (the mid plane) and broken ones are for $h/R = 1$ (the end planes). Fig. 3 indicates that the difference between the view factors at $h/R = 0$ and $h/R = 1$ for $s/R = 0$ at a given α_1 and $r/R < 1$ increases with increasing α_1, but that it decreases for $r/R \geq 1$. However, for $s/R > 0$, the difference rapidly decreases and goes to zero when either r/R or s/R or both increase. Thus, when s/R is large the view factors for $0 \leq h/R \leq 1$ are functions only of α_1, and are therefore identical to the view factor from a sphere of the same radius. For these conditions the conclusions concerning the behavior of the view factor from spheres also apply to cylinders.

2 The view factor from a finite surface A_1 to sphere 2 is evaluated by $F_{12} = 1/A_1 \int_{A_1} F_{dA_1-2} dA_1$. For flat plates F_{dA_1-2} is substituted by equation (7) or (8) depending on whether the plane of dA_1 intersects the sphere or not.

As an example, substituting F_{dA_1-2} by equation (7) and $dA_1 = \Delta\gamma L dL$, the view factor from a sector $\Delta\gamma$ of a coaxial disk with radius L_2 to a sphere is by closed form integration $F_{12} = 2(R/L_2)^2(1 - H/\sqrt{L_2^2 + H^2})$. This expression also represents the view factor from a coaxial disk and agrees with [5].

For curved surfaces the integration is carried out after selecting a suitable coordinate system and applying the proper transformations to equations (4) and (5). However, this procedure is not valid for a concave surface facing the sphere if the radiation from any dA_1 which strikes the sphere is partly reduced due to obstruction by parts of surface A_1.

Conclusion

The expressions for the view factor from a differential plane source to a sphere are derived by using a new integration scheme which gives the integral equation in a form suitable for closed form integration without involving any transformations. The expressions are applied to obtain the view factors to a sphere from differential areas located on flat plates, spheres and cylinders. The results are presented graphically and yield detailed information about behavior of the view factor which is concealed by general numerical integration programs.

References

1 Cunningham, F. G., "Power Input to Small Flat Plate from a Diffusely Radiating Sphere, with Application to Earth Satellites," NASA TN D-710, Aug. 1961.

2 Hottel H. C., and Sarofim, A. F., *Radiation Transfer*, McGraw-Hill, 1967, pp. 65–67.

3 Chung, B. T. F., and Sumitra, P. S., "Radiation Shape Factors from Plane Point Sources,", ASME JOURNAL OF HEAT TRANSFER, Vol. 94, August, 1972, pp. 328–330.

4 Hamilton D. C., and Morgan, W. R., "Radiant-Interchange Configuration Factors," NACA TN 2836, Dec. 1952, p. 23.

5 Feingold A., and Gupta K. G., "New Analytical Approach to the Evaluation of Configuration Factors in Radiation from Spheres and Infinitely Long Cylinders," ASME JOURNAL OF HEAT TRANSFER, Vol. 92, No. 1, Feb. 1970, pp. 69–76.

6 Juul, N. H., "Investigation of Approximate Methods for Calculation of the Diffuse Radiation Configuration View Factor Between Two Spheres," *Letters in Heat and Mass Transfer Journal*, Vol. 3, No. 6, Nov./Dec. 1976, pp. 513–522.

7 Campbell J. P., and McConnell, D. G., "Radiant-Interchange Configuration Factors for Spherical and Conical Surfaces to Spheres," NASA Report TN D-4457, 1968.

Shielding of Heat Transfer from a Boundary

A. S. Popel[1]

Nomenclature

a, b, d = geometric parameters
F = elliptic integral of the first kind
k = elliptic modulus, equation (8)
K = complete elliptic integral of the first kind
T = temperature
T_0 = temperature of the boundary
T_1 = temperature of the strips
T_∞ = temperature at the infinity
t = dimensionless temperature
t_∞ = dimensionless temperature at the infinity
w, w_1, w_2 = complex variables
x, y = rectangular coordinates
ξ_1, ξ_2 = dimensionless parameters, equation (7)

Introduction

In some practical situations it is desirable to limit the heat transfer into a volume from the boundary surface, e.g., to maintain a prescribed temperature in the volume independent of variations of the surface temperature. One possible way to achieve this is to situate a control array of heat sources or sinks near the surface. In order to illustrate a practical application of the problem, consider a volume of material with constant thermoconductivity contained in a rectangular box with thermoisolating walls; the box is open from one side. Suppose that an experiment requires a controlled uniform temperature in the bulk of the volume, but the mass transfer with the ambient medium through the open surface must be retained. A possible experimental solution of this task would be situating an array of temperature-controlled strips below the surface which should not influence the mass transfer processes; at some depth below the strips the temperature distribution in the volume should be close to uniform.

In the present communication, the problem of heat transfer in the half-space containing a control one-dimensional periodic array of flat strips parallel to the surface is considered; and it is shown that an efficient shielding of heat transfer from the boundary can be achieved with this arrangement. A simple expression is derived for the temperature in the bulk of the volume in terms of the temperatures of the surface and the strips, and the geometrical parameters of the problem.

Analysis and Results

Consider the problem of steady-state heat transfer in the half-space bounded by a plane surface, and containing a periodic array of strips of infinite length; geometry of the problem is illustrated in Fig. 1(a) where the cross section perpendicular to the strips and to the bounding plane is shown. Let the temperature of the bounding surface be T_0, and the temperature of the strips be T_1 where T_0 and T_1 are given constants. The problem is to determine the temperature distribution in the half-space. Since due to the symmetry of the problem

[1] Departments of Chemical Engineering and Aerospace and Mechanical Engineering, University of Arizona, Tucson, AZ 85721, Mem. ASME.

Contributed by the Heat Transfer Division for publication in the JOURNAL OF HEAT TRANSFER. Manuscript received by the Heat Transfer Division August 11, 1978.

in [6]. The results obtained here are in agreement with [7] which only presents values for $r/R = 1$ using numerical integration.

Case c. The location of dA_1 on the curved surface of a cylinder is determined by s/R, r/R, α_1 and the distance ratio from the symmetry plane, h/R, as shown in Fig. 3.

For this coordinate system x/R and λ are given by

$$x/R = ((1 + s/R + r/R(1 - \cos\alpha_1))^2 + (h/R)^2 + (r/R(1 - \cos\alpha_1))^2)^{1/2}$$

and

$$\lambda = \cos^{-1}(((1 + s/R + r/R(1 - \cos\alpha_1))\cos\alpha_1 - r/R\sin^2\alpha_1)/(x/R))$$

When substituted into equations (4) and (5), the view factor from a differential plane source lying on the curved surface of a cylinder to the sphere is obtained.

The limits of α_1 for application of equations (4) and (5) are identical to case b. Fig. 3 presents the curves of the view factor for $r/R = 0.1$, 1, 10 as a function α_1 and with s/R as a parameter. The solid curves are for $h/R = 0$ (the mid plane) and broken ones are for $h/R = 1$ (the end planes). Fig. 3 indicates that the difference between the view factors at $h/R = 0$ and $h/R = 1$ for $s/R = 0$ at a given α_1 and $r/R < 1$ increases with increasing α_1, but that it decreases for $r/R \geq 1$. However, for $s/R > 0$, the difference rapidly decreases and goes to zero when either r/R or s/R or both increase. Thus, when s/R is large the view factors for $0 \leq h/R \leq 1$ are functions only of α_1, and are therefore identical to the view factor from a sphere of the same radius. For these conditions the conclusions concerning the behavior of the view factor from spheres also apply to cylinders.

2 The view factor from a finite surface A_1 to sphere 2 is evaluated by $F_{12} = 1/A_1 \int_{A_1} F_{dA_1-2} dA_1$. For flat plates F_{dA_1-2} is substituted by equation (7) or (8) depending on whether the plane of dA_1 intersects the sphere or not.

As an example, substituting F_{dA_1-2} by equation (7) and $dA_1 = \Delta\gamma L dL$, the view factor from a sector $\Delta\gamma$ of a coaxial disk with radius L_2 to a sphere is by closed form integration $F_{12} = 2(R/L_2)^2(1 - H/\sqrt{L_2^2 + H^2})$. This expression also represents the view factor from a coaxial disk and agrees with [5].

For curved surfaces the integration is carried out after selecting a suitable coordinate system and applying the proper transformations to equations (4) and (5). However, this procedure is not valid for a concave surface facing the sphere if the radiation from any dA_1 which strikes the sphere is partly reduced due to obstruction by parts of surface A_1.

Conclusion

The expressions for the view factor from a differential plane source to a sphere are derived by using a new integration scheme which gives the integral equation in a form suitable for closed form integration without involving any transformations. The expressions are applied to obtain the view factors to a sphere from differential areas located on flat plates, spheres and cylinders. The results are presented graphically and yield detailed information about behavior of the view factor which is concealed by general numerical integration programs.

References

1 Cunningham, F. G., "Power Input to Small Flat Plate from a Diffusely Radiating Sphere, with Application to Earth Satellites," NASA TN D-710, Aug. 1961.

2 Hottel H. C., and Sarofim, A. F., *Radiation Transfer*, McGraw-Hill, 1967, pp. 65–67.

3 Chung, B. T. F., and Sumitra, P. S., "Radiation Shape Factors from Plane Point Sources,", ASME JOURNAL OF HEAT TRANSFER, Vol. 94, August, 1972, pp. 328–330.

4 Hamilton D. C., and Morgan, W. R., "Radiant-Interchange Configuration Factors," NACA TN 2836, Dec. 1952, p. 23.

5 Feingold A., and Gupta K. G., "New Analytical Approach to the Evaluation of Configuration Factors in Radiation from Spheres and Infinitely Long Cylinders," ASME JOURNAL OF HEAT TRANSFER, Vol. 92, No. 1, Feb. 1970, pp. 69–76.

6 Juul, N. H., "Investigation of Approximate Methods for Calculation of the Diffuse Radiation Configuration View Factor Between Two Spheres," *Letters in Heat and Mass Transfer Journal*, Vol. 3, No. 6, Nov./Dec. 1976, pp. 513–522.

7 Campbell J. P., and McConnell, D. G., "Radiant-Interchange Configuration Factors for Spherical and Conical Surfaces to Spheres," NASA Report TN D-4457, 1968.

Shielding of Heat Transfer from a Boundary

A. S. Popel[1]

Nomenclature

a, b, d = geometric parameters
F = elliptic integral of the first kind
k = elliptic modulus, equation (8)
K = complete elliptic integral of the first kind
T = temperature
T_0 = temperature of the boundary
T_1 = temperature of the strips
T_∞ = temperature at the infinity
t = dimensionless temperature
t_∞ = dimensionless temperature at the infinity
w, w_1, w_2 = complex variables
x, y = rectangular coordinates
ξ_1, ξ_2 = dimensionless parameters, equation (7)

Introduction

In some practical situations it is desirable to limit the heat transfer into a volume from the boundary surface, e.g., to maintain a prescribed temperature in the volume independent of variations of the surface temperature. One possible way to achieve this is to situate a control array of heat sources or sinks near the surface. In order to illustrate a practical application of the problem, consider a volume of material with constant thermoconductivity contained in a rectangular box with thermoisolating walls; the box is open from one side. Suppose that an experiment requires a controlled uniform temperature in the bulk of the volume, but the mass transfer with the ambient medium through the open surface must be retained. A possible experimental solution of this task would be situating an array of temperature-controlled strips below the surface which should not influence the mass transfer processes; at some depth below the strips the temperature distribution in the volume should be close to uniform.

In the present communication, the problem of heat transfer in the half-space containing a control one-dimensional periodic array of flat strips parallel to the surface is considered; and it is shown that an efficient shielding of heat transfer from the boundary can be achieved with this arrangement. A simple expression is derived for the temperature in the bulk of the volume in terms of the temperatures of the surface and the strips, and the geometrical parameters of the problem.

Analysis and Results

Consider the problem of steady-state heat transfer in the half-space bounded by a plane surface, and containing a periodic array of strips of infinite length; geometry of the problem is illustrated in Fig. 1(*a*) where the cross section perpendicular to the strips and to the bounding plane is shown. Let the temperature of the bounding surface be T_0, and the temperature of the strips be T_1 where T_0 and T_1 are given constants. The problem is to determine the temperature distribution in the half-space. Since due to the symmetry of the problem

[1] Departments of Chemical Engineering and Aerospace and Mechanical Engineering, University of Arizona, Tucson, AZ 85721, Mem. ASME.

Contributed by the Heat Transfer Division for publication in the JOURNAL OF HEAT TRANSFER. Manuscript received by the Heat Transfer Division August 11, 1978.

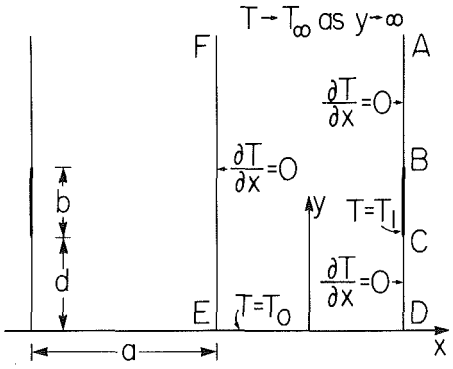

Fig. 1(*a*) Geometry of the problem

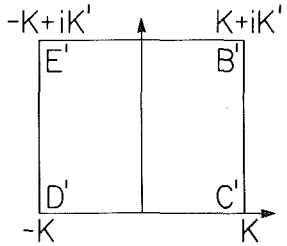

Fig. 1(*b*) Rectangle in the complex w_2-plane

the temperature distribution is two-dimensional and is spatially periodic, we can restrict ourselves to consideration of a semi-infinite strip $ABCDEF$ shown in Fig. 1(*a*) ($DE = a$, $DC = d$, $BC = b$). Introducing a coordinate system (x, y) with the origin located in the middle of DE, we can formulate the mathematical problem as follows:

$$\frac{\partial^2 T}{\partial x^2} + \frac{\partial^2 T}{\partial y^2} = 0 \text{ for } -a/2 < x < a/2, y > 0 \tag{1}$$

$$T = T_0 \text{ at } y = 0, -a/2 \leq x \leq a/2 \tag{2}$$

$$T = T_1 \text{ at } x = a/2, b \leq y \leq d + b \tag{3}$$

$$\partial T/\partial x = 0 \text{ at } x = -a/2 \text{ and } x = a/2, 0 < y < d \text{ and } y > d + b \tag{4}$$

The problem may be solved by conformal mapping the semi-infinite strip $ABCDEF$ in the complex w-plane into a rectangle $B'C'D'E'$ in the w_2-plane so that BC maps into $B'C'$ and DE into $D'E'$ (Fig. 1(*b*)). The transformation is given by the relationships [1]

$$w_1 = \frac{[\xi_1 + 1 - k(\xi_1 - 1)] \sin^2(\pi w/a) - 2\xi_1}{[\xi_1 - 1 - k(\xi_1 + 1)] \sin^2(\pi w/a) + 2\xi_1 k} \tag{5}$$

$$w_2 = \int_0^{w_1} (1 - t^2)^{-1/2} (1 - k^2 t^2)^{-1/2} \, dt \tag{6}$$

where $w = x + iy$, w_1, and w_2 are complex variables, and

$$\xi_1 = \cosh^2 \frac{\pi d}{2a}, \; \xi_2 = \cosh^2 \frac{\pi(d + b)}{2a} \tag{7}$$

$$k = \frac{\xi_2(\xi_1 - 1)}{(\xi_2 - \xi_1) + \xi_1(\xi_2 - 1) + 2[\xi_1(\xi_2 - 1)(\xi_2 - \xi_1)]^{1/2}} \tag{8}$$

The latter parameter satisfies the condition $0 \leq k \leq 1$. The temperature distribution may be expressed in a simple form in terms of the variable w_2:

$$T = \frac{T_1 - T_0}{2K(k)} \operatorname{Re} w_2 + \frac{T_1 + T_0}{2} \tag{9}$$

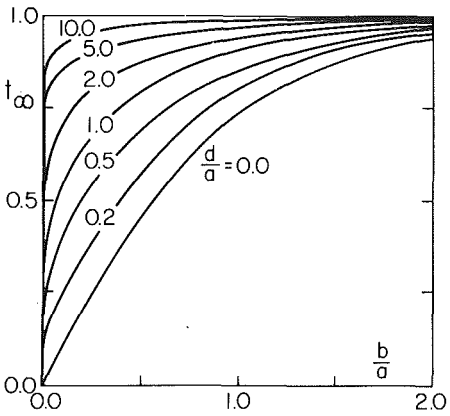

Fig. 2 Dimensionless temperature at the infinity as function of geometric parameters b/a and d/a

or in dimensionless form

$$t = \frac{T - T_0}{T_1 - T_0} = \tfrac{1}{2}\left(1 + \frac{\operatorname{Re} w_2}{K(k)}\right) \tag{10}$$

where $K(k)$ is the complete elliptic integral of the first kind [2], $K' = K(\sqrt{1 - k^2})$, and Re w_2 designates the real part of the complex variable. Relationships (5–9) completely solve the problem.

Let us calculate the temperature T_∞ far away from the surfaces, i.e., at $y \to \infty$. It can be shown that the infinity in the w-plane corresponds to a finite point on the real axis in the w_1-plane:

$$w_1^* = \frac{\xi_1 + 1 - k(\xi_1 - 1)}{\xi_1 - 1 - k(\xi_1 + 1)} \tag{11}$$

where $|w_1^*| > 1/k$. Using the solution (10) we can express the dimensionless temperature at the infinity in the form

$$t_\infty = \frac{T_\infty - T_0}{T_1 - T_0} = \tfrac{1}{2}\left[1 + (\operatorname{sgn} w_1^*) \frac{F(\arcsin k^{-1}|w_1^*|^{-1}, k)}{K(k)}\right] \tag{12}$$

where

$$F(\phi, k) = \int_0^\phi (1 - k^2 \sin^2\theta)^{-1/2} \, d\theta \tag{13}$$

is the elliptic integral of the first kind. Relationships (12) imply $t_\infty \to 0$ as $t_\infty \to T_0$, $t_\infty \to 1$ as $T_\infty \to T_1$, and min $(T_0, T_1) \leq T_\infty \leq$ max (T_0, T_1). When $d/a \to 0$ the solution assumes a simpler form

$$t_\infty = 0.5 + \pi^{-1} \arcsin(1 - 2/\xi_2) \tag{14}$$

The quantity t_∞ given by (12) is plotted in Fig. 2 as a function of the parameters b/a and d/a. As d/a increases, the temperature T_∞ approaches the temperature of the strips T_1 even for small values of b/a.

These results make it possible to simply calculate one of the temperatures T_∞, T_0, T_1 if the other two are specified. To consider a numerical example, let $d/a = 0.5$, $b/a = 0.2$ then from Fig. 2 we find $t_\infty \approx 0.5$. Thus, for example, if the surface temperature is $T_0 = 0°C$, and the temperature in the volume should be $T_\infty = 20°C$, then the temperature of the strips has to be maintained at $T_1 = 40°C$.

Acknowledgment

This work was supported in part by NIH Grant HL-17421.

References

1 Churchill, R. V., *Introduction to Complex Variables and Applications*, McGraw-Hill, New York, 1948.

2 Abramowitz, M. and Stegun, I. A., *Handbook of Mathematical Functions*, Dover, New York, Ch. 17, 1972.

Triangular Fin Performance by the Heat Balance Integral Method

L. C. Burmeister[1]

Nomenclature

B = dimensionless parameter, $B^2 = 1/(1 - \theta_0/\tan\theta_0)$

Biot = dimensionless Biot number based on fin base width, Biot = $hR\theta_0/k$

$F(a, b, c; x)$ = hypergeometric function, $F(a, b, c; x) = \dfrac{\Gamma(c)}{\Gamma(a)\Gamma(b)} \sum_{n=0}^{\infty} \dfrac{\Gamma(a+n)\Gamma(b+n)}{\Gamma(c+n)} \dfrac{x^n}{n!}$

h = convective film coefficient of heat transfer, constant

I_0 = zero-order modified Bessel function of the first kind

I_1 = first-order modified Bessel function of the first kind

k = thermal conductivity of fin

t = local temperature in fin

t_∞ = environmental temperature, constant

t_{ba} = average temperature at the straight base of the fin

T = dimensionless temperature, $T = (t - t_\infty)/(t_{ba} - t_\infty)$

T_{tip} = dimensionless temperature of the fin tip

y = average dimensionless temperature, $y = \theta_0^{-1} \int_0^{\theta_0} T(r, \theta)d\theta$

Z = dimensionless radial distance from fin tip, $Z = (hr/k\theta_0)(1 - \theta_0/\tan\theta_0)$

Z_R = maximum value of Z, $Z_R = (hR/k\theta_0)(1 - \theta_0/\tan\theta_0)$

Z_{1d} = dimensionless parameter from one-dimensional analysis, $Z_{1d} = hR/k \tan\theta_0$

$\Gamma(a)$ = gamma function, $\Gamma(a) = \int_0^\infty t^{a-1}e^{-t}dt$

$\Psi(a)$ = digamma function, $\Psi(a) = d\ln\Gamma(a)/da$

Introduction

Because of their utility and simplicity, it is desirable to ascertain the conditions under which the results of one-dimensional analyses of fin efficiencies retain their accuracy. Exact solutions have been presented for this purpose for a pin fin [1], for an infinitely wide rectangular fin [2], and for an annular fin of constant thickness [3].

More recently, an integral method was employed by Sfeir [4] to approximately account for a fin's transverse temperature variation. He showed that for annular and straight fins of constant thickness, compensation for the effects of transverse temperature variations could be accomplished by a simple modification of the one-dimensional analysis parameter since the resulting differential equations are of the same form as for a one-dimensional analysis. But, for a triangular fin no similar success was enjoyed.

The purpose of the present study is to further the work begun by Sfeir on a triangular fin, utilizing the heat balance integral method. In addition to determining the conditions under which the one-dimensional prediction of triangular fin efficiency is accurate, these results would be useful in the optimization of such fins with respect to weight [5].

Analysis

The triangular fin with a straight base illustrated in Fig. 1 has a steady temperature distribution, with a constant temperature along the straight base, described by

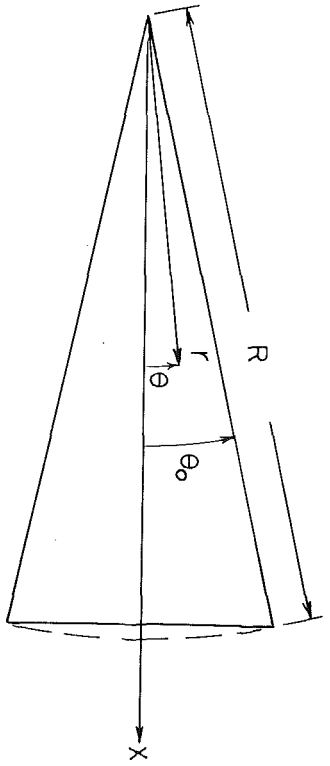

Fig. 1 Physical configuration and coordinate system

$$\partial(r\partial T/\partial r)/\partial r + r^{-1}\partial^2 T/\partial\theta^2 = 0, \quad 0 < r < R \qquad 0 \le \theta < \theta_0 \tag{1}$$

and the boundary conditions

$$\partial T(r, \theta_0)/\partial\theta = -(hr/k)T(r, \theta_0) \tag{2}$$

$$\partial T(r, 0)/\partial\theta = 0 \tag{3}$$

$$T(0, \theta) \text{ finite} \tag{4}$$

$$T(R\cos\theta_0/\cos\theta, \theta) = 1 \tag{5}$$

Following Sfeir in the application of the integral method, equation (1) is integrated with respect to θ from 0 to θ_0 to obtain, after introducing equations (2) and (3),

$$d(rdy/dr)/dr - (h/k\theta_0)T(r,\theta_0) = 0 \tag{6}$$

A transverse temperature variation of the form

$$T(r, \theta) = A_0(r) + A_1(r)\cos(\theta)$$

is next assumed and is subjected to the boundary conditions of equations (2) and (3) to give the relation between the local temperature and the average temperature, y, at that radius as

$$T(r, \theta) = y(r)[1 - (B^2 - 1)(1 - \cos\theta/\cos\theta_0)Z]/(1 + Z) \tag{7}$$

Equation (7) inserted into equation (6) gives

$$d(Z\,dy/dZ)/dZ - B^2 y/(1 + Z) = 0 \tag{8}$$

Sfeir's assumed quadratic form for the transverse temperature distribution gave a result which is of the same form as equation (8).

Solution

The solution to equation (8), not pointed out by Sfeir, is a hypergeometric function. This can be seen by employing the transformation $x = -Z$ [6] to get the standard form of the hypergeometric differential equation (7)

$$x(1 - x)d^2y/dx^2 + [c - (a + b + 1)x]dy/dx - aby = 0 \tag{9}$$

[1]Professor, Mechanical Engineering Department, University of Kansas, Lawrence, KA 66045.

Contributed by the Heat Transfer Division for publication in the JOURNAL OF HEAT TRANSFER. Manuscript received by the Heat Transfer Division January 11, 1979.

where here $a = -b = B$ and $c = 1$. The two solutions of the hypergeometric differential equation are given in terms of hypergeometric functions [8] as

$$y_{1(0)} = F(a, b, c; x) \tag{10a}$$

and

$$y_{2(0)} = F(a, b, c; x) \ln(x) + \sum_{n=1}^{\infty} \frac{(a_n)(b_n)}{(n!)^2} x^n [\Psi(a+n) - \Psi(a) + \Psi(b+n) - \Psi(b) - 2\Psi(n+1) + 2\Psi(1)] \tag{10b}$$

Consideration of the requirement that $y(0)$ be finite and the logarithmic term in equation (10b) reveals that only $y_{1(0)}$ can be retained. Then

$$y = C[1 + B^2Z/(1!)^2 + (B^2 - 1^2)B^2Z^2/(2!)^2 + (B^2 - 2^2)(B^2 - 1^2)B^2Z^3/(3!) + \cdots] \tag{11}$$

which is convergent only for $|Z| < 1$ unless B exactly equals an integer, in which case the polynomial represents the solution for all Z.

The constant C in equation (11) can be evaluated from the integral form of equation (5), $\theta_0^{-1} \int_0^{\theta_0} y(R \cos\theta_0/\cos\theta)\{[1 + (B^2 - 1)Z_R(1 - \cos\theta_0/\cos\theta)]/(1 + Z_R \cos\theta_0/\cos\theta)\}d\theta$, as

$$1/C = 1 + B_1Z_R + B_1^2Z_cZ_RL/\theta_0 + B_1[B_2(1 + B_1Z_R - 2^2B_1]Z_c^2(t_1/\theta_0)/(2!)^2 + \cdots \tag{12}$$

where $Z_c = Z_R \cos\theta_0$, $L = \ln[\tan(\pi/4 + \theta_0/2)]$, $t_1 = \tan\theta_0$, $B_1 = B^2 - 1^2$, $B_2 = B^2 - 2^2$.

The efficiency of the triangular fin is obtained from its definition to be

$$\eta = \left[kR \int_0^{\theta_0} \frac{\partial T(R, \theta)}{\partial r} d\theta\right] \Big/ (hR)$$

$$= C[1 + 2(B^2 - 1^2)Z_R/(2!)^2 + 3(B^2 - 2^2)(B^2 - 1^2)Z_R^2/(3!)^2 + \cdots] \tag{13}$$

Discussion

The Biot number, Biot, based on the fin's base width is related to the parameters Z_R and Z_{1d} by

$$\text{Biot} = Z_R(B\theta_0)^2 = Z_{1d}(B\theta_0)^2/(B^2 - 1) \tag{14}$$

Because the parameter Z_R is proportional to Biot, the convergence criterion for equation (11), $|Z| < 1$, offers no practical difficulty since interest is centered on cases where a fin's transverse conductive resistance to heat flow is relatively small.

It is pertinent to observe in equations (11) and (13) that the temperature distribution and fin efficiency depend separately upon included angle and the dimensionless parameter, Z, in contrast to a one-dimensional analysis which predicts that

$$T = I_0[2Z_{1d}^{1/2}(x/R \cos\theta_0)^{1/2}]/I_0[2Z_{1d}^{1/2}] \tag{15}$$

from which it is found that

$$\eta_{1d}(Z_{1d}) = (Z_{1d}^{1/2})^{-1} I_1(2Z_{1d}^{1/2})/I_0(2Z_{1d}^{1/2}) \tag{16}$$

Fig. 2 shows that at small included angles the integral method's efficiency prediction does not differ appreciably from the one-dimensional prediction since then the Biot number is small. As the included angle increases, the departure from the one-dimensional prediction becomes greater and occurs at a smaller value of Z_{1d}. It can be shown with the aid of equation (14) that this departure first becomes noticeable at Biot = 1.

To assess the accuracy of the integral method's results, numerical solutions of equations (1–5) were obtained by a finite-difference method. When the temperature along the straight base in the finite-difference method equals the distribution required by the integral method, excellent agreement results. When the temperature along the straight base equals unity in the finite-difference method, the efficiency noticeably exceeds that predicted by the integral method due to the inability of the assumed temperature profile to give a temperature of unity along the straight-line base. In such a case, however, the efficiency variation with included angle still seems to follow the trend predicted by the integral method.

When the Biot number becomes large, the surface temperature at the fin's base is shown by the integral method to be substantially depressed below the unity value stated in equation (5). Numerical studies of rectangular fins [9–10] showed similar base-temperature profiles, but of opposite curvature. The temperature of the fin tip is in noticeable disagreement with the numerical solutions for both unity and cosine base-temperatures when $Z_{1d} > 5$.

To construct a modification to the one-dimensional prediction for triangular fin efficiency, the effective distance from tip to base is first set equal to the average of R and $R \cos\theta_0$, as was similarly done by Harper and Brown [11], to give $R^* = R(1 + \cos\theta_0)/2$. Next the $1/(1 + Z)$ term in equation (8) is replaced by its average over R^*, giving a modified parameter for equation (8) which is

$$B^{*2} = B^2 \ln(1 + Z_R^*)/Z_R^* \tag{17}$$

Equation (8) then has the form found from a one-dimensional analysis and its solution is

$$y \approx I_0(2B^*Z^{1/2})/I_0(2B^*Z_R^{1/2})$$

The efficiency is then approximately given by

$$\eta \approx \left[kR^* \int_0^{\theta_0} \frac{\partial T}{\partial r}(R^*, \theta)d\theta\right] \Big/ hR^*$$

$$\approx \{B^*Z_R^{*1/2})^{-1} I_1(2B^*Z_R^{*1/2})/I_0(2B^*Z_R^{*1/2}]\ln(1 + Z_R)/Z_R^*$$

The term in braces is recognized as the one-dimensional prediction of fin efficiency evaluated at $B^{*2}Z_R^*$. Restated,

$$\eta \approx \{\eta_{1d}(B^2Z_R^*)\}\{Z_R^{*-1} \ln(1 + Z_R^*)\} \tag{18}$$

Equation (18) represents the integral method's predictions with less than 4 percent error.

Consideration of equations (17) and (14) together with the fact that $B^2\theta_0^2 \approx 3$ reveals that when Biot < 1 and θ_0 is small

$$\eta \approx \{\eta_{1d}(\text{Biot}/12 + Z_{1d})\}\{1 - \text{Biot}/6\} < \eta_{1d}(Z_{1d}) \tag{19}$$

where Biot $\approx Z_{1d}\theta_0^2$ with θ_0 in radians. Equation (19) more strongly shows that the effect of the Biot number is to reduce (slightly in most cases) efficiency below the prediction of a one-dimensional analysis.

This study does not account for the probable variation of the film coefficient which was experimentally found [12] to vary nearly linearly from low base values to high tip values in a forced convection situation and to lower fin efficiency about 7 percent below that for constant h.

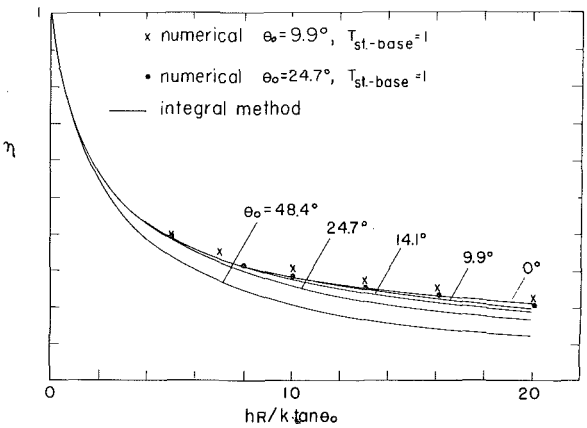

Fig. 2 Triangular fin efficiency versus one-dimensional parameter for several half-angles. The curve for $\theta_0 = 0$ deg also represents the one-dimensional solution

References

1 Irey, R. K., "Errors in the One-Dimensional Fin Solution," ASME JOURNAL OF HEAT TRANSFER, Vol. 90, 1968, pp. 175–176.

2 Avrami, M. and Little, J. B., "Diffusion of Heat Through a Rectangular Bar and the Cooling and Insulating Effect of Fins," *Journal of Applied Physics*, Vol. 13, 1942, pp. 255–264.

3 Keller, H. H. and Somers, E. V., "Heat Transfer From an Annular Fin of Constant Thickness," ASME JOURNAL OF HEAT TRANSFER, Vol. 81, 1959, pp. 151–156.

4 Sfeir, A. A., "The Heat Balance Integral in Steady Heat Conduction," JOURNAL OF HEAT TRANSFER, Vol. 98, 1976, pp. 466–470.

5 Schnurr, N. M., Shapiro, A. B., and Townsend, M. A., "Optimization of Radiating Fin Arrays with Respect to Weight," ASME JOURNAL OF HEAT TRANSFER, Vol. 98, 1976, pp. 643–648.

6 Murphy, G. M., *Ordinary Differential Equations and Their Solutions*, Van Nostrand, 1960, p. 357, item 409.

7 Abramowitz, M. and Stegun, I. A., *Handbook of Mathematical Functions*, National Bureau of Standards, Applied Mathematics Series 55, 1965, pp. 562–564.

8 Morse, P. M. and Feshbach, H., *Methods of Theoretical Physics*, McGraw-Hill, 1953, pp. 541–547, pp. 587–593, and pp. 668–671.

9 Sparrow, E. M. and Hennecke, D. K., "Temperature Depression at the Base of A Fin," ASME JOURNAL OF HEAT TRANSFER, Vol. 92, 1970, pp. 204–206.

10 Kleff, D. E. and McCulloch, J. W., "The Effect of Thermal Conductivity and Base-Temperature Depression on Fin Effectiveness," ASME JOURNAL OF HEAT TRANSFER, Vol. 94, 1972, pp. 333–334.

11 Harper, W. B. and Brown, D. R., "Mathematical Equations for Heat Conduction in the Fins of Air-Cooled Engines," NACA Report No. 158, Washington, D. C., 1922, pp. 679–708.

12 Stachiewicz, J. W., "Effect of Variation of Local Film Coefficients on Fin Performance," ASME JOURNAL OF HEAT TRANSFER, Vol. 91, 1969, pp. 21–26.

Fin Thickness for an Optimized Natural Convection Array of Rectangular Fins

A. Bar-Cohen[1]

Nomenclature

A_p = fin cross-sectional area
b = fin width
c_p = specific heat at constant pressure
g = gravitational acceleration
h = convective heat transfer coefficient
k = thermal conductivity of fin material
k_a = thermal conductivity of ambient air
L = length of fin
Nu = hS/k_a
β = volume coefficient of expansion
δ = fin thickness
θ = average temperature difference between fin and ambient
P = array parameter, $S/\mathrm{Ra}^{1/4}$
Pr = Prandtl number $c_p\mu/k_a$
q = heat dissipation of single fin
Q = heat dissipation
r = number of inter-fin spaces in array

$$\mathrm{Ra} = \frac{g\beta\theta_0 \mathrm{Pr} S^4}{L\nu^2}$$

S = inter-fin spacing
W = width of fin array
θ_0 = temperature difference between fin root and ambient
η = fin efficiency
ν = kinematic viscosity

Subscripts

lm = least material
max = maximum
opt = optimum

Introduction

The heat rejection capability of a natural convection fin array (see Fig. 1) is dependent on both the convective heat transfer coefficient at the fin surface and the thermal efficiency of the fins. The literature contains many analyses of heat transfer by natural convection from parallel, vertical plates of rectangular profile [1–5] but unfortunately, nearly all of these assume the plates to be isothermal [1, 2, 3] or constant flux surfaces [5] and are thus inapplicable to the determination and optimization of heat transfer from an array of finite thermal conductivity fins.

The experimental study by Elenbaas [1] was the first to establish the relationship between the separation distance, S, of adjacent isothermal plates and the convective coefficient on the plate surface. As the spacing was reduced, the surface Nusselt Number, Nu, was found to fall below values normally associated with an isolated plate in an infinite medium [1]. The Elenbaas results were later shown to also agree with the average heat transfer coefficients obtained in natural convection airflows in vertical channels formed by plates subjected to a constant heat flux [5]. Maximization of total heat transfer from an array of parallel plates or fins of known thickness thus requires finding the plate spacing for which the product of plate surface area and local heat transfer coefficient is a maximum.

Based on his experimental results, Elenbaas determined that this optimum spacing could be obtained by setting the Rayleigh Number (based on the plate spacing and aspect ratio) equal to 50. The associated optimum Nu was found to equal 1.05. A later theoretical study by Bodoia and Osterle [2], found Ra_{opt} to equal 70 for idealized two-dimensional flow between the plates and related the slight deviation from the Elenbaas result to three-dimensional flow effects in the Elenbaas apparatus.

In view of the agreement between the constant flux [5] and isothermal surface [1] Nu variation, it appears possible to generalize the Elenbaas optimum spacing result to all surfaces, by basing the Rayleigh Number on the average surface-to-air temperature difference. In a fin, this average temperature difference is given by the product of the temperature difference at the base and the fin efficiency, i.e., $\theta = \eta\theta_0$. Consequently, the optimum fin spacing, $S_{opt} = (50/\eta)^{1/4}P$, is dependent on both the array fluid parameters contained in P and the efficiency of the fin.

Optimum Fin Dimensions

In the design of fin arrays for electronic equipment, manufacturing, weight and cost considerations generally dictate that the requisite thermal load be dissipated with rectangular, longitudinal fins of minimum volume and weight. This requirement can be met by choosing rectangular fin dimensions which maximize heat dissipation per unit fin profile area (A_p in Fig. 1) and it is this particular fin geometry that will serve as a reference point for array design.

The heat rejection capability of a single, rectangular, least-material fin, subjected to a constant heat transfer coefficient, is expressible as [6]

$$\frac{q_{lm}}{L} = 1.258(hk)^{1/2}\delta^{1/2}\theta_0 \tag{1}$$

This heat transfer rate is attained at a prescribed relationship between fin thickness and fin width, according to

$$b_{lm} = 1.4192(k/2h)^{1/2}\delta^{1/2} \tag{2}$$

[1] Department of Mechanical Engineering, Ben-Gurion University of the Negev, Beer Sheva, Israel, Mem. ASME.

Contributed by the Heat Transfer Division for publication in the JOURNAL OF HEAT TANSFER. Based on ASME Paper 77-DE-37, presented at the Design Engineering Conference, Chicago, 1977. Revised Manuscript received by the Heat Transfer Division June 13, 1978.

References

1 Irey, R. K., "Errors in the One-Dimensional Fin Solution," ASME JOURNAL OF HEAT TRANSFER, Vol. 90, 1968, pp. 175–176.

2 Avrami, M. and Little, J. B., "Diffusion of Heat Through a Rectangular Bar and the Cooling and Insulating Effect of Fins," *Journal of Applied Physics*, Vol. 13, 1942, pp. 255–264.

3 Keller, H. H. and Somers, E. V., "Heat Transfer From an Annular Fin of Constant Thickness," ASME JOURNAL OF HEAT TRANSFER, Vol. 81, 1959, pp. 151–156.

4 Sfeir, A. A., "The Heat Balance Integral in Steady Heat Conduction," JOURNAL OF HEAT TRANSFER, Vol. 98, 1976, pp. 466–470.

5 Schnurr, N. M., Shapiro, A. B., and Townsend, M. A., "Optimization of Radiating Fin Arrays with Respect to Weight," ASME JOURNAL OF HEAT TRANSFER, Vol. 98, 1976, pp. 643–648.

6 Murphy, G. M., *Ordinary Differential Equations and Their Solutions*, Van Nostrand, 1960, p. 357, item 409.

7 Abramowitz, M. and Stegun, I. A., *Handbook of Mathematical Functions*, National Bureau of Standards, Applied Mathematics Series 55, 1965, pp. 562–564.

8 Morse, P. M. and Feshbach, H., *Methods of Theoretical Physics*, McGraw-Hill, 1953, pp. 541–547, pp. 587–593, and pp. 668–671.

9 Sparrow, E. M. and Hennecke, D. K., "Temperature Depression at the Base of A Fin," ASME JOURNAL OF HEAT TRANSFER, Vol. 92, 1970, pp. 204–206.

10 Kleff, D. E. and McCulloch, J. W., "The Effect of Thermal Conductivity and Base-Temperature Depression on Fin Effectiveness," ASME JOURNAL OF HEAT TRANSFER, Vol. 94, 1972, pp. 333–334.

11 Harper, W. B. and Brown, D. R., "Mathematical Equations for Heat Conduction in the Fins of Air-Cooled Engines," NACA Report No. 158, Washington, D. C., 1922, pp. 679–708.

12 Stachiewicz, J. W., "Effect of Variation of Local Film Coefficients on Fin Performance," ASME JOURNAL OF HEAT TRANSFER, Vol. 91, 1969, pp. 21–26.

Fin Thickness for an Optimized Natural Convection Array of Rectangular Fins

A. Bar-Cohen[1]

Nomenclature

A_p = fin cross-sectional area
b = fin width
c_p = specific heat at constant pressure
g = gravitational acceleration
h = convective heat transfer coefficient
k = thermal conductivity of fin material
k_a = thermal conductivity of ambient air
L = length of fin
Nu = hS/k_a
β = volume coefficient of expansion
δ = fin thickness
θ = average temperature difference between fin and ambient
P = array parameter, $S/\mathrm{Ra}^{1/4}$
Pr = Prandtl number $c_p\mu/k_a$
q = heat dissipation of single fin
Q = heat dissipation
r = number of inter-fin spaces in array

$$\mathrm{Ra} = \frac{g\beta\theta_0 \mathrm{Pr} S^4}{L\nu^2}$$

S = inter-fin spacing
W = width of fin array
θ_0 = temperature difference between fin root and ambient
η = fin efficiency
ν = kinematic viscosity

Subscripts

lm = least material
max = maximum
opt = optimum

Introduction

The heat rejection capability of a natural convection fin array (see Fig. 1) is dependent on both the convective heat transfer coefficient at the fin surface and the thermal efficiency of the fins. The literature contains many analyses of heat transfer by natural convection from parallel, vertical plates of rectangular profile [1–5] but unfortunately, nearly all of these assume the plates to be isothermal [1, 2, 3] or constant flux surfaces [5] and are thus inapplicable to the determination and optimization of heat transfer from an array of finite thermal conductivity fins.

The experimental study by Elenbaas [1] was the first to establish the relationship between the separation distance, S, of adjacent isothermal plates and the convective coefficient on the plate surface. As the spacing was reduced, the surface Nusselt Number, Nu, was found to fall below values normally associated with an isolated plate in an infinite medium [1]. The Elenbaas results were later shown to also agree with the average heat transfer coefficients obtained in natural convection airflows in vertical channels formed by plates subjected to a constant heat flux [5]. Maximization of total heat transfer from an array of parallel plates or fins of known thickness thus requires finding the plate spacing for which the product of plate surface area and local heat transfer coefficient is a maximum.

Based on his experimental results, Elenbaas determined that this optimum spacing could be obtained by setting the Rayleigh Number (based on the plate spacing and aspect ratio) equal to 50. The associated optimum Nu was found to equal 1.05. A later theoretical study by Bodoia and Osterle [2], found Ra_{opt} to equal 70 for idealized two-dimensional flow between the plates and related the slight deviation from the Elenbaas result to three-dimensional flow effects in the Elenbaas apparatus.

In view of the agreement between the constant flux [5] and isothermal surface [1] Nu variation, it appears possible to generalize the Elenbaas optimum spacing result to all surfaces, by basing the Rayleigh Number on the average surface-to-air temperature difference. In a fin, this average temperature difference is given by the product of the temperature difference at the base and the fin efficiency, i.e., $\theta = \eta\theta_0$. Consequently, the optimum fin spacing, $S_{opt} = (50/\eta)^{1/4}P$, is dependent on both the array fluid parameters contained in P and the efficiency of the fin.

Optimum Fin Dimensions

In the design of fin arrays for electronic equipment, manufacturing, weight and cost considerations generally dictate that the requisite thermal load be dissipated with rectangular, longitudinal fins of minimum volume and weight. This requirement can be met by choosing rectangular fin dimensions which maximize heat dissipation per unit fin profile area (A_p in Fig. 1) and it is this particular fin geometry that will serve as a reference point for array design.

The heat rejection capability of a single, rectangular, least-material fin, subjected to a constant heat transfer coefficient, is expressible as [6]

$$\frac{q_{lm}}{L} = 1.258(hk)^{1/2}\delta^{1/2}\theta_0 \tag{1}$$

This heat transfer rate is attained at a prescribed relationship between fin thickness and fin width, according to

$$b_{lm} = 1.4192(k/2h)^{1/2}\delta^{1/2} \tag{2}$$

[1] Department of Mechanical Engineering, Ben-Gurion University of the Negev, Beer Sheva, Israel, Mem. ASME.

Contributed by the Heat Transfer Division for publication in the JOURNAL OF HEAT TANSFER. Based on ASME Paper 77-DE-37, presented at the Design Engineering Conference, Chicago, 1977. Revised Manuscript received by the Heat Transfer Division June 13, 1978.

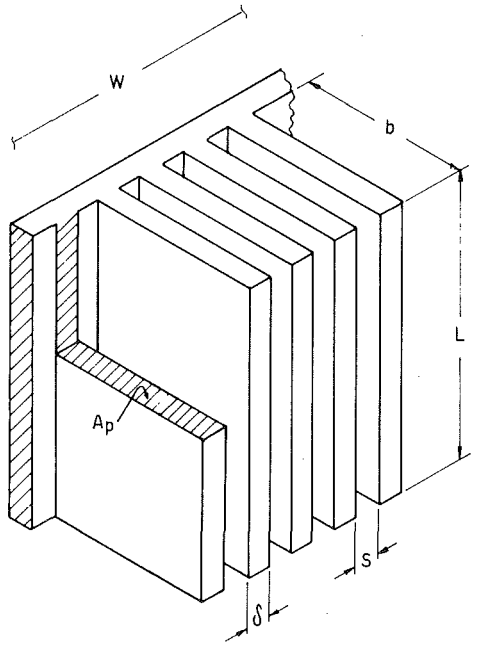

Fig. 1 Geometric definition of rectangular, vertical fin array

Using the heat transfer coefficient value determined by Nu_{opt} = 1.05 and noting that the efficiency of a least material, rectangular fin equals 62 percent [6], the fin width associated with the optimum fin spacing is given by

$$b_{opt} = 1.597(k/k_a)^{1/2}(L\nu^2/g\beta\mathrm{Pr}\theta)^{1/8}\delta^{1/2} = 1.7(kP/k_a)^{1/2}\delta^{1/2} \quad (3)$$

This relation is, strictly speaking, valid only for least material fins with a constant heat transfer coefficient and may, thus, not be applicable to fin arrays where spatial variation in h may be encountered. However, when the Elenbaas optimum spacing is used, fully-developed flow can be expected to prevail over much of the "channel" height [2] and consequently h will be uniform or near-uniform over almost all the fin surface area. Furthermore, due to the 1/4 power dependence of the optimum spacing on the surface-to-air temperature difference, modest variations in fin efficiency resulting from slight non-uniformities in the heat transfer coefficient, can be expected to yield near-negligible variations in the optimum spacing (less than ±1 percent for a ±4 percent change in η).

Equation (3) is shown graphically in Fig. 2, where it may be noted that, as a consequence of the relatively low heat transfer coefficients associated with natural convection in air, the values of b_{opt} vary from 0.1 to 1 m for typical array parameters.

Fin Array Dissipation

Heat rejection from the array is comprised of two components—thermal transfer from each of the fins in the array and heat dissipation from the area between the fins. Assuming that the number of fins is large, the number of fins can be taken equal to the number of inter-fin spaces and each equal approximately to $W/(S + \delta)$. Assuming, furthermore, that h_{opt} can be used to characterize the heat transfer coefficient in the area between the fins, the total heat dissipation of the array is expressible as

$$(Q/L) = (q_{opt}/L + h_{opt}S_{opt}\theta_0)W/(S_{opt} + \delta) \quad (4)$$

Following substitution for q_{opt}/L, h_{opt}, and S_{opt}, with η = 0.62, equation (4) can be modified to yield

$$Q/LW\theta_0 = [0.75(k_a k\delta/P)^{1/2} + 1.05k_a]/[3P + \delta] \quad (5)$$

A graphical presentation of equation (5) for an aluminum array of least material fins, dissipating heat to ambient air is shown in Fig. 3, for a typical parametric range. Array dissipation is seen to vary strongly with both the array parameter, P, and the thickness of the optimum fin δ_{opt}. Furthermore, a maximizing value of δ_{opt} appears to exist for each value of P.

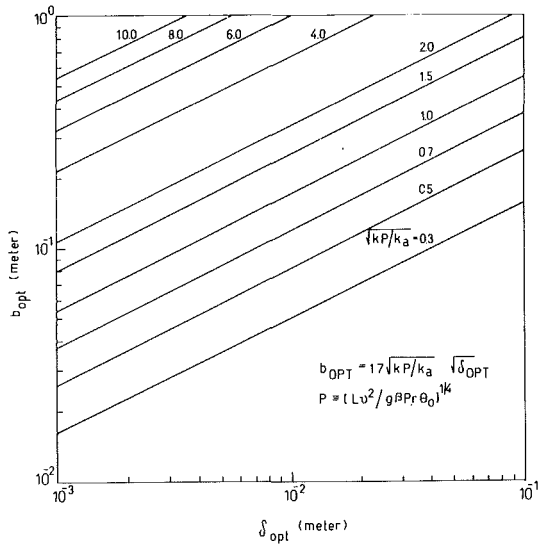

Fig. 2 Optimum fin width as a function of fin thickness and array parameter

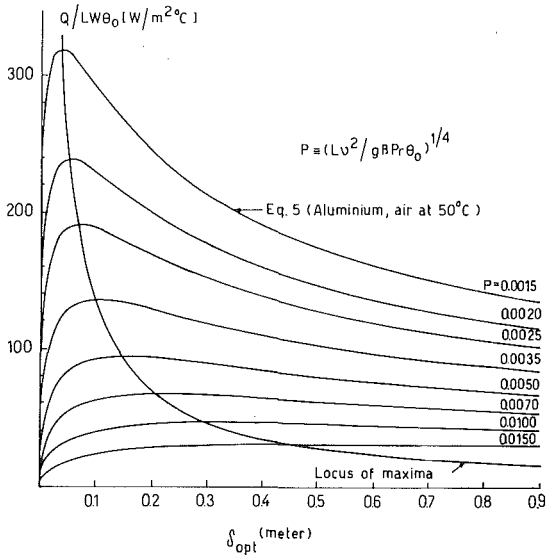

Fig. 3 Free convection heat dissipation of an array of optimally spaced, vertical, rectangular, least-material fins (aluminum)

The locus of the array dissipation maxima can be obtained by differentiation of equation (5) or, more simply, by differentiation of an approximate form of this relation, in which heat transfer from the area between the fins is neglected. With this assumption, clearly justified by the large width of the optimum natural convection fin, equation (4) yields

$$\frac{Q}{LW\theta_0} \simeq 1.258(hk)^{1/2}\delta_{opt}^{1/2}/(S_{opt} + \delta_{opt}) \quad (6)$$

Differentiating equation (6) relative to δ_{opt} and setting the derivative to zero, the maximizing value of δ_{opt} is found to equal S_{opt}. Consequently, maximum array dissipation in air is obtained when fin thickness is approximately equal to the optimum fin spacing. Substitution of this value in equation (5) yields the peak dissipation capability of a vertical array of rectangular least-material fins as

$$\left.\frac{Q}{LW\theta_0}\right|_{max} = 1.3(kk_a)^{1/2}/6P \quad (7)$$

It must be noted that the validity of this relation and, indeed, the above analysis, is limited to configurations in which the primary area is or can be assumed isothermal. Fortunately, this is a frequently encountered situation in the thermal control of electronic components, where relatively massive "cold-plates" are used to smooth temporal variations in heat dissipation and separate the electronic components

from the dirt and humidity laden cooling air [7]. A similar situation is generally encountered in fin arrays on the exterior surfaces of liquid-filled enclosures [8], as may be found in the chemical industry, in the immersion cooling of electronic components or in thermal storage devices.

Discussion

The results of the present analysis can be conveniently characterized by examining the behavior of $Q/LW\theta_0$, which constitutes an effective array heat transfer coefficient referenced to the primary area. Examination of Fig. 3 and equation (5) shows $Q/LW\theta_0$, for the configuration studied, to be governed by two key parameters: P—embodying the influence of geometric, thermal and air property variations, and δ_{opt}—the individual optimum fin thickness. A factor of two increase in the fin array parameter typically doubles the value of the effective heat transfer coefficient. Alternately, at fixed values of P, a maximizing value of δ_{opt} exists, although at larger P values the array dissipation is only weakly dependent on δ_{opt} and a maximizing "plateau" is encountered. At effective heat transfer coefficients other than the maximum, either many, short, thin fins or fewer, longer, thicker fins can be used to achieve the same thermal results and it is to be expected that mechanical strength, manufacturing and/or packaging considerations will dictate the appropriate choice. Significantly, however, in the parametric range where array dissipation is substantial, fin thickness is decidedly not negligible, relative to the fin spacing, in determining the number of fins that can be accommodated per unit width of primary area.

Turning now to the array configuration at which the peak heat dissipation rates are encountered, it is apparent that by proper design it is possible to attain effective (array) heat transfer coefficients in natural convection, i.e., $Q/LW\ \theta_0$, that are comparable to values normally associated with forced convection transfer (in air) from the primary surface alone. In particular, for aluminum fins in air, the maximum effective heat transfer coefficient, as presented in Fig. 3, is seen to range from 100 to 320 W/m^2°C (18 to 57 Btu/hr-ft^2°F) in the parametric range of interest, providing a 15 to 45 fold improvement over natural convection heat transfer from an unfinned surface. These transfer rates are attained when the fins are optimally spaced (based on the modified Elenbaas criteria), the thickness of each fin closely approximates the optimum spacing and the width of the fins is determined by the least-material criterion equation (2).

Array design, which compromises any one of these three requirements, cannot be expected to yield the above-mentioned heat transfer rates. Thus, for example, a more conventional aluminum fin array, consisting of 0.2 cm thick and 5 cm wide, optimally-spaced fins would offer a theoretical effective heat transfer coefficient of approximately 43 W/m^2-°C for conditions associated with an array parameter, P, of 0.002. Comparison with the values shown in Fig. 3 reveals that this transfer rate is approximately 1/6 of what could be obtained at P = 0.002 by use of 0.6 cm thick and 40 cm wide fins, constituting the maximizing configuration.

Concluding Remarks

The preceding development reveals that in natural convection arrays superior thermal performance is generally associated with relatively thick fins. Consequently, fin thickness cannot be neglected in optimizing total array heat transfer as it influences both the efficiency of individual fins and the number of fins that can be accommodated on the primary area.

Analysis of the thermal performance of an array of least-material, optimally spaced, vertical, rectangular fins further suggests that a maximizing value of fin thickness exists for each distinct combination of environmental, geometric and material constraints. In air, this value of fin thickness closely approximates the optimum fin spacing and results in effective heat transfer coefficients that offer a 15 to 45-fold improvement over natural convection transfer from an unfinned surface.

The array heat transfer rate obtained by setting fin thickness equal to the optimum spacing would appear to offer a good first approximation of the maximum attainable natural convection heat dissipation at a specified temperature difference between the primary surface and ambient air for a least-material array. With the derived relations and a geometric constraint on the fin width or thickness, it is thus possible to determine, a priori, whether the necessary thermal control can, in principle, be provided by natural convection transfer or whether one must resort to an alternate heat transfer technique.

Acknowledgment

The technical aid of Gershon Perlman in the preparation of this manuscript is gratefully acknowledged.

References

1 Elenbaas, W., "Heat Dissipation of Parallel Plates by Free Convection," *Physica*, Vol. 9, No. 1, Holland, 1942.

2 Bodoia, J. R. and Osterle, J. F., "The Development of Free Convection Between Heated Vertical Plates," ASME JOURNAL OF HEAT TRANSFER Vol. 84, 1964, pp. 40–44.

3 Levy, E. K., "Optimum Plate Spacings for Laminar Natural Convection Heat Transfer from Parallel Vertical Isothermal Flat Plates," ASME JOURNAL OF HEAT TRANSFER, Vol. 93, 1971, pp. 463–465.

4 Aung, W., Kessler, T. J., and Beitin, K. I., "Free Convection Cooling of Electronic Systems," *IEEE Transactions on Parts, Hybrids and Packaging*, Vol. PHP-9, No. 2, 1973, pp. 75–86.

5 Sobel, N., Landis, F. and Mueller, W. K., "Natural Convection Heat Transfer in Short Vertical Channels Including the Effect of Stagger," *Proceedings—Third International Heat Transfer Conference*, Vol. 2, 1966, pp. 121–125.

6 Kern, D. Q. and Kraus, A. D., *Extended Surface Heat Transfer*, McGraw Hill, New York, 1972.

7 Kraus, A. D., *Cooling Electronic Equipment*, McGraw Hill, New York, 1962.

8 Bar-Cohen, A. and Distel, H., "Thermal Characteristics of Multiple Surface Submerged Condensers," *Proceedings 1978 HTFMI*, edited by C. T. Crowe and W. L. Grosshandler, Stanford University Press, 1978, pp. 131–142.

Natural Convection from Spheres and Cylinders Immersed in a Thermally Stratified Fluid

C. C. Chen[1] and R. Eichhorn[2]

Nomenclature

a = ambient temperature gradient, dT_∞/dz
C = Pr − dependent parameter
D = cylinder or sphere diameter
g = gravitational acceleration
g_x = component of gravitational acceleration tangent to the body surface
k = thermal conductivity
L = body height
$\overline{\mathrm{Nu}}$, $\overline{\mathrm{Nu}}_{iso}$ = average Nusselt number based on ΔT_m and L for the stratified and unstratified case, respectively
Pr = Prandtl number
q = local heat transfer rate
R = radial distance from a surface element
Ra = Rayleigh number, $g\beta\Delta T_m L^3/\nu\alpha$
S = stratification parameter, defined in equation (6)
T_w = surface temperature
T_∞ = local ambient temperature
x = coordinate along the body surface
y = coordinate normal to the body surface
z = coordinate measured vertically
α = thermal diffusivity
β = coefficient of thermal expansion
ν = kinematic viscosity

[1] Gould Inc., Gould Lab-Energy Research, Associate Mem. ASME
[2] Professor, University of Kentucky, Fellow ASME.
Contributed by the Heat Transfer Division for publication in the JOURNAL OF HEAT TRANSFER. Manuscript received by the Heat Transfer Division June 16, 1979.

from the dirt and humidity laden cooling air [7]. A similar situation is generally encountered in fin arrays on the exterior surfaces of liquid-filled enclosures [8], as may be found in the chemical industry, in the immersion cooling of electronic components or in thermal storage devices.

Discussion

The results of the present analysis can be conveniently characterized by examining the behavior of $Q/LW\theta_0$, which constitutes an effective array heat transfer coefficient referenced to the primary area. Examination of Fig. 3 and equation (5) shows $Q/LW\theta_0$, for the configuration studied, to be governed by two key parameters: P—embodying the influence of geometric, thermal and air property variations, and δ_{opt}—the individual optimum fin thickness. A factor of two increase in the fin array parameter typically doubles the value of the effective heat transfer coefficient. Alternately, at fixed values of P, a maximizing value of δ_{opt} exists, although at larger P values the array dissipation is only weakly dependent on δ_{opt} and a maximizing "plateau" is encountered. At effective heat transfer coefficients other than the maximum, either many, short, thin fins or fewer, longer, thicker fins can be used to achieve the same thermal results and it is to be expected that mechanical strength, manufacturing and/or packaging considerations will dictate the appropriate choice. Significantly, however, in the parametric range where array dissipation is substantial, fin thickness is decidedly not negligible, relative to the fin spacing, in determining the number of fins that can be accommodated per unit width of primary area.

Turning now to the array configuration at which the peak heat dissipation rates are encountered, it is apparent that by proper design it is possible to attain effective (array) heat transfer coefficients in natural convection, i.e., $Q/LW\ \theta_0$, that are comparable to values normally associated with forced convection transfer (in air) from the primary surface alone. In particular, for aluminum fins in air, the maximum effective heat transfer coefficient, as presented in Fig. 3, is seen to range from 100 to 320 W/m^2°C (18 to 57 Btu/hr-ft^2°F) in the parametric range of interest, providing a 15 to 45 fold improvement over natural convection heat transfer from an unfinned surface. These transfer rates are attained when the fins are optimally spaced (based on the modified Elenbaas criteria), the thickness of each fin closely approximates the optimum spacing and the width of the fins is determined by the least-material criterion equation (2).

Array design, which compromises any one of these three requirements, cannot be expected to yield the above-mentioned heat transfer rates. Thus, for example, a more conventional aluminum fin array, consisting of 0.2 cm thick and 5 cm wide, optimally-spaced fins would offer a theoretical effective heat transfer coefficient of approximately 43 W/m^2-°C for conditions associated with an array parameter, P, of 0.002. Comparison with the values shown in Fig. 3 reveals that this transfer rate is approximately 1/6 of what could be obtained at P = 0.002 by use of 0.6 cm thick and 40 cm wide fins, constituting the maximizing configuration.

Concluding Remarks

The preceding development reveals that in natural convection arrays superior thermal performance is generally associated with relatively thick fins. Consequently, fin thickness cannot be neglected in optimizing total array heat transfer as it influences both the efficiency of individual fins and the number of fins that can be accommodated on the primary area.

Analysis of the thermal performance of an array of least-material, optimally spaced, vertical, rectangular fins further suggests that a maximizing value of fin thickness exists for each distinct combination of environmental, geometric and material constraints. In air, this value of fin thickness closely approximates the optimum fin spacing and results in effective heat transfer coefficients that offer a 15 to 45-fold improvement over natural convection transfer from an unfinned surface.

The array heat transfer rate obtained by setting fin thickness equal to the optimum spacing would appear to offer a good first approximation of the maximum attainable natural convection heat dissipation at a specified temperature difference between the primary surface and ambient air for a least-material array. With the derived relations and a geometric constraint on the fin width or thickness, it is thus possible to determine, a priori, whether the necessary thermal control can, in principle, be provided by natural convection transfer or whether one must resort to an alternate heat transfer technique.

Acknowledgment

The technical aid of Gershon Perlman in the preparation of this manuscript is gratefully acknowledged.

References

1 Elenbaas, W., "Heat Dissipation of Parallel Plates by Free Convection," *Physica*, Vol. 9, No. 1, Holland, 1942.

2 Bodoia, J. R. and Osterle, J. F., "The Development of Free Convection Between Heated Vertical Plates," ASME JOURNAL OF HEAT TRANSFER Vol. 84, 1964, pp. 40–44.

3 Levy, E. K., "Optimum Plate Spacings for Laminar Natural Convection Heat Transfer from Parallel Vertical Isothermal Flat Plates," ASME JOURNAL OF HEAT TRANSFER, Vol. 93, 1971, pp. 463–465.

4 Aung, W., Kessler, T. J., and Beitin, K. I., "Free Convection Cooling of Electronic Systems," *IEEE Transactions on Parts, Hybrids and Packaging*, Vol. PHP-9, No. 2, 1973, pp. 75–86.

5 Sobel, N., Landis, F. and Mueller, W. K., "Natural Convection Heat Transfer in Short Vertical Channels Including the Effect of Stagger," *Proceedings—Third International Heat Transfer Conference*, Vol. 2, 1966, pp. 121–125.

6 Kern, D. Q. and Kraus, A. D., *Extended Surface Heat Transfer*, McGraw Hill, New York, 1972.

7 Kraus, A. D., *Cooling Electronic Equipment*, McGraw Hill, New York, 1962.

8 Bar-Cohen, A. and Distel, H., "Thermal Characteristics of Multiple Surface Submerged Condensers," *Proceedings 1978 HTFMI*, edited by C. T. Crowe and W. L. Grosshandler, Stanford University Press, 1978, pp. 131–142.

Natural Convection from Spheres and Cylinders Immersed in a Thermally Stratified Fluid

C. C. Chen[1] and R. Eichhorn[2]

Nomenclature

a = ambient temperature gradient, dT_∞/dz
C = Pr − dependent parameter
D = cylinder or sphere diameter
g = gravitational acceleration
g_x = component of gravitational acceleration tangent to the body surface
k = thermal conductivity
L = body height
$\overline{\mathrm{Nu}}$, $\overline{\mathrm{Nu}}_{iso}$ = average Nusselt number based on ΔT_m and L for the stratified and unstratified case, respectively
Pr = Prandtl number
q = local heat transfer rate
R = radial distance from a surface element
Ra = Rayleigh number, $g\beta\Delta T_m L^3/\nu\alpha$
S = stratification parameter, defined in equation (6)
T_w = surface temperature
T_∞ = local ambient temperature
x = coordinate along the body surface
y = coordinate normal to the body surface
z = coordinate measured vertically
α = thermal diffusivity
β = coefficient of thermal expansion
ν = kinematic viscosity

[1] Gould Inc., Gould Lab-Energy Research, Associate Mem. ASME
[2] Professor, University of Kentucky, Fellow ASME.
Contributed by the Heat Transfer Division for publication in the JOURNAL OF HEAT TRANSFER. Manuscript received by the Heat Transfer Division June 16, 1979.

Introduction

Thermally stratified environments exist in nature and in many engineering applications. Consequently, there have been a number of recent studies which discuss the effect of stratification on natural convection heat transfer. Cheesewright [1] and Yang, et al. [2] obtained boundary layer solutions for cases which admit similarity transformations. For vertical plate problems which do not have a similarity solution, Eichhorn [3] and Takeuchi, et al. [4] used a perturbation method and Chen and Eichhorn [5] used the local nonsimilarity method. To our knowledge, there are no published papers which treat the boundary layer problems for more complex geometries such as the horizontal cylinder or the sphere in a stratified fluid.

It is well known that the boundary layer equations for horizontal cylinders and spheres do not admit a similarity solution even when the ambient fluid is isothermal. For these cases there are many analyses available. However, the results from different analyses for the upper half of the body are not consistent. Since ambient stratification is an additional complexity, we can expect these methods to give more uncertain results.

Recently, Raithby, et al. [6, 7] developed an approximate method to calculate natural convection heat transfer rates. They have applied the method with good success to a number of complex problems. In this work, we apply their approach to derive an equation for the heat transfer rate from axisymmetric bodies to a thermally stratified fluid. The results for the average heat transfer rate are shown to compare very favorably with the experimental data reported in [8] for heated horizontal cylinders and spheres in stratified water. The analysis parallels Raithby and Hollands application [9] of the approximate method to our data [5] for the vertical plate.

Approximate Boundary Layer Solution

Fig. 1 shows the coordinate system for a closed-end axisymmetric body. The z-coordinate is measured from the forward stagnation point of the body and is parallel to the direction of gravity. Based on the approach of Raithby, et al. [6], we find the equation for the local heat transfer rate from the body surface to a stratified fluid to be

$$q = Ck(\beta/\nu\alpha)^{1/4}(R^i)^{1/3}g_x{}^{1/3}(T_w - T_\infty)^{5/3}(F/G)^{1/4} \tag{1}$$

where superscript i is equal to 0 for two-dimensional bodies, and 1 for axisymmetric bodies, and

$$F = \exp\left[\frac{4}{3}(n+1)\int_0^x \frac{(dT_\infty/dx)}{(T_w - T_\infty)}dx\right] \tag{2}$$

$$G = \int_0^x (R^i)^{4/3}g_x{}^{1/3}(T_w - T_\infty)^{5/3}F dx \tag{3}$$

The other standard symbols are defined in the Nomenclature.

There are two undetermined constants in the approximate solution: C in equation (1) and n in equation (2). Since equation (1) is intended to be valid for either two-dimensional or axisymmetric bodies, and for either uniform or non-uniform T_w and T_∞, the value of C is only Prandtl number dependent and can be determined by comparing the approximate solution with available exact solutions or experimental results. In contrast, the value of n actually depends on the velocity and temperature distributions. However, as a result of the approximations assumed in deriving equation (1), its value is restricted to depend on the ambient fluid stratification and the Prandtl number.

If the ambient fluid is at a uniform temperature, whether or not the surface is isothermal, the function $F(x)$ is unity and n is not a parameter in the solution. For the case of an isothermal surface in a stratified fluid, equation (2) can be simplified to give

$$F = (T_w - T_\infty)^{-4(n+1)/3} \tag{4}$$

Application of the Approximate Solution

It is of interest to know the accuracy of the approximate heat transfer prediction. The method is even more desirable if it gives reasonable results for problems which do not have similarity solutions. For this, we consider the problem of an isothermal body at T_w immersed in a stratified fluid. The temperature of the fluid far from the body surface increases linearly with vertical distance, i.e.,

$$T_\infty = T_0 + az \tag{5}$$

where T_0 is the ambient temperature at $z = 0$ (or $x = 0$). We further specify that T_0 is different from T_w. Thus, the problem does not have a similarity solution even if the heat transfer body is a vertical plate.

As shown in [5], the effect of stratification on natural convection heat transfer can be expressed in terms of a stratification parameter, S, which has been defined as

$$S = (L/\Delta T_m)dT_\infty/dz = aL/\Delta T_m \tag{6}$$

where L is the height of the body and ΔT_M is the temperature difference, $T_w - T_\infty$ at the midheight of the body. If $(T_w - T_\infty)$ is positive through the height of the body, the value of S lies between 0 and 2. If $(T_w - T_\infty)$ changes sign between $z = L/2$ and L, the value of S is greater than 2.

To see the effect of stratification on the heat transfer rate, we express the results of the approximate method as

$$\overline{\mathrm{Nu}}/\overline{\mathrm{Nu}}_{\mathrm{iso}} = G(n,S) \tag{7}$$

where $\overline{\mathrm{Nu}}$ is the average Nusselt number for the stratified case and the subscript iso refers to the unstratified case with a constant temperature difference, T_m. As has been done in [5], the gross heat transfer rate from the body surface is used to calculate $\overline{\mathrm{Nu}}$.

Vertical Plates

Raithby and Hollands [9] determined the constant in the approximate solution for the vertical plate case by comparison with the similarity solution of Yang, et al. [2]. However, the ambient temperature in the similarity solution varies differently from that given by equation (5). For the case used for comparison in [9], the temperature difference is not defined at the leading edge of the plate and decreases non-linearly with the plate height.

In this work we find $n(\mathrm{Pr})$ by comparing the approximate solution with the local nonsimilarity solution in [5] for the vertical plate. The results for the average Nusselt number ratio for values of n between 1.5 and 4.5 are plotted in Fig. 2. In this figure, the local nonsimilarity solution for Pr = 0.7 and 6.0 from [5] are also included. We find that the approximate solution with $n = 2.5$ agrees remarkably well with the local non-similarity solution for Pr = 6.0. While the agreement for Pr = 0.7 is not as good as this, the difference between the approximate solution for $n = 4.0$ and the nonsimilar solution is less than 3 percent over the range of S between 0 and 2.

The values of n given in [9] are quite close to those we have found. It seems that n does not strongly depend on stratification of the ambient fluid.

Horizontal Cylinder

For the horizontal cylinder of diameter D, $z = (D/2)(1 - \cos 2x/D)$, $g_x = g \sin 2x/D$, and $R^i = 1$ in equation (1). The local or overall heat transfer rates can be found by numerical integration.

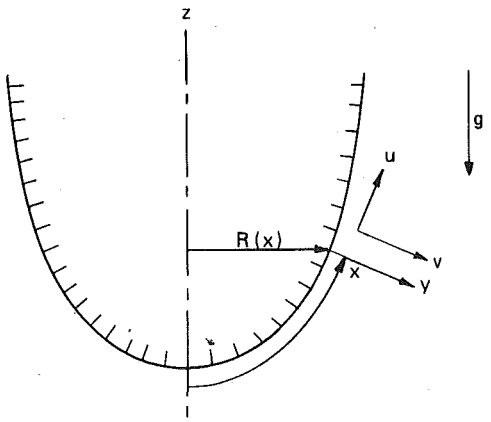

Fig. 1 Coordinate system for an axisymmetric body

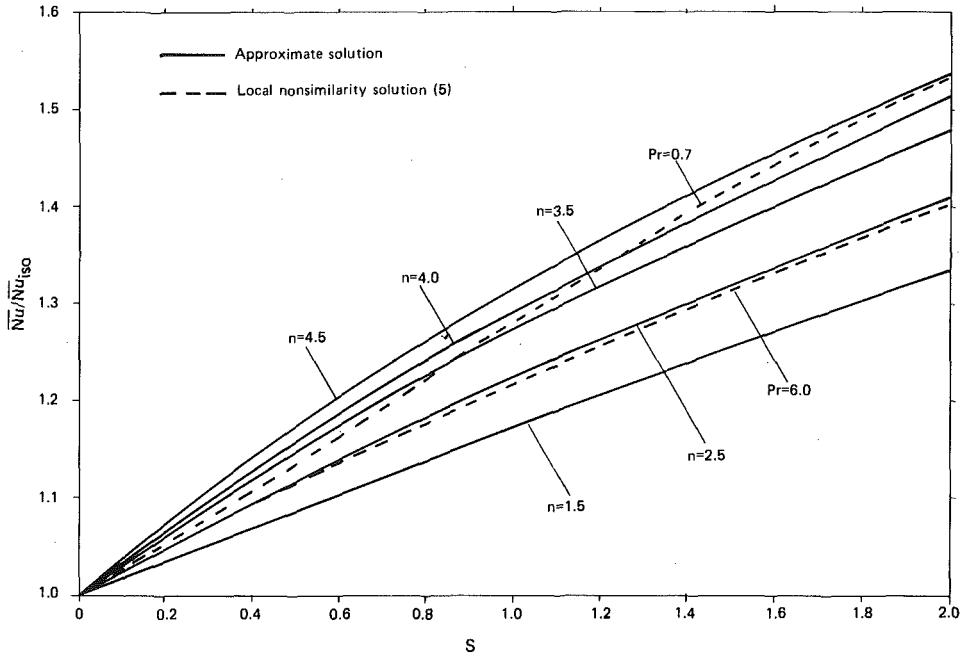

Fig. 2 Comparison between the approximate solution and the local nonsimilarity solution for the vertical plate case

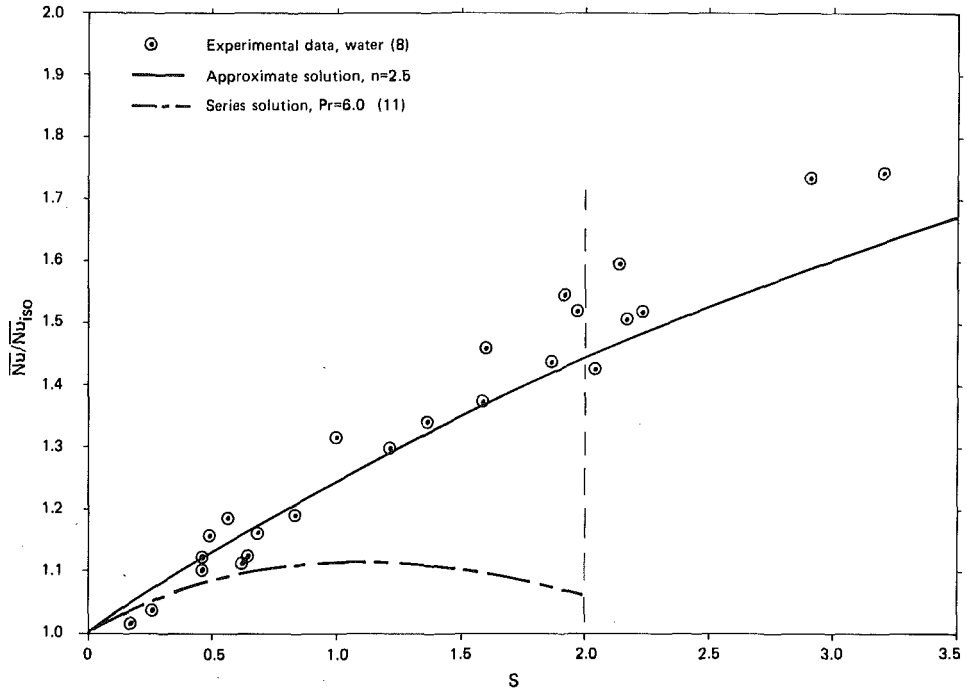

Fig. 3 Influence of stratification on heat transfer from horizontal cylinders

To compare the theory with experimental data from [8], the curvature effect was considered. The effect becomes significant for large S because the boundary layer thickens. As shown in the studies of Raithby and Hollands [6] and Eichhorn and Wang [10], the curvature effect on heat transfer from a horizontal cylinder can be corrected by the formula

$$\overline{Nu} = 2/[\exp(2/\overline{Nu}_m) - 1] \tag{8}$$

where $\overline{Nu}$ is the mean Nusselt number as $Ra \to \infty$, and $\overline{Nu}_m$ is the measured mean Nusselt number for finite Ra. The experimental data from [8, 12] for an isothermal environment, modified by equation (8), correlate very well with the purely theoretical result [13]

$$\overline{Nu}_{iso} = 0.5\, Ra^{1/4} \tag{9}$$

With equations (8) and (9), the data from [8] for a stratified environment were used to calculate the mean Nusselt number ratio, $\overline{Nu}/\overline{Nu}_{iso}$. The results and the present theory for $n = 2.5$ are shown in Fig. 3. In the figure, the Goertler type series solution for $Pr = 6.0$ from [11] is also included for comparison. Apparently, the approximate solution is in reasonable agreement with experiment while the series solution predicts low values of mean Nusselt number ratio for large S.

Spheres

For a sphere of diameter D, $z = (D/2)(1 - \cos 2x/D)$, $g_x = g \sin 2x/D$, and $R^i = (D/2) \sin 2x/D$ in equation (1). As in the horizontal cylinder case, numerical integration is required to compute the heat transfer rate.

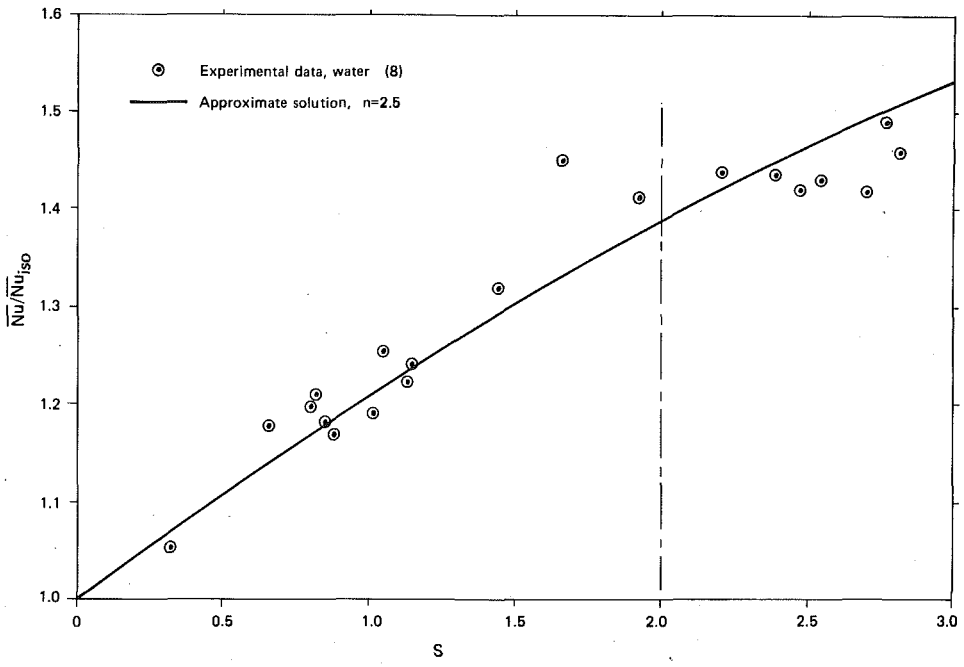

Fig. 4 Influence of stratification on heat transfer from spheres

The curvature effect was also considered in comparing theoretical predictions and experimental data for the case of spheres. The effect is well known and can be estimated with good approximation by

$$\overline{Nu} = \overline{Nu}_m - 2 \tag{10}$$

where $\overline{Nu}$ and $\overline{Nu}_m$ were defined previously. For an isothermal environment, the data for water from [8] fit very well with the correlation equation (9), recommended by McAdams [14] for spheres.

Equations (9) and (10) were used to obtain the mean Nusselt number ratio for the data given in [8] for spheres in stratified water. Fig. 4 shows the present solution for $n = 2.5$ and the experimental results; fair agreement is obtained.

Conclusions

1 An approximate solution has been obtained for the problem of natural convection from an axisymmetric body to a thermally stratified fluid.

2 For an isothermal horizontal cylinder or sphere in a linearly stratified fluid, the average heat transfer rate predicted by the approximate solution compares very well with available experimental data for water.

Acknowledgment

We gratefully acknowledge the support of the National Science Foundation under Grant ENG 72-03904. Professor Raithby kindly permitted us to inspect an advance copy of [9] and shared with us a similar analysis of the cylinder problem.

References

1 Cheesewright, R., "Natural Convection from a Plane, Vertical Surface in Nonisothermal Surroundings," *Int. Jour. Heat Mass Transfer*, Vol. 10, 1967, pp. 1847–1859.

2 Yang, K. T., Novotny, J. L., and Cheng, Y. S., "Laminar Free Convection from a Non-isothermal Plate Immersed in a Temperature Stratified Medium" *Int. Jour. of Heat and Mass Transfer*, Vol. 15, 1972, pp. 1097–1109.

3 Eichhorn, R., "Natural Convection in a Thermally Stratified Fluid," *Progress in Heat and Mass Transfer*, Vol. 2, 1969, pp. 41–53.

4 Takeuchi, M. Ota, Y. and Tanaka, Y., "Laminar Natural Convection Heat Transfer from a Flat Plate in a Thermally Stratified Fluid," *Heat Transfer—Japanese Research*, Vol. 4, 1975, pp. 48–63.

5 Chen, C. C., and Eichhorn, R., "Natural Convection from a Vertical Surface to a Thermally Stratified Fluid," ASME JOURNAL OF HEAT TRANSFER, Vol. 98, 1976, pp. 446–451.

6 Raithby, G. D., and Hollands, K. G. T., "A General Method of Obtaining Approximate Solutions to Laminar and Turbulent Free Convection Problems," *Advances in Heat Transfer*, Academic Press, Vol. 11, 1975, pp. 266–315.

7 Raithby, G. D., Hollands, K. G. T., and Unny, T. E., "Free Convection Heat Transfer Across Fluid Layers of Large Aspect Ratio," Paper 76-HT-37, ASME/AIChE Heat Transfer Conference, St. Louis, MO., 1976.

8 Eichhorn, R., Lienhard, J. H., and Chen, C. C., "Natural Convection from Isothermal Spheres and Horizontal Cylinders Immersed in a Stratified Fluid," *Proc. 5th Int. Heat Transfer Conference*, Tokyo, Vol. 3, 1974, pp. 10–14.

9 Raithby, G. D., and Hollands, K. G. T., "Heat Transfer by Natural Convection between a Vertical Surface and a Stably Stratified Fluid," ASME JOURNAL OF HEAT TRANSFER, Vol. 100, 1978, pp. 378–381.

10 Eichhorn, R., and Wang, G. S., "Natural Convection from Vertical Plates with Semicircular Leading Edgs," To appear in *The E.R.G. Eckert Festschrift*, Hemisphere Publishing, 1979.

11 Chen, C. C., and Eichhorn, R., "Natural Convection from Simple Bodies Immersed in Thermally Stratified Fluids," Tech. Report UKY-TR105-ME14-77, University of Kentucky, 1977.

12 Gentry, C. C., "Local Free Convection to Non-Newtonian Fluids from a Horizontal, Isothermal Cylinder," Ph.D. Thesis, University of Missouri—Columbia, 1972.

13 Saville, D. A., and Churchill, S. W., "Laminar Free Convection in Boundary Layers near Horizontal Cylinders and Axisymmetric Bodies," *Jour. Fluid Mech.*, Vol. 29, pp. 391–399, 1967.

14 McAdams, W. H., *Heat Transmission*, 3rd Edition, McGraw-Hill, 1954.

Laminar Free Convection in Small Aspect Ratio Rectangular Enclosures with Isothermal Boundary Conditions

M. N. A. Said[1,2] and A. C. Trupp[2]

Nomenclature

Gr = Grashof number, $g\,\beta(\theta_h - \theta_c)\,w^3/\nu^2$
h = overall average heat transfer coefficient, $\overline{q}/(\theta_h - \theta_c)$
H = height of gap
L = aspect ratio, H/w
Nu = Nusselt number, hw/k
Pr = Prandtl number, ν/α
$\overline{q}$ = average wall heat flux
Ra = Rayleigh number, (Gr)(Pr)

[1] Associate Member ASME

[2] Department of Mechanical Engineering, University of Manitoba, Winnipeg, Manitoba, Canada.

Contributed by the Heat Transfer Division for publication in the JOURNAL OF HEAT TRANSFER. Manuscript received by the Heat Transfer Division December 14, 1979.

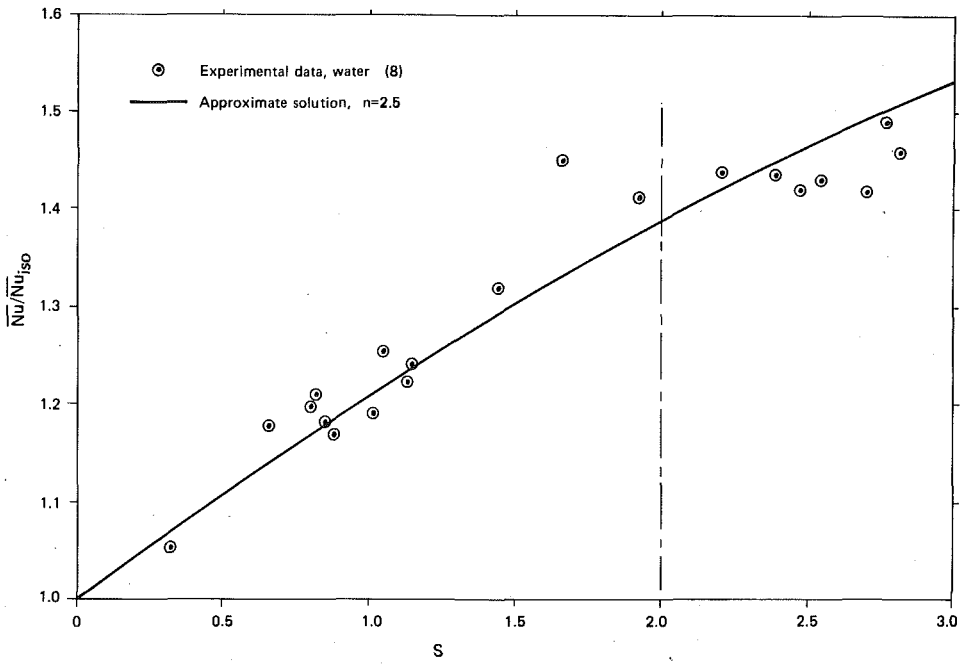

Fig. 4 Influence of stratification on heat transfer from spheres

The curvature effect was also considered in comparing theoretical predictions and experimental data for the case of spheres. The effect is well known and can be estimated with good approximation by

$$\overline{Nu} = \overline{Nu}_m - 2 \tag{10}$$

where $\overline{Nu}$ and $\overline{Nu}_m$ were defined previously. For an isothermal environment, the data for water from [8] fit very well with the correlation equation (9), recommended by McAdams [14] for spheres.

Equations (9) and (10) were used to obtain the mean Nusselt number ratio for the data given in [8] for spheres in stratified water. Fig. 4 shows the present solution for $n = 2.5$ and the experimental results; fair agreement is obtained.

Conclusions

1 An approximate solution has been obtained for the problem of natural convection from an axisymmetric body to a thermally stratified fluid.

2 For an isothermal horizontal cylinder or sphere in a linearly stratified fluid, the average heat transfer rate predicted by the approximate solution compares very well with available experimental data for water.

Acknowledgment

We gratefully acknowledge the support of the National Science Foundation under Grant ENG 72-03904. Professor Raithby kindly permitted us to inspect an advance copy of [9] and shared with us a similar analysis of the cylinder problem.

References

1 Cheesewright, R., "Natural Convection from a Plane, Vertical Surface in Nonisothermal Surroundings," *Int. Jour. Heat Mass Transfer*, Vol. 10, 1967, pp. 1847–1859.

2 Yang, K. T., Novotny, J. L., and Cheng, Y. S., "Laminar Free Convection from a Non-isothermal Plate Immersed in a Temperature Stratified Medium" *Int. Jour. of Heat and Mass Transfer*, Vol. 15, 1972, pp. 1097–1109.

3 Eichhorn, R., "Natural Convection in a Thermally Stratified Fluid," *Progress in Heat and Mass Transfer*, Vol. 2, 1969, pp. 41–53.

4 Takeuchi, M. Ota, Y. and Tanaka, Y., "Laminar Natural Convection Heat Transfer from a Flat Plate in a Thermally Stratified Fluid," *Heat Transfer—Japanese Research*, Vol. 4, 1975, pp. 48–63.

5 Chen, C. C., and Eichhorn, R., "Natural Convection from a Vertical Surface to a Thermally Stratified Fluid," ASME JOURNAL OF HEAT TRANSFER, Vol. 98, 1976, pp. 446–451.

6 Raithby, G. D., and Hollands, K. G. T., "A General Method of Obtaining Approximate Solutions to Laminar and Turbulent Free Convection Problems," *Advances in Heat Transfer*, Academic Press, Vol. 11, 1975, pp. 266–315.

7 Raithby, G. D., Hollands, K. G. T., and Unny, T. E., "Free Convection Heat Transfer Across Fluid Layers of Large Aspect Ratio," Paper 76-HT-37, ASME/AIChE Heat Transfer Conference, St. Louis, MO., 1976.

8 Eichhorn, R., Lienhard, J. H., and Chen, C. C., "Natural Convection from Isothermal Spheres and Horizontal Cylinders Immersed in a Stratified Fluid," *Proc. 5th Int. Heat Transfer Conference*, Tokyo, Vol. 3, 1974, pp. 10–14.

9 Raithby, G. D., and Hollands, K. G. T., "Heat Transfer by Natural Convection between a Vertical Surface and a Stably Stratified Fluid," ASME JOURNAL OF HEAT TRANSFER, Vol. 100, 1978, pp. 378–381.

10 Eichhorn, R., and Wang, G. S., "Natural Convection from Vertical Plates with Semicircular Leading Edgs," To appear in *The E.R.G. Eckert Festschrift*, Hemisphere Publishing, 1979.

11 Chen, C. C., and Eichhorn, R., "Natural Convection from Simple Bodies Immersed in Thermally Stratified Fluids," Tech. Report UKY-TR105-ME14-77, University of Kentucky, 1977.

12 Gentry, C. C., "Local Free Convection to Non-Newtonian Fluids from a Horizontal, Isothermal Cylinder," Ph.D. Thesis, University of Missouri—Columbia, 1972.

13 Saville, D. A., and Churchill, S. W., "Laminar Free Convection in Boundary Layers near Horizontal Cylinders and Axisymmetric Bodies," *Jour. Fluid Mech.*, Vol. 29, pp. 391–399, 1967.

14 McAdams, W. H., *Heat Transmission*, 3rd Edition, McGraw-Hill, 1954.

Laminar Free Convection in Small Aspect Ratio Rectangular Enclosures with Isothermal Boundary Conditions

M. N. A. Said[1,2] and A. C. Trupp[2]

Nomenclature

Gr = Grashof number, $g\,\beta(\theta_h - \theta_c)\,w^3/\nu^2$
h = overall average heat transfer coefficient, $\overline{q}/(\theta_h - \theta_c)$
H = height of gap
L = aspect ratio, H/w
Nu = Nusselt number, hw/k
Pr = Prandtl number, ν/α
$\overline{q}$ = average wall heat flux
Ra = Rayleigh number, (Gr)(Pr)

[1] Associate Member ASME

[2] Department of Mechanical Engineering, University of Manitoba, Winnipeg, Manitoba, Canada.

Contributed by the Heat Transfer Division for publication in the JOURNAL OF HEAT TRANSFER. Manuscript received by the Heat Transfer Division December 14, 1979.

T = dimensionless temperature, $(\theta - \theta_c)/(\theta_h - \theta_c)$
w = width of gap
x = vertical coordinate
y = horizontal coordinate
θ = temperature
θ_c = cold wall temperature
θ_h = hot wall temperature

Introduction

The laminar free convection in a fluid enclosed by two vertical isothermal surfaces (at different temperatures) and two horizontal insulated surfaces has been widely investigated both experimentally [1, 2] and theoretically [3–6]. However, whereas most reported results have been either for the square cavity or for aspect ratios of 2 or more where many engineering applications occur, only a few studies [6, 7] have involved $L < 1$. The purpose of this communication is to help fill in the range of aspect ratios from 0.5 to 5 for gas-filled cavities at low Grashof number. This range is of considerable interest for non-insulating applications since Nu peaks in the vicinity of $L = 1$ [7], and here the Nu dependence on L reverses.

The results reported here were obtained from a theoretical investigation in which the two-dimensional laminar free convective heat transfer was predicted numerically for a gas enclosed in a rectangular enclosure with isothermal side boundaries and adiabatic top and bottom walls. Specifically, the computation involved atmospheric air ($\Pr \approx 0.7$), a fixed gap (w) of 1.905 cm (0.75 in) thickness, one vertical wall (the cold wall) held at a fixed uniform temperature (θ_c) of 18.3°C (65°F), and the other (the hot wall) held at a uniform temperature (θ_h) in the range 23.3 to 58.3°C (74–137°F). The height of the cavity (H) was varied to provide aspect ratios in the range 0.5 to 5. The formulation of this boundary value problem using the Boussinesq approximation is well documented [8], and the governing equations and boundary conditions show that the velocity and temperature fields are dependent on Gr, Pr, and L. The time-dependent governing vorticity, stream function and energy equations [3] were solved using a modified Alternating-Direction Implicit finite difference method coupled with the Gauss-Seidel successive over-relaxation iterative technique. This approach as applied to the mixed boundary conditions problem is outlined in detail in [9].

Results and Discussion

Eight solutions using increments in $\Delta\theta$ of 5 C°, were obtained at each of the aspect ratios listed in Table 1. An additional 17 runs were also made for the square cavity spanning Grashof numbers of (1.05–55.5) 10^3 which included one result in the conduction regime. Air properties were evaluated at $(\theta_h + \theta_c)/2$. The grid systems were square with mesh spacing of $\Delta x = \Delta y = 0.05w$ which was determined to be the most practical (in terms of accuracy and computer time) after running several test cases with $\Delta x/w$ of 0.10, 0.05, 0.033 and 0.025.

1. **Flow Regimes.** Following Eckert and Carlson [1], the temperature distribution across the gap at the mid-height of the channel was used to distinguish between the three flow regimes, viz. conduction, asymptotic and laminar boundary layer. Using this convention, the boundary between the asymptotic and boundary layer regimes occurs when $dT/d(y/w) = 0$ where the gradient is evaluated at $y/w = 0.5 = x/H$. This boundary was obtained from the numerical values of the temperature fields, and the results are reported in Fig. 1. The lowest boundary Rayleigh (~6300) occurred in the vicinity of $L = 1.5$. For the square cavity, the boundary was located at about Ra = 7500 which is in fair agreement with the findings of De Vahl Davis [4] and MacGregor and Emery [10]. There were no cases in the laminar boundary layer regime (within the investigated Ra range) for $L = 0.6$ and 0.5 which is not surprising. For $L = 0.7$, the temperature distribution at the mid-height gap for the highest Ra test ($\text{Ra} = 2.15 \times 10^4$) was near the boundary ($dT/d(y/w) = 0.119$). For $L > 3$, the present variation of boundary Ra with L appears to merge reasonably well with the results of Thomas and De Vahl Davis [11] who have reported that their criterion ($\text{Ra}/L = 3000, L > 5$) properly categorized not only their data, but also all but one of the data of Eckert and Carlson [1].

2. **Heat Transfer Results.** The computed results for average Nusselt number are shown in Fig. 2. Nusselt values near the peak are almost constant between $L \approx 1.4$ to 1.8 and hence essentially independent of L. The maximum Nusselt numbers shift slightly with Grashof number from about $L = 1.6$ at the lowest Grashof number to about $L = 1.45$ at the highest Grashof number. This trend is also present in the results of Boyack and Kearney [7].

For a fixed Grashof number, the flow pattern is obviously optimum for heat transfer at $L \approx 1.5$. This is related to flow regime. For Gr = 9740 (for example), only aspect ratios between about 1 and 2 (i.e., in the vicinity of the Nu peak) are in the boundary layer regime. Simi-

Table 1 L S F data for $\text{Nu} = C\,(\text{Ra})^m$

L	N	C	m	Std. Dev.*	Range**
0.5	7	0.037	0.386	1.50	b
0.6	8	0.048	0.382	2.09	a
0.7	8	0.054	0.385	0.35	a
0.8	8	0.071	0.365	0.27	a
1.0	8	0.116	0.322	0.49	a
1.0	24	0.120	0.318	0.64	c
1.2	8	0.149	0.299	0.50	a
1.4	8	0.167	0.288	0.42	a
1.5	8	0.172	0.285	0.41	a
1.6	8	0.175	0.283	0.44	a
1.8	8	0.176	0.282	0.47	a
2.0	8	0.174	0.283	0.54	a
2.5	8	0.166	0.285	0.49	a
3.0	8	0.156	0.289	0.39	a
4.0	8	0.142	0.293	0.33	a
5.0	8	0.132	0.295	0.66	a

* Std. Dev. = $[(1/N)\ \Sigma\ (\text{Nu}_{\text{corr.}} - \text{Nu}_{\text{pred.}})^2]^{1/2}$ and is expressed here as a percent of the average $\text{Nu}_{\text{corr.}}$ in the range.
** Range a: $5078 \le \text{Gr} \le 30650$; $0.706 \le \text{Pr} \le 0.703$. b: $9737 \le \text{Gr} \le 30650$; $0.706 \le \text{Pr} \le 0.703$. c: $2085 \le \text{Gr} \le 55550$; $0.706 \le \text{Pr} \le 0.692$.

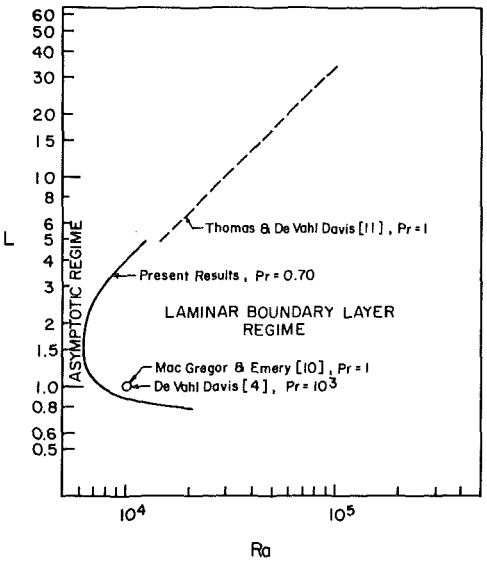

Fig. 1 Boundary between asymptotic and laminar boundary layer regimes

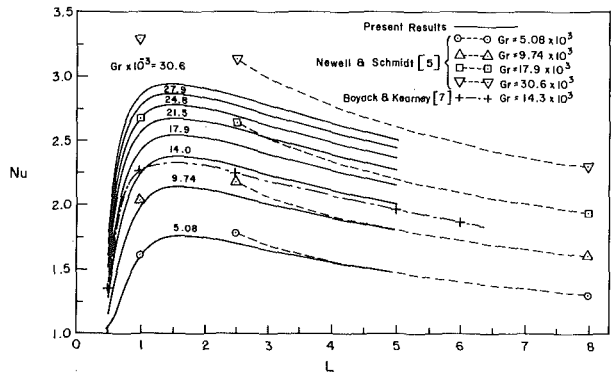

Fig. 2 Variation of Nusselt with aspect ratio for fixed Grashof

larly, for higher Gr, the flow character at $L \approx 1.5$ is further advanced into the boundary layer regime than higher aspect ratios whereas lower aspect ratio cross-sections may still be in asymptotic flow. The shape of the boundary line in Fig. 1 suggests for a given Ra (viewed as fixed w and $\Delta\theta$), that the upper limit in L occurs when the physical height is such that the growing thermal boundary layers begin to interfere significantly with each other, whereas at the lower limit, H is inadequate for the heat transfer to be accomplished by convection alone.

Fig. 3 shows Nu as a function of Ra for selected fixed aspect ratios. It includes the additional data at $L = 1$ not shown in Fig. 2. In general, Nu increases non-linearly with Ra, however, the relationship is almost linear at $L = 0.5$. Within the investigated range, the square cavity and the rectangular cavity of $L = 2.5$ perform similarly as do several other pairs pivoted about $L = 1.5$.

Heat transfer correlations (involving all computed data from both regimes)[3] were obtained by least-squares-fit and are given in Table 1 where the coefficient (C) incorporates the L dependence where it exists. All of the computed Nu values were correlated by $\mathrm{Nu} = C(\mathrm{Ra})^m$ with a standard deviation of 0.65 percent of the average Nusselt in the set.

As shown in Fig. 3, the present Nu results are in excellent agreement with the results of previous investigators for $L = 0.5$ and 1. Also Fig. 2 shows reasonable consistency with the predictions of Boyack and Kearney [7] for $\mathrm{Ra} = 10^4$ (equivalent to $\mathrm{Gr} = 14.3 \times 10^3$ for $\mathrm{Pr} = 0.70$). Fig. 2 also includes the results of Newell and Schmidt [5]. Their correlation for air ($2.5 \leq L \leq 20, 4 \times 10^3 < \mathrm{Gr} < 1.4 \times 10^5$) represents (at $L \approx 5$) a median of the published correlations such as those in [2] and [10]. As can be seen, the present results merge reasonably well with it. For the square cavity, the present results agree well with the correlation of Newell and Schmidt [5] at the lowest Grashof number, but are about 13 percent lower at the highest Grashof number. A similar divergence occurs at $L = 2.5$. Although the solution procedure of Newell and Schmidt [5] differs in detail from the present method (e.g., handling of vorticity boundary conditions), the above noted discrepancies are likely due mainly to differences in mesh size. Heat transfer results can be very sensitive to mesh size particularly for low aspect ratio cavities operating in the laminar boundary layer regime. For example, for $L = 1$, Wilkes and Churchill [3] found a 12 percent decrease in Nu when a square mesh of $0.10w$ was replaced by a finer mesh of $0.05w$ for $\mathrm{Gr} = 2 \times 10^4$ and $\mathrm{Pr} = 0.733$. Newell and Schmidt [5] used $\Delta y = 0.083w = 2\,\Delta x$ for $L = 1$ and 2.5, which is marginal for small L at the larger Grashof numbers [6, 7].

Conclusions

Results have been presented from which the laminar free convective heat transfer across air-filled rectangular enclosures can be calculated for aspect ratios in the range 0.5 to 5. For fixed $\Delta\theta$, the heat transfer is maximum at $L \approx 1.5$, and it is here that the boundary Rayleigh number attains its minimum value.

[3] It was found in an earlier study [9] that there is little advantage to be gained by separating the data according to flow regime.

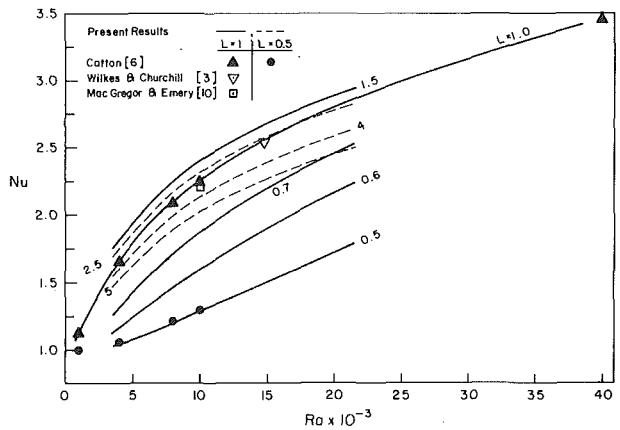

Fig. 3 Variation of Nusselt with Rayleigh for fixed aspect ratio

Acknowledgment

The authors gratefully acknowledge the support provided for this research by National Research Council of Canada.

References

1 Eckert, E. R. G., and Carlson, W. O., "Natural Convection in an Air Layer Enclosed Between Two Vertical Plates with Different Temperatures," *Int. J. Heat Mass Tr.*, Vol. 2, 1961, pp. 106–120.

2 Yin, S. H., Wung, T. Y., and Chen K., "Natural Convection in an Air Layer Enclosed Within Rectangular Cavities," *Int. J. Heat Mass Tr.*, Vol. 21, 1978, pp. 307–315.

3 Wilkes, J. O. and Churchill, S. W., "The Finite-Difference Computation of Natural Convection in a Rectangular Enclosure," *A.I. Ch. E. Journal*, Vol. 12, No. 1, 1966, pp. 161–166.

4 De Vahl Davis, G., "Laminar Natural Convection in an Enclosed Rectangular Cavity," *Int. J. Heat Mass Tr.*, Vol. 11, 1968, pp. 1675–1693.

5 Newell, M. E., and Schmidt, F. W., "Heat Transfer by Laminar Natural Convection Within Rectangular Enclosures," ASME JOURNAL OF HEAT TRANSFER, Vol. 92, 1970, pp. 159–167.

6 Catton, I., "Natural Convection in Enclosures," *6th International Heat Tr. Conf.*, Vol. 6, 1978, pp. 13–31.

7 Boyack, B. E., and Kearney, D. W., "Heat Transfer by Laminar Natural Convection in Low Aspect Ratio Cavities," ASME Paper 72-HT-52, 1972.

8 Ostrach, S. "Natural Convection in Enclosures," *Advances in Heat Transfer*, Vol. 8, Academic Press, New York, 1972, pp. 161–227.

9 Said, M. N. A., "Numerical Investigation of Laminar Free Convection in Vertical Air Filled Cavities with Mixed Boundary Conditions," M.Sc. Thesis, Dept. of Mech. Engg. Univ. of Manitoba, Winnipeg, Canada, May 1978.

10 MacGregor, R. K., and Emery, A. F., "Free Convection Through Vertical Plane Layers-Moderate and High Prandtl Number Fluids," ASME JOURNAL OF HEAT TRANSFER, Vol. 91, 1969, pp. 391–401.

11 Thomas, R. W., and De Vahl Davis, G., "Natural Convection in Annular and Rectangular Cavities—a Numerical Study," Fourth International Heat Transfer Conference (Paris—Versailles, 1970), *Heat Transfer 1970*, Vol. 4, Elsevier, Amsterdam, 1970, NC 2.4.

Method for Visualizing High Prandtl Number Heat Convection[1]

M. Vedhanayagam,[2] J. H. Lienhard,[3] and R. Eichhorn[3]

Baker [1] described the so-called "thymol blue" method for visualizing boundary layer flows, in 1966. The method has been used to advantage by others (see e.g., [2–4]). Eichhorn, Lienhard, and Chen's [4] use of the method in their study of convection in thermally stratified environments led to a need for visualizing convection at Prandtl Numbers, Pr, greater than those for warm water. Hide and Ibbestson [2] varied viscosity in their work by mixing sucrose with water, but they did not provide physical properties of the mixture nor did they note any limitations on the method. In this note we show how the thymol blue method can be used while the Prandtl Number, Pr, is changed at will from 7 to 10,000 by mixing water with any desired fraction of pure glycerol.

The Prandtl number, $\mathrm{Pr} = \mu c_p/k$, requires the evaluation of three properties for water and glycerol mixtures. The properties of pure water [5] and glycerol [6] are readily available and the viscosity, μ, [7], and thermal conductivity, k, [8] of glycerol-water mixtures have been measured as well. Only a few values of c_p for glycerol-water mixtures are available at 15 and 32°C. We have passed solid lines through these data in Fig. 1. The dashed lines in Fig. 1 are interpolations at other temperatures, with the same general shape as the solid lines, but they are stretched to fit the known values of c_p for pure water and glycerol.

[1] This work was part of a larger study of natural convection funded by the N.S.F. under Research Grant No. ENG 72-03904.

[2] Research Assistant, Mechanical Engineering Department, University of Kentucky, Lexington, KY 40506.

[3] Professor, Mechanical Engineering Department, University of Kentucky, Lexington, KY 40506, Fellow ASME.

larly, for higher Gr, the flow character at $L \approx 1.5$ is further advanced into the boundary layer regime than higher aspect ratios whereas lower aspect ratio cross-sections may still be in asymptotic flow. The shape of the boundary line in Fig. 1 suggests for a given Ra (viewed as fixed w and $\Delta\theta$), that the upper limit in L occurs when the physical height is such that the growing thermal boundary layers begin to interfere significantly with each other, whereas at the lower limit, H is inadequate for the heat transfer to be accomplished by convection alone.

Fig. 3 shows Nu as a function of Ra for selected fixed aspect ratios. It includes the additional data at $L = 1$ not shown in Fig. 2. In general, Nu increases non-linearly with Ra, however, the relationship is almost linear at $L = 0.5$. Within the investigated range, the square cavity and the rectangular cavity of $L = 2.5$ perform similarly as do several other pairs pivoted about $L = 1.5$.

Heat transfer correlations (involving all computed data from both regimes)[3] were obtained by least-squares-fit and are given in Table 1 where the coefficient (C) incorporates the L dependence where it exists. All of the computed Nu values were correlated by $\mathrm{Nu} = C(\mathrm{Ra})^m$ with a standard deviation of 0.65 percent of the average Nusselt in the set.

As shown in Fig. 3, the present Nu results are in excellent agreement with the results of previous investigators for $L = 0.5$ and 1. Also Fig. 2 shows reasonable consistency with the predictions of Boyack and Kearney [7] for $\mathrm{Ra} = 10^4$ (equivalent to $\mathrm{Gr} = 14.3 \times 10^3$ for $\mathrm{Pr} = 0.70$). Fig. 2 also includes the results of Newell and Schmidt [5]. Their correlation for air ($2.5 \leq L \leq 20, 4 \times 10^3 < \mathrm{Gr} < 1.4 \times 10^5$) represents (at $L \approx 5$) a median of the published correlations such as those in [2] and [10]. As can be seen, the present results merge reasonably well with it. For the square cavity, the present results agree well with the correlation of Newell and Schmidt [5] at the lowest Grashof number, but are about 13 percent lower at the highest Grashof number. A similar divergence occurs at $L = 2.5$. Although the solution procedure of Newell and Schmidt [5] differs in detail from the present method (e.g., handling of vorticity boundary conditions), the above noted discrepancies are likely due mainly to differences in mesh size. Heat transfer results can be very sensitive to mesh size particularly for low aspect ratio cavities operating in the laminar boundary layer regime. For example, for $L = 1$, Wilkes and Churchill [3] found a 12 percent decrease in Nu when a square mesh of $0.10w$ was replaced by a finer mesh of $0.05w$ for $\mathrm{Gr} = 2 \times 10^4$ and $\mathrm{Pr} = 0.733$. Newell and Schmidt [5] used $\Delta y = 0.083w = 2\,\Delta x$ for $L = 1$ and 2.5, which is marginal for small L at the larger Grashof numbers [6, 7].

Conclusions

Results have been presented from which the laminar free convective heat transfer across air-filled rectangular enclosures can be calculated for aspect ratios in the range 0.5 to 5. For fixed $\Delta\theta$, the heat transfer is maximum at $L \approx 1.5$, and it is here that the boundary Rayleigh number attains its minimum value.

[3] It was found in an earlier study [9] that there is little advantage to be gained by separating the data according to flow regime.

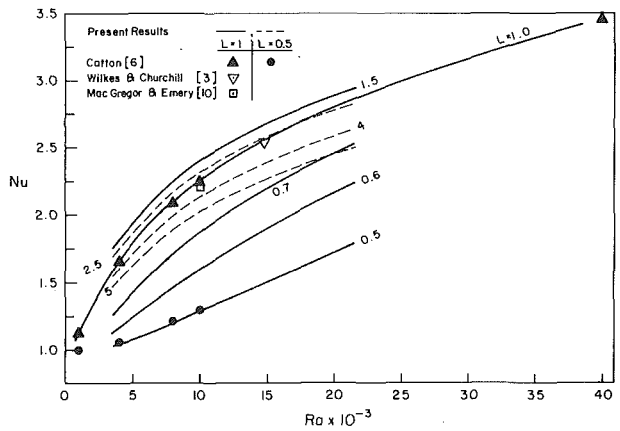

Fig. 3 Variation of Nusselt with Rayleigh for fixed aspect ratio

Acknowledgment

The authors gratefully acknowledge the support provided for this research by National Research Council of Canada.

References

1 Eckert, E. R. G., and Carlson, W. O., "Natural Convection in an Air Layer Enclosed Between Two Vertical Plates with Different Temperatures," *Int. J. Heat Mass Tr.*, Vol. 2, 1961, pp. 106–120.

2 Yin, S. H., Wung, T. Y., and Chen K., "Natural Convection in an Air Layer Enclosed Within Rectangular Cavities," *Int. J. Heat Mass Tr.*, Vol. 21, 1978, pp. 307–315.

3 Wilkes, J. O. and Churchill, S. W., "The Finite-Difference Computation of Natural Convection in a Rectangular Enclosure," *A.I. Ch. E. Journal*, Vol. 12, No. 1, 1966, pp. 161–166.

4 De Vahl Davis, G., "Laminar Natural Convection in an Enclosed Rectangular Cavity," *Int. J. Heat Mass Tr.*, Vol. 11, 1968, pp. 1675–1693.

5 Newell, M. E., and Schmidt, F. W., "Heat Transfer by Laminar Natural Convection Within Rectangular Enclosures," ASME JOURNAL OF HEAT TRANSFER, Vol. 92, 1970, pp. 159–167.

6 Catton, I., "Natural Convection in Enclosures," *6th International Heat Tr. Conf.*, Vol. 6, 1978, pp. 13–31.

7 Boyack, B. E., and Kearney, D. W., "Heat Transfer by Laminar Natural Convection in Low Aspect Ratio Cavities," ASME Paper 72-HT-52, 1972.

8 Ostrach, S. "Natural Convection in Enclosures," *Advances in Heat Transfer*, Vol. 8, Academic Press, New York, 1972, pp. 161–227.

9 Said, M. N. A., "Numerical Investigation of Laminar Free Convection in Vertical Air Filled Cavities with Mixed Boundary Conditions," M.Sc. Thesis, Dept. of Mech. Engg. Univ. of Manitoba, Winnipeg, Canada, May 1978.

10 MacGregor, R. K., and Emery, A. F., "Free Convection Through Vertical Plane Layers-Moderate and High Prandtl Number Fluids," ASME JOURNAL OF HEAT TRANSFER, Vol. 91, 1969, pp. 391–401.

11 Thomas, R. W., and De Vahl Davis, G., "Natural Convection in Annular and Rectangular Cavities—a Numerical Study," Fourth International Heat Transfer Conference (Paris—Versailles, 1970), *Heat Transfer 1970*, Vol. 4, Elsevier, Amsterdam, 1970, NC 2.4.

Method for Visualizing High Prandtl Number Heat Convection[1]

M. Vedhanayagam,[2] J. H. Lienhard,[3] and R. Eichhorn[3]

Baker [1] described the so-called "thymol blue" method for visualizing boundary layer flows, in 1966. The method has been used to advantage by others (see e.g., [2–4]). Eichhorn, Lienhard, and Chen's [4] use of the method in their study of convection in thermally stratified environments led to a need for visualizing convection at Prandtl Numbers, Pr, greater than those for warm water. Hide and Ibbestson [2] varied viscosity in their work by mixing sucrose with water, but they did not provide physical properties of the mixture nor did they note any limitations on the method. In this note we show how the thymol blue method can be used while the Prandtl Number, Pr, is changed at will from 7 to 10,000 by mixing water with any desired fraction of pure glycerol.

The Prandtl number, $\mathrm{Pr} = \mu c_p/k$, requires the evaluation of three properties for water and glycerol mixtures. The properties of pure water [5] and glycerol [6] are readily available and the viscosity, μ, [7], and thermal conductivity, k, [8] of glycerol-water mixtures have been measured as well. Only a few values of c_p for glycerol-water mixtures are available at 15 and 32°C. We have passed solid lines through these data in Fig. 1. The dashed lines in Fig. 1 are interpolations at other temperatures, with the same general shape as the solid lines, but they are stretched to fit the known values of c_p for pure water and glycerol.

[1] This work was part of a larger study of natural convection funded by the N.S.F. under Research Grant No. ENG 72-03904.

[2] Research Assistant, Mechanical Engineering Department, University of Kentucky, Lexington, KY 40506.

[3] Professor, Mechanical Engineering Department, University of Kentucky, Lexington, KY 40506, Fellow ASME.

Interpolated values of μ, k, c_p, and the compressibility, β, are tabulated at four temperatures in Table 1. Values of β in the table were evaluated numerically using the specific volume data for mixtures given in [8].

Baker describes the method for preparing a thymol blue solution for visualization as follows: First, enough thymol blue is dissolved in the water to produce a 0.01 percent by weight solution. This solution is then titrated to the end point, which lies slightly on the acid side, by adding 1-N NaOH, drop by drop, until the solution turns dark blue, and a drop of 1-N HCl to bring the color back to yellow. He also prescribed a d-c voltage level of 5V with a current flow of about 5mA for an electrode spacing of 0.5 cm.

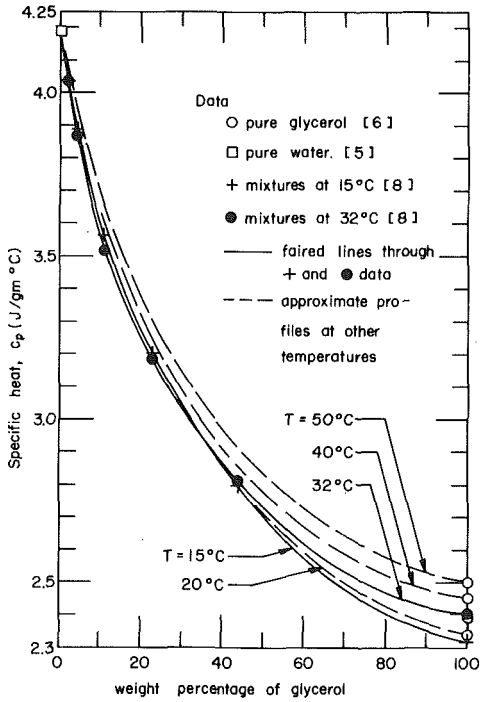

Fig. 1 Specific heat of glycerol solutions at various temperatures

We were able to use the same procedure, with the following slight modifications, in the various mixtures of glycerol and water. The working fluid is prepared by mixing measured quantities of water and glycerol to obtain any desired Prandtl number. Enough thymol blue is dissolved in the mixture to produce a 0.01 percent by weight solution. A small pellet of solid NaOH is dropped in this solution and stirred continuously until the solution turns dark blue. The excess undissolved NaOH is quickly removed and a drop of 1-N HCl is added to bring the end point to acid side turning the color of the solution to orange. Addition of a very small amount of NaOH, when the thymol blue is being dissolved, increases its solubility. The use of solid NaOH, instead of a 1-N solution, reduces the quantity of unaccounted water present in the mixture.

As the glycerol concentration increases in the mixture, a higher d.c. voltage is required between the electrodes (up to 30V). This is because the conductivity of the mixture goes down with an increasing concentration of glycerol. The cathode is the ink-generating heated body and the anode is a copper plate in contact with the working fluid away from the field of observation.

As an example, we have prepared Figs. 2 and 3. These show natural convection from two horizontal cylinders. In each case the Grashof number based on the heating rate per unit length, q, the heater diameter, D, and properties evaluated at the bath temperature: $Gr^* = \beta q g \rho^2 D^3 / k \mu^2$, is 5.65.

The Prandtl numbers for the two cases differ by a factor of 783.5. This was accomplished by using a 1.905 cm dia cylinder in a 96 percent glycerol mixture for the photograph in Fig. 2 and a 0.046 cm dia wire in pure water for the photograph in Fig. 3.

The resulting wake behavior differs dramatically in the two cases. At Pr = 5500 the wake extends only two diameters above the cylinder, but at Pr = 7.02 it extends 300 diameters.

Thus the use of predictable glycerol-water mixtures provide means for exposing independent Pr effects in natural convection. These would previously have been hard to identify.

Table 1 Physical properties of glycerol-water solutions

		Percent, by weight, of Glycerol in solution										
	T°C	0	10	20	30	40	50	60	70	80	90	100
k $\frac{W}{m-k}$	20	0.590	0.557	0.519	0.481	0.448	0.414	0.381	0.352	0.327	0.301	0.285
	30	0.607	0.574	0.532	0.490	0.452	0.419	0.381	0.356	0.327	0.301	0.285
	40	0.624	0.586	0.540	0.502	0.461	0.423	0.385	0.356	0.327	0.301	0.285
	50	0.636	0.599	0.553	0.511	0.469	0.431	0.389	0.360	0.331	0.301	0.285
c_p $\frac{kJ}{kg-K}$	20	4.18	3.60	3.25	3.03	2.85	2.72	2.59	2.50	2.43	2.38	2.35
	30	4.18	3.55	3.23	3.01	2.85	2.72	2.61	2.54	2.47	2.43	2.40
	40	4.18	3.64	3.30	3.08	2.90	2.78	2.66	2.56	2.52	2.48	2.46
	50	4.18	3.70	3.36	3.14	2.96	2.84	2.70	2.64	2.57	2.53	2.52
μ $\frac{N-s}{m^2} \times 10^3$	20	1.01	1.31	1.76	2.50	3.72	6.00	10.8	22.5	60.1	219	1412
	30	0.80	1.03	1.35	1.87	2.72	4.21	7.91	14.1	33.9	109	612
	40	0.656	0.826	1.07	1.46	2.07	3.10	5.08	9.40	20.8	60.0	284
	50	0.549	0.680	0.879	1.16	1.62	2.37	3.76	6.61	13.6	35.5	142
ρ $\frac{kg}{m^3}$	20	998	1022	1047	1073	1099	1126	1154	1181	1209	1235	1261
	30	996	1019	1043	1069	1095	1121	1148	1176	1203	1229	1255
	40	992	1016	1039	1064	1090	1116	1143	1170	1197	1223	1249
	50	988	1011	1035	1059	1085	1111	1137	1164	1191	1217	1243
β $\frac{1}{K} \times 10^3$	20	0.21	0.25	0.31	0.37	0.41	0.45	0.48	0.50	0.51	0.51	0.48
	30	0.30	0.32	0.36	0.41	0.45	0.48	0.50	0.52	0.52	0.52	0.49
	40	0.39	0.39	0.41	0.45	0.48	0.51	0.52	0.53	0.53	0.52	0.49
	50	0.45	0.44	0.46	0.49	0.51	0.53	0.53	0.53	0.53	0.52	0.50
Pr	20	7.2	8.5	11.1	15.7	23.7	39.4	73.4	159.9	447.2	1729.1	11630.2
	30	5.5	6.4	8.2	11.5	17.1	27.4	49.3	100.6	258.5	878.7	5161.2
	40	4.4	5.1	6.5	9.0	13.0	20.4	35.1	67.6	160.5	493.6	2450.9
	50	3.6	4.2	5.3	7.1	10.2	15.6	26.1	48.5	105.7	297.9	1254.4

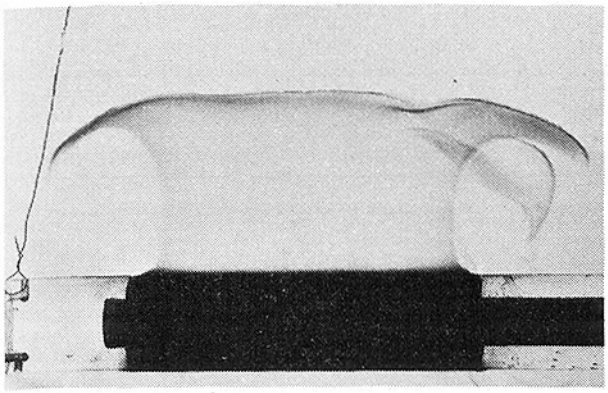

Fig. 2 The visualization of natural convection from a 1.905 cm dia cylinder in a glycerol-water mixture, 96 percent by weight glycerol, $Gr^* = 5.65$, $Pr = 5500$, surface heat flux = 202 W/m^2

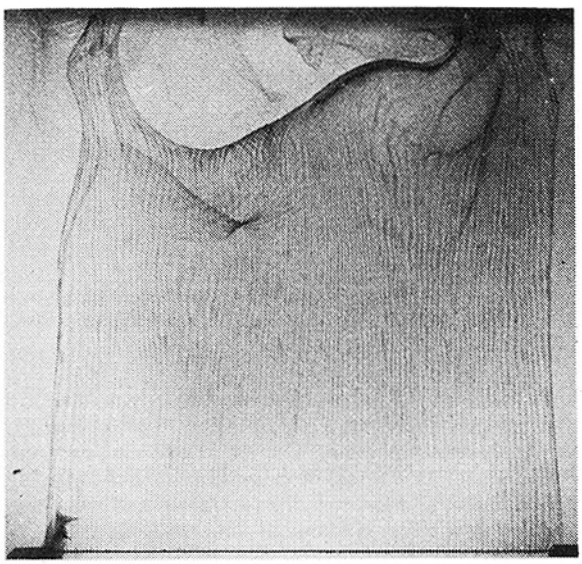

Fig. 3. The visualization of natural convection from a 0.46 mm dia wire in pure water. $Gr^* = 5.65$, $Pr = 7.02$, surface heat flux, $q_w = 12{,}000$W/m^2. (Some as-yet-unexplained thermal phenomenon at the wire leads to vertical striations of the thymol blue which were absent at the gentler heat rate used in Fig. 2)

References

1 Baker, D. J., "A Technique for the Precise Measurement of Small Fluid Velocities," *Journal of Fluid Mech.*, Vol. 26, pp. 573–575.

2 Hide, R., Ibbestson, A., and Lighthill, M. J., "On Slow Transverse Flow Past Obstacles in a Rapidly Rotating Fluid," *Journal of Fluid Mech.*, Vol. 32, 1968, pp. 251–272.

3 Sparrow, E. M., Husar, R. B., Goldstein, R. J., "Observations and Other Characteristics of Thermals," *Journal of Fluid Mech.*, Vol. 41, 1970, pp. 793–800.

4 Eichhorn, R., Lienhard, J. H., and Chen, C. C., "Natural Convection from Isothermal Spheres and Cylinders immersed in a Stratified Fluid," Paper NC 1.3, *Proc., Vth Int. Heat Trans. Conf.*, Tokyo, 1974.

5 *CRC Handbook of Chemistry and Physics,* CRC Press, Cleveland, 58th ed., 1977–78, p. D-518.

6 Touloukian, Y. S., and Makita, T., eds., *Specific Heat of Nonmetalic Liquids and Gases,* TPRC Data Series, IFI/Plenum, New York-Washington, Vol. 6, 1970, p. 230.

7 Segur, J. B., and Oberstar, H. E., "Viscosity of Glycerol and Its Aqueous Solutions," *Industrial and Engineering Chemistry,* Vol. 43, 1951, pp. 271–220.

8 Miner, C. S., and Dalton, N. N., *Glycerol,* American Chemical Society Monograph Series No. 117, Reinhold Publishing, New York, 1953, p. 313.

9 *International Critical Tables,* Vol. V, McGraw-Hill, New York, 1933, p. 116.

Mechanism of Heat and Momentum Transfer of Combined Free and Forced Convection with Opposing Flow

S. Tsuruno[1] and I. Iguchi[2]

Nomenclature

C_f = friction factor, $\mu \left(\frac{\partial u}{\partial y}\right)_{y=0} \Big/ \rho u_\infty^2$

f = dimensionless stream function, $\Psi(x, y)/K\sqrt{u_\infty \nu x}$

g = gravitational acceleration

Gr = Grashof number, $g\beta(T_w - T_\infty)x^3/\nu^2$

h = coefficient of heat transfer, $k \left(\frac{\partial T}{\partial y}\right)_{y=0} \Big/ (T_w - T_\infty)$

k = thermal conductivity

K = constant which is so chosen that a coefficient of each term in equations (5) and (6) becomes an integer

Nu = Nusselt number, hx/k

Pr = Prandtl number, ν/α

Re = Reynolds number, $u_\infty x/\nu$

u, v = velocity component of x and y-direction

α = thermal diffusivity

β = coefficient of volumetric expansion

η = pseudo-similarity variable, $\frac{y}{K}\sqrt{u_\infty/\nu x}$

ξ = ratio of Gr and Re^2

θ = dimensionless temperature, $T - T_\infty/T_w - T_\infty$

μ = viscosity

ν = kinematic viscosity

Ψ = stream function

Introduction

This note is concerned with the opposing flow of combined free and forced convection along an isothermal vertical plate with free stream velocity varying as $u_\infty(x) \approx x^m$. Various authors have reported their theoretical [1–4] and experimental work [5] on this problem. In [2] and [3], the characteristics of the heat transfer and the friction factor were reported in connection with the isothermal vertical flat plate at Pr = 0.7–10. Sparrow, et al. [1] gave similar solutions for the cases $u_\infty(x) \approx x^{1/2}$, $T_w - T_\infty$ = const. and $u_\infty(x) \approx x^{3/5}$, $T_w - T_\infty \approx x^{1/5}$. Wilks [4] presented the numerical solution to the case of the constant heat flux at Pr = 1 and investigated the mechanism of this convective flow around the separation point.

However, in these investigations, the examination of the mechanism of buoyancy effect on fluid flow and heat transfer is not yet considered to be sufficient. That is, thus far the buoyancy effect on the transfer phenomena has been treated only from the point of view of how skin friction and heat transfer vary due to the increase of buoyance force; and no discussion on the fundamental property which probably exists through the various Prandtl numbers has been written.

This note attempts to supplement the aforementioned insufficient points that have not yet been examined for flow along the isothermal vertical plate with free stream velocity varying as $u_\infty(x) \approx x^m$.

[1] Lecturer, Department of Mechanical Engineering, The National Defense Academy, Hashirimizu, Yokosuka, Japan.

[2] Professor, Department of Mechanical Engineering, The National Defense Academy, Hashirimizu, Yokosuka, Japan.

Contributed by the Heat Transfer Division for publication in the JOURNAL OF HEAT TRANSFER. Manuscript received by the Heat Transfer Division October 17, 1978.

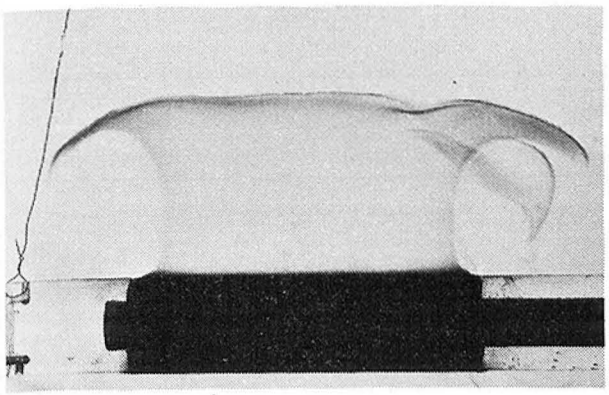

Fig. 2 The visualization of natural convection from a 1.905 cm dia cylinder in a glycerol-water mixture, 96 percent by weight glycerol, $Gr^* = 5.65$, $Pr = 5500$, surface heat flux = 202 W/m²

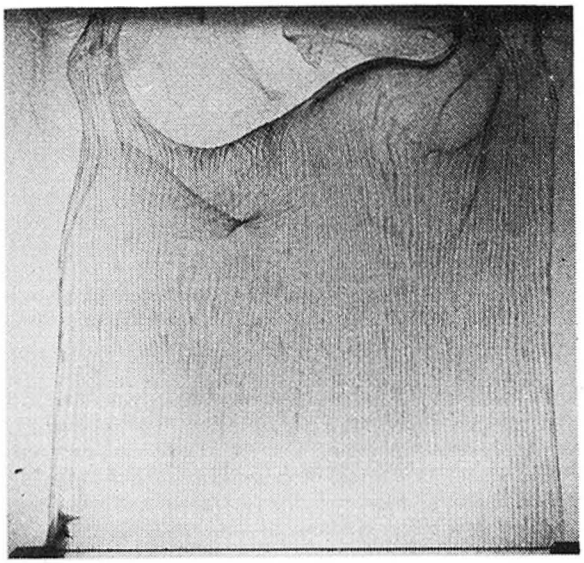

Fig. 3. The visualization of natural convection from a 0.46 mm dia wire in pure water. $Gr^* = 5.65$, $Pr = 7.02$, surface heat flux, $q_w = 12{,}000 W/m^2$. (Some as-yet-unexplained thermal phenomenon at the wire leads to vertical striations of the thymol blue which were absent at the gentler heat rate used in Fig. 2)

References

1 Baker, D. J., "A Technique for the Precise Measurement of Small Fluid Velocities," *Journal of Fluid Mech.*, Vol. 26, pp. 573–575.

2 Hide, R., Ibbestson, A., and Lighthill, M. J., "On Slow Transverse Flow Past Obstacles in a Rapidly Rotating Fluid," *Journal of Fluid Mech.*, Vol. 32, 1968, pp. 251–272.

3 Sparrow, E. M., Husar, R. B., Goldstein, R. J., "Observations and Other Characteristics of Thermals," *Journal of Fluid Mech.*, Vol. 41, 1970, pp. 793–800.

4 Eichhorn, R., Lienhard, J. H., and Chen, C. C., "Natural Convection from Isothermal Spheres and Cylinders immersed in a Stratified Fluid," Paper NC 1.3, *Proc., Vth Int. Heat Trans. Conf.*, Tokyo, 1974.

5 *CRC Handbook of Chemistry and Physics*, CRC Press, Cleveland, 58th ed., 1977–78, p. D-518.

6 Touloukian, Y. S., and Makita, T., eds., *Specific Heat of Nonmetalic Liquids and Gases*, TPRC Data Series, IFI/Plenum, New York-Washington, Vol. 6, 1970, p. 230.

7 Segur, J. B., and Oberstar, H. E., "Viscosity of Glycerol and Its Aqueous Solutions," *Industrial and Engineering Chemistry*, Vol. 43, 1951, pp. 271–220.

8 Miner, C. S., and Dalton, N. N., *Glycerol*, American Chemical Society Monograph Series No. 117, Reinhold Publishing, New York, 1953, p. 313.

9 *International Critical Tables*, Vol. V, McGraw-Hill, New York, 1933, p. 116.

Mechanism of Heat and Momentum Transfer of Combined Free and Forced Convection with Opposing Flow

S. Tsuruno[1] and I. Iguchi[2]

Nomenclature

C_f = friction factor, $\mu \left(\frac{\partial u}{\partial y}\right)_{y=0} \Big/ \rho u_\infty^2$

f = dimensionless stream function, $\Psi(x, y)/K\sqrt{u_\infty \nu x}$

g = gravitational acceleration

Gr = Grashof number, $g\beta(T_w - T_\infty)x^3/\nu^2$

h = coefficient of heat transfer, $k \left(\frac{\partial T}{\partial y}\right)_{y=0} \Big/ (T_w - T_\infty)$

k = thermal conductivity

K = constant which is so chosen that a coefficient of each term in equations (5) and (6) becomes an integer

Nu = Nusselt number, hx/k

Pr = Prandtl number, ν/α

Re = Reynolds number, $u_\infty x/\nu$

u, v = velocity component of x and y-direction

α = thermal diffusivity

β = coefficient of volumetric expansion

η = pseudo-similarity variable, $\frac{y}{K}\sqrt{u_\infty/\nu x}$

ξ = ratio of Gr and Re^2

θ = dimensionless temperature, $T - T_\infty/T_w - T_\infty$

μ = viscosity

ν = kinematic viscosity

Ψ = stream function

Introduction

This note is concerned with the opposing flow of combined free and forced convection along an isothermal vertical plate with free stream velocity varying as $u_\infty(x) \approx x^m$. Various authors have reported their theoretical [1–4] and experimental work [5] on this problem. In [2] and [3], the characteristics of the heat transfer and the friction factor were reported in connection with the isothermal vertical flat plate at Pr = 0.7–10. Sparrow, et al. [1] gave similar solutions for the cases $u_\infty(x) \approx x^{1/2}$, $T_w - T_\infty$ = const. and $u_\infty(x) \approx x^{3/5}$, $T_w - T_\infty \approx x^{1/5}$. Wilks [4] presented the numerical solution to the case of the constant heat flux at Pr = 1 and investigated the mechanism of this convective flow around the separation point.

However, in these investigations, the examination of the mechanism of buoyancy effect on fluid flow and heat transfer is not yet considered to be sufficient. That is, thus far the buoyancy effect on the transfer phenomena has been treated only from the point of view of how skin friction and heat transfer vary due to the increase of buoyance force; and no discussion on the fundamental property which probably exists through the various Prandtl numbers has been written.

This note attempts to supplement the aforementioned insufficient points that have not yet been examined for flow along the isothermal vertical plate with free stream velocity varying as $u_\infty(x) \approx x^m$.

[1] Lecturer, Department of Mechanical Engineering, The National Defense Academy, Hashirimizu, Yokosuka, Japan.

[2] Professor, Department of Mechanical Engineering, The National Defense Academy, Hashirimizu, Yokosuka, Japan.

Contributed by the Heat Transfer Division for publication in the JOURNAL OF HEAT TRANSFER. Manuscript received by the Heat Transfer Division October 17, 1978.

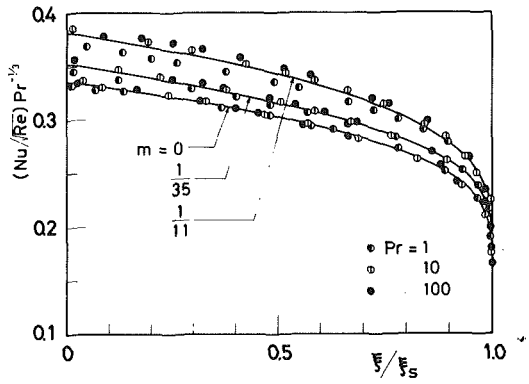

Fig. 1 Nusselt number

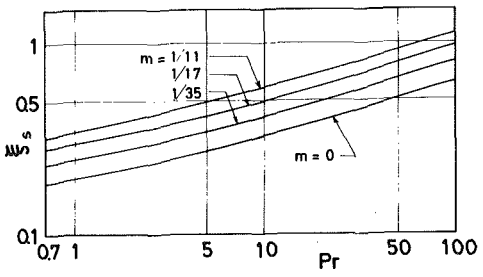

Fig. 2 Position of separation

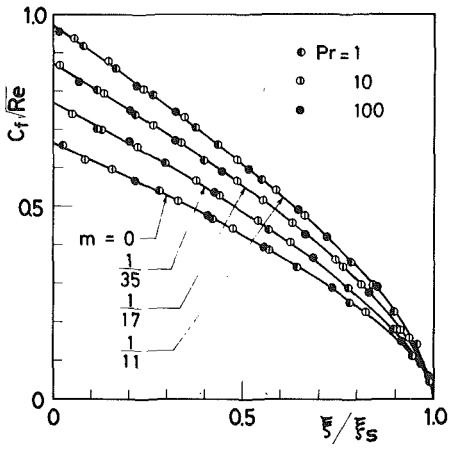

Fig. 3 Friction factor

Analysis

The problem discussed in this note is that of the opposing flow of combined free and forced convective flow along an isothermal plate where the index, m, is varied from $m = 0$ to 1/11. The x-coordinate is measured from the leading edge and the y-coordinate is measured normal to the wall surface where the positive x-axis is directed vertically downwards. The free stream is assumed to flow downwards along the surface of the plate with T_w where $T_w > T_\infty$ (T_∞ is the temperature in the free stream). Based on the assumption that the fluid properties are constant independent of the temperature and that the viscous heating is negligible, the governing equations are:

$$\frac{\partial u}{\partial x} + \frac{\partial v}{\partial y} = 0 \tag{1}$$

$$u\frac{\partial u}{\partial x} + v\frac{\partial u}{\partial y} = \nu\frac{\partial^2 u}{\partial y^2} + u_\infty\frac{du_\infty}{dx} - g\beta(T - T_\infty) \tag{2}$$

$$u\frac{\partial T}{\partial x} + v\frac{\partial T}{\partial y} = \alpha\frac{\partial^2 u}{\partial y^2} \tag{3}$$

The boundary conditions are:

$$u = v = 0,\ T = T_w \text{ at } y = 0;\ u = u_\infty,\ T = T_\infty \text{ at } y = \infty \tag{4}$$

Equations (1–4) are transformed into the nondimensional partial differential equations (5–7) by the use of the usual boundary layer theory, where the new variables employed are shown in the nomenclature.

$$\frac{\partial^3 f}{\partial \eta^3} + K^2\left\{\frac{m+1}{2}f\frac{\partial^2 f}{\partial \eta^2} - m\left(\frac{\partial f}{\partial \eta}\right)^2 + m - \xi\theta + (2m-1)\xi\left(\frac{\partial f}{\partial \eta}\frac{\partial^2 f}{\partial \xi \partial \eta} - \frac{\partial^2 f}{\partial \eta^2}\frac{\partial f}{\partial \xi}\right)\right\} = 0 \tag{5}$$

$$\frac{\partial^2 \theta}{\partial \eta^2} + \Pr \cdot K^2\left\{\frac{m+1}{2}f\frac{\partial \theta}{\partial \eta} + (2m-1)\xi\left(\frac{\partial f}{\partial \eta}\frac{\partial \theta}{\partial \xi} - \frac{\partial \theta}{\partial \eta}\frac{\partial f}{\partial \xi}\right)\right\} = 0 \tag{6}$$

$$f = \frac{\partial f}{\partial \eta} = 0,\ \theta = 1, \text{ at } \eta = 0$$

$$\frac{\partial f}{\partial \eta} = 1,\ \theta = 0, \text{ at } \eta = \infty \tag{7}$$

The numerical solutions were carried out for the cases of $m = 0 \sim 1/11$ and $\Pr = 0.7 \sim 100$, where the numerical procedure employed is based on the implicit finite difference scheme [6]. In particular, the calculation in the very near region of the separation point, ξ_s, was carefully carried out, changing the step length in ξ according to the decrease of $\partial^2 f/\partial \eta^2|_{\eta=0}$; but it is difficult to go on with the computation to the region more advanced than ξ corresponding to $\partial^2 f/\partial \eta^2|_{\eta=0} < 10^{-3}$, where the smallest step length in ξ is 10^{-6}. Therefore, ξ corresponding to $\partial^2 f/\partial \eta^2|_{\eta=0} \approx 10^{-3}$ might be considered to be the approximate separation point ξ_s. Moreover, the reason why the calculation was terminated at $m = 1/11$ is mainly the numerical difficulty.

Table 1 Coefficients of equation (8)

$m \backslash a_i$	a_0	a_1	a_2	a_3	a_4
0	0.3358	0.005828	−0.3761	0.7035	−0.4707
1/35	0.3472	0.01417	−0.3676	0.6137	−0.3836
1/17	0.3614	−0.03801	−0.09022	0.1423	−0.1470
1/11	0.3808	−0.01710	−0.2795	0.5089	−0.3575

Table 2 The values of ξ_s

$\Pr \backslash m$	0	1/35	1/17	1/11
1	0.1970	0.2482	0.3001	0.3450
5	0.2774	0.3433	0.4163	0.4887
10	0.3232	0.4072	0.4928	0.5832
100	0.6274	0.8036	0.9632	1.129

Results and Discussions

The obtained results are shown in Figs. 1–3. Fig. 1 shows the characteristic of the transfer, where the ordinate is $(Nu/\sqrt{Re})\cdot Pr^{-1/3}$ and the abscissa is ξ/ξ_s. ξ is Gr/Re^2 and ξ_s is the value of ξ at the separation point. One should note in Fig. 1 that the relationship between $(Nu/\sqrt{Re})\cdot Pr^{-1/3}$ and ξ/ξ_s approximately results in a curved line independent of the Prandtl number for each value of m. As is seen in Fig. 1, slight differences arise due to the Prandtl number, which increases with the increase of the value of m. At $m = 0$, the differences due to the Prandtl number are below $\pm 1 \sim 2$ percent, but, at $m = 1/11$, those become below ± 3 percent. However, in the regions of $m = 0 \sim 1/11$, the differences arising from the Prandtl number may be considered to be small enough; and therefore, it is possible to consider that the Nusselt number is a function of $Pr^{-1/3}$ and ξ/ξ_s. Such a characteristic, as seen in the opposing flow, is a peculiar one which characterizes the opposing flow of the combined free and forced convection. On the other hand, the characteristic shown in Fig. 1 also suggests that it is capable of deriving the correlation of the heat transfer coefficient. Then approximating the relation shown in Fig. 1 with the polynomial expression gives the correlation of the transfer coefficient:

$$\frac{Nu}{\sqrt{Re}}\cdot Pr^{-1/3} = \sum_{i=0}^{i=4} a_i(\xi/\xi_s)^i \tag{8}$$

where the coefficients a_i were tabulated in Table 1, the values for which were obtained by use of the method of least squares based on the mean values of the numerical results obtained. The degree of agreement is below maximum ± 3 percent from the standard values

(the mean values) for the regions of $0 \leq \xi/\xi_s < 0.99$. The position of the separation point, ξ_s, plays an important role in predicting the heat transfer coefficient from equation (8); then, the values of ξ_s are shown in Fig. 2 and in Table 2, where ξ_s gradually increases with the Prandtl number. This signifies that the buoyancy effect on the flow field decreases as the Prandtl number increases. Furthermore, the gradients of those lines change around $\mathrm{Pr} = 7 \sim 8$, which are divided into two approximately straight lines corresponding to the regions of $0.7 \leq \mathrm{Pr} < 7$ and $8 < \mathrm{Pr} \leq 100$. Therefore, it can be seen that there are two patterns concerning the dependency of the Prandtl number on this convective flow field. Fig. 3 indicates the characteristic of the skin friction where the figure was drawn in the same manner as Fig. 1; the ordinate is $C_f \cdot \sqrt{Re}$ and the abscissa is ξ/ξ_s. As is proved by Fig. 3, it is found that the characteristic of skin friction also depends on the ratio of ξ and ξ_s similar to the case of Fig. 1, where the differences arising from the Prandtl number are smaller than in the case of Fig. 1, so that they are hardly perceptible.

From the discussions above it is proved that ξ/ξ_s is the most convenient parameter in scaling the characteristics of heat transfer and friction factor in the opposing flow with Prandtl number. Such scaling might be established in the friction factor for the wide range of m, while, as regards the Nusselt number, it gradually collapses with the increase of m, and has a tendency to get lost; but it should be noted that the scattering due to Prandtl number may be very small in the case of m.

Acknowledgment

The authors wish to express their thanks to Professor N. Seki of Department of Mechanical Engineering of University of Hokkaido, for his guidance and numerous helpful suggestions during the course of the investigation.

References

1 Sparrow, E. M., Eichhorn, R. and Gregg, J. L., "Combined Forced and Free Convection in a Boundary Layer Flow," *The Physics of Fluids*, Vol. 2, 1959, pp. 319–328

2 Merkin, J. H., "The Effect of Buoyancy Forces on the Boundary Layer Flow over a Semi-Infinite Vertical Flat Plate in a Uniform Stream," *Journal of Fluid Mechanics*, Vol. 35, 1969, pp. 439–450

3 Oosthuizen, P. H. and Hart, R. "A Numerical Study of Laminar Convective Flow over Flat Plates," ASME JOURNAL OF HEAT TRANSFER, Vol. 95, 1973, pp. 60–63.

4 Wilks, G., "A Separated Flow in Mixed Convection," *Journal of Fluid Mechanics*, Vol. 62, 1974, pp. 359–368.

5 Kliegel, J. R., "Laminar Free and Forced Convective Heat Transfer From a Vertical Flat Plate," University of California, PhD thesis, 1959.

6 Terril, R. M., "Laminar Boundary-Layer Flow near Separation with and without Suction," *Philosophy Transaction of Royal Society*, Vol. 253, A, 1960, pp. 55–100.

ERRATA

Erratum: R. S. Basu and J. V. Sengers, "Viscosity of Nitrogen near the Critical Point," published in the February 1979 issue of the *Journal of Heat Transfer*, pp. 3–8.

Equation (10) should read:

$$\chi_T^{*-1} = |\Delta\rho^*|^{\gamma/\beta}\left[\left(\frac{\beta+\gamma}{\beta}\right)h(x) - \frac{x}{\beta}h'(x)\right]$$

ERRATA

Erratum: Md. Alamgir and J. H. Lienhard, "The Temperature Dependence of Surface Tension of Pure Fluids," published in the May 1978 issue of the *Journal of Heat Transfer*, pp. 324–329.

We are sorry to announce that our recent paper on surface tension is seriously in error. In that paper we conjectured that the surface tension, σ, varied as follows with the reduced limiting liquid superheat of a van der Waals substance, $(\Delta T_{rm})_{vdW}$, and the Pitzer accentric factor, ω.

$$\sigma = \sigma_0'[(\Delta T_{r_m})_{vdW}]^{f_3(\omega)} \tag{1}$$

where σ_0' was a lead constant and $f_3(\omega)$ was an undetermined function. On the basis of this equation we wrote:

$$\left.\frac{\partial \ln \sigma}{\partial T_{r_s}}\right|_{\omega} \Big/ \frac{d \ln (\Delta T_{r_m})_{vdW}}{dT_{r_s}} = f_3(\omega) \tag{2}$$

where T_{r_s} is the reduced saturation temperature. The l.h.s. was easily calculable using σ data and the established function $(\Delta T_{r_m})_{vdW}$. We plotted the l.h.s. against ω for known substances and obtained an extraordinarily good correlation of data, from which the function $f_3(\omega)$ was set as

$$f_3(\omega) = 1.06 - 0.68\omega \tag{3}$$

Equation (3) is shown in Fig. 7. The reduced data all appeared to lie within a few percent of this line, as was shown in Fig. 1 of the original paper.

Recently, our laboratory undertook to extend the correlation equation (1) using a slightly different temperature function in the r.h.s. In the course of this work it became clear that the original correlation was invalid, so we reworked the entire correlation. Fig. 7 shows where the reduced data actually lie.

It is clear that there is no correlation such as we originally claimed. Without this correlation there is virtually no merit in the remaining ideas in the paper. It is still possible that σ can be correlated with an equation similar to (1), but that remains to be shown.

The relatively simple calculations of $f_3(\omega)$ were made without making a proper written record. Consequently our attempts to reconstruct how the original calculations led to an almost perfect correlation, have failed. We wish to apologize to the ASME readership and editorship for publishing the original paper.

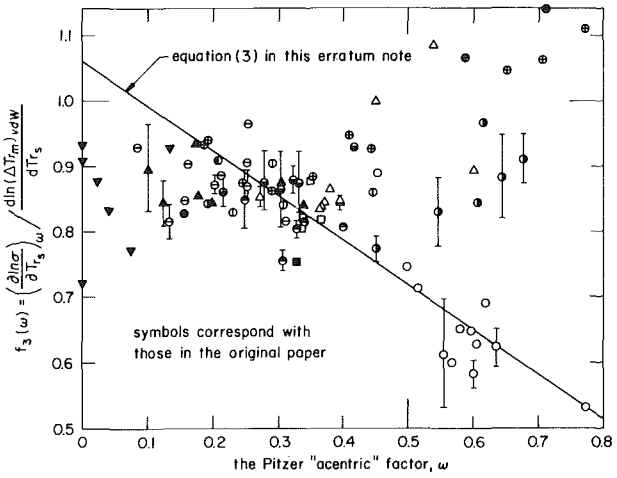

Fig. 7 Re-correlation of the surface tension data